

DTIC FILE COPY

AGARD-CP-465

AGARD-CP-465

AD-A223 680

AGARD

ADVISORY GROUP FOR AEROSPACE RESEARCH & DEVELOPMENT

7 RUE ANCELLE 92200 NEUILLY SUR SEINE FRANCE

AGARD CONFERENCE PROCEEDINGS No.465

Aerodynamics of Combat Aircraft Controls and of Ground Effects

(L'Aérodynamique des Commandes des Avions de Combat
et des Effets de Sol)

DISTRIBUTION STATEMENT A

Approved for public release
Distribution Unlimited

DTIC
ELECTE
JUL 05 1990
S DCS D

NORTH ATLANTIC TREATY ORGANIZATION



DISTRIBUTION AND AVAILABILITY
ON BACK COVER

90 07 3 182

NORTH ATLANTIC TREATY ORGANIZATION
 ADVISORY GROUP FOR AEROSPACE RESEARCH AND DEVELOPMENT
 (ORGANISATION DU TRAITE DE L'ATLANTIQUE NORD)

AGARD Conference Proceedings No.465

Aerodynamics of Combat Aircraft Controls and of Ground Effects

(L'aérodynamique des commandes des avions de combat
 et des effets de sol)



Accession To:	
NTIS - GRA&I	<input checked="" type="checkbox"/>
DTIC - TAB	<input type="checkbox"/>
Unannounced	<input type="checkbox"/>
Justification:	
By:	
Distribution:	
Availability Codes	
Dist	Availability of Special
A-1	

Papers presented and discussions held at the Symposium of the Fluid Dynamics Panel in Madrid,
 Spain, 2nd—5th October 1989.

The Mission of AGARD

According to its Charter, the mission of AGARD is to bring together the leading personalities of the NATO nations in the fields of science and technology relating to aerospace for the following purposes:

- Recommending effective ways for the member nations to use their research and development capabilities for the common benefit of the NATO community;
- Providing scientific and technical advice and assistance to the Military Committee in the field of aerospace research and development (with particular regard to its military application);
- Continuously stimulating advances in the aerospace sciences relevant to strengthening the common defence posture;
- Improving the co-operation among member nations in aerospace research and development;
- Exchange of scientific and technical information;
- Providing assistance to member nations for the purpose of increasing their scientific and technical potential;
- Rendering scientific and technical assistance, as requested, to other NATO bodies and to member nations in connection with research and development problems in the aerospace field.

The highest authority within AGARD is the National Delegates Board consisting of officially appointed senior representatives from each member nation. The mission of AGARD is carried out through the Panels which are composed of experts appointed by the National Delegates, the Consultant and Exchange Programme and the Aerospace Applications Studies Programme. The results of AGARD work are reported to the member nations and the NATO Authorities through the AGARD series of publications of which this is one.

Participation in AGARD activities is by invitation only and is normally limited to citizens of the NATO nations.

The content of this publication has been reproduced directly from material supplied by AGARD or the authors.

Published April 1990

Copyright © AGARD 1990
All Rights Reserved

ISBN 92-835-0555-7



*Printed by Specialised Printing Services Limited
40 Chigwell Lane, Loughton, Essex IG10 3TZ*

Foreword

The complex shapes of modern combat aircraft, in combination with ever-widening flight-envelopes and increasing demands for greater manoeuvrability and controllability, have intensified the need to improve the aerodynamic design of aircraft controls. However, the basic understanding of aerodynamic controls is still deficient in many areas and aircraft designers are still very dependent on results from wind tunnels and flight tests. Though computational methods are proving increasingly effective in basic vehicle design, application to controls has met with limited success because of the dominance of unsteady viscous and separated-flow effects, which lead to poorer control performance than predicted, often coupled with high buffet levels.

It was the purpose of the Symposium to review the aerodynamic design of controls at take-off and landing conditions, for manoeuvring at subsonic, transonic and supersonic speeds, for high angles of attack and yaw, and for departure prevention and post-stall manoeuvring. Also, part of the Symposium was concerned with novel control devices. With regard to ground effects, computational and experimental methods were reviewed and included jet effects, flow-field forces and intake flows.

* * *

Les formes complexes des avions de combat modernes, associées aux domaines de vol qui s'étendent sans cesse et aux demandes croissantes pour une plus grande manoeuvrabilité et une plus grande contrôlabilité, ont fait croire le besoin d'améliorer les moyens de conception et de définition de leurs gouvernes.

Cependant les connaissances de base sur le fonctionnement des gouvernes sont encore insuffisantes sur bien des points et les concepteurs d'avions doivent encore se reposer beaucoup sur les résultats d'essais en soufflerie et en vol. Bien que les méthodes de calcul se montrent de plus en plus efficaces pour les projets, leur utilisation pour les gouvernes a un succès limité à cause de l'importance des effets visqueux et de la présence de décollements qui conduisent à des performances inférieures à celles qui sont calculées et, en plus, à des niveaux de tremblement élevés.

C'était le but de ce symposium que de faire le point sur la définition aérodynamique des gouvernes:

- dans les configurations de décollage et d'atterrissage,
- pour les manoeuvres en subsonique, transsonique et supersonique,
- pour les grands angles d'attaque et de dérapage,
- pour la prévention de la mise en vrille,
- et pour les manoeuvres après décrochage.

Une partie du symposium a également été consacrée aux nouveautés en matière de contrôle aérodynamique.

En ce qui concerne l'effet de sol, les méthodes expérimentales et les méthodes de calcul ont été passées en revue. Leur aptitude à évaluer les effets de jet sur les efforts aérodynamiques et sur les écoulements d'entrée a été examinée.

D.H. Peckham and J. Leynaert
Co-Chairmen

Fluid Dynamics Panel

Chairman: Mr D.H. Peckham
Superintendent AF2 Division
Royal Aerospace Establishment
R141 Building
Farnborough Hants GU14 6TD
United Kingdom

Deputy Chairman: Dr W.J. McCroskey
Senior Staff Scientist
US Army AeroFlightdynamics
Directorate-Mail Stop N258-1
NASA Ames Research Center
Moffett Field, CA 94305-1099
United States

PROGRAMME COMMITTEE

Mr D.H. Peckham (Co-Chairman)
Superintendent AF2 Division
Royal Aerospace Establishment
R141 Building
Farnborough
Hants GU14 6TD
United Kingdom

M.J. Leynaert (Co-Chairman)
Directeur Adjoint
Direction Grands Moyens d'Essais
B.P. 72
ONERA
92322 Chatillon
France

Dr K.J. Orlik-Ruckemann
National Aeronautical Establishment
National Research Council - Montreal Rd
Ottawa, Ontario K1A 0R6
Canada

M.G. Emzivat
DCAe/STPA/EG.2
4 Avenue de la Porte d'Issy
75996 Paris Armées
France

Dipl.-Ing. P.W. Sacher
Messerschmitt-Bölkow-Blohm GmbH - FE 11
Postfach 80 11 60
D-8000 München 80
Federal Republic of Germany

Prof. C. Bergeles
Dept. of Mech. Eng. Fluids Section
National Technical University of Athens
10682 Athens, Hellas
Greece

Dr Ing. G. Bucciattini
Aeritalia-Società Aerospaziale Italiana
Gruppo Aerei Difesa
Corso March 41
10146 Torino
Italy

Mr J. Simon
CASA - Project Division
Aerodynamic Department
Avda. John Lennon s/n
GETAFFE
28065 Madrid
Spain

Prof. A.D. Young
30 Gilbert Road
Cambridge CB4 3PD
United Kingdom

Mr D.L. Powers
Aeromechanics Div., Flight Dynamics Lab.
WRDC/FIMM
Wright-Patterson AFB, OH, 45433-6553
United States

Dr J.E. Campbell M/S 294
Transonic Aerodynamics Division
NASA Langley Research Center
Hampton, VA 23665
United States

PANEL EXECUTIVE

Mail from Europe:
Dr W. Goodrich
AGARD/OTAN
7 rue Ancelle
92200 Neuilly sur Seine
France

Mail from US and Canada:
Dr W. Goodrich
AGARD/NATO
APO New York

Tel. (1) 4738-5775 -- Telex 61076 (France) -- Telefax (1) 4738-5799

Contents

	Page
FOREWORD	iii
FLUID DYNAMICS PANEL/PROGRAMME COMMITTEE	iv
	Reference
<u>SESSION I — OVERVIEW AND FUTURE REQUIREMENTS</u>	
Chairman: F.J.Simon	
AERODYNAMIC AND PROPULSIVE CONTROL DEVELOPMENT OF THE STOL AND MANEUVER TECHNOLOGY DEMONSTRATOR by D.J.Moorhouse, J.A.Laughrey and R.W.Thomas	1
COMBAT AIRCRAFT CONTROL REQUIREMENTS by T.B.Saunders and J.H.Tucker	2
CONTROL RESEARCH IN THE NASA HIGH-ALPHA TECHNOLOGY PROGRAM by W.P.Gilbert, L.T.Nguyen and J.Gera	3
COMBAT AIRCRAFT CONTROL REQUIREMENTS FOR AGILITY by J.R.Chody, J.Hodgkinson and A.M.Skow	4
<u>SESSION II — CURRENT EXPERIENCE OF CONTROL DESIGN</u>	
Chairman: A.D.Young	
AERODYNAMIC CONTROL DESIGN: EXPERIENCE AND RESULTS AT AERMACCHI by B.Bufacchi, M.Lucchesini, L.Manfrani and E.Valtorta	5
SOME RECENT EXPERIMENTAL INVESTIGATIONS INTO AERODYNAMIC ASPECTS OF CONTROLS FOR CANARD COMBAT AIRCRAFT LAYOUTS by D.A.Lovell	6*
EFFECTS OF CANARD POSITION ON THE AERODYNAMIC CHARACTERISTICS OF A CLOSE-COUPLED CANARD CONFIGURATION AT LOW SPEED by D.Hummel and H.C.Oelker	7
THE EFFECTS OF FOREPLANES ON THE STATIC AND DYNAMIC CHARACTERISTICS OF A COMBAT AIRCRAFT MODEL by C.O.O'Leary and B.Weir	8
THE INTERFERENCE OF CONTROLS AT HIGH ANGLE OF ATTACK AND AT LOW SPEED by F.J.Simon (Withdrawn)	9
<u>SESSION III — HIGH ALPHA AND INNOVATIVE CONTROL CONCEPTS</u>	
Chairman: J.F.Campbell	
INNOVATIVE CONTROL CONCEPTS AND COMPONENT INTEGRATION FOR A GENERIC SUPERCruise FIGHTER by B.A.Marks and D.E.Hahne	10
DEVELOPMENT OF NON-CONVENTIONAL CONTROL METHODS FOR HIGH ANGLE OF ATTACK FLIGHT USING VORTEX MANIPULATION by G.N.Malcolm, T.T. Ng, L.C.Lewis and D.G.Murri	11

* Printed in classified publication CP 465 (Supplement)

	Reference
CONTROL OF VORTEX AERODYNAMICS AT HIGH ANGLES OF ATTACK by L.Roberts and N.J.Wood	12
A LOOK AT TOMORROW TODAY by L.A.Walchli	13
 <u>SESSION IV - DYNAMIC AND UNSTEADY EFFECTS</u> Chairman: K.J.Orlik-Ruckemann	
UNSTEADY AERODYNAMICS OF CONTROLS by G.J.Hancock and D.G.Mabey	14
THE STEADY AND TIME-DEPENDENT AERODYNAMIC CHARACTERISTICS OF A COMBAT AIRCRAFT WITH A DELTA OR SWEEP CANARD by D.G.Mabey, B.L.Welsh and C.R.Pyne	15
THE EFFECT OF RAPID SPOILER DEPLOYMENT ON THE TRANSIENT FORCES ON AN AEROFOIL by P.W.Bearman, J.M.R.Graham and P.Kalkanis	16
 <u>SESSION V - IMPLICATION OF THRUST VECTORING, AND ENGINE GROUND EFFECT</u> Chairman: P.W.Sacher	
IN-FLIGHT THRUST VECTORING - A FURTHER DEGREE OF FREEDOM IN THE AERODYNAMIC/FLIGHTMECHANICAL DESIGN OF MODERN FIGHTER AIRCRAFT by P.Mangold and G.Wedekind	17
A PROPULSION VIEW OF GROUND EFFECTS RESEARCH by M.Holmes, J.E.Flitcroft and C.J.Penrose	18*
AERODYNAMIC INTERFERENCES OF IN-FLIGHT THRUST REVERSERS IN GROUND EFFECT by G.Wedekind and P.Mangold	19
 <u>SESSION VI - AIRCRAFT GROUND EFFECTS AND TESTING TECHNIQUES I</u> Chairman: J.Leynaert	
ETUDE DE L'EFFET DE SOL AU CEAT EXPLOITATION DES RESULTATS par G.Vidal et J.Deschamps	20
DYNAMIC GROUND EFFECTS by J.W.Paulson Jr, G.T.Kemmerly and W.P.Gilbert	21
ETUDE DE L'EFFET DE SOL SUR MAQUETTE EN VOL par J.L.Cocquerez, P.Coton et R.Verbrugge	22
 <u>SESSION VII - AIRCRAFT GROUND EFFECTS AND TESTING TECHNIQUES I</u> Chairman: G.Bucciantini	
AN IN-FLIGHT INVESTIGATION OF GROUND EFFECT ON A FORWARD SWEEP-WING AIRPLANE by R.E.Curry, B.J.Moulton and J.Kresse	23
DETERMINATION DE L'EFFET DE SOL SUR LES CARACTERISTIQUES DE L'AVION A320 par A.Condaminas et J.P.Becle	24
TECHNICAL EVALUATOR'S REMARKS/ROUND TABLE DISCUSSION	RTD

* Printed in classified publication CP 465 (Supplement)

AERODYNAMIC AND PROPULSIVE CONTROL DEVELOPMENT OF THE STOL AND MANEUVER TECHNOLOGY DEMONSTRATOR

by

David J. Moorhouse and James A. Laughrey
Wright Research & Development Center
Wright-Patterson AFB, Ohio 45433
United States

Richard W. Thomas
McDonnell Aircraft Company
St Louis, MO
United States

INTRODUCTION

The STOL and Maneuver Technology Demonstrator (S/MTD) program was structured to investigate, develop and validate through analysis, experiment and flight test, four specific technologies related to providing current and future high performance fighters with both STOL capability and enhanced combat mission performance. The four technologies are:

- o Two-dimensional thrust vectoring and reversing exhaust nozzle
- o Integrated Flight/Propulsion Control (IFPC) System
- o Advanced Pilot Vehicle Interface (PVI)
- o Rough/soft field landing gear.

In addition to the required technologies, all-moving canard surfaces were also incorporated into the baseline F-15R (see Figure 1). As stated previously, the intent of the demonstration program is to validate specific technologies, it is neither a prototype nor an explicit research program. Starting with an existing aircraft, many wind tunnel tests were performed to define the incremental effects of the specific technology items. A single data base was defined that was used by all the different functional design groups. The components of most interest to this conference are the canard and jet effects, both in and out of ground effect, and their use as control effectors.

Reference 1 was published in 1984 with the following concluding remarks: "At this point in time, a program has been initiated to develop technology to give a supersonic fighter STOL capability while also enhancing mission performance. The key elements of the program are a fully vectoring and reversing exhaust nozzle and an Integrated Flight/Propulsive Control System. The intent is to achieve a level of control integration beyond any attempted so far, and to achieve an unsurpassed precision of controllability and maneuverability in all flight phases. This will involve solving new problems and generating new criteria to mature the technologies through to flight test demonstration. We expect to report the successful results to a similar conference in 4-5 years". The intent of this paper is to present the progress of the S/MTD configuration towards meeting those goals. First, the design requirements and their rationale are discussed. Second, the aerodynamics of the canards and jet effects of vectoring and reversing are discussed followed by their implementation and impact on the control system. Ground effects with and without reversing are discussed, including a comparison of static and moving model test approaches. The results of a test to define inlet ingestion are presented. Then the control laws to counter the ground effects are discussed. Lastly, some preliminary flight test correlations are presented (the flight test program will continue into 1990).

DESIGN REQUIREMENTS

As much as possible, the program requirements were stated in operational terms rather than design parameters. As an example: "A design requirement and technology driver for this program is to takeoff with payload and land with a ground roll (including dispersion tolerances) of 1500 feet or less under adverse weather conditions (night, in wet, gusty weather)." Another premise was that the technologies would not be acceptable to the using commands if enhanced takeoff and landing performance came at the expense of degraded up-and-away capability. There was also a requirement to "emphasize mission flexibility using the technologies". This came in a rather general statement as follows:

"A fully integrated flight/propulsion control system, including in-flight thrust vectoring and in-flight reversing, may also be needed in the next generation fighter for enhancing the survivability and attack capabilities, such as the following:

- a. Increased range and/or loiter time by coordinated management of aircraft drag, angle-of-attack and sideslip, and inlet/engine/nozzle controls.
- b. Increased survivability during penetration and/or attack by maneuver enhancement, dash acceleration increase, engine up-trimming, and drag modulation.
- c. Aircraft deceleration to its maximum turn rate condition (corner speed) for rapid pitching/pointing and weapon launch.
- d. Positive control at those flight conditions where aerodynamic surfaces are ineffective (low dynamic pressure and/or high angle of attack)."

Speeds

Requirements on minimum speed were stated as "The aircraft shall demonstrate precise control of flight path at speeds as low as 1.1 V_{min} " supported also by "Lift-off and final approach speeds are not less than 1.2 V_{min} for the appropriate aircraft configuration(s)." This requirement was intended to ensure that level 1 flying qualities (i.e. precise flight path control) would exist for significant perturbations away from the nominal approach speed. Obviously, the concern was with preventing degradation in controllability if the aircraft slowed down. In addition, V_{min} was used consistent with

powered-lift STOL requirements - it could be defined either by maximum trimmed lift coefficient or by controllability in all axes. Up-and-away requirements were simply for supersonic capability, Mach 1.5 at 26,000 ft and a dynamic pressure of 1200 psf. The premise was that it would be a more significant test of the technologies to maintain or enhance the mission capabilities of a supersonic configuration.

Takeoff and Landing

The basic design requirement for the program is the usable runway dimensions - 1500 ft by 50 ft. These dimensions form implicit, and very stringent, requirements on flight path control and touchdown dispersion. Longitudinal touchdown dispersion is typically measured in hundreds of feet - a significant proportion of the available length. The specified length of 1500 ft, therefore, became a design requirement on precision of airspeed and flightpath control. Although not expressed as an explicit requirement, the Air Force took the position that such precision would only be accomplished by decoupling airspeed control from pitch control (leaving open the question of whether pitch rate, pitch attitude or flight path angle was the most appropriate commanded variable).

Lateral and directional flying qualities design requirements are dictated by the 50 ft. runway width in conjunction with specified crosswind, turbulence and windshear (numerical values given in MIL-F-8785C). The severity of this requirement applies throughout a STOL approach and flare to ground rollout. This last phase is also aggravated by the necessity for high values of reverse thrust and specified slippery surface conditions coupled with crosswinds. Early in the program, questions were raised as to whether the techniques used in Navy carrier landings would satisfy the program requirements. The difference, of course, is the ground rollout phase which is not required for carrier landings. A Navy fighter either catches an arresting wire or goes around. It was believed that the task as specified for the STOL/MTD program was a 'new problem' beyond the capability of any current fighter system.

Propulsive Control

The first requirement was for pitch vectoring, on the ground and in the air, at all operating conditions with the nozzle open (i.e. not reversing). A value of $\pm 20^\circ$ was chosen as the requirement at dynamic pressures up to 300 psf. This deflection was chosen somewhat arbitrarily as 'enough to exercise the technology' without being 'too much'. The requirement was also for at least $\pm 5^\circ$ between 300 and 900 psf. These requirements have been essentially validated during the design process, although the deflections have been limited to give a maximum normal force to avoid over-designing the structure. The vectoring function was also required to be part of the primary flight control system, which becomes a requirement on nozzle actuation rate.

The reverser flow (either by itself or in conjunction with vectoring) was to provide pitch, yaw and roll control functions. The intent was stated to be "to enhance stability and controllability of the aircraft in the STOL operating mode both in flight and on the ground". The actuation rates, however, were dictated by a requirement to go "from the nominal steady state approach position to full reverse or to maximum dry forward thrust in less than one second". The intent of this requirement was to minimize delay in obtaining reverse thrust for stopping or forward thrust for a go-around. The rollout was a control bandwidth more than adequate for all other control functions.

IPTC System Capabilities

The overriding requirement of the IPTC system was stated to be "capable of functionally integrating all aspects of flight, engine, and vehicle control including aerodynamic control surfaces, engine thrust, thrust vectoring, thrust reversing and differential efflux modulation, control and stability augmentation, high lift system, steering and braking". The intent was to convey the understanding that integration was an objective of the demonstration program, not just a means to achieve mission requirements. The IPTC system was required to provide "good inner-loop stability and positive manual control in all axes of the air vehicle throughout its intended operating envelope both in flight and on the ground (satisfying the intent of MIL-F-8785C)". This subjective requirement was intended to convey that we were seeking good flying qualities over the whole envelope guided more by the intent than the letter of the specification. This recognizes that, while the intent is to provide flying qualities clearly adequate for the mission, the letter of the specification is no guarantee. In addition, the requirement for 'positive manual control' was intended to preclude consideration of automatic landing systems, for instance. It was also recognized that MIL-F-8785C had no requirement to apply (even for guidance) to the proposed landing task. This led to an explicit requirement that "special emphasis shall be placed on precise flight path control for minimum dispersion landing (defined as a Category A Flight Phase tracking task per MIL-F-8785C)". This yields both a qualitative requirement to treat the landing as a tracking task and a quantitative effect of raising the minimum acceptable values of short period frequency. The one other flying qualities requirement that was explicitly called out in the Statement of Work was to minimize time delay, i.e. lag in aircraft response to pilot control input. Although the importance of time delay is more widely accepted now, it still should be an explicit, hard requirement in any control system to be designed for any precise task. The general system requirements were completed with departure resistance and spin recovery.

Mission Task Oriented Control Modes

Specific flight control modes were required with the rationale: "In order to provide the ability to assess task performance and minimize pilot workload in the flight vehicle, the integrated system shall also provide the flexibility to permit: intelligent selection of mission task oriented control modes as determined by analysis and simulation. Mode switching transients shall not produce unsafe aircraft responses. As a minimum the following modes are required.

A conventional mode shall be designed for satisfactory performance over the flight task envelope, including conventional landing, without the use of the added technologies. This mode will serve as a

baseline for performance evaluation and as a backup in the event of multiple failure of the new technology components.

A STOL mode shall be designed to provide precise manual control of flight path trajectory, airspeed and aircraft attitudes. The integrated control system and other technologies shall be combined to provide short field performance in weather and poor visibility. The purpose of this mode is to minimize pilot workload during precise manual landings, high reverse thrust ground operations and maximum performance takeoffs.

A cruise mode shall be designed to enhance normal up-and-away and cruise task performance, with and without external stores. The purpose of this mode is to use the integrated control system and other technologies to optimize appropriate measures of merit representing an improvement over the cruise capability of the baseline aircraft.

A combat mode shall be designed to enhance up-and-away maneuverability, with and without external stores. The purpose of this mode is to use the integrated control system and other technologies to optimize appropriate measures of merit representing an improvement over the combat maneuvering or weapon delivery performance of the baseline aircraft."

The different modes were called out in this form for technology demonstration purposes, with general guidance as to the intent of each mode. Once the benefits of the technologies have been identified, it was expected that they would be implemented differently in any production application.

Control System Design

The basic structure of the integrated control system was required to "be digital fly-by-wire, to provide flexibility, precision and fault tolerance". Originally there was to be the option for a hybrid system with the intent of requiring that functions be partitioned either digital or analog as appropriate. In practice, a modern digital system satisfies this requirement to a large degree whereas the term hybrid would have been ambiguous. The Statement of Work also allowed distributed or federated processing, leaving the choice open to the designers.

The system was required to be designed with the stability margins of MIL-F-9490B as design goals, followed by: "Such single-input/single-output parameters may be too restrictive or too lenient for different aspects of the IFEC system in achieving the desired compromise between stability and performance. The contractor shall analyze and document deviations from the MIL-F-9490B requirements". This was, therefore, a requirement to validate or correct the bdb gain margin and 45° phase margin for such a complex system.

Although not in the Statement of Work, an 'informal requirement' to use modern control theory in the system design was also imposed. The intent of this was to achieve the most benefit from the multiple control effectors, and to support the objective of integration as a supporting technology.

AERO DATA BASE DEVELOPMENT

The baseline F-15 is a conventional 1960's fighter design featuring a significant level of static stability in all axes and the usual aerodynamic control surfaces. The S/MTD aerodynamic data base was uniquely constructed using wind tunnel data and the F-15 flight derived data base. A comprehensive set of wind tunnel tests were performed to identify both the aerodynamic characteristics associated with the airframe modifications, and the jet induced effects associated with vectoring and with vane operation. Extensive testing was also performed in ground effects to provide a complete data base for ground handling analyses. The addition of canards, a vectoring nozzle and reverser vanes introduced complex aerodynamic interactions that are not present on the F-15. An extensive analysis of the wind tunnel data was performed to define these effects. Guidelines were established to dictate when an interaction was large enough to warrant inclusion in the data base. As an example, only moment effects equivalent to 1/4 deg of stabilator or 1/2 deg of aileron and rudder were included.

The static stability characteristics at low to moderate angles of attack (up to 24 degrees) were defined by adding wind tunnel measured increments due to the canard, nozzle and rotating vanes to the F-15 flight derived data base. The wind tunnel tests used for this are defined in Figure 2. Also shown are the baseline configurations tested from which the increments were measured. Above 30 degrees angle of attack the F-15 data were completely replaced with the S/MTD high angle of attack wind tunnel results. Since the high angle of attack data were only obtained at low speed, the data above 30 degrees is invariant with Mach number. Between 24 and 30 degrees, the data were faded from one data set to the other. Differences in the two data sets were generally small in this angle of attack region, minimizing the fading that was needed.

The effectiveness of the various control effectors was taken directly from wind tunnel test data. This included both the control devices common to the basic F-15 and the added control effectors. Comparisons with the F-15 data base were made where possible to check the validity of the results. Similarly, the F-15 ground effects data were completely replaced with wind tunnel test data. The baseline configuration used to define the ground effects increments was the S/MTD out of ground effects.

The dynamic derivatives were obtained from forced oscillation wind tunnel data obtained at angles of attack from 0 to 90 degrees. In some areas significant data scatter from repeat runs occurred. In these cases the data were compared with data from other sources. These included F-15 estimated, wind tunnel and flight derived data, wind tunnel data from other F-15 modification programs and S/MTD estimated dynamic derivatives using the strip theory program DYNAMIC (Reference 2). If the information from the additional data sources was inconclusive, the most critical test data were used. The dynamic derivatives at higher subsonic, transonic and supersonic Mach numbers were estimated using DYNAMIC.

All data presented are in body axes, and are for a 1G trim conditions. The trim angle of attack, stabilator, canard and, where applicable, nozzle position are included for reference.

Canard Effects

The most obvious effect of the canards is a destabilizing increment of pitching moment versus angle of attack. Figure 3 shows the comparison of S/MFD controls-fixed neutral point with the F-15B. There are shifts of approximately 15% MAC at subsonic speeds and 12% at supersonic speeds, the differences being attributed to the canard downwash effect on the wing changing from subsonic to supersonic conditions. The flaps-down neutral point is also seen to be the same as the low-speed flaps-up value.

Control effectiveness of the canards in pitch is shown in Figure 4 to be very close to the predictions and approximately half the value of the stabilators. An expected change in stabilator effectiveness was not seen in the wind tunnel results, which also verified that canard deflection did not affect any of the other control surfaces.

As can be seen from Figure 1, the canards are at a significant dihedral angle so that they also de-stabilize the yaw axis significantly. Figure 5 shows the reduction supersonically - the static directional stability is actually zero at Mach 2.0. At the same time, it can be seen that the contribution of differential canards to yaw control power is approximately the same as the rudders. Figure 6 gives the level of dynamic stability and also contains an example of the effect of different wind tunnel data sources. The two sources agree up to 3° angle of attack but differ significantly above that value. The most conservative, least stability, data was used in the design leading to an arbitrary limit of 30° for the initial flight tests to avoid the expense of clearing a high angle-of-attack flight envelope.

Vectoring Effects

Pitching moment due to vectoring is shown in Figure 7 compared with the stabilator and canard powers. The expected results are indicated: the aerodynamic controls are most effective at high subsonic and low supersonic speeds; thrust vectoring becomes comparable at high supersonic speeds; pitch vectoring exceeds aerodynamic controls at low speed. A more practical assessment of this last result is to consider that the aerodynamic control effectiveness is tending towards zero whilst thrust vectoring retains its effectiveness. This is illustrated most effectively by the low speed nose-down recovery moment shown in Figure 8 - more than five times the pitch rate is generated in one second. Obviously, the configuration has the capability with pitch vectoring of meeting the recovery criteria at an angle of attack much higher than 30°. In addition, there are moderate increases in zero lift drag at subsonic speeds and negative or very slightly positive drag increments at supersonic speeds. Longitudinal stability is not affected, but there is a slight drag polar rotation. Increments due to up vectoring are generally less than those due to down vectoring. The basic increments due to differential vectoring are small. For comparison, 120° of differential vectoring give a rolling moment coefficient equivalent to approximately 3° of differential aileron deflection. More significant, however, the differential vectoring effect is independent of angle of attack (Figure 9). There are also sideforce and yawing moments consistent with the up-vector generating a positive pressure on the inside of the vertical tail.

Reverser Effects

Samples of the longitudinal effects of reverser vane angle are shown in Figures 10 (subsonic) and 11 (supersonic). There are large nose-down pitching moments even though the effect on lift is insignificant. The largest increment is when the reverser is first deployed to an angle of 45° (there is no steady-state operation in the transition region from stowed or zero deflection to 45° deflection). Nose-down moments continue to increase up to the maximum vane angle of 135°. Static longitudinal stability is not significantly affected. The induced drag increments are quite large subsonically and relatively small supersonically, but show an apparent rotation. It can also be seen in Figure 10 that the induced drag has a maximum and is reducing again at a vane angle of 135°. None of the longitudinal increments due to reversing are affected by sideslip angle.

The lateral and directional data shows large and widely varying effects of vane angle and nozzle pressure ratio (NPR). Figures 12 (subsonic) and 13 (supersonic) present the data in the form of increments of sideforce, yawing moment and rolling moment at 5° of sideslip angle, i.e. a representation of the derivatives. At Mach 0.4, Figure 12a shows relatively minor effects of vane angle on directional stability at NPR of 2.2. For an NPR of 4, Figure 12b shows an extreme loss in directional stability for vane angle greater than 90°. At supersonic speeds, Figure 13 shows large losses in directional stability at any vane angle. Lateral stability shows an initial increase then a decrease with increasing vane angle at subsonic speeds. Again, the largest decrease is at the higher NPR in Figure 12b. Supersonically, Figure 13 shows small increases in lateral stability.

Differential reversing effects (i.e. zero on one engine and maximum on the other) are shown in Figures 14 and 15, with modest yawing moments equivalent to approximately 5° of rudder and negligible rolling moments. It is interesting to note that the influence of NPR is negligible subsonically and significant supersonically. Complete testing was done of the effect of vane angle and nozzle pressure ratio on the other control surfaces.

CONTROL SYSTEM DEVELOPMENT

Although some aspects of the S/MFD development were constrained by modifying an existing aircraft, the Integrated Flight/Propulsion Control (IFPC) system is an all-new implementation between the existing cockpit controls and the control surfaces. The existing mechanical control system with analogue Command Augmentation System has been replaced with a quadruplex digital fly-by-wire system designed to the requirements stated previously. Figure 16 shows the overall layout of the IFPC system. Electrical signals from Linear Variable Differential Transducers (LVDT's) representing stick and pedal

deflections are summed with appropriate sensor inputs in the Flight Controller. Control commands are sent either to new direct-drive-valve actuators for the aerodynamic surfaces or to the Nozzle Controller for vectoring and reversing commands. The Nozzle Controller integrates the commands with nozzle exit area requests from the Digital Electronic Engine Control (which is given priority in case of conflict) to position either the convergent and divergent flap positions or the reverser vane angle. These control capabilities have provided the ability to meet all the requirements stated previously; the final complement of control modes is listed in Figure 17. Note that the required "STOL" mode is implemented as three separate modes in the final design. The final content of the CRUISE and COMBAT modes is also presented.

Canard Implementation

Figure 18 summarizes how the canards are used in the control laws, i.e. scheduled with angle of attack and also used for control in various axes. The pitch control power of the canards affords a convenient way to restore subsonic static stability. Canard deflection is scheduled as a linear function of angle of attack. Figure 19 provides an example at Mach 0.9, showing also the difference between the CRUISE and COMBAT modes. The slope is the same, yielding the same level of static stability in both modes, but the intercepts were chosen to give minimum drag at 1g in the CRUISE mode and at higher load factors in the COMBAT mode. At supersonic speeds the canard schedule satisfies more than one design requirement. Of course, the configuration suffers excess stability as the canards are scheduled to reduce stability. In addition, hinge moments are kept within limits and sufficient differential capability is retained to provide yaw control. Figure 20 shows the data at Mach 1.6, the canard schedule is destabilizing over a range corresponding to approximately 1-5g in all control modes. The schedule at higher angles of attack is stabilizing to support an overall design philosophy of always having a stable pitching moment break. The same characteristics are also exhibited in the flaps-down configuration shown in Figure 21. Tailoring static stability in this fashion also had an indirect benefit. Multivariable control theory (i.e. Honeywell's Linear Quadratic Gaussian with Loop Transfer Recovery) was used in the design process, References 3 and 4. An unstable configuration requires special treatment in this design process, but it was very convenient and straight forward to design to the stable configuration with canards on their angle of attack schedule. Choice of the canard/angle of attack schedule was also influenced by considerations of lateral directional stability. Figure 22 shows $C_{Y\beta}$ as a function of angle of attack for different canard deflections. The data in this Figure is for a sideslip angle of 2° because stability increases above that value. As can be seen, there are significant regions of negative $C_{Y\beta}$ which are avoided with the canards on their schedule.

In the 'enhanced' control modes (i.e. other than CONVENTIONAL) the canards are also used as short-term pitch control effectors. They deflect as a function of pilot-stick input, but are then "washed out" and return to the AoA schedule leaving the stabilizer as the long term trim control. Differential canard deflection is used as a control effector in different ways. In the flaps-up modes, differential canards are used to augment the yaw control power of the rudders including dynamic stability augmentation. As an example, the additional control power plus yaw rate feedback combine to make a high speed loss of augmentation on one engine into a benign transient.

Flaps down, differential canard is used most effectively in combination with rudder deflection to command direct sideforce to meet the crosswind requirements. On final approach, direct sideforce is commanded by the rudder pedals which is a natural pilot action in a crosswind landing. The overall effect is to give the appearance of a crosswind that is approximately half the actual value. After touchdown, in the ground handling mode to be described later, direct sideforce is commanded by lateral stick into the wind - again a natural pilot action.

Vectoring Implementation

In simple terms, pitch vectoring is integrated into the enhanced modes not just added as an incremental control effector. Thus, Figure 23 represents the difference between two modes designed to meet requirements on flying qualities, gain and phase margin, etc. - it is the realistic increment in pitching capability. It shows the ability to pitch up for a 'snap shot' with maybe a half second advantage even at power for level flight, not full capability. Equally important in combat is the reduction in time required to pitch back down again in order to regain energy (already shown in Figure 7). Another benefit of vectoring comes in maximum performance takeoffs. Fighters at heavy weights are frequently limited by the pitching moment required to rotate to takeoff attitude. With pitch vectoring at maximum afterburning thrust, rotation is available at the optimum speed for takeoff.

The nozzle vector angle is also on an angle-of-attack schedule to minimize drag in both CRUISE and COMBAT modes at supersonic speeds (see Figure 24). This schedule relieves the stabilizer required for trim at the high levels of static stability. Examples of the drag polars which result from the combined canard and vector schedules are given in Figure 25. Subsonically there is a zero-lift drag penalty but the benefits at higher lift coefficients are apparent. An optimum blend of the two modes would obviously be used in a production application. Drag benefits at all lift coefficients are realized at supersonic conditions.

Reverser Implementation

In the CRUISE and COMBAT modes, vane control to provide in-flight thrust reversing is integrated into normal throttle action, Figure 26. Pulling the throttles slowly back from maximum afterburner to intermediate (full dry power) to idle produces absolutely conventional response with the engine spooling down to the flight idle speed. Movement aft of the idle detent will deploy the vane to 45° and then to 135° with continued movement. When the vane is at 135°, further aft movement of the throttles will spool the engine up to 100% RPM at the maximum reverse thrust point. For rapid movement of the throttle, the engine is not expected to spool down. The pilot can therefore snatch the throttle back to command maximum reverse thrust as desired, up to the software limits. A maximum reverser

command of 2g "eyeh.lla out" is implemented where this capability is available, and at high speeds forward deflection of the vanes is limited to avoid exceeding vertical tail bending moments.

Thrust reversing as implemented in the SLAND control mode is the key to the short landing capability, predicated on making the approach with the engine at 100% RPM and exhausting through the reverser vanes at a trim angle of approximately 60°. At touchdown the vanes are commanded forward so that thrust reversing is available with virtually no time delay. Also contributing to the landing capability is minimum touchdown dispersion achievable with this mode (see also References 4 and 5). The characteristics of the reverser vanes give high-bandwidth control of the speed axis, and the control laws were designed to decouple the speed axis from the pitch axis (Figure 27). To achieve this the control effectors were ganged into a "moment" effector and a "thrust" effector. The stabilator, canard, trailing edge flap, and differential (top and bottom) rotating vanes are used to produce pitching moment. The three aerodynamic surfaces are scheduled with the inverse of dynamic pressure to maintain a constant pitch effectiveness over the STOL envelope. A 2-sec washout is used on the canard, flap, and vanes so that the stabilator will provide the pitching moment required to trim the aircraft. The trailing edge flap and canard are used "out of phase": a nose-up moment command commands a trailing edge down flap and canard deflection. In this way, lift lost from the stabilator is compensated for, and minimum-phase flight path angle response is achieved. The thrust effector is composed of the top and bottom rotating vanes coordinated to produce zero pitching moment. Body angle is added to the thrust command to compensate for rotation of the gravity vector as the aircraft pitches. The result to the pilot is that throttle position commands airspeed which is held constant by the airspeed feedback, and stick commands pitch rate which is effectively flight path angle rate command because of the speed hold. This control strategy, including the differential canard implementation discussed previously, has been validated by piloted simulation as facilitating landings within a "touchdown box" 60 ft long by 20 ft wide under all required conditions of wind, wind shear and turbulence.

GROUND EFFECTS

Numerous wind tunnel investigations (References 6-10) have indicated large changes in the stability and control characteristics of the aircraft induced by the reverse flow. These studies found the proximity of the reverser to the tail surfaces, the reverser efflux angle, and the reverser jet to free-stream dynamic pressure ratio to be key parameters affecting the reverser induced aerodynamics. As a part of the S/MTD development program, static wind tunnel tests were conducted to determine the jet induced effects on the aircraft during the approach and landing phases. The objective of these tests was to generate a data base for use in control law development and simulation. Key results from these tests are presented, and where appropriate, a qualitative explanation of the phenomena in terms of the classical V/STOL flow effects are postulated. Most of the stability and control results are presented in terms of force and moment coefficient increments, defined as the jet-on minus the jet-off values. Reference 10 gives a more indepth analysis of the basic flow field interactions induced by thrust reversers. Another recently completed series of tests (Reference 11) used a moving-model method to investigate the influence of rate of descent while reversing on the approach aerodynamics of the S/MTD. A comparison of this investigation to the static wind tunnel test results is also presented. Finally, results from a hot gas ingestion test are presented.

Static Wind Tunnel Test Approach

Ground simulation was achieved using a fixed ground board which had a trailing edge flap for controlling the leading edge stagnation point. This allowed for flow angularity control ahead of the ground board. The test was conducted in two phases. During the first phase, testing of the 7.5% scale model (Figure 28) was conducted in free air; at three intermediate ground heights (0.20, 0.35, and 0.5 h/b), at angle of attack from zero to twenty. Testing was also conducted at landing gear height (0.17 h/b), but only at zero angle of attack. The second phase of the test was conducted solely at landing gear height, and angles of attack up to six degrees. During this phase, a shortened ground board was used in order to minimize the ground board boundary layer effects. During both phases, testing was conducted at three nozzle pressure ratio settings; 1.0 (jet off), 7.2 (reduced power), and 2.7 (nominal approach power setting). The angle of sideslip and nozzle pressure ratio were held constant, while the angle of attack and tunnel speed were varied. Due to the crosswind requirement on the S/MTD program, the sideslip angles tested varied from -30 to +30 degrees while on the ground. Parametric variations on all control surfaces (canard, tail, rudder, flap, and aileron) were tested to determine the impact of the reverser induced flow fields. The upper vanes were set at 155 degrees for all runs at landing gear heights. The only exception to this was the series of differential (left/right) upper reverser runs. A matrix of lower reverser vane settings and forward velocities was tested to determine the impact of decreasing the lower vane angle during rollout on the stability and control characteristics. This reduction in lower vane angle with velocity is intended to preclude hot gas ingestion on the full scale aircraft.

Wind Tunnel Results in Free Air

Lift and pitching moment coefficient increments at zero angle of attack in free air are presented in Figures 29 and 30 for combinations of upper and lower vane angles. When the upper and lower vane angles are equal, the lift and moment coefficient increments are both about zero. When the upper vane is deflected less than the lower vane, the induced lift is positive. Similarly, when the lower vane is deflected less than the upper vane, the induced lift is negative. The moment increments are very small compared to the lift increments, which indicates that the center of pressure of the induced forces is near the center of gravity. This rules out interpretations which assume the induced effects act on the horizontal tail. It is consistent, however, with the idea of flow entrainment ahead of the ports. The induced lift forces shown in Figure 29 are in the same direction as the direct jet lift forces. While the induced moment produced is small, the direct jet moment is large.

As seen in Figure 31, horizontal tail effectiveness is affected by reverser angle. The increase in effectiveness results for the 45 degree vanes probably results from an increase in the tail dynamic pressure due to increased local velocities resulting from flow entrainment. The reverser ports are

located 0.45 root chords aft of the horizontal tail leading edge, (0.14 chords forward of the hinge line). With the lower reverser vane at 135 degrees, there is a reduction in the horizontal tail effectiveness for negative (trailing edge up) deflections, which is not evident at the positive deflection. With this vane setting, the reverser efflux opposes the free stream flow, and significant mixing will occur. This may result in a local dynamic pressure ratio decrease. With a negative tail setting, the leading edge of the tail is in this region, and this could account for the non-linearity. A similar non-linearity was not found with the upper reversers at high settings, presumably because of the presence of the vertical tails.

The reverser induced increment in directional stability as a function of upper vane angle is presented in Figure 32. All data represent a nozzle pressure ratio of 2.7 and a lower vane angle of 110 degrees. Also included is a full reverse case (135 degree setting) taken from testing at landing gear height. For all vane angles less than 90 degrees, an increase in the directional stability is found. This may be due to an increase in the local dynamic pressure due to entrainment. Negligible changes were found in lateral stability with thrust reversers in free air.

The reverser induced rudder effectiveness increment as a function of upper vane angle is presented in Figure 33. Included with the free air data is a full reverse (135 degree upper vane) case taken from testing at landing gear height. The trends are similar to the directional stability trend, the largest increase in rudder effectiveness is found with the reverser angles near vertical. It is interesting to note that the 110 degree vane results in no change compared to the jet off value, while it did result in a moderate loss in directional stability at the same flight condition.

Wind Tunnel Results During Transition

Jet-induced lift and pitching moment coefficient increments as a function of height above the ground and lower vane angle are presented in Figures 34 and 35. Both curves show increasing effects near the ground as the lower vane angle is increased. There is a large increase in the pitching moment increment, as the height decreases, while the lift increment changes from positive to negative. As the aircraft moves into ground effect, the ground vortex and associated suckdown region begin to form, and become larger as the height above the ground decreases. The magnitude of the induced pitching moment coefficients near the ground is larger than the free air effects noted above, and in a direction to oppose attaining a three-point attitude for control during the rollout. These effects were a strong concern in the control law development.

Increments at zero and twelve degrees angle of attack are presented in Figures 36 and 37. Twelve degrees is the nominal approach angle of attack for the S/MTD. Near the ground, larger increments are found at the higher angles of attack. This is not surprising in that, as angle of attack increases, the horizontal tail and reverser ports move closer to the ground. In addition, positive angle of attack increases the effective lower reverser angle. As a result, the suckdown region becomes larger.

Wind Tunnel Results at Gear Height

The presence of a ground board boundary layer will influence the flow field induced by the lower reversers. The upstream penetration of the ground vortex and the associated suckdown region should be primarily affected. During the second phase of the tests, runs were made on a shortened ground board (Figure 38), in order to analyze the effect of the ground board boundary layer on the reverser induced flow field. The distance from the leading edge of the ground board to the nose of the model was decreased from 92" to 50". Theoretically, with a thinner ground boundary layer the forward penetration of the ground vortex should be reduced. This should result in a smaller suckdown region, with a corresponding decrease in the lift loss. The results of repeat runs made following the ground board change showed an increase in both the lift loss and the pitching moment (Figures 39 and 40). The reason for the added lift loss is not clear at this time. The nozzle pressure ratio varied slightly (2.67 vs 2.86) between the repeat runs, so the minor changes that were found may not be entirely attributable to the thinner boundary layer.

The effect of lower reverser vane angle and forward speed on the reverser induced lift and pitching moment is shown in Figures 41 and 42. A loss in lift coefficient of about 0.7 was induced at vane angles above 110 degrees, for all velocities. The smaller lift loss as the lower vane angle decreases is due to the smaller suckdown region caused by the resultant aft movement of the ground vortex. As the lower vane angle decreases (or the ground and the ground vortex move aft, so the center of pressure of the net suckdown force moves rearward, which results in an increase in pitching moment (Figure 42). A loss in lift coefficient of about 0.7 was induced at vane angles above 110 degrees, for all velocities. The smaller lift loss as the lower vane angle decreases is due to the smaller suckdown region caused by the resultant aft movement of the ground vortex. As the lower vane angle decreases (or the forward velocity increases), both the point of reverser impingement on the ground and the ground vortex move aft so the center of pressure of the net suckdown force moves rearward, which results in an increase in pitching moment. (Figure 42). The pitching moment increments begin to decrease as the ground vortex moves back to the vicinity of the wing trailing edge. As the lower reverser angle decreases, the direct jet force will give positive lift and nose down pitching moment increments (assuming a constant 135 degree upper reverser setting), both of which act to offset the induced effects.

During the second phase of testing, each reverser configuration was tested over an alpha range of zero to six degrees. The results of these runs are presented in Figures 43 and 44. An additional lift loss was found at six degrees angle of attack for all lower vane angles tested. This was accompanied by a decreasing moment increment back to about a 100 degree vane setting, where the moment increment then started to increase. Two key changes happen at angle of attack: the effective reverser efflux angle increases from the vane angle to the vane angle plus the angle of attack, and the distance between the reverser ports and the ground decreases. The net effect is a forward movement of the ground vortex, so the suckdown region becomes larger. This forward movement results in a forward shift

of the suckdown center of pressure, which gives the decreased moment increment. This is encouraging from an operational viewpoint, in that the reverser induced increments are stable.

The impact of reversing on horizontal tail effectiveness as a function of the reverser jet to free-stream dynamic pressure ratio for a 110 degree vane setting is shown in Figure 45. Two curves are presented, one based on the difference in pitching moment at zero and plus fifteen degrees elevator deflection, the other based on the difference at zero and minus fifteen degrees. A dynamic pressure ratio of 50 is representative of the touchdown condition. As the ground speed decreases, the dynamic pressure ratio increases (for a fixed nozzle pressure ratio). At high values of the dynamic pressure ratio, both curves show a decrease from the jet off value. At this condition, the ground vortex is far forward of the tail; the flow seen by the tail is the wake behind the ground vortex. For low dynamic pressure ratios, the tail effectiveness becomes highly nonlinear with tail deflection. At a dynamic pressure ratio of 50, the center of the ground vortex is estimated to be under the wing trailing edge. The complex interactions between the wing, tail, and ground vortex result in a significant loss in the tail effectiveness for the negative deflection.

One interesting result from these tests was a large variation in the induced lift and pitching moment with sideslip angle (Figures 46 and 47). As seen in Figure 47 the pitching moment increments at high angles of sideslip are much higher than those found at zero sideslip for the 135 and 110 degree lower reverser settings. These increments were accompanied by a large reduction in the induced lift loss (Figure 46), which indicates that a source of the additional moment is a positive lift force. In addition, a large negative increase in the rolling moment was found at positive sideslip, possibly indicating a greater lift on the windward side of the aircraft. These pieces of evidence point to the cause of the increased pitch-up being a shift of the ground vortex to the lee side of the aircraft. This moves the windward inboard and forward portion of the windward wing out of the suckdown region and into the free-stream. An additional contributing factor may be induced upwash on the windward canard from the leading edge of the shifted ground vortex. The shift in the stagnation line was confirmed by flow visualization (Figure 48). As the lower reverser vane angle decreases, the ground vortex and thus the induced center of pressure moves rearward, resulting in a decreased moment arm. Hence, the additional moment due to sideslip decreases with lower vane angle.

For the upper reverser setting of 135 degrees, a reduction in the directional stability was found for all flight conditions representative of ground rollout. As shown in Figure 49, the induced directional stability increment is negative and roughly constant over the dynamic pressure ratio range from 50 to 115. This loss is due to the reverser efflux penetrating forward (approximately two root chords) of the vertical tail leading edge. This results in negative pressures between the tails, due to entrainment. The resultant inboard tail loads act to reduce the directional stability. The dynamic pressure ratio of 50 corresponds to a nozzle pressure ratio of 2.7 at touchdown speed. Data taken at very low dynamic pressure ratios during high speed test of the S/MTD conducted at the Arnold Engineering Development Center (AEDC) are also presented. At these conditions, directional stability is regained, and increases slightly over the jet off value. Here, the efflux penetration does not project forward of the vertical tail, so the tails experience blockage-induced positive pressures. Outboard tail loads result which act to increase the directional stability. The induced directional stability was found to be independent of the lower vane angle. This supports the indication that, at landing gear height, the upper reverser interaction with the vertical tail is the dominant effect directionally.

The effect of jet dynamic pressure ratio on lateral stability is shown in Figure 50. A large increase in lateral stability is found as the dynamic pressure ratio increases. Increasing the lower vane angle at a constant dynamic pressure ratio also increased the induced lateral stability. These increases are due to the shift in the ground vortex induced flow field towards the leeward side of the aircraft (see Figure 48). This shift causes the center of pressure of the induced lift losses to move to the leeward side of the aircraft. It also causes portions of the windward wing and canard to move from the suckdown region into the free-stream. Both of these effects act to cause positive rolling moments at a negative sideslip angle, so the lateral stability is increased. It would be expected that the upper reverser/vertical tail interaction would also contribute to lateral stability changes. Due to the decreased tail effectiveness, this interaction should result in a decrease in the lateral stability. It is impossible to assess this contribution, because no vertical tail-off runs were conducted.

Differential upper reversing (differing upper left/right vane settings) was tested in order to investigate the induced aerodynamic effects to determine the potential for using differential upper vanes for yaw control. Incremental yawing moment coefficient data versus sideslip angle are presented in Figure 51 for a fixed left upper vane setting. For asymmetric settings, a zero beta yawing moment increment of about -0.025 is present for all cases. This is in the same direction as the induced forces, and is equivalent to about a fifteen degree rudder deflection. Even though the trends are non-linear, all of the differential settings tested induce roughly neutral directional stability. An asymmetric yawing moment is apparent in the symmetric 135/135 upper vane setting. It is believed that this asymmetry may arise from small differences in the left/right reverser nozzle pressure ratio settings.

The induced effect of differential upper reversing on rudder effectiveness is given in Figure 52. The trend is identical to that found with symmetric upper vanes (Figure 33). The magnitude of the increases with differential reversing is smaller than with symmetrical reversing. With differential reversing, the left upper reverser remains at the 135 degree setting, so only the right hand vertical tail benefits from the vane angle reduction. It should be noted that while differential upper reversing favorable impacts the stability and control characteristics, it also causes significant (possibly unacceptable) losses in reverse thrust.

Summary of Wind Tunnel Reverser Tests

As concluded in Reference 10, for low speed wind tunnel tests using a fixed ground board, the S/MTD thrust reversers were found to induce:

- a. Small lift and negligible pitching moment increments in free air.
- b. Increasing lift and pitching moment increments during transition into ground effect.
- c. Large lift losses and nose-up pitching moment increments at landing gear height. These increments varied with the lower vane angle, velocity, nozzle pressure ratio, and sideslip angle.
- d. Non-linear horizontal tail effectiveness characteristics in all flight regimes.
- e. Negligible changes in lateral stability in free air.
- f. Large increases in lateral stability at landing gear height.
- g. Changes in directional stability and rudder effectiveness, which were strongly affected by the upper vane angle. These changes were independent of the height above the ground.
- h. Large favorable yawing moment increments with differential upper reversing.

Moving Model Test Approach

The Vortex Research Facility (VRF) (Figure 53) at the NASA-Langley Research Center was used for the study discussed in Reference 11. In that facility, the model is suspended on a variable-length strut extending from the bottom of the gasoline-engine powered cart. The strut supports the model, sting, and airline assembly as well as the instrumentation. Angle of attack was changed by pitching the entire strut, sting, and model assembly at the point where the strut was attached to the cart. Velocity was controlled by a cruise-control system on the cart. High-pressure air bottles on the cart provided compressed air for the jets.

For the test, the test region of the VRF was modified to incorporate a 150-foot long ground plane near the center of the test section. The ground board consisted of two parts: a ramp which was inclined upward 4° for a distance of 100 feet, followed by a horizontal section which extended for an additional 50 feet. The height of the model over the fixed horizontal portion of the ground board was set by adjusting the length of the model support strut. As the model moved horizontally over the inclined portion, the distance from the ground board to the model reduced, thereby simulating an approach along a glide slope of 4° with rate of descent dependent on the test velocity. After moving across the ramp, the model passed over the horizontal section to simulate roll-out or constant altitude flight (see Figure 54).

Figure 55 illustrates some of the important differences between conventional static ground effects test methods and the moving model method. Static test techniques involve setting a model at a given height above the ground plane, allowing the flowfield to reach a steady state, and measuring the aerodynamic loads. The moving-model technique, on the other hand, involves measuring the aerodynamics while the model is in motion and the flowfield is in a dynamic state, similar to conditions in an actual approach. Simulations of normal approaches (without thrust reversers) have indicated only small, but discernable, differences in model aerodynamics measured statically and at various rates of descent. With thrust reversers or similar jet devices operating, however, the two techniques could yield significantly different results. There are two primary reasons for the expected differences. The first is the time dependent (unsteady) aerodynamic effects related to the motion of the model and the developing jet exhaust plume. The other difference is due to the different model attitudes (relative to the ground plane) required to set a particular angle of attack. The vertical component of velocity inherent in the moving model technique reduces the incidence angle of the model (in comparison to the static test technique) necessary to achieve a given angle of attack. This reduced incidence angle changes both the impingement angle and the impingement point of the jet on the ground plane resulting in distinctly different plumes in the two test techniques.

Comparison of Results: Moving Model to Wind Tunnel

There are two major differences between the static wind-tunnel database and the measurements made using the moving model at the VRF. The first principal difference is that the VRF data were obtained while simulating a rate of descent. The other significant difference is that the wind tunnel measurements were made in the presence of a ground boundary layer which has been shown to have a significant impact on the development of the ground vortex created by vectored jets near a ground plane. This impact is detailed in Reference 12. In short, the presence of a ground boundary layer allows the ground vortex to penetrate significantly farther upstream (approximately 30 percent) than would be possible in its absence. These two major differences are believed to be the source of the differences between the two data sets discussed below. For the data shown in Figures 56 through 61 the angle of attack was 12° , the flaps and ailerons were set at 20° , the canard at -13° and the horizontal tail at 2° .

In Figure 56 the lift increment in ground effect for the approach configuration has been plotted for Lower Vane Angles (LVA) of 45° and 60° . As height decreases to touchdown height the static wind-tunnel data consistently predicts a greater lift increment due to ground effect than that predicted by the VRF data set. This difference is attributed to the effects of rate-of-descent modeling in the VRF. Once at the minimum ground height for some time, the results from the VRF testing are seen to have the same steady state lift increment levels as those in the wind-tunnel database.

As the thrust reverser vanes were vectored farther forward, the presence of the ground boundary layer is seen to have a greater effect. This is illustrated in Figure 57. For LVA of both 80° and 110° not only is the lift increment different as h/b reduces to the minimum ground height, but also, the steady state levels measured once the models were at that minimum height are different. The reason for the differences at the minimum ground height is believed to be due to the presence of a ground boundary layer in the wind tunnel testing. The differences at the other ground heights are due to both

rate-of-descent modeling in the VRF and the presence of a ground boundary layer in the wind tunnel testing - these two effects can not be separated for this particular set of data. All test data points shown in Figures 56-61 represent interpolations of the data base discussed in Reference 10.

The differences in pitching moment are similarly illustrated in Figures 58 and 59. The thrust reverser configuration LVA = 45° and LVA = 60° are shown in Figure 58. At LVA = 45°, much like the results seen for the lift coefficient, the wind tunnel database predicts greater nose-down pitching moment than the dynamic measurements from the VRF as the model height is reduced to the minimum ground height. However, once at that height for some time, and the VRF flowfield transitions to a steady state, the level of nose-down pitching moment measured by the two techniques are nearly equal. Again this difference at heights greater than that corresponding to wheel touchdown is attributed to the modeling of a rate of descent in the VRF testing.

As the thrust reverser jet is vectored further to LVA = 60°, the comparison is similar down to a model height to wing span of approximately 0.3. Below that height the wind-tunnel database indicates that the configuration experiences progressively less nose-down pitching moment as the model approached the ground. This is, again, believed to be due to the presence of the ground boundary layer in the wind tunnel testing. This boundary layer allows the thrust reverser jets to penetrate farther upstream before forming the ground vortex. In this situation it is believed that the ground vortex has developed under the horizontal stabilizer and the low pressure vortex has reduced the lift on that surface. The greater penetration of the ground vortex also induced greater upwash at the wing. The net effect is as seen in Figures 56 and 58: increased steady state pitching moment increment and no difference in lift increment between the VRF data and the wind-tunnel database.

The effect of the ground boundary layer is even more pronounced as the thrust reverser jets are vectored further forward. This is presented in Figure 59. In these configurations, more upwash might be induced at the canard in the wind tunnel database than was indicated in the VRF results because the ground vortex could not penetrate as far upstream in the absence of a ground boundary layer.

Similar results were found in the drag measurements as shown in Figures 60 and 61. Again, at LVA = 45°, where the jets are blown well aft, the presence of the ground boundary layer in the wind tunnel test had little effect on the steady state aerodynamics, but, as the thrust reverser was directed progressively farther forward, the boundary-layer effect was intensified as was seen in both lift and pitching moment. For all settings, a significant effect is evident due to rate-of-descent modeling in the VRF at all model heights greater than the minimum height.

It is concluded in Reference 11 that, relative to the conventional static wind tunnel ground-effects tests, the rate-of-descent modeling produced substantially less lift increase in ground effect, more nose-down pitching moment, and less increase in drag. These differences became more prominent at the larger reverser vane angles. The results of the moving model technique indicate no safety-of-flight problems with the lower reverser vectored up to 80° on approach. They also indicate that the S/MTD configuration could employ a nozzle concept using lower reverser vane vector angles up to 110° on approach if a procedure were adopted in which rate of descent was not arrested near the ground and if inlet reingestion were found not to pose a problem. These moving model tests, however, were performed too late for consideration in the S/MTD development.

INLET INGESTION OF REVERSER FLOW

Another major constraint on the use of reversed thrust during ground roll out can be hot gas ingestion in the inlet. Key results from a hot gas ingestion tests using the 7.57 scale model of the S/MTD are presented and evaluated in Reference 13. The data acquired during these tests were used along with the data from the static wind tunnel tests to derive an appropriate schedule for the lower reverser vanes during ground deceleration. The primary findings were:

- The temperature rise at the engine face following the onset of ingestion is rapid and large. Peak temperatures are about 20% of the difference in the jet exit and free stream temperatures.
- Reductions in the reverser vane angle reduce the ingestion velocity. Sideslip angle further reduces the ingestion velocity, due to the introduction of an effective cant angle.
- Variations in free-stream velocity, nozzle pressure ratio, and jet temperature can be collapsed using the reverser jet to free-stream mass flux ratio. Ingestion schedules for arbitrary engine face temperature rises can be constructed from curves of mass-flux ratio vs temperature rise.
- Ground pressure data indicate that the stagnation line position is a very conservative indicator of ingestion onset. Temperature measurements under the inlet lip are a better indicator of incipient ingestion.

Based on these test results, a schedule of lower vane angle with airspeed has been defined to preclude ingestion for the initial flight tests.

GROUND HANDLING CONTROL LAWS

During the configuration development it was found necessary to design a special ground handling mode (STOL-GH) in order to control the wind-tunnel ground effects discussed above, and also to ensure adequate control of the ground track in meeting the landing requirements with minimum pilot workload. A pictorial summary of the reconfiguration from approach to rollout is presented in Figure 62. Figure 62a gives the nominal approach configuration and also the limits on vane deflection in this mode. Maximum angle before touchdown is 75° so that the pilot cannot command deceleration to a speed less than V_{min} . At touchdown some changes are switched by a combination of weight on wheels (WOW) and/or wheel spin-up, others require the selection of reverse thrust. First, positive WOW introduces a nose-down pitch rate bias of 6 deg/sec to provide a rapid and repeatable rotation from touchdown

attitude to the three-point attitude, reducing any bounce or float tendencies. The canard schedule intercept also is changed from +1.55 deg to -11.56 deg. This aids the nose-down pitching moment, smooths canard travel as angle of attack changes during the rotation and provides ample differential canard control power during crosswind landings. Other control law changes take place when the throttles are in the reverse thrust range (3 deg to 17 deg in Figure 26). First, the flaperons are snatched from 20 deg to 1 deg and the ailerons from 20 deg to zero. This reduces wing lift to enhance braking effectiveness, but also gives more differential aileron capability for crosswind landings. The top reverser vanes go full forward with both WOV and throttle angle less than 14 deg. This provides deceleration with minimum time delay to maximize ground roll performance. Since the lower vanes can induce strong nose-up moments, their forward deflection is limited as a function of pitch attitude. This ensures controllability at the expense of some loss of deceleration. During rollout the bottom vanes are scheduled with speed to preclude hot air ingestion into the inlets, and the pilot can select either manual or auto braking.

To provide good ground handling flying qualities, all integrators, the speed hold, the lateral-directional interconnect and lateral acceleration feedback are all switched off. Yaw rate is feedback to nosewheel steering to enhance ground directional stability. Lastly, command of direct sideforce is switched from rudder pedals to lateral stick. To enhance control of ground track in crosswinds, lateral stick into the wind commands both roll control and rudders plus differential canards, leaving the rudder pedals for directional control.

FLIGHT TEST RESULTS

At this time only limited and preliminary results can be reported. A Phase I flight test was accomplished between 7 Sep 88 and Feb 89 using production engines and nozzles. This phase allowed an evaluation of the basic aerodynamics, the TFPC CONVENTIONAL mode characteristics, landing gear, displays and subsystems. The 2-D thrust vectoring and reversing nozzles have been installed and a second phase of flight testing commenced 10 May 1989, to run through February 1990, for evaluation of vectoring and reversing in the enhanced control modes. Initial pilot comments indicate that the enhanced modes are exactly like the simulation, however, processed data is available only from the first phase. The data presented below is from the Phase I program.

Longitudinal Characteristics

The trim characteristics of the S/MTD aircraft are strongly influenced by the canards, which provide an additional control effector, as well as decreasing the static longitudinal stability. In the CONVENTIONAL mode the canard position is determined by its angle of attack schedule. The stabilator is then used to trim out any residual pitching moment. A longitudinal integrator is used to provide IG at zero stick position below 18 degrees angle of attack with flaps up. This provides neutral speed stability throughout the envelope. With the flaps down, angle of attack feedback is used to provide a sense of speed stability to the pilot. The trim characteristics at IG in the CONVENTIONAL mode with the flaps up are indicated in Figure 63. The trim angle of attack, stabilator and canard deflection angle are presented as a function of Mach number. These data were obtained in IG accel and decels. Below Mach 1.0, the trim stabilator is close to predicted. Supersonically, a more leading edge up trim stabilator is needed, indicating an unanticipated nose up C_m shift. The canard setting is close to expected, although a small offset is indicated in some cases. This is caused by offsets in the flight control angle of attack.

Wind-up turns at Mach 0.9 and 1.6 at 40,000 feet are shown in Figure 64. Good agreement with predictions is evident, although at supersonic Mach numbers the difference in trim stabilator observed in IG accel is again evident. Note that the canard variation with angle of attack reverses sign from the subsonic slope to decrease the static stability, as discussed previously. From the wind-up turns that were performed, a normal force coefficient was extracted and compared with data from the F-15 similarly extracted from flight test data. Subsonically, the S/MTD demonstrated an increase in C_n at all angles of attack, with the increment increasing at higher AOA. At Mach 1.6, 40,000 feet, an increase in C_n is indicated, but is smaller in magnitude.

The static stability in flight differed somewhat from that predicted. Data extracted from flight test results were used to identify the actual neutral point which is shown compared to predictions in Figure 65. In general, good agreement is indicated, however the transonic shift in neutral point begins at a lower Mach number than predicted.

The longitudinal control laws use stick deflection, along with feedbacks of normal acceleration, pitch rate and angle of attack to achieve the desired response. The stick input and each feedback have both proportional and integral paths to the stabilator. The integral path produces the desired steady state response to stick input. A linear stick gradient of 6.0 lbs per inch is used. This, combined with the control law gains provide a constant stick force per G of 3.5 lbs per G above 300 KCAS. This increases on a 1/KCAS schedule to 9.8 lbs/G at and below 107 KCAS. Above 18 degrees angle of attack, AOA feedback increases this gradient further, providing the pilot with a force cue. At all conditions the gradient is close to that designed.

The flight test program included clearing the angle of attack envelope to 20 degrees subsonically. This angle of attack region was explored in both IG flight and at elevated load factors, and included both flaps up and flaps down test points. A summary of the points, along with the pilot comments pertaining to the aircraft characteristics, is presented in Figure 66. Although a 20 degree AOA limitation was in effect for this phase of the S/MTD flight test program, an angle of attack of 30 degrees AOA was attained at one test condition. This resulted when the pilot inadvertently commanded a higher angle of attack than intended. As is evident from the pilots comments, the characteristics of the aircraft at elevated angles of attack were considered satisfactory. The aircraft was very stable, with positive control about all three axes. There was no evidence of wing rock in any condition tested. Although buffet onset occurred at about the same angle of attack as with the F-15, the buffet intensity reportedly remained light to medium as the angle of attack increased. At 20 degrees AOA, it

was much less than the F-15, which can only be attributed to the canard influence on the wing flow field. Full stick roll maneuvers were performed at angles of attack up to 20 degrees at selected flight conditions. The maneuvers were well coordinated, with good bank angle capture characteristics.

The 30 degree test point provided insight into the nose down control power available at high AOA. Because of the canard, the nose down pitching moment available decreases with increasing angle of attack, reaching a minimum at 30 to 32 degrees. In the case flown, the pilot abruptly neutralized the stick at about 31 degrees AOA. A time history of the maneuver is shown in Figure 67. Included are the stick command, stabilator response, angle of attack and pitch rate. The pitch rate response was immediate, even though only half of the nose down moment was used (since forward stick was not applied). The pilot considered the nose down response to be satisfactory. The flight test data were analyzed to identify the aerodynamic pitching moment during the pushover. The moment, shown in coefficient form in Figure 67, is a total aerodynamic moment, and includes effects of angle of attack, stabilator deflection, pitch rate, etc. Using the aircraft state variables and surface deflections during the maneuver, the total aerodynamic pitching moment predicted by the data base was also determined, and is compared to the flight test data. As indicated, the negative peak in pitching moment is very close to that predicted. However, the increment in C_m due to the pilot neutralizing the stick is about 80% of that anticipated.

Lateral Characteristics

Full stick roll performance was evaluated throughout the flight envelope. Rolls were performed using abrupt full lateral stick inputs, maintaining the longitudinal stick at the initial trim position throughout the roll. The rolls included 360 degree 1G rolls, -1G 180 degree rolls, and 3G and 5G (up to 20 degrees AOA) bank to bank rolls (RPO's).

The time to bank characteristics in 1G 360 degree rolls was measured from the initial stick motion. Typically, full lateral stick was applied in about 0.1 seconds. Requirements from the F-15 detailed spec, served as the design guideline. Subsonically, the requirements are met up to about 370 KCAS. At higher airspeeds the time to bank exceeds the Level 1 limit and at supersonic Mach numbers, the roll response essentially meets the requirements.

Directional Characteristics

Steady heading sideslips were performed throughout the flight envelope to assess the directional stability and control power. Maneuvers were performed to full pedal deflection in both directions. The results obtained are summarized in Figure 68. The maximum sideslip angle, lateral acceleration, rudder and differential canard deflection at max pedal are presented as a function of calibrated airspeed. Also shown are the predicted values. In general good agreement is indicated. The maximum lateral acceleration is a little less than predicted, but the sideslip agrees closely. Some asymmetry in the surface deflections is evident, which may be indicative of an aircraft asymmetry. However, the directional response was linear with pedal deflection up through full pedal input. Data extracted from directional doublets using the parameter identification program indicated that both the static directional stability and the rudder effectiveness were higher than predicted in some areas. However, it was difficult to separate the control effectiveness from the directional stability. In cases where one parameter was higher than predicted, the other was also. Because of this, and the large uncertainties in the extracted data, it was difficult to identify actual differences from the predicted values.

CONCLUSIONS

The STOL and Maneuver Technology Demonstration Program has incorporated thrust vectoring and reversing exhaust nozzles and all-moving canards into an F-15 to meet a stringent set of design requirements. A digital fly-by-wire Integrated Flight Propulsion Control system has integrated these new control capabilities with the existing aerodynamic control surfaces. Pilot use of stick, rudder pedals and throttle is completely conventional for both STOL performance and enhanced up-and-away maneuvering. This paper has presented the aerodynamic characteristics of the vectoring, reversing and canards and discussed their implementation in the control system. Next is a discussion of the very strong jet effects/ground effects interactions, controlled by a special ground handling control mode. Last, some initial flight test data is presented.

REFERENCES

1. Moorhouse, D.J., and D.R. Selegan, "The STOL and Maneuver Technology Program Integrated Control System Development," AGARD Conference on Active Control Systems, AGARD CP 384, October 1984.
2. Thomas, R.W., "Analysis of Aircraft Stability and Control Design Methods," AFWAL-TR-84-3038, May 1984.
3. Mooney, R., and D. Lowry, "Application of Multivariable Control to the STOL and Maneuver Technology Demonstrator," AIAA Paper 87-2403, August 1987.
4. Moorhouse, D.J., and R.L. Kisslinger, "Lessons Learned in the Development of a Multivariable Control System," NAECON 89, Dayton, Ohio, May 1989.
5. Moorhouse, D.J., D.B. Leggett and K.A. Feaser, "Flying Qualities Criteria for Precise Landing of a STOL Fighter," AIAA Paper 89-3390, August 1989.
6. Tolhurst, W.H., and Kelly, M.W., "Full Scale Wind-Tunnel Investigation of the Effects of a Target-Type Thrust Reverser on the Low-Speed Aerodynamic Characteristics of a Single-Engine Jet Airplane," NASA TN D-72, September 1959.

7. Kelly, M.W., Greif, R.K., and Tolhurst, W.H., "Full-Scale Wind-Tunnel Tests of a Swept-Wing Airplane With a Cascade-Type Thrust Reverser," NASA TN D-311, April 1960.
8. Joshi, P.B., and Compton, M., "Approach and Landing Thrust Reverser Testing in Ground Effect," AIAA Paper 85-3075, October 1985.
9. Giezer, A., Hughes, R.V., and Hunt, B.L., "Thrust Reverser Effects on Fighter Aircraft Aerodynamics," *Journal of Aircraft*, Vol. 22, June 1985, pp. 455-467.
10. Blake, W.B., "F-15 S/MTD Low Speed Jet Effects Wind Tunnel Test Results," NASA CP 10008, 1987 Ground Vortex Workshop, April 1987.
11. Kemmerly, G.T., "A Comparison of the Ground Effects Measured With and Without Rate-of-Descent Modeling on the F-15 S/MTD Configuration," AIAA Paper 89-3280, August 1989.
12. Steward, V., and Kemmerly, G.T., "Characteristics of the Ground Vortex Formed by a Jet Moving Over a Fixed Ground Plane," AIAA Paper 89-0650, January 1989.
13. Blake, W.B. and Laughrey, J.A., "F-15 SMTD Hot Gas Ingestion Wind Tunnel Test Results," AIAA Paper 87-1922, July 1987.

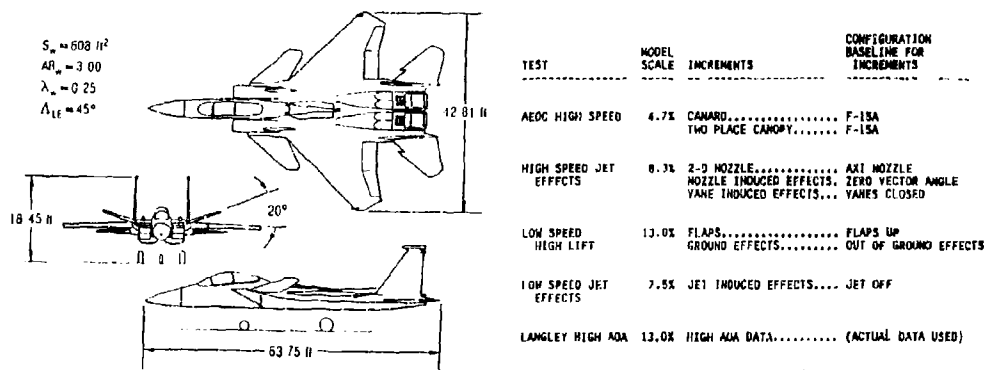


Figure 1. F-15 S/MTD Three View

TEST	MODEL SCALE	INCREMENTS	CONFIGURATION BASELINE FOR INCREMENTS
AEDC HIGH SPEED	4.7X	CANARD.....	F-15A
		TWO PLACE CANOPY.....	F-15A
HIGH SPEED JET EFFECTS	8.3X	2-D NOZZLE.....	AXI NOZZLE
		NOZZLE INDUCED EFFECTS.....	ZERO VECTOR ANGLE
		YANE INDUCED EFFECTS.....	YANES CLOSED
LOW SPEED HIGH LIFT	13.0X	FLAPS.....	FLAPS UP
		GROUND EFFECTS.....	OUT OF GROUND EFFECTS
LOW SPEED JET EFFECTS	7.5X	JET INDUCED EFFECTS.....	JET OFF
LANGLEY HIGH AOA	13.0X	HIGH AOA DATA.....	(ACTUAL DATA USED)

Figure 2. Wind Tunnel Tests

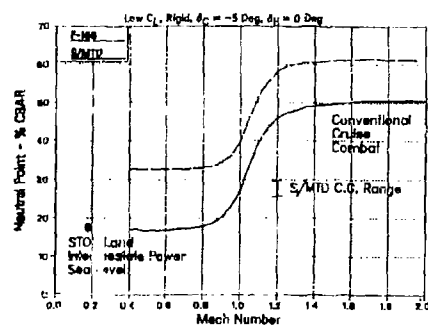


Figure 3. Canard Effect on Static Stability

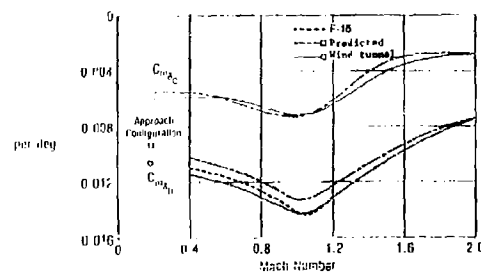


Figure 4. Stabilator and Canard Effectiveness

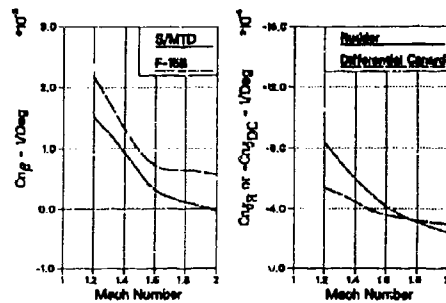


Figure 5. Canard Impact on Directional Stability and Control

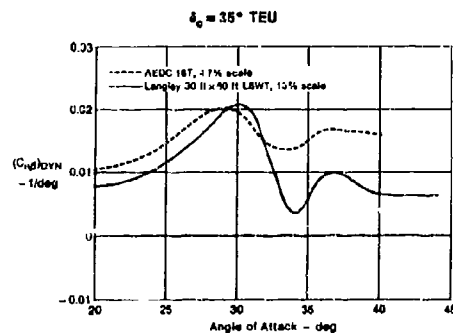


Figure 6. Dynamic Directional Stability

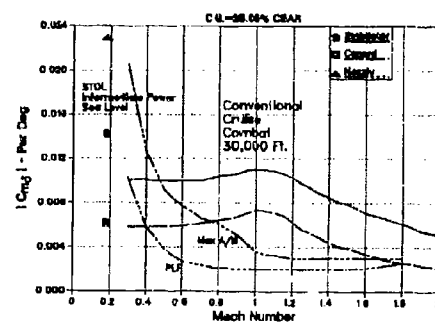


Figure 7. Vectoring Pitch Control Power

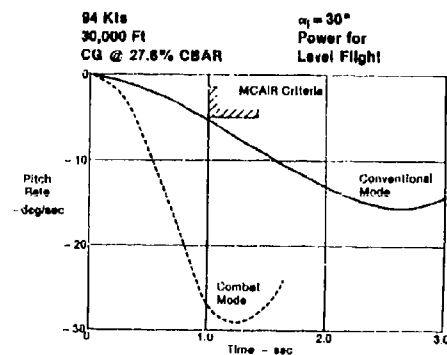


Figure 8. Nose Down Pitch Response

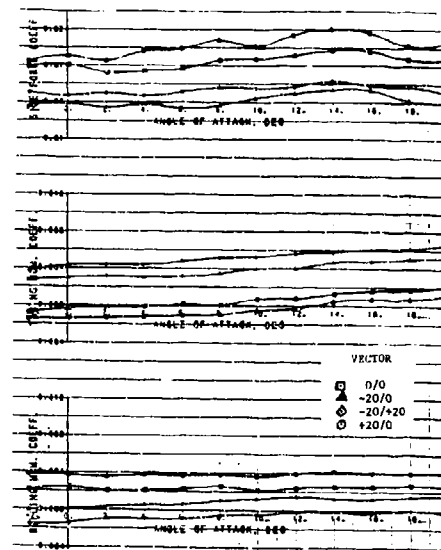


Figure 9. Differential Vectoring Effects

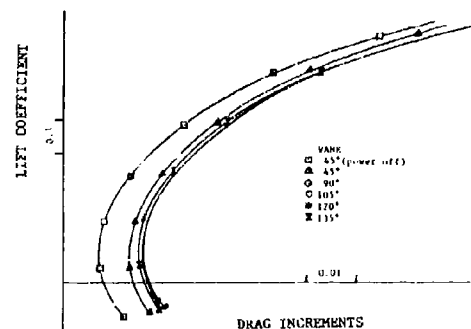


Figure 10. Subsonic Longitudinal Reverser Effects

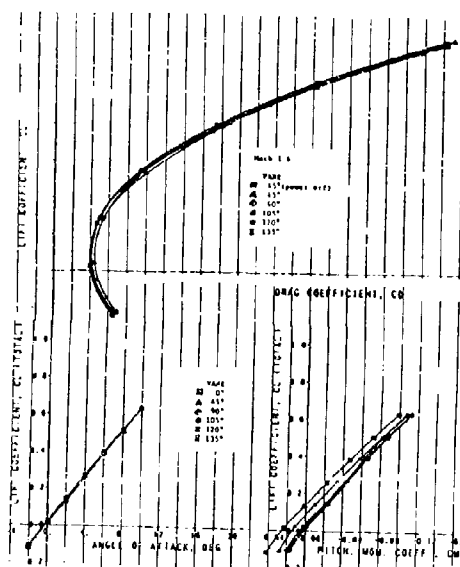


Figure 11. Supersonic Longitudinal Reverser Effects

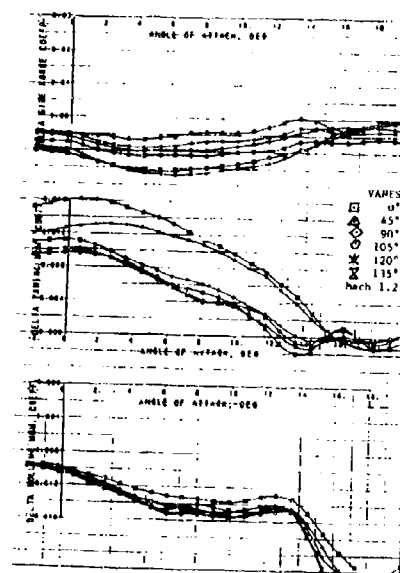


Figure 13. Supersonic Reverser Effects on Stability

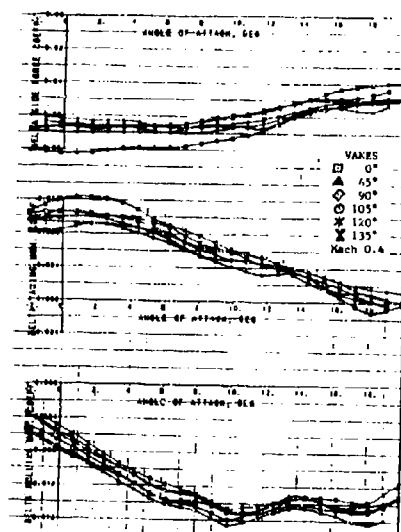


Figure 12a. Reverser Effects on Stability, NPR = 2.2

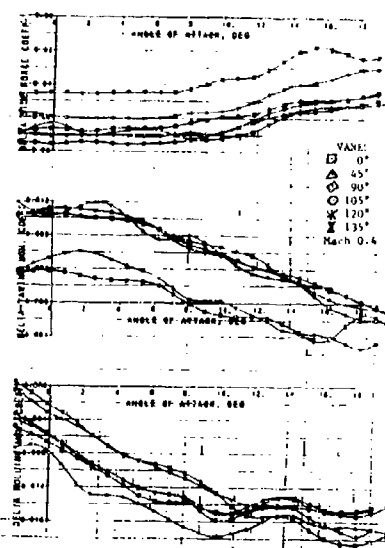


Figure 12b. Reverser Effects on Stability, NPR = 4

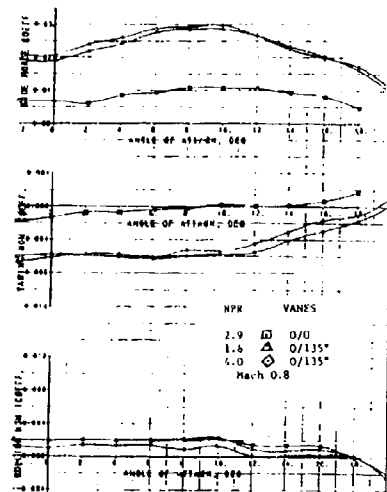


Figure 14. Differential Reverser Effects, Subsonic

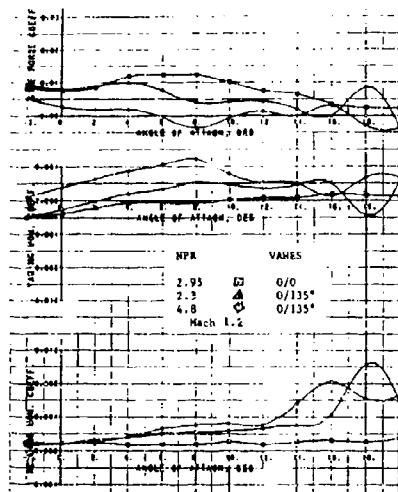


Figure 15. Differential Reverser Effects, Supersonic

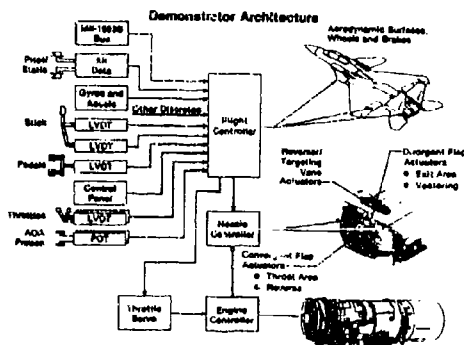


Figure 16. Control System Architecture

Mode	Capability
1 CONVENTIONAL	- Flaps Up - Flaps Down All effectors except vectoring/reversing
2 CRUISE	- Flaps Up Optimum flight path control Minimum drag at 1g
3 COMBAT	- Flaps Up Optimum attitude control Minimum drag at load factor
4 STOL-LAND	- Flaps Down - TGA - GA Maximum performance approach Maximum performance takeoff and normal approach Minimum stopping distance and ground handling
5 SPIN RECOVERY	- Flaps Up Full surface deflections with no feedback

Figure 17. Modes of Control

- Angle of Attack Schedule (All Modes)
 - Augment longitudinal static stability
 - Optimize drag
 - Provide high AoA lateral stability
- Control Augmentation
 - Longitudinal control (Enhanced modes)
 - Directional control (All modes)
- Direct Sideforce (Flaps down)
 - Approach in crosswind
 - Ground handling

Figure 18. Canard Usage in Control Laws

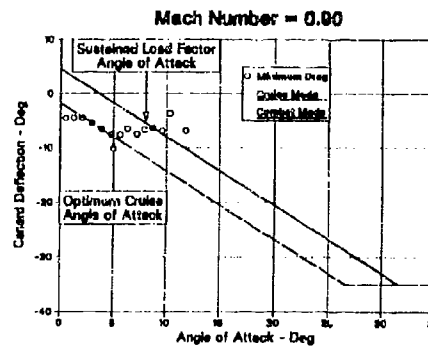


Figure 19. Subsonic Canard Schedule

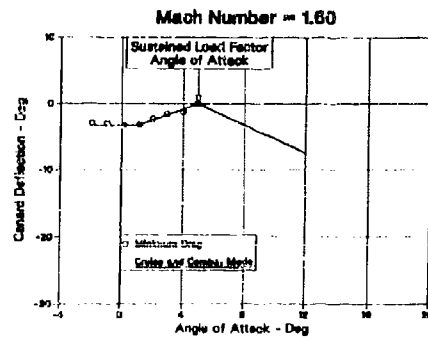


Figure 20. Supersonic Canard Schedule

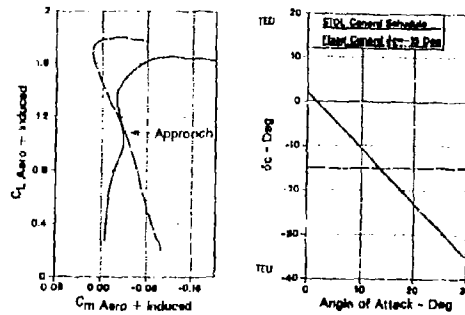


Figure 21. Flaps Down Canard Schedule

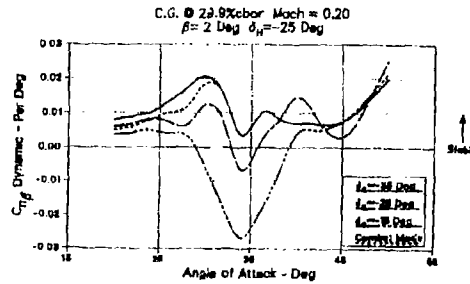


Figure 22. Departure Resistance

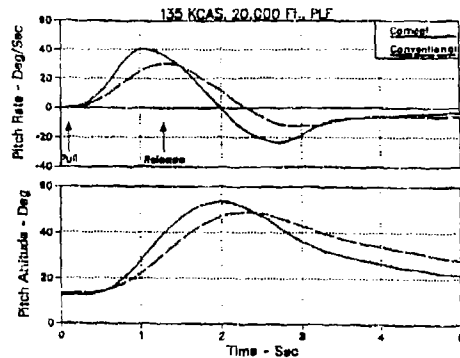


Figure 23a. Peak Pitch Rate Capabilities

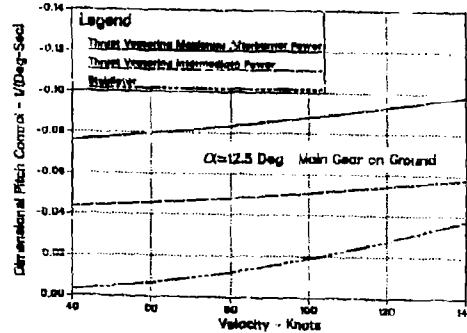


Figure 23b. Takeoff Pitch Control

Figure 21. Pitch Control from Vectoring

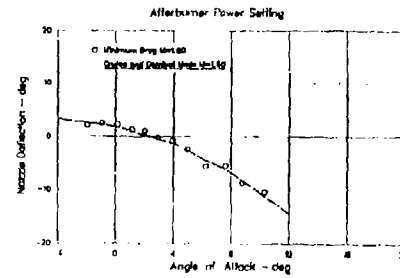
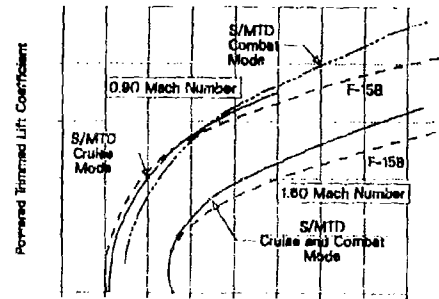


Figure 24. Thrust Vector Schedule



Powered Trimmed Drag Coefficient

Figure 25. Maneuvering Drag Effects

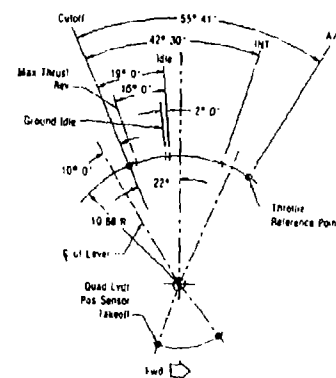


Figure 26. Thrust Geometry

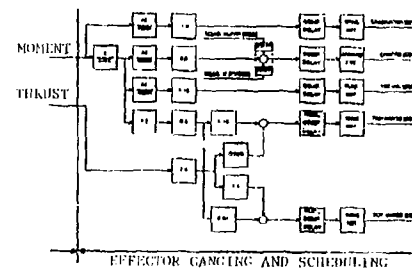


Figure 27. Control Arrangement in STAND Mode

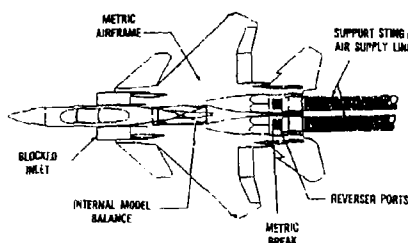


Figure 28. Jet Effects Model Schematic (Ref. 10)

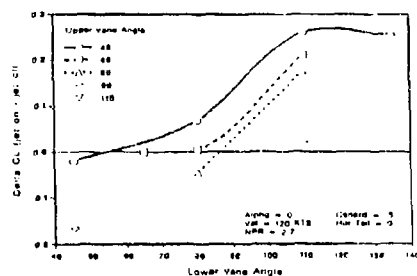


Figure 29. Lift Coefficient Increment, Free Air (Ref. 10)

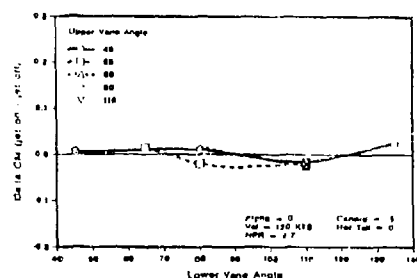


Figure 30. Pitching Moment Increment, Free Air (Ref. 10)

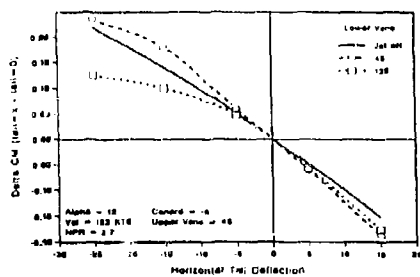


Figure 31. Horizontal Tail Effectiveness, Free Air (Ref. 10)

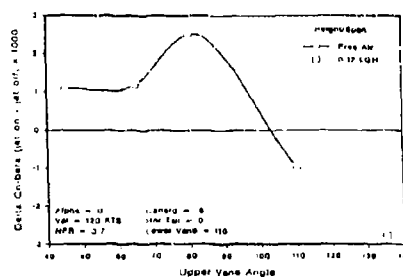


Figure 32. Directional Stability Increments, Free Air (Ref. 10)

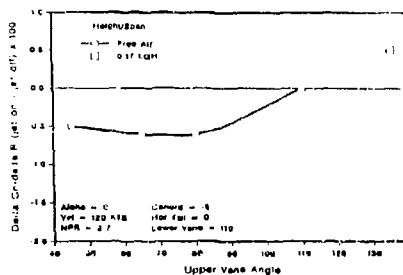


Figure 33. Rudder Effectiveness Increments, Free Air (Ref. 10)

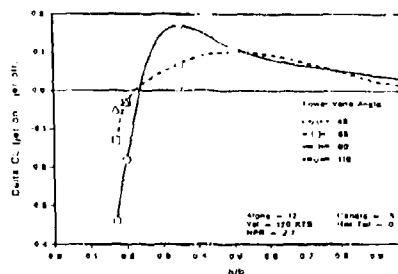


Figure 34. Lift Coefficient Increment in Transition (Ref. 10)

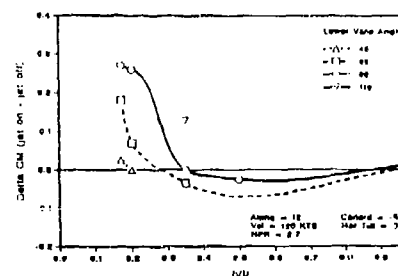


Figure 35. Pitching Moment Increment in Transition (Ref. 10)

Figure 36. Lift Coefficient vs Angle of Attack, Transition (Ref. 10)

Figure 37. Pitching Moment vs Angle of Attack, Transition (Ref. 10)

Figure 18. Comparison of Ground Board Installations
(Ref. 10)

Figure 30. Effect of Ground Board Length on Lift Coefficient (Ref. 10)

Figure 40. Effect of Ground Board Length on Pitching Moment (Ref. 10)

Figure 42. Pitching Moment Increment vs. Gear Height (Ref. 10)

Figure 43. Lift Coefficient vs Angle of Attack, Gear Height (Ref. 10)

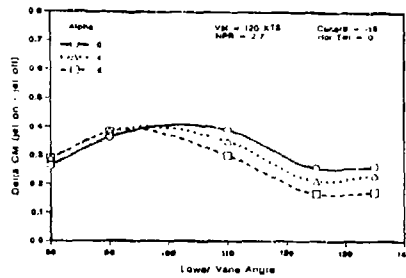


Figure 44. Pitching Moment vs Angle of Attack, Gear Height (Ref. 10)

LOWER VANE ANGLE = 110 VELOCITY = 80 KTS NPR = 2.7

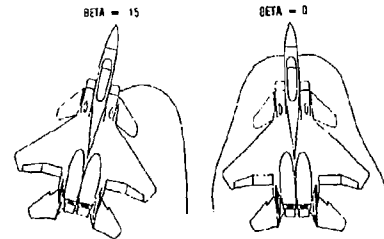


Figure 48. Sideslip Effect on Ground Stagnation Line (Ref. 10)

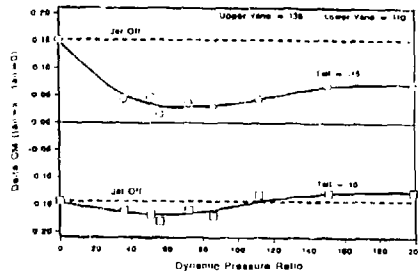


Figure 45. Horizontal Tail Effectiveness, Gear Height (Ref. 10)

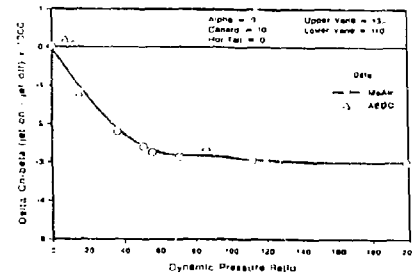


Figure 49. Directional Stability Increments, Gear Height

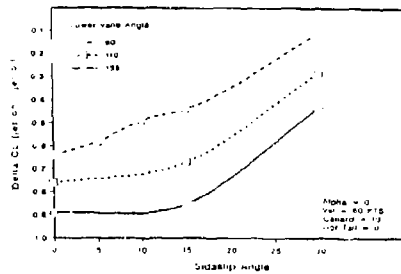


Figure 46. Lift Coefficient vs Sideslip, Gear Height

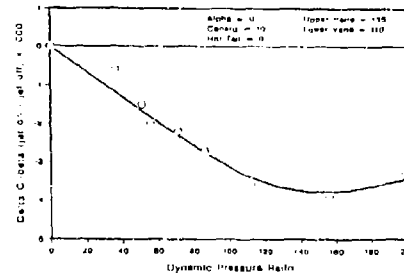


Figure 50. Lateral Stability Increments, Gear Height

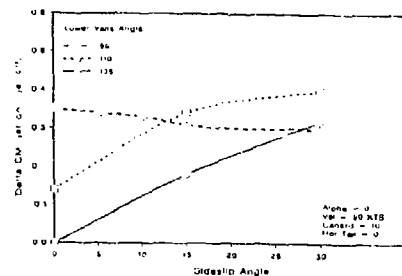


Figure 47. Pitching Moment vs Sideslip, Gear Height

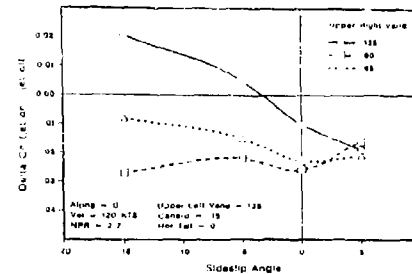


Figure 51. Yawing Moment Increments, Gear Height

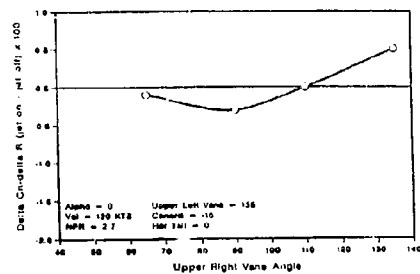


Figure 52. Rudder Effectiveness, Gear Height (Ref. 10)

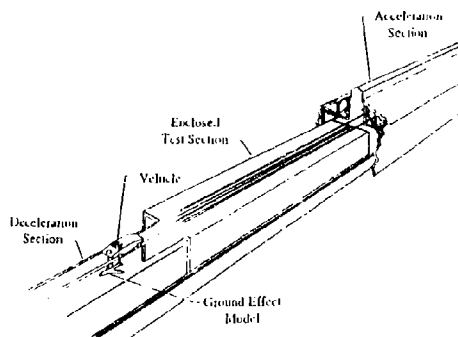


Figure 53. VRF Schematic (Ref. 11)

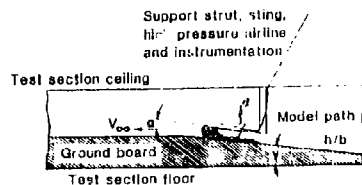


Figure 54. VRF Test Section (Ref. 11)

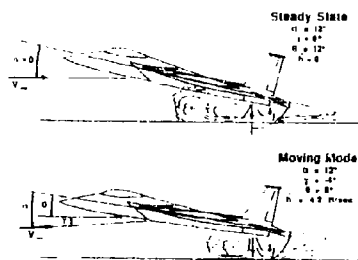


Figure 55. Dynamic vs Steady State Ground Effects (Ref. 11)

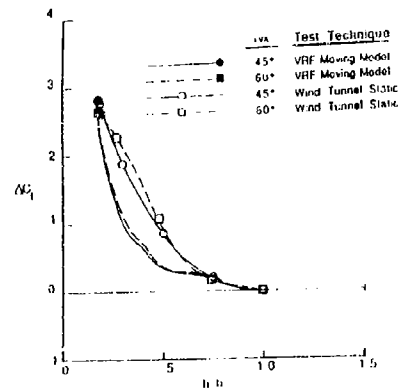


Figure 56. Comparison of Dynamic and Steady State Lift Coefficients (Ref. 11)

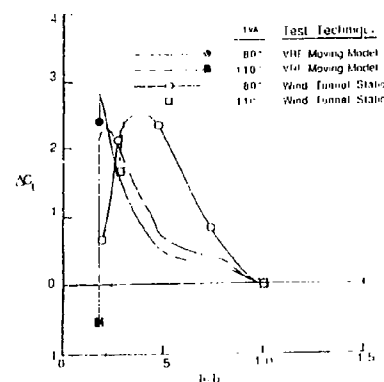


Figure 57. Comparison of Dynamic and Steady State Lift Coefficients (Ref. 11)

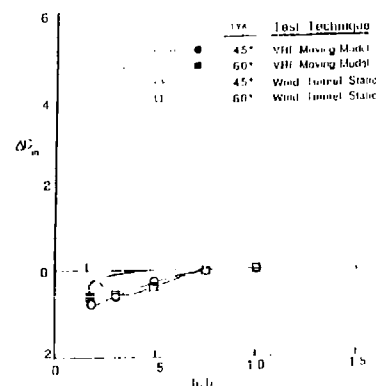


Figure 58. Comparison of Dynamic and Steady State Pitching Moments (Ref. 11)

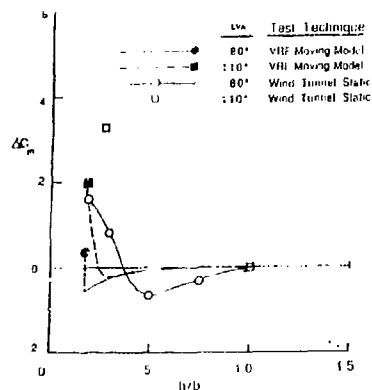


Figure 59. Comparison of Dynamic and Steady State Pitching Moments (Ref. 11)

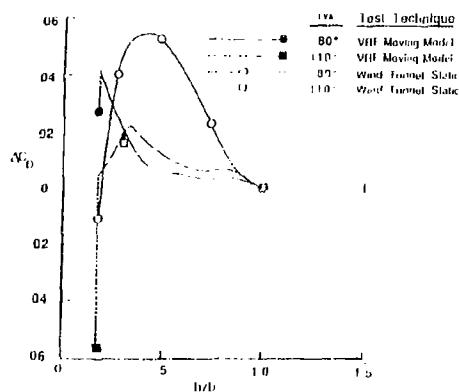


Figure 61. Comparison of Dynamic and Steady State Drag Increments

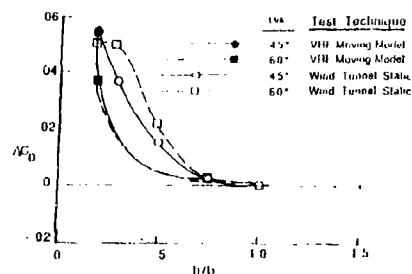


Figure 60. Comparison of Dynamic and Steady State Drag

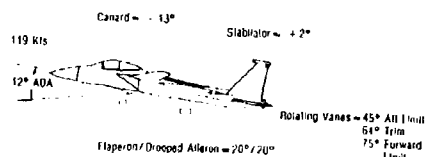


Figure 62a. SLAND Approach Configuration

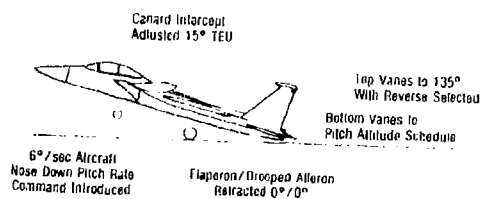


Figure 62b. STOL-SH at Touchdown

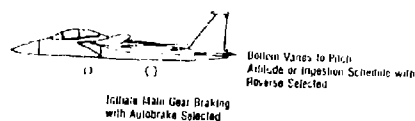


Figure 62c. STOL-SH During Rollout

Figure 62. Touchdown Control Law Reconfiguration

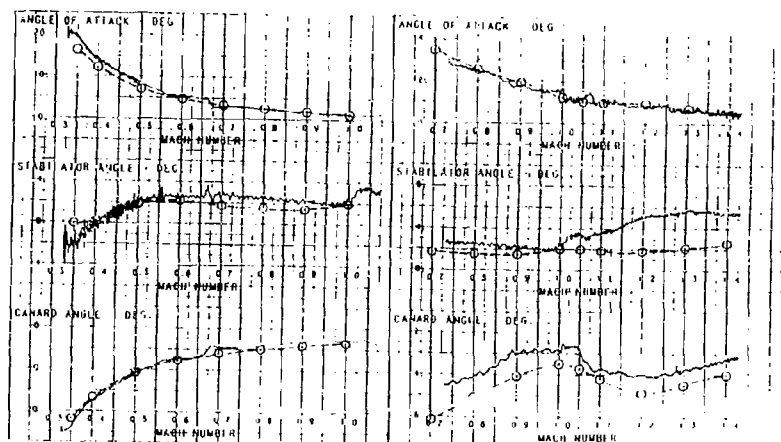


Figure 63. Longitudinal Trim Characteristics

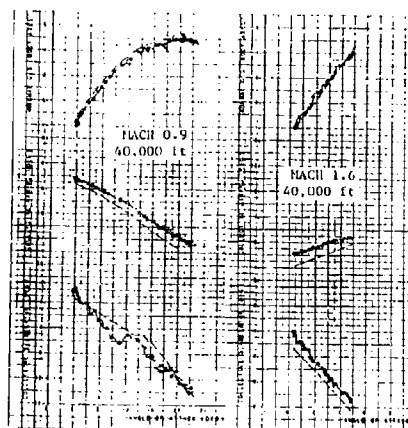


Figure 64. Wind-Up Turn Results

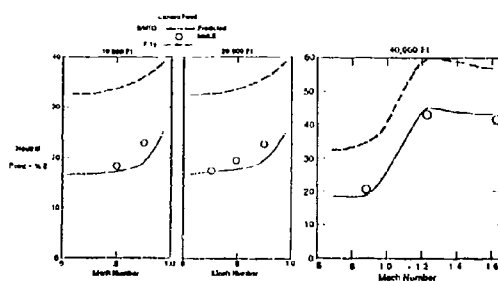


Figure 65. Neutral Point vs Mach No.

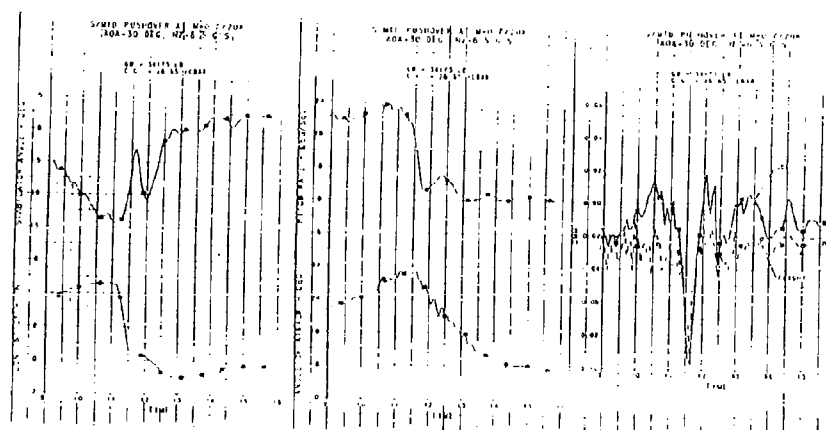


Figure 67. Pitch Control Power

FLT NO	MANEUVER	PILOT COMMENTS
1587	* 1G decel from 0.4/20K to 20 deg * MUT to 20 deg, 0.4/20K * MUT to 20 deg, 150Kts/20K * 1G decel from 0.8/30K to 20 deg	At 20 deg control very positive. Buffet started at 12 deg, increased to low and pounding at 15-17 deg. At 20 deg it was much less than F-15. Chase F-15 needed win AB, S/MTO was at about 85% rpm.
1604	* PID maneuvers, 0.9/40K 15 and 20 deg * 1G decel from 0.3/10K to 20 deg	Good, solid aircraft control. Aircraft response very good to all control inputs. No wing rock. Buffet increased to medium intensity, much less than F-15. Aircraft responsive and predictable in all axes.
1605	* 1G decel from 0.3/10K to 20 deg flaps down	Very stable and well controlled. Control response was positive. No wing rock and only light buffet.
1606	* 1G decel from 0.3/12K to 20 deg flaps down	
1607	* 5G decel to 20 deg at 40K * 5G decel to 20 deg at 30K	20 deg AGA at 5G produced heavy buffet, but small amount of sideslip. Aircraft handled nicely.
1608	* PID maneuvers, 0.7/40K * 40K to 17K decel at 20 deg	Aircraft response was benign. Felt very comfortable.
1618	* MUT to 20 deg, 0.8/20K * MUT to 30 deg, 0.7/20K	The aircraft handled very well with no adverse nose movement. Buffet build up to medium intensity was smooth.
1622	* 1G decel from 0.5/30K to 20 deg (upwash point)	
1625	* 1G decel from 0.7/40K to 20 deg (upwash point)	Very controllable. Appeared there was plenty of stabilator left for pitch control. Directional stability is positive.

Figure 66. Elevated Angle of Attack Characteristics

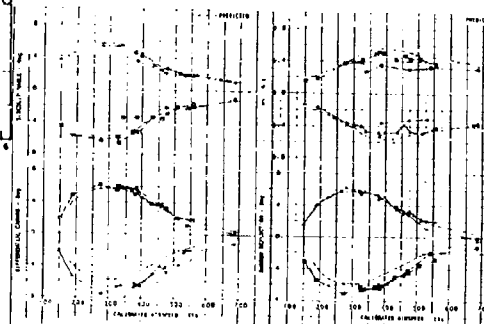


Figure 68. Steady Heading Sideslip

COMBAT AIRCRAFT CONTROL REQUIREMENTS

T B SAUNDERS
J H TUCKER

BRITISH AEROSPACE (MILITARY AIRCRAFT) LIMITED
WARTON AERODROM:
PRESTON PR4 LAX
LANCASHIRE
ENGLAND

SUMMARY

The paper reviews the various functions and requirements for combat aircraft controls which arise from consideration of the flight envelope, agility, handling qualities specifications, control system design criteria etc. Examples are drawn from supersonic and subsonic combat aircraft designed by British Aerospace including those employing powered lift (Harrier) and those which use a basically unstable airframe to enhance performance (EAP/EFA). The subject is discussed in terms of the basic functions of aircraft controls which are to trim, manoeuvre and stabilise. These functions require certain forces and moments to be generated over the full design envelope of speed, Mach number and angle of attack. A certain minimum level of linearity is desirable although, with some redundancy of controls, trim schedules can be chosen to avoid limited areas of ineffectiveness provided other constraints allow it. The achievable rate of application of control is an important variable which can have a serious impact on the sizing of actuators and power systems.

1. INTRODUCTION

Throughout the history of flying the final, vital action which a pilot carries out before committing his aircraft to flight, is to confirm full and free movement of the controls. This gives some clue to the importance attached to correct operation of the controls in ensuring the safe flight of the aircraft.

In recent years a number of developments have made the requirements for combat aircraft controls more demanding. The flight envelope in terms of speed and angle of attack has been greatly increased. Early subsonic jet aircraft operated near to the limits of elevator trim, or control power at maximum speed, Figure 1. Aircraft have also operated near this limit on the approach, with a heavily flapped wing. Extension into the supersonic speed regime led to the almost universal employment of fully powered controls on high speed combat aircraft. More recent developments, such as the use of powered lift and the increasing emphasis on agility, have led to novel configurations and imposed even more challenging requirements on the flight control designer. This paper will deal with this latter period and will examine the novel challenges presented to the Aerodynamicist designing the controls for current and future generations of combat aircraft. We aim to set the scene for the many, varied papers to follow on the specifics of control design and experience.

The first aspect to be considered will concern the functions which the controls have to carry out and we shall then go on to examine some of the requirements brought about by new design trends.

2. FUNCTIONS OF CONTROLS2.1 Contribution to Natural Stability

In the classical flapped arrangement of the tailplane/elevator or fin/rudder, the fixed part of the surface was considered as providing stability, but the moving part of the control itself would also contribute in this way; although generally the aim was to give only a small contribution to stability. In fact with unpowered controls, geared tabs etc., it was relatively easy to get the hinge moments/balance wrong and very careful design and indeed redesign was needed. This problem was largely removed by powered controls. With the common use of all moving controls, or tailplanes, foreplanes and fins, the stabilising or destabilising effect is an important consideration in sizing of the control surface.

2.2 Trim

Lateral Directional Control trim requirements, for conventional aircraft, are confined to cross wind landing, engine failure or asymmetric store carriage cases, which are mainly of interest at low speed or high angle of attack. Increasingly with large, sophisticated and expensive stores carried underwing, the choice of roll control can be dictated by asymmetric store carriage.

In the pitch axis, in addition to coping with zero lift pitching moment, it is necessary to trim the varying pitching moment resulting from the natural stability or instability of the aircraft. Figure 2 shows the envelope of pitching moment of a stable combat aircraft at zero control angle and has superimposed the control power available from the control surface, showing the necessary margin for trim throughout

the flight envelope. The benefit of reduced trim requirement and hence reduced trim drag from reducing the stability of the aircraft is well known, Figure 3. Of course if the control surface in question is a tailplane, reducing the size of the tailplane to reduce stability will also reduce pitching moment available for trim. The tailplane may well be sized by stability considerations subsonically, e.g. with large stores underwing.

The effect of the control surface on lift has also to be considered. Allowing for a neutrally stable wing body, a larger tailplane will of course contribute more stability and a larger foreplane more instability. In an aircraft with a stable wing-body and a tailplane, the trimming forces produce a negative trimming lift component and unstable aircraft of this type would have a positive contribution to the lift. This is illustrated somewhat simplistically by the familiar photograph of a Tornado ADV with its positive stability, flying in formation with the fly-by-wire Jaguar, which had had its wing modified to make it unstable (Figure 4). Both aircraft are controlled by tailplanes and the large negative trimming lift contribution from the tailplane of the stable Tornado is very obvious on the picture.

We shall be discussing the functions of controls for manoeuvring the aircraft next, but it is probably appropriate to mention here the need for controls to trim out moments in an axis due to manoeuvres in the other axes of the aircraft. For instance, a rapid roll would produce a significant pitch up, which has to be trimmed out. This is of particular importance in the design of an unstable aircraft, where the inertial pitch up in a rolling pull out is in the same sense as the natural instability of the aircraft and both of these must be resisted by the controlling moment (Figure 5). The usual design case is one of high commanded roll rate at high angle of attack, but the case of recovery from an incipient stall in which uncommanded roll rates may result from the deterioration in lateral directional characteristics must not be neglected.

2.3 Powered Lift

Where powered lift is used, there must be an appropriate balance between powered lift moments, control moments from the reaction control system and aerodynamic moments during hover and transition. Figure 6 indicates the flight regimes to be considered and Figure 7, some of the basic design concepts for this type of aircraft. The performance and handling benefits to be gained from the careful design of these aspects are considerable. Figure 8 shows that with an aft thrust centre, front pitch reaction valves are necessary, whereas in Figure 9, there is a possibility that this part of the control system could be completely eliminated and replaced by a two directional trimming valve at the rear of the aircraft, if the thrust centre is slightly forward of the c.g.

In the future, it is possible to consider designs with remote augmented lift systems, where the thrust from the main nozzles could be modulated to assist trimming. Although this will allow much greater trimming moments to be generated, the basic requirement for care in relating the c.g. range of the aircraft to the range of thrust centres remains a very important aspect of design.

2.4 Manoeuvre

Since the controls are the means whereby the pilot can change the state of the aircraft, some margin must be defined to enable this to happen. In the rolling axis the trim requirements are relatively modest, resulting as they do from asymmetries, but the agility of the aircraft is vitally affected by the roll accelerations and rates that can be obtained at all operational parts of the flight envelope. Figure 10 illustrates roll performance requirements, traditionally deemed necessary to provide the necessary agility for combat aircraft.

In the pitch axis the control powers are usually designed by low speed high angle of attack or nosewheel lift considerations for aeroelastically efficient surfaces and the margin for manoeuvring (producing pitch acceleration) at high speed is automatically established.

2.5 Stabilisation

Controls have always been used by the pilot to stabilise the aircraft dynamically, but automatic stability augmentation has become an increasingly important and powerful function of the aircraft's controls. Starting from the need for dampers about all three axes in subsonic and early supersonic aircraft, we have now progressed to the need for increased stiffness in the yaw and pitch axes, due to the use of instability to enhance the turning performance of combat aircraft. The increasing degree of pitching instability over the years is illustrated in Figure 11.

2.6 Control in Turbulence

The power and sensitivity of the aerodynamic controls are important factors in enabling the pilot to control the aircraft's response to external disturbances, such as gusts. Pilots will sometimes criticise aircraft with ineffective or sluggish controls as being "susceptible to gusts". On the other hand automatic gust alleviation systems can be introduced to operate the controls in such a way as to reduce the effects of gusts.

2.7 Control of the Structure

With the availability of high performance, fast and high integrity control systems for other purposes, it is becoming natural to use the aerodynamic control for structural load alleviation and flutter suppression. This requires a comprehensive knowledge of the control surface unsteady aerodynamic/structural interactions, for significant let alone full benefits on configuration and weight to be gained.

2.8 Acceleration and Deceleration

We should not forget the speedbrakes on combat aircraft. Their function is to produce deceleration with as little effect on pitching and yawing moment and buffet as possible. We should really include the engine amongst the important controls which have a vital function in the operation of the aircraft. The natural agility of an aircraft can be seriously impaired if the engine itself is not agile and is not able to change its thrust level rapidly at the command of the pilot.

3. REQUIREMENTS

3.1 General

Figure 12 shows the percentage of empty mass of a number of recent aircraft, which is taken up by the flying control surfaces, actuators, control computers and associated hydraulics. Two things should be noted. First, the flying controls comprise a surprisingly high percentage of the empty mass exceeding 10% in some cases. Secondly, those aircraft which have a high degree of instability or control augmentation generally reflect this in a larger percentage of the empty mass being taken up by the associated controls and the heavier actuators that are needed to provide the necessary power and integrity. In these circumstances, careful consideration of control requirements and the optimisation of the design of the aerodynamic control surfaces is important, if the overall mass of the aircraft is to be controlled. We will now go on to consider some of the specific requirements relating to the control functions described in Section 2.

3.2 Control Power

The maximum controlling moment available about a given axis needs to be considered for low speed design cases and occasionally at high supersonic speeds where, for instance, fin and rudder combinations can become ineffective due to aeroelastics for both stabilisation and for control, Figure 13. At low speeds the directional control power must be sufficient to kick off drift when landing at the maximum design cross wind with an adequate margin in roll to counter the dihedral effect. Additionally the control of sideslip excursions at the angle of attack limit in a combat configuration, must also be considered.

There must always be enough pitching moment control to achieve any point within the flight envelope, including high angle of attack and high normal load factor. For an unstable canard configuration foreplane stall must be avoided. For a stable aircraft the lack of sufficient control power merely limits the flight envelope itself and the result of running out of control power is a safe retreat to within the existing flight envelope. There can be exceptions to this, where tailplane stall is involved. An interesting example was met on a Hawk variant, where it was possible for the tailplane to stall and lead to a stable low incidence situation in recovery from a stall with full flap undercarriage up, in which the aircraft could only be recovered by the retraction of flaps. This situation, although not relating to the essential part of the flight envelope, was in fact eliminated in development in an interesting way by the addition of a small fixed leading edge strake near the tailplane apex. Figure 14 shows the pitching moment characteristic and Figure 15 the strake. (Reference 1).

3.3 Control Power Gradient

The gradient of controlling moment for small control deflections is usually sufficient if the maximum controlling moment available has been achieved for reasonable maximum control deflections. It is necessary, however, to consider the gradient, particularly in cases where control characteristics are non-linear and where a large degree of stability augmentation may be required. In such cases inadequate or significantly varying control power gradient would lead to excessive system gains, resulting in large inertial effects on the structure and excessive demands from the hydraulic system and actuators.

3.4 Linearity

Whereas the control system designer would naturally prefer linear characteristics, considerable levels of non-linearity are often dealt with, or avoided. A particular example is, in the case of the use of spoilers for roll control, as shown in Figure 16 where the non-linearity can be markedly different for flaps up and down, with significant implications on the design of the control to minimise this effect and on the P.C.S. to deal with the characteristic. Also in the case of foreplane characteristics, where the interaction with the wing leads to a loss of pitching moment control from the foreplane in certain areas of incidence as illustrated in

Figure 17. If flaps are employed as an additional pitch control, the area of low fore-plane control effectiveness can be avoided by appropriate scheduling.

3.5 Control Rate

The specification of maximum actuator rates for aerodynamic controls is an important part of the design in highly augmented aircraft. When actuators are operated on their rate limit at high amplitude, the phase lags produced are greater than those which would result from a pure mathematical rate limit leading to risk of PIO Figure 18. This can be avoided by careful design of rate limits on the electrical signals within the flight control system, related to the specified performance of the actuator and of course by adequately sited accumulators in the hydraulic system.

3.6 Hinge Moments

Control surface hinge moments are still an important parameter in aircraft design. For combat aircraft with a wide flight envelope, it is important to position the spigot hinge line of all moving controls, so as to minimise the maximum hinge moments in both directions, thus optimising the mass of actuators and structural back up. In fact in the drive to minimise weight we may be going full circle back to a real degree of aerodynamic balance. Figure 19. In flight, excessive hinge moments can lead to changes in trimmed stick position, or restriction in the control surface angle available due to jack sink and aeroelastic deflections. On the Jaguar aircraft, where a non-linear gearing was used with a fixed feel spring to simulate Q feel, the jack sink, due to the altered jet plume characteristics in re-heat, led indirectly to light stick forces. For this reason the tailplane hinge moments were trimmed by a large chord trim tab at the inboard edge of the tailplane trailing edge, Figure 20.

3.7 Structural Interactions

Flutter has always been a major concern to the Aerodynamic Control Designer. Structural stiffness and jack impedance could be defined with the possibility of additional mass balance to ensure a sufficiently high flutter speed. With increasing levels of stability augmentation, the coupling of the FCS with the structure has become more difficult to deal with. Initially, structural notch filters could be introduced to ensure that the system was stable on the ground and flight at higher speeds would then be dealt with by the scheduled reduction in gains as dynamic pressure increased. With higher levels of augmentation for unstable aircraft and separated flows, however, this assumption can no longer be made and the aero-structural characteristics of the aircraft at high speed have to be included in the calculation. Up to the present time all aircraft flown by BAe have been purely gain stabilised in respect of FCS structure coupling, but in order to accommodate large numbers of external stores on future aircraft, with high levels of augmentation, phase stabilisation must be considered. At the same time the reliability of highly augmented flight control systems would allow us to use the system for active flutter suppression on future aircraft. This has been demonstrated a number of times in Wind Tunnels and in flight, but has yet to be used routinely in an operational aircraft. This is likely to result in a requirement for even higher rate actuators.

3.8 Thrust Vectoring - Control Implications for VIPing

On a jet-borne or even partially jet-borne aircraft the controls must cater for direct thrust moments, jet induced/aerodynamic effects and the effects of ground proximity. Control of jet-borne flight is currently, e.g. on Harrier, by reaction control jets, however, it is becoming realistic to consider modulation at the main nozzles for control of an operational aircraft.

Jet-Borne Phase

With Harrier in ground effect sideslip and aircraft attitude affect the significant overall forces and moments induced by the presence of the ground. The basic control requirements here are to trim the aircraft over the operational e.g. range, including asymmetric stores and to ensure the necessary aircraft responsiveness to operate from small secluded sites in a wide range of weather conditions.

Reaction Control System Requirements

Roll control requirement and capability are illustrated in Figure 21. It is worth noting here that the reaction control system on the original Kestrel was found to have inadequate capability, particularly in the roll axis, and was resized. The control problems were noted to be as a result of sideslip in low speed flight and control margin in ground effect. Subsequent autostabilisation improved the situation, particularly sideslip elimination. In this context the yaw control is designed to provide a yaw acceleration of 0.26 rad/sec^2 .

Figure 21 shows pitch response in relation to the e.g. limits for the aircraft, with the forward e.g. giving the design case.

VIFFing

In forward flight deflecting thrust to augment lift induces marked trim changes, which must be controlled in such a manner as to fully capitalise on the lift gain. Basically the Harrier pitches nose-up as the nozzles are deflected in forward flight. This is mainly due to the variation of downwash and local dynamic pressure at the tailplane. Obviously the offset of the thrust centre position from the c.g. will cause additional pitching moment to be generated. The majority of the induced pitching moment is generated between 10 and 25° nozzle deflection. Figure 23 shows the effect of lowering the nozzles with fixed tailplane angle from a nominal 16 degree AOA, as a function of Mach number and height (hence q). Figure 24 shows the incidence required to maintain a 5 'g' turn at a variety of nozzle angles at 10000 feet.

The nozzle drive motor capability is such that the full range of nozzle deflection is not achieved at high dynamic pressure due to nozzle hinge moment limits. Figure 25 shows the maximum nozzle angle as a function of dynamic pressure. Plotted on the same figure are the corresponding tailplane angles required to trim. The nozzle aft (i.e. normal trim) is around 1 degree.

4. FUTURE CONTROL TECHNOLOGY

Much of the aerodynamic control design, even on modern combat aircraft, is based on well founded technology, but there are some questions still to be answered for future aircraft projects. Some of the major technology challenges are as follows:-

- 1) A better understanding of agility and its relation to the operational use of the aircraft.
- 2) Increasing use of deflected thrust and thrust modulation.
- 3) Integration of the powerplant and the aerodynamic controls into a common control system.
- 4) A greater understanding of separated flows and their control.
- 5) Improved prediction of structural effects both static aeroelastic and the coupling of the FCS with structural dynamics.

CANBERRA: SPEED LIMITS DEFINED BY TRIM AUTHORITY

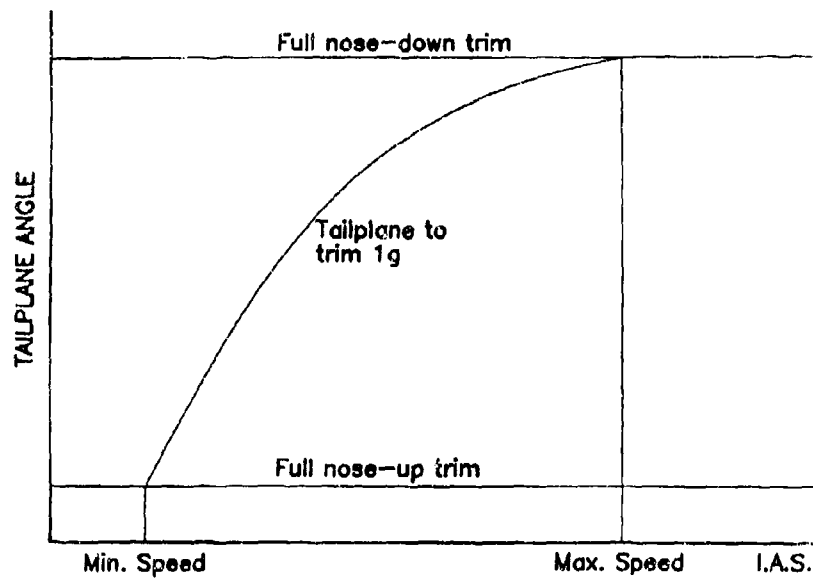
**BRITISH
AEROSPACE**

FIGURE 1

STABLE AIRCRAFT: AVAILABLE TAILPLANE AUTHORITY

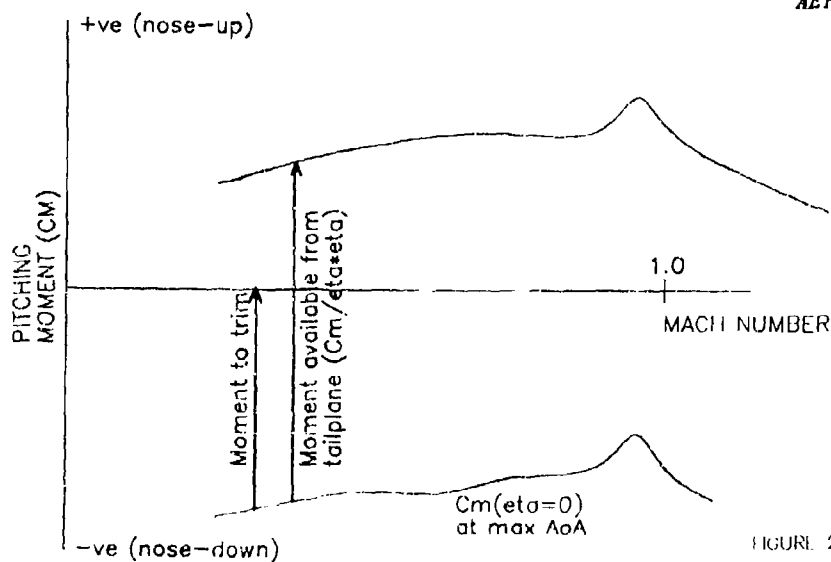
**BRITISH
AEROSPACE**

FIGURE 2

UNSTABLE AIRCRAFT: AVAILABLE FLAP/FOREPLANE AUTHORITY

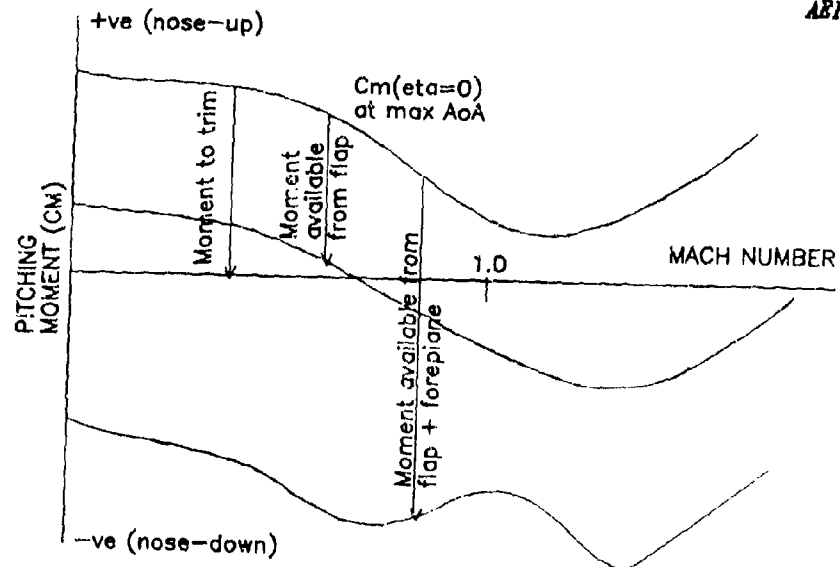
**BRITISH
AEROSPACE**

FIGURE 3

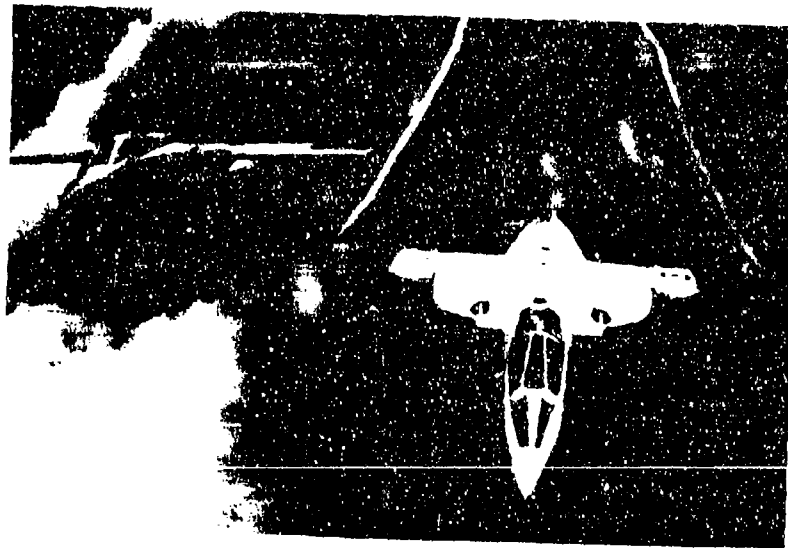


FIGURE 4

EAP: INERTIAL PITCH COMPENSATION DESIGN

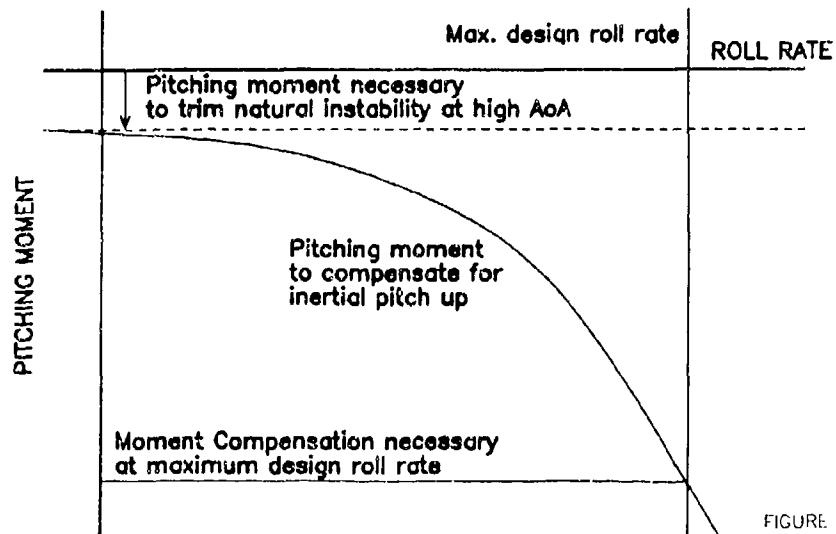
**BRITISH
AEROSPACE**

FIGURE 5

BRITISH
AEROSPACETHRUST CENTREFLIGHT REGIMESJETBORNE

- . AIRCRAFT WEIGHT SUPPORTED BY ENGINE THRUST
- . NOZZLES AT OR NEAR VERTICAL

SEMI-JETBORNE

- . AIRCRAFT WEIGHT SUPPORTED BY ENGINE THRUST AND AERODYNAMIC LIFT
- . NOZZLES BETWEEN VERTICAL AND AFT

WINGBORNE

- . AIRCRAFT WEIGHT SUPPORTED BY AERODYNAMIC LIFT
- . NOZZLES AFT

FIGURE 6

THRUST CENTRE

BRITISH
AEROSPACE

BASIC CONCEPTS

AIM: FOR ALL MODES OF FLIGHT, AND AT ALL ENGINE CONDITIONS,
TO CONTROL THE MOMENT PRODUCED BY THE ENGINE THRUST ABOUT
THE AIRCRAFT CENTRE OF GRAVITY, SO AS TO MINIMISE TRIM
REQUIREMENTS FROM THE FLIGHT CONTROL SYSTEM

RESULTING BENEFITS

- MINIMISE TRIM BLEED DEMANDS FROM R.C.S., HENCE:-
- MAXIMISED ENGINE PERFORMANCE
- MAXIMISED R.C.S. BLEED AVAILABLE FOR CONTROL
- REDUCED PILOT WORKLOAD TO TRIM THE AIRCRAFT

FIGURE 7

ALL THRUST CENTRE

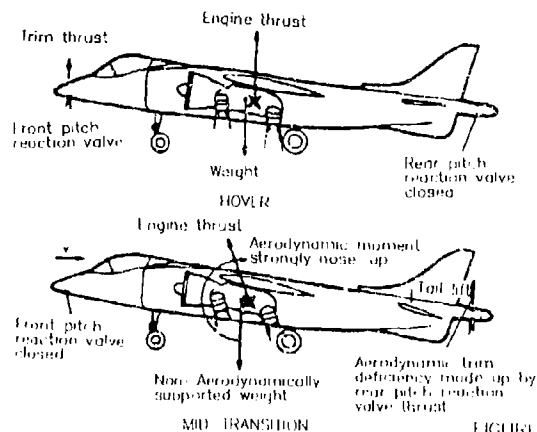


FIGURE 8

FORWARD THRUST CENTRE

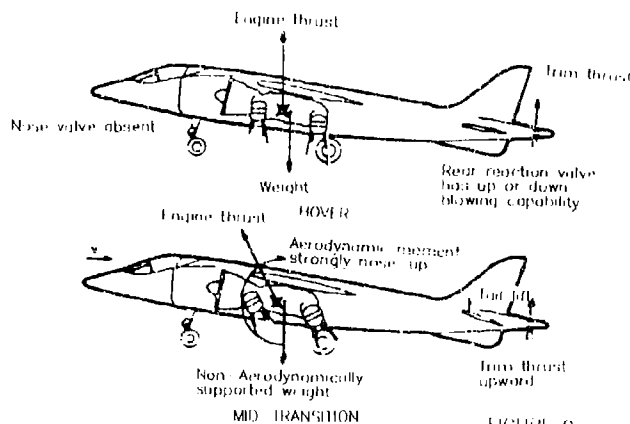


FIGURE 9

ROLL PERFORMANCE REQUIREMENTS

CLASS	FLIGHT PHASE CATEGORY	LEVEL 1	LEVEL 2	LEVEL 3
IV	A	$\theta_t = 90^\circ$ in 1.5 sec	$\theta_t = 90^\circ$ in 1.7 sec	$\theta_t = 90^\circ$ in 2.6 sec
	B	$\theta_t = 90^\circ$ in 1.7 sec	$\theta_t = 90^\circ$ in 2.5 sec	$\theta_t = 90^\circ$ in 3.4 sec
	C	$\theta_t = 50^\circ$ in 1.0 sec	$\theta_t = 50^\circ$ in 1.5 sec	$\theta_t = 50^\circ$ in 2.0 sec

FIGURE 10

TRENDS IN COMBAT AIRCRAFT PITCH STABILITY

**BRITISH
AEROSPACE**

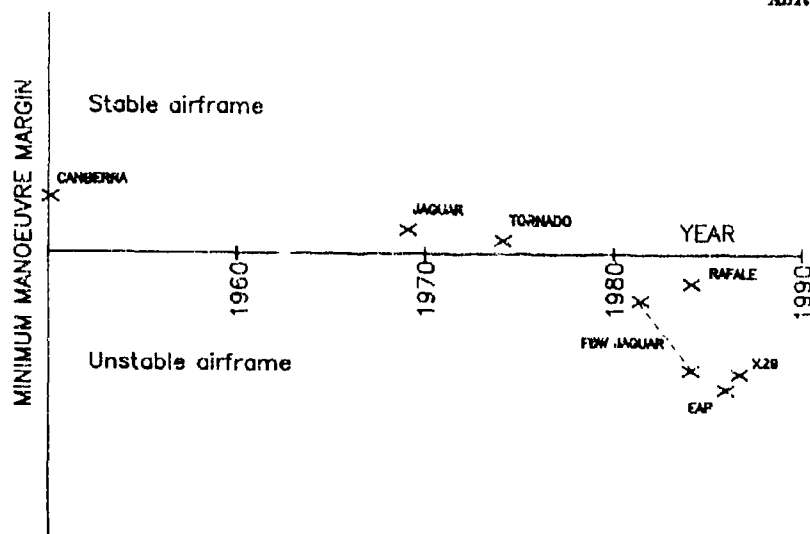


FIGURE 11

MASS OF AERODYNAMIC CONTROLS

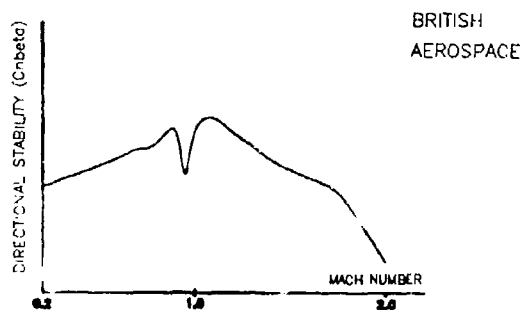
<u>AIRCRAFT</u> <u>TYPE</u>	<u>PERCENTAGE</u> <u>OF EMPTY MASS</u>
Jaguar	9.2%
Tornado	12.2%
Jaguar FBW	11%
EAP	13.2%

Note: "Aerodynamic controls" includes:-

- Control surfaces
- Actuators
- Control circuits & inceptors
- Flight control computers

FIGURE 12

AEROELASTIC EFFECTS UPON DIRECTIONAL STABILITY



AEROELASTIC EFFECTS UPON RUDDER POWER

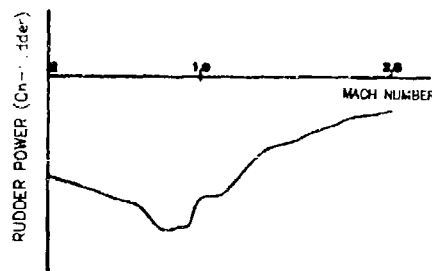


FIGURE 13

HAWK VARIANT: TAILPLANE STALL PHENOMENUM

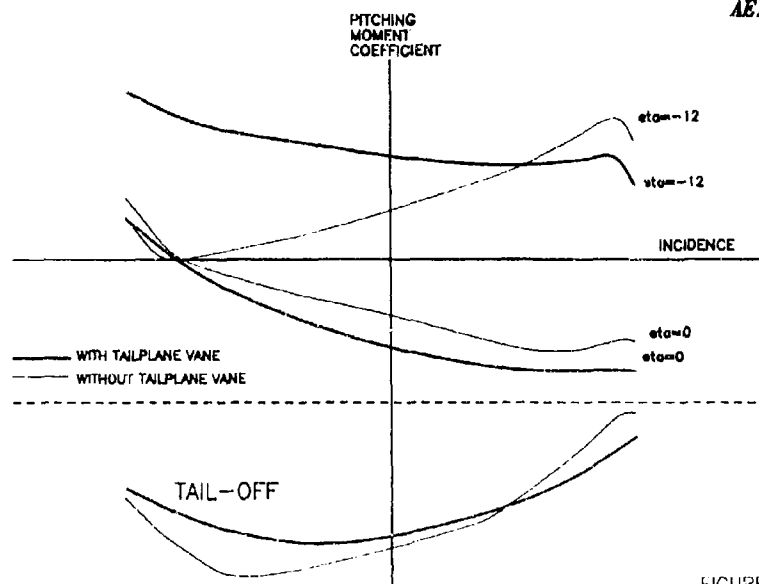
BRITISH
AEROSPACE

FIGURE 14



TAILPLANE VANES SET AT 0 DEGREES - TAILPLANE NEUTRAL

FIGURE 15A



TAIL PLANE LE FULLY DOWN
FIGURE 15B

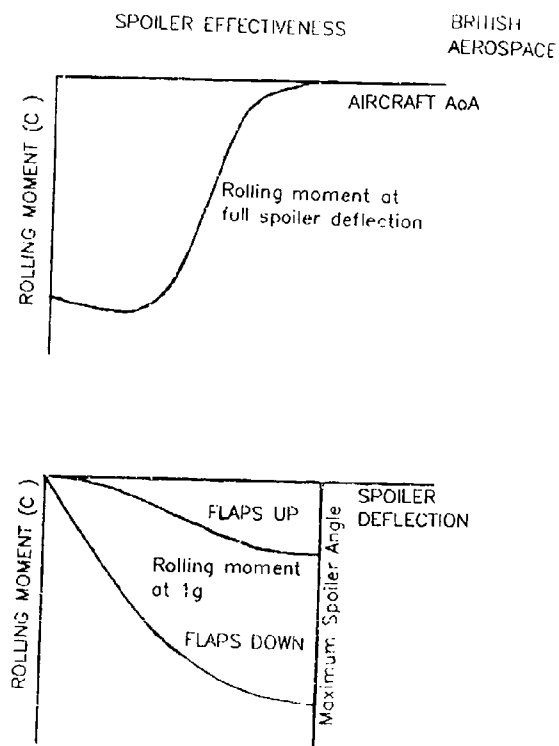


FIGURE 16

EAP FOREPLANE NECKING CHARACTERISTIC

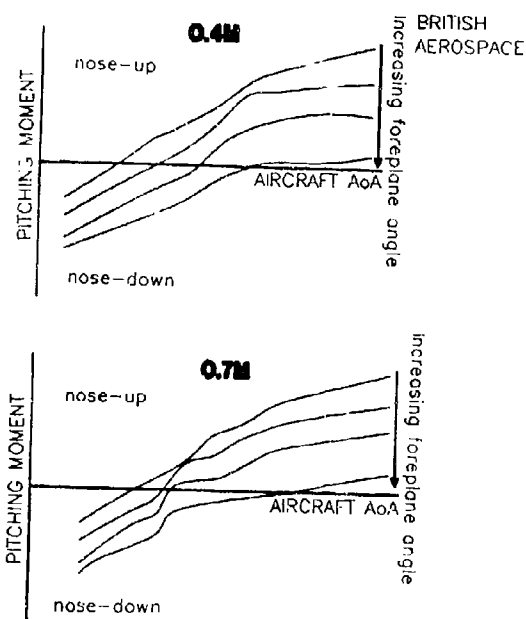


FIGURE 17

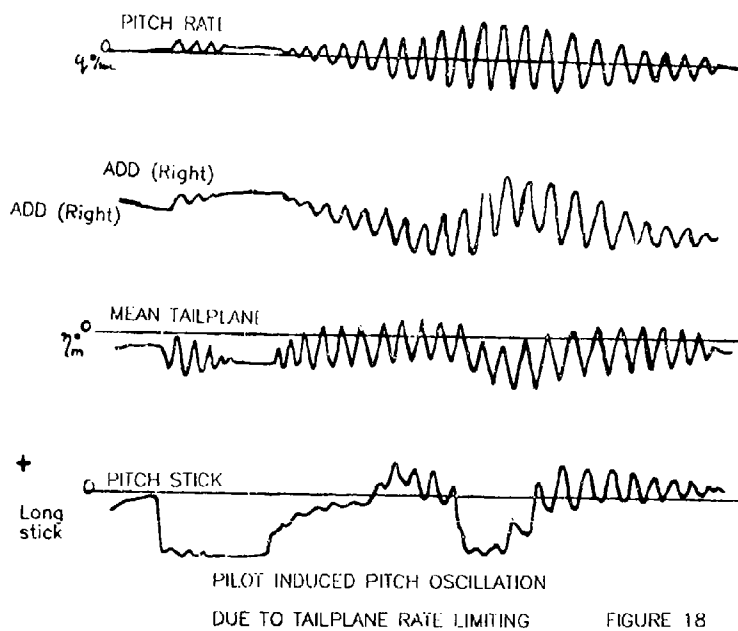


FIGURE 18

EFA: FOREPLANE HINGE MOMENTS AS A FUNCTION OF MACH NO.

**BRITISH
AEROSPACE**

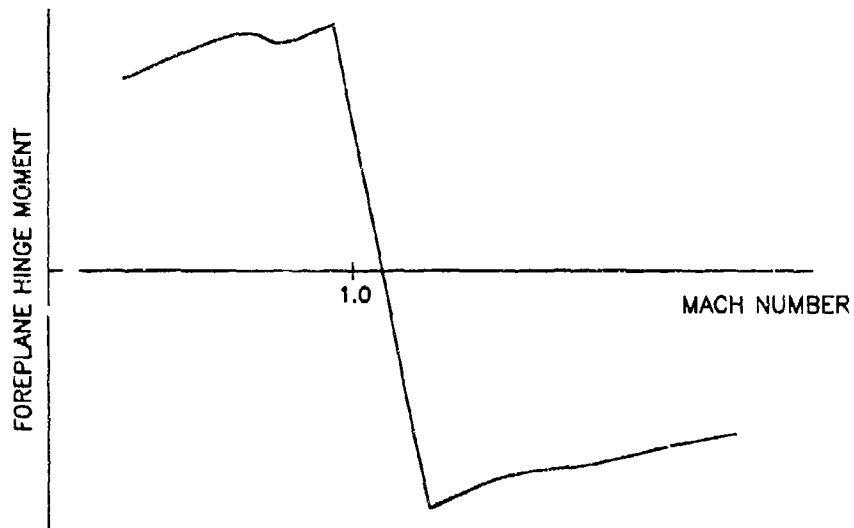


FIGURE 19

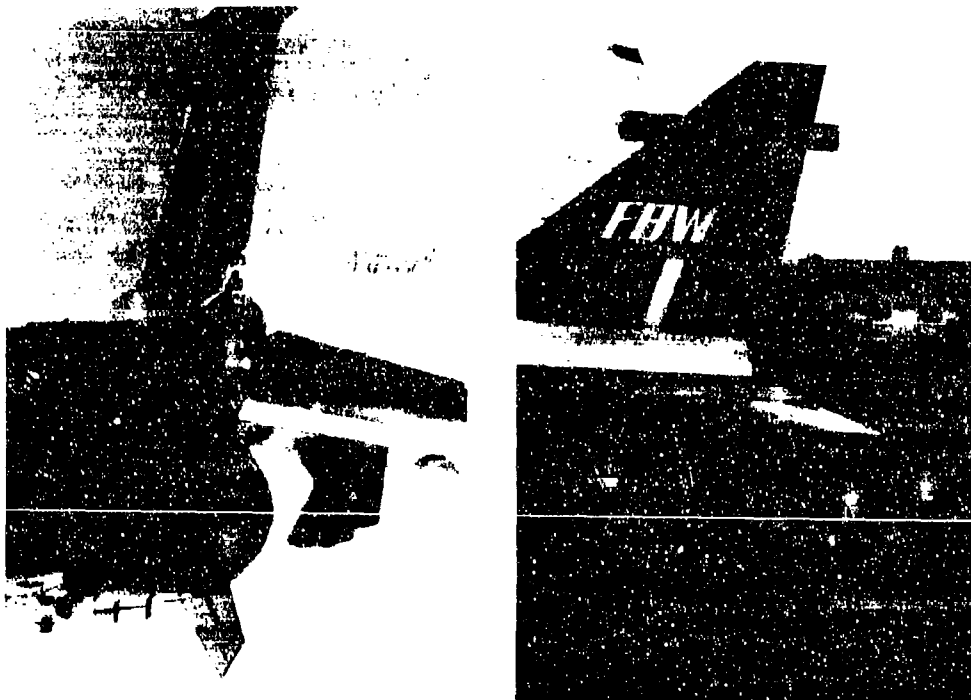


FIGURE 20

JETBORNE CONTROLLABILITY UNDER ADVERSE FLIGHT CONDITIONS

ROLL CONTROL RESPONSE

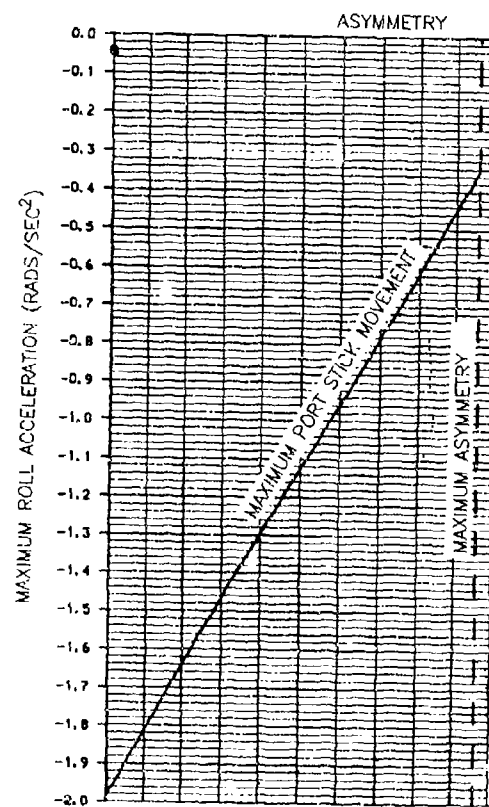


FIGURE 21

JETBORNE CONTROLLABILITY UNDER
ADVERSE FLIGHT CONDITIONS
PITCH CONTROL RESPONSE

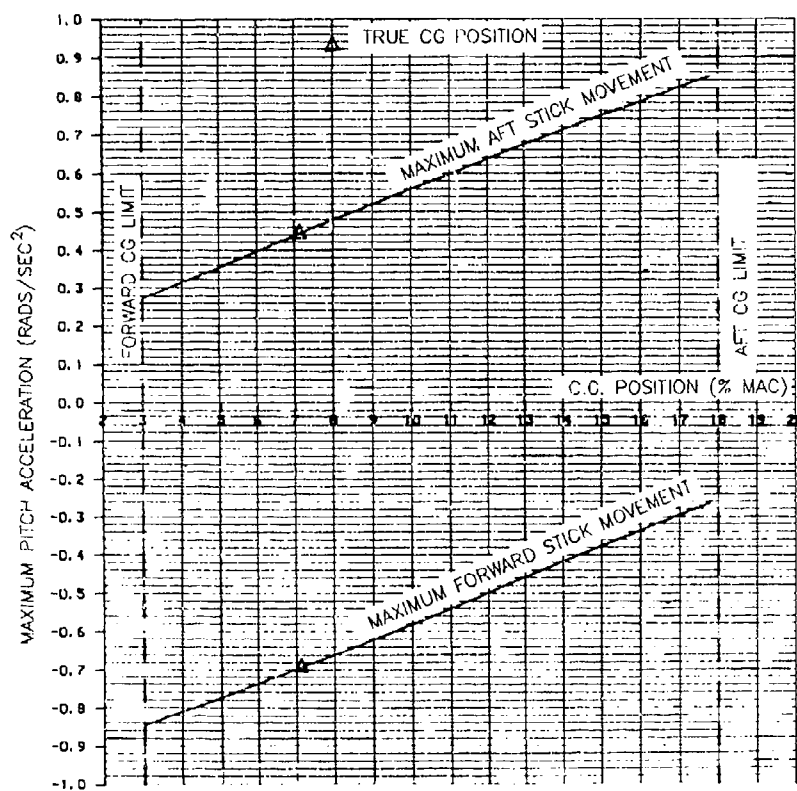


FIGURE 22

EFFECT OF MACH NUMBER AND ALTITUDE
ON INCIDENCE
NOZZLE TRANSIENTS $\alpha_j = 0-60^\circ$
TARGET 16° AOA ENTRY

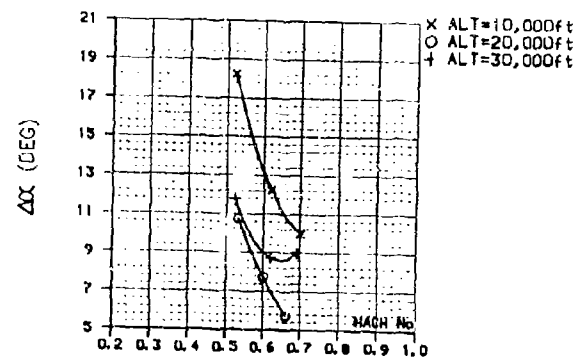


FIGURE 23

EFFECT OF NOZZLE DEFLECTION ON
INCIDENCE TO MAINTAIN 5g TURNS
PULL UPS WITH DEFLECTED NOZZLES
ALTITUDE 10,000FT

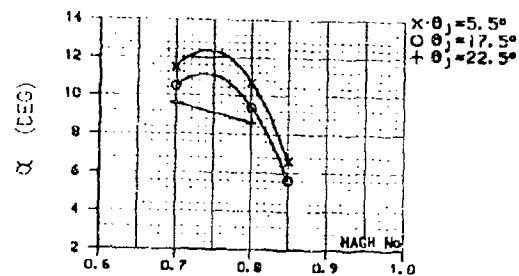


FIGURE 24

EFFECT OF DYNAMIC PRESSURE ON MAXIMUM
NOZZLE ANGLE AND REQUIRED TRIM
NOZZLE DEMAND TO HOVER STOP
ALTITUDE 10,000FT

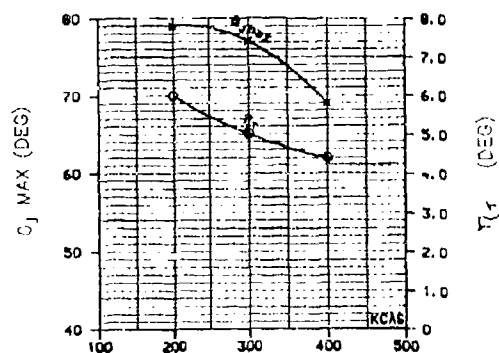


FIGURE 25

CONTROL RESEARCH IN THE NASA HIGH-ALPHA TECHNOLOGY PROGRAM

by

William PGilbert
Mail Stop 246A
NASA Langley Research Center
Hampton VA 23665-5225
United States

and

Luat T. Nguyen
Mail Stop 355
NASA Langley Research Center
Hampton, VA 23665-5225
United States

and

Joseph Gera
Mail Stop D-OFV
NASA Ames-Dryden Flight Research Facility
Edwards, CA 94523
United States

SUMMARY

The NASA is conducting a focused technology program, known as the High-Angle-of-Attack Technology Program, to accelerate the development of flight-validated technology applicable to the design of fighters with superior stall and post-stall characteristics and agility. A carefully integrated effort is underway combining wind-tunnel testing, analytical predictions, piloted simulation, and full-scale flight research. A modified F-18 airplane has been extensively instrumented for use as the NASA High-Angle-of-Attack Research Vehicle used for flight verification of new methods and concepts. This program stresses the importance of providing improved airplane control capabilities both by powered control (such as thrust-vectoring) and by innovative aerodynamic control concepts. The program is accomplishing extensive coordinated ground and flight testing to assess and improve available experimental and analytical methods and to develop new concepts for enhanced aerodynamics and for effective control, guidance, and cockpit displays essential for effective pilot utilization of the increased agility provided.

NOMENCLATURE

Symbols

x	longitudinal body axis
p	roll rate about body axis
r	yaw rate about body axis
α	angle of attack (alpha)
β	angle of sideslip (beta)
N	body axis yawing moment
L	body axis rolling moment
I _z	moment of inertia in yaw (body axis)
I _x	moment of inertia in roll (body axis)
M	pitching moment (body axis)
Mach	Mach number
Re	Reynolds number based on wing mean aerodynamic chord
Mil	military (or intermediate) power setting

Acronyms

CFD	Computational fluid dynamics
HATP	High Angle-of-Attack Technology Program
HARV	High-Angle Research Vehicle
LEX	Leading edge extension
TVCS	Thrust-Vectoring Control System

RFCS Research Flight Control System
PVI Pilot vehicle interface

Subscripts

stab stability axis
IC inertial coupling

1.0 INTRODUCTION

The projected scenario for future air combat engagements emphasizes an extremely demanding environment in which the participants must possess highly agile aircraft in order to survive and win. This demand for agility will result in intentional flight at high angles of attack (high alpha) in order to generate the angular accelerations and positional maneuver advantages required for a successful engagement. Unfortunately, the current state-of-the-art in design methodology for high-alpha flight conditions is relatively poor, typically resulting in extensive cut-and-try efforts to fix vehicles in an untimely and costly fashion. Chambers (reference 1) presents an excellent summary of recent experience with high-alpha problems for high-performance aircraft and solutions defined. These design shortcomings have been dramatically illustrated in the past by a large number of accidents and flight restrictions caused by deficiencies in high-alpha behavior. The magnitude of the problem is illustrated by the data presented in figure 1, which lists the documented high-alpha-related losses for high-performance military vehicles during the last decade. The large losses experienced with the older aircraft are an indication of deficient designs which resulted from an intention to avoid the high-angle-of-attack environment by using stand-off or slashing attacks.

Although the current safety record has dramatically improved for aircraft like the F-15 and F-16, current fighters are relatively limited in effective maneuver capability at elevated angles of attack, in large part due to inadequate control power. In addition, certain aircraft such as the F-16 must use artificial angle-of-attack limiters to constrain the flight envelope and avoid loss of stability and control. The foregoing considerations represent a severe impediment to the aggressive, "care-free" maneuver philosophy required in current and future air combat.

As just noted, improved control power is a primary need to obtain high-alpha maneuverability in current and future fighters. The ability to generate rapid body axes angular rates at high-alpha flight conditions requires effective control capability about all three aircraft axes, with the most critical requirements being in yaw and pitch as described in reference 2. The yaw requirement is illustrated in figure 2. Because rolling about the body x-axis at high angles of attack generates large sideslip excursions due to kinematic coupling, modern fighter aircraft are designed to roll more nearly about the velocity vector. It is clear that this conical rotational motion (indicated by "p_{stab}") eliminates the coupling between angle of attack and sideslip. Resolving p_{stab} into the body-axis system shows that this motion involves body-axis yaw rate (r) as well as roll rate (p) and that these rates are related by the expression $r = p \tan(\alpha)$. Converting this relationship to reflect control requirements gives the expression:

$$N/L = (I_z/I_x) \tan(\alpha)$$

The $\tan(\alpha)$ term in the expression shows that the required yaw control (N) increases nonlinearly with increasing angle of attack. Furthermore, because I_z/I_x can be large (5 to 10) for slender, fuselage-heavy fighter airplanes, the ratio of yaw control to roll control (L) required can become quite large at higher angles of attack corresponding to stall and post-stall conditions as illustrated in figure 2.

In the pitch axis, the nose-up pitch control requirement is driven primarily by the desire to be able to trim the airplane to stall and post-stall angles of attack and to generate large pitch angular rates for rapid nose pointing. In addition, however, it is critical to have sufficient nose-down control to counter inertial coupling effects. Due to the fuselage-dominated mass distribution of modern fighters, a nose-up inertial coupling pitching moment is produced during velocity vector rolls as given by the expression:

$$M_{ic} = (1/2)(I_z - I_x)p^2 \sin^2(\alpha)$$

This nose-up moment can be quite large during rapid rolls at high angles of attack and must be counteracted by the available nose-down pitch control to prevent loss of control. The challenge today is to provide effective control concepts at high angles of attack that do not create unacceptable penalties in other parts of the flight envelope of advanced fighters.

Briefly outlined in figure 3 are the problems with the current state-of-the-art in high-angle-of-attack technology. They are caused, in large part, by the lack of reliable design methods to address the extremely complex, separated flows present at high angles of attack. The nature of these flows is evident in the water tunnel photograph presented in figure 4.

Several emerging technologies (noted in part in reference 3) offer the potential to eliminate the traditional limitations imposed on designers due to considerations of high-angle-of-attack characteristics. These technologies include:

- Thrust Vectoring Concepts
- Digital Flight Controls
- Computational Aerodynamics
- High Thrust/Weight Engines

The dramatic increases in control effectiveness provided by multi-axis thrust vectoring combined with the versatility and options provided by advanced aerodynamic controls, displays, and expert systems provide for unprecedented levels of agility and tactical options. Rapidly maturing computational fluid dynamics (CFD) methods offer a significant saving in cut-and-try wind-tunnel testing, improved analysis capabilities, and preliminary design methods which are not currently available. High T/W engine technology offers the capability to rapidly accelerate from low-speed conditions following extended maneuvers at high angles of attack, thus providing a new energy-management option which minimizes one of the current concerns regarding the tactical usage of high-angle-of-attack capability.

The implementation of these advanced technologies offers immediate payoff from three viewpoints as depicted in figures 5 to 7. As shown in figure 5, all current fighters exhibit a marked decrease in agility (particularly in lateral-directional motions) at high angles of attack. In addition, many of these fighters exhibit severe aerodynamic instabilities at angles of attack near maximum lift, requiring artificial alpha limiting by use of the flight control system. Incorporation of these advanced technologies will dramatically improve the agility of future fighters both within the normal flight envelope, as well as at extremely high angles of attack. Piloted simulation studies conducted recently (reference 4) have shown clearly that substantial tactical advantage accrues to the pilot with the option to use high-alpha maneuvers with good controllability; multi-axis thrust vectoring offers this capability without undue compromise in other critical flight regimes. Highly undesirable alpha limiters will no longer be needed, and the operational envelope can be extended into the post-stall regime.

If the classical alpha limits are removed, new operational tactics and capabilities can be used to provide a dominant advantage in certain scenarios. For example, shown in figure 6 are two maneuvers which are easily effected with advanced technology. The ability to gain an additional nose-pointing angle provides a solution to a commonly experienced limitation in air combat. The ability to reposition the airplane for a firing opportunity makes use of the ability to exchange kinetic and potential energy with the use of high angles of attack to rapidly change maneuver states and obtain the first shot advantage. Herbst addressed these possibilities in post stall maneuverability in depth in his discussions of supermaneuverability (See reference 5.) Finally, the elimination of traditional high-alpha limitations provides the designer with a revolutionary option in airplane design. As illustrated in figure 7, the designer has previously had to penalize relatively efficient supersonic configurations by geometric redesign for compliance with low-speed, high-alpha stability and control requirements. This process has been especially undesirable for aircraft which spend an extremely small portion of their operational lives at low-speed, high-alpha conditions. If the advanced concepts provide alternative means for satisfying these requirements, the designer can take a fresh look at the configuration and possibly enhance the relative efficiency of the vehicle at the design point. Thus, solutions to high alpha limitations can provide significant benefits across the speed range and operational envelope.

Several ongoing advanced technology flight demonstrator programs being conducted by the U.S. Department of Defense are based on a recognition of the large potential of the increased operational flexibility and the air combat maneuverability likely to be derived from successful application of thrust-vectoring for control. These programs include the U.S. Air Force STOL and Maneuver

Demonstrator (highly modified F-15 with canard and vectoring) and the Defense Advanced Research Projected Agency X-31. (See references 6 and 7.) Each of these programs is attempting to quantify the gains possible from advanced control capabilities when properly integrated and properly used in air combat.

The revolutionary gains previously discussed will only be obtained if the pertinent technologies are advanced in an aggressive, accelerated manner with a cohesive, well-coordinated focus. This realization was the stimulus for developing the High Angle-of-Attack Technology Program (HATP) described in this paper. Although many contributions to high-alpha technology have emerged from NASA efforts in aircraft development programs and via basic research and development programs, they have lacked a focus and validation cycle, resulting in high-risk applications from an industry viewpoint.

The need for the flight validation step has become particularly apparent in recent airplane development efforts for the F-16 and F-18, wherein significant discrepancies were encountered between ground test facilities and between some ground facilities and flight. Reference 8 describes the problems encountered with predicting the deep stall of the F-16 and reference 9 describes the problems encountered in prediction of the low lateral stability encountered on the F-18 near maximum lift. Such results strongly suggest that principle high-alpha design capabilities should be carried through flight validation to ensure confidence.

Many aerodynamic stability and control problems encountered during aircraft development efforts were solved by cut-and-try methods to meet time constraints and the underlying fluid mechanics problems were not understood to the level needed for improved design methods in the future; failure to take time to learn from such experiences will result in repeating the problems and the cut-and-try solution approach. The development and maturation of high-alpha technology would minimize these surprises at the development stage and ensure that the tactical capabilities of future U.S. high-performance military vehicles are superior to potential threats.

This paper addresses the controls research opportunities and plans in the NASA HATP by providing a program description highlighting the unique aspects of the program that will enable the exploration of advanced controls for the high-alpha flight regime. Included is a brief description of the program, with the rationale behind its structure, a description of the flight validation vehicle current and planned capabilities, and how NASA is conducting the flight research aspects of the program. Highlights of recent results obtained in the program to date are presented. A description is given of the current focus for development of new control concepts and the plans to flight-validate these ideas in the near future.

2.0 PROGRAM DESCRIPTION

The NASA program conceived to address the high-alpha problems and the advanced technology opportunities for high-performance aircraft is now known as the High-Angle-of-attack Technology Program (HATP). This program not only addresses the advanced technologies of interest but, indeed, relies on them to carry out the high-alpha technology effort. The primary objectives of the HATP are (See figure 8.): (1) provide flight-validated prediction/analysis methodology including experimental and computational methods that accurately simulate high-angle-of-attack aerodynamics, flight dynamics, and flying qualities; and (2) improve agility at high angles of attack and expand the usable high-alpha envelope. Accomplishment of these objectives will significantly improve the airplane design process; minimize the occurrence of unexpected deficiencies; and permit routine, unprecedented use of high alpha in tactical situations, including flight at post-stall conditions. The program provides the critically needed focus for key technologies in an integrated manner and uses the unique expertise and facilities of NASA's leading aeronautics research centers, including the Langley, Ames, and Lewis Centers. Technical direction for and coordination of the program is provided by a steering committee composed of representatives of each participating center and NASA Headquarters.

As noted in the Introduction, full-scale flight validation is essential in the development of high-alpha technology. To provide this critical element, the High Angle-of-Attack Research Vehicle (HARV) is being used and developed in the program. A photograph of the HARV is presented in figure 9. Selection of the F-18 for the flight vehicle was done after careful consideration of the research thrusts and the potential capabilities of several available U.S. fighters. Important advantages of the F-18 for this role are listed in figure 10. The airplane was obtained from the U.S. Navy where it was used as the high-alpha test airplane (known as F-6) during the F-18 development program. To provide the precise control needed for aerodynamic measurements and maneuverability at post-stall

angles of attack, the HARV is being modified to incorporate a simple, low-cost multi-axis thrust-vectoring control system (TVCS) as shown in figure 11. No attempt is being made in the program to develop a multi-axis vectoring nozzle suitable for production application; a simple vane-type system conceived by Lacey (reference 10) was selected to avoid complexity and cost; and the same type of system is being used in the X-31 Program. As part of this modification, a research flight control system (RFCS) will also be installed to allow investigating flight control laws for the high alpha flight regime. A summary of the capabilities being developed on the HARV is given in figure 11. A more detailed description of the HARV system and the flight research approach is provided later in this paper.

The research approach being taken in the HATP is a balanced one involving the close integration of ground-based and flight activity as depicted in figure 13. Wind-tunnel experiments, computational aerodynamics, piloted simulation, and flight tests of the HARV are being orchestrated to provide integrated program results. This approach is felt to be essential since today no single method offers reliable answers and a combination of these methods is used in development of new aircraft concepts. Therefore the HATP will seek to provide improvements in the effectiveness of each of these tools used in the prediction of high-alpha characteristics.

The HATP is designed to focus in three key technology areas as depicted in figure 14: high-alpha aerodynamics, advanced high-alpha control concepts, and maneuver management; a detailed breakdown of each area is shown in figure 14. It is recognized that these technologies constitute only a subset of the full set needed to produce an advanced, highly maneuverable fighter airplane; other pivotal technologies include propulsion, engine inlets, vectoring nozzles, weapons release, etc. However, the set included in the HATP is essential to the success of future highly maneuverable aircraft, is not currently being addressed aggressively elsewhere, and fits the skills and resources available within NASA.

Specific technology experiments have been defined and formulated in each of the key technology areas so as to provide valid prediction/analysis methods needed in design methods for future aircraft. Ground-based research is being conducted to define these experiments at the research centers in a coordinated manner leading to appropriate flight experiments to be carried out on the HARV for validation or evaluation. As the experiments mature in each technology area, the HARV will be modified to fly the needed full-scale experiments.

The emphasis in the aerodynamics research is to develop a sound understanding of the steady and unsteady flow physics of 3-D separated flows, particularly strong vortex flows; to develop and validate computational and experimental methods for the prediction of such phenomena; and to develop and evaluate concepts to control separated flows to provide improved high-alpha characteristics. That is, the approach is to understand, predict, and control. Experience with the F-18 aerodynamics during the aircraft development (reference 9) showed the high-alpha stability characteristics near and above maximum lift are dominated by the forebody and wing-body-strake (or LEX) flowfields. Therefore, these portions of the aircraft configuration were taken as the initial focus for instrumentation and study.

In advanced controls, the emphasis is on the development and evaluation of unconventional aerodynamic controls and control laws designed for high-alpha conditions and on application of multi-axis thrust-vectoring to augment aerodynamic controls at low-speed conditions. A strong emphasis is placed on the methods used in developing the advanced aerodynamic controls, including both experimental and analytical schemes, to insure that after the best concepts are verified in flight, there is a sound methodology available for application to new aircraft designs. In many instances, concepts are evolved in generic experiments and are then redefined for application to the HARV configuration to achieve validation. This process provides valuable exercising of the development methods to check their robustness or dependability.

Maneuver management research is developing the unique guidance laws, displays, handling quality requirements, and advisory systems required for satisfactory flying qualities at extreme angles of attack. The expected levels of expanded maneuverability will make improved cockpit display and advisory schemes essential to enable the pilot to fully utilize the expanded capabilities.

The HATP is being carried out in three phases as indicated in figure 15. These phases are defined both by a rational step-by-step research approach and by the efforts needed to expand the HARV flight envelope. Phase I activities are focusing several ongoing generic research areas toward achieving assessment and validation on the HARV. Particular emphasis is placed on aerodynamic

studies, documentation of the HARV baseline agility, correlation of inflight and ground-based predictions for aerodynamics and flight dynamics, the development of future technology experiments, and the expansion of the HARV capabilities. For Phase I, the available angle-of-attack range for precise aerodynamic measurements is limited to about 40 degrees, or less, (although the airplane can be trimmed to near 55 degrees) since the loss of control effectiveness and aerodynamic damping limits usefulness at higher angles of attack until some form of control augmentation is provided. During Phase I, the TVCS is being developed for the HARV to provide that needed control power (discussed further later).

The installation and flight demonstration of the HARV TVCS will initiate Phase II of the program and will double the available flight envelope of the HARV; good levels of controllability are expected to near 70 degrees angle of attack. During Phase II the aerodynamic correlation work of Phase I will be extended to the post-stall regime; the new expanded flight envelope and maneuver capabilities of the HARV will be explored and compared with predictions. Concepts developed for agility metrics, maneuver management, and high-alpha flight control laws and advanced control concepts, carefully defined in ground-based experiments, will be carried to flight for assessment and verification. Ground-based efforts will continue in Phase II to define flight experiments for validation of improved aerodynamic and control design methods. Actual flight tests of the more complex and extensive experiments will be accomplished in Phase III. In this last phase, the HATP will focus on key validation experiments for each of the primary technology areas; most of these experiments are expected to require modifications to the airframe. For example, aerodynamic prediction codes will be exercised in the design of new forebody and/or wing-body-strake components for the HARV (as illustrated in figure 16) to demonstrate the maturity of these methods; references 11 and 12 are good examples of the powerful influence specific forebody shaping can have on total configuration stability. Similarly comprehensive experiments are expected in cockpit advanced displays and in new aerodynamic control concepts.

Throughout the HATP, special emphasis will be placed on conducting experiments wherein a close coordination between predictions and flight results is achieved. Special emphasis will be placed on the use of extensive instrumentation to provide the essential information for checking the results of predictive methods and analyses of discrepancies which occur between wind-tunnel, computational, and flight-derived results. The primary goal of the program is to provide valid prediction and analysis methods in each technology area. This goal will be achieved if industry teams are able to use previously unavailable predictive methods and options at all stages of the design process to ensure superior high-alpha qualities.

Description of High-Alpha Research Vehicle (HARV)

Basic HARV Capabilities

The test airplane selected for the HATP is F-18 No. 160780 obtained on loan from the U.S. Navy. This particular aircraft was previously used for high-angle-of-attack and spin testing and has unique modifications which have been retained by NASA. A photograph of the airplane without the thrust vectoring control system (TVCS) was shown in figure 9, while figure 17 shows the installation details of the six thrust vectoring vanes to be installed on the aft fuselage.

The test airplane is a single-seat version of the F-18 powered by two F404-GE-400 afterburning turbofan engines with pilot-selectable continuous ignition system. With the installation of the TVCS, the divergent portion of the nozzles and the external nozzle flaps will be removed from the engine. The HARV is equipped with a flight test nose boom and wing-tip mounted test pods. Additionally, the airplane has an emergency spin recovery parachute system mounted on the upper portion of the aft fuselage.

The HARV is instrumented extensively as noted in figures 18 and 19; the research instrumentation system allows the monitoring of over 700 flight test parameters. These parameters include conventional flight test parameters, the output of pressure transducers from about 500 surface pressure orifices, from a pressure rake, and a flush air data system (FADS), the output of an inertial navigation system, and 256 words from the data bus. For the purposes of flow visualization, the airplane is equipped with a smoker system and a surface flow visualization system. Smoke can be ejected to visualize the forebody and LEX off-surface flow fields (extending aft to the vertical tails) and colored glycol can be ejected to define the surface streamlines on the forebody and the LEX. Visual data can be obtained by two black-and-white video cameras mounted on the inboard side of the vertical tails, a color video camera on the right wing-tip pod, a still 35-mm

camera on the left wing-tip pod, and another color video camera located in the cockpit looking aft. A more detailed description of the flow visualization system and some recent flight test results are contained in reference 13.

The telemetry system consists of two independent, asynchronous Pulse Code Modulation (PCM) data encoders each with a basic PCM word size of 10 bits. The output of the encoders is telemetered to the ground; no on-board recording of the PCM data is provided in the airplane. Special provisions are incorporated in the data acquisition system for higher resolution of certain types of data. For example, data collected from rate gyros, linear accelerometers and the inertial measuring system are encoded into 14-bit words. The 16-bit words from the MIL-STD-1553B bus are inserted in two 10-bit PCM words for the purpose of monitoring the digital flight control system.

Expanded Capabilities

Computer hardware architecture input/output.- The implementation of the thrust vectoring control system (TVCS) required the modification of the production F-18 flight control computers. The latter is a 4-channel system that is packaged in two identical boxes. Due to a recent change in the production F-18 flight control computer set, sufficient space now exists in the two boxes to house not only the dual-redundant research flight control computers (RFCS), but also all of the additional servo-drive electronics that are required for the six turning vane actuators. The RFCS is projected to use the PACE-1750 microprocessor that communicates with the modified F-18 production system through dual port memory as illustrated in figure 20. A memory size of 32K 16-bit words is allotted in the RFCS for research control laws which will be programmed in ADA. The research control laws will be executed in the RFCS at the basic 80 Hz frequency of the F-18 flight control system. The system will be functionally identical to the standard F-18 when it is not in the RFCS mode, and it is designed to accommodate research control laws that will be generated throughout the duration of the flight test program. It is anticipated, however that little or no change will be made either to the executive and communication portion of the RFCS software or to the modified production F-18 software during the research program.

The HARV flight control system is projected to have the reliability of the production F-18 when it is not in the RFCS mode; that is, dual fail-operate/fail-safe. For the demonstration of the thrust vectoring, however, the system is only required to have fail-safe capability. These reliability requirements will be achieved by leaving the redundancy management/fault reaction portion of the standard F-18 system intact, and by designing dual hydraulic and electrical redundancy into the added, thrust-vectoring portion of the system. Since all redundancy management and fault reaction logic functions reside in the standard F-18 flight control computer set, actuator commands are issued only by the F-18 flight control computer set even when the control system is in the RFCS mode. The thrust vane hydraulic actuators are standard F-18 aileron actuators. The redundancy management and failure status monitoring of this added hardware constitutes the bulk of the added software in the F-18 HARV flight control computer set.

Control laws.- The control laws in the standard F-18 flight control computer set of the HARV are functionally identical to those of the production airplane in its basic configuration so that there will not be a need for extensive envelope clearance or flight qualification. The research control laws, however, which reside in the RFCS will be written in ADA and will have the flexibility to accommodate the requirements of NASA's high-angle-of-attack research during the next few years. The requirements range from merely stabilizing the HARV at angles of attack up to 70 degrees to demonstrating the tactical advantages of thrust vectoring during simulated air combat maneuvers. Currently, there are several control law configurations under development by NASA and the McDonnell Douglas Company.

The initial control laws are designed for the functional demonstration of thrust vectoring, verification of the predicted control effectiveness derivatives of the turning vanes, and stabilizing the airplane at angles of attack well beyond the capability of the aerodynamic control surfaces. Figure 21 shows the form of the maneuvering requirements specified for the control laws throughout the angle-of-attack capability of the HARV. These requirements grew out of several years of simulator experience with other highly maneuverable fighter-type aircraft in the Differential Maneuvering Simulator (DMS) of the Langley Research Center. The actual levels to be specified (not available for publication at this time) will not constitute unique levels associated with specific maneuvers but will rather be the minimum set needed to perform the research mission of the HARV.

Regardless of the details of the control laws, at high angles of attack where the effectiveness of the aerodynamic controls begins to diminish, pitch and yaw control will be augmented by the moments induced by deflecting the jet exhaust of both engines. The amount of deflection or jet turning angle is primarily a function of vane deflection. The determination of each of the six vane deflections from the pitch and yaw jet turning angles will be an integral part of the control laws and will take place in the RFCS. Initially, the vane deflections will be calculated from the two-nozzle average envelopes that are based on single nozzle cold-jet tests. A typical average jet turning envelope is shown in figure 22. It is important to note that the use of average envelopes for a twin-engine airplane neglects vane-mounting asymmetries or split throttle settings. Engine parameters required for real-time thrust calculations, however, allow detection of any gross thrust asymmetries which will result in a downmode to aerodynamic controls-alone operation. Refinement of the calculations for vane deflections and the technique of optimal jet turning are important research objectives of the initial TVCS tests.

An important design feature of the RFCS is the ability to revert to the modified production F-18 flight control system as a result of either a pilot-initiated action or of a RFCS cross-channel miscomparison. Since the production F-18 has been subjected to extensive flight tests at high angles of attack, including spins, an aggressive flight test program can be pursued with the HARV as soon as the TVCS is installed. As a precaution, however, the spin recovery parachute system has been reinstalled on the HARV since the TVCS provides the HARV with a much higher level of maneuverability and could produce changes in the basic stability characteristics.

NASA High-Alpha Flight Research Approach

Integration of simulation and flight. The approach to flight testing the HARV equipped with the TVCS, noted in figure 23, will be similar to other high-alpha flight tests which have been performed at Dryden in the past on airplanes such as the F-14 and the X-29A. This approach includes integrating a high-fidelity simulation into the flight program. Throughout the flight tests, extreme care is taken to validate the ability of the simulator to predict reliably the dynamic response of the airplane not only to small, single-axis control inputs, but also to large amplitude, complex inputs. The simulator aerodynamic data base consists of the best currently known information about the aerodynamics of the F-18 HARV and includes data from static, forced-oscillation, and rotary-balance tests. The data tables are defined over an angle-of-attack and sideslip range of -15 to 90 and + or -25 degrees, respectively. As flight data are becoming available at high angles of attack, parameter estimation efforts are underway at both Ames and Langley to refine the aerodynamic data base for the HARV. In fact, an important research objective of the HATP is the improved modeling of aircraft dynamics at elevated angles of attack and sideslip. Flight tests and flight control system software testing will be supported by several types of simulation:

- Iron bird with hydraulic system
- Hardware-in-the-loop
- All-FORTRAN with control laws in ADA
- Off-line, all-FORTRAN batch
- Off-line, linearized

In these simulations, which are listed in decreasing levels of complexity, many of the modules such as equations of motion, table look-up routines, etc., are identical. It has been the experience at Dryden that each simulation has a particular advantage for certain applications during the course of major flight research program.

Additionally, the Differential Maneuvering Simulator at Langley will be used for maneuver management and advanced display research in direct support the HATP.

Flight test blocks. The flight testing of the TVCS will proceed to clear the envelope shown in figure 24 according to several major tests blocks. Each block covers approximately three months' duration, however, the blocks will be revised monthly to incorporate research objectives that were unanticipated at the start. Detailed procedures for the following test blocks are now being developed:

- (1) Complete ground tests of the TVCS system. The tests will ensure proper operation of the mechanical and hydraulic components of the turning vane system, and will verify and validate the software in the modified F-18 flight control computers and in the RFCS.

(2) Airworthiness tests to validate the conventional envelope of the HARV with the TVCS installed. The tests will include the engagement of RFCS, control inputs designed for parameter estimation, and demonstration of safe transition into the modified production F-18 flight control system from the RFCS.

(3) Envelope clearance of the TVCS below 200 knots and a 3-g normal load factor with unlimited positive angles of attack. At increasing angles of attack the simulator response will be compared to that of the airplane and data base adjustments will be made as needed.

(4) Envelope clearance of the TVCS up to a Mach number of 0.7 and a 6-g normal load factor from 15,000 to 40,000 feet altitude. This clearance will be performed with control laws that may include modifications dictated by block (4) results.

(5) Complete demonstration and optimization of the post-stall performance of the HARV. This block will include agility studies, benefits of the TVCS during limited tactical engagements, and wind-tunnel/computational fluid mechanics correlation and flow visualization studies at extreme angles of attack heretofore inaccessible.

Flight planning.- Detailed flight planning will be accomplished on the hardware-in-the-loop simulator. These simulator sessions allow the complete definition of the altitude-airspeed profile of each flight taking into consideration available fuel, airspace usage, and the most efficient mix of flight test maneuvers requested by the various engineering disciplines involved in a particular flight.

Safety and test control.- Responsibility for the safe conduct and control of each research flight rests with Dryden. The various engineering and operations team members of this organization have established the preflight and post-flight requirements, communication protocol, go/no-go parameters, chase aircraft, and minimum data requirements.

Recent Results

At this writing the HATP is approaching the end of Phase I and the HARV will soon be grounded for installation of the TVCS and RFCS. During Phase I primary attention has been given to defining the basic F-18 high-alpha flow field using wind-tunnel, CFD, and flight tests. Experimental results have been obtained in the form of force and moment data, on- and off-surface flow visualization, and surface pressures with particular emphasis on the forebody and wing-body-strake (LEX) portion of the airplane. Emphasis has been placed on this region based on previous experience with the F-18 (reference 9) which showed the forebody/LEX region to dominate the high-alpha lateral-directional aerodynamics. To date, CFD math models have been developed and calculations made only for this forward portion (from the wing-body juncture forward) of the HARV airframe. Analysis is in progress to correlate these results and to provide insight into understanding the data discrepancies observed in predicting the F-18 high-alpha aerodynamics as noted in reference 9. Additionally, emphasis is being placed on defining improved methods for subscale wind-tunnel testing at high alphas to better simulate full-scale flows.

Comparisons of forebody/LEX surface flows are shown in figure 25 for wind-tunnel scale model results (16-percent scale) and flight results. These results indicate what appears to be a fully turbulent flow on the airplane versus a transitional flow on the model. However, the location of the primary flow separation lines on the forebody and LEX seem to be in close agreement between the airplane and the model. Comparison of the total force and moment aerodynamics measured on this model with similar results extracted from parameter identification analysis of flight data shows substantial agreement despite these noticeable differences in the surface flow patterns. Further analysis is needed to understand the significance of these differences in surface flow patterns as well as the differences noted between different size subscale models at equivalent total Reynolds numbers. Dramatic visualization of the off-surface flows has been obtained in flight showing the forebody and LEX vortices and their interaction in the angle-of-attack region near maximum lift. These results are being compared with wind tunnel and CFD predictions both qualitatively and quantitatively.

A valuable tool in correlation and analysis of these results has been the CFD results developed at Langley and Ames. As shown in figure 26, results predicted using a fully turbulent Navier-Stokes

prediction method (reference 14) appear strikingly similar to the patterns observed on the airplane. Such results are providing increased confidence that these CFD tools can be used to understand principal features in the airplane flowfields and to help in sorting out differences observed in subscale wind-tunnel results. The CFD models in use are currently being extended to model the complete HARV configuration. Until predictions are obtained from these complete models, comparisons of available flight data and predictions as shown in figure 27, while encouraging, may be expected to show differences until the full configuration is properly modelled. As CFD methods applicable to the high-alpha regime continue to mature and become easier to set up and run for specific geometries, they will be applied in exploring advanced airframe features to provide desired levels of stability and control.

The final inflight measurements scheduled for Phase I will be the detailed surface pressure measurements on the HARV forebody and LEX. These results will be obtained during the summer and fall of 1989. Other ground-to-flight correlation work has included studies of tail buffet and correlation of vortex burst locations for the wing-body-strake vortex.

Other important activities in the HATP have included efforts to expand the research capabilities of the HARV and ground-based work to prepare flight experiments for Phase II and III. Several alternate air data sensors concepts have been explored for providing reliable measurements of airspeed and angles of attack and sideslip at extreme angles of attack and low airspeeds--such measurements are essential for operation of effective flight control laws at these conditions. Wind-tunnel tests have been conducted to support the development of the thrust-vectoring system for the HARV. Piloted simulations are in progress exploring the use of this vectoring capability and the effectiveness of advanced aerodynamic control concepts as described next in this paper. Ground-based analysis and piloted simulation work on controls, guidance, and PVI areas are well underway and expected to lead to new methods and concepts for flight validation in the next several years.

Controls Research

As noted already, operation at high alphas is greatly dependent on having effective controls to stabilize the airplane and execute the tactical maneuvers needed. The HATP is stressing research in controls for the high-alpha regime and addressing both powered controls, such as blowing for boundary-layer control and thrust-vectoring, and advanced aerodynamic control concepts. The approach being used in the HATP high-alpha controls technology is to develop a sound definition of the levels of control power needed in realistic scenarios and to then develop and validate options to provide the control needed.

Achieving the desired levels of control effectiveness at high angles of attack, as noted in the introduction, with conventional aerodynamic controls is difficult due to extensive flow separation and breakdown that occur at these conditions. For example, rudders typically lose their effectiveness due to being immersed in the low energy separated wake of the wing and fuselage, as illustrated in figure 28. However, as discussed earlier, yaw control requirements to maintain roll coordination actually increase with increasing angle of attack. Thus, an "ideal" yaw control device would have characteristics similar to those shown by the dashed curve. Vectoring of the engine thrust is a very promising method for achieving the desired control capability. As shown by the square symbols, 10 degrees of vectoring on a typical current fighter airplane matches or exceeds the effectiveness of the "ideal" control at the low-speed flight condition. Because of this potential, extensive thrust vectoring controls research has been conducted in a number of wind-tunnel and simulation facilities at Langley. The results have verified the potentially large payoffs of this technology (See reference 4.) and have been used to develop the TVCS for the HARV. The oral version of this paper will present a brief video to illustrate these results. The TVCS will be used to explore tactically significant high-alpha maneuvers and to define the levels of control power needed in these maneuvers.

Parallel research activities are also being conducted to explore and develop advanced aerodynamic control concepts with effectiveness characteristics approaching the "ideal" shown in figure 28. These efforts are spurred by the potentially large payoffs offered by these concepts, particularly at the higher speed maneuvering conditions as illustrated in figure 29. Plotted are the yaw acceleration capability versus Mach for a typical fighter airplane provided by 10 degrees of yaw thrust vectoring and the "ideal" aerodynamic yaw control at $\alpha = 35$ degrees and $h = 20,000$ feet. The data show that at low airspeeds (Mach < 0.3), the propulsive control is much more effective because of the low dynamic pressures at these conditions. However, at higher airspeeds corresponding to the region near corner velocity (M = 0.6 to 0.7), the "ideal" aerodynamic control provides much higher control capability. Thus, it may be that a combination of thrust vectoring and

highly effective aerodynamic controls will provide the desired high level of control effectiveness over the complete maneuvering flight regime.

The strong vortex flows generated by the slender forebodies and wing-body-strakes of current and future fighter airplanes at high angles of attack (as evident in figure 4) offer an attractive opportunity to generate large aerodynamic control forces and moments (due to the long moment arm from the center of gravity) if effective means for controlling these vortices can be developed. Several very promising control concepts have been identified in wind-tunnel tests of research models and are illustrated in figure 30. Variable incidence wing-body strakes can produce large pitch and roll control moments at high angles of attack. Actuated forebody strakes and nose blowing have been shown to be highly effective yaw control devices at stall and post-stall conditions (references 15 and 16). Each of these concepts is being considered for flight testing on the HARV with the initial focus being placed on the actuated forebody strake concept.

Extensive exploratory wind-tunnel tests have been conducted on the actuated forebody strake concept using generic fighter models. An example result which illustrates the concept and its effectiveness is presented in figure 31. In this implementation, strakes on either side of the forebody would deflect individually from their conformal positions depending on the direction of the yaw control required. Analysis of the resulting flow behavior shows that the strake acts as a spoiler by pushing the vortex away from the forebody and thus reducing the suction pressure on that side; at the same time, the vortex on the opposite side moves closer to the surface hence increasing the suction pressure. The combination of reduced suction pressure on the strake side and increased suction pressure on the other side produces a net side force in the direction opposite the strake. As shown in the figure, the resulting moment can be very large at stall and post-stall angles of attack. It is interesting to note that combining the rudder and forebody strake results in a yaw control with characteristics approaching those of the "ideal" aerodynamic device shown earlier in figure 28.

The actuated forebody strake concept has been adapted to the HARV configuration and extensive wind-tunnel testing has been conducted using a 0.16-scale dynamic model (figure 32). Static force and moment data show high levels of yaw control similar to those obtained on the generic models. The high-alpha control capabilities provided by these characteristics were studied by conducting tethered free-flight tests of the model in the Langley 30- by 60-Foot Tunnel (figure 33). The results demonstrate dramatically enhanced controllability at low-speed, high-alpha flight conditions as compared to the baseline configuration with only the rudders for yaw control. Piloted simulation studies show even larger payoffs at higher speed maneuvering conditions as suggested earlier in figure 29.

Based on these promising results, plans have been developed to carry the actuated forebody control concept to full-scale flight tests on the HARV. The overall process is illustrated in figure 34. Additional experimental and analytical studies are underway to further understanding and refinement of the strake aerodynamics. Wind-tunnel tests are investigating Reynolds number and Mach number effects and the impact of the strakes on aerodynamic damping characteristics. The HARV forebody with conformal strakes has been modeled for performing aerodynamic predictions using advanced Navier-Stokes codes and preliminary calculations correlate well with experimental results. An engineering feasibility study is being completed to establish approaches for implementation on the HARV and to define constraints on strake size, shape, and location. The combined results from all of these studies will provide the basis for development of the final strake design to be flight tested. This design will then undergo a comprehensive series of wind tunnel tests, CFD analysis, and piloted studies leading to implementation and flight testing on the HARV. This systematic use of a matrix of experimental and analytical tools will assure maximum effectiveness of the flight program. The flight results will, in turn, serve to validate these tools so that they can be applied with confidence to new airplane designs. The current schedule calls for HARV flight tests of the actuated forebody strakes to begin in mid-1992.

CONCLUDING REMARKS

The NASA (See figure 35.) has embarked on an aggressive technology development program to provide flight validated methods and concepts for use in the development of future fighter aircraft. The approach and content of the program is derived from many years of experience in solving the high-alpha problems of developing new aircraft designs. Program scope is set to include key facets of R and D involved in advanced aircraft development, including wind-tunnel, CFD, simulation, and flight tests. The goal of the program is to obtain substantial improvements in the capabilities of each of these key tools for high-alpha predictions and to thereby support the development of

improved design methods by industry. Additionally, the program seeks to define the increased high-alpha maneuverability afforded by control power augmentation via thrust-vectoring and advanced aerodynamic control concepts.

Program results to date are confirming the expectations that indepth aerodynamic measurements could be obtained and correlated with coordinated ground tests and analysis to improve the understanding of the complex, nonlinear flows encountered at high angles of attack. A high level of interest has developed among NASA researchers in each of the technology thrusts--the program is viewed as offering a unique opportunity for full-scale method and concept verification. Current progress indicates the HARV will be equipped with the TVCS and the RFCS to provide an greatly expanded flight envelope during the first half of 1990.

The HATP presents a unique and unprecedented opportunity to explore high-alpha flight control technology. The multi-axis thrust-vectoring system and the RFCS being implemented in the HARV will allow full-scale verification of the substantial high-alpha maneuverability improvements predicted in simulation to date. Equally important, the program will develop new concepts for improved high-alpha control and will provide validation of the methods needed to apply such new ideas as well as flight demonstration of the effectiveness of such innovative concepts such as the actuated forebody strake.

REFERENCES

1. Chambers, J.R.: High-Angle-of-Attack Aerodynamics: Lessons Learned. AIAA Paper No. 86-1774-CP, June 1986.
2. Nguyen, L.T.; Gilbert, W. P.; and Ogburn, M. E.: Control-System Techniques for Improved Departure/Spin Resistance for Fighter Aircraft. NASA TP 1689, August 1980.
3. Dollyhigh, S.M.; and Foss, W. E., Jr.: The Impact of Technology on Fighter Aircraft Requirements. SAE TP 851841, October 1985.
4. Ogburn, M. E.; et. al.: Simulation Study of Flight Dynamics of a Fighter Configuration with Thrust-Vectoring Controls at Low Speeds and High Angles of Attack. NASA TP 2750 (Confidential), March 1988.
5. Herbst, W. B.: Supermaneuverability. DGLR 83-106, S/PUB/120, October 1983.
6. Roberts, F. D.: The F-15 STOL and Maneuver Technology Demonstrator (S/MTD) Program. SAE 87-2383, Dec. 1987.
7. Sluru, Bill: Agile Aircraft: The Search for Supermaneuverability. Mechanical Engr., Dec. 1988, page 28.
8. Hammett, L. N., Jr.: An Investigation of the F-16 High-Angle-of-Attack Pitching-Moment Discrepancy. Technical Report AFWAL-TR-81-3107.
9. Erickson, Gary E.: Water Tunnel Flow Visualization and Wind-Tunnel Data Analysis of the F/A-18. NASA CR 165859, May 1982.
10. Lacey, David W.; and Murphy, Richard D.: Jet-Engine Thrust Turning by the Use of Small Externally Mounted Vanes. DTNSRDC-82/080, U. S. Navy, Jan. 1983.
11. Carr, P. C.; and Gilbert, W. P.: Effects of Fuselage Forebody Geometry on The Low-Speed Lateral-Directional Characteristics of Twin-Tail Fighter Model at High Angles of Attack. NASA TP-1592, Dec. 1979.
12. Brandon, J. M.; and Nguyen, L. T.: Experimental Study of Effects of Forebody Geometry on High-Angle-of-Attack Static and Dynamic Stability. AIAA-86-0331, Jan. 1986.
13. Fisher, David F.; Richwine, D.M.; and Banks, D.W.: Surface Flow Visualization of Separated Flows on the Forebody of an F-18 Aircraft and Wind-Tunnel Model. NASA TM-100436, June 1988.

14. Thomas, J. L.; et. al.: A Patched-Grid Algorithm for Complex Configurations Directed Towards the F/A-18 Aircraft. AIAA-89-0121, Jan. 1989.
15. Rao, D. M.; Moskovitz, Cary; and Murri, D. G.: Forebody Vortex Management for Yaw Control at High Angles of Attack. Journal of Aircraft, Vol. 24, No. 4, Pages 248-254, April 1987.
16. Skow, A. M.; et. al.: Forebody Vortex Blowing-A Novel Control Concept to Enhance Departure/Spin Recovery Characteristics of Fighter and Trainer Aircraft. AGARD CP No. 262, Paper No. 24, 1979.

USAF	
F-4	43
F-5	7
F-111	11
F-15	10
F-16	5
<hr/>	
TOTAL	76

Service total: 177 Aircraft

Figure 1.- Stall/spin losses.

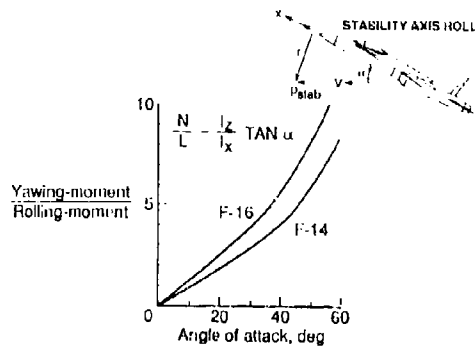


Figure 2.- High-alpha yaw control requirement for roll coordination.

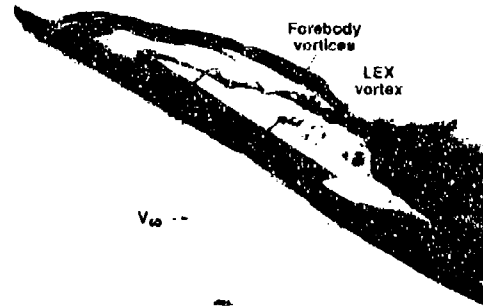


Figure 4.- High-alpha flow over model in water tunnel.

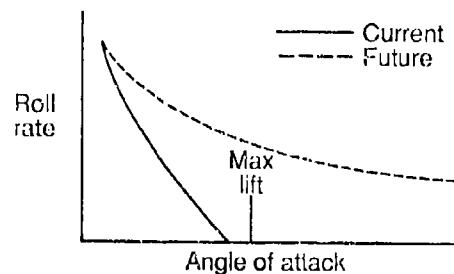


Figure 5.- Opportunity for envelope expansion.

THE PROBLEM

- Complex aerodynamics and lack of design methods
- Maneuver limitations and degraded performance

IMPACT OF EMERGING TECHNOLOGIES

- Highly lethal all-aspect weapons demand unprecedented agility
- New technologies enable use of high alpha:

- Thrust vectoring concepts
- Aerodynamic design methods
- High T/W
- Advanced controls and guidance

THE OPPORTUNITY

- Provide technology for revolutionary fighter capabilities
- Remove the traditional *Stall Barrier*

Figure 3.- The high-alpha problem and opportunity for fighters.

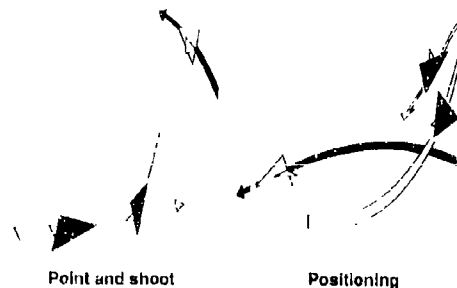


Figure 6. Maneuver options with improved high-alpha behavior.

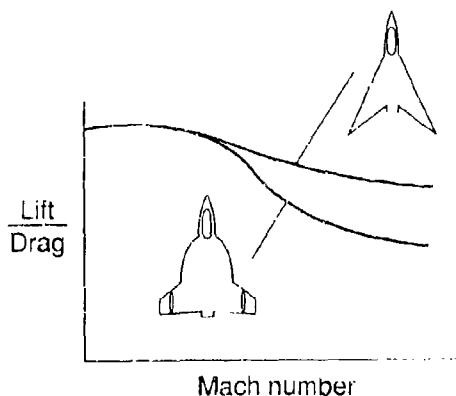


Figure 7.- Opportunity for performance gains via configuration.

- Provide flight validated high-alpha prediction/analysis methods for superior design methods
- Enable expanded high alpha maneuverability and flight envelopes

Figure 8.- HATP objectives.



Figure 9.- The High-Alpha Research Vehicle (HARV).

Advantages of F-16 as High Alpha Research Vehicle (HARV)

- Exceptional high alpha capability ($\alpha > 55^\circ$)
- Satisfactory spin recovery behavior
- Outstanding engine reliability
- Versatile digital flight controls with separable surfaces
- Exhibits aerodynamic phenomena of interest:
 - Vortex flows
 - Forebody/wing interactions
 - Wing Rock
- Large aero data base exists
- Availability of high alpha test airplane with emergency spin recovery systems

Figure 10.- Selection rationale for HARV.



Figure 11.- Artists concept of HARV with TVCS.

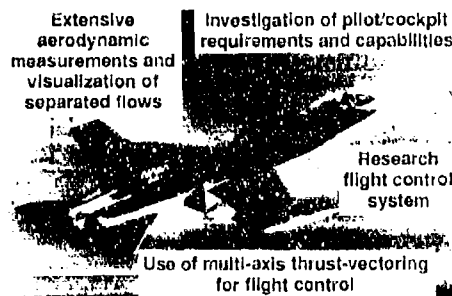


Figure 12.- HARV research capabilities.

HATP SCOPE AND APPROACH

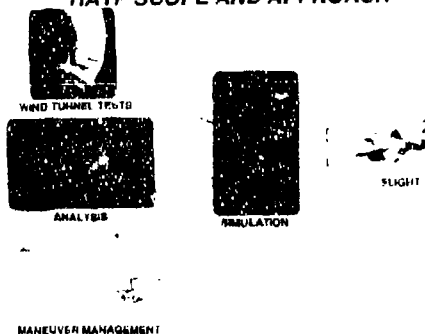


Figure 13.- HATP scope and approach.

AERODYNAMICS	ADVANCED CONTROLS	MANEUVER MANAGEMENT
<ul style="list-style-type: none"> ● Forebody flows <ul style="list-style-type: none"> - Unsteady flow - Separation control - Shaping ● Vortex flows <ul style="list-style-type: none"> - Formation - Position and strength - Interactions - Breakdown ● Configuration area <ul style="list-style-type: none"> - Forward flow interaction - Tail fin flow - Dynamic stall - Wing rock 	<ul style="list-style-type: none"> ● Aerodynamic control <ul style="list-style-type: none"> - Forebody controls - Movable FLX ● Propulsive control <ul style="list-style-type: none"> - Thrust vectoring - Control levels - Integration - Interf. zero ● Control design <ul style="list-style-type: none"> - Blending - Optimum response 	<ul style="list-style-type: none"> ● Agility metrics <ul style="list-style-type: none"> - Nose pointing - Unpredictability ● Handling qualities <ul style="list-style-type: none"> - Response criteria ● Guidance <ul style="list-style-type: none"> - Maneuvers ● Displays <ul style="list-style-type: none"> - Helmet mounted - Advisory ● Expert systems <ul style="list-style-type: none"> - Maneuver decision - Attack engineering - Advanced displays

Figure 14.- HATP key technology areas.

FLIGHT PHASES AND SCHEDULE

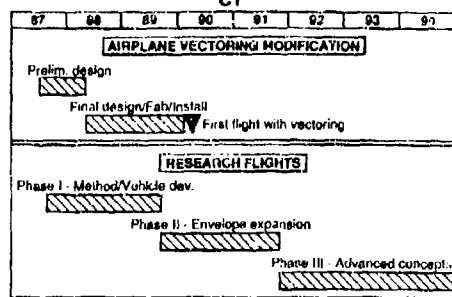


Figure 15.- HATP principal phases.

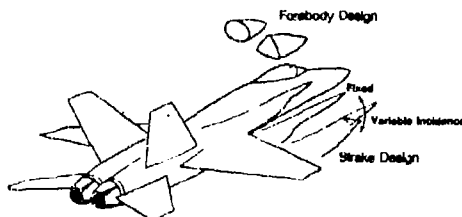


Figure 16.- Possible future aerodynamic and control experiments.

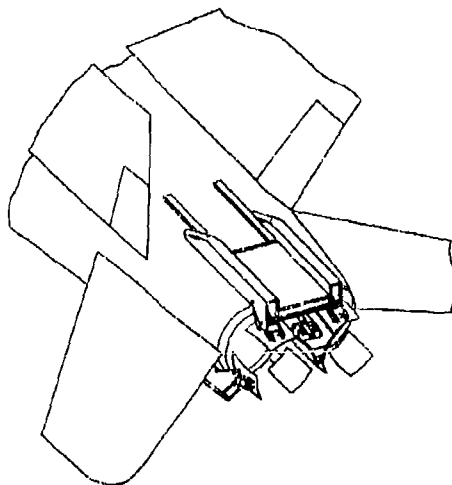


Figure 17.- Installation sketch of HARV tuning vanes.

● Data acquisition system

- 2 telemetry systems with 700 total measurements including 500 surface pressures
- 5 video cameras; 2 radiated, 2 recorded onboard in VHS
- 2 35mm stereo still cameras

● Flow visualization systems

- Smoke generator system
 - + 12 cartridges, 20-40 sec each
 - + 4 ports, 2 at a time
- Surface flow visualization
 - + Dyed PGME
 - + Emitted through pressure ports on forebody and LEX
 - + One point per flight

Figure 18.- HARV research instrumentation and flow visualization systems.

● Air data system

- Fixed NACA probe on right wingtip
- Swiveling pilot probe on left wingtip
- Alpha and beta vanes on both wingtips
- Flush Air Data System (FADS) on nose

● Maneuver Guidance

- Uses analog pointer and ILS cross hair as display
- Uplink error signal as pilot command

● Emergency systems

- Battery pack in gun bay provides 15 minutes of electrical and hydraulic power, both engines off line
- Fuel boost for engine start
- Spin recovery parachute

Figure 19.- HARV research subsystems and emergency system.

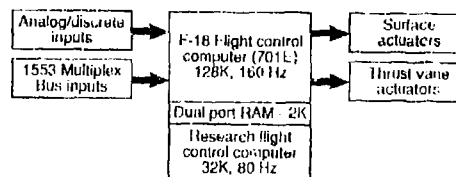
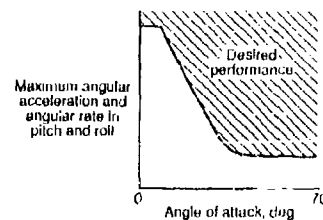


Figure 20.- Relation of HARV FCC and F11 CS.



- Maximum time to reach peak acceleration and rate
- Time to bank 90° (wind axes)
- 1-g and accelerated (Mach ~ 0.6)

Figure 21.- Manuevar specifications for HARV with TVCS.

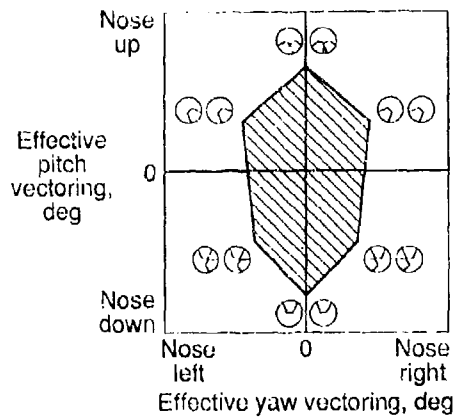


Figure 22.- Typical two nozzle average jet turning envelope.

- Integration of high fidelity ground-based simulations with flight programs
 - Careful simulator validation; used for flight plans
 - Simulation with and without hardware-in-the-loop
- Flight tests organized in test blocks, e.g.
 - Ground tests of TVCS
 - Airworthiness of HARV with TVCS
 - Clearance of TVCS envelope (low and high speed)
 - Exploration of HARV TVCS maneuver capabilities
- Safety and test control by Dryden Flight Facility

Figure 23.- NASA high-alpha flight research approach.

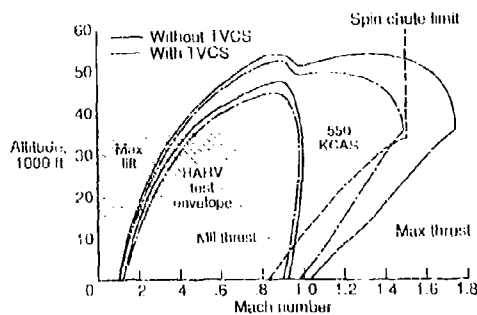


Figure 24.- HARV flight envelopes.

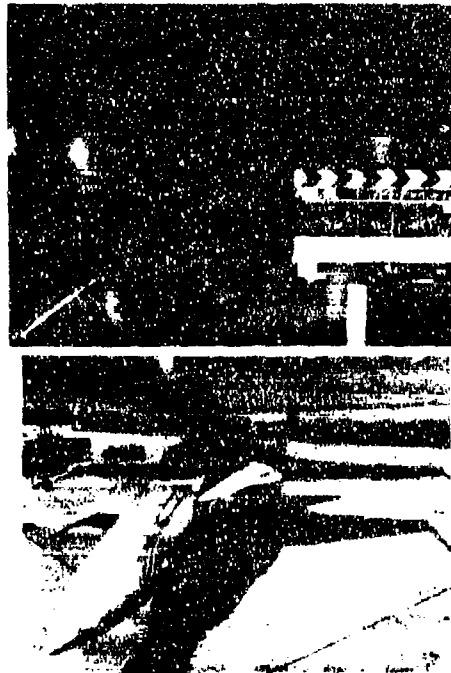


Figure 25.- Comparison of tunnel and flight surface flows near 35° angle of attack (model Reynolds number of $\approx 10^6$ versus flight of $\approx 10^7$).



Figure 26.- Correlation of CFD and flight surface flows at $\alpha = 30^\circ$, Reynolds number $\approx 10^7$, Mach = 0.3.

Aerodynamics
Typical Off-Surface (Vortex) CFD to Flight Comparison

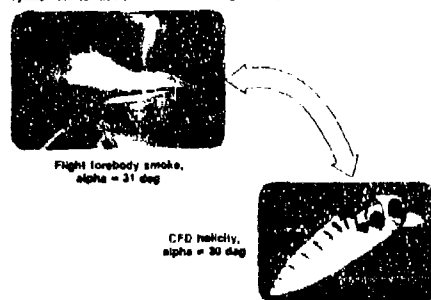


Figure 27.- Correlation of CFD and flight off-surface flows.

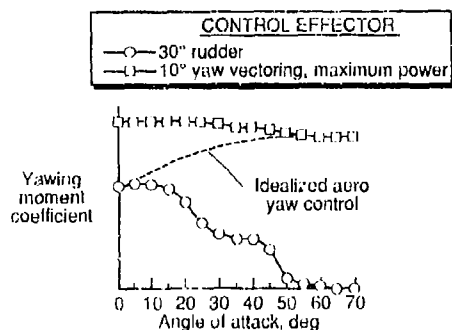


Figure 28.- Low-speed yaw control effectiveness.

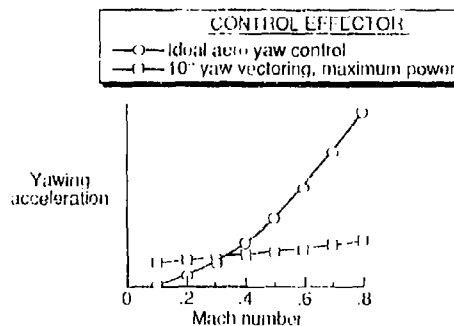


Figure 29.- Yaw control capability near maximum lift versus Mach number.

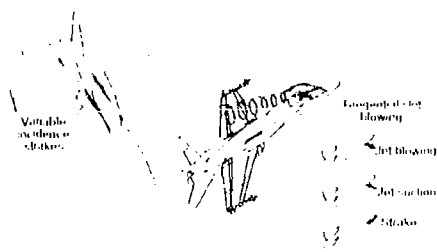


Figure 30.- Vortex flow control concepts.

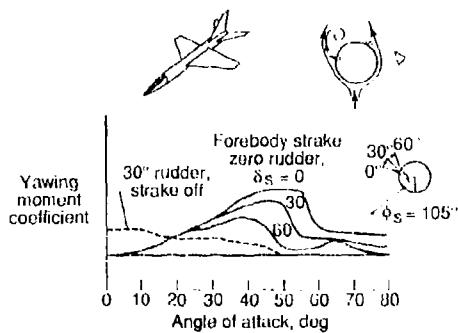


Figure 31.- Forebody strake control characteristics.



Figure 32.- Free-flight model with forebody strake controls.

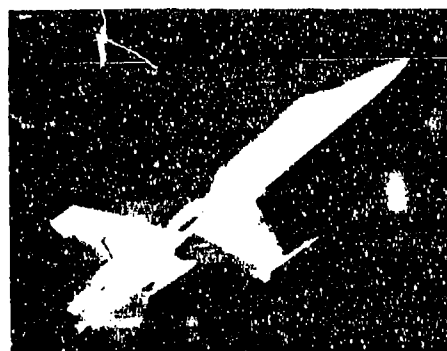


Figure 33.- Free-flight tests with forebody strake controls.

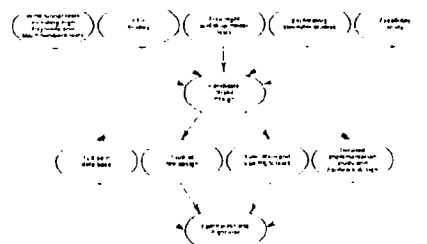


Figure 34.- Forebody strake controls research approach.

- NASA HATP an aggressive technology development effort
- Scoped to improve key prediction methods to provide reliable design methods
- Excellent research team providing exciting results
- Program a unique and unprecedented opportunity to explore high-alpha flight control technology

Figure 35.- Summary remarks.

COMBAT AIRCRAFT CONTROL REQUIREMENTS FOR AGILITY

by

Joseph R. Chody, John Hodgkinson and Andrew M. Skow
 Eidetics International, Inc.
 3415 Lomita Blvd.
 Torrance, CA 90505-5010
 United States

SUMMARY

The positive effect of increased aircraft agility on air-to-air combat effectiveness has created a need to quantify the impact of preliminary design decisions on the agility potential of candidate aerodynamic configurations. Recently developed measures of agility can provide an important supplement to traditional energy maneuverability measures like specific excess power and turn rate. The very nature of agility, characterized by the combination of traditional energy maneuverability plus controllability, places additional controllability and departure resistance requirements on the aircraft design. The major purpose of this paper is to highlight specific issues of aircraft controllability that require close attention during the preliminary design process. This will help ensure that the agility potential of the final configuration is not compromised at some point in the design process due to inadvertent oversight. Methods for estimating agility potential early in the design process are given as well as extensions of currently used departure susceptibility prediction techniques. The paper begins by giving a brief synopsis of agility from a historical standpoint and discussing several agility measures of merit currently being used. The benefits of improved lateral agility are illustrated by mapping potential lateral agility improvements as a function of angle of attack onto a typical energy-maneuverability envelope showing regions of enhanced combat capability.

SYMBOLS

V	Total velocity
g	Acceleration due to gravity
q	Dynamic pressure
S	Wing area
b	Wing span
c	Wing mean aerodynamic chord
P	Angular rate component about X-body axis
Q	Angular rate component about Y-body axis
R	Angular rate component about Z-body axis
L	Rolling moment about X-body axis
M	Pitching moment about Y-body axis
N	Yawing moment about Z-body axis
I _x	Moment of inertia about X-body axis
I _y	Moment of inertia about Y-body axis
I _z	Moment of inertia about Z-body axis
I _{xz}	Product of inertia about X- and Z-body axes
α	Angle of attack (AOA)
β	Angle of sideslip
θ	Pitch angle

ϕ	Bank angle
ψ	Heading angle
C_L	Non-dimensional lift coefficient \Rightarrow Lift/qS
C_l	Non-dimensional rolling moment coefficient L/qSb
C_m	Non-dimensional pitching moment coefficient M/qSc
C_n	Non-dimensional yawing moment coefficient N/qSb
C_{n0}	Asymmetric ($\beta = 0^\circ$) yawing moment coefficient
$C_{n\beta}$	Change in non-dimensional yawing moment coefficient WRT sideslip
$C_{l\beta}$	Change in non-dimensional rolling moment coefficient WRT sideslip
$C_{l\delta_A}$	Rolling moment due to aileron deflection (δ_A)
$C_{n\delta_A}$	Yawing moment due to aileron deflection
$C_{n\beta_{DYN}}$	$C_{n\beta} \cos \alpha + l_z/l_x (C_{l\beta}) \sin \alpha$ -- Bare airframe
$LCDP$	$C_{n\beta} - C_{n\delta_A}/C_{l\delta_A} (C_{l\beta})$ -- Bare airframe
C_{lp}	Change in rolling moment coefficient due to roll rate
C_{lr}	Change in rolling moment coefficient due to yaw rate
C_{np}	Change in yawing moment coefficient due to roll rate
C_{nr}	Change in yawing moment coefficient due to yaw rate
L_β	Dimensional rolling moment derivative WRT sideslip
N_β	Dimensional yawing moment derivative WRT sideslip
$N_{\beta_{stab}}$	Stability axis $N_\beta = N_{\beta} \cos \alpha + L_\beta \sin \alpha$
L_p	Dimensional rolling moment derivative WRT roll rate
L_r	Dimensional rolling moment derivative WRT yaw rate
N_p	Dimensional yawing moment derivative WRT roll rate
N_r	Dimensional yawing moment derivative WRT yaw rate
L_{δ_A}	Dimensional rolling moment derivative WRT aileron deflection
N_{δ_A}	Dimensional yawing moment derivative WRT aileron deflection
τ_R	Roll mode time constant
t_f	Time required for full deflection ramp input (δ/δ)
ω_ϕ	Frequency of numerator quadratic of ϕ/δ_A transfer function
ω_D	Dutch roll frequency
(\cdot)	Derivative WRT time
$(\cdot)_0$	Initial value
$(\cdot)_{ramp}$	Parameter response to ramp input
$(\cdot)_{step}$	Parameter response to step input
$(\cdot)_{max}$	Maximum achievable value
$(\cdot)_{EQ}$	Equivalent value
$(\cdot)_{IC}$	Effect of inertial coupling

1.0 THE NEED FOR AGILITY

1.1 Historical Background

A general definition of agility is: "The ability to orient the state vector of the aircraft rapidly and precisely." Prior to the mid 1960's, the combat effectiveness of aircraft was traditionally measured using point performance data. As a result of the work of Col. John Boyd and Mr. Tom Christie, energy maneuverability, an element of agility, has become the current standard measure for comparison. Energy maneuverability, a steady-state quantity, can be graphically displayed as a plot of specific excess power against turn rate, or as turn rate vs. speed or Mach number (Fig. 1). These plots are defined by configuration characteristics like the maximum lift capability of the aircraft at low speeds and by its structural limits at high speeds. The control response of the aircraft does not directly affect its energy maneuverability, which is more a measure of structural, aerodynamic and propulsive efficiency.

From the beginnings of aerial combat, however, the transient control response of the aircraft, its agility, has been part of the lexicon of pilots, in spite of its omission from energy maneuverability analysis. There have been many references to the value of unpredictability and to the element of surprise that accrue to the pilot of an agile aircraft. These qualities were part of the effectiveness of the Fokker Dr 1 vs. the Royal Aircraft Factory S.E.5a and the Focke-Wulf 190 vs. the early Vickers-Supermarine Spitfire, to mention examples from the two World Wars. For these examples, conventional combinations of aircraft configuration and control effectiveness (stability and control, if you like), were the enabling technologies for agility. The Fokker Dr 1 was inferior to the S.E.5 in conventional performance but with its superior flying qualities, was able to defeat S.E.5 opponents even when outnumbered (Refs. 1 and 2). In the case of the Spitfire, its excellent maneuvering aerodynamic efficiency was not sufficient to counter the superior roll agility of the FW 190. Adoption of clipped wings in the later Mark Spitfires allowed better roll control response without modifying the aileron control itself.

Experiences from the Korean, Vietnam, and Falkland wars also confirmed the value of agility on more modern aircraft. For reasons of space, they will not be repeated here, however, the general lessons of earlier conflicts still apply (Ref. 2).

1.2 The Present Need for Agility

Agility has also continued to attract attention and be a feature of current fighter aircraft, including Soviet designs (Ref. 3), so there has always been a need for agility. Today there is increasing recognition of that need because of emerging combat imperatives that may increasingly stress within-visual-range (WVR) combat. Though beyond-visual-range (BVR) combat is naturally preferred by whoever has the advantage, it is not always possible to remain BVR. Once WVR combat is entered, escape is difficult because air-to-air missiles are highly lethal against a close-in adversary who tries to turn away from the battle and run. So, WVR combat is a kill-or-be-killed situation whose outcome can be decided by the quick shot opportunities created by high levels of agility. Other developments favor WVR engagements; the all-aspect missile allows transient snapshots; low observables technology increases the possibility of an inadvertent encounter with a stealthy adversary, with a WVR engagement resulting; rules of engagement can call for visual identification and limited missile supplies mean that in a protracted war, close-in gunshots may soon become the only option left to a surviving pilot.

With this background, it can be seen that agility measures would be valuable supplements to the point performance and energy maneuverability methods of comparing configuration design choices, even in preliminary design.

1.3 Near Term Improvements in Combat Agility Using Existing Technology

The agility-dominated combat of WVR engagements involves frequent excursions to high angles of attack. This is to take advantage of shot opportunities with guns or all-aspect missiles, as well as to perform maneuvers to evade missiles. The pilot in these circumstances has elected to lose, or bleed, energy for the sake of an advantage that briefly presents itself. Many aircraft have been capable of transient flight, without loss of control, beyond the angle of attack for maximum lift coefficient (CL_{max}). However, to control aircraft attitude with the rapidity and precision needed to be effective, new control

* Energy maneuverability is sometimes referred to as a form of agility. In this paper, we are discussing more recent developments in transient agility.

concepts are required. These concepts are the enabling technologies that allow us to examine the potential of new levels of transient agility and eventually of "superagility" or "supermaneuverability."

Recent developments in high angle-of-attack (AOA) control power technologies such as Thrust Vectoring for Control (TVC) and Vortex Manipulation for Control (VMC) have made controllable flight at AOA's at and above C_{Lmax} possible. This includes two principal effects (Fig. 2):

- 1) The maximum AOA range up to which the aircraft can be flown with precision can be increased from current levels of 25° to 30° up to perhaps 60° to 70° .
- 2) The loaded roll capability of the aircraft, i.e., its ability to roll with precision about its velocity vector at elevated load factor or AOA's, can be increased.

To illustrate the correlation between enhanced controllability and enhanced maneuverability as used in the combat environment, Fig. 3 shows EFM "mapped" in a controllability domain and in the traditional energy-maneuverability (EM) domain. The only additional control features required for current aircraft to achieve these EFM enhancements are:

- 1) Increased nose-down pitch control power at stall/post-stall AOA's.
- 2) Increased yaw control power at near-stall/stall/post-stall AOA's.

The benefit of maneuvering at very high AOA has been demonstrated anecdotally from combat experience and via analyses in, for example, Refs. 12 through 14. These combat analyses have demonstrated the benefit of loaded rolling as discussed below.

1.4 Recent Combat Analysis Results

Under contract to the USAF Aeronautical Systems Division (ASD), Eidetics has recently completed a study which quantified the combat effectiveness of agility using digital air combat simulation (Ref. 4) analysis. In this study "nominal" Red aircraft were flown against "enhanced agility" Blue aircraft in close-in air combat with varying scenario sizes ranging from 1v1 to 2v2 and 4v4. Conservative (high speed) tactics were employed in the simulation with no maneuvering below 400 KIAS. Both forces were equipped with all-aspect AIM-9L missiles.

The simulation results, summarized in Figs. 4a & 4b (Ref. 5), show that enhanced agility produced a combat effectiveness increment roughly equivalent to the increment derived from a 30% increase in thrust plus a 23% decrease in wing loading. It is important to note that the agility enhancements were limited in our model to those that would be achievable through conventional controls technology. Further, the simulation results show that lateral (torsional) agility was found to be nearly twice as significant in improving combat effectiveness as either pitch or axial agility. For this reason, much of this paper will focus on lateral agility.

We can summarize the above by pointing out first that agility has always been important, and today, this is no less true, according to combat experience and to recent analyses. Second, because the fundamental balance between stability and control defines agility, we would expect to re-examine this balance as we evaluate new control devices, stability and control criteria, and test methods. In the following, we will amplify this second point.

2.0 CONSIDERING AGILITY IN THE DESIGN PROCESS

There is no shortage of engineering definitions of agility, ranging from highly theoretical concepts to easily-measured flight test measures (Refs. 7-11). The quantification techniques shown in Fig. 5 (Refs. 2 and 6) have been developed by Eidetics to compare aircraft response characteristics in essentially all the aircraft degrees of freedom. Whatever the definition, it is intuitively obvious that control power is of primary importance in defining initial response, and so, control effector performance at maneuvering angles of attack to a great extent establishes agility.

2.1 The Additional Control Power Requirements for Agile Maneuvering

To consider agility in design means that controllability must be considered early in the design and to a greater extent than is the current practice. For example, when specifying control surface rate requirements, the emphasis has been traditionally placed on the terminal flight phases (takeoff and powered approach) where low dynamic pressure and the tight tracking type requirements combine with potentially adverse atmospheric conditions (gusts, crosswinds, wind shears, etc.) to create a very

demanding controllability problem. However, the rapid initial response required when maneuvering at high AOA produces even greater demands in an equally demanding environment. Also, the aircraft rotation rates and attitudes are at much higher values in maneuvering flight and create additional factors that need to be considered when analyzing control power requirements.

As an example, the two main control power considerations for agile maneuvering are the control of pitch and yaw acceleration while maintaining angles of attack where aerodynamic pitch and yaw control power are greatly reduced. Roll control is also important but body axis roll control power is not a key limiting factor. To illustrate, consider the pitch (\dot{Q}) and yaw (\dot{R}) acceleration equations as shown below:

$$\begin{aligned}\dot{Q} &= \frac{M}{I_y} + \frac{I_z - I_x}{I_y} PR + \frac{I_{xz}}{I_y} (R^2 - P^2) \\ &= \dot{Q}_{AERO} + \dot{Q}_{INERTIAL} \\ \dot{R} &= \frac{N}{I_z} + \frac{I_x - I_y}{I_z} PQ + \frac{I_{xz}}{I_z} (\dot{P} - QR) \\ &= \dot{R}_{AERO} + \dot{R}_{INERTIAL}\end{aligned}$$

To maintain control, the aerodynamic contribution to the above equations must be greater than the inertial coupling portion, as shown graphically in Figure 6. In this figure, we constrain the rolling motion to be about the stability axis, so that $R = P \tan \alpha$, and assume that the roll is initiated while performing a coordinated turn, so that $Q = \dot{\psi} \sin \phi$. The two lines shown on each figure represent two different sets of inertial characteristics. As illustrated, Configuration 1 would be control power limited at a lower AOA than Configuration 2. This could be representative of two fuel and/or store loadings for any particular aircraft.

Most aircraft exhibit some reduction of control power at high AOA which further exacerbates the inertial coupling problem. Figure 7 illustrates typical fighter characteristics as examples. Also shown on the figure are the critical AOA regions where control power should be enhanced. It is important to note that although we focus here on inertial coupling effects, the stability vs. control balance of the aerodynamic terms (\dot{Q}_{AERO} and \dot{R}_{AERO}) is what is ultimately important. For example, the contribution of the stability and damping derivatives, $C_{n\dot{\beta}}$ and C_{nr} , can influence the total restoring moment of the configuration as much as control power in overcoming the inertial effects. Our point is that total aircraft aerodynamics need to be considered when evaluating the acceptability of the control power capability.

It should also be noted that exceedance of the controllability limits discussed above does not necessarily imply that a departure will occur. If the aircraft is stable without augmentation, the aircraft could return to controlled flight.

2.2 The Need to Re-evaluate Current Stability Requirements

Closely associated with increased aircraft agility is the potential for increased departure susceptibility. Highly agile maneuvering has historically produced departures from controlled flight in many aircraft. Also, the availability of modern fly-by-wire control technologies have tended to give the modern aircraft designer a false sense of security -- i.e. "Don't worry, we'll fix it in the software!" Unfortunately, due to the controllability considerations mentioned previously, there is not always an over-abundance of control power with which to solve problems. Thus, there continues to be a great need to emphasize the importance of bare airframe stability at high AOA's where control power is especially limited and uncertain. For this reason, new techniques need to be developed which can be used early in the design process that will enable the designer to have a more accurate estimate of aircraft departure resistance. In Section 3 we discuss techniques which have been developed which have the potential to help fill this need.

2.3 The Need For Approximate Forms for Transient Agility Analysis

The agility of an aircraft depends on all the factors that define initial response. While the effectiveness of the control surface or device is the primary parameter, an aircraft's agility will also be affected by control laws, control surface limiting, and even unsteady aerodynamic effects and structural flexibility. These factors cannot be included accurately until there is a reasonably complete simulation of the aircraft and its flight control system -- usually too late in the design cycle to contemplate any major changes to the configuration, even if those changes would be beneficial. Preliminary designers

need a way of examining a configuration for which no simulation or control laws are yet developed and assessing its agility potential.

We have used a general concept called Equivalent Potential Agility (EPA) for this type of assessment. The word "equivalent" is used because we are approximating aircraft dynamics which can be very complex. The word "potential" reflects our need to know how much agility is inherent in the configuration even if that potential will not be realized until much later in the design cycle when appropriate control laws have been developed. The EPA concept uses the decoupling and linearization concepts of vehicle approximate factors (Ref. 25), the idealized feedback concepts of limiting forms (Ref. 26) and the order reduction concepts of equivalent systems (Ref. 27) while adding key nonlinearities (such as surface rate limits) that affect agility. Briefly, EPA estimates give insight into the fundamental aerodynamic parameters that govern the agility of a configuration. In the following discussion, we show how the EPA concept can be used to estimate the lateral agility of an advanced fighter aircraft. Various levels of estimation fidelity are also discussed to illustrate the flexibility of the concept.

2.4 Equivalent Potential Lateral Agility at High Angles of Attack

To quantify lateral agility (defined here as the time required to bank to $\phi = 90^\circ$ and stop) at high AOA's, the effect of rolling about the stability axis needs to be included in the analysis. To include the important effects of control surface rate, our EPA model of the time required to bank and stop the aircraft includes an input that is ramped in at a finite rate and then ramped out at the appropriate time. The remainder of the EPA form includes modal parameters and was developed using an inverse Laplace transform technique (Ref. 6):

$$1) \quad \phi_{90} = \phi_i + \frac{90}{P_{ss}} + \tau_R \ln \left[\frac{\dot{P}_{MAX} \tau_R}{10} \left(e^{10/P_{ss}} - e^{-90/\tau_R P_{ss}} \right) \right]$$

Where,

$$t_i = \text{time to get input in } \left(t_i = \frac{\delta_A}{\dot{\delta}_A} < \frac{(90 + 10\tau_R)}{P_{ss}} \right)$$

$$P_{ss} = L_{\delta_A} \delta_A \tau_R$$

$$2) \quad \dot{P}_{MAX} = \frac{P_{ss}}{t_i} (1 - e^{-t_i/\tau_R})$$

Equation 1) can be used to quantify the effect of changes in control power, control rate, and roll mode time constant of any preliminary design.

Another EPA method examines maximum roll acceleration capability (Equation 2 above). When a roll acceleration parameter (RAP) is defined as the ratio of the actual roll acceleration to a rate limited input to the roll acceleration to a perfect step input, i.e.:

$$RAP = \frac{\dot{P}_{MAXRAMP}}{\dot{P}_{MAXSTEP}} = \frac{\tau_R}{t_i (1 - e^{-t_i/\tau_R})}$$

RAP can then be plotted as a function of input time (Fig. 8) showing the effect of surface rate on the lateral EPA of the configuration.

To more closely represent the maneuvering capabilities of modern aircraft, the roll mode time constant, τ_R , should reflect stability axis rolling at high AOA's. Normally, the low AOA approximation, $\tau_R = -1/L_p$, is used in estimating roll dynamics but, as shown in Ref. 6, the EPA ϕ/δ_A transfer function for a stability axis roll with sideslip held to zero ($\beta = 0$) is:

$$\frac{\phi}{\delta_A} = \frac{L_{\delta_A}}{(S^2 - (L_p + L_T \tan \alpha) S - L_T g/V)}$$

Note that if L_T and AOA are small, the equation reduces to a first order roll response with $\tau_R = -1/L_p$. However, since L_T is a function of (among other things) the lift of the wing, the roll and spiral modes are no longer completely decoupled at high AOA giving rise to a new equivalent roll mode time constant.

At AOA's above 10° to 20° , an aerodynamicist might require a prediction of the lateral EPA, even if the rolling motion is not a "perfect" stability axis roll, i.e., ϕ/S_A sideslip is not zero. If, in fact, sideslip is not eliminated from the equation, the roll mode time constant can be approximated as:

$$\tau_R = \frac{-N_{\beta \text{ stab}}}{N_{\beta} L_{\Omega} \cdot L_{\beta} (N_{\Omega} - \frac{g \cos \alpha}{V})}$$

Where,

$$\begin{aligned} L_{\Omega} &= L_p \cos \alpha + L_r \sin \alpha \\ \& \quad N_{\Omega} &= N_p \cos \alpha + N_r \sin \alpha \end{aligned}$$

But even this approximation can be significantly in error if an aileron input excites the dutch roll mode of the vehicle (i.e., $\omega_{\phi}/\omega_D \neq 1$). Fortunately, further refinement of the approximation can be made to define an equivalent roll mode time constant (τ_{REQ}), as follows:

$$\frac{\tau_{REQ}}{(\tau_{REQ}S+1)} \sim \frac{\tau_R}{(\tau_RS+1)} \frac{S^2+2\zeta_{\phi}\omega_{\phi}S+\omega_{\phi}^2}{S^2+2\zeta_D\omega_DS+\omega_D^2}$$

$$\text{Where, } \tau_{REQ} = \tau_R \frac{\omega_{\phi}^2}{\omega_D^2} \sim \tau_R \frac{LCDP}{Cn_{\beta DYN}}$$

These different levels of EPA fidelity demonstrate that the EPA concept is flexible and can embrace different degrees of approximation depending on the amount of data available and the accuracy desired. In the case of lateral EPA as just discussed, equation 1) is used at all levels with only τ_R changing in computational complexity. Thus, the result is a relatively simple expression which can give a rough estimate of agility as well as yield insight into the influence of aerodynamic parameters on agility.

As an example of the use of lateral EPA, Fig. 9 shows flight test, simulation, and EPA predicted time to bank and stop data for a typical fighter aircraft. Method 1 uses the simple one degree of freedom ($\tau_R = -1/L_p$) estimation technique while Method 2 uses the three degree of freedom method ($\tau_R = \tau_{REQ}$). Note that, while the Method 1 estimate just gives a rough order of magnitude approximation, Method 2 is fairly accurate -- especially in predicting the trend as a function of AOA. The ultimate lateral agility of a configuration is obviously a function of many dynamic quantities, including flight control and structural effects. However, as can be seen from the figure, the lateral EPA estimate can yield a fairly accurate estimation of lateral agility without actually including these other effects.

3.0 PROPOSED NEW DESIGN METHODOLOGIES FOR EFM AIRCRAFT

Control criteria and stability criteria need to be evaluated together, but because controls always have some inherent limit, designers have usually begun by defining the stability of the configuration.

3.1 Lateral-Directional Stability Criteria

To take full advantage of recent advances in high AOA aerodynamic technologies, new preliminary design criteria need to be developed for assessing unaugmented departure resistance. For example, $Cn_{\beta DYN}$ and LCDP (Lateral Control Departure Parameter) were proposed in 1958 (Ref. 15) and established empirically as a prediction method by Weissman in 1972 (Ref. 16). The resulting Weissman Criterion specified regions on the plane of $Cn_{\beta DYN}$ and LCDP using flight data of a large group of aircraft, by calculating their levels of $Cn_{\beta DYN}$ and LCDP from wind tunnel data, and correlating these data with actual flight test behavior. Subsequent workers have modified the boundaries considerably to match emerging flight data. Figure 10 from Ref. 17 is an example, showing regions where correlation is "heavily affected by secondary factors," clear evidence that some key phenomena are missing from the criterion. In addition to these regions, there are many examples of current technology fighters and research aircraft whose behavior at high angles of attack were found in flight tests to be dramatically different from that predicted by $Cn_{\beta DYN}$ vs. LCDP. Reference 18 contains examples indicating that the Weissman boundaries are "configuration dependent" -- more evidence that the effects of some generic phenomena are missing.

In spite of its imperfections, the $C_{n\beta DYN}$ vs. LCDP plane continues to be used throughout the industry to predict susceptibility to lateral-directional departure and to aid designers in developing spin-resistant aircraft. The industry needs criteria that retain the simplicity of the $C_{n\beta DYN}$ vs. LCDP concept and yet which correlate better with modern aircraft characteristics.

3.2 Current Criteria Shortfall

In examining the substantiating data used by Weissman, we reviewed the characteristics of the aircraft that made up the data base, noting that they rarely maneuvered above 25° AOA, and possessed certain design features and characteristics that are substantially different from aircraft of the 70's and 80's. Table 1 lists differences between today's aircraft and those used by Weissman.

Table 1 - FIGHTER AIRCRAFT DESIGN CHARACTERISTICS

	50's - 60's	70's - 90's
CL_{max}	$17 - 23^\circ$	$30^\circ - 40^\circ$
CL_{Lmax}	Relatively Low	High
I_z/I_x	Med - High	High
Forebody Fineness (I/d)	2 - 2.5	4 - 6
Asymmetric Yawing Moment (C_{n0})	0 - 0.01	0.05 - 0.12
Directional Weathercock Stability ($C_{n\beta}$)	Dominated by aft located vertical tail	Dominated by forebody (nose/ l_{cx} */canard) vortices
Effect of Increasing $C_{n\beta}$ on Directional Damping (C_{nr})	Increased damping due to forces acting aft of aircraft CG	Decreased damping due to forces acting ahead of CG
Impact of Rotary Cross Derivatives (C_{lr} , C_{np})	Low due to relatively low CL_{Lmax}	High due to increased CL_{Lmax}

*Leading edge extension

Figure 11 points out that more modern configurations are dominated by nose vortices at high AOA with consequent dynamic characteristics like high static stability but poor dynamic stability. Dynamic data influenced the departure characteristics of the aircraft in Weissman's correlation data base, but were not the dominant factors.

The non-dimensional lateral-directional dynamic, or rotary derivatives (C_{np} , C_{lp} , C_{nr} and C_{lr}) can no longer be ignored when determining the minimum acceptable departure resistance for today's aircraft. NASA and other agencies have shown that high AOA damping characteristics clearly affect aircraft flight mechanics (Refs. 20-23), and that when the aerodynamics of a configuration at high AOA are dominated by the forebody, there is a fundamental interchange between static stability and damping. Specifically, if the forebody is altered to increase static directional stability ($C_{n\beta}$) at high AOA, yaw damping (C_{nr}) will invariably decrease at high AOA. Conversely, if the forebody is altered to improve C_{nr} , $C_{n\beta}$ will invariably decrease.

3.3 Revised Lateral-Directional Stability Criteria

We have recently proposed new criteria (Ref. 24) which define minimum levels of $C_{n\beta DYN}$ and LCDP for departure resistance and which include the key dynamic effects of the dimensional rotary derivatives N_p , L_p , N_r , and L_r . The new criteria include the effect of vehicle attitudes and inertial coupling relevant to high angle of attack maneuvering. The "primed" terms are defined as the aerodynamic terms plus inertial terms as follows:

$$\begin{aligned}
 N'_p &= N_p + (R_0 I_{yz} + Q_0 (I_{xx} - I_{yy}) + 2 P_0 I_{xy})/I_{zz} \\
 N'_r &= N_r + (-Q_0 I_{xz} + P_0 I_{yz})/I_{zz} \\
 L'_p &= L_p + (-R_0 I_{xy} + Q_0 I_{xz})/I_{xx} \\
 L'_r &= L_r + (-P_0 I_{xy} + Q_0 (I_{yy} - I_{zz}) - 2 R_0 I_{xz})/I_{xx}
 \end{aligned}$$

The resulting minima can be plotted with $C_{n\beta_{DYN}}$ and LCDP as a function of angle of attack as shown in Fig. 12. One interpretation of these criteria is that the currently defined minimum value requirements for $C_{n\beta_{DYN}}$ and LCDP should not be constant for all configurations. Instead, minimum acceptable values should be based on the quantity defined by the configuration-specific dynamic derivatives as illustrated by the shaded line. Though we have refined it, this criterion is still a stability test on the coefficient of S^2 in the lateral-directional characteristic equation. The effect of feedback stabilization can be included in the criterion by using augmented derivatives in place of bare airframe derivatives. Criteria such as these are obviously not meant to replace current closed-loop flight control design techniques, but rather are intended to: 1) provide a simple "quick look" design guide for the aerodynamicist and 2) provide insight into the dominant vehicle characteristics at various angles of attack.

Similarly, Eidetics has postulated (Ref. 5) that, for stability,

$$C_{nr} + \frac{I_z}{I_x} C_{lp} < 0$$

is required, as shown graphically in Fig. 13. This, and the previous discussion above, emphasize the need for accurate knowledge of aircraft rotary derivatives early in the design process.

3.4 Longitudinal Control Design Considerations

There has been a recent trend toward less inherent longitudinal stability to improve aircraft performance -- especially at supersonic cruise speeds. Statements are often made that this relaxed static stability enhances pitch agility. This is not necessarily the case, however, for two main reasons:

- 1) Due to handling qualities considerations, the maximum achievable pitch rate must be limited. The upper bound of the control anticipation parameter (CAP), for example, is one limit on pitch responsiveness (Ref. 5).
- 2) Control authority and control rate limits necessarily impose restrictions on the "quickness" of the response. In addition to effects similar to those shown previously in the lateral discussion, there is also the problem of maintaining vehicle stability and avoiding the deep stall.

The relationship between agility and handling qualities hinted at in 1) above, is actually quite complex. Work has been proposed to clarify the issue of "how much is enough and how much is too much?" Since this work is just beginning (Ref. 28 presents lateral results on this question), we will focus on the second issue addressed above.

3.5 Relaxed Static Stability (RSS) vs. Pitch Agility

Figure 14 shows typical pitch agility data for an aircraft with progressively decreased static stability. The data were generated by a full non-real-time simulation of an aircraft representative of a modern RSS fighter. They also reflect results obtained with a simplified longitudinal EPA model consisting of short period dynamics with a nonlinear pitching moment term (Ref. 6). Agility certainly increases at first as stability is decreased. However, the reduced nose-down control power at high AOA due to the instability eventually reduces agility quite sharply.

The impact of a lack in pitch control authority is illustrated by the potential deep-stall entry of RSS aircraft (Fig. 15). Traditionally, pitch control power is sized for the low speed, terminal flight phases -- takeoff and landing. As shown in the figure, the positive (unstable) slope of the pitching moment curve decreases the nose-down pitching moment capability as angle of attack is increased. This not only introduces the potential for a deep stall, but also explains the data of Fig. 14.

The notional data of Fig. 15 indicate that to predict the existence of a deep stall, accurate pitching moment data is required at extremely high AOA's. However, accurately predicting data at AOA's above CL_{max} is very difficult, especially from wind tunnel tests of small scale models. The data of Ref. 29 indicate several sources of measurement error: 1) engine nozzle position, 2) model support interference, and 3) Reynolds number effects. Mach and dynamic pressure effects have also been shown to be significant. Finally, model scale effects alone can be enough to sufficiently underestimate this potential for a deep stall. For these reasons, great care should be taken when developing the preliminary aerodynamic database for a new RSS fighter design, and high AOA aerodynamic characteristics must be considered as early as possible in the design process.

3.6 The Impact of Inertial Coupling on Pitch Control Requirements

The problem of maintaining adequate nose-down pitch authority is further worsened by inertial cross-coupling inherent in high AOA stability axis rolling. The nose-up pitch acceleration due to coupling, \dot{Q}_c , is:

$$\begin{aligned}\dot{Q}_c &= R * P * (I_z - I_x) / I_y \\ &= P^2 * \tan(\alpha) * (I_z - I_x) / I_y \quad (\text{Stability Axis Roll})\end{aligned}$$

where P and R are body axis roll and yaw rates and I_x , I_y , and I_z are the moments of inertia about the respective axes. This equation can be shown in terms of pitching moment due to coupling coefficient, $C_{m\dot{c}}$, as follows:

$$\begin{aligned}C_{m\dot{c}} &= \dot{Q}_c I_y / q S c \\ &= P^2 * \tan(\alpha) (I_z - I_x) / q S c\end{aligned}$$

Figure 16 shows representative $C_{m\dot{c}}$ values for a typical RSS fighter vs. AOA for several roll rates at $M=3$ and 15,000 ft. Also shown on the figure is the total available nose-down C_m from full elevator/tail deflection. The summation of these two values is shown in Fig. 17. Note that where the total value becomes positive indicates insufficient nose-down capability to prevent an uncontrolled pitch-up. This, coupled with the "stable break" in the pitching moment curve, creates a deep-stall potential which can be catastrophic.

3.7 Minimum Pitching Moment Requirements

The above discussion of inertial cross-coupling has been included here to emphasize the need to accurately predict total nose-down pitch capability at all angles of attack. It can be the single most restrictive aerodynamic characteristic regarding high AOA maneuverability and agility. In fact, the F-16 flight control law incorporates a roll rate limiter to avoid uncontrolled pitch up's while rolling. This is in addition to the AOA limiter and has the effect of degrading the aircraft's otherwise excellent lateral agility potential.

Obviously, from the above discussion, it is impractical to define a minimum pitching moment coefficient to apply to all aircraft. Instead, the desired maneuvering capabilities of the particular configuration should be used in conjunction with the inertial properties, the desired level of longitudinal stability and the desired level of nose down pitch agility to determine the minimum acceptable high AOA nose-down pitching moment margin.

The question arises -- are our test techniques today sufficient to avoid discrepancies like a deep stall? Control laws can be used to stabilize the aircraft and limit the maximum AOA as demonstrated by the F-16, but a deep stall is still undesirable and cannot be eliminated by the flight controls group through software alone.

4.0 NEW TESTING REQUIREMENTS FOR BFM AIRCRAFT

In view of the above discussion, current requirements for early wind tunnel tests need to be modified to ensure that appropriate data are collected for correct design decisions. For example, new emphasis needs to be placed on good rotary balance data early in the design process. The data of Figs. 18 and 19 show that increasing yaw stability, $C_{n\beta}$, can decrease yaw damping, $C_{n\dot{\beta}}$. If only static wind tunnel data are available, trade-off's between static stability and damping cannot be made. The new design criteria discussed earlier in this report will allow these trade off's if good rotary balance data are available.

It is a fact of life that most future final aircraft designs will have a full authority closed-loop augmentation system. This does not remove the need for a good understanding of the unaugmented aircraft. The ability to design the augmentation system requires adequate control authority. In fact, adequate control authority at high AOA's is paramount for a successful overall design. If, for example, the rudders (or any other control effector) cannot produce sufficient yawing moments, feedback stabilization will be of no use in ameliorating a bare airframe design deficiency in the directional axis. Thus, a full matrix of force and moment data, including inter-axis coupling terms, is required to evaluate the design. This control power information can be used, if available, early in the design process to create augmented stability derivatives for use in the design criteria discussed earlier or in a preliminary control law analysis if the resources are available.

5.0 QUANTIFYING THE EFFECT OF STRUCTURAL FLEXIBILITY ON AGILITY

An often overlooked area in the stability and control preliminary design process is the impact of structural flexibility on control power. While it may be obvious to many, the impact of structural flexibility on controllability is frequently de-emphasized early in the design process. Thus, to further assure that agility is maximized, the communication link between the structures group and the aerodynamic design group needs to be firmly established. This will help prevent over-optimistic agility assessments early in the design process and should lead to a more adequate assessment of the impact of design changes on the agility of the configuration. Additionally, Equivalent Potential Agility (EPA) analyses at high dynamic pressure flight conditions could include an estimate of the effective elastic-to-rigid (E/R) ratios of stabilizing surfaces and control effectors. If adequate levels of agility are predicted, these E/R estimates could then be carried forward as the design matures as actual structural stiffness criteria. Trade studies could also be conducted early in the design process to quantify the trade-off between structural weight (stiffness) and agility. Finally, EPA analyses could also be used to help verify the more sophisticated aero-structural models as they are developed later in the design process.

6.0 CONCLUSIONS

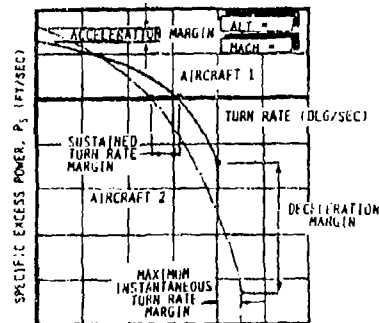
1. Transient agility, governed largely by control power, is of great importance to combat effectiveness.
2. Analysis of control power must be accompanied by examination of the basic aircraft stability -- static and dynamic.
3. Simplified analyses using Equivalent Potential Agility (EPA) parameters are insightful tools for preliminary design estimates.
4. New stability criteria are proposed to augment the use of traditional lateral-directional stability criteria for use in preliminary design.
5. Nose-down pitch control power limits how much agility, both pitch and roll, is gained by relaxing longitudinal static stability.
6. Flying qualities requirements can set upper limits on agility.
7. New emphasis needs to be placed on high angle of attack preliminary design test techniques including earlier testing to determine dynamic derivatives.
8. The effect of aircraft flexibility on agility can (and should) be quantified early in the design process.

7.0 REFERENCES

1. Hallion, Richard P., "Rise of Fighter Aircraft: 1914-1918," Nautical and Aviation Publishing, 1984.
2. Skow, A.M., Foltyn, R.W., Taylor, J.H., and Parker, R.W., "Transient Performance and Maneuverability Measures of Merit for Fighter/Attack Aircraft," Eidetics Report TR86-201, January 1986.
3. Fink, D.E., et al, "Agile Sukhoi SU-27 Leads Strong Soviet Presentation," Aviation Week and Space Technology, p. 28, June 19, 1989.
4. McDonagh, G.M., "Advanced Air-to-Air System Performance Evaluation Model (AASPEM) Analyst Manual," Boeing Document D180-29122-1, November 1985.
5. Hodgkinson, J., Skow, A.M., Ettinger, R.C., Lynch, U.H.D., Laboy, O.J., Chody, J.R. and Cord, T.J., "Relationships Between Flying Qualities, Transient Agility, and Operational Effectiveness of Fighter Aircraft," AIAA Atmospheric Flight Mechanics Conference, Minneapolis, Minnesota, August 1988.
6. Hodgkinson, J., Ettinger, R.C., Skow, A.M., Parker, R.W., Foltyn, R.W., Lynch U.H.D., Laboy, O.J., Lynch A.M.P. and Chody, J.R., "Transient Agility Enhancements for Tactical Aircraft -- Tasks 1, 2, & 3 Final Report," Eidetics Report TR89-001, Vol. I, II, and III, January 1989.
7. Scott, W., "Air Force, NASA Conduct Tests to Define Fighter Aircraft Agility," p. 45, Aviation Week and Space Technology, 9 January 1989.

8. Tamrat, B.F., "Fighter Aircraft Agility Assessment Concepts and Their Implications on Future Agile Fighter Design," AIAA 88-4400, September 1988.
9. Taylor, J.H., et al, "Flight Test Validation of Advanced Agility Metrics," Eidetics Report TR86-212, September 1986.
10. Shelley, F.E., et al, "RF-4C/F-16B Agility Metrics Evaluation - Agile Thunder," USAF TPS-TR-87A-S05, December 1987.
11. Brown, P.T., et al, "F-38/F-16B Agility Metrics Evaluation - Agile Lightning," USAF TPS-TR-87A-S04, December 1987.
12. Hamilton, W.L. and Skow, A.M., "Operational Utility Survey, Supermaneuverability," Eidetics Report R85-002 September 1984.
13. Foltyn, R.W., et al. "Development of Innovative Air Combat Measures of Merit for Supermaneuverable Fighters," AFWAL-TR-87-3073, October 1987.
14. Herbst, W., "Dynamics of Air Combat," AIAA Journal, Vol. 20, 1983.
15. Moul, M.T. and Paulson, J.W., "Dynamic Lateral Behavior of High Performance Aircraft," NACA RM L58E16, August 6, 1958.
16. Weissman, Robert, "Criteria For Predicting Spin Susceptibility of Fighter Type Aircraft," ASD TR 72-48, June 1972.
17. Beaufre, H., "Flight Plan Development for a Joint NASA/Navy High Angle of Attack Flight Test Program," Grumman Contract No. NASA 2965, March 1983.
18. Johnston, D.E. and Heffley, R.K., "Investigation of High AOA Flying Qualities Criteria and Design Guides," AFWAL-TR-81-3108, December 1981.
19. Nguyen, L.T., Whipple, R.D. and Brandon, J.M., "Recent Experiences of Unsteady Aerodynamic Effects on Aircraft Flight Dynamics at High Angle of Attack," NASA Langley, May 1985.
20. Butler, R.W., "Aircraft Motion Sensitivity to Cross and Cross-Coupling Derivatives," AEDC TR 76-138, November 1976.
21. Butler, R.W. and Langham, T.F., "Sensitivity of Aircraft Spinning Motion to Dynamic Cross-Coupling and Acceleration Derivatives," AEDC-TR-79-11, January 1980.
22. Langham, T.F., "Missile Motion Sensitivity to Dynamic Stability Derivatives," AEDC TR 80-11, September 1980.
23. Langham, T.F., "Aircraft Motion Sensitivity to Dynamic Stability Derivatives," AEDC TR-80-11, September 1980.
24. Chody, J.R., "High Angle of Attack Departure Criteria," Eidetics Report TR88-013, 7 October 1988.
25. McRuer, D., Ashkenas, I. and Graham, D., "Aircraft Dynamics and Automatic Control," Princeton University Press, 1973.
26. Hoh, R.H., et al, "Development of Handling Quality Criteria for Aircraft with Independent Control of Six Degrees of Freedom," AFWAL-TR-81-3027, April 1981.
27. Hodgkinson, J., "Equivalent Systems Criteria for Handling Qualities of Military Aircraft," AGARD CP333, April 1982.
28. Riley, D.R. and Drajeste, M.H., "An Experimental Investigation of Torsional Agility in Air-to-Air Combat," AIAA Paper, 1989.
29. Hammett, L.N., Jr., "Investigation of F-16 High Angle of Attack Pitching Moment Discrepancy," AFWAL-TR-81-3107, September 1981.

USE OF ENERGY MANEUVERABILITY TO COMPARE TWO AIRCRAFT



TYPICAL 'DOGHOUSE' PLOT

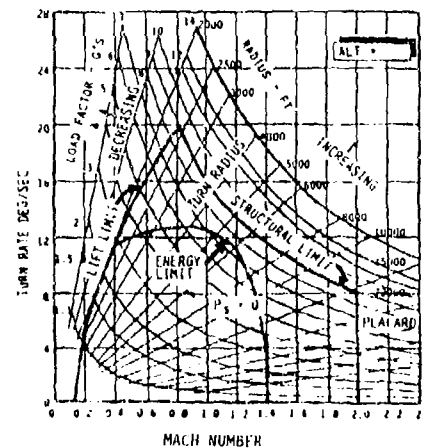


Figure 1 Traditional Agility Metrics

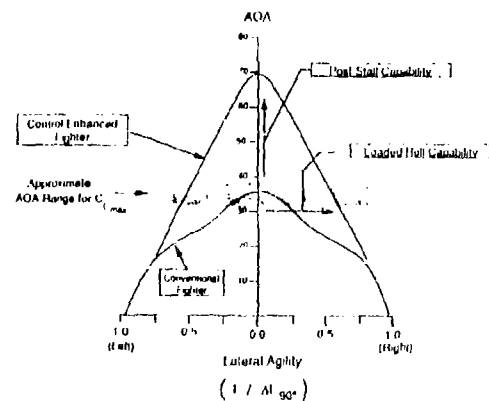
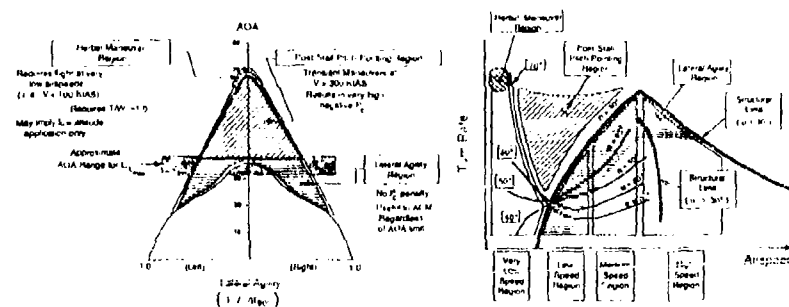


Figure 2 Controllability Envelope Expansion



Lateral Agility Region

Lateral Agility Region with Energy Maneuverability Region

Figure 3 Enhanced Fighter Maneuverability Flight Regions

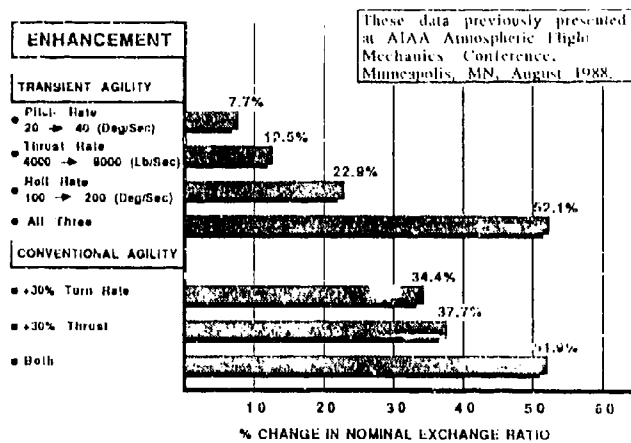


Figure 4a AASPLM 2v2 Combat Summary

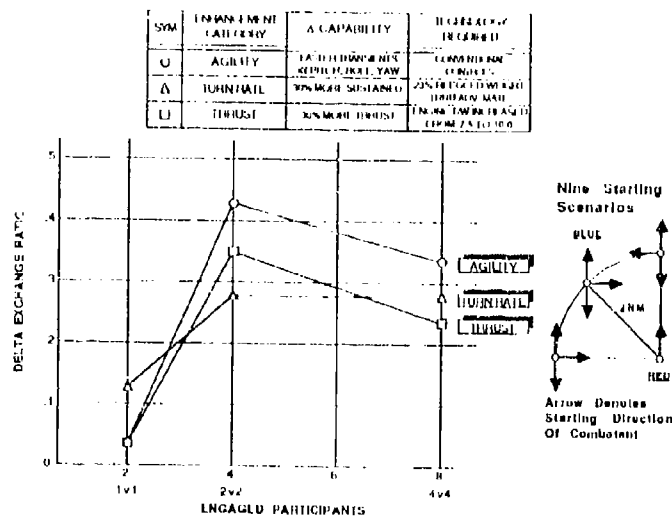


Figure 4b AASPLM Combat Exchange Summary

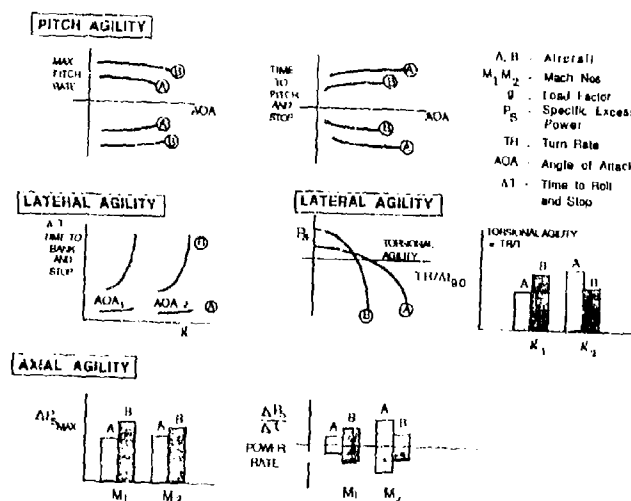


Figure 5 Bidetics' Proposed Agility Metrics

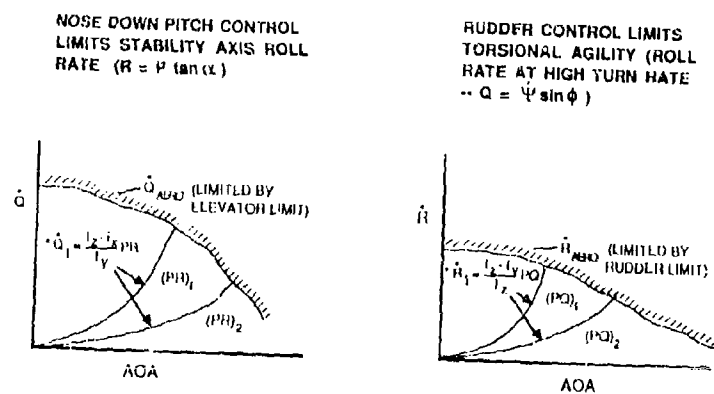
NOTE: I_{xz} Effects Are Not Shown.

Figure 6 Maneuvering Limitations Due to Inertial Coupling

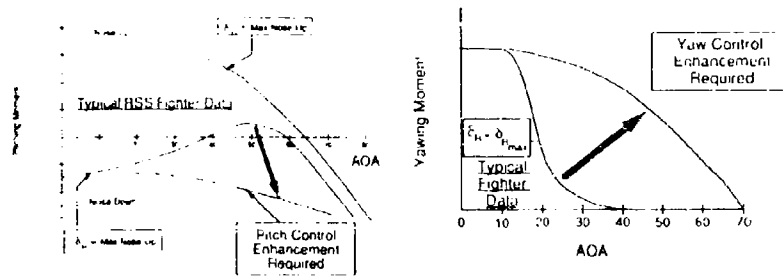


Figure 7 Required Control Power Enhancements for EFM Aircraft

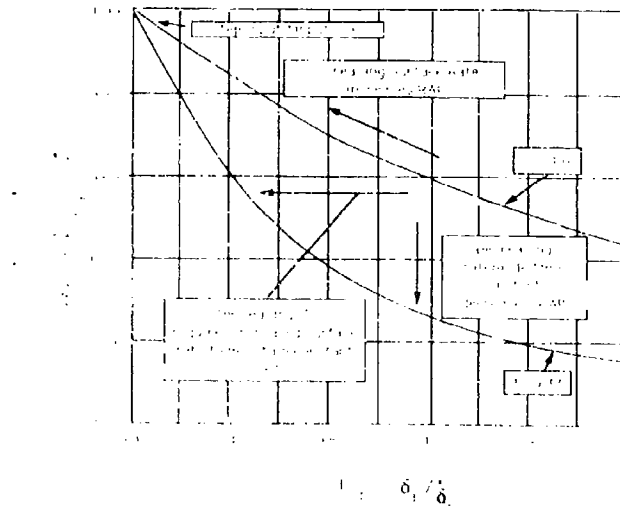


Figure 8 Roll Acceleration Parameter

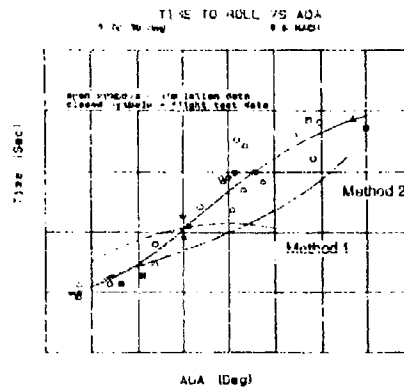


Figure 9 EPA Prediction Comparison

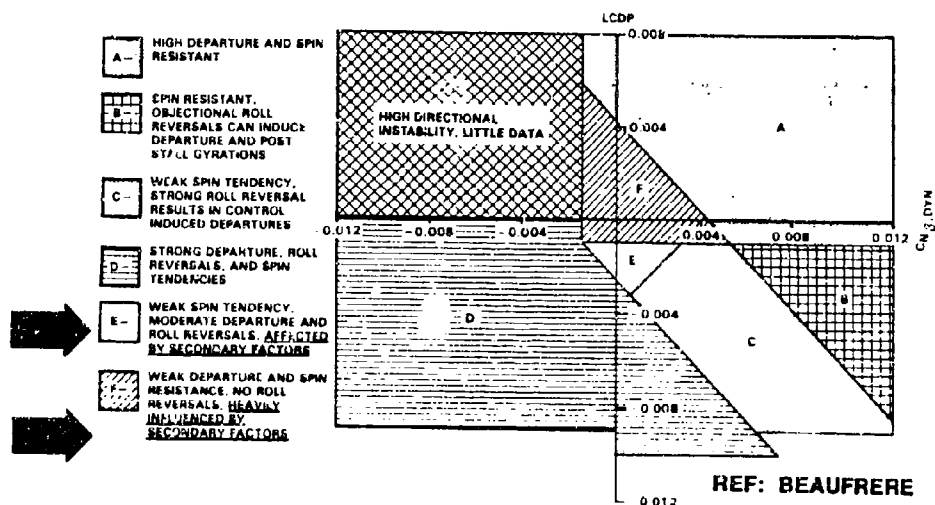


Figure 10 Weissman Criterion (Ref. 17)

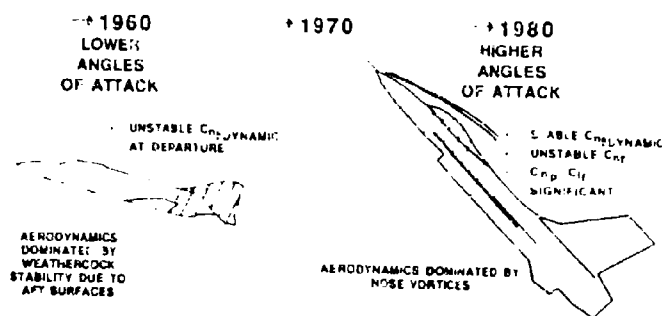


Figure 11 Nose Dominated High AOA Aerodynamics

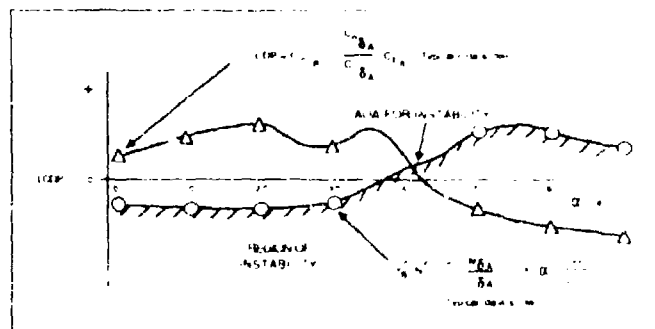
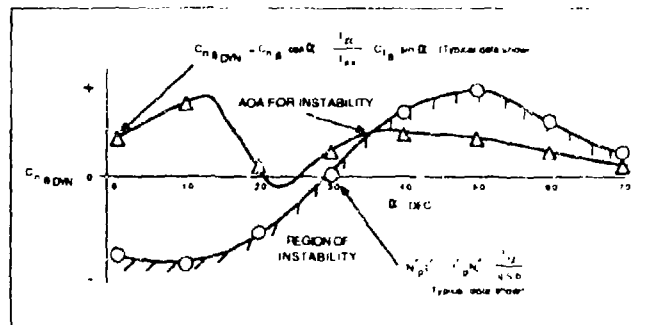
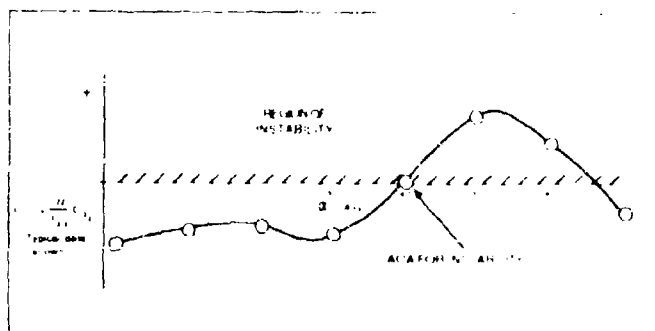
Figure 12 Minimum Values of $C_n \delta_{DN}$ & $LDCP$ for Stability

Figure 13 Lateral Directional Damping for Stability

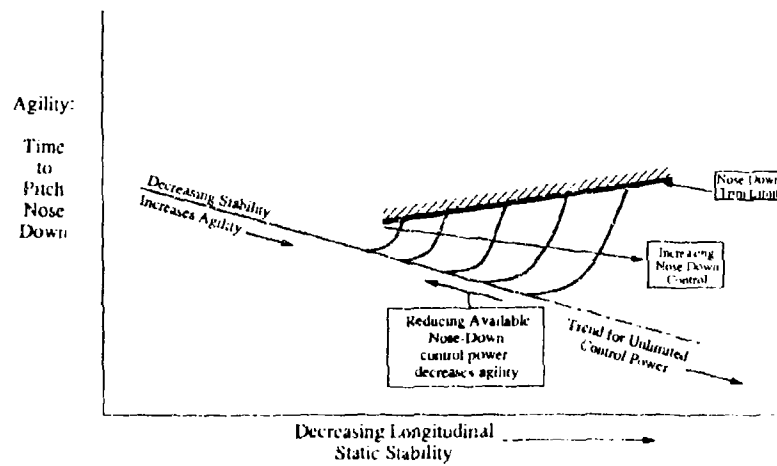


Figure 14 Nose-Down Control Capability Limits Agility Gains
From Relaxing Longitudinal Stability

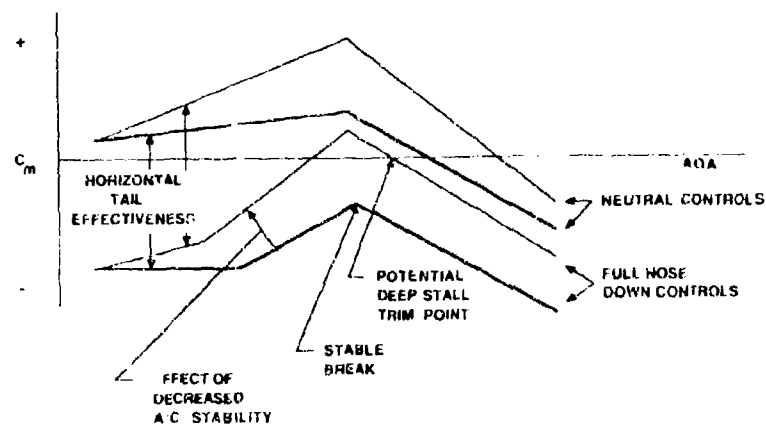
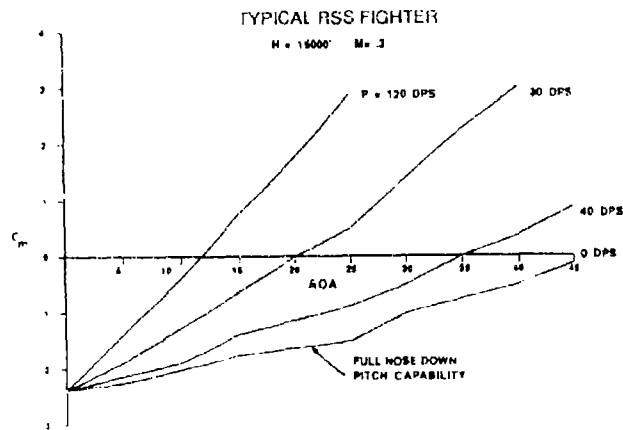
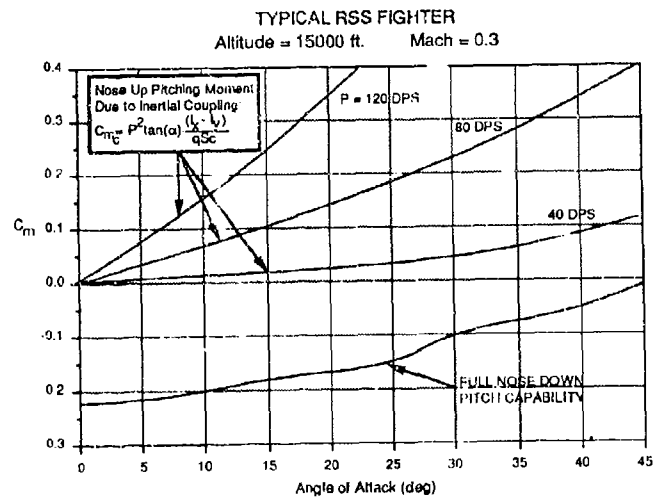


Figure 15 Deep-Stall Potential of RSS Aircraft



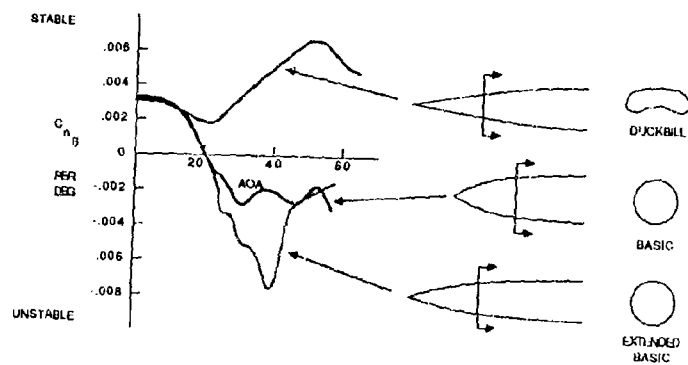


Figure 18 The Effect of Nose Shape on High AOA Directional Stability

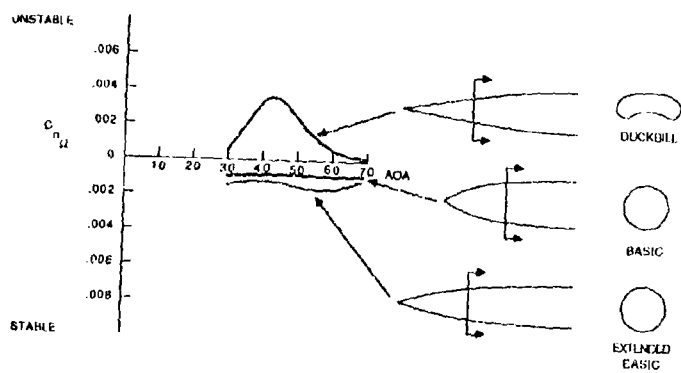


Figure 19 The Effect of Nose Shape on High AOA Directional Damping

AERODYNAMIC CONTROL DESIGN:
EXPERIENCE AND RESULTS AT AERMACCHI

B. Bufacchi, M. Lucchesini, L. Manfrani, E. Valtorta
Technical Department
AERMACCHI S.p.A.
Via Sanvito, 80
21100 - Varese
ITALY

SUMMARY

A review of Aermacchi activities in the field of aerodynamic control design is presented. The aerodynamic balancing of the MB-326/339 elevator and of the AM-X control surfaces for the manual backup mode are described. The use of rotary balance wind tunnel testing and of simulation in assessing controllability at high angle of attack is discussed. Preliminary design studies of unconventional layouts are described and some features of novel control techniques on an unstable canard design are illustrated using wind tunnel results and flow visualisations.

NOTATION

b	- wing span	(m)
c	- local chord length	(m)
C_h	- hinge moment coefficient	
C_L	- lift coefficient	
C_D	- drag coefficient	
C_Y	- side force coefficient	
C_l	- rolling moment coefficient	
C_m	- pitching moment coefficient	
C_n	- yawing moment coefficient	
g	- acceleration due to gravity	(m/s ²)
n_x	- longitudinal load factor	("g")
n_y	- lateral load factor	("g")
n_z	- normal load factor	("g")
p	- roll rate	(rad/s)
\bar{p}	- non-dimensional roll rate, $pb/2V$	
q	- pitch rate	(rad/s)
\bar{q}	- non-dimensional pitch rate, $qb/2V$	
r	- yaw rate	(rad/s)
\bar{r}	- non-dimensional yaw rate, $rb/2V$	
V	- flight speed	(m/s)
α	- angle of attack	(deg)
β	- angle of sideslip	(deg)
Δ, δ	- incremental value	

Subscripts

a	- aileron
b	- balance
e	- elevator
ref	- reference value of coefficient
sp	- spoiler
sto	- stores

Note: All aerodynamic coefficients are referred to stability axes.

1. INTRODUCTION

Aermacchi has long been associated with the design and manufacture of military trainer and light combat aircraft. Its MB-326 and MB-339 jet trainers have enjoyed worldwide success thanks to their reputation for excellent flying qualities and precise handling over a wide range of operating conditions. One of the factors contributing to this reputation was the attention given to aerodynamic control design in order

to obtain good handling qualities with simple and reliable control systems. It is established practice in the company to support this type of design work with dedicated wind tunnel tests to assess control effectiveness in static and rotating flowfields over a wide angle of attack range. This allows controllability at the stall and in spin to be analysed as well as in normal operating conditions. Finally, flight testing plays an important part in aerodynamic refinement of the controls. The above approach has been built upon in subsequent projects and now includes tools such as real-time simulation and water tunnel flow visualisation. This paper illustrates this approach by presenting some results and experience obtained on production aircraft such as the MB-326 and MB-339 trainer/light combat aircraft and the AM-X ground attack fighter, as well as design studies and research projects in which the aerodynamic design of controls has been emphasized.

2. MB-326/MB-339 EXPERIENCE

The MB-326 basic jet trainer (Figure 2.1) was designed by a team led by Ermanno Mazzocchi in 1955, paying considerable attention to the aerodynamic aspects of controllability at all angles of attack. Aerodynamic design of controls relied on handbook methods such as those of Refs. 1 and 2 in the preliminary phase and produced detailed and accurate estimates of flying qualities in all three axes (Ref. 3). The designers were backed up by experience gained with the MB-323 piston-engined trainer and extensive wind tunnel tests conducted at Aermacchi (low speed) and R.A.E. Farnborough (high speed, Ref. 4). This attention to detail produced an aircraft with good flying qualities, well suited to its tasks as a basic trainer.

Early flight tests showed that the aerodynamic configuration of the elevator resulted in good stick force per 'G' characteristics; this configuration remained unchanged for all MB-326 trainer versions. The basic philosophy was to provide a student pilot with a safe aircraft having a relatively high stick force per 'G' gradient at high speeds to avoid inadvertent overstressing of the airframe. Different operating requirements applied to the MB-326K light fighter calling for more control responsiveness at both high and low speeds as well as improved performance. A higher thrust version of the engine was installed, hydraulic aileron servos were added and the elevator was modified to give lighter stick forces and better trim accuracy at maximum speed.

The speed stability curve of the MB-326, shown in Figure 2.2, is characterised by a zone of shallow negative slope at higher speeds indicating marginal stick-fixed instability. This phenomenon is common to many aircraft and is acceptable provided that the negative stick force gradient which may result does not exceed certain limits, such as those of U.S. Military Specifications (Mil-Spec, Ref. 5). With a manual system, careful aerodynamic control balancing allows a positive stick force gradient to be maintained despite a negative elevator deflection slope. This is clearly shown in Figure 2.3 which compares the original elevator with that developed for the MB-326K. The elevator of the MB-339A was designed to combine the longitudinal control feel of the MB-326 with the favourable stick-free speed stability of the MB-326K. Figure 2.4 presents the stick force per 'G' characteristics of all three elevator configurations, and highlights the effect of aerodynamic control design on this particular handling requirement (Ref. 5).

Figure 2.5 shows the hinge moment characteristics for the elevator configuration of the MB-339A.

The MB-326K elevator layout resulted in control force characteristics similar to modern fighters and was adopted for both the MB-339C advanced avionic trainer and the MB-339K light fighter. These are the latest additions to a family of aircraft sharing the philosophy of fine handling qualities obtained with simple and reliable systems.

A further area of attention in the initial design stages was flying qualities at high angles of attack. The fin was placed well forward of the tailplane to maintain rudder effectiveness in the spin and testing in a vertical wind tunnel was carried out to evaluate spin behaviour (Ref. 6). This layout is common to all derivatives of the MB-326 and MB-339 which have consistently demonstrated good controllability in all flight attitudes as well as the ability to recover easily from erect and inverted spins.

3. AM-X EXPERIENCE

3.1 Control characteristics in the manual backup mode

While the trainer fleet of the Italian Air Force was being re-equipped with the MB-339, attention was shifted to the replacement of the FIAT G91 in the ground attack role.

Aermacchi had been undertaking preliminary design studies of this type for some time and was invited to join the AM-X consortium formed with Aeritalia and Brazil's EMBRER to design and manufacture the aircraft to a joint requirement of the Italian and Brazilian air forces. Aermacchi's studies had centred around a manually controlled vehicle and emphasized controllability and manoeuvrability at all angles of attack. Aeritalia benefitted from experience gained on the Tornado program and was considering a heavier aircraft with all-powered controls. The final specification called for Level 1 flying qualities in normal operation; a speed range of up to 550 KCAS, or Mach 0.9, and the ability to tolerate a high degree of battle damage. This was met by the AM-X aircraft in its present form, designed jointly by the three partner companies under the leadership of Aeritalia (Figure 3.1.1).

The AM-X control system is fully powered with manual back-up in pitch and roll, making use of the experience gained by Aeritalia and Aermacchi in control design. It is characterized by two independent hydraulic subsystems which actuate the elevators, ailerons and rudder. Pilot stick inputs are directly transmitted to the elevator and aileron actuators by mechanical linkages which provide manual back-up if both hydraulic systems fail. There are also two independent electrical circuits, each connecting a flight control computer to electrically signalled actuators which drive the stabiliser, spoilers and rudder. These surfaces are used for stability augmentation as well as control.

The control system was designed to a precise set of operating requirements which specify the level of controllability to be guaranteed in case of system failure. In normal operation, all hydraulic and electrical circuits are active. Manual back-up only comes into play when both hydraulic and both electrical systems fail and is sufficient to allow the pilot to return to base although the mission must be aborted. Figure 3.1.2 shows the active control functions in both the normal and manual modes.

The aerodynamic design of the control surfaces used for manual back-up was driven by the same requisites as any manual system: to limit and control hinge moments within the full flight envelope of the aircraft, which in this case extends to high transonic Mach numbers. Various types of aerodynamic balance were evaluated using handbook methods and experimental data. A Westland-Irving internal balance was eventually selected for the ailerons and elevators (Figure 3.1.3). Wind tunnel testing was used to finalise the balance ratios and hinge axis positions as well as to provide a full set of hinge moment coefficients as functions of angle-of-attack, deflection and Mach number. The tests were carried out on a 1/3 scale model of the complete aircraft with balanced controls and a 1/2 scale model of the horizontal stabiliser with balanced elevators.

Figure 3.1.4 is a non-dimensional plot of some results of this activity, which yielded data now included in the aerodynamic data bank used for flying quality predictions.

The wind tunnel results were regarded as conservative because the effectiveness of the Irving balance is strongly dependent on the scaling between upper and lower balance chambers and the size of the vent gaps. These effects are difficult to reproduce at reduced scale and the hinge moments obtained from these tests were expected to be higher than those obtained from flight test. In fact flight test results show higher stick forces due to friction in the mechanical linkage, but the aerodynamic balancing was proved effective by an (unplanned) return to base and successful landing in manual mode with both electric and hydraulic systems inoperative.

3.2 Analysis of control effects at high angles of attack

The AM-X requirements for controllability at angles of attack close to the stall were met by exploiting Aermacchi's experience with the MB 326 and MB 339 aircraft. The basic requisites are that controllability must be maintained up to the stall; that spin entry must be free of violent departures and that recovery from the spin should occur within 1-1/2 turns after the application of simple recovery procedures. Design and development involved dedicated wind tunnel tests, specific analysis techniques and the development of a mathematical model sufficiently accurate to allow simulation of the spin. These activities allowed the dynamics of aircraft behaviour at the stall and beyond to be quantified and understood well before flight testing. Test pilots were able to assess flying qualities at high angle of attack using Aeritalia's fixed base simulator. The results of piloted and off-line simulations were largely confirmed by flight tests and showed that analytical methods can be used to investigate the effects of changes in the aircraft's aerodynamic configuration on stall/spin behaviour.

High angle of attack wind tunnel tests were used to build up aerodynamic data banks for numerical analysis. The rotary balance shown in Figure 3.2.1 was used to obtain pitching and rolling moment coefficients as functions of non-dimensional rate of rotation (see Ref. 7). These are important in modelling departure and spin conditions as they show non-linearities which depend on angle of attack and control deflection.

Experience has shown that rotary balance testing is the best way of obtaining accurate

control effectiveness coefficients at high angle of attack because they can then be treated separately from autorotation effects. In practice it is necessary to analyse wind tunnel data as functions of $pb/2V$ to distinguish these effects. Fig. 3.2.2 compares typical results obtained using fixed and rotary balances at high angles of attack. While the fixed balance results often tend to mask the effects of control deflection near the stall, the rotary balance allows these to be quantified quite easily. In fact fixed balance results can be misleading at these incidences because they tend to show rapid fluctuations due to asymmetry of the stall which could mistakenly be ascribed to changes in control effectiveness. Figure 3.2.3 presents rotary balance data which illustrate the effects of control deflections on the overall aerodynamic characteristics of the aircraft.

Rotary balance test techniques were originally used at Aermacchi for the MB-326 and MB-339 and have since been employed, with a good measure of success, to predict control effectiveness at high incidences for the Tornado as well as the AM-X and the EFA. The use of simulation with rotary balance data has proved to be a practical and effective means of predicting behaviour close to the stall and in the spin.

The mathematical model used for high alpha simulation includes relevant damping terms and stores effects and allows the control effectiveness terms to be modelled as functions of rate of rotation (Figure 3.2.4). The possibility of matching flight test with simulation results allows the accuracy of the aerodynamic data to be assessed rapidly and can be used in conjunction with parameter identification techniques (Ref. 8) to improve the modelling of the aircraft.

Flight test results obtained so far have shown that the wind tunnel data are comprehensive enough to allow the general behaviour of the aircraft to be predicted with a high degree of confidence. The only discrepancies between simulation and flight test were encountered for certain manoeuvres near the stall. These were found to be largely due to sudden variations in control effectiveness which could be identified in wind tunnel tests but had to be matched with the angle of attack at which the stall occurred on the real aircraft. Some flight test traces obtained during a cross-control manoeuvre are compared with simulation results in Figure 3.2.5.

4. STUDIES OF UNCONVENTIONAL LAYOUTS

Aermacchi has been studying unconventional layouts for some time including some stable and unstable canard configurations. Early efforts were inspired by the SAAB Viggen and a similar layout was tested in the wind tunnel using static and rotary balances. Some generic models were built which allowed the changes in stability and controllability due to different relative positions of the wing, canard and fin to be investigated (Fig. 4.1). The results of tests on these models were used to fix the geometry of the MB-341 design study, of which a flying scale model was constructed (Fig. 4.2). This model was used to obtain a practical appreciation of the controllability of the configuration and it was interesting to compare the points that emerged with the wind tunnel results.

Some of the characteristics which became evident were:

- Strong interference effects between the wing and canard which allow the wing to develop lift up to very high angles of attack, but only with certain canard deflections and wing/canard positioning.
- A marked reduction in longitudinal stability at high incidences and the possibility of pitch-up problems due to canard effects.
- The need for leading edge droop on the regions of the wing not affected by the canard flowfield to avoid tip stalling and reduced effectiveness of the outboard elevons.
- A reduction of yaw control at high incidence due to the reduced fin arm.

The experience gained in these studies provided a useful base for current activity dedicated to layouts incorporating reduced longitudinal static stability coupled with active control systems. Most current trainer and fighter designs take advantage of the performance improvements offered by this technique; the amount of instability desirable from the performance point of view must, however, be checked against flight control system capabilities. At high angles of attack, instability means high nose-up pitching moments that must be counteracted by adequate control power to avoid pitch-up divergence. This is a crucial problem for modern fighter configurations where high wing sweep, leading edge extensions or canards and long, pointed forebodies contribute strongly to the pitching moment buildup.

Tds and other control problems of unstable aircraft were evident in an unstable canard configuration for an advanced jet trainer studied in Aermacchi (Figure 4.2).

The canard surface is all-moving and is sized to give 10% m.a.c. longitudinal instability. The elevons are the primary pitch control surfaces and the canard is scheduled to maximise lift/drag ratio. If the aerodynamic balancing of the canard is correct the surface may be allowed to float in case of actuator failure, resulting in a stable and easily controllable configuration.

Figure 4.4 shows the pitching moment curves of this aircraft for various combinations of control deflections; a solid line indicates the minimum recovery pitching moment according to a criterion proposed in Ref. 9 ($C_{M}^{\alpha} = 0.10$). At high angle of attack the canard schedule calls for a nose-down deflection of 10° to get maximum lift coefficients. Elevon effectiveness decreases noticeably above 20° alpha; with full nose-down elevon control input, the aircraft is trimmed at 26° angle of attack. In these conditions, pitch-up recovery can only be obtained by unloading the canard; very large deflections are required because of the strong upwash field produced by the wing-body. With 60° nose-down canard deflection the criterion is met up to 38° angle of attack; therefore it may be necessary to incorporate an angle of attack limiter to avoid uncontrollable pitch-up.

Current studies of fighter aircraft agility show that the capability of flying and manoeuvring at extreme angle of attack gives significant advantages in close-in combat. It is therefore desirable to raise the angle of attack limit as far as possible. This particular configuration incorporated a split airbrake on the rear fuselage "helves" (Figure 4.3) designed to give Mil-Spec deceleration without undesirable trim effects. Wind tunnel tests showed that this airbrake could also be used as a very effective "tail flap". In particular, a constant increment of nose-down pitching moment was obtained up to very high angles of attack, as shown in Fig. 4.4. This could be utilised to improve the recovery from pitch-up.

Another well documented problem in the design of agile aircraft is the loss of roll control and of directional stability at very high angles of attack, leading to lateral departure and spin entry. Figure 4.5 shows how leading edge droop and canard deflection can improve lateral-directional stability at high angles of attack. In vortex-flow dominated configurations the loss of directional stability at high alpha is due to the asymmetric sidewash generated by wing vortices on the vertical tail rather than to flow separation, as depicted in Figure 4.6.

In sideslip, as the angle of attack increases the sidewash field changes and eventually reverses the effective angle of attack of the fin. Nose droop and canard deflection influence vortex flow development and therefore have an impact on lateral-directional stability and control.

Water-tunnel flow visualisations did effectively show that canard deflection had a substantial influence on the development of forebody and wing vortices; the possibility of using asymmetrical canard deflections for lateral control was then investigated. The effect of such a manoeuvre depends on angle of attack, as shown by the curves in Figure 4.7 corresponding to 20° nose down deflection of one canard surface, the other remaining neutral. At low incidence the rolling moment produced by the canard is compensated by an opposing wing rolling moment caused by the canard downwash field; the asymmetry of forebody vortices generates a small but noticeable side force and yawing moment in the same direction of the deflected canard.

At high incidence, the wing on the same side of the deflected canard stalls abruptly and a large rolling moment is generated (Figure 4.8); at the same time, a stronger yawing moment of the opposite sign appears and the side force increases substantially. The water tunnel flow visualisations taken at the same conditions (Figure 4.9) show a clear asymmetry of the forebody vortices, with the vortex that is on the same side as the deflected canard being higher and closer to the vertical tail. In presence of sideslip angle, different effects can be obtained by deflecting the leeward or the windward canard surface; the directional stability at high angle of attack is worsened in the first case, greatly improved in the second.

The potential of asymmetric canard deflection to improve stability and control at high angles of attack is evident, though the strong non linear behaviour of this manoeuvre could pose some problems in control law design. At low incidence differential canards can be used in combination with rudder and ailerons in an conventional control modes such as direct side force control and yaw pointing. These manoeuvres can be used in air combat to aim the aircraft nose without changing the heading.

5. CONCLUDING REMARKS

Aermacchi has acquired a fair amount of experience in the aerodynamic design of controls for combat aircraft, starting with light trainer and ground-attack designs which provide excellent controllability at all angles of attack using simple and effective manual systems. It participated in the design of a dedicated ground-attack fighter, the AM-X, contributing to the optimisation of controls which guarantee recovery from extreme flight attitudes and fully developed spins as well as full controllability with acceptable stick forces in case of electrical and hydraulic

Failure.

These results were made possible by systematic wind tunnel tests using fixed and rotating balances. First estimates of hinge moments can be obtained by calculation and optimised in flight tests to obtain good control characteristics for a manual system. A thorough analysis of pre- and post-stall phenomena is necessary to guarantee predictable and satisfactory handling qualities at high angles of attack. Aermacchi has developed wind tunnel test techniques, largely based on the use of the rotary balance, which allow the controllability of a new configuration to be assessed with sufficient accuracy in preliminary design. The Aermacchi wind tunnel was used for rotary balance tests on the Tornado and is currently in use for the EFA as well as the advanced trainer project mentioned above. A water tunnel has recently been acquired to visualise and manipulate vortex dominated flows.

REFERENCES

1. Perkins, Hage, Aircraft Performance, Stability and Control, Wiley 1949.
2. Royal Aeronautical Society Data Sheets: Wings and Controls, Her Majesty's Stationery Office, 1955.
3. R.Caula, Analisi preventiva delle qualità di volo del velivolo MB-326, Aermacchi Rep. No. 2004, 1 Dec. 1957.
4. J.E.Romiter, Longitudinal Stability Tests at Subsonic Speeds on a 1/13th Scale Model of a Jet Trainer Aircraft (Macchi MB.326), R.A.E., Report No. AERO.2624, June 1959.
5. Military Specification, Flying Qualities of Piloted Airplanes, U.S. D.O.D., MIL-F-8785C, 5 Nov. 1980.
6. D.R.Dennis, Model Spinning on a Jet Trainer (Macchi MB-326), R.A.E. Report No. AERO.2489, December 1956.
7. E.Bazzocchi, Rotary Balance Wind Tunnel Tests in the Design of Modern Aircraft, Lecture held at China Defence Science and Technology Information Center - Beijing April 1988, (Available from Aermacchi Public Relations Dept.).
8. M.Laschenini, P.Maerzelli, L.Manfritani, P.Chimetto, Results and Practical Experience using Parameter Identification Techniques on the AM X Program at Aermacchi, AGARD CP-452, October 1988.
9. G.Wedekind, P.Mangold, Integration of Aerodynamic, Performance, Stability and Control Requirements into the Design Process of Modern Unstable Fighter Aircraft Configurations, AGARD 133-153, June 1987.
10. A.Mentasti, Commento preliminare alle visualizzazioni in galleria ad acqua sul modello ATX/2, Aermacchi Internal MEMO PRA/012/87.

ACKNOWLEDGMENTS

The work described in this paper has been crowned with successes in the marketplace which were made possible by the dedication and perseverance of many people at Aermacchi. In particular, Ermanno Bazzocchi and the late Renato Caula, whose contributions were fundamental to these successes, deserve special mention.



FIGURE 2.1 MD-326 PROTOTYPE IN FLIGHT

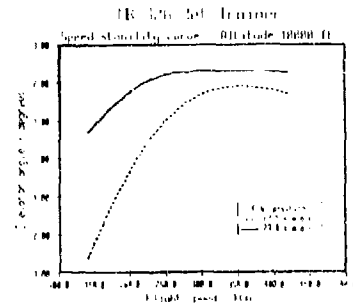


FIGURE 2.2

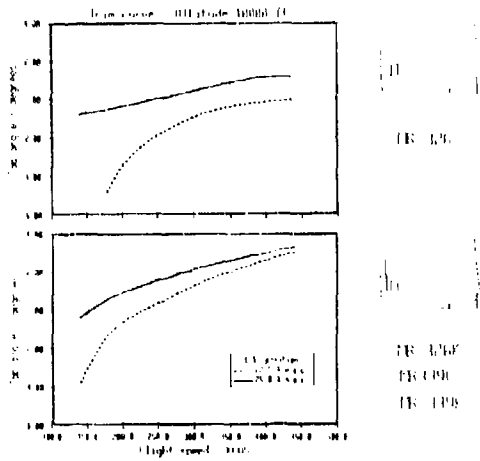


FIGURE 2.3 TRIM CURVES WITH VARIOUS ELEVATOR CONFIGURATIONS

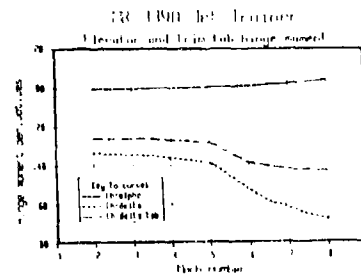


FIGURE 2.4 HINGE MOMENT CHARACTERISTICS OF THE MD-326

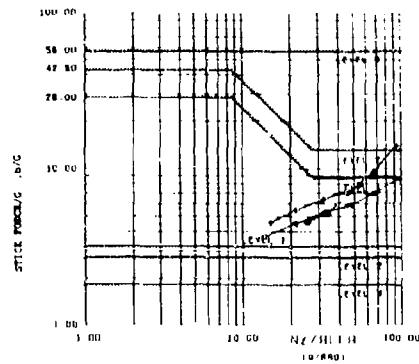


FIGURE 2.4 STICK FORCE CHARACTERISTICS WITH VARIOUS ELEVATOR CONFIGURATIONS

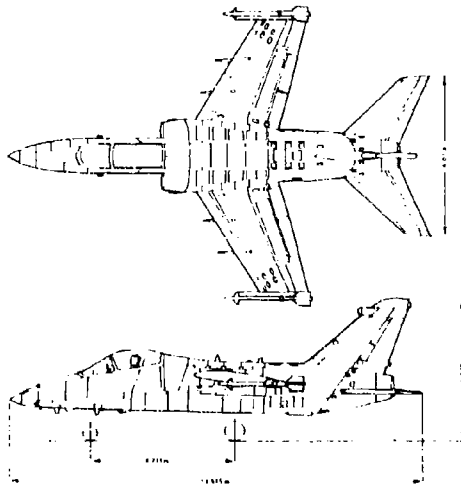
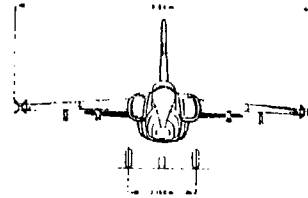


FIGURE 3.1.1 - AM-X GROUND ATTACK FIGHTER



CONTROL SUBSYSTEM	LONGITUDINAL		LATERAL		DIRECTIONAL	
	Control Surface	Control Mode	Control Surface	Control Mode	Control Surface	Control Mode
AUTOMATIC		✓		✓		✓
HYDRAULIC POWER		✓		✓		✓
FLY BY WIRE SCHEDULING CONTROL AUTHORITY	ELEVATOR	✓	Ailerons	✓	Rudder	✓
WING ON	✓		Spoilers	✓	✓	
STABILITY AUGMENTATION AND DAMPING FUNCTIONS	STABILIZER	✓	Spoilers	✓	Rudder	✓
WING ON	✓		✓		✓	
NORMAL TRIM	STABILIZER	✓	Ailerons	✓	Rudder	✓
WING ON	✓		Spoilers	✓	✓	
EMERGENCY TRIM	STABILIZER	✓	Ailerons	✓	Rudder	✓
WING ON	DEFLECTOR	✓	Spoilers	✓	✓	
MANUAL CONTROL		✓		✓		✓
WING ON	ELEVATOR	✓	Ailerons	✓	Rudder	✓

FIGURE 3.1.2 - AM-X: ACTIVE CONTROL FUNCTIONS IN NORMAL AND EMERGENCY MANUAL MODE

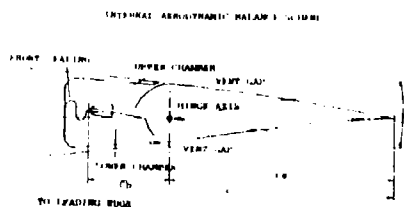


FIGURE 3.1.3 - AM-X: AERODYNAMIC BALANCING FOR AILERONS AND ELEVATOR

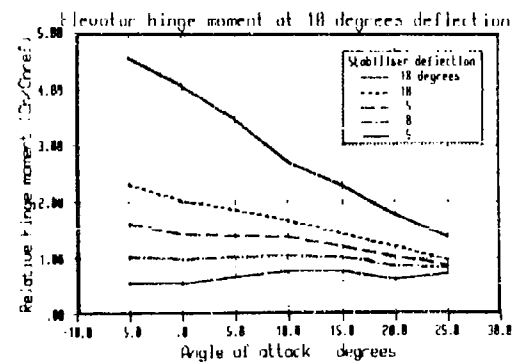


FIGURE 3.1.4 - AM-X: TYPICAL HINGE MOMENT CHARACTERISTICS

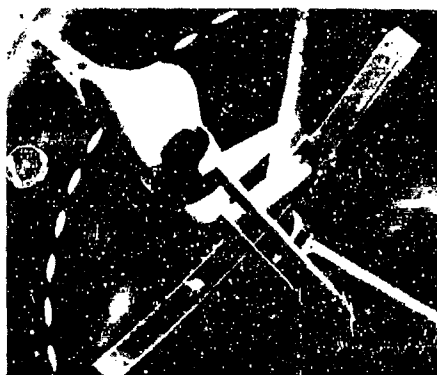


FIGURE 3.2.1 - WIND TUNNEL MODEL OF AM-X
MOUNTED ON ROTARY BALANCE

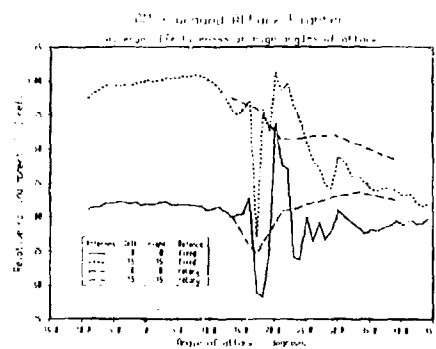


FIGURE 3.2.2 - COMPARISON OF FIXED AND
ROTARY BALANCE RESULTS

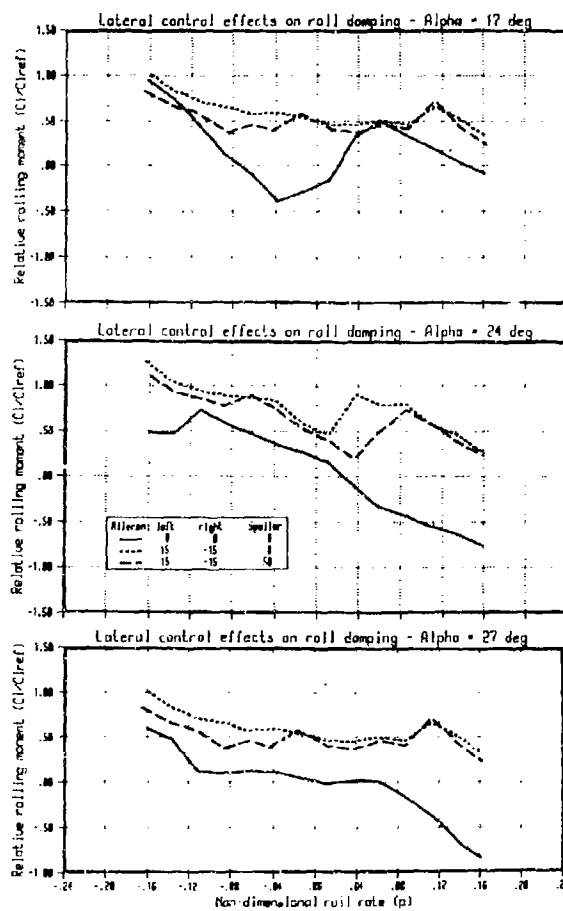


FIGURE 3.2.3 - TYPICAL ROTARY BALANCE RESULTS
AT HIGH INCIDENCE

$$\begin{aligned}
C_L &= C_L(\alpha, M) + C_{L\delta_a}(\alpha)\delta_a + C_{L\delta_{ap}}(\alpha)\delta_{ap} + \Delta C_{Lato}(\alpha, M) \\
C_D &= C_D(\alpha, M) + C_{D\delta_a}(\alpha)\delta_a + C_{D\delta_{ap}}(\alpha)\delta_{ap} + \Delta C_{Dato}(\alpha, M) \\
C_M &= C_m(\alpha, M) + C_{m\delta_a}(\alpha)\delta_a + C_{m\delta_{ap}}(\alpha)\delta_{ap} + C_{mq}(\alpha)\dot{q} + \Delta C_{mato}(\alpha, M) \\
C_L &= C_L(\alpha, \beta) + C_{L\delta_a}(\alpha, \dots)\delta_a + C_{L\delta_{ap}}(\alpha, \dots)\delta_{ap} + \\
&\quad + C_{L\delta_r}(\alpha, \dots)\delta_r + \Delta C_L(\hat{p}, \alpha, \beta) + C_{Lr}(\alpha)\hat{r} + \Delta C_{Lato}(\alpha, \beta) \\
C_N &= C_N(\alpha, \beta) + C_{N\delta_a}(\alpha, \dots)\delta_a + C_{N\delta_{ap}}(\alpha, \dots)\delta_{ap} + \\
&\quad + C_{N\delta_r}(\alpha, \dots)\delta_r + \Delta C_N(\hat{p}, \alpha, \beta) + C_{Nr}(\alpha)\hat{r} + \Delta C_{Nato}(\alpha, \beta) \\
C_Y &= C_Y(\alpha) + C_{Y\delta_a}(\alpha)\delta_a + C_{Y\delta_{ap}}(\alpha)\delta_{ap} + C_{Y\delta_r}(\alpha)\delta_r + C_{Yp}(\alpha)\hat{p} \\
&\quad + C_{Yr}(\alpha)\hat{r} + \Delta C_{Yato}(\alpha, \beta)
\end{aligned}$$

FIGURE 3.2.4 - MATHEMATICAL MODEL FOR HIGH ANGLE OF ATTACK SIMULATION

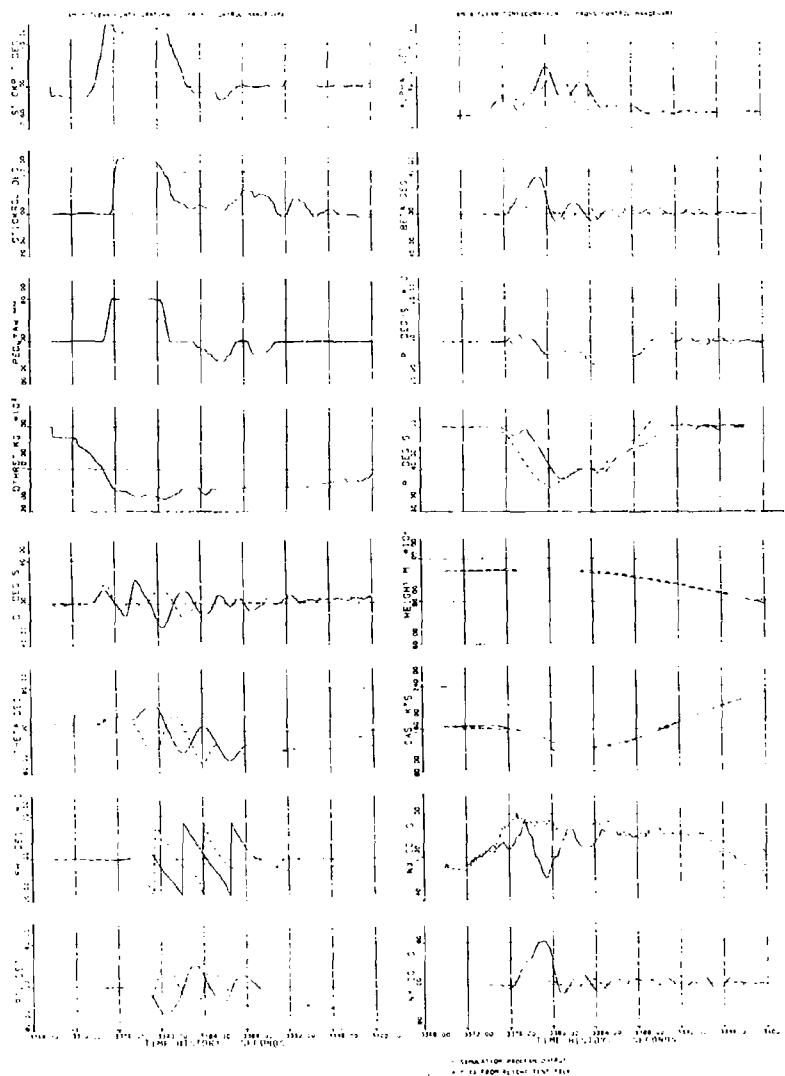


FIGURE 3.2.5 - MATCHING OF SIMULATION AND FLIGHT TEST RESULTS

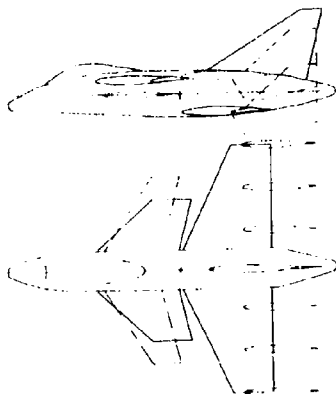


FIGURE 4.1 - RECONFIGURABLE WIND TUNNEL MODEL USED IN STUDIES OF A STABLE CANARD CONFIGURATION



FIGURE 4.2 - FLYING MODEL OF THE MB-341
DESIGN STUDY

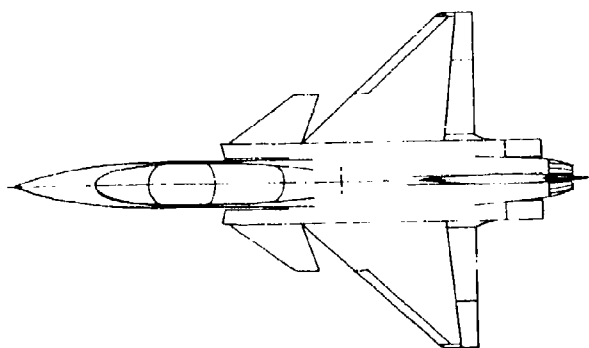


FIGURE 4.3 - ADVANCED TRAINER STUDY WITH DETAIL OF AIRBRAKE/TAIL FLAP LAYOUT

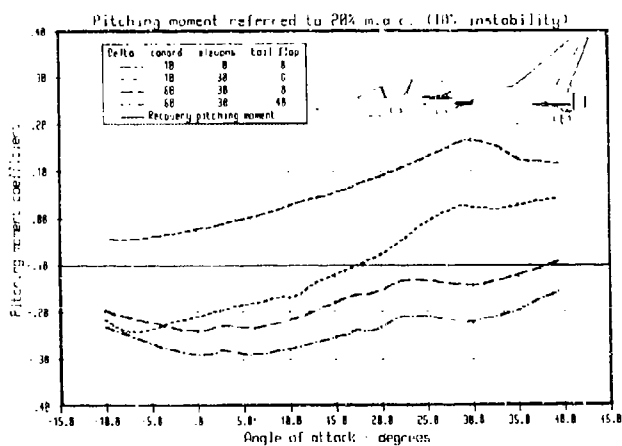
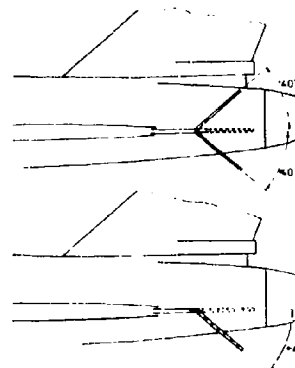


FIGURE 4.4 - ADVANCED TRAINER
STUDY.
CONTROL.
REQUIREMENTS FOR
RECOVERY FROM
PITCH-UP

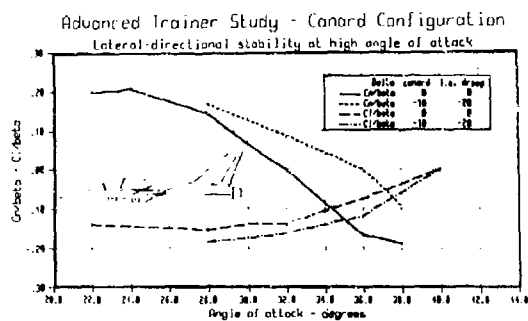


FIGURE 4.5 - EFFECT OF LEADING EDGE DROOP AND CANARD DEFLECTION ON LATERAL-DIRECTIONAL STABILITY

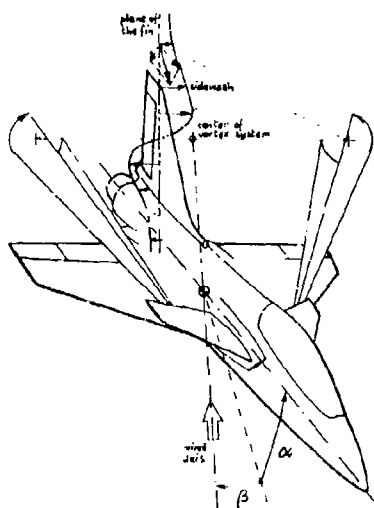


FIGURE 4.6 - VORTEX SIDEWASH ON THE VERTICAL TAIL IN SIDESLIP.

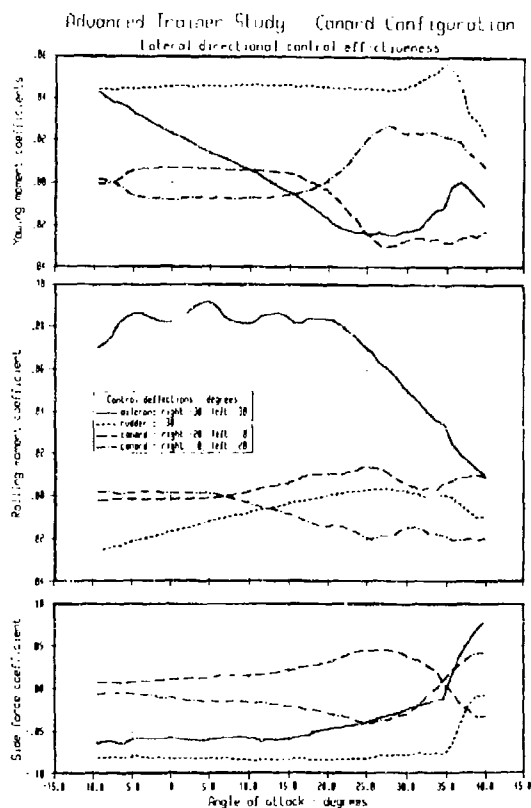


FIGURE 4.7 - DIFFERENTIAL CANARD DEFLECTION FOR LATERAL-DIRECTIONAL CONTROL.

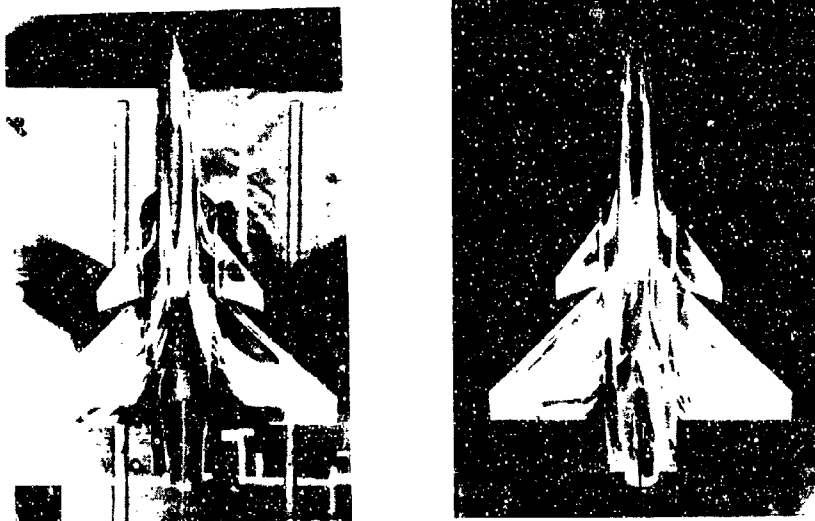


FIGURE 4.8 - EFFECT OF DIFFERENTIAL CANARD DEFLECTION ON WING FLOWFIELD
 ($\alpha = 32^\circ$, $\beta = 0^\circ$)
 LEFT) BOTH CANARD SURFACES NEUTRAL;
 RIGHT) RIGHT CANARD SURFACE DEFLECTED 20° NOSE DOWN.

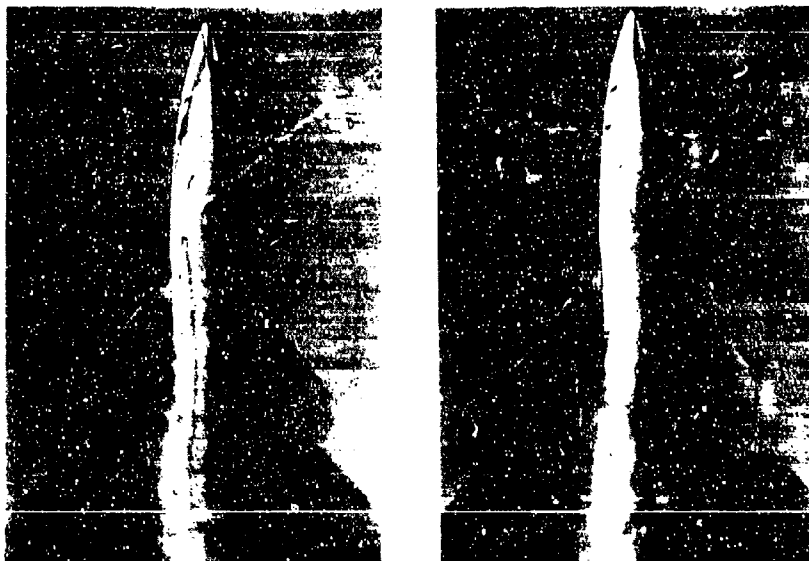


FIGURE 4.9 - WATER TUNNEL FLOW VISUALISATION AT $\alpha = 32^\circ$
 LEFT) BOTH CANARD SURFACES NEUTRAL;
 RIGHT) RIGHT CANARD SURFACE DEFLECTED 20° NOSE DOWN.

EFFECTS OF CANARD POSITION ON THE AERODYNAMIC CHARACTERISTICS OF A CLOSE-COUPLED CANARD CONFIGURATION AT LOW SPEED^{*)}

by

D. HUMMEL and H.-CHR. OELKER
Institut für Strömungsmechanik
Technische Universität Braunschweig
Hienroder Weg 3, D-3300 Braunschweig
Federal Republic of Germany

SUMMARY

Comprehensive wind-tunnel investigations have been carried out on a close-coupled $A = 2.31$ delta-canard configuration at low speed. Based on three-component, surface pressure and flowfield measurements as well as on oilflow patterns, the flow about the coplanar "normal" configuration may be regarded as well understood. Three parameters describing the position of the canard relative to the wing have been varied systematically within certain limits: Vertical distance (3 locations: high, coplanar, low), longitudinal distance (3 locations: front, mid, rear) and canard setting angle ($-12^\circ \leq \alpha \leq 412^\circ$). The results of three-component measurements are presented and the corresponding flow structure is analyzed by means of pressure distribution measurements and oilflow patterns. For a large variety of parameter combinations in the vicinity of the "normal" configuration the same state of the flow with two separate vortex systems for canard and wing has been found, and the effects of different canard positions relative to the wing on the aerodynamic coefficients could be explained by this flow mechanism. For low canard positions and large setting angles, however, the formation of vortices on the lower surface of the wing as well as the merging of the canard vortices with the wing vortex system on the upper surface has been observed. This flow structure leads to abrupt changes in the aerodynamic coefficients which are unacceptable for practical flight conditions.

LIST OF SYMBOLS

Geometric Quantities

$A = b^2/S$	Aspect ratio of canard or wing	h_F	Height of the fuselage
$H = \bar{h}/c_{rw}$	Dimensionless vertical position of the canard	\bar{h}	Distance of the canard's geometric neutral point N_{25c} from the fuselage axis
N_{25}	Geometric neutral point of canard or wing	l_F	Length of the fuselage
$R = (\bar{x} - \bar{x}_0)/c_{rw}$	Dimensionless relative forward position of the canard	l_F, l_F^1, l_F^2, l_F^3	Length of front, cylindrical and rear part of the fuselage
S	Area of canard or wing (extended to $y_C = y_W = 0$ according to Fig. 1)	\bar{x}	Horizontal distance between the geometric neutral points of canard and wing
$b = 2s$	Span of canard or wing	$\bar{x}_0 = (c_{rw}^2 + c^2)/2$	Horizontal distance between the geometric neutral points of canard and wing for canard's trailing-edge located at wing apex
$c(\gamma)$	Local chord of canard or wing	s	Half span of canard or wing
$c_r = c(\gamma = 0)$	Root chord of canard or wing	$s_1(\cdot)$	Local half span of canard or wing
$\bar{c} = \frac{1}{S_W} \int_{-s_W}^{+s_W} \frac{1}{2} c_W dy_W$	Mean aerodynamic chord of the wing	t	Maximum thickness of canard or wing or fuselage
e	Distance between fuselage apex and wing geometric neutral point	x, y, z	Body-fixed coordinates, origin at canard or wing apex
^{*)} These investigations have been supported by DEUTSCHE FORSCHUNGSGEMEINSCHAFT under contract number DFG Hu 254/8		$x_{N25} = c/2$	Distance of geometric neutral point from origin of coordinate system for wing or canard

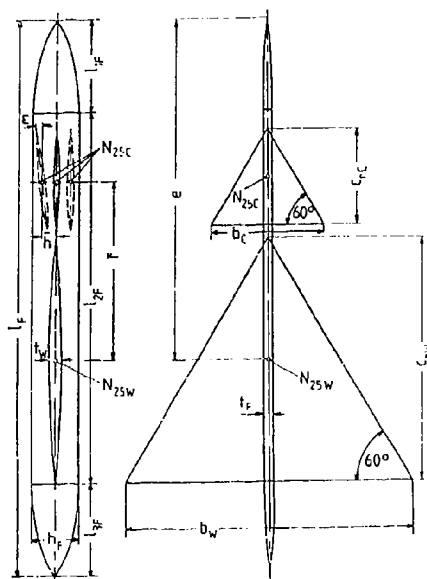
ϵ	Setting angle of the canard; angle between the planes of canard and wing	V_∞	Free stream velocity
$l = x/c_x$	Dimensionless body-fixed coordinate for canard or wing	$C_D = D/q_\infty S_W$	Drag coefficient
$\eta = y/s_1$	Dimensionless local spanwise coordinate for canard or wing	$C_q = (q-p)/q_\infty$	Total pressure coefficient
$\bar{\eta}_W = y_W/s_{1W}$	Dimensionless aerodynamic coordinates with the origin at the intersection of the measuring plane and the x_W -axis	$C_L = L/q_\infty S_W$	Lift coefficient
$\bar{\zeta}_W = z_W \cdot \cos \alpha / s_{1W}$	Dimensionless aerodynamic coordinates with the origin at the intersection of the measuring plane with an axis parallel to the free stream, which passes through the point $x_W = c_{xW}$, $y_W = 0$, $z_W = 0$ at the trailing-edge of the wing	$C_m = M/q_\infty S_W \bar{c}$	Pitching moment coefficient (reference point N_{25W} , nose-up positive)
$\bar{\eta}_C = y_C/s_C$	Dimensionless aerodynamic coordinates with the origin at the intersection of the measuring plane with an axis parallel to the free stream, which passes through the point $x_W = c_{xW}$, $y_W = 0$, $z_W = 0$ at the trailing-edge of the wing	$C_p = (p-p_\infty)/q_\infty$	Static pressure coefficient
$\bar{\zeta}_C = z_C \cdot \cos \alpha / s_C$	Dimensionless aerodynamic coordinate system with the origin at $x_W = c_{xW}$, $y_W = 0$, $z_W = 0$	q	Total pressure
ϕ	Leading-edge sweep of canard or wing	p	Static pressure
Aerodynamic Quantities		q_∞	Free stream dynamic pressure
$Re = V_\infty \cdot c_{xW} / \nu$	Reynoldsnnumber	α	Angle of attack; angle between free stream and wing plane, $z_W = 0$
		ν	Kinematic viscosity
		Subscripts	
		C	Canard
		F	Fuselage
		W	Wing

1. INTRODUCTION

The application of close-coupled canard configurations for modern fighter design, e.g. in Israel Aircraft-Industries (IAI) Lavi, SAAB-Viggen and Kraken and the European Fighter Aircraft (EFA), has considerably increased in the last years. Canard configurations are well known since the Wright Flyer in 1903. An early series of experimental investigations has been carried out at NASA in the 1950's, Refs. [1] to [7], which were concerned with long-coupled canard configurations. Since H. Behrbohm [8] it is known that close-coupled canard configurations with canard and wing of small aspect ratios in the range of $1 \leq A \leq 3$ have substantial advantages. The values of maximum lift coefficient c_{Lmax} and of the corresponding angle of attack $\alpha(c_{Lmax})$ can be considerably increased by adding a delta canard to a delta wing. This advantage is due to favourable interference between the vortex system of canard and wing. A second series of measurements has been performed at Naval Ship Research and Development Center (NSRDC), Refs. [9] to [12], and a third one at NASA, Refs. [13] to [21]. These two last series were concerned with close-coupled canard configurations. They confirmed the results of H. Behrbohm [8] and added a lot of new details. It turned out that a canard's benefits are largest for a high canard location. In this case the maximum lift coefficient c_{Lmax} as well as the corresponding angle of attack $\alpha(c_{Lmax})$ are higher than for the clean configuration. The wing has a positive effect on the flow over the canard: its effective angle of attack is increased and its stall is delayed. For a high canard location the largest values for L/D are achieved. Concerning the longitudinal stability a destabilizing pitching moment occurs for all canard configurations which depends linearly on the canard's longitudinal distance from the wing. The trimming capabilities of close-coupled canard configurations in comparison with conventional configurations have been investigated by R.B. Eberle et al. [22] and S.E. Goldstein, C.P. Combs [23]. Similar studies related to the regime beyond stall have been carried out by H. John, W. Kraus [24] and W. Kraus [25]. Investigations on the interference between a canard and a forward swept wing have been performed by K.E. Griffin et al. [26], [27], [28] in the course of the development of the research aircraft X-29.

Investigations on the physics of interfering vortex systems of canard and wing are very rare. B.B. Gloss, D.D. Miner [18], D.J. Lorincz [29] as well as J. Kr-EI, A. Seginer [30] gave some qualitative insight into the flow structure by means of flow visualization. Flowfield measurements have been carried out by R. Gallington, G. Sisson [31] as well as for configurations with a forward swept wing by K.E. Griffin et al. [27], [28].

The calculation of the flow around canard configurations and the corresponding design of configurations by means of aerodynamic theory are presently at the very beginning. To promote substantial progress in this field the "International Vortex Flow Experiment for Computer Code Validation" was initiated by G. Brougge [32]. As the basic configuration to be investigated both theoretically and experimentally a close-coupled canard configuration was chosen. The Institut für Strömungsmechanik at Technische Universi-



Canard:	Aspect ratio	$A_C = 2.31$
	Leading-edge sweep	$\tau_C = 60^\circ$
	Thickness-ratio	$(t/c)_C = 0.05$
Wing:	Aspect ratio	$A_W = 2.31$
	Leading-edge sweep	$\tau_W = 60^\circ$
	Thickness-ratio	$(t/c)_W = 0.05$
Fuselage:	Height-ratio	$(h/l)_F = 1/12$
	Thickness-ratio	$(t/l)_F = 1/60$
Combination Wing-Fuselage:		
	Relative fuselage length	$l/b_W = 2.0$
	Relative fuselage width	$t_F/b_W = 1/30$
	Rear position of N_{25W}	$e/l_F = 0.617$
Combination Canard-Wing:		
	Relative canard size	$b_C/b_W = 0.4$
		$S_C/S_W = 0.16$
	Vertical position	$-0.04 \leq H \leq +0.04$
	Horizontal position	$-0.01 \leq R \leq +0.16$
	Setting angle	$-12^\circ \leq \alpha \leq +12^\circ$

Tab. 1: Geometric data of the configuration

Fig. 1: Wing-fuselage-canard configuration

tät Braunschweig took part in this international cooperation by means of experimental investigations on two different configurations. Apart from the international configuration [32] a sharp-edged delta wing/canard configuration with $A_C = A_W = 2.31$ and $b_C/b_W = 0.4$ according to Fig. 1 has been studied in detail. Three-component, surface pressure and flowfield measurements using a conventional five-hole probe as well as flow visualizations by means of oilflow patterns have been performed in the institute's 1.3-m low speed wind-tunnel and additional flow visualizations have also been carried out in a small water-tunnel. The investigations were mainly concerned in the wing alone as well as in a coplanar canard-wing combination -called the "normal" configuration- in order to detect the basic interference effects and to provide a set of experimental data on aerodynamic coefficients, surface pressure distributions and flowfield structure for comparison with results of theoretical investigations. The experimental data for the normal canard configuration have been published by D. Hummel, H.-Chr. Oelker [33], [34], [35], [36]. As a result of these investigations the flow structure, the corresponding surface pressure distributions and the aerodynamic coefficients as well as the mechanisms of interference between canard and wing may be regarded as well understood for this coplanar configuration.

The wind-tunnel model according to Fig. 1 was equipped with a flat fuselage in order to fix the position of the canard relative to the wing. This flat fuselage provided the possibility of varying the canard position and attitude to some extent. Three-component and surface pressure distribution measurements as well as flow visualizations by means of surface oilflow patterns have been carried out for different longitudinal and vertical positions and for various setting angles of the canard. The results of these investigations are presented subsequently and they are discussed on the basis of the well known structure of the flow about the normal configuration. The performance and the effectiveness of the canard will be related to the flow structure and to the mechanisms of interference present in these configurations.

2. EXPERIMENTAL SET-UP AND TEST PROGRAM

The experimental investigations have been carried out in the 1.3-m wind-tunnel of the Institut für Strömungsmechanik at Technische Universität Braunschweig.

2.1 Models

The investigations have been performed for a wing-fuselage-canard configuration, which is shown in Fig. 1. The geometric data may be taken from Tab. 1. Wing and canard have delta planforms of aspect ratio $A_C = A_W = 2.31$ and a corresponding leading-edge sweep of $\tau_C = \tau_W = 60^\circ$. In both cases symmetric parabolic arc airfoils for the root section and parabolic contours in spanwise direction have been used. The leading-edges are sharp. Both wing and canard are equipped with a tube system underneath the surface and with pressure holes in order to measure the surface pressure distribution. A very flat fuselage has been chosen to keep the canard in position relative to the wing, to provide some variation of this position and to cover some volume necessary for the rubber tubes in the case of pressure distribution measurements. The fuselage consists of a cylindrical portion of length $l_{2F} = 2h_F$ and attached are front and rear parts of length $l_{1F} = l_{3F} = 2h_F$. Their shape has been taken as a polynomial of fourth order which meets the cylindrical part continuously with respect to slope and curvature. The wind-tunnel model was produced with $b_W = 600$ mm.

The geometric data of the combinations wing-fuselage and canard-wing are collected in Tab. 1. The wing was added to the fuselage in such a way, that the trailing-edge of the wing coincided with the rear end of the cylindrical part of the fuselage. Concerning the canard-wing combination some variations in vertical and horizontal position as well as in setting angle of the canard were possible. The corresponding ranges may be taken from Tab. 1. A typical configuration has been chosen as a basis for comparisons. Its parameters are $\epsilon = 0^\circ$, $H = 0$, $R = 0.05$ and it is called subsequently "normal" configuration.

2.2 Description of the tests

The wind-tunnel investigations have been carried out at free stream velocities of $V_\infty = 30$ m/s and $V_\infty = 40$ m/s, which correspond to Reynolds numbers of $Re = 10^6$ and $Re = 1.4 \cdot 10^6$.

Three-component measurements (lift, drag and pitching moment) have been performed for $-5^\circ \leq \alpha \leq +40^\circ$ with $\Delta\alpha = 2.5^\circ$. The surface pressure measurements have been carried out on the suction side for 7 selected angles of attack only. The flow on the upper surface of the configuration has been studied by means of oilflow patterns. For this purpose the black model surface was painted by a mixture of aluminumoxide-powder and petroleum and benzine (ratio of components : 1g aluminumoxide : 3cm petroleum : 1cm benzine) and exposed to the flow for about half a minute.

Flowfield measurements were carried out in planes perpendicular to the free stream using a conical five-hole probe of 2 mm diameter [36]. These measurements were performed with the normal configuration at stations $x/w = 0, 0.3, 0.6$ and 0.8 over the wing as well as at stations $x/w = 1.01$ and 1.125 downstream of the wing. The angle of attack was $\alpha = 8.7^\circ$, where vortex breakdown is not present.

A large variety of canard positions has been investigated. Concerning the vertical location of the canard three different heights corresponding to $H = -0.04$ (low), $H = 0$ (coplanar, mid) and $H = +0.04$ (high) were tested. The longitudinal distance of the canard from the wing was adjusted in different locations corresponding to $R = 0.16$ (front), 0.05 (mid), -0.01 (rear). The canard's setting angle ϵ was altered in steps of $\Delta\epsilon = 6^\circ$ as $\epsilon = -12^\circ/-6^\circ/0^\circ/+6^\circ/+12^\circ$.

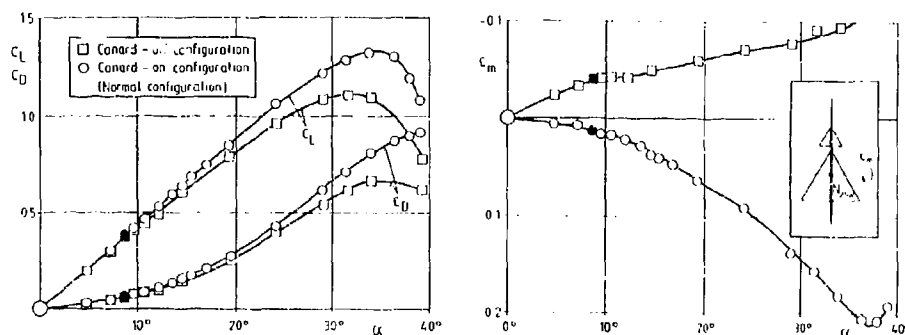


Fig. 2: Results of three-component measurements for the canard-off and the canard-on normal configuration at $Re = 10^6$.

3. RESULTS

3.1 Normal configuration

The basic interference effects between canard and wing have been studied by means of the canard-on normal configuration and the canard-off configuration, see section 2. The results of these investigations have been published in Refs. [33], [34] and [36]. The main findings are to be repeated here, since their knowledge is essential for the understanding of the effects of canard position presented in this paper.

At first the results of the three-component measurements for the canard-off and the canard-on normal configuration are presented in Fig. 2. For low angles of attack both configurations have nearly the same lift and drag. The addition of the canard to the wing-fuselage configuration changes a formerly nose-down pitching moment to a nose-up pitching moment. The results of the corresponding surface pressure measurements at $\alpha = 8.7^\circ$, marked in Fig. 2 by the black symbols, are presented in Fig. 3. The traces of the leading-edge vortices can be detected from the suction peaks on both configurations and it can clearly be seen, that vortex breakdown does not take place at this angle of attack. A comparison between Figs. 3a and 3b reveals two characteristics of the flow around the canard configuration. The pressure distribution on the canard is very similar to the one on the wing alone and in both cases the flow is fairly conical, apart from the trailing-edge region. On the wing of the canard configuration the pressure distribution shows considerably lower suction peaks in the front part, which lie closer to the leading-edge than in the non-interfering case, and the flow on the wing of the canard configuration is distinctly non-conical. The

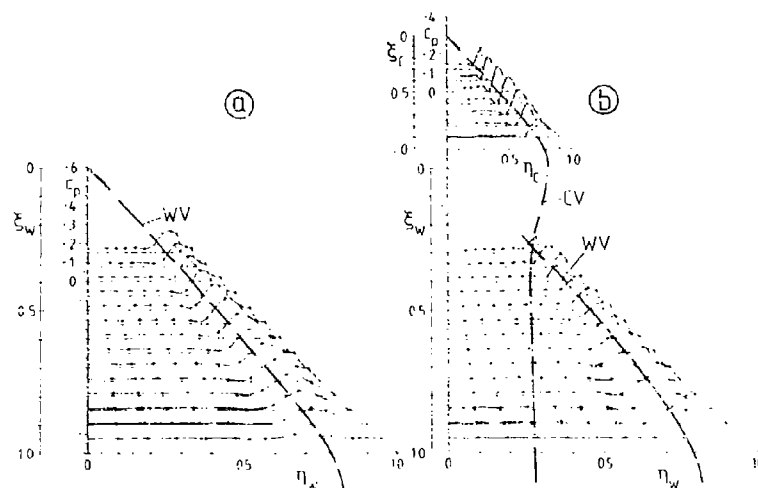


Fig. 3: Upper surface pressure distribution at $\alpha = 8.7^\circ$ and $Re = 1.4 \times 10^6$.
a) canard-off configuration; b) canard-on normal configuration, $k = 0.65$ (solid), $k = 0$ (dashed),
 $t = 0$. CV Canard Vortex; WV Wing vortex.

results of flow visualizations by means of oilflow patterns on the upper surface at $\alpha = 8.7^\circ$ are presented in Fig. 4. For the non-interfering case, Fig. 4a, one can detect the traces of the vortices with the aid of primary attachment and secondary separation lines. The flow is fairly conical. Fig. 3b shows a very similar pattern on the canard of the canard configuration. The streamlines on the wing of this configuration, however, are distinctly different from the non-interfering case. Primary attachment and secondary separation lines indicate, that the wing vortices start a fair distance downstream of the wing apex. On the inner portion of the leading-edge either an attached flow or a very weak flow separation is present. This delay in the formation of leading-edge vortices coincides with the smaller suction peaks of the pressure distributions, which are indicated in Fig. 3b. It can also clearly be seen, that the flow on the wing of the canard configuration is highly non-conical. Fig. 4 shows again, that no vortex break-down is present in this case.

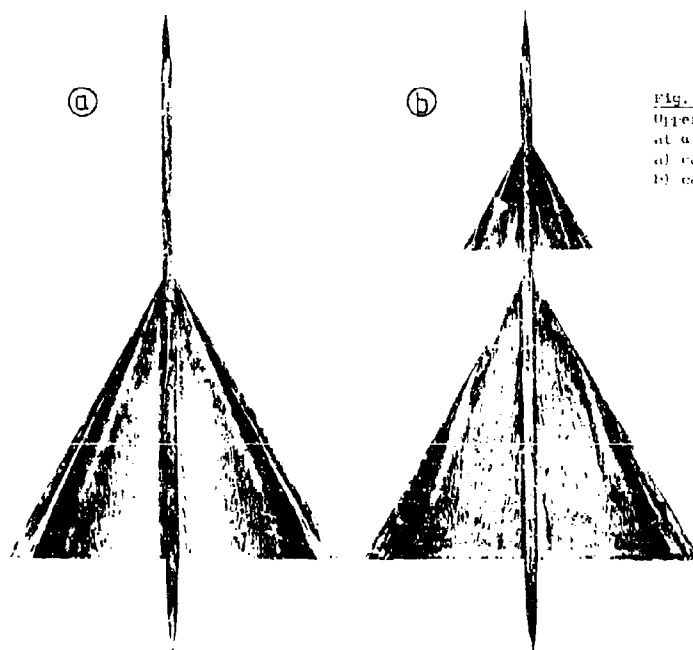
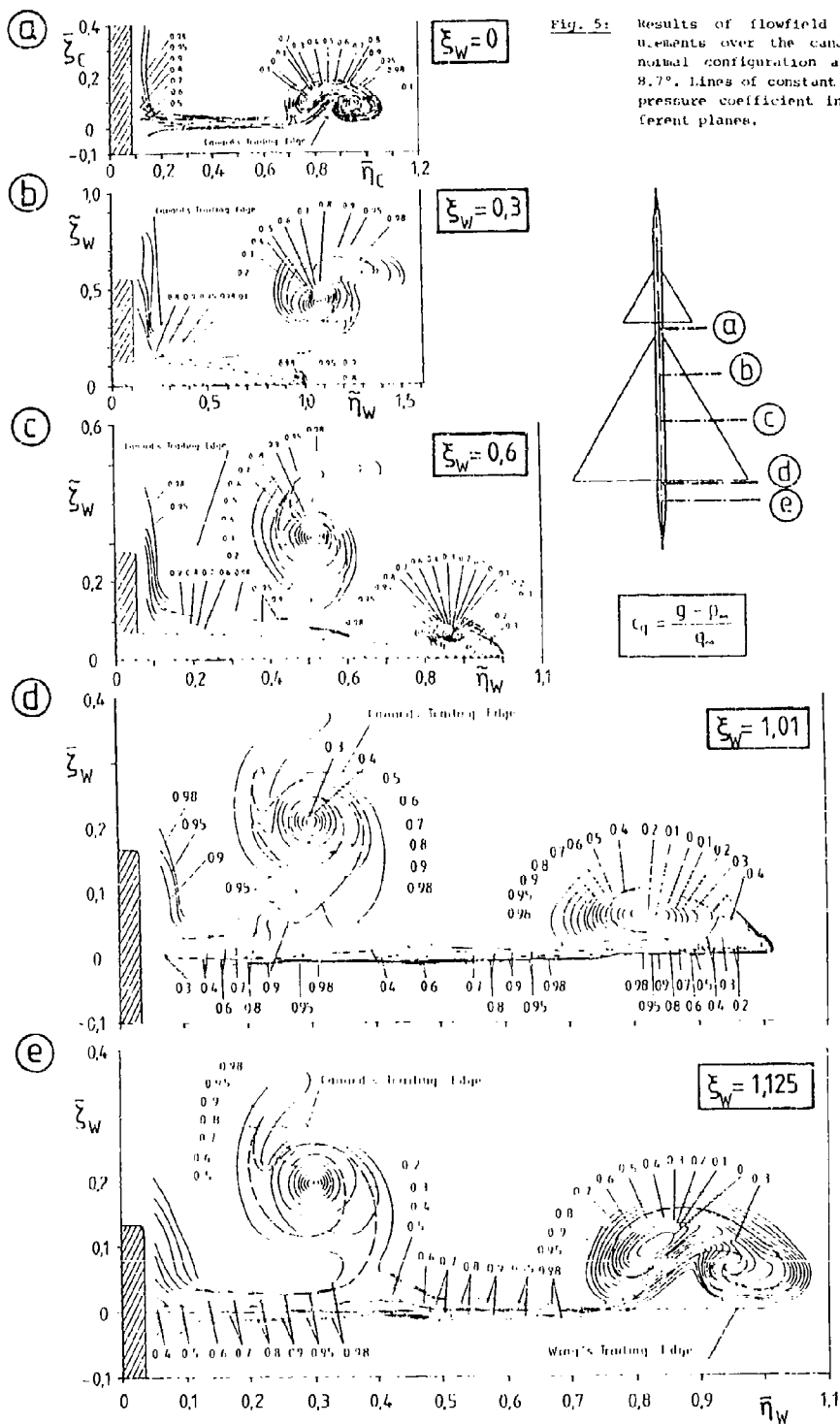


Fig. 4:
Upper surface oilflow patterning
at $\alpha = 8.7^\circ$ and $Re = 1.4 \times 10^6$.
a) canard-off configuration;
b) canard-on normal configuration.



The presentation of these results reveals, that there is a strong influence of the canard on the wing at this small angle of attack. The canard induces behind its trailing-edge a downwash field within its span and an upwash field outside its span. The downwash field reduces the effective angle of attack in the forward and inner portion of the wing considerably. This leads to a suppression of flow separation there. The upwash field increases the effective angle of attack in the outside and rear portion of the wing, which supports flow separation there. This mechanism leads to a delayed formation of the wing vortex downstream of the wing apex, because of the nonuniform distribution of the effective angle of attack along the leading-edge of the wing. The wing vortex is fed with vorticity in a different manner than it is known from the non-interfering case. In total the wing works at a lower angle of attack than in the non-interfering case, which leads to a compensation of the additional lift at the canard through a loss of lift at the wing. Therefore both configurations have almost the same lift. At this angle of attack of $\alpha = 8.7^\circ$ the influence of the wing on the canard is very small.

The results of flowfield measurements over the canard-on normal configuration at $\alpha = 8.7^\circ$ are shown in Fig. 5. The first measuring plane is located at the apex of the wing at $x_w = 0$ which is equal to $x_c = 1.125$. The regions with relatively large total pressure losses represent the vortex system of the canard. It consists of the canard's primary vortex at $\eta_c = 0.0$ and of an already fully developed counter-rotating trailing-edge vortex at $\eta_c = 0.93$. This vortex results from a rolling-up process of the trailing vortex sheet behind the canard which is similar to the well-known behaviour of the flow downstream of a delta wing as described by D. Hummel [17]. The canard's secondary vortex could hardly be detected.

Further downstream over the wing the canard vortex system remains separate from the wing vortex system. The vorticity sheet originating from the trailing-edge of the canard touches the upper surface of the wing and a fusion with the suction side boundary layer takes place in the inner portion of the wing. At some spanwise station the canard's vorticity sheet again separates from the wing and rolls into the canard's trailing-edge vortex. Marching downstream the center of this vortex turns around the canard's primary vortex in the sense of rotation of this primary vortex. Due to the downwash of the canard the vortex formation at the wing leading-edge is delayed up to $x_w = 0.1$. More downstream a strong wing leading-edge vortex system with a corresponding secondary vortex develops. Between the separate vortex systems of canard and wing some interference takes place. The canard vortices approach the wing very high above the plane of the wing and under the influence of the developing wing vortices the canard vortices move inboard and downwards. Behind the trailing-edge of the wing the vortex systems of canard and wing are still separate. The trailing vortex sheet of the wing again rolls up into a corresponding counter-rotating trailing-edge vortex. Fig. 6 shows a schematic overview of the flow field above the canard-on normal configuration low angle of attack.

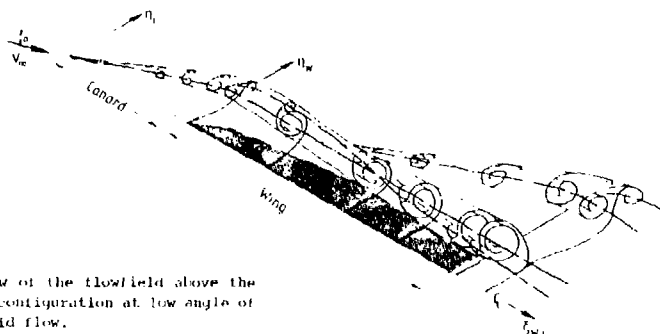


Fig. 6: Schematic overview of the flowfield above the canard-on normal configuration at low angle of attack and inviscid flow.

With increasing angle of attack the flowfield around the normal configuration remains virtually the same. The vortex systems from canard and wing are always separate. However, the distance of the canard's wake from the wing increases at larger angles of attack. This means that the canard induced downwash at the wing is reduced and correspondingly the lift of the wing increases. On the other hand, the canard's angle of attack is also increased by an upwash induced by the wing. At very large angles of attack vortex breakdown within the canard vortices is considerably delayed by the acceleration of the flow over the upper surface of the wing near the wing leading-edge. On the other hand vortex breakdown within the wing vortices is also delayed due to the downwash induced by the canard. Both effects lead to high lift coefficients at very large angles of attack, but these favourable mutual interference effects are limited. Thus for further increased angles of attack vortex breakdown suddenly moves upstream in the canard's and the wing's vortex systems and correspondingly the maximum lift coefficient is reached.

Starting from the normal configuration the effects of variation of the canard's longitudinal and vertical position and of its setting angle are discussed subsequently. For this purpose two of these parameters are kept constant at the values of the normal configuration and the third parameter is varied systematically within certain limits. This leads to an overview of the aerodynamic characteristics in the vicinity of the normal configuration. Finally the behaviour of the configuration is analyzed in detail for some selected parameter combinations which lead to remarkable aerodynamic coefficients and related flow structures.

3.2 Variation of canard's longitudinal position

The influence of variations of the canard's longitudinal position on the lift and pitching moment coefficients may be taken from Fig. 7. Results are shown for coplanar canard-wing configurations ($H = 0$, $\epsilon = 0$) for which the parameter range $-0.01 \leq R \leq +0.16$ could be investigated. The main effects are larger nose-up pitching moments with increasing longitudinal distance of the canard from the wing. This influence is well known, see e.g. D.W. Lacey, S.J. Chorney [9], and it is due to the increased distance of the canard from the pitching moment reference point. The lift coefficient is almost the same for various longitudinal distances R , but a close view indicates that the highest values are achieved for the most forward canard position.

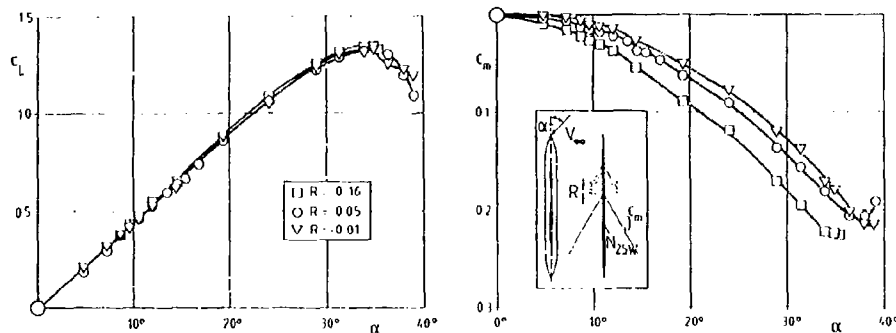


Fig. 7: Results of the three-component measurements for canard-on configurations at $Re = 10^6$. Variation of canard forward position R for $\epsilon = 0$, $H = 0$ (mid).

Pressure distributions at $\alpha = 8.7^\circ$ for different longitudinal position of the canard are shown in Fig. 8. Those for the canard itself are virtually the same, but distinct differences occur in the front part of the wing. With increasing longitudinal distance of the canard from the wing the vertical distance of the canard's wake from the wing plane increases as well. This means that the canard's downwash at the wing decreases and correspondingly the vortex formation at the wing leading-edge starts closer to the wing apex. This effect may be taken from Fig. 8: In the section at $L_w = 0.3$ for $R = +0.16$ a suction peak due to a leading-edge vortex is found whereas in the same section for $R = -0.01$ the pressure distribution indicates just the onset of separation. Thus the wing lift coefficient increases for larger longitudinal distances of the canard from the wing. On the other hand the wing induced upwash at the canard and correspondingly the canard's lift coefficient decrease with increasing longitudinal distance of the canard. The latter effect turns out to be secondary and therefore the overall lift coefficient increases slightly with increasing longitudinal distance of the canard from the wing.

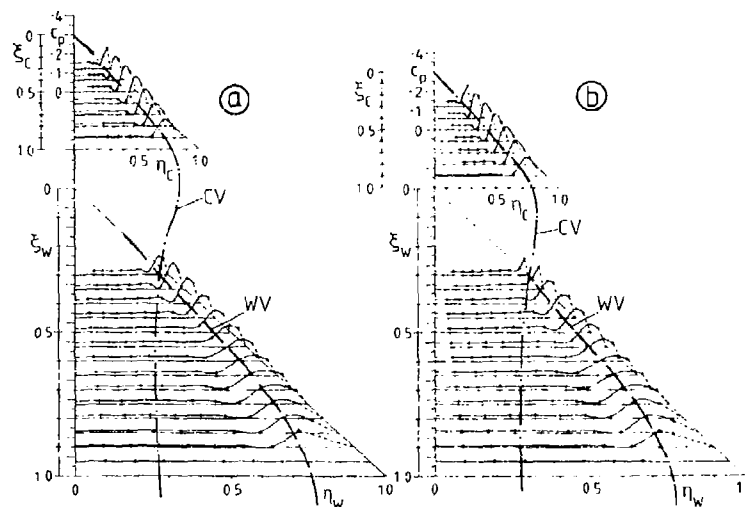


Fig. 8: Upper surface pressure distribution at $\alpha = 8.7^\circ$, $Re = 1.4 \cdot 10^6$, $H = 0$, $\epsilon = 0$ for different longitudinal positions of the canard a) $R = 0.16$ (front), b) $R = -0.01$ (rear). For $R = 0.05$ (mid) see Fig. 3. CV Canard vortex, WV Wing vortex.

3.3 Variation of canard's vertical position

Results of three-component measurements for various canard's vertical positions are presented in Fig. 9. Concerning the lift coefficient only small effects can be detected, but a close view shows that for the high canard location slightly larger lift coefficients as well as higher L/D ratios are obtained. The destabilizing nose-up pitching moment depends nonlinearly on the angle of attack. Increasing the vertical distance of the canard from the wing plane increases the pitching moment, but the nonlinearity of the pitching moment curve is reduced. These results coincide with the findings according to D.W. Lacey, S.J. Chorney [9], R.B. Gloss [14], [17] and others.

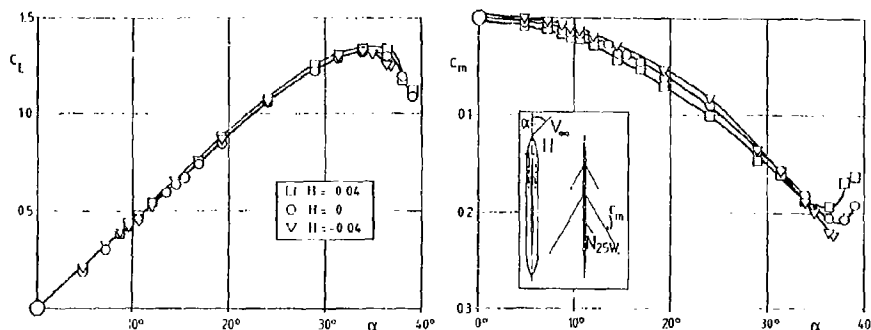


Fig. 9: Results of the three-component measurements for canard-on configurations at $Re = 10^6$. Variation of canard height H for $c = 0$, $R = 0.05$ (mid).

The upper surface pressure distribution at $\alpha = 8.7^\circ$ is shown for different vertical positions of the canard in Fig. 10. For high and low canard positions the canard's pressure distributions are identical. Substantial differences can be identified in the front part of the wing. In the section $\xi_w = 0.3$ e.g. a vortex induced pressure distribution is found for a high canard location, whereas in the case of a low canard an attached flow pressure distribution occurs in the same section. This means that lowering the canard's vertical position leads to a delay of the vortex formation along the leading-edge of the wing. This effect can clearly be detected from Fig. 11, in which oilflow patterns from the upper surface are presented for different vertical positions of the canard. Flow visualizations of this kind have shown that even for low canard positions and angles of attack $\alpha \geq 10^\circ$ the canard's vortex system passes downstream above the upper surface of the wing.

Regarding the interference mechanism for different vertical locations of the canard, the main effects at low angles of attack result from the canard-induced velocities at the wing: Lowering the canard's vertical position leads to an increased downwash in the inner portion and an increased upwash in the outer

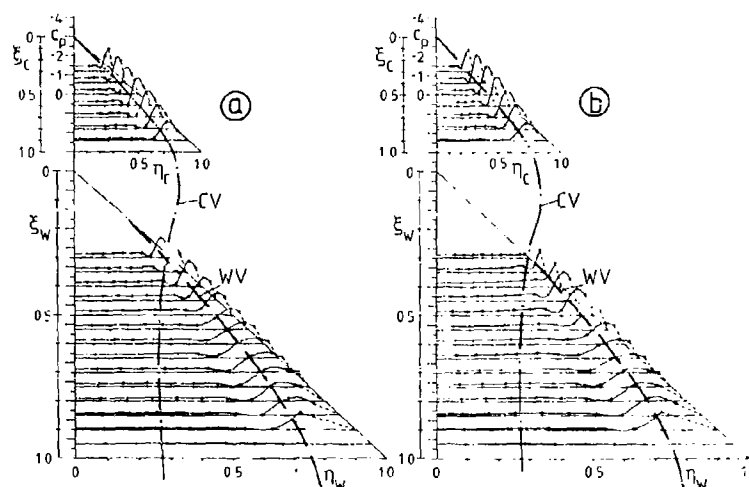
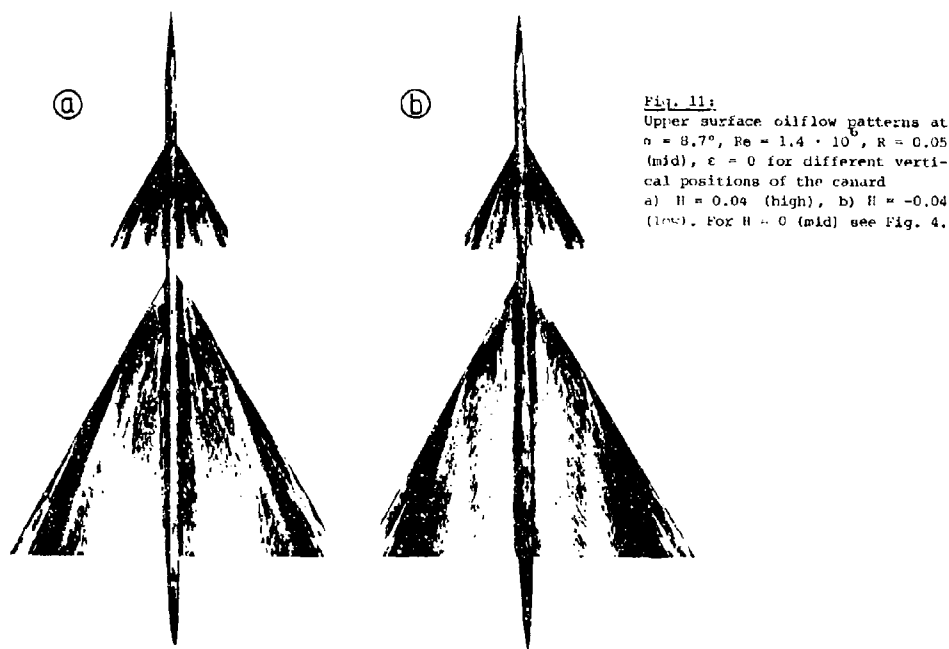
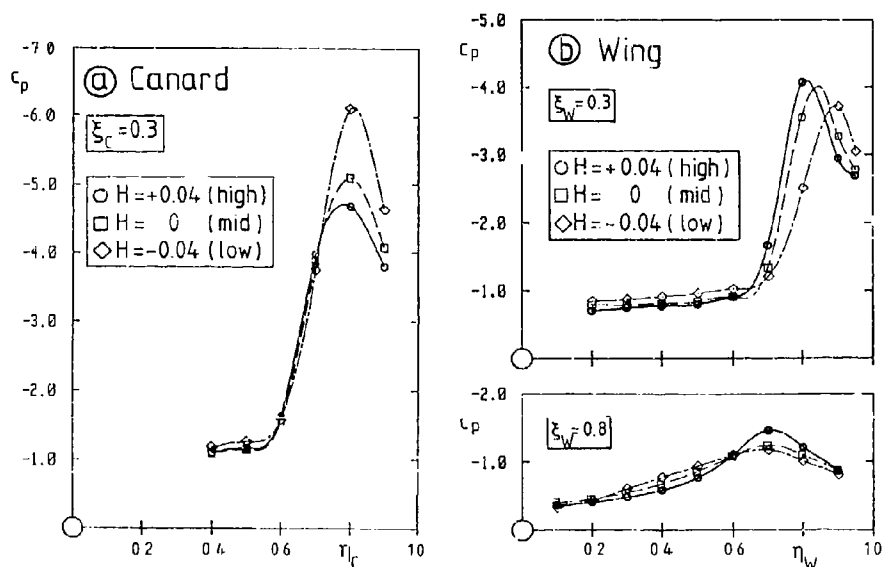


Fig. 10: Upper surface pressure distribution at $\alpha = 8.7^\circ$, $Re = 1.4 \cdot 10^6$, $R = 0.05$ (mid), $\epsilon = 0$ for different vertical positions of the canard a) $H = +0.04$ (high), b) $H = -0.04$ (low). For $H = 0$ (mid) see Fig. 3. CV Canard vortex, WV Wing vortex.



portion of the wing. Apart from the delay in the onset of vortex formation along the leading-edge of the wing, a close view of Fig. 10 indicates larger suction in the central portion of the wing for low canard positions. This may be due to an additional nonlinear interference effect, which results from the lower distance of the canard vortices from the wing surface. Since the lift of the canard does not depend on its vertical location, the reduction of the wing's effective angle of attack at low canard positions should lead to a decrease of the lift coefficient, but due to the additional interference effect mentioned above the lift coefficient is fairly independent of the canard's vertical location. Concerning the pitching moment coefficient, for the low canard locations the destabilizing nose-up tendency is reduced.



For large angles of attack the same effects of the canard on the wing flow are present. This may be taken from the pressure distributions on the wing shown in Fig. 12 for an angle of attack of $\alpha = 29.0^\circ$. In this case, however, also a remarkable effect of the wing on the canard flow can be recognized. For mid and low canard locations the suction in the front part of the canard is considerably increased. This is caused by the wing-induced upwash at the canard, which is largest for low canard positions due to the unsymmetry of the wing flowfield at high angles of attack. However, in the rear part of the canard, the vortex breakdown region is enlarged and the downwash at the wing is increased. Correspondingly the canard lift is slightly increased and the wing lift is decreased for low canard positions. Although the total lift remains fairly constant, a certain shift of lift towards the canard is present and therefore the additional nose-up pitching moment as well as the nonlinearity of the pitching moment curve are largest for low canard locations.

3.4 Variation of canard's setting angle at mid canard position

Fig. 13 shows the result of the three-component measurements with variation of the canard's setting angle ϵ . Forward and vertical position of the canard are the same as for the normal configuration. In the angle of attack range $\alpha < \alpha_{\text{max}}$ only little influence of the setting angle ϵ on the lift coefficients is present. This is due to the effect of the canard wake on the wing. With increasing setting angle ϵ more lift is produced at the canard. The consequence is a stronger downwash at the wing. Thus the effective angle of attack of the wing is even more reduced and the loss of lift on the wing becomes larger. This means for the overall configuration that the gain of lift, which is produced at the canard with increasing setting angle ϵ , is almost completely compensated by the loss of lift at the wing through the reduction of the effective angle of attack. With increasing setting angle ϵ of the canard larger nose-up pitching moments occur at constant angle of attack and it is the shift of lift from the wing to the canard which causes these nose-up pitching moments.

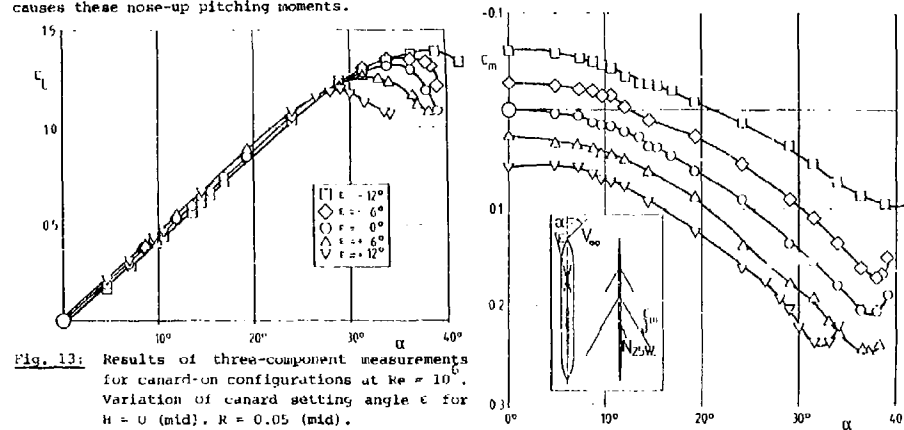


Fig. 13: Results of three-component measurements for canard-on configurations at $Re = 10^6$. Variation of canard setting angle ϵ for $H = 0$ (mid), $R = 0.05$ (mid).

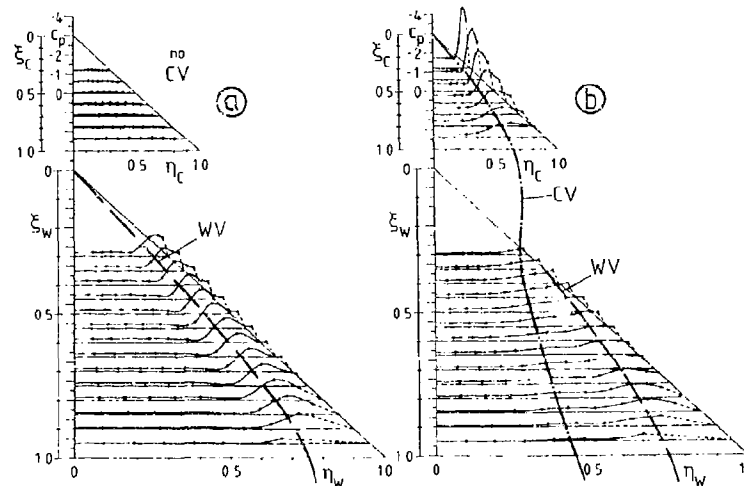


Fig. 14: Upper surface pressure distribution at $\alpha = 8.7^\circ$, $Re = 1.4 \cdot 10^6$, $H = 0$ (mid), $R = 0.05$ (mid), for different canard setting angles ϵ . a) $\epsilon = -12^\circ$, b) $\epsilon = +12^\circ$. For $\epsilon = 0^\circ$ see Fig. 3. CV Canard vortex, WV Wing vortex

The upper surface pressure distribution at $\alpha = 8.7^\circ$ is shown in Fig. 14 for two different setting angles. At $\epsilon = -12^\circ$ no vortex formation takes place on the upper surface of the canard. The canard-induced downwash at the wing is small and the formation of a wing leading-edge vortex starts close to the apex of the wing as indicated in Fig. 14a. The results for $\epsilon = 0^\circ$ may be taken from Fig. 3. The corresponding flowfield consists of a canard vortex system and a wing vortex system as presented in Fig. 5 and sketched schematically in Fig. 6. In this case the canard vortices are located far inboard and so high above the wing, that its upper surface pressure distribution is virtually not affected by these vortices. The results for $\epsilon = +12^\circ$ according to Fig. 14b indicate a strong canard vortex system. Above the wing this vortex system is still separate from the wing vortex system, but the canard vortex is located more outboard and closer to the wing surface. The trace of the canard vortex on the wing as marked in Fig. 14 has been located by the increased suction marked in the pressure distribution. Although the two vortex systems are still separate, a tendency towards merging due to mutual induced velocities is clearly indicated.

The upper surface pressure distribution at a much larger angle of attack $\alpha = 29.0^\circ$ is shown in Fig. 15 for two different setting angles. At $\epsilon = -12^\circ$, Fig. 15a, the effective angle of attack at the wing is much larger than at the canard. Two vortex systems are produced at the configuration which remain separate above the wing since the canard's trailing-edge is located well above the wing surface and no indications of the presence of the canard vortices are found in the wing pressure distribution. Some results for $\epsilon = 0^\circ$ may be taken from Fig. 12. In this case the wing vortices are clearly marked by the suction peaks close to the wing leading-edge and some additional suction in the inner portion of the wing indicates the presence of the separate canard vortex system above the wing. The results for $\epsilon = +12^\circ$ according to Fig. 15b show a strong vortex formed at the canard. Since its trailing-edge is located well below the wing surface this canard vortex passes downstream above the wing leading-edge at a low vertical distance. In the front part of the wing the suction due to the canard vortex as well as due to the wing vortex is distinctly marked, but further downstream the two vortex systems merge and separate suction contributions can no longer be identified. The pressure distributions in Fig. 15b indicate that for large setting angles ϵ and at high angles of attack α the vortex systems above the upper surface of the configuration undergo a merging process which ends up with a single vortex on each side at the trailing-edge of the wing.

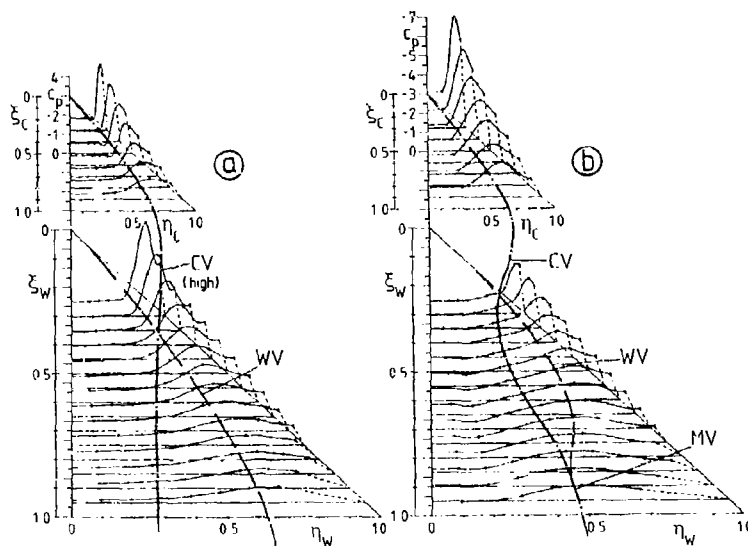


Fig. 15: Upper surface pressure distribution at $\alpha = 29.0^\circ$, $Re = 1.4 \cdot 10^6$, $R = 0$ (mid), $R = 0.05$ (mid), for different canard setting angles ϵ . a) $\epsilon = -12^\circ$, b) $\epsilon = +12^\circ$. CV Canard vortex, WV Wing vortex, MV Merged vortex.

In the region of maximum lift another distinct influence of the canard setting angle turns out. With increasing setting angle ϵ the maximum lift coefficient c_{Lmax} as well as the corresponding angle of attack $\alpha(c_{Lmax})$ decreases, see Fig. 13. This effect can be interpreted as follows: For positive setting angles ϵ the canard has a larger geometrical angle of attack than the wing. Therefore the canard reaches its maximum lift coefficient earlier than the wing. When this happens the influence of some favourable interference effects is lost: The downwash behind the canard becomes weaker and therefore the effective angle of attack of the wing increases. This leads to a stronger vorticity shedding particularly in the front part of the wing, which increases the local lift there. On the other hand these stronger vortices break down earlier in the rear part of the wing which leads to a loss of lift for the wing too. The whole configuration reaches its maximum lift coefficient when the canard reaches its maximum lift coefficient. The local lift gain in the front part and the local lift loss in the rear part of the wing produce an additional nose-up pitching moment which counteracts the nose-down pitching tendency from the loss of lift at the canard. Maximum pitching moment occurs therefore at $\alpha > \alpha(c_{Lmax})$, when the canard effect is finally the dominating one.

3.5 Variation of canard's setting angle at low canard position

The canard's setting angle was also varied for high and low positions of the canard. For high canard locations the vortex systems of the canard and the wing were always separate even at large setting angles ϵ and high angles of attack α . The aerodynamic characteristics were similar to those of the normal configuration and they are not discussed in detail subsequently.

The results of three-component measurements for the variation of the setting angle ϵ in the low canard position are shown in Fig. 16. For $-3^\circ \leq \epsilon \leq +6^\circ$ the low canard configuration's behaviour is similar to that of the normal configuration as discussed already in Fig. 13. For the large setting angle $\epsilon = +12^\circ$, however, two steep jumps in the pitching moment curve can be recognized at $\alpha = 19^\circ$ and at $\alpha = 31^\circ$. For $\alpha < 19^\circ$ the increase of nose-up pitching moment with increasing angle of attack is delayed and at $\alpha = 19^\circ$ the ordinary and expected values of the pitching moment are suddenly achieved. On the other hand at $\alpha = 31^\circ$ the second jump leads to considerable lower values of the nose-up pitching moment.

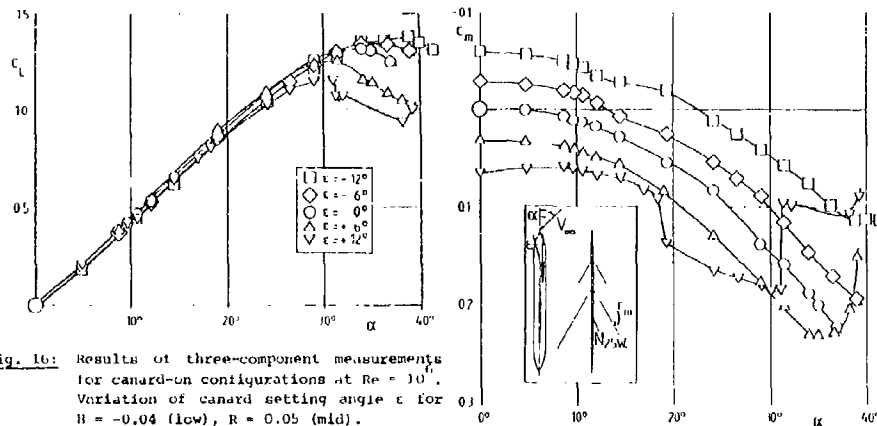


Fig. 16: Results of three-component measurements for canard-on configurations at $Re = 10^6$. Variation of canard setting angle ϵ for $H = -0.04$ (low), $R = 0.05$ (mid).

Details of the flow structure may be detected from the pressure distributions shown in Fig. 17 for $\alpha = 14.5^\circ$ and different canard's setting angles ϵ . At $\epsilon = 0^\circ$, Fig. 17a, the canard vortex system passes downstream above the wing and the pressure distributions indicate that it is everywhere separate from the wing vortex system. At constant angle of attack the strength of the canard vortices increases with increasing setting angle of the canard. Since the canard's trailing-edge moves downwards with increasing setting angle ϵ the canard vortex system comes closer to the upper surface of the wing and the tendency towards merging with the wing vortex system increases. At $\epsilon = +6^\circ$ both vortex systems are still separate as indicated by the pressure distributions in Fig. 17b, and at $\epsilon = +12^\circ$ both vortex systems merge as marked in Fig. 17c where different suction contributions can no longer be separated.

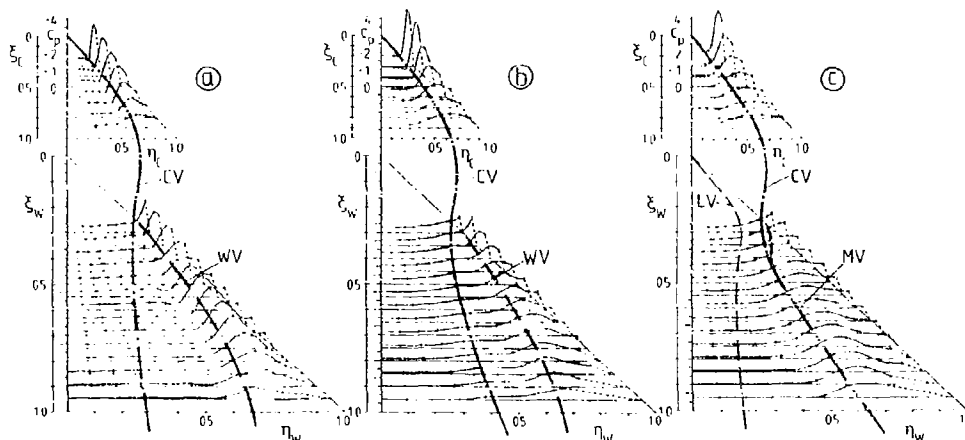


Fig. 17: Upper surface pressure distribution at $\alpha = 14.5^\circ$, $Re = 1.4 \cdot 10^6$, $H = -0.04$ (low), $R = 0.05$ (mid), for different canard setting angles ϵ . a) $\epsilon = 0^\circ$, b) $\epsilon = +6^\circ$, c) $\epsilon = +12^\circ$. CV Canard vortex, WV Wing vortex, MV Merged vortex, LV Lower side vortex.

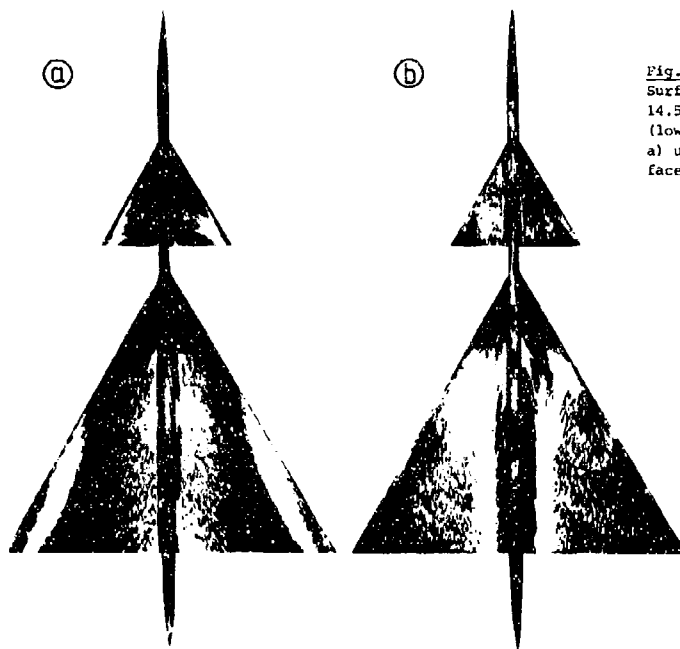


Fig. 18:
Surface oilflow patterns at $\alpha = 14.5^\circ$, $Re = 1.4 \cdot 10^6$, $H = -0.04$ (low), $R = 0.05$ (mid), $\epsilon = +12^\circ$ on a) upper surface and b) lower surface of the configuration.

For $\epsilon = +12^\circ$ the canard vortex system induces a large downwash in the front part of the wing. In the present situation at $\alpha = 14.5^\circ$ the local angle of attack near the apex of the wing is negative. This means that in the front part of the wing the flow around its leading-edge is directed from the upper to the lower surface. Correspondingly a leading-edge vortex is formed in this region on the lower surface of the wing as indicated in Fig. 17c, and this vortex may be identified from the flow visualization according to Fig. 18. The reversed vortex shedding mechanism can easily be recognized: The front part of the wing's

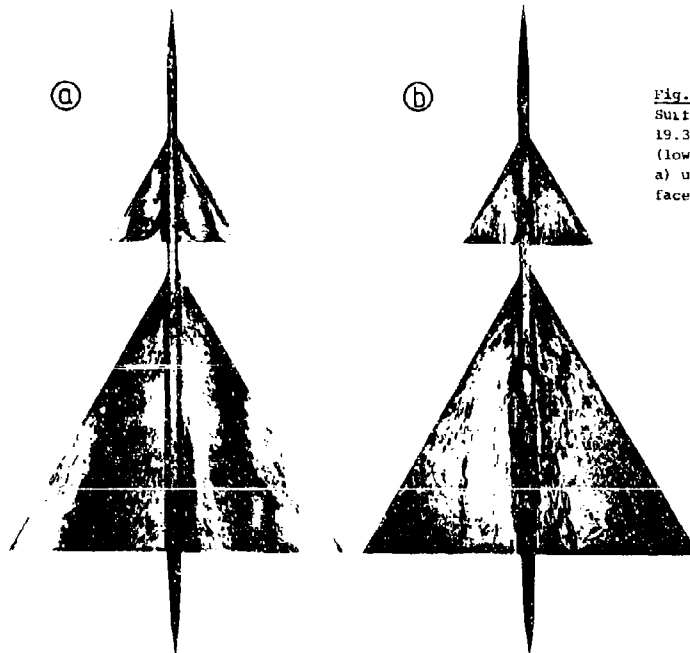


Fig. 19:
Surface oilflow patterns at $\alpha = 19.3^\circ$, $Re = 1.4 \cdot 10^6$, $H = -0.04$ (low), $R = 0.05$ (mid), $\epsilon = +12^\circ$ on a) upper surface and b) lower surface of the configuration.

upper surface, Fig. 18a, acts as a "pressure side" and the rear part as a "suction side" and on the lower surface the situation is vice versa. The reversed flow field in the vicinity of the wing's apex leads to a substantial upstream influence on the canard flow in the sense that the high pressures on the upper surface of the wing cause vortex breakdown within the canard vortex system. This effect is indicated in Fig. 17c by the low and very flat suction distribution in the rear part of the canard. The corresponding reduction of the canard's lift leads to the weaker increase the nose-up pitching moment with angle of attack for $\alpha \leq 19^\circ$ as found in Fig. 16.

With increasing angle of attack the vortex formation on the lower surface of the wing decreases and according to Fig. 19 it disappears at an angle of attack of $\alpha = 19^\circ$. Thus, at this angle of attack the reversal of suction and pressure in the vicinity of the wing apex comes to an end. Now, near the canard's trailing-edge favourable wing-induced pressure gradients appear which suddenly shift the vortex breakdown position in the canard vortices more downstream. This effect may be taken from the canard's pressure distribution at $\alpha = 19.3^\circ$ shown in Fig. 20a in comparison with the results for $\alpha = 14.5^\circ$ in Fig. 17c. The sudden reduction of vortex breakdown at $\alpha = 19^\circ$ leads to a considerable increase of suction at the canard and it is this effect which produces again large nose-up pitching moments according to Fig. 16.

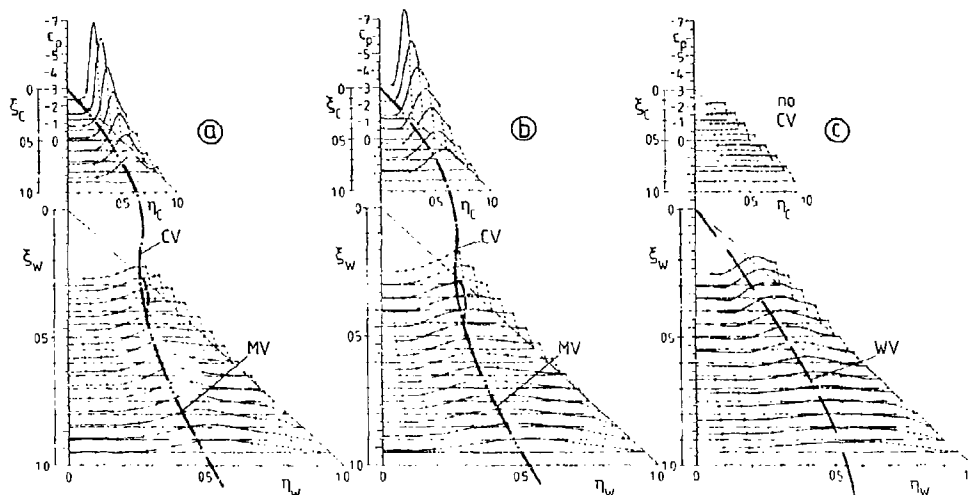


Fig. 20: Upper surface pressure distribution at $Re = 1.4 \cdot 10^6$, $H = -0.04$ (low), $R = 0.05$ (mid), $\epsilon = +12^\circ$ for different angles of attack. a) $\alpha = 19.3^\circ$, b) $\alpha = 29.0^\circ$, c) $\alpha = 33.9^\circ$. CV Canard vortex, WV Wing vortex, MV Merged vortex.

Pressure distributions at very large angles of attack are shown in Figs. 20b and 20c. The flow structure at $\alpha = 29.0^\circ$ is principally the same as for $\alpha = 19.3^\circ$ according to Fig. 20a. At larger angles of attack the influence of the wing on the canard flow is no longer capable to prevent the upstream movement of the vortex breakdown position within the canard vortices. At $\alpha = 33.9^\circ$ vortex breakdown has reached the canard apex. The vortical flow over the canard has completely broken down and a deadwater type flow with constant pressure on the upper surface is present. The wing vortex system starts again at the wing apex and vortex breakdown takes place well upstream of the trailing-edge. The sudden breakdown of the vortical flow over the canard causes a steep loss of lift and a corresponding additional nose-down pitching moment, see Fig. 16. With decreasing setting angle ϵ this phenomenon occurs at larger angles of attack and therefore c_m as well as $\alpha(c_m)$ increase with decreasing setting angle ϵ .

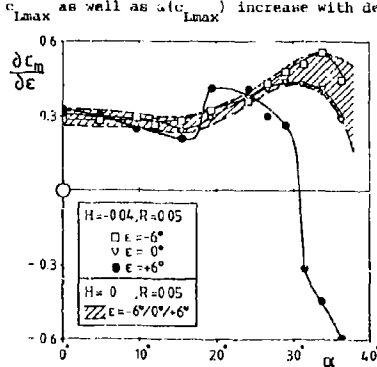


Fig. 21: Canard effectiveness $c_m = \frac{dc_m}{d\alpha}$ as function of the angle of attack.

Fig. 21 shows the canard's effectiveness with respect to the nose-up pitching moment $c_{mc} = dc/d\alpha$ as a function of the angle of attack. These derivatives have been evaluated from Fig. 16 by spline interpolation through the measuring points for three different setting angles ϵ at constant angle of attack α . Three curves for $\epsilon = -6^\circ, 0^\circ, +6^\circ$ turn out. For low angles of attack an effectiveness of $c_{mc} = 0.3$ is achieved and for large angles of attack the effectiveness still increases due to the favourable effects of the wing on the canard vortex system by which vortex breakdown is delayed. The results for other vertical locations lie within the band marked in the figure. For larger setting angles, $\epsilon = +6^\circ$, however, steep jumps in the canard's effectiveness take place at $\alpha \approx 19^\circ$ and $\alpha \approx 31^\circ$ due to the changes of the flow structure mentioned above. At $\alpha \approx 19^\circ$ a considerable improvement of the canard's effectiveness takes place, but at $\alpha \approx 31^\circ$ an abrupt loss of efficiency occurs for this configuration which is unacceptable for practical flight conditions.

4. CONCLUSIONS

For a canard configuration with an $A_w = 2.31$ delta wing and an $A_c = 2.31$ delta canard low speed wind-tunnel tests have been carried out for various longitudinal and vertical canard locations and different setting angles. Three-component and pressure distribution measurements as well as flow visualizations by means of oilflow patterns have been performed. The main results can be summarized as follows:

- 1) The canard induces at the wing a non-uniform angle of attack distribution, which suppresses flow separation in the front part and supports vortex shedding in the rear part. The vortex formation on the wing is thus non-conical. Due to the downwash vortex breakdown is delayed within the wing vortex system.
- 2) The wing induces at the canard an upwash field as well as additional longitudinal velocities. Thus the canard's lift is increased and vortex breakdown is considerably delayed. At very high angles of attack, however, these favourable effects are no longer sufficient to prevent the upstream movement of vortex breakdown and the reduction of the canard's lift. It is this mechanism which leads to the maximum lift coefficient of the configuration.
- 3) The basic state of the flow around the configuration, investigated here, consists of two separate vortex systems produced by the canard and by the wing. With increasing angle of attack there exists a tendency towards merging of both vortex systems above the wing.
- 4) With increasing longitudinal distance of the canard from the wing additional nose-up pitching moments occur which depend linearly on the canard's position.
- 5) The effects of the canard's vertical position on the aerodynamic coefficients and flow structure are relatively small apart from the fact that the tendency towards merging of the two vortex systems increases for lowering the canard's vertical position.
- 6) With increasing setting angle the nose-up pitching moments are enlarged. The corresponding effects on the lift coefficient are relatively small, but the maximum lift coefficient reduces considerably with increasing setting angle due to earlier vortex breakdown in the canard vortex system. For large setting angles and high angles of attack the canard vortices and the wing vortices merge above the wing.
- 7) For low canard positions and large setting angles at low angles of attack flow separation takes place in the front part of the lower side of the wing. This leads to increased vortex breakdown in the canard vortices and to reduced nose-up pitching moments. At a certain angle of attack these phenomena suddenly disappear which causes a steep increase of nose-up pitching moment. Due to the large setting angle the increased vortex breakdown at high angles of attack finally leads to a complete breakdown of vortical flow at the canard. Correspondingly abrupt reductions of lift and nose-up pitching moment coefficients occur.

5. REFERENCES

- [1] W.R. Bates: Low-speed static longitudinal stability characteristics of a canard model having a 60° triangular wing and horizontal tail. NACA RM L9H17 (1949).
- [2] W.R. Bates: Low-speed static lateral stability characteristics of a canard model having 60° triangular wing and horizontal tail. NACA RM L9J12 (1949).
- [3] J.W. Draper: Low-speed static stability characteristics of a canard model with a 45° sweptback wing and a 60° triangular horizontal control surface. NACA RM L50G11 (1950).
- [4] J.L. Johnson Jr.: A study of the flow field behind the triangular horizontal tail of a canard airplane at approximately the vertical-tail location by means of a tuft grid. NACA RM L52H11 (1952).
- [5] D.L. Burrows: Large-scale low-speed wind-tunnel tests of a model having a 60° delta horizontal canard control surface and wing to obtain static-longitudinal-stability and canard-surface hinge-moment data. NACA RM L54D16a (1954).

- [6] W.C. Sleeman Jr.: Investigation at high subsonic speeds of the static longitudinal and lateral stability characteristics of two canard airplane configurations. NACA RM L57J08 (1957).
- [7] W.I. Scallion: Low-speed static longitudinal and lateral aerodynamic characteristics of a model with a low-aspect-ratio variable-incidence wing and with a free-floating and a programmed high-lift canard control. NASA TN-D 1381 (1962).
- [8] H. Behrbohm: Basic low speed aerodynamics of the short-coupled canard configuration of small aspect ratio. SAAB TN 60 (1965).
- [9] D.W. Lacey, S.J. Chorney: Subsonic aerodynamic characteristics of close-coupled canards with varying area and position relative to a 50° swept wing. Naval Ship Research and Development Center, Techn. Note AL-199 (1971).
- [10] J.R. Krouse: Effects of canard planform on the subsonic aerodynamic characteristics of a 25° and a 50° swept-wing research aircraft model. Naval Ship Research and Development Center, Evaluation Report AL-91 (1972).
- [11] J. Ottensmeyer: Wind tunnel data on the transonic aerodynamic characteristics of close coupled canards with varying planform position and deflection relative to a 50° swept wing. Naval Ship Research and Development Center, Test Report AL-88 (1972).
- [12] D.W. Lacey: Transonic characteristics of close-coupled canard and horizontal tail installed on a 50 degree sweep research aircraft model. Naval Ship Research and Development Center, Evaluation Report AL-81 (1972).
- [13] B.B. Gloss, L.W. McKinney: Canard-wing lift interference related to maneuvering aircraft at subsonic speeds. NASA TM X-2897 (1973).
- [14] B.B. Gloss: Effect of canard location and size on canard-wing interference and aerodynamic-center shift related to maneuvering aircraft at transonic speeds. NASA TN D-7505 (1974).
- [15] W.P. Henderson: The effect of canard and vertical tails on the aerodynamic characteristics of a model with a 59° sweptback wing at a Mach number of 0.30. NASA TM X-3088 (1974).
- [16] B.B. Gloss: The effect of canard leading-edge sweep and dihedral angle on the longitudinal and lateral aerodynamic characteristics of a close-coupled canard-wing configuration. NASA TN D-7814 (1974).
- [17] B.B. Gloss: Effect of wing planform and canard location and geometry on the longitudinal aerodynamic characteristics of a close-coupled canard wing model at subsonic speeds. NASA TN D-7910 (1975).
- [18] B.B. Gloss, D.D. Miner: Flow visualization study of close-coupled canard-wing and strake-wing configurations. NASA TM X-75663 (1975).
- [19] K.P. Boyden: Subsonic dynamic stability characteristics of two close-coupled canard-wing configuration. NASA TP 1291 (1978).
- [20] B.B. Gloss: Effect of camber on the trimmed lift capability of a close-coupled canard-wing configuration. NASA TM 78686 (1978).
- [21] B.B. Gloss, E.J. Ray, K.E. Washburn: Effect of canard vertical location, size and deflection on canard-wing interference at subsonic speeds. NASA TN 78790 (1978).
- [22] R.B. Eberle, R.T. Stancil, W.C. Fowler: A critical review of canard relative to aft horizontal tail based on low- and high-speed tunnel tests of a fighter/attack configuration. AIAA-Paper No. 71-8 (1971).
- [23] S.E. Goldstein, C.P. Combs: Trimmed drag and maximum flight efficiency of aft tail and canard configurations. AIAA-Paper No. 74-69 (1974).
- [24] H. John, W. Kraus: High angle of attack characteristics of different fighter configurations. AGARD-CP-247 (1978), 2-1 to 2-12.
- [25] W. Kraus: Delta canard configuration at high angle of attack. Z. Flugwiss. Weltraumforsch. 7 (1983), 41-46.
- [26] K.E. Griffin: Measurement of wake interactions of a canard and a forward swept wing. USAFA-TN-82-4 (1982), US Air Force Academy, Colorado Springs 80840, Colorado.
- [27] K.E. Griffin, F.C. Haerter, B.R. Smith: Wake characteristics and interactions of the canard/wing lifting surface configurations of the X-29 forward swept wing flight demonstrator. USAFA-TN-83-7 (1983), US Air Force Academy, Colorado Springs 80840, Colorado.

- [28] K.E. Griffin, F.M. Jonas: Wake characteristics and interactions of the canard/wing lifting surface configuration of the X-29 forward swept wing flight demonstrator. AIAA-Paper 83-1835 (1983).
- [29] D.J. Lorincz: Flow visualization study of the HIMAT RPRV. NASA-CP-163094 (1980).
- [30] J. Er-El, A. Seginer: Vortex trajectories and breakdown on wing-canard configurations. J. Aircraft 22 (1985), 641-648.
- [31] R. Callington, G. Sisson: Flow visualization using a computerized data acquisition system. Preprints of the Contributed Papers, International Symposium on Flow Visualization, 9. - 12. Sept. 1980, Ruhr Universität Bochum (1980), 134-141.
- [32] G. Drougge: The international vortex flow experiment for computer code validation. ICAS-Proceedings 1988, Vol. 1, XXXV-XLI.
- [33] D. Hummel, H.-Chr. Oelker: Vortex interference effects on close-coupled canard configurations in incompressible flow. Proceedings of the Symposium on "International Vortex Flow Experiment on Euler Code Validation", Stockholm October 1-3 1986, Flygtekniska, Forsöksanstalten, Bromma, Sweden (1986), 47-61.
- [34] H.-Chr. Oelker, D. Hummel: Experimentelle Untersuchungen an Entenkonfigurationen. DGLR-Bericht 86-03 (1986), 172-191.
- [35] D. Hummel: Documentation of separated flows for computational fluid dynamics validation. AGARD-CP-437 (1988), Vol. 2, P15-1 to P15-24.
- [36] H.-Chr. Oelker, D. Hummel: Investigations on the vorticity sheets of a close-coupled delta-canard configuration. ICAS-Proceedings 1988, Vol. 1, 649-662. See also: J. Aircraft 26 (1989), 657-666.
- [37] D. Hummel: On the vortex formation over a slender wing at large angles of incidence. AGARD-CP-247 (1978), 15-1 to 15-17.

THE EFFECTS OF FOREPLANES ON THE STATIC AND DYNAMIC
CHARACTERISTICS OF A COMBAT AIRCRAFT MODEL

by

C O O'Leary

B Weir

Royal Aerospace Establishment, Aerodynamics Department, Bedford, MK41 6AE, England

SUMMARY

On a close coupled canard configuration there are strong aerodynamic interactions between the forebody, foreplanes and wings which are likely to affect both the longitudinal characteristics and the lateral/directional stability of the aircraft, especially at high angle-of-attack. The nature and strength of these interactions is likely to depend on the planform and deflection of the foreplanes.

Tests were made to investigate these effects on the RAE HIRM2 model in the 4m x 2.7m Low Speed Wind Tunnel. The model was tested with trapezoidal and gothic foreplanes on a static force balance and on a lateral oscillatory rig.

Effects on lift and pitching moment were similar for the different types of foreplane. There were significant effects on lateral and directional stability due to foreplane and foreplane deflection.

LIST OF SYMBOLS

b wing span
 \bar{c} aerodynamic mean chord
 C_L rolling moment coefficient, $L/\rho V S b$
 C_L lift coefficient
 C_m pitching moment coefficient
 C_n yawing moment coefficient, $N/\rho V S b$
 C_y sideforce coefficient, $Y/\rho V S$
 p rate of roll
 r rate of yaw
 S reference wing area
 V free stream velocity

α angle of attack
 β angle of sideslip
 δ_G foreplane deflection (gothic)
 δ_T foreplane deflection (trapezoidal)
 ρ air density

Derivatives:

$$C_{L_\alpha} = \frac{\partial C_L}{\partial \alpha}, \quad C_{n_\beta} = \frac{\partial C_n}{\partial \beta}, \quad C_{y_\beta} = \frac{\partial C_y}{\partial \beta}$$

$$C_{L_p} = \frac{\partial C_L}{\partial (\frac{pb}{2V})}, \quad C_{n_p} = \frac{\partial C_n}{\partial (\frac{pb}{2V})}, \quad C_{y_p} = \frac{\partial C_y}{\partial (\frac{pb}{2V})}$$

$$C_{L_\beta} = \frac{\partial C_L}{\partial (\frac{\beta b}{2V})}, \quad C_{n_\beta} = \frac{\partial C_n}{\partial (\frac{\beta b}{2V})}, \quad C_{y_\beta} = \frac{\partial C_y}{\partial (\frac{\beta b}{2V})}$$

$$C_{L_r} = \frac{\partial C_L}{\partial (\frac{rb}{2V})}, \quad C_{n_r} = \frac{\partial C_n}{\partial (\frac{rb}{2V})}, \quad C_{y_r} = \frac{\partial C_y}{\partial (\frac{rb}{2V})}$$

1 INTRODUCTION

The canard configuration has become popular in the design of advanced combat aircraft since there can be significant aerodynamic advantages from such a layout^{1,2}. For a close coupled canard there is a strong aerodynamic interaction between the foreplane and the wing which affects not only the longitudinal characteristics but may also influence the lateral and directional stability of the aircraft, especially at high angle-of-attack. Interaction between the flow around the forebody and the foreplane may also have a significant effect. Both these effects are likely to depend on the planform and deflection of the foreplane. Results from previous tests³ on a model with a trapezoidal foreplane of 50° leading edge sweep showed significant non-linearities in the variation of pitching moment with angle-of-attack. It was thought possible that slender gothic foreplanes with sharp leading edges may eliminate these non-linearities without adversely affecting other aerodynamic advantages of the configuration.

This paper presents results from low-speed wind-tunnel tests on an agile fighter-type delta-canard model to assess the effects on longitudinal and lateral characteristics of (a) the presence of foreplanes of trapezoidal and gothic planform and (b) foreplane deflection. Static forces were measured on a conventional strain gauge balance and lateral aerodynamic derivatives on an oscillatory balance.

2 DESCRIPTION OF MODEL

A general arrangement of the second RAE High Incidence Research Model (HIRM 2) is shown in Fig 1 and principal dimensions are given in Table 1. The configuration is typical of a delta-canard agile fighter with a wing leading edge sweep of 58°. It has been the subject of a research programme at RAE, including extensive wind-tunnel and free flight model testing⁴.

The fuselage of the model is of rectangular cross section which transitions to a circular section forward of the foreplanes. It consists of a tubular steel core, incorporating the strain gauge balance housing, onto which is built a glass reinforced-plastic shell to form the fuselage shape. The bore in the steel core is increased towards the tail of the model to allow enough clearance for small amplitude pitch and yaw oscillations (up to 2°). A motor, gearbox and displacement transducer are built onto the forward end of the core for remote control of the foreplanes which can be deflected through the range +10° to -40°. The foreplane and/or fin can be removed and replaced by blanks. Wings, foreplanes and fin are made from aluminium alloy and the total model mass is approximately 70 kg.

During previous tests⁴, wing fences and rear fuselage strakes were fitted when the basic configuration was found to suffer a loss in directional stability at moderate angle-of-attack.

Planforms of the foreplanes are shown in Fig 1. Trapezoidal foreplanes have a symmetrical thin aerofoil cross-section but gothic foreplanes are flat plate sections with sharp leading and trailing edges. Gothic foreplanes are 0.92 x area of trapezoidal foreplanes.

3 DESCRIPTION OF TESTS

3.1 Static tests

The tests were made in the 4m x 2.7m Low Speed, Atmospheric Wind Tunnel at RAE Bedford at a wind speed of 60 m/s. Reynolds number based on c was 2.3×10^6 and all tests were made with transition free. The model was sting mounted on a six-component strain gauge balance. Tests made were as follows:

(A) Longitudinal

$\alpha = 0^\circ$ to 36° in 2° steps, $\beta = 0^\circ$

(i) Trapezoidal foreplanes $\delta_T^* = 10, 0, -10, -20, -40$

(ii) Gothic foreplanes $\delta_G^* = 10, 0, -10$

(iii) Foreplanes off

(B) Lateral

$\alpha = 8^\circ$ to 36° in 4° steps, $\beta = -10^\circ$ to $+10^\circ$ at each

(i) Trapezoidal foreplanes $\delta_T^* = 10^\circ, 0^\circ, -10^\circ$

(ii) Gothic foreplanes $\delta_G^* = 10^\circ, 0^\circ, -10^\circ$

(iii) Foreplanes off

3.2 Lateral oscillatory tests

These tests were also made in the 4m x 2.7m Wind Tunnel. The angle-of-attack range was 0° to 30° with $\delta = 0^\circ$ and wind speed was again 60 m/s. A description of the rig and calibration procedures is given in Ref 5.

The test procedure was to excite oscillations in one of the three lateral modes and take data at each angle-of-attack throughout the test range. The mode was then changed and the procedure repeated. The three modes approximated to yaw, sideslip and roll. Tests were made foreplanes-off and with trapezoidal and gothic foreplanes set at -10° , 0° and 10° .

4 RESULTS AND DISCUSSION

All results are referred to a Moment Reference Centre (MRC) at 0.17 c. Derivatives are defined in the List of Symbols.

4.1 Longitudinal static results

4.1.1 Effects on lift

Lift characteristics for the model with trapezoidal and gothic foreplanes on at zero deflection ($\delta_L = \delta_G = 0^\circ$) are compared with foreplanes-off in Fig 2. The increment in lift due to foreplanes increases steadily from $\alpha = 10^\circ$ until C_{Lmax} , which is approximately 20% greater with foreplanes-on. Trapezoidal foreplanes give a small (1.5%) increment above that for gothic foreplanes. With foreplanes-off C_{Lmax} is reached at $\alpha = 30^\circ$ but with foreplanes-on C_{Lmax} is at $\alpha = 35^\circ$. Effects of foreplane deflection are shown in Figs 3 and 4 for trapezoidal and gothic foreplanes respectively. For trapezoidal foreplanes there is little effect on gradient for deflections $\delta_L = 0^\circ$, -10° , and -20° but some reduction for $\delta_L = 10^\circ$. For $\delta_L = -40^\circ$ there is a marked reduction in gradient and a decrement in C_{Lmax} of approximately 15% compared with the maximum lift for $\delta_L = 0^\circ$. The highest value of C_L is achieved when $\delta_L = -20^\circ$. With gothic foreplanes also there is no significant effect of deflection until near C_{Lmax} (Fig 4).

It is apparent that, on this close coupled configuration at high angles-of-attack, there is maximum beneficial interaction between foreplane and wing flows when the foreplane is set at approximately -20° , and foreplane planform has little effect.

4.1.2 Effects on Pitching moment

Pitching moment characteristics for $\delta_L = \delta_G = 0^\circ$ and foreplanes-off are compared in Fig 5. With foreplanes-on the model is still marginally stable up to $\alpha = 20^\circ$ after which stability decreases, with markedly unstable characteristics at high angles-of-attack. With foreplanes-off stability is maintained up to $\alpha = 29^\circ$. The initial instability above C_{Lmax} diminishes to neutral at $\alpha = 18^\circ$. At low and moderate angles-of-attack gothic foreplanes probably generate less direct lift than trapezoidal foreplanes and this is reflected in slightly more stability for $\delta_L = 0^\circ$ up to $\alpha = 20^\circ$. At higher angles-of-attack it is likely that because of stronger vortex flow over the slender gothic foreplane more normal force is generated forward of the MRC and the model is then slightly less stable as shown in Fig 5. There is, however, little difference in the linearity of pitching moment variation with angle-of-attack for the two types of foreplane.

Effects of foreplane deflection on pitching moment are shown in Figs 6 and 7. In general, deflection of either type of foreplane has only minor effects on the gradient and linearity of pitching moment. For $\delta_L = -40^\circ$, however, stability is markedly increased at low angles-of-attack. In this condition flow on the foreplane lower surface is likely to be separated, so the gradient of pitching moment is similar to foreplanes-off with a negative increment due to a steady download from pressure on the upper foreplane surface. For $\delta_L = \delta_G = 0^\circ$ and -10° Figs 6 and 7 show that there is little difference in linearity due to foreplane planform but for $\delta_L = \delta_G = 10^\circ$ gothic foreplanes give a more linear variation of pitching moment.

4.2 Lateral static results

In this section results are presented for the 'static' derivatives, $C_{n\beta}$, $C_{y\beta}$ and $C_{\xi\beta}$. These were obtained from the slopes of C_n , C_y and C_ξ vs β over the β range $\pm 2^\circ$.

4.2.1 Effects on $C_{y\beta}$ and $C_{n\beta}$

A comparison of the sideslip derivative $C_{y\beta}$ foreplanes on and off, in Fig 8a shows that the presence of either foreplane at zero deflection significantly reduces

the magnitude of $C_{y\beta}$ throughout the angle of attack range. The corresponding comparison for $C_{n\beta}$ (Fig 9a) is more complicated: at low to moderate angles of attack ($\alpha < 16^\circ$), either foreplane reduces directional stability from the near-constant value of 0.12 obtained with foreplane-off. At higher angles of attack, $C_{n\beta}$ is reduced and becomes zero near $\alpha = 30^\circ$, foreplanes on or off. The trapezoidal foreplane makes little difference to the level of $C_{n\beta}$, so adding this foreplane moves the lateral centre of pressure further aft. However, the level of $C_{n\beta}$ for gothic foreplane continues to be reduced, with near-zero value at $\alpha = 24^\circ$, and recovery only at $\alpha = 28^\circ$.

Deflection of the foreplanes has marked nonlinear effects on both $C_{y\beta}$ and $C_{n\beta}$ as shown in Fig 8b&c, Fig 9b&c respectively. Negative deflection (10° LE down) causes a larger magnitude $C_{y\beta}$, but more negative $C_{n\beta}$, compared with positive deflection. $C_{n\beta}$ becomes negative as α increase through 24° and 21° for trapezoidal and gothic foreplanes respectively. It is possible that negative deflection induces larger areas of streamlined flow over the nose, enhancing the differential sidelforce on the forebody. Positive deflection causes the level of $C_{n\beta}$ to be maintained up to $\alpha \approx 24^\circ$, but then reduction occurs more quickly.

4.2.2 Effects on $C_{l\beta}$

Fig 10a shows that at all angles-of-attack tested $C_{l\beta}$ is more negative, ie more stable, with foreplanes-on, indicating that foreplane-induced effects increase differential lift on the wings during sideslip. There is a loss in stability for $\alpha > 17^\circ$, but with foreplanes-on $C_{l\beta}$ becomes zero at an angle-of-attack about 5° higher than with foreplanes-off. Differences due to foreplane type are insignificant.

As shown in Fig 10b&c, change in deflection of either type of foreplane from -10° to 10° causes a significant (20% to 30%) increase in the magnitude of $C_{l\beta}$ for $\alpha < 25^\circ$. This result indicates that a positive foreplane deflection generates greater differential lift on the wings.

4.3 Lateral oscillatory results

4.3.1 Effects on dynamic measurements of $C_{y\beta}$, $C_{n\beta}$ and $C_{l\beta}$

Results from oscillatory tests include the so-called 'stiffness' derivatives $C_{y\beta}$, $C_{n\beta}$ and $C_{l\beta}$ which are shown in Figs 11, 12 and 13. The results in Figs 11 and 12 may be compared with the static measurements of $C_{y\beta}$ and $C_{n\beta}$ in Figs 8 and 9. Oscillatory tests were made at smaller intervals of angle-of-attack than corresponding static lateral tests and the results show more variation with angle-of-attack. Figs 11a and 12a show that with foreplanes-off, for $\alpha < 13^\circ$, $C_{y\beta}$ increases in magnitude while $C_{n\beta}$ is fairly constant but for $13^\circ < \alpha < 17^\circ$ there are large variations in both quantities. With foreplanes-on the variation is similar but displaced in a negative direction for $C_{y\beta}$, and a positive direction for $C_{n\beta}$. The signs of the changes in $C_{y\beta}$ and $C_{n\beta}$ are such as to suggest that the probable cause is a temporary loss of fin effectiveness due to wake effects. Results from previous tests⁶ on the basic model showed similar excursions in $C_{n\beta}$ which reached large negative values and prompted the fitting of wing fences and rear fuselage strakes which reduced the losses to a level acceptable for free-flight tests. A comparison of static and oscillatory results in Figs 9a and 12a shows that at moderate angle of attack $C_{n\beta}$ from static tests is about 20% larger, a result which has been consistently obtained in tests on other models^{6,7} and ascribed to lag effects in oscillatory tests.

Differences in $C_{y\beta}$ and $C_{l\beta}$ due to foreplane deflection follow similar trends to results from static tests, but the 'drop out' in directional stability at $\alpha \approx 14^\circ$ does not occur when $\delta_T = \delta_G = 10^\circ$.

Rolling moment due to sideslip (Fig 13) is similar to the static result (Fig 10) but for $\alpha > 20^\circ$ oscillatory results are more negative. Here again the differences may be due to lag effects.

At all angles-of-attack below 30° there is a consistent negative increment in $C_{l\beta}$ when the foreplanes are deflected from -10° to 10° , as is the case for static results in Fig 10b&c.

4.3.2 Effects on derivatives due to rate of yaw

The yaw damping derivative, $C_{n\dot{\beta}} = C_{n\dot{\beta}} \cos \alpha$ (Fig 14a) remains negative (positive damping) for all angles-of-attack tested, both with and without foreplanes, but there is considerable variation with angle of attack. There is, however, less variation with gothic foreplanes, for $15^\circ < \alpha < 25^\circ$. During the tests it was found that with foreplanes-off, at high angle-of-attack, the yawing mode was very unsteady. Accuracy of measurement was affected and may explain some of the large variation in the results at high α .

As shown in Figs 14b,c, for $15^\circ < \alpha < 25^\circ$, negative foreplane deflection results in more negative values of $C_{n\dot{\beta}}$, $C_{n\dot{\beta}} \cos \alpha$. In section 4.2.1 it was stated that results for $C_{y\dot{\beta}}$ and $C_{n\dot{\beta}}$ shown in Figs 8 and 9 suggested that negative foreplane increased the destabilising sideforce on the nose due to sideslip. Fig 15 shows how a sideforce on the nose can have a destabilising effect on $C_{n\dot{\beta}}$ but a stabilising effect on $C_{n\dot{\beta}} = C_{n\dot{\beta}} \cos \alpha$. In Fig 15a the fuselage is in a steady positive sideslip with the same value of β at the nose and at the c of g. The increment in sideforce on the nose due to negative δ is destabilising. In Fig 15b the fuselage is yawing positively. β is zero at the c of g but since the relative wind vector is curved there is positive sideslip at the nose. This local sideslip produces a side-force opposing the yawing motion and therefore stabilising, ie more negative, as shown in Fig 14.

Results for the cross derivative $C_{l\dot{p}} = C_{l\dot{p}} \cos \alpha$ are shown in Fig 16. Generally, this derivative is generated by differential lift on the wings due to yawing motion. For a positive rate of yaw there is an increment of lift on the port wing and a decrement on the starboard wing leading to a positive rolling moment which is proportional to lift coefficient. Results from the present tests (Fig 16a) show a general increase with angle-of-attack. There are no significant effects of foreplane at low and moderate angles-of-attack but for $\alpha > 20^\circ$ there is considerable variation in the measurements with foreplanes off.

Fig 16b,c show the effects of foreplane deflection on $C_{l\dot{p}} = C_{l\dot{p}} \cos \alpha$. For $\alpha < 25^\circ$ there is an increment of approximately 0.03 when foreplanes are deflected from 10° to -10° . Although there is no significant increment in total lift due to foreplane deflection at low angle-of-attack (Figs 3 and 4), the results suggest that there is an increase in foreplane-induced differential lift on the wings for a negative foreplane deflection.

4.3.3 Effects on derivatives due to rate of roll

As shown in Fig 17a, the roll damping derivative $C_{l\dot{p}} + C_{l\dot{p}} \sin \alpha$ is fairly constant with angle-of-attack and is maintained at about -0.24 up to $\alpha = 30^\circ$. Foreplanes at zero deflection have no significant effect on this derivative. There is some variability, foreplanes off, at high angle-of-attack but this may be due to measurement inaccuracy.

Roll damping derives mainly from differential lift on the wings due to positive and negative increments in effective angle-of-attack on the outer wing panels. Fig 17b,c show an increment in the magnitude of $C_{l\dot{p}} + C_{l\dot{p}} \sin \alpha$ between results for $\delta = 10^\circ$ and $\delta = -10^\circ$. So, as for $C_{l\dot{p}} = C_{l\dot{p}} \cos \alpha$, there is an apparent increase in the induced differential wing lift for negative foreplane deflection.

The cross-derivative $C_{n\dot{p}} + C_{n\dot{p}} \sin \alpha$ is shown in Fig 18. Up to $\alpha = 12^\circ$ Fig 18a shows that the derivative increases negatively from near zero to approximately -0.16. At higher angles-of-attack there is some scatter in the range -0.4 to 0.1. There is no consistent effect due to foreplanes. Fig 18b,c show that foreplane deflection between -10° and 10° also has no consistent effect.

4.4 Effects on stability parameter $C_{n\dot{\beta}}$ (dynamic)

The possibility of directional divergence at high angles-of-attack can be examined by means of the parameter $C_{n\dot{\beta}}$ (dyn) which is defined:

$$C_{n\dot{\beta}}(\text{dyn}) = C_{n\dot{\beta}} \cos \alpha - C_{l\dot{\beta}} \frac{I_z}{I_x} \sin \alpha$$

where I_z and I_x are the moments of inertia about the yaw and roll axes applicable to the free flight model of the HIRM 2 configuration. Negative values of this parameter indicate susceptibility to directional divergence.

The effect of foreplanes (trapezoidal) is shown in Fig 19 for static and oscillatory test data. Fig 19a shows that using static data, the criterion indicates that foreplanes delay the onset of instability from $\alpha \approx 28^\circ$ to $\alpha \approx 33^\circ$ but for oscillatory test data, Fig 19b, there is no indication of a negative trend for either configuration at $\alpha = 30^\circ$. The reason for this disagreement is primarily due to the difference in the static and oscillatory measurements of $C_{n\dot{\alpha}}$ (Figs 10 and 13) since the second term in the equation for $C_{n\dot{\alpha}(\text{dyn})}$ is much larger than the first at high angle-of-attack. In the static test data (Fig 10) $C_{n\dot{\alpha}}$ becomes positive but in oscillatory data it remains substantially negative (Fig 13).

The effects of foreplane deflection are shown in Fig 20. Here again $C_{n\beta}(\text{dyn})$ from static data (Fig 20a) indicates instability at high angle-of-attack, for positive and negative deflection of foreplanes, but there is no indication of instability, up to $\alpha \approx 30^\circ$, with oscillatory data (Fig 20b).

The derivative $C_{L\delta}$ is mainly a function of the flow over the wings. Thus the difference in wing flow for a static model and an oscillating model, where there may be substantial modification of the forces on the wing due to lag effects, could be expected to cause the observed differences in $C_{L\delta}$ and hence $C_{n\delta}(\text{dyn})$.

5 CONCLUSIONS

Static and lateral oscillatory tests have been made on an agile fighter configuration to investigate the effects of close-coupled trapezoidal and gothic foreplanes. Results show the following:

- (1) Foreplanes of either planform increase lift at moderate and high angle-of-attack and optimum negative deflections may be chosen.
- (2) As compared with trapezoidal foreplanes, gothic foreplanes do not significantly improve the linearity or gradient of the pitching moment characteristic for moderate negative deflection.
- (3) At moderate angle-of-attack, addition of foreplanes at zero or negative deflection reduces directional stability $C_{n\beta}$. Yaw damping, however, is increased under these conditions.
- (4) The derivative $C_{L\beta}$ is more negative (increased stability) with foreplanes-on and positive deflection increases this effect.
- (5) Foreplanes at zero deflection have only a small effect on derivatives $C_{L_p} + C_{L\dot{\beta}}$, $\sin \alpha$, $C_{L_r} - C_{L\delta} \cos \alpha$ and $C_{n_p} + C_{n\dot{\beta}} \sin \alpha$, but deflecting the foreplanes causes some changes in levels.
- (6) As in previous tests, results for derivatives $C_{n\beta}$ and $C_{L\beta}$ from static and oscillatory tests are not in agreement, reflecting the difference in flow conditions in the two types of test. The tendency to directional divergence, indicated by the parameter $C_{n\beta}(\text{dyn})$, is greater if static data are considered more appropriate.

Table 1
PRINCIPAL DIMENSIONS OF MODEL.

	mm or mm
Wing area, S x 10 ⁻⁶	0.5367
Aerodynamic mean chord, \bar{c}	559.7
Wing span, b	1111.1
Foreplane area x 10 ⁻⁶ : trapezoidal (each surface)	0.0268
gothic	0.0220
Foreplane span	480.3
Fin area x 10 ⁻⁶	0.0466
Fin height above horizontal fuselage datum	365.8
Moment reference centre (MRC)	0.17 \bar{c}

REFERENCES

- 1 B.B. Gloss, Effect of wing planform and canard location and geometry of the longitudinal aerodynamic characteristics on a close-coupled canard wing model at subsonic speeds, NASA TN D-7910, 1975.
- 2 J. Er-El, A Seginer, The leading edge vortex trajectories of close-coupled wing-canard configurations and their breakdown characteristics, AIAA-83-1817, 1983.
- 3 A. Jean Ross, G.E.A. Reid, The development of mathematical models for a high incidence research model, Part 1 - analysis of static data, RAE Technical Report 83037, 1983.
- 4 C.O. O'Leary, E.N. Rowthorn, Low speed dynamic tests on a canard configured High Incidence Research Model (HIRM 2), RAE Technical Report 88024, 1988.
- 5 C.O. O'Leary, Wind-tunnel measurement of aerodynamic derivatives using flexible sting rigs, RAE Technical Memorandum 1875, 1980.
- 6 C.O. O'Leary, Dynamic tests on a high incidence research model (HIRM) in a low speed wind tunnel, RAE Technical Report 84111, 1984.
- 7 C.O. O'Leary, The aerodynamic effects of leading edge strakes on a combat aircraft: a wind-tunnel investigation including oscillatory measurements of lateral aerodynamic derivatives, RAE Technical Report 83021, 1983.

Copyright © Controller HMSO London 1989

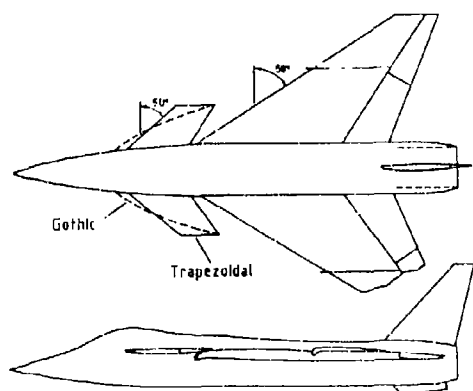


Fig 1 General arrangement of BIRM-2

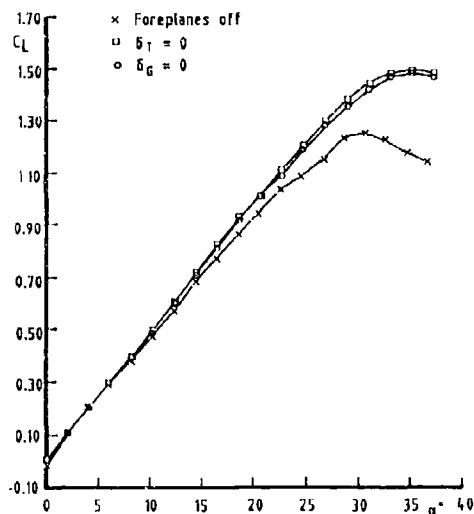


Fig 2 Effect of foreplanes on lift

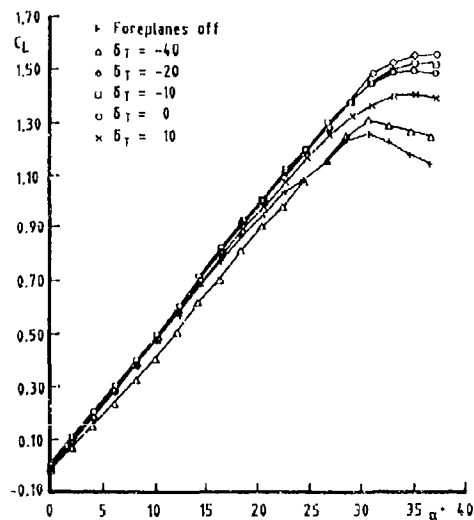


Fig 3 Effect of trapezoidal foreplane deflection on lift

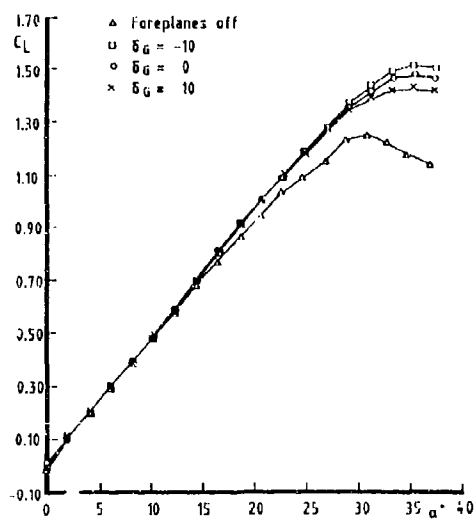


Fig 4 Effect of gothic foreplane deflection on lift

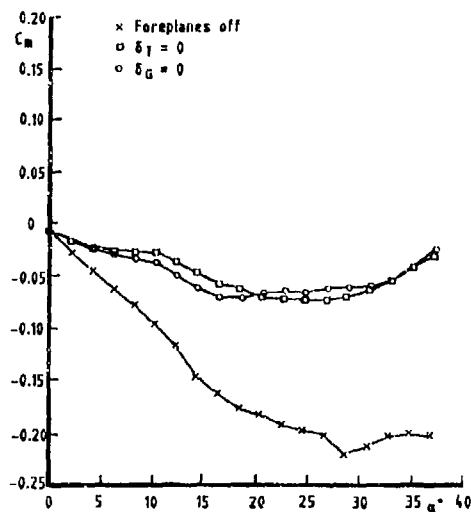


Fig 5 Effect of foreplanes on pitching moment

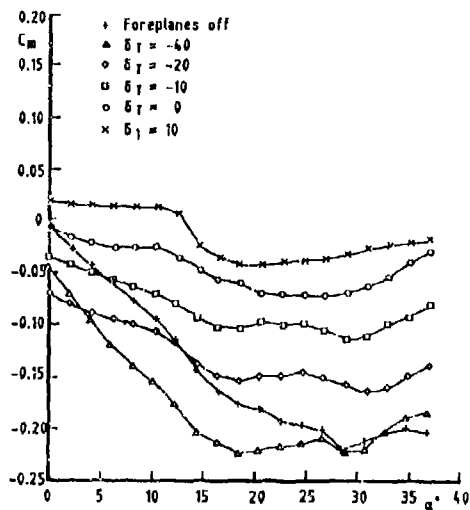


Fig 6 Effect of trapezoidal foreplane deflection on pitching moment

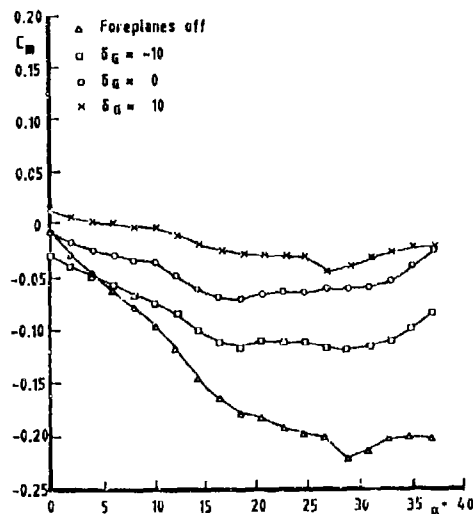


Fig 7 Effect of gothic foreplane deflection on pitching moment

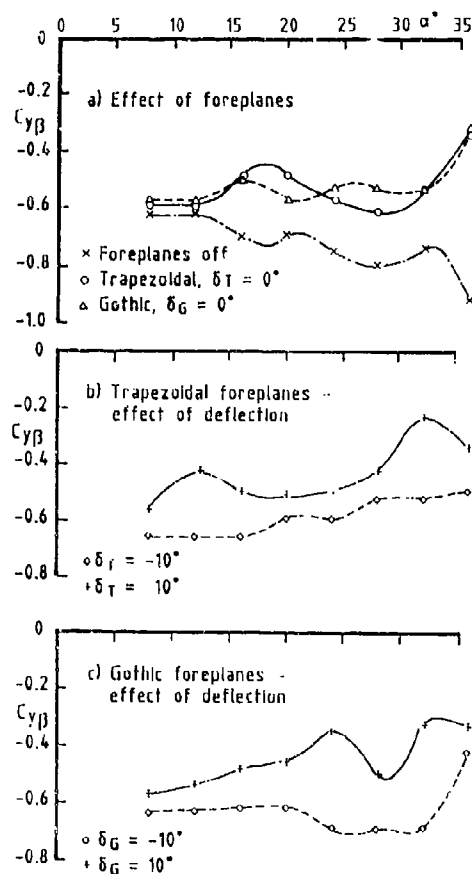


Fig 8 Sideforce due to sideslip, $C_{Y\beta}$
from static tests

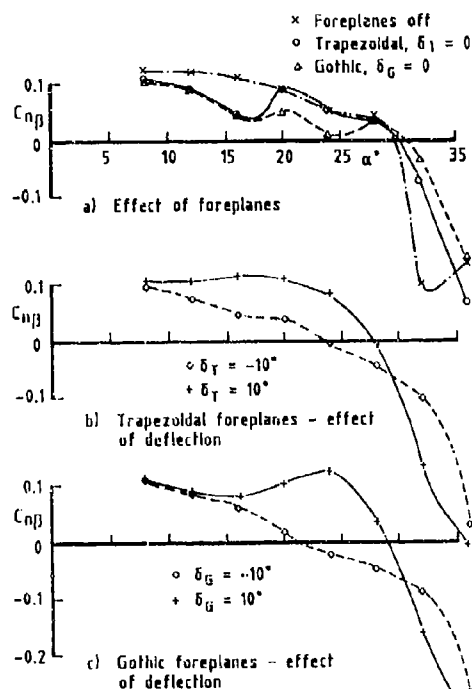


Fig 9 Directional stability, $C_{N\beta}$ from
static tests

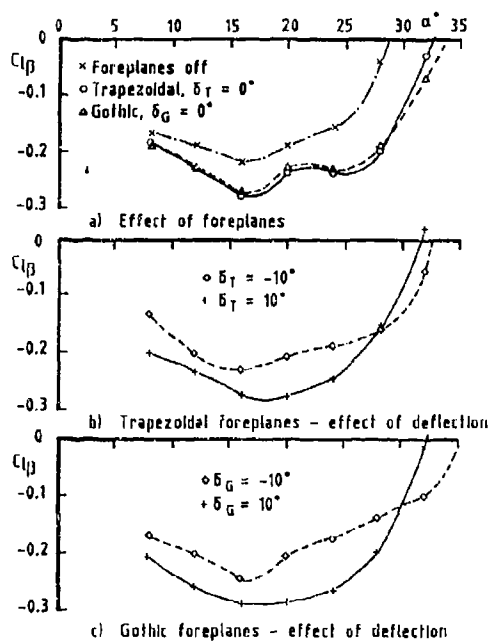


Fig 10 Rolling moment due to sideslip, $C_{l\beta}$ from static tests

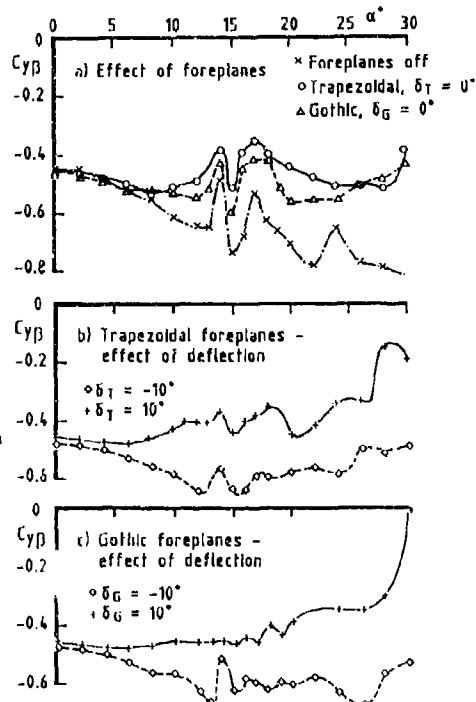


Fig 11 Sideforce due to sideslip, $C_{Y\beta}$ from oscillatory tests

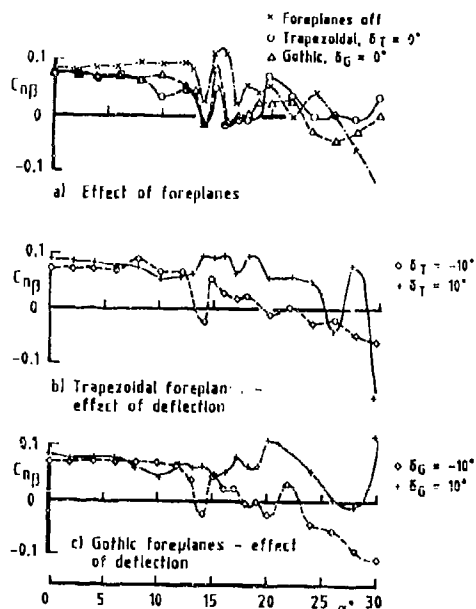


Fig 12 Directional stability, $C_{n\beta}$ from oscillatory tests

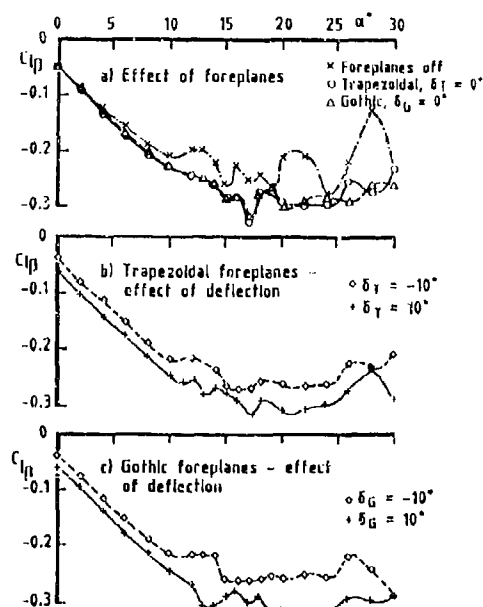


Fig 13 Rolling moment due to sideslip, $C_{l\beta}$ from oscillatory tests

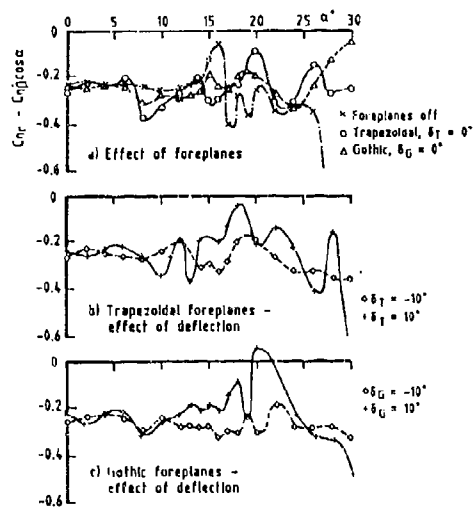
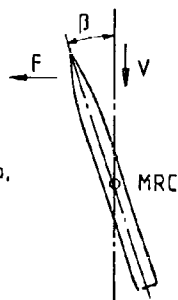


Fig 14 Yaw damping derivative, $C_{Yr} - C_{Yr} \cos \alpha$ from oscillatory tests

a) Steady sideslip, zero yaw rate



b) Zero sideslip at MRC, steady yaw rate

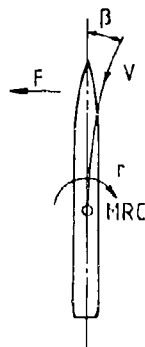


Fig 15 Sideforce developed on forward fuselage due to negative foreplane deflection

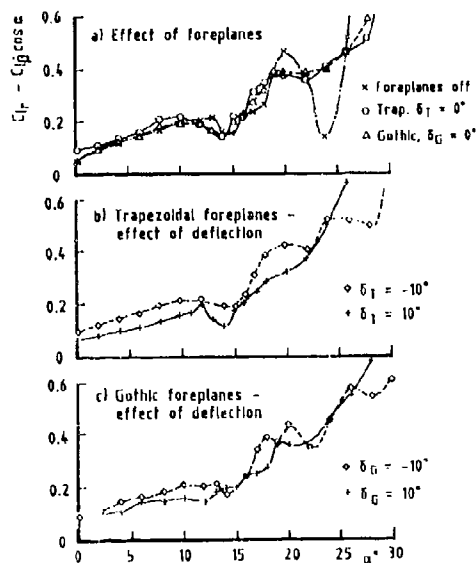


Fig 16 Cross damping derivative, $C_{Yp} - C_{Yp} \cos \alpha$ from oscillatory tests

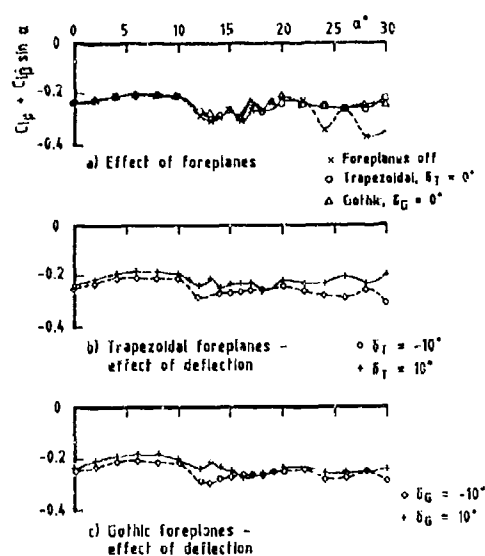


Fig 17 Roll damping derivative, $C_{lp} + C_{l\dot{\beta}} \sin \alpha$ from oscillatory tests

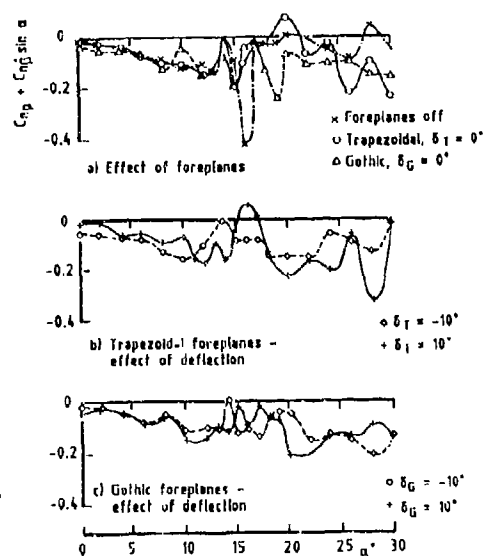


Fig 18 Cross damping derivative, $C_{np} + C_{n\dot{\beta}} \sin \alpha$ from oscillatory tests

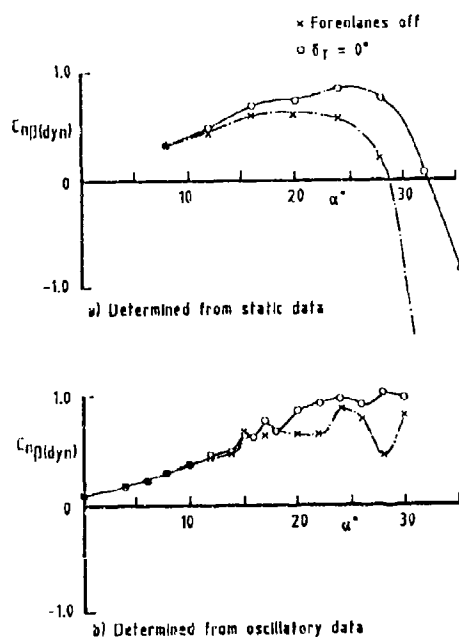


Fig 19 Effect of foreplanes on lateral stability parameter $C_{n\beta}(\text{dyn})$

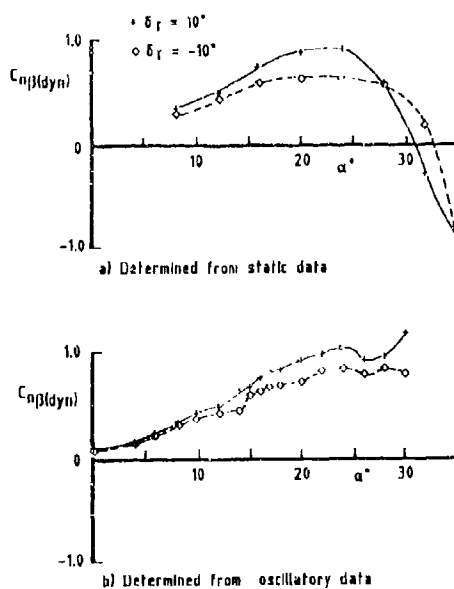


Fig 20 Effect of foreplane deflection on lateral stability parameter $C_{n\beta}(\text{dyn})$

Innovative Control Concepts and Component Integration for a Generic Supercruise Fighter

Bret A. Marks
McDonnell Aircraft Company
McDonnell Douglas Corporation
St. Louis, Missouri 63166
U.S.A.

David E. Hahne
National Aeronautics and Space Administration
Langley Research Center
Hampton, Virginia 23665
U.S.A.

Summary

This paper highlights the results of a series of low speed wind tunnel tests conducted in the NASA Langley Research Center (LaRC) 12 Ft Low Speed Wind Tunnel (LSWT). The main objectives of the tests were to provide generalized component integration guidelines and to investigate a variety of innovative control concepts designed to improve the high angle of attack (AOA) controllability of a generic class of supercruise fighters.

List of Symbols

Aerodynamic Symbols

AR	wing aspect ratio
b	wing span (ft)
\bar{c}	mean geometric chord (ft)
C_{ℓ}	rolling moment coefficient (body axis)
C_{ℓ_a}	lift curve slope (deg^{-1})
C_{ℓ_β}	static lateral stability derivative, $\partial C_{\ell} / \partial \beta$ (deg^{-1})
C_m	pitching moment coefficient
C_N	normal force coefficient
C_n	yawing moment coefficient (body axis)
C_{n_β}	static directional stability derivative, $\partial C_n / \partial \beta$ (deg^{-1})
C_Y	side force coefficient
IB	inboard
HL	hinge line
ℓ_t	distance from aircraft moment reference center to tail aerodynamic center
MS	model station (in)
OB	outboard
Re	Reynolds number referenced to mean geometric chord
S_{ref}	wing reference area (ft^2)
\bar{V}	control surface volume
$2y/b$	semispan fraction (normalized distance from aircraft plane of symmetry)

Greek Symbols

α	aircraft angle of attack (deg)
β	slideslip angle (deg)
Γ	vortical tail cant angle (deg)
δ	control surface deflection angle relative to control surface hingeline (deg)
Λ	sweep angle (deg)

Unclassified. Copyright McDonnell Douglas 1988. All rights reserved.
McDonnell Douglas, Boeing and proprietary names are trademarks of the McDonnell Douglas Corporation. Reproduction or translation of this information without the written consent of McDonnell Douglas Corporation is prohibited. This document is intended for use by the McDonnell Douglas Corporation and its subsidiaries and is not to be distributed outside the McDonnell Douglas Corporation.
Copyright 1988, McDonnell Douglas Corporation.
Reprinted with permission.

Export Authority: 22CFR125.4(b)(13)

Subscripts

A	aileron
B	body flap
c	canard
F	wing trailing edge extension flap
H	horizontal stabilator
le	leading edge flap
LE	leading edge
L,R	left, right
r	rudder
s	strake
T	tiperon
TE	trailing edge

1.0 Introduction

Aircraft designed for projected combat threat performance will require unprecedented levels of transonic maneuverability as well as sustained supersonic cruise capability. Unconventional, high fineness ratio forebodies and highly swept, low aspect ratio wings, which are characteristic of advanced supersonic cruise concepts, are conducive to the formation of complex, nonlinear flowfields and to degraded high AOA stability. In addition, conventional aerodynamic control surfaces lose effectiveness at high angles of attack resulting in reduced maneuverability and inadequate recovery control. Consequently, new design and analysis methods are needed, and unconventional control concepts need to be explored.

Under a cooperative program between the McDonnell Aircraft Company (MCAIR) and the NASA LaRC Flight Dynamics Branch (FDB), component integration was investigated to provide generalized design guidelines for optimum high AOA lateral-directional stability of advanced fighter configurations. In addition, a variety of innovative control concepts designed to improve high AOA controllability were evaluated. A series of wind tunnel tests were conducted in the NASA LaRC 12 ft LSWT. A 7.5% scale NASA model of the generic MCAIR Supersonic Persistence Fighter (SSPF), illustrated in Figure 1, was used in these investigations. The baseline wing has a 65° leading edge sweep and a cranked, 0°/35° sweep trailing edge. This wing was selected based on the results of a high speed wing planform study conducted in the NASA LaRC Unitary Plan Wind Tunnel using a 4% scale SSPF model, Reference 1.

Included in the high speed investigation were 25° trapezoidal, 65° delta, and 70°/66° and 70°/90° cranked wing planforms. The 70°/66° cranked wing planform exhibited the most favorable supersonic cruise drag characteristics. Weight estimates and sizing analyses based upon a supersonically biased mission also identified the 70°/66° wing as the best design. For these reasons, the 70°/66° cranked wing planform was selected for initial low speed testing. The desire to reduce structural complexity without compromising aerodynamic characteristics led to the design of the baseline wing illustrated in Figure 1.

The 7.5% scale SSPF model was designed to be highly versatile to provide maximum configuration flexibility. All conventional lifting surfaces (e.g. wing, canard, horizontal and vertical tails) are composed of flat plates with beveled leading and trailing edges. Static force and moment data were obtained at a Mach number of 0.05 ($Re = 0.64 \times 10^6$) for angles of attack ranging from 0° to 60° and sideslip angles between ± 30°. A number of the control concepts investigated are illustrated in Figure 2. Several of the more promising concepts have been selected for detailed discussion. Detailed analyses of all of the concepts illustrated may be found in References 2 through 4.

In addition to the concepts shown in Figure 2, a wide variety of nose shapes were tested to determine their effect on static lateral-directional stability at high angles of attack, References 2 and 3. The baseline nose, illustrated in Figure 3, is triangular in cross section near the apex and blends to a circular cross section approximately 4 inches (model scale) aft of the apex. This nose shape provides a considerable reduction in asymmetric yawing moment at high angles of attack compared to a conventional circular nose, Reference 3.

2.0 Component Integration

Aircraft component integration effects were investigated early in the program. In addition to the baseline 65° wing, a 70°/66° and two 55° sweep cranked wings were evaluated. These wing planforms are compared to the baseline wing in Figure 4. One of the purposes of this wing parametric study was to determine the effects of leading edge sweep and aspect ratio on component integration optimization.

One of the more significant discoveries was the superior lateral-directional stability afforded by twin, wing-mounted vertical tails as compared to twin, fuselage mounted or single-centerline tails, Figure 5. The data presented in Figure 5 were obtained with the 70°/66° cranked wing planform. As

illustrated, moving the vertical tails outboard greatly increases directional stability ($C_{n\dot{\delta}}$) at high angles of attack. High AOA lateral stability ($C_{l\dot{\delta}}$) is also increased by moving the vertical tails outboard on the wing. These improvements are due to a favorable interaction between the vertical tails and the strong vortices generated at the wing leading edge.

Figure 6 illustrates the effect of vertical tail spanwise location on lateral-directional stability at 5° and 30° AOA for each of the wing planforms investigated. Incremental data (tails on - tails off) are presented to isolate the effects of the vertical tails on each wing planform. Note that the data presented in Figure 6 have been normalized by vertical tail volume (S_{vt}/S_{ref}) to account for the differences in the sizes of the tails investigated.

At low angles of attack, the directional stability provided by the vertical tails is fairly insensitive to vertical tail spanwise location. The increased effectiveness of the centerline vertical tail over that of the twin fuselage or wing mounted tails results from the end plating effect of the fuselage and wing trailing edge extension. Using the method described in Reference 5 to account for this end plating effect, the theoretical low AOA directional stability of the centerline vertical tail was determined and is illustrated in Figure 6.

The vertical tails contribute to lateral stability in varying degrees, depending on spanwise location, for each of the wing planforms investigated. However, the variation in lateral stability as a function of tail location is not as consistent from planform to planform as the variation in directional stability at low angles of attack.

At 30° AOA, placing the vertical tails inboard of 40% wing semispan degrades both lateral and directional stability. Stated another way, at 30° AOA, the lateral-directional stability characteristics of the configurations studied are actually more favorable without vertical tails than with tails placed inboard of 40% wing semispan. Lateral-directional stability is augmented by vertical tails located outboard of 40% wing semispan, with the optimum location being between 50% and 60%. These results are independent of the wing planforms tested and are due to the interaction of the vertical tails with the wing leading edge vortices.

The effects of vertical tail cant angle on the lateral-directional stability of the baseline wing configuration are illustrated in Figure 7. The data presented were obtained for a twin vertical tail root location of 50% of the wing semispan. As shown, inboard cant reduces both lateral and directional stability. Similar results were obtained for the forward swept tails illustrated in Figure 2. Tail sweep was also found to have little effect on the overall levels of lateral-directional stability, as reported in Reference 3.

In comparing the data presented in Figure 7, note that as the vertical tails are canted in either direction, the sideward projected area of the tails is reduced. Theoretically, the planform area required to maintain the same effectiveness as the uncanted tails (at low angles of attack) is determined by dividing the uncanted tail area by the square of the cosine of the tail cant angle ($\cos^2 \tau$). A detailed derivation clarifying the application of the $1/\cos^2 \tau$ term is provided in the Appendix. This term has been applied to the data presented in Figure 8, which illustrates the effects of vertical tail cant angle on lateral-directional stability at 5° and 30° AOA for several of the wing planforms tested. The effects of vertical tail cant angle on lateral-directional stability were not investigated on the 70°/66° cranked wing.

At low angles of attack ($\alpha = 5^\circ$), vertical tail cant angle has little effect on directional stability, however, lateral stability increases as the tails are canted outboard and decreases as they are canted inboard. At high angles of attack ($\alpha = 30^\circ$), the vertical tails are more effective in improving both lateral and directional stability as cant angle is increased. As with the effects observed by varying vertical tail spanwise location, the cant angle effects seen at 30° AOA result from the interaction of the twin vertical tails with the wing leading edge vortices. In general, the magnitudes of lateral-directional stability generated by the vertical tails at 30° AOA are greater for the 65° sweep wing than for either of the 55° sweep wings. This is attributed to the stronger leading edge vortices associated with the 65° sweep wing.

3.0 Control Concepts

3.1 Pitch Control

Structural integration of twin, wing-mounted vertical tails will probably require the use of a wing trailing edge extension. Incorporation of such a device would effectively eliminate the use of a conventional horizontal tail. Pitch control, therefore, would have to be obtained by other means.

Figure 9 compares the nose-down pitch control provided by wing trailing edge extension flaps to that available from canard-wing and wing-horizontal tail configurations. Generally speaking, wing trailing edge extension flaps are as effective as conventional horizontal tail or canard surfaces in generating nose down pitch control. With the addition of a buoy flap, the nose down pitch control available from the wing trailing edge extension flaps is improved across the entire AOA range investigated, as indicated by the shaded region in Figure 9.

3.2 Roll Control

Roll control for highly swept, low aspect ratio wings can be seriously degraded at high angles of attack due to the predominance of wing spanwise flow. As spanwise flow develops, conventional ailerons having aft swept hingelines lose effectiveness. To take advantage of this spanwise flow, skewed hingelines, deflectable wing tips (tipperons) were developed on the SSPV as high AOA roll control devices.

Figure 10 compares the roll control provided by skewed hingeline tipperons to that provided by conventional ailerons. Below 22° AOA, conventional ailerons generate an average of approximately 17% more roll control than tipperons. However, above 32° AOA, the roll control provided by the tipperons is as much as four times that provided by the ailerons. In addition, differentially deflected tipperons generate very little adverse yawing moment at low angles of attack. Above approximately 40° AOA, the tipperons generate proverse yawing moment which is beneficial when attempting to coordinate a stability axis (zero sideslip angle) roll. Conversely, the adverse yawing moment generated by the ailerons is substantial at high angles of attack.

In Figure 10, note that deflecting the ailerons in combination with the tipperons completely eliminates the proverse yawing moment generated by the tipperons at high angles of attack. In fact, the yawing moment characteristics of the combined ailerons and tipperons are nearly identical to those of the ailerons. These results suggest that through proper tailoring of control surface geometry and location, it may be possible to provide increased roll control at high angles of attack while maintaining proverse levels of yawing moment to aid in roll coordination.

One way to take advantage of the proverse yaw generated by the tipperons at high angles of attack without sacrificing the increased roll control provided by combined ailerons and tipperons at lower angles is to schedule differential aileron deflection with AOA. By restricting maximum differential aileron deflection as shown in Figure 11a, it is possible to achieve the roll/yaw characteristics illustrated in Figure 11b. Above 40° AOA, the ailerons are not used at all when roll is commanded. The roll control provided by the tipperons alone at these angles of attack is greater than that provided by conventional ailerons (Figure 10) and full advantage is taken of the proverse yaw associated with the tipperons.

3.3 Yaw Control

A large number of unconventional yaw control devices were investigated with the goal of substantially increasing yaw control at high angles of attack. Conventional rudder effectiveness is rapidly degraded as angle of attack is increased and the angle of the flowfield surrounding the vertical tails approaches that of the rudder hingelines. In addition, the shielding effect of the wing at high angles of attack reduces the kinetic energy of the vertical tail flowfield, further reducing yaw control.

Figure 12 illustrates the effect of vertical tail cant angle on conventional rudder effectiveness. At moderate to high angles of attack, rudder effectiveness increases as the vertical tails are canted inboard 15° . Conversely, effectiveness is reduced considerably as the tails are canted outboard 15° . Also shown in Figure 12 are the variations in tip rudder effectiveness with vertical tail cant angle. Operating on the same principle as the tipperon, the tip rudders were designed to take advantage of the spanwise flow acting on the swept tails ($\Lambda_{LE} = 47.7^\circ$) at high angles of attack.

Referring to the 0° vertical tail cant angle data, the tip rudders begin to gain effectiveness at approximately 20° AOA. The effectiveness of the tip rudders is short-lived, however, and becomes erratic above 40° AOA. Contrary to the trend observed with the conventional rudders, tip rudder effectiveness increases as the tails are canted outboard 15° . When the tails are canted inboard 15° , tip rudders are ineffective across the entire AOA range investigated.

Conventional and tip rudders were also tested in combination. With no vertical tail cant, combined rudders improve yaw control between 20° and 40° AOA compared to conventional rudders alone, Reference 4. However, simply increasing the size of the conventional rudders to match the control volume of the combined rudders resulted in larger improvements.

All-movable twin vertical tails were also evaluated for their ability to improve yaw control at high angles of attack. The results are presented in Figure 13. Yaw control is increased substantially, compared to conventional rudders (Figure 12), at low angles of attack. However, all-movable tail effectiveness decays rapidly between 13° and 20° AOA before leveling off at slightly less than half its initial value (which is still considerably greater than conventional rudder effectiveness in this AOA range). Effectiveness then decays further above 30° to 40° , depending on vertical tail cant angle. This two-stage decay was also exhibited, to a lesser extent, by the conventional rudders, Figure 12. One possible explanation for this phenomenon is that the initial reduction in control surface effectiveness is related to the blanketing effect of the wing and the subsequent reduction in kinetic energy in the vertical tail flowfield. The surfaces retain some effectiveness due to the influence of the strong wing leading edge vortices. When these vortices burst (between 30° and 40° AOA), the effectiveness of the vertical tail control surfaces is reduced further. This explanation is purely conjecture and needs to be substantiated with additional data or through flow visualization.

Vertical tail cant has a substantial effect on the levels of adverse roll generated by the all-movable vertical tails at low angles of attack. Below 10° AOA, the adverse roll generated by 30° of tail deflection is nearly three times as large with 15° outboard tail cant as with 15° inboard cant. The Figure 13 data illustrate that if tail cant is used to augment control effectiveness, a trade-off exists between high AOA yaw control effectiveness and low AOA roll degradation.

Forebody cross-section shape significantly influences aircraft aerodynamic characteristics at high angles of attack, Reference 2. This is especially true for high fineness ratio forebodies, characteristic of fighter configurations. A unique approach to increasing yaw control at high angles of attack is the use of asymmetrically deployed nose strakes to influence forebody vortex formation and downstream trajectory. This concept has been evaluated extensively at NASA LARC on a number of different configurations, References 6 through 9. It involves the use of nose strakes to establish a fixed location for forebody flow separation and provide a pair of enhanced forebody vortices. Yaw control is achieved by controlling the level of forebody vortex asymmetry generated by the strakes. Deflectable nose strakes were also investigated on the 7.5% scale SSPM model (Figure 2). Nose strake parameters investigated included variations in strake length, circumferential and axial location and deflection angle. A detailed analysis of the yaw control characteristics of the nose strakes tested is provided in Reference 4. These devices showed great promise at high angles of attack and warrant further investigation.

To establish the validity of the low Reynolds number data obtained in the 12 ft LSWT, a 14% scale model of the SSPF was tested in the NASA LaRC 30x60 ft LSWT. Figure 14 illustrates the 14% scale SSPF model installation. Somewhat more sophisticated than the highly versatile 7.5% scale model, the baseline 14% scale model wing and vertical tails are comprised of modified NACA 65A series airfoil sections. The baseline wing is uncambered and has a predominately linear twist distribution. The wing twist distribution selected for the baseline SSPF wing is a compromise based on previous MCAIR experience with similar wings designed using the MCAERO design method, Reference 10, at transonic cruise conditions and the Carlson-Walkley design method, Reference 11, at supersonic cruise.

Static force and moment data were obtained at a Mach number of 0.10 ($Re = 1.876 \times 10^6$) at angles of attack ranging from 0° to 65° and sideslip angles between $\pm 30^\circ$. Preliminary results obtained from the 30x60 ft LSWT test conducted in January 1989 indicate reasonable agreement with the overall trends predicted using the 7.5% scale SSPF model.

4.0 Conclusions

A number of general conclusions may be drawn from the data presented:

- (1) Vertical tail spanwise location and cant angle have substantial influences on aircraft lateral-directional stability at high angles of attack. Significant improvements in the levels of static stability may be achieved through proper integration of the vertical tails.
- (2) Structural integration of vertical tails positioned for optimum high AOA lateral-directional stability will most likely require the use of unconventional pitch control devices.
- (3) Skewed hingeline tipperons provide increased roll control on highly swept, low aspect ratio wings up to post-stall angles of attack.
- (4) All-movable twin vertical tails provide a substantial increase in yaw control over conventional rudders and thus extend roll coordination capability to higher angles of attack. However, the adverse roll generated by all-movable vertical tails presents a potential problem, depending on the level of roll acceleration required and the roll control available from other surfaces.

5.0 References

1. Wood, R. M., Miller, D. S., Hahne, D. E., Niedling, L. G. and Klein, J. R., NASA Langley Research Center and McDonnell Aircraft Company, "Status Review of a Supersonically Biased Fighter Wing-Design Study," 13 July 1983, AIAA-83-1857.
2. Klein, J. R., Walck, K. J. and Hahne, D. E., McDonnell Aircraft Company and NASA Langley Research Center, "Airframe Component Integration Effects on the Aerodynamic Stability and Control Characteristics of Supersonic Cruise Fighter Aircraft at High Angles of Attack," 21 August 1984, AIAA-84-2110.
3. Glaze, L. W. and Marks, B. A., McDonnell Aircraft Company, "Advanced Concepts for High Angle of Attack Control - LaRC 12 Ft Low Speed Wind Tunnel Test No. 153," 3 December 1985, MDC A9190.
4. Marks, B. A. and Hogan, J. K., McDonnell Aircraft Company, "Advanced Concepts for High Angle of Attack Stability and Controllability of a Supercruise Fighter - NASA LaRC 12 Ft Low Speed Wind Tunnel Test No. 181," 19 June 1987.
5. Perkins, C. D. and Hage, R. E., Airplane Performance Stability and Control, Sixth Printing, New York, John Wiley & Sons, February 1957, pp. 323-325.
6. Rao, D. M. and Murri, D. G., Vigyan Research Associates and NASA Langley Research Center, "Exploratory Investigation of Deflectable Forebody Strakes for High-Angle-of-Attack Yaw Control," 6 January 1986, AIAA-86-0333.
7. Brandon, J. M. and Nguyen, L. T., NASA Langley Research Center, "Experimental Study of Effects of Forebody Geometry on High Angle of Attack Static and Dynamic Stability," 6 January 1986, AIAA-86-0331.
8. Brandon, J. M., Murri, D. G. and Nguyen, L. T., NASA Langley Research Center, "Experimental Study of Effects of Forebody Geometry on High Angle of Attack Static and Dynamic Stability," 7 September 1986, Presented at the 15th Congress of the International Council of the Aeronautical Sciences (ICAS), London, England, UK.
9. Murri, D. G. and Rao, D. M., NASA Langley Research Center and Vigyan Research Associates, "Exploratory Studies of Actuated Forebody Strakes for Yaw Control at High Angles of Attack," 1987, AIAA-87-2557.
10. Hawk, J. D. and Bristow, D. R., McDonnell Aircraft Company, "Development of MCAERO Wing Design Panel Method with Interactive Graphics Module," NASA CR-3775, April 1983.
11. Carlson, H. W. and Walkley, K. B., "Numerical Methods and a Computer Program for Subsonic and Supersonic Aerodynamic Design and Analysis of Wings with Attainable Thrust Considerations," NASA CR-3808, August 1984.

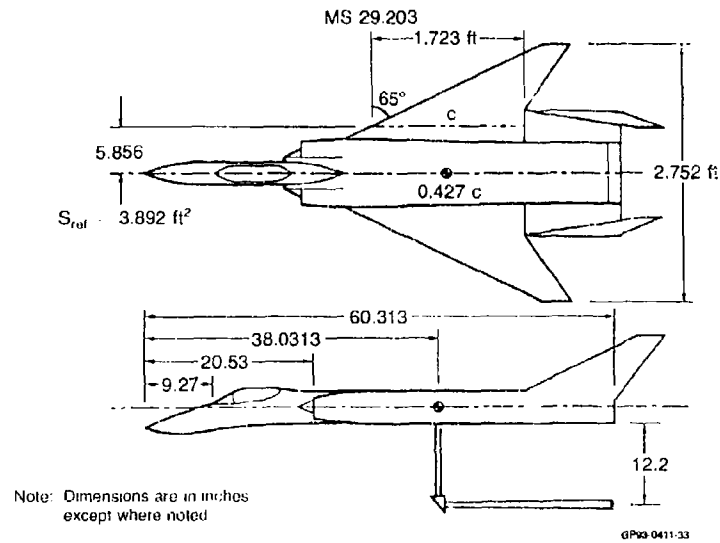


Figure 1. 7.5% Scale Supersonic Persistence Fighter (SSPF) Model

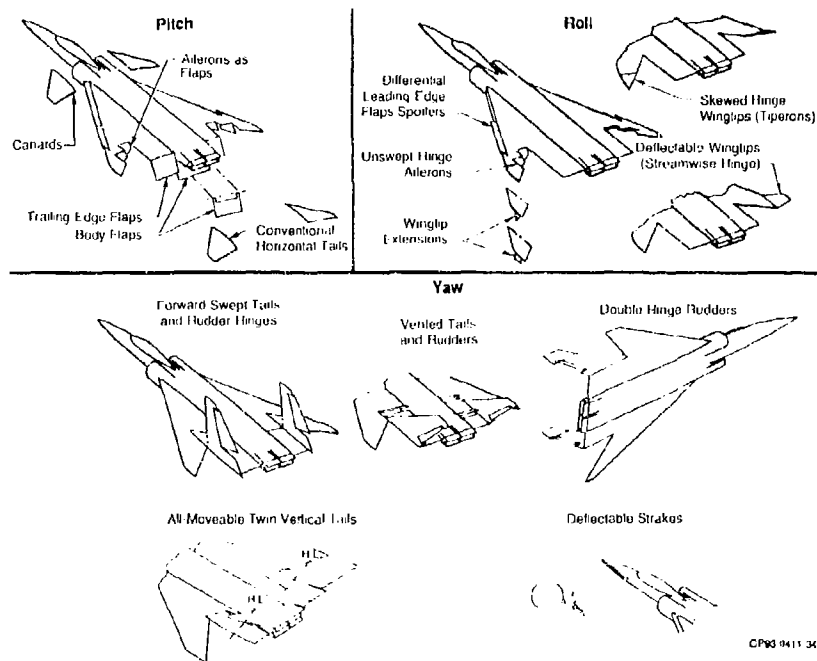
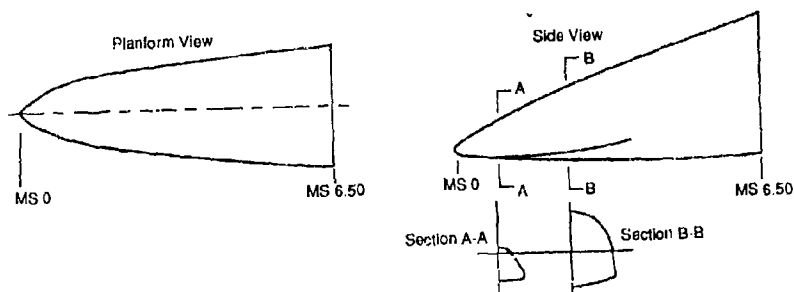
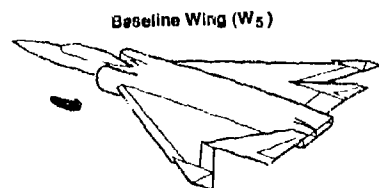


Figure 2. Control Concepts Investigated in NASA LaRC 12 ft Low Speed Wind Tunnel

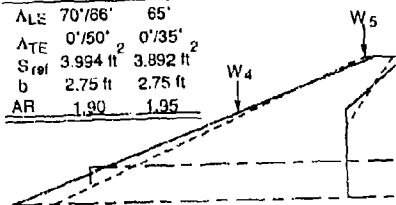


GP93-0411-25-D

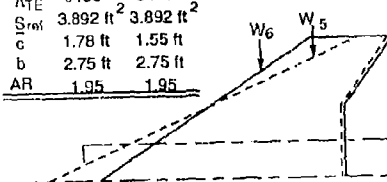
Figure 3. Baseline Nose Shape



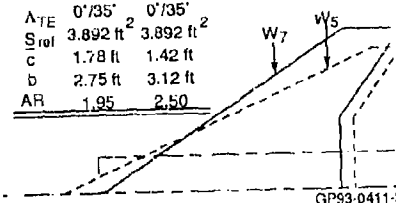
Wing	W ₄	W ₅
Λ_{LE}	70°/66°	65°
Λ_{TE}	0°/50°	0°/35°
S_{ref}	3.994 ft ²	3.892 ft ²
b	2.75 ft	2.75 ft
AR	1.90	1.95



Wing	W ₅	W ₆
Λ_{LE}	65°	55°
Λ_{TE}	0°/35°	0°/35°
S_{ref}	3.892 ft ²	3.892 ft ²
c	1.78 ft	1.55 ft
b	2.75 ft	2.75 ft
AR	1.95	1.95

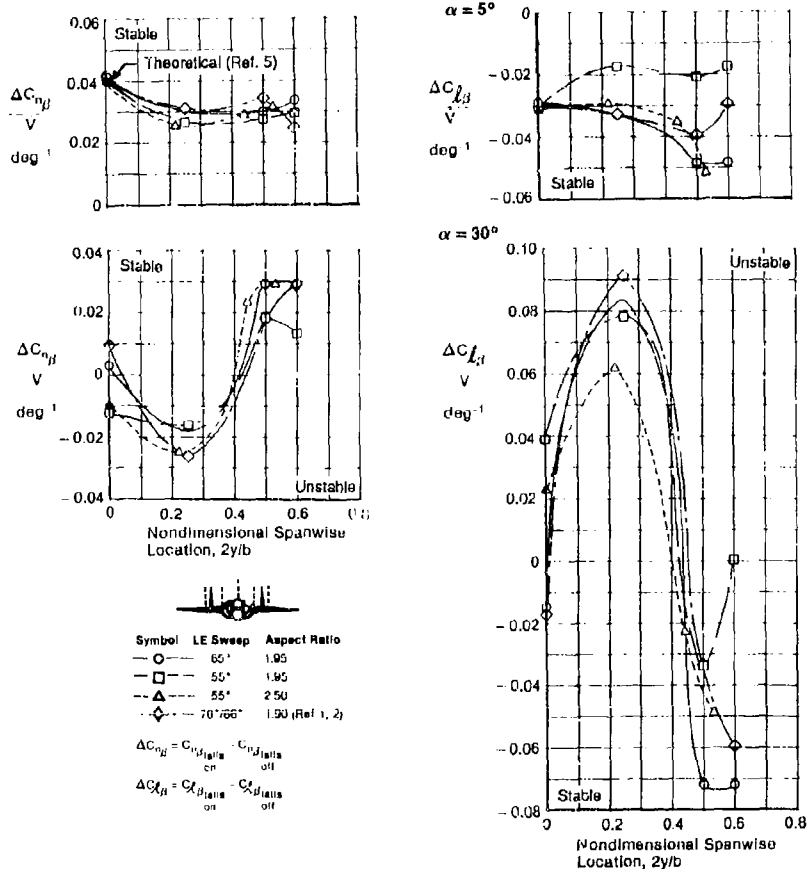
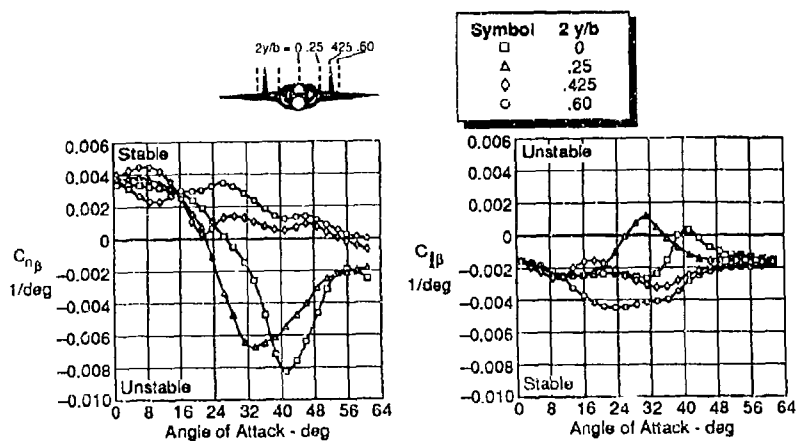


Wing	W ₅	W ₇
Λ_{LE}	65°	55°
Λ_{TE}	0°/35°	0°/35°
S_{ref}	3.892 ft ²	3.892 ft ²
c	1.78 ft	1.42 ft
b	2.75 ft	3.12 ft
AR	1.95	2.50



GP93-0411-31-D

Figure 4. Planform Comparison of Wings Tested



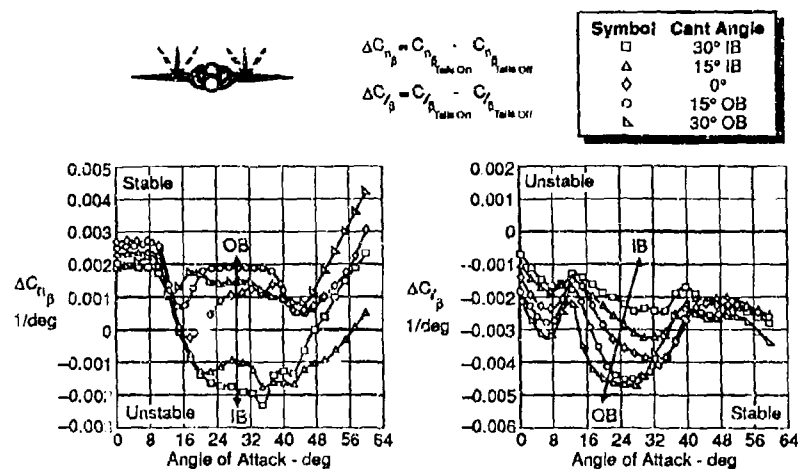


Figure 7. Effect of Vertical Tail Cant Angle on Lateral-Directional Stability
 NASA LaRC 12 ft LSWT Test Data
 $2y/b = 0.50$ Body Axes Mach 0.05

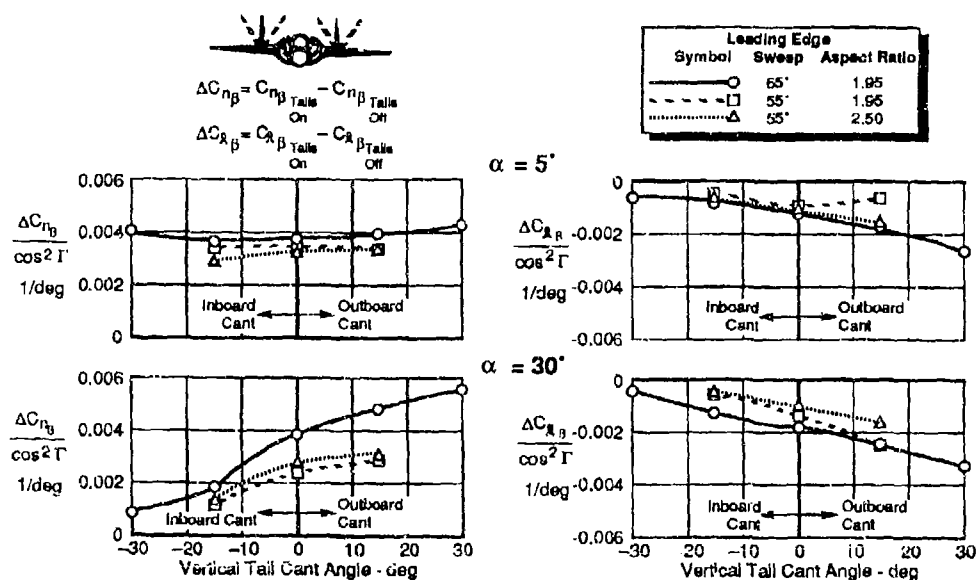


Figure 8. Effect of Cant Angle on Vertical Tail Contribution to Lateral-Directional Stability
 NASA LaRC 12 ft LSWT Test Data
 $2y/b = 0.50$ Body Axes Mach 0.05

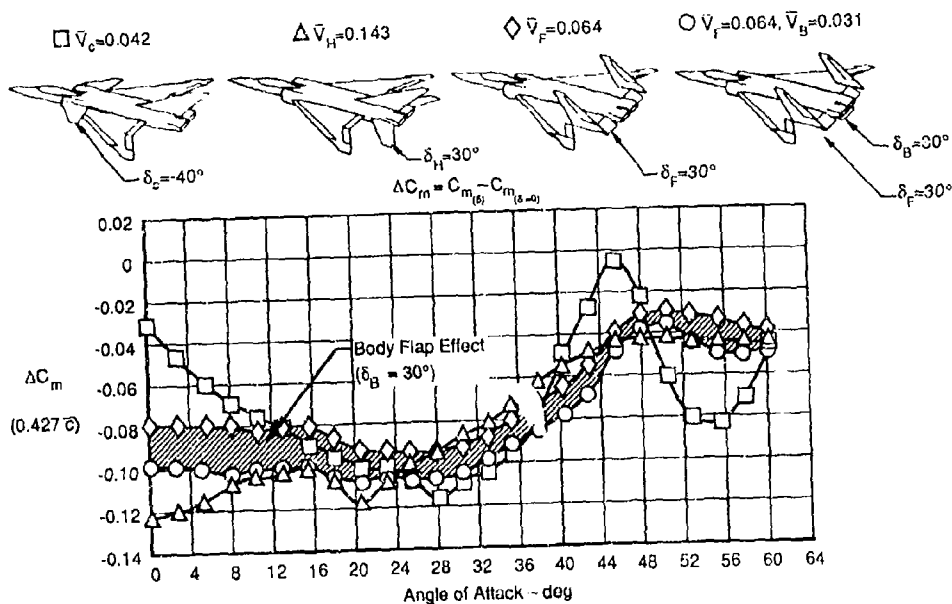


Figure 9. Nose Down Pitch Control
 NASA LaRC 12 ft LSWT Test Data
 $\delta_{/e} = 30^\circ$ Mach 0.05

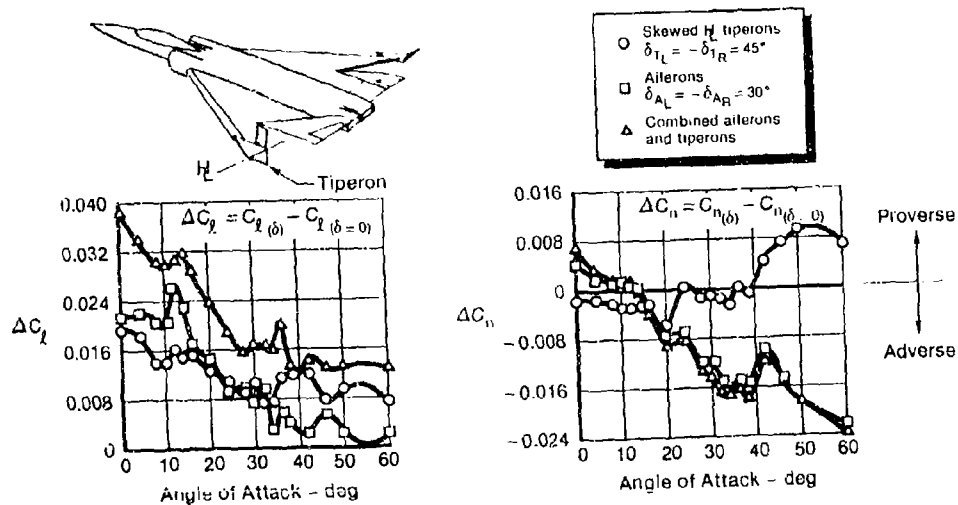


Figure 10. Deflectable Wing Tips Provide Improved High Angle of Attack Roll Control
 NASA LaRC 12 ft LSWT Test Data
 $\delta_{/e} = 30^\circ$ 15° Inboard Tail Cant Mach 0.05

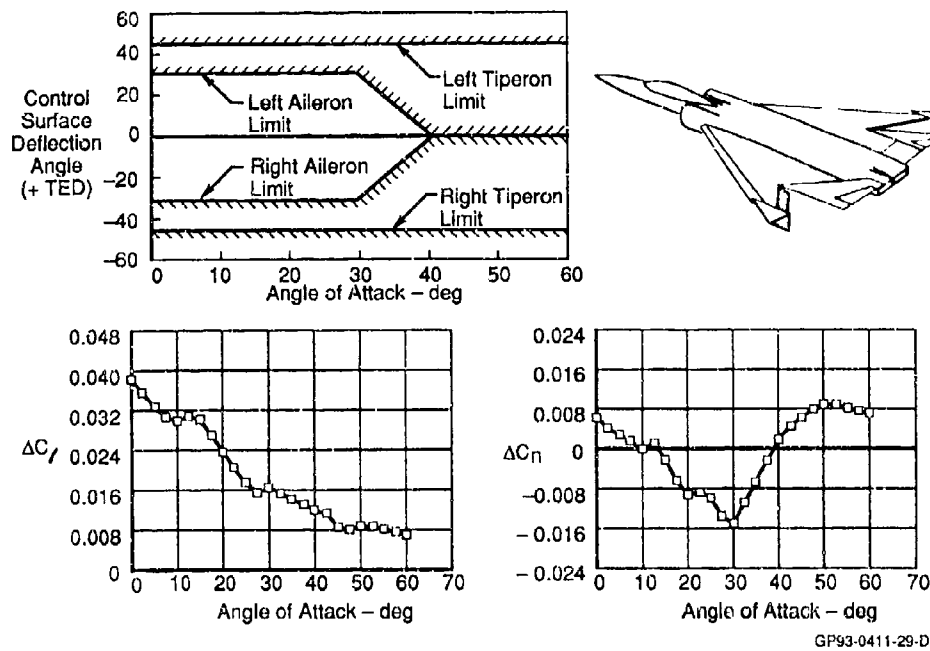


Figure 11. Roll/Yaw Resulting From Scheduling Maximum Aileron Deflection With AOA
NASA LaRC 12 ft LSWT Test Data

$\delta_{\delta} = 30^\circ$ 15° Inboard Tail Cant Mach 0.05

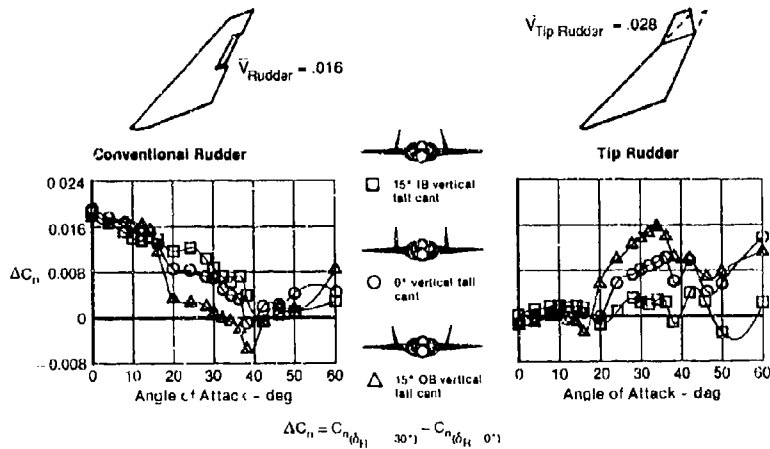


Figure 12. Effect of Vertical Tail Cant on Rudder Effectiveness
NASA LaRC 12 ft LSWT Test Data

$\delta_{\delta} = 30^\circ$ $\delta_{\delta} = -30^\circ$ (TER) Mach 0.05

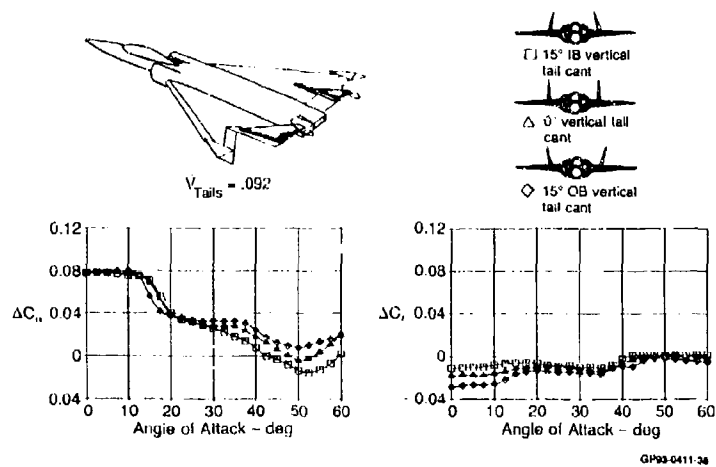


Figure 13. Effect of Vertical Tail Cant Angle on All-Moveable Twin Vertical Tail Power
 NASA LaRC 12 ft LSWT Test Data
 $\delta\gamma_{\theta} = 30^\circ$ $\delta\gamma_{\phi} = -30^\circ$ (TER) Mach 0.05

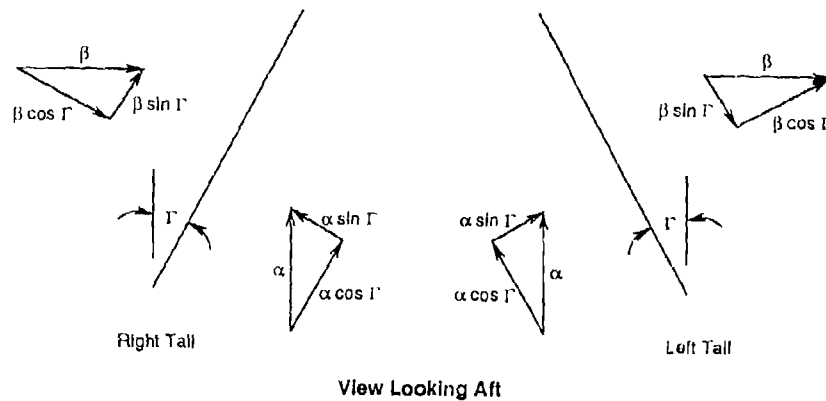


Figure 14. 14% Scale SSPF Model Installed in NASA LaRC 30x60 ft
 Low Speed Wind Tunnel

Appendix

Derivation of $\cos^2 \Gamma$ Term for Sizing Canted Vertical Tails

The $\cos^2 \Gamma$ term is used to account for the reduction in projected area in the x-z plane (body axes) resulting from canting the vertical tails. In canting the vertical tails, the planform area required to maintain the same low AOA directional stability as the uncanted tails is determined by dividing the uncanted tail area by $\cos^2 \Gamma$. This is illustrated by the following derivation:



GP93-0411-24-D

$$C_{N_{\text{right tail}}} = (C_{L_{\alpha \text{ right tail}}})(\beta \cos \Gamma - \alpha \sin \Gamma)$$

$$\begin{aligned} C_{Y_{\text{right tail}}} &= (C_{N_{\text{right tail}}})(\cos \Gamma) \\ &= (C_{L_{\alpha \text{ right tail}}})(\beta \cos^2 \Gamma - \alpha \cos \Gamma \sin \Gamma) \\ &= (C_{L_{\alpha \text{ right tail}}})(\beta \cos^2 \Gamma - \frac{\alpha}{2} \sin 2\Gamma) \end{aligned}$$

$$C_{N_{\text{left tail}}} = (C_{L_{\alpha \text{ left tail}}})(\beta \cos \Gamma + \alpha \sin \Gamma)$$

$$\begin{aligned} C_{Y_{\text{left tail}}} &= (C_{N_{\text{left tail}}})(\cos \Gamma) \\ &= (C_{L_{\alpha \text{ left tail}}})(\beta \cos^2 \Gamma + \frac{\alpha}{2} \sin 2\Gamma) \end{aligned}$$

$$C_{L_{\alpha \text{ left tail}}} = C_{L_{\alpha \text{ right tail}}} = C_{L_{\alpha \text{ tail}}}$$

$$\begin{aligned} C_{Y_{\text{tails}}} &= C_{Y_{\text{left tail}}} + C_{Y_{\text{right tail}}} \\ &= (C_{L_{\alpha \text{ tail}}})(\beta \cos^2 \Gamma - \frac{\alpha}{2} \sin 2\Gamma + \beta \cos^2 \Gamma \\ &\quad + \frac{\alpha}{2} \sin 2\Gamma) \end{aligned}$$

$$= 2(C_{L_{\alpha \text{ tail}}})(\beta \cos^2 \Gamma)$$

For $\Gamma = 0$,

$$C_{Y_{\text{tails}}(\Gamma=0)} = 2(C_{L_{\alpha \text{ tail}}}(\beta))$$

therefore,

$$\frac{C_{Y_{\text{tails}}(\Gamma=0)}}{C_{Y_{\text{canted tails}}}} = \frac{2(C_{L_{\alpha \text{ tail}}}(\beta))}{2(C_{L_{\alpha \text{ tail}}}(\beta \cos^2 \Gamma))} = \frac{1}{\cos^2 \Gamma}$$

$$C_{Y_{\text{tails}}(\Gamma=0)} = \frac{C_{Y_{\text{canted tails}}}}{\cos^2 \Gamma}$$

$$\text{Tail Area}_{\text{canted}} = \frac{\text{Tail Area}_{(\Gamma=0)}}{\cos^2 \Gamma}$$

Similarly,

$$C_{n_{\text{tails}}(\Gamma=0)} = \frac{C_{n_{\text{canted tails}}}}{\cos^2 \Gamma}$$

DEVELOPMENT OF NON-CONVENTIONAL CONTROL METHODS FOR HIGH ANGLE OF ATTACK FLIGHT USING VORTEX MANIPULATION

by

Gerald N. Malcolm, T. Terry Ng and Liane C. Lewis
Eidetics International, Inc
3415 Lomita Blvd.
Torrance, CA 90505-5610
United States

and

Daniel G. Murri
NASA Langley Research Center
Hampton, VA 23665-5225
United States

SUMMARY

Methods of manipulating the forebody vortices on a generic fighter model to produce controlled yawing moments at high angles of attack have been investigated. Forces and moments were measured on the complete configuration and on the isolated forebody. Two schemes for vortex control on the forebody were evaluated: (1) individually-controlled tip strakes and (2) individually-controlled blowing ports. The effectiveness of the forebody strakes in controlling forebody side forces was strongly dependent on the size and location of the strakes. A yawing moment can be produced by deploying the forebody strakes asymmetrically, or can be eliminated by deploying the strakes symmetrically. The most effective strake position was found to be near the primary separation point, between 105° and 120° from windward. Blowing on the surface of the model was also shown to have a strong effect on the yawing moment. Blowing either forward or aft tangential to the surface appears to be more effective than blowing normal to the surface. The most effective method to control the yawing moment on the forebody was to minimize the natural asymmetry with a pair of small symmetrically mounted tip strakes and to perturb the vortex system away from the symmetric condition with asymmetric blowing.

SYMBOLS

- b Wing span, 3.968 ft (1.209 m)
- \bar{c} Mean aerodynamic chord, 1.854 ft (0.565 m)
- CM Pitching moment coefficient, pitching moment/ $q_\infty S \bar{c}$, $X_{ref} = 4.018$ ft (1.226 m) from the nose tip
- CN Yawing moment coefficient, yawing moment/ $q_\infty S b$, $X_{ref} = 4.018$ ft (1.226 m) from the nose tip
- CN-F Yawing moment coefficient contributed by forebody alone, referenced to complete aircraft configuration moment reference location, $X_{ref} = 4.018$ ft (1.226 m) from the nose tip
- C_{μ} Blowing momentum coefficient,

$$C_{\mu} = \frac{\dot{m} v_j}{q_\infty S}$$
- d Forebody base diameter, 5.5 in (13.97 cm)
- h_{ST} Height of strake
- l_{ST} Length of strake
- \dot{m} Mass flow rate for blowing jet
- q_∞ Dynamic pressure, $\frac{1}{2} \rho v_\infty^2$
- S Wing reference area, 6.564 ft² (0.610 m²)
- v_j Velocity of blowing jet
- v_∞ Free-stream velocity
- X_{ref} Moment reference center, measured from nose tip, 4.018 ft (1.226 m)
- α Angle of attack
- β Sideslip angle

- ϕ Radial location on forebody measured from windward ray
- ρ Air density

1.0 INTRODUCTION

A key technology to increase the overall angle of attack capability of present and future fighter aircraft is aerodynamic control. The flight envelopes of current aircraft have been limited at least in part by controllability problems at high angles of attack, typically represented by sudden departures in roll and yaw and, in some cases, by nose pitch-up or deep stall. Reduced controllability places undesirable limits on the maneuverability of the aircraft but, even worse, often leads to unrecoverable flight modes such as spins. The objective of this research program is to demonstrate the potential to extend the angle of attack range for controllable flight by locally controlling the vortex flowfield around the aircraft with nonconventional techniques.

The flowfield around a modern fighter aircraft at moderate to high angles of attack is dominated by vortices. One of the problems on aircraft with slender forebodies is the presence of large uncontrollable yawing moments generated by asymmetric vortices on the forebody at high angles of attack, even at zero sideslip angles. The inability to overcome these large moments with conventional control surfaces has led to a number of studies to search for alternate methods of controlling the vehicle. One of the potential schemes is to effectively utilize the vortices that are the cause of the problem.

Research experiments on a series of generic fighter configurations have investigated several methods of controlling the forebody vortices including movable forebody strakes and blowing on the forebody surface. Figure 1 illustrates, with sketches, the vortex patterns typical of forebody flows and the two schemes investigated to control their orientation and strength. Figure 2 schematically shows the objective of this research program. The typical effectiveness of the vertical tail and rudder to control the yawing moment falls off as the angle of attack increases because the vertical tail gradually becomes enveloped in the wake of the wing and fuselage. At the time the rudder effectiveness is decreasing, the asymmetric forces of the forebody vortices are increasing. If the vortices can be controlled, then they can be used for generating a controlled yawing moment to replace the lost yaw controllability from the rudder.

A number of studies have previously been conducted to investigate the effects of forebody strakes and forebody blowing. The use of forebody strakes has been shown (Refs. 1-3) to be an effective method of forcing naturally occurring asymmetric vortices at high angles of attack to be symmetric, or nearly symmetric, and to therefore eliminate the large forebody sideforces and resulting yawing moments at zero sideslip. The use of asymmetrically deployed forebody strakes have been investigated in Ref. 4 for possible application to controlling the yawing moments. Investigations of forebody blowing techniques to control the forebody vortex orientation have also been conducted in both water and wind tunnel experiments (Refs. 5-10).

The primary focus of this paper is the results from a series of wind tunnel tests of a generic fighter configuration conducted in the NASA Langley 12-Foot Low Speed Wind Tunnel. The main objective was to evaluate the effect on the forces and moments of the complete aircraft configuration and, in some cases, of the isolated forebody, from forebody strakes (both symmetrically and asymmetrically placed) and local blowing from the surface of the forebody at various span locations. This paper will discuss some of the results from this study and show a number of examples of the effectiveness of various schemes.

2.0 TEST FACILITY AND MODEL

The experiment was conducted in the NASA Langley Research Center 12-Foot Low Speed Wind Tunnel. The tests were conducted at a dynamic pressure of approximately 5 psf and a Reynolds number based on c of 0.75×10^6 . The model was sting-mounted on a 6-component balance. The model attitude was varied from 0 to 70° angle of attack and from -20° to +20° in sideslip. The model used for the majority of the tests and the one to be discussed in this paper is the generic fighter aircraft configuration shown in Fig. 3. It consists of a circular fuselage section, $l/d=4.0$ tangent ogive forebody, 45° clipped delta wing with a leading edge extension, and typical horizontal and vertical tail components. The basic model was originally designed and constructed at NASA Langley. Eldetics International constructed a number of new components specifically for this test including new forebody components. A separate forebody was constructed to be used with an isolated forebody balance to measure the forces and moments of the forebody alone in addition to the total forces and moments recorded simultaneously by the main 6-component balance in the fuselage. The test was conducted in two tunnel entries. The first entry provided for the separate forebody balance and the evaluation of many forebody strake configurations. The available strake sizes and radial locations for attachment are shown in Fig. 4, although not all combinations were tested.

The second entry used the same configuration except the isolated forebody balance was eliminated and two new forebodies were built to provide for detailed studies of both the forebody strakes and blowing. One new forebody was needed to incorporate a remotely adjustable pair of strakes at a radial location judged to be the most effective from results of the first test, i.e., at a radial angle 105° from the windward meridian. The strakes were 1.0d in length and could be varied in height up to 0.08d. The pivot point of the strakes was as close to the tip of the forebody as feasible, approximately .013d. The wings were made from a flat plate made of plywood and the fuselage consisted of an aluminum frame, steel balance block, and wood side pieces shaped to provide a circular cross section. The horizontal tail deflection angles were adjustable from 10° trailing edge down to 30° trailing edge up. The rudder was adjustable from -30° to +30°. An additional forebody was built and used to conduct the forebody blowing tests. It was constructed with several blowing tubes mounted internally with ports at different locations. The ports available are

shown in Fig. 5 and could be used for blowing normal to the surface and tangentially either in an aft or a forward direction. The tangential blowing was accomplished by using a small 90° elbow that could be inserted into the blowing port at the surface. Figure 6a is a photograph of the model in the tunnel and Figs. 6b and 6c are photographs of the forebody with strakes and blowing nozzles for the aft blowing case. The nozzles are 0.125 inches (0.3175 cm) in diameter. The mass flow was regulated by changing the supply pressure.

3.0 TEST RESULTS

The experimental results discussed in the following section are intended to show the effectiveness of various methods of controlling the forebody vortices and the resulting influence on the yawing moment. Some examples will be shown with both the total yawing moment of the airplane configuration and the yawing moment contributed by the forebody alone. For this configuration, changes in the forebody vortex structure had little influence on either the rolling moment or the pitching moment, thus providing a means of controlling the yawing moment nearly independently of moments in other axes.

The configurations to be discussed are:

- 1) Baseline with clean forebody
- 2) Baseline with symmetric and asymmetric forebody strakes
- 3) Baseline with clean forebody and blowing symmetrically and asymmetrically (normal, forward and aft)
- 4) Baseline with fixed strakes on the forebody and blowing symmetrically and asymmetrically (forward and aft)
- 5) Baseline with fixed strakes on the forebody and blowing differentially on right and left sides (forward and aft)

3.1 Baseline Configuration

The yawing moment coefficient for the baseline configuration (Fig. 3) is shown in Fig. 7 as a function of angle of attack for sideslip angles of 0 and $\pm 5^\circ$. The development of asymmetric forebody vortices resulting in a non-zero yawing moment coefficient at zero sideslip begins to appear at about $\alpha = 25^\circ$ where the yawing moment is shown to depart rapidly from zero with increasing angle of attack. Figure 7a, which shows the yawing moment for the complete airplane, indicates that the directional stability is positive (i.e., at $\beta = +5^\circ$, a restoring yawing moment, $C_{N\beta}$ positive, is experienced to angles of attack of approximately 30°). This directional stability is provided by the vertical tail, which loses its effectiveness in the wake of the wing at $\alpha = 30^\circ$. The forebody contribution to the total aircraft yawing moment coefficient is shown in Fig. 7b. The effect of the forebody on the directional stability is destabilizing throughout the angle of attack range, i.e., the moment is in the same direction as the direction of the nose movement. It is also obvious that the magnitude of the yawing moment asymmetry is quite large in comparison to the yawing moment generated with moderate sideslip angles. Figure 8 shows the effectiveness of the rudder deflection to 30° for comparison to the magnitude of the yawing moment produced by the asymmetric forebody vortices. The maximum rudder effectiveness is at low angles of attack, as expected, and decreases to near zero as angle of attack approaches 40° . It should be noted that the maximum rudder effectiveness is only half of the magnitude of the yawing moment at angles of attack near 40° caused by asymmetric vortices. It is clear that the forces produced by forebody asymmetric flows are very large and that the conventional rudder cannot overcome them beyond about $\alpha = 30^\circ$.

3.2 Forebody Strakes

An effort was made to find an optimum location for symmetrically mounting a set of strakes on the leeward side of the forebody to minimize the asymmetry at zero sideslip and also to improve the directional stability characteristics with increased angle of attack. Since the vertical tail is ineffective at angles of attack above 30° , then the improved directional stability must come from favorable contributions from the forebody. The addition of small strakes at the appropriate location on the forebody controls the location of flow separation and can be chosen to minimize or eliminate the flow asymmetry associated with leeward vortices.

3.2.1 Symmetric Forebody Strakes

Strakes were investigated at several radial angles from 165° to 90° , from the windward meridian of the forebody. For comparison, Figs. 9 and 10 show the yawing moment coefficient for strakes at $\phi = 150^\circ$ and $\phi = 105^\circ$, respectively. At $\phi = 150^\circ$, the effectiveness of the strakes is very poor. They do not reduce the zero sideslip asymmetry, and the contribution to directional stability is significantly negative, e.g., the magnitude of the yawing moment in the direction of the sideslip angle above $\beta = 0$ is much larger than that for the clean forebody. As the strakes were placed closer to the windward side of the forebody, they became increasingly beneficial.

Figure 10 shows a large improvement by placing the strakes at $\phi = 105^\circ$. Not only is the yawing moment at $\beta = 0$ nearly zero for the entire angle of attack range, but the directional stability, $C_{N\beta}$, is positive to angles of attack of approximately 50° , a large improvement over the cases shown in Figs. 3 and 9.

The configuration with strakes at $\phi = 105^\circ$ was chosen as the baseline configuration for the remaining investigation of controlling the forebody vortices with strakes. The manipulation of the forebody vortices with different strake sizes, i.e., lengths and heights, in pairs and with left and right side alone will be illustrated. The following figures will show the dependency of the forebody yawing moment on strake size and deploying a single strake. Figure 11 shows the effectiveness of a pair of strakes of the same length as those in Fig. 10b (i.e., $l_{ST} = 1.5d$) but with half the height ($h_{ST} = 0.5d$ instead of $0.1d$). The large strake is slightly more effective in maintaining symmetry at $\beta = 0$ but the small strake is significantly more effective at contributing to positive directional stability above $\alpha = 30^\circ$ (i.e., $C_{N\beta}$ is more positive for $\beta = +5^\circ$ and more negative for $\beta = -5^\circ$). Comparing Fig. 10 with Fig. 12 shows that for strakes with the same height of $h_{ST} = 0.1d$, there is little difference between strakes with lengths of $1.0d$ and $1.5d$. However, for strakes with less height ($h_{ST} = 0.05d$), the difference in length can be somewhat important as shown by comparing Fig. 13 with strake lengths of $0.5d$ to Fig. 11 with strake lengths of $1.5d$. In summary, if the strake height is $0.1d$, there is little

difference in effectiveness between $l_{ST} = 1.0d$ and $l_{ST} = 1.5d$. If the strake height is $.05d$, longer strakes ($l_{ST} = 1.5d$) are more effective than shorter ones ($l_{ST} = 0.5d$).

3.2.2 Asymmetric Forebody Strakes

Following the study of symmetric pairs of strakes to reduce the zero sideslip asymmetry and to improve directional stability, an investigation was conducted to evaluate single strakes. Figure 14 shows the effectiveness of a single strake in changing the yawing moment over the angle of attack range. The asymmetric yawing moment produced by the clean forebody (no strakes) is shown for reference. The placement of a single strake at $\phi = 105^\circ$ on the right side only is shown for three different strake sizes. All three have a height of $0.1d$ but vary in length with $l_{ST} = 0.5d$, $1.0d$, and $1.5d$. The longest strake is the most effective over the entire angle of attack range. As indicated, with this particular strake height, a strake on the right side reverses the natural asymmetry for this forebody with no strakes and forces a negative yawing moment. The effect of the strake is to separate the flow on the right side of the forebody, forcing the right side vortex to be positioned above the left side vortex. The left side vortex is closer to the forebody, resulting in a forebody side force to the left creating a negative yawing moment. The shorter strakes are not as effective at the higher angles of attack and the flow reverts to the preferred orientation of the left vortex above the right. For example, the short strake is similar in effectiveness to the long strake until $\alpha = 35^\circ$, where the negative yawing moment is maximum and for angles above $\alpha = 40^\circ$, the yawing moment is positive. In Fig. 15, it appears that if the strake is long enough (i.e., $l_{ST} = 1.5d$), the effect of the difference in height (i.e., $h_{ST} = 0.05d$ and $0.1d$) is insignificant.

The second phase of the wind tunnel tests investigated, in more detail, the effectiveness of variable forebody strake height on the control of the resulting yawing moment. The forebody component was constructed so that the left and right strakes were independently and remotely controllable and could be varied from 0 to $0.08d$. The strake length was $1.0d$ and left and right strakes were both located at $\phi = 105^\circ$. The strakes were pivoted about a point approximately $.013d$ from the forebody tip, the most forward point about which the strakes could be mechanized to pivot. Figure 16 shows that the variation in height on either side alone can have pronounced effects on the magnitude of the yawing moment, but even more important, on the direction of the yawing moment. For example, if the right strake is deployed from zero to $0.04d$ (Run 533) at $\alpha = 45^\circ$, the yawing moment is positive or in the same direction as the strake. If the strake is deployed further to $0.08d$ (Run 535), the yawing moment is reversed and is in the opposite direction of the strake deployment. Similar comparison for deployment of the left strake produces a near mirror image.

A more detailed study of yawing moment variation with strake deployment height is shown in Fig. 17 at $\alpha = 45^\circ$. The yawing moment is plotted as a function of strake height for right and left strakes independently. Referring to Fig. 17a, with neither strake deployed, i.e., $h_{ST} = 0$, the yawing moment is negative. If the right strake only is deployed (Run 552), the vortices respond by orienting themselves in the reverse pattern, i.e., the right side vortex is closest to the body resulting in a positive C_n . The maximum yawing moment coefficient of 0.06 is obtained with the strake at about $.027d$. At $h_{ST} = .06d$, the yawing moment crosses through zero and becomes negative with increasing height. It is believed that the effect of the strake at small heights is to separate the cross-flow boundary layer but not with sufficient adverse pressure gradient to maintain a separated flow and the flow re-attaches further around the body before eventually separating again and forming a vortex. This effect in delaying the final separation location is to allow the flow to maintain a higher suction on that side of the body with the vortex positioned closer to the body than the vortex on the opposite side. Since the two vortices do not want to occupy the leeward side of the body in a stable symmetric orientation naturally, if the result of the controlled side of the body is to force the vortex closer to the body, then the opposite side will respond with a vortex above and further from the body. If the strake is deployed to an increased height, eventually the separation that occurs is strong enough that re-attachment cannot take place and the vortex is forced further away from the body. The result is that the opposite vortex will occupy a position closer to the body and the yawing moment will be in the direction opposite the strake. Deployment of the left strake (Run 551) is seen to produce a near mirror image of the effect of deployment of the right strake alone.

Figure 17b also shows the case at $\alpha = 45^\circ$ where one strake is fixed at $.027d$ (the position for maximum yawing moment) and the other strake is varied in height from 0 to $.08d$. For example, if the right strake is fixed at $.027d$ and the left strake is fully retracted, the initial yawing moment is in the nose-right direction. As the left strake height is varied from 0 to $.027d$ (at which time the strakes are now symmetrically deployed) the yawing moment approaches zero. Further increase in strake height on the left strake does not produce large yawing moments. Utilization of this variation of yawing moment with strake deployment would suggest that, at least at $\alpha = 45^\circ$, the basic configuration should be a forebody with symmetrically deployed strakes at $.027d$ to minimize asymmetry, and then the individual strake on either side would be varied between $.027d$ and zero to achieve the maximum impact on yawing moment. It is also clear that the variation of the yawing moment with strake height from zero to $.027d$ is nearly linear. The reverse of the orientation, that is, holding the left strake at $.027d$ and varying the right strake height is a mirror image of the case just described. This particular behavior of yawing moment variation with differential strake height variation is an attractive approach to high angle of attack control. It produces moments in excess of the maximum yawing moment that the rudder can produce at low angles of attack (approximately twice as much) and it is nearly linearly variable with the movement of the control surface, i.e., an individual strake. These are examples of the potential power of using forebody strakes to control the forebody vortices and therefore control the yawing moment at angles of attack well above that where the rudder is effective. The selection of the optimum strake size, height of deployment, location and method of combining the motions of each strake would depend on the forebody configuration and the requirements for the level of augmented control level. The effectiveness of the controllability also needs to be evaluated at sideslip angles to insure that the method is adequate for nonzero sideslip as well. The importance of Reynolds number in the selection of strake placement and the sensitivity of the forebody flow to strake height also needs to be evaluated.

3.3 Forebody Blowing

The forebody forces can also be manipulated by direct injection of air into the forebody vortex flowfield. Experiments have shown that with relatively low blowing ratios, the forebody vortices can be influenced. The principal

objective was to optimize the location and direction of blowing ports on the forebody to produce the maximum yawing moment with the minimum required blowing.

As discussed earlier in the description of the model, the variables for the blowing forebody tests were blowing port location, direction of the blowing jet and the blowing momentum coefficient. Refer to Fig. 5 for the location of the ports. For these tests the blowing momentum coefficient is defined as:

$$\text{Blowing coefficient} = C_{\mu} = \frac{\dot{m} v_j}{q_{\infty} S}$$

Where:

\dot{m} = Mass flow rate from the jet

v_j = Velocity of the jet

q_{∞} = Dynamic pressure, $\frac{1}{2} \rho v_{\infty}^2$

S = Reference area, i.e., wing area

Previous research results (Refs. 5-7) have shown that the effectiveness of the blowing is increased the closer the jet can be located near the tip of the forebody. Initial experiments were conducted with blowing ports at $x/d = 0.5, 1.0, \text{ and } 1.5$, and at circumferential locations of $\phi = 120^\circ \text{ to } 165^\circ$. Blowing directions included normal to the surface and tangential to the surface in both aft and forward directions. The circumferential location that was selected as the most effective and chosen for detailed experimentation was at the most forward location, $x/d = 0.5d$ and $\phi = 135^\circ$. The most effective location for minimizing the blowing required is generally in the location between the primary separation and the secondary vortex. The following figures and discussion will illustrate some of the results of the blowing experiments.

3.3.1 Clean Forebody with Blowing Normal to the Surface

The initial blowing direction that was investigated was normal to the surface. Figure 18 shows the case with blowing ports located at $x/d = 0.5d$, the most forward location that could practically be implemented on this model. The indication is that the blowing is most effective at the lower angles of attack and is not particularly successful in altering the vortex flowfield at the higher angles of attack where the yawing moment is asymmetric with the clean forebody. The change in the yawing moment measured at low angles of attack due to blowing can be shown to be nearly equal to the component of yawing moment produced by the local thrust of the blowing jet. In other words, the contribution of blowing normal to the surface is primarily a local thrust effect. At higher angles of attack, i.e., above $\alpha = 15^\circ$, where forebody vortices are present, the predominant change in the yawing moment is still seen to be the contribution from local thrust effects. At angles of attack above about 35° , where the vortex flowfield becomes asymmetric, the blowing does not have a particularly significant effect on altering the yawing moment in a controllable manner. Clearly, an improved method of controlling the vortices and the resulting yawing moments was needed. The following discussion will show some examples of blowing tangential to the surface, both in an aft direction and in a forward direction. An example of simultaneous blowing aft on one side and blowing forward on the opposite side will also be shown.

3.3.2 Clean Forebody with Tangential Blowing Aft

Figure 19 shows an example of simultaneous blowing at $\phi = 135^\circ$ from left and right ports at a body station $0.5d$ from the nose tip in an aft direction. The baseline case (Run 334) shows the yawing moment with no blowing. The other cases show the results of blowing at equal rates on both sides (symmetric blowing). The results show that symmetric blowing does not necessarily produce symmetric yawing moments. It is speculated that with simultaneous blowing on both sides the flow is still very sensitive to minor perturbations in the flowfield, much as it is to surface perturbations in the case of no blowing. Figure 20 shows the case where blowing is implemented on the right and left sides individually at different rates. The natural asymmetry for the non-blowing case is oriented to produce a positive yawing moment, which coincides with a vortex pattern where the right side vortex is closer to the forebody thereby providing a higher suction force in the nose-right direction. By blowing on the right side, the already asymmetric condition is enhanced and the asymmetry persists to even higher angles of attack than for the non-blowing case. Blowing on the left side of the forebody is effective in changing the yawing moment in the opposite direction, but it is not effective in completely overcoming the natural asymmetry for all angles of attack. It would appear that the most effective technique for utilizing blowing to provide effective and controllable variation of the yawing moment would be to start with a baseline configuration which has a yawing moment inherently near zero thru the angle of attack range and to perturb the moment away from zero. The approach illustrated in the next few figures is to provide a forebody with symmetrically mounted nose strakes $1.0d$ in length and $.05d$ in height at $\phi = 105^\circ$, as described earlier for the baseline configuration. The effectiveness of blowing on this baseline configuration is discussed in the following figures.

3.3.3 Forebody with Symmetric Strakes and Blowing Aft

Figure 21 shows a case with blowing individually aft on left and right sides. This particular case is for the maximum blowing rate tested. Figure 21a is the case for the forebody with the strakes described above, i.e., placed symmetrically at $105^\circ, 1.0d$ long, and $.05d$ in height. The result of the blowing is a significant yawing moment in the direction of the side on which the blowing is taking place. The effect of the aft blowing is to strengthen the vortex and position it closer to the forebody surface than the vortex on the opposite side. Blowing left and right produces opposite effects, as shown, although not necessarily an exact mirror image about the non-blowing case. In Figure 21b, the strake height has been doubled to $0.1d$. The result is that the vortex is more difficult to perturb from symmetry. This would suggest that with larger strakes, the vortices are forced into a near symmetric orientation that requires a stronger input to alter. The point is that in an effort to force the baseline to be symmetric, one can make the symmetric

condition so stable that desired perturbations by blowing cannot effectively overcome the local symmetric pressure distribution. The effects of varying the blowing rate on either side where the baseline is essentially symmetric flow due to symmetric strakes is shown in Fig. 22. Increased blowing produces increased yawing moment in the direction of the side on which the blowing occurs. While the effects of blowing left and right are not exactly mirror images, the effects are very similar. The effect on the pitching moment from increased blowing rate is shown in Fig. 23 for angles of attack of 45° and 60° . At 45° , the pitching moment appears to be invariant with the blowing. At 60° , there is a small increase in the nose-up pitching moment with increased blowing, which is what one would expect if the forebody vortex on either side is being strengthened by the blowing.

An indication of the effectiveness of blowing with different sideslip angles is shown in Fig. 24. The case shown is for an angle of attack of 60° . The progression of increased yawing moment with blowing rate in the direction of blowing seems to hold reasonably well with sideslip angles to at least 20° . The significance of the results shown in this figure is that with blowing on the appropriate side, a yawing moment can be generated that will overcome the negative directional stability which is evident without blowing, i. e., C_N is negative for positive β . With blowing it is possible, for example, to generate positive C_N for positive β .

3.3.4 Clean Forebody with Blowing Forward

The next few figures will illustrate the effects of blowing tangentially to the surface in a forward direction. The baseline configuration initially had a clean forebody, i. e., no forebody strakes. Figure 25 shows the effect on the yawing moment coefficient of blowing forward at two different longitudinal locations, $x/d = 0.5d$ and $1.0d$ at a radial location of 135° . Comparing Figs. 25a and 25b, it is apparent that for blowing forward, it is more effective to be at $x/d = 1.0d$ in terms of generating a larger yawing moment over a larger angle of attack range. It should be noted that the baseline runs in Figs. 25a and 25b for no blowing are somewhat different. The location of the blowing ports was changed by manually moving the small blowing nozzles from one longitudinal location to another. The forebody is essentially identical for both sets of data except that the nozzles are located differently. The yawing moment variation is asymmetric in both cases but varies with angle of attack differently for the two cases. The important point to note is that blowing forward from a more aft position is more effective over the angle of attack range. The magnitude of the yawing moment is greater and there is not as much tendency to reverse directions with a given blowing rate as the angle of attack is increased. For example, in Fig. 25a the yawing moment switches direction at $\alpha = 36^\circ$. With the blowing ports further aft (Fig. 25b), the yawing moment has the same direction until about 50° angle of attack and is larger in magnitude through most of the range. The other important point is that in the angle of attack range prior to the reversal, blowing on the right side produces a nose-right yawing moment. It is also interesting to note that, compared to aft blowing, the forward blowing is more effective at lower angles of attack. There appears to be some significant influence at angles of attack as low as 10° .

3.3.5 Forebody with Symmetric Strakes and Blowing Forward

Figure 26 shows the effect of varying the forward blowing rate for the case where the forebody has symmetric forebody strakes as discussed before for the aft blowing, i. e., length = $1.0d$, height = $0.05d$, and placed at 105° . The non-blowing case shows a yawing moment near zero for the entire angle of attack range. Blowing at low rates has the opposite effect of blowing at higher rates. At low rates, at least at angles of attack less than that where the yawing moment changes sign with angle of attack, the yawing moment is in the opposite direction to the side where the blowing is occurring. At higher rates the blowing has the effect of producing a yawing moment in the opposite direction, i. e., in the same direction as the side where blowing is. It is not clear what the exact fluid mechanism is that reverses the direction of the yawing moment with increased blowing rate. From a controls standpoint, forward blowing would not be as desirable as aft blowing since it does not have the characteristics of continually increasing yawing moment in the same direction with increasing blowing rate.

3.3.6 Forebody with Symmetric Strakes and Blowing Differentially (Aft, Forward, and Aft/Forward)

The cases examined so far have shown the effects of blowing at various rates on both sides simultaneously or on one side only at various rates. The next few examples will illustrate the effectiveness of blowing at different rates on each side.

3.3.7 Blowing Differentially Aft

The first is shown in Fig. 27 where blowing is tangentially aft at $x/d=0.5$. The ability to vary the yawing moment at any given angle of attack by holding one side at the maximum blowing rate and then varying the blowing rate on the opposite side is evaluated in Fig. 27. This plot shows the change in the yawing moment from the baseline case of maximum blowing on the left, which generates a nose-left yawing moment to the case where there is equal blowing on both sides. As the blowing on the right side is gradually increased, the effect is to shift the yawing moment towards the positive, or nose-right. The opposite trend is seen when the right blowing port is maximum and the left side has variable blowing rates. The effects are not identical on both sides but show similar trends. One does not see complete symmetry because the case where the blowing is identical on both sides does not necessarily produce a zero yawing moment, as can be seen for the case where left and right blowing are both maximum. It does show that for any specific angle of attack there is a combination of blowing rates that should be able to force the yawing moment to be near zero. A good example is the case shown in Fig. 27 where $C_{y\text{left}} = .03$ and $C_{y\text{right}} = .015$ at angle of attack of 50° . From a flight controls point of view, it would be important to examine a large number of variations to select a systematic variation of blowing on both sides simultaneously that minimized the total blowing required while at the same time produced the maximum predictable moment. It might be that blowing on one side only at a time is still the most desirable. The degree that the differential blowing would provide a finer vernier adjustment on the yawing moment would be an important consideration.

3.3.8 Blowing Differentially Forward

Another example of differential blowing is shown in Fig. 28 where blowing ports are situated at $x/d=1.0d$ blowing tangentially forward. In this case it appears that the range of yawing moments that are achievable with various combinations of blowing are similar in magnitude to aft blowing, but as seen before for individually blowing on one side, the forward blowing is more effective at lower angles of attack. It also appears, for example in Fig. 28, that the influence of blowing rate on the magnitude of the yawing moment is very nonlinear with blowing rate. This case shows that there is little difference in the moment due to differential rates until the rate on the right side is nearly equal to the left side. The left side blowing is completely dominating until the blowing rate is the same as the left side at which point the yawing moment is nearly zero.

3.3.9 Blowing Differentially Forward/Aft

It is now appropriate to examine the effects of differential blowing where one side is blowing tangentially forward and the other side is blowing tangentially aft. In the data to be shown the forward blowing port is located at $x/d=1.0d$ and the aft blowing port is located at $x/d = 0.5$. Figure 29 shows the case for blowing forward on the left and blowing aft on the right. Blowing forward on the left side alone produces a moment to the left as observed previously. Blowing aft on the right side alone produces a moment to the right as shown before. The most interesting result is the result of combining these two blowing schemes to blow simultaneously. The initial presumption would be that the resulting moment would have a value that would be between the values for each of the two individual results. Figure 29 shows that the moment generated by forward blowing on the left is enhanced significantly in the same direction by blowing aft on the right instead of being modified in the direction of aft blowing alone. In fact, it appears that the magnitude of the additional moment created by the aft blowing is nearly equal to the magnitude of the aft blowing alone, but the direction is reversed. There is an extremely effective synergistic effect of the simultaneously blowing which cannot be achieved with either individual blowing scheme alone. Figure 30 shows the case where the blowing ports are reversed. The right port is blowing forward and the left port is blowing aft. The result is basically a mirror image of Fig. 29 considering the same cases, i.e., for maximum blowing individually and maximum blowing for both sides simultaneously. In addition in Fig. 30, there are curves plotted for intermediate values of blowing. In Fig. 30a the blowing is constant at the maximum rate on the left in the aft direction and the right port is blowing forward at various rates from zero to maximum. In Fig. 30b, the right forward-blowing port is held constant at maximum while the left port blowing aft is varied. It is clear from Fig. 30b that the forward blowing is the dominant force, and that increased blowing in the aft direction is an increasingly effective enhancement in the same direction as the forward blowing. The enhanced yawing moment is approximately proportional to the magnitude of the aft blowing rate in the angle of attack range up to 60° . It is also interesting to note in Fig. 30a that when the right-side forward blowing is at a low value the moment to the left caused by aft blowing is enhanced in the direction of aft blowing. At higher rates of forward blowing, the yawing moment direction moves toward the direction of the forward blowing. This variation in blowing direction with increased blowing in the forward direction is similar to that discussed in Fig. 26 for forward blowing alone.

4.0 CONCLUSIONS

Experiments have been conducted on a generic fighter configuration to investigate the effectiveness of deployable forebody strakes and forebody blowing to produce controllable yawing moments at high angles of attack. Strategically placed symmetric strakes can be located on the forebody to minimize the asymmetric forces and moments. Individually movable strakes can be used to control the magnitude and direction of the yawing moment. Blowing from outlets in the forebody can be used effectively to alter the leeward vortex flowfield and generate forebody side forces and resulting yawing moments.

For this generic configuration, asymmetric side forces and yawing moments at zero sideslip angle were minimized by a pair of strakes $1.0d$ in length and $0.05d$ in height mounted at the forebody tip at 105° from the windward side. Significant forebody side forces could be generated by deploying a single strake on either side with the magnitude (and direction) controlled by the height of the strake from the forebody surface. For strake deflections from 0 to $0.07d$, the forebody side force is in the same direction as the strake side. If the strake height is increased beyond $0.07d$, the side force is in the opposite direction as the strake side. The difference is believed to be due to the effect of the strake height on the separation and/or reattachment of the flow on the strake side and the resulting effect on the overall orientation of the forebody vortices.

Forebody blowing experiments showed that aft blowing is most effective closest to the tip of the forebody and at a location on the leeward side approximately 135° from the windward side, while forward blowing is more effective at a farther aft position from the tip at the same meridian. At a longitudinal location of $0.5d$ from the tip, blowing normal to the surface was not very effective in generating forebody side forces or yawing moments. Blowing tangential to the surface in either an aft or forward direction was much more effective. Blowing forward showed that at low blowing rates the yawing moment was in a direction opposite to the side where blowing occurred. At higher blowing rates the yawing moment was in the same direction as the blowing side. Aft blowing produced a yawing moment in the direction of the blowing side for all blowing rates and the moment continually increased with increased blowing. The level of yawing moment could be controlled by variation in the blowing rate on both sides individually. Differential blowing with one side forward and one side aft was very effective in producing controllable yawing moments. It was concluded that the most effective method to control the yawing moment on the forebody was to minimize the natural asymmetry with a pair of symmetrically mounted tip strakes and to perturb the vortex system away from the symmetric condition with blowing on either side. Control of the flowfield with blowing only, i.e., with no strakes on the forebody to reduce the asymmetry, is more difficult than starting with symmetric condition. It is also important to minimize the size of the strake, because the larger the strake, the more difficult it is to overcome the forced symmetry with asymmetric flow produced by blowing.

Overall, significant yawing moments (twice that available from the rudder at low angles of attack) can be produced at high angles of attack by either independently moving a pair of forebody strakes or by independently controlling blowing rates from ports located on the model surface.

REFERENCES

1. Chapman, G. T., Keener, E. R., and Malcolm, G. N., "Asymmetric Aerodynamic Forces on Aircraft Forebodies at High Angles of Attack - Some Design Guides," November 1975, Conference on Stall/Spin Problems of Military Aircraft, Rhode Saint Genese, Belgium, AGARD CP-199.
2. Skow, A. M. and Titinga, A., "A Survey of Analytical and Experimental Techniques to Predict Aircraft Dynamic Characteristics at High Angles of Attack," May 1978, Conference on Dynamic Stability Parameters, Athens, Greece, AGARD CP-235.
3. Headley, J. W., "Analysis of Wind Tunnel Data Pertaining to High Angle of Attack Aerodynamics," July 1978, AFFDL-TR-78-94, Volume I.
4. Murri, D. G. and Rao, D. M., "Exploratory Studies of Actuated Forebody Strakes for Yaw Control at High Angles of Attack," August 1987, AIAA Paper No. 87-2557-CP.
5. Skow, A. M., Moore, W. A., and Lorincz, D. J., "Forebody Vortex Blowing - A Novel Concept to Enhance the Departure/Spin Recovery Characteristics of Fighter Aircraft," May 1979, Conference on Aerodynamics of Controls, Naples, Italy, AGARD CP-262.
6. Moore, W. A., Skow, A. M., and Lorincz, D. J., "Control of the Forebody Vortex Orientation by Asymmetric Air Injection - Application to Enhance Departure/Spin Recovery," January 1980, AIAA 18th Aerospace Sciences Meeting, Pasadena, CA, AIAA Paper No. 80-0173.
7. Peake, D. J., and Owen, F. K., "Control of Forebody Three-Dimensional Flow Separation," May 1979, AGARD-CP-262-15.
8. Peake, D. J., Owen, F. K., and Johnson, D. A., "Control of Forebody Vortex Orientation to Alleviate Side Forces," January 1980, AIAA-80-0183.
9. Malcolm, G. N. and Skow, A. M., "Enhanced Controllability Through Vortex Manipulation on Fighter Aircraft at High Angles of Attack," August, 1986, AIAA Paper No. 86-2277-CP.
10. Malcolm, G. N., Ng, T. T., Lewis, L. C., and Murri, D. G., "Development of Non-Conventional Control Methods for High Angle of Attack Flight Using Vortex Manipulation," July 1989, AIAA Paper No. 2192.

ACKNOWLEDGEMENTS

The authors wish to recognize Mr. Bert Ayers and Mr. Anthony Arand of Eidetics International for their substantial contributions to the design and construction of the various model components and to the personnel of the Flight Dynamics Branch at NASA Langley Research Center who assisted in the wind tunnel tests.

The work is sponsored in part by the US Air Force Flight Dynamics Laboratory, WPAFB, Ohio (Contract No. F33615-86-C-3623). The technical monitors are Mr. Stan Lash and Mr. Dieter Multhopp of the Flight Controls Branch.

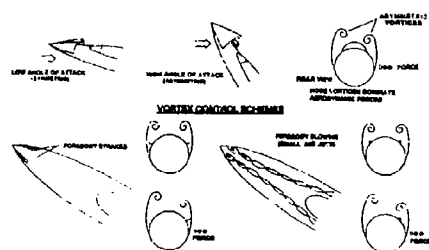


Fig. 1 - Forebody vortex patterns and proposed methods of vortex control.

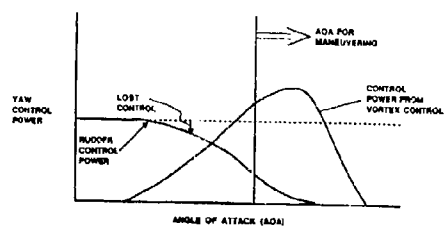


Fig. 2 - Illustration of typical loss of yaw control power with increasing angle of attack and potential benefits of vortex control.

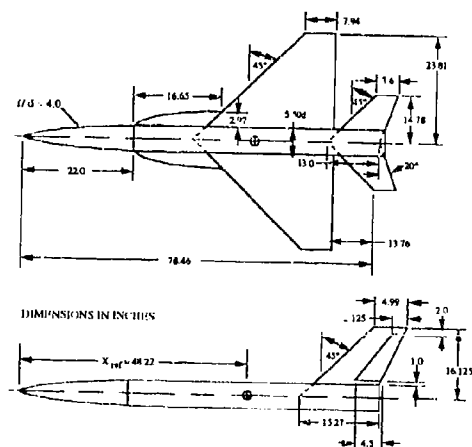


Fig. 3 - Planform and side views of generic fighter configuration.

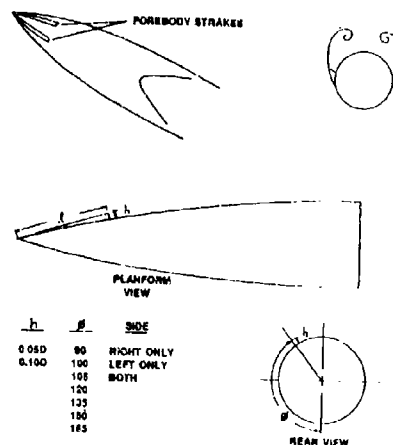


Fig. 4 - Matrix of forebody strake sizes and locations tested.

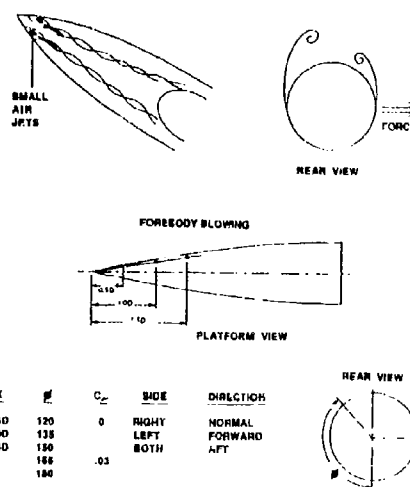


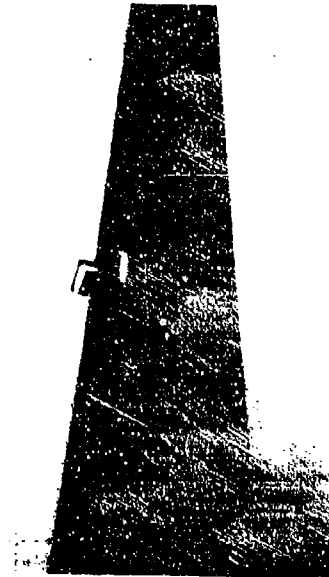
Fig. 5 - Matrix of forebody blowing port locations and directions tested.



a. Complete model



b. Forebody with strakes



c. Forebody with blowing nozzles

Fig. 6 - Generic fighter model in NASA Langley 12-foot Low Speed Wind Tunnel.

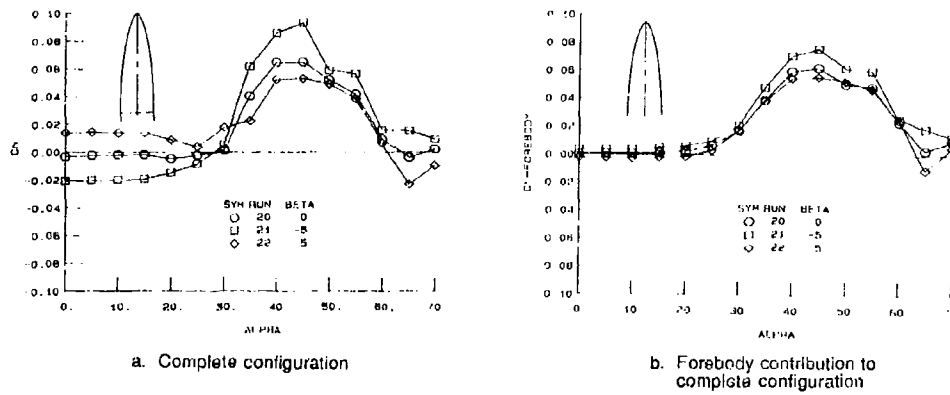


Fig. 7 - Yawing moment coefficient for baseline configuration with clean forebody.

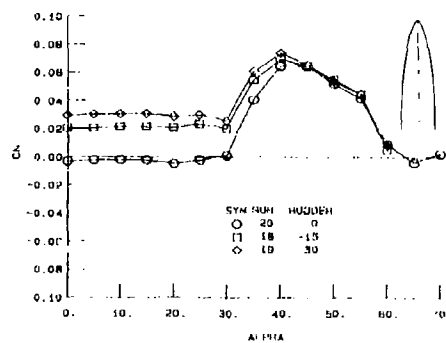


Fig. 8 - Yawing moment coefficient for baseline configuration for various rudder deflections.

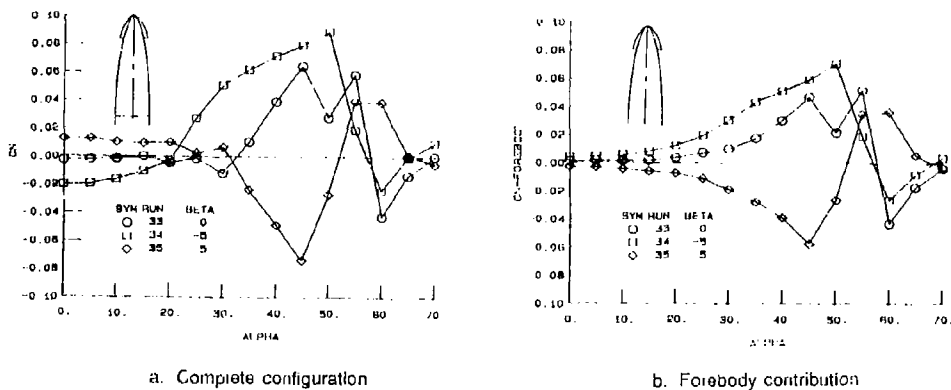
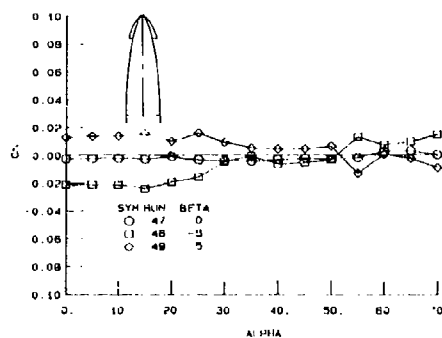
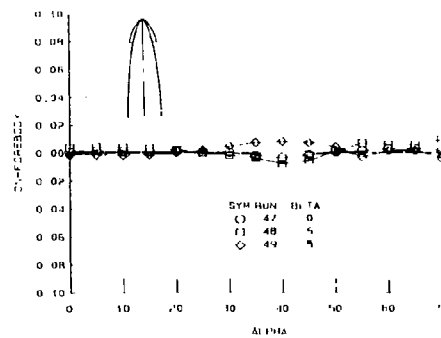


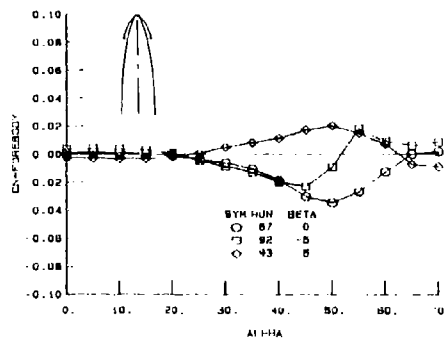
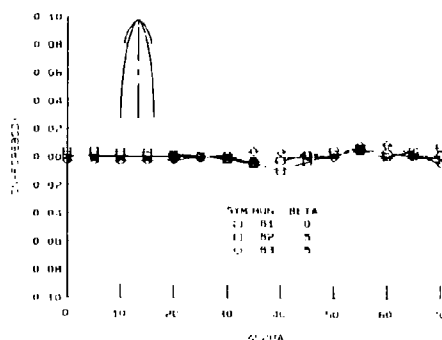
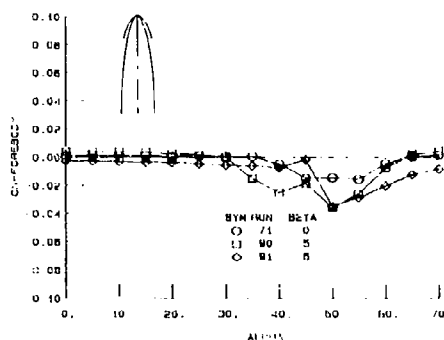
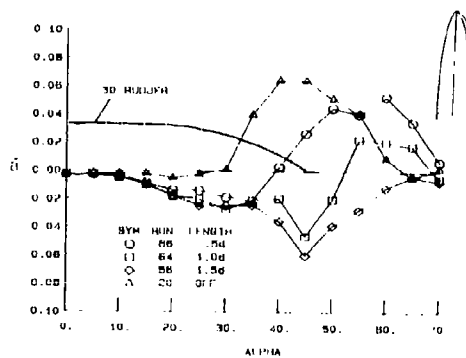
Fig. 9 - Yawing moment coefficient for configuration with symmetric forebody strokes $\phi = 150^\circ$, $l_{ST} = 1.5d$, $h_{ST} = 0.1d$



a. Complete configuration



b. Forebody contribution

Fig. 10 - Yawing moment coefficient for configuration with symmetric forebody strakes, $\phi = 105^\circ$, $l_{ST} = 1.5d$, $h_{ST} = 0.1d$ Fig. 11 - Yawing moment contribution of forebody with symmetric strakes, $\phi = 105^\circ$, $l_{ST} = 1.5d$, $h_{ST} = 0.05d$ Fig. 12 - Yawing moment contribution of forebody with symmetric strakes, $\phi = 105^\circ$, $l_{ST} = 1.0d$, $h_{ST} = 0.1d$ Fig. 13 - Yawing moment contribution of forebody with symmetric strakes, $\phi = 105^\circ$, $l_{ST} = 0.5d$, $h_{ST} = 0.05d$ Fig. 14 - Comparison of yawing moment coefficient produced by single strakes ($h_{ST} = 0.1d$) of different lengths on the right-hand side of the forebody and that produced by a 30° rudder deflection.

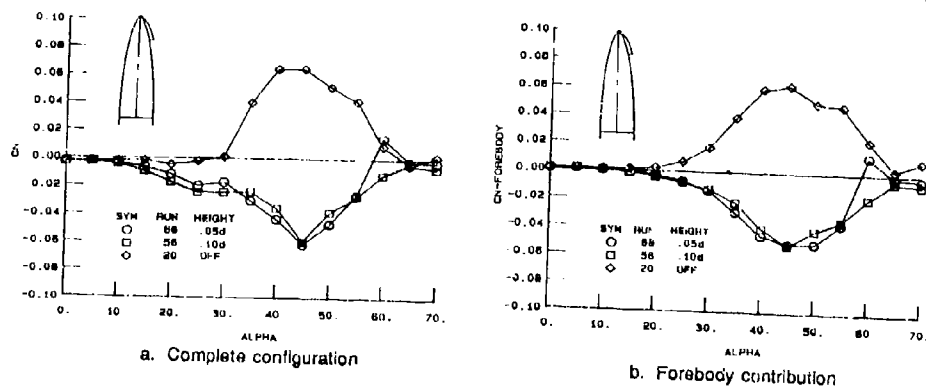


Fig. 15 - Effect on the yawing moment of varying the height of a single stroke on the right side, $l_{ST} = 1.5d$.

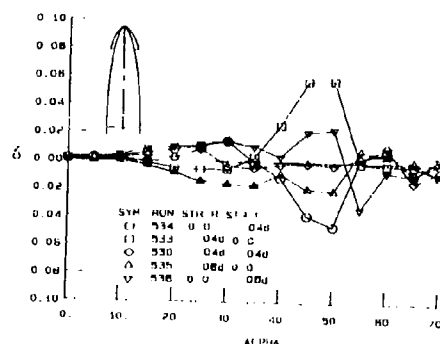


Fig. 16 - Yawing moment coefficient for left and right strokes at $\phi = 105^\circ$, deployed individually and together, $l_{ST} = 1.0d$.

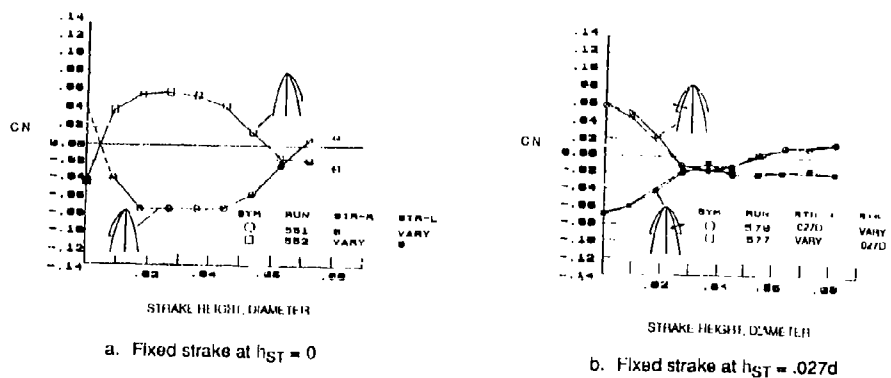


Fig. 17 - Yawing moment coefficient variation with stroke height, $l_{ST} = 1.0d$, $\alpha = 45^\circ$, $\phi = 105^\circ$.

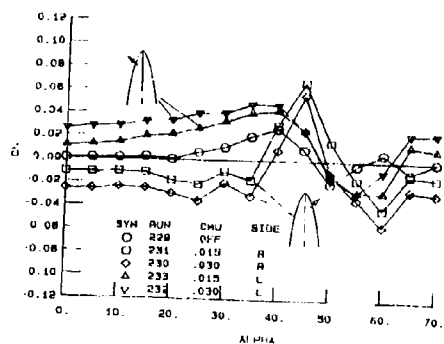


Fig. 18 - Yawing moment coefficient for baseline configuration without forebody strakes, with forebody blowing normal to the surface at $x/d = 0.5$ and $\phi = 135^\circ$.

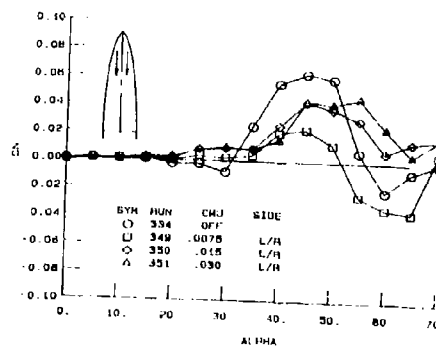


Fig. 19 - Yawing moment coefficient for baseline configuration without forebody strakes blowing simultaneously in tangential aft direction at $x/d = 0.5$ and $\phi = 135^\circ$.

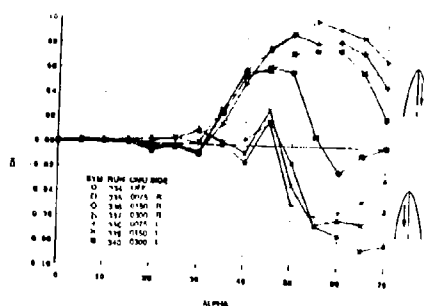
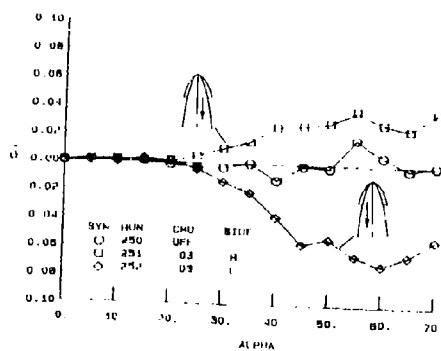
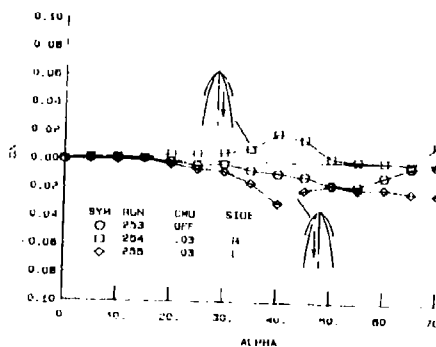


Fig. 20 - Yawing moment coefficient for baseline configuration, clean forebody, blowing aft at various rates from right or left ports at $x/d = 0.5$ and $\phi = 135^\circ$.



a. $l_{ST} = 1.0d$, $h_{ST} = 0.05d$



b. $l_{ST} = 1.0d$, $h_{ST} = 0.10d$

Fig. 21 - Yawing moment coefficient for configuration with symmetric forebody strakes of different heights at $\phi = 105^\circ$. Blowing aft left or right, $\phi = 135^\circ$, $x/d = 0.5d$, $C_{\mu} = 0.3$.

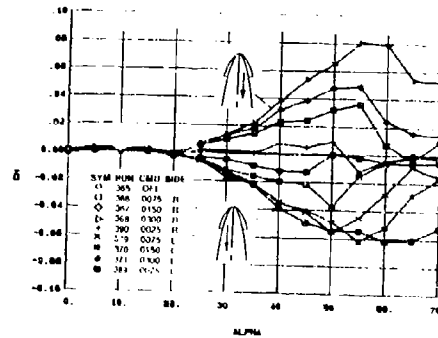
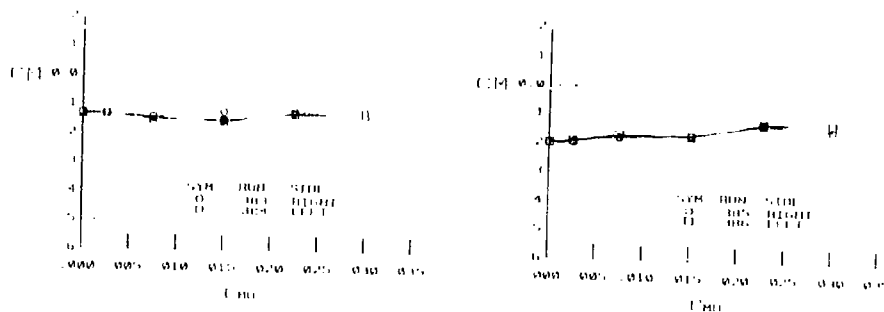


Fig. 22 - Yawing moment coefficient variation for several blowing rates for configuration with symmetric strakes, $\phi = 105^\circ$, $l_{ST} = 1.0d$, $h_{ST} = 0.05d$. Blowing aft on left or right side at $\phi = 135^\circ$, $x/d = 0.5$.



a. $\alpha = 45^\circ$

b. $\alpha = 60^\circ$

Fig. 23 - Pitching moment coefficient variance with blowing rate on configuration with symmetric strakes, $\phi = 105^\circ$, $l_{ST} = 1.0d$, $h_{ST} = 0.05d$. Blowing aft left or right at $\phi = 135^\circ$, $x/d = 0.5$.

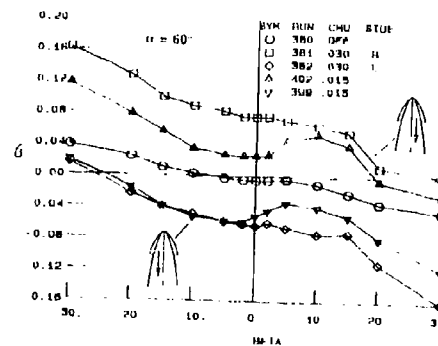


Fig. 24 - Effect of sideslip angle at $\alpha = 60^\circ$ on yawing moment coefficient for configuration with symmetric strakes, $\phi = 105^\circ$, $l_{ST} = 1.0d$, $h_{ST} = 0.05d$. Blowing aft left or right at $\phi = 135^\circ$, $x/d = 0.5$.

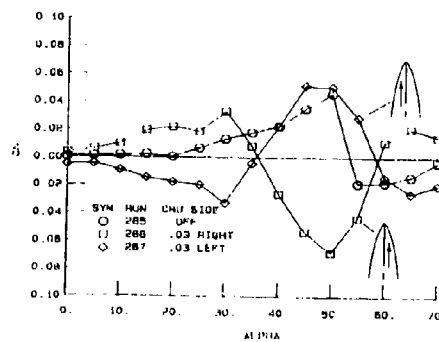
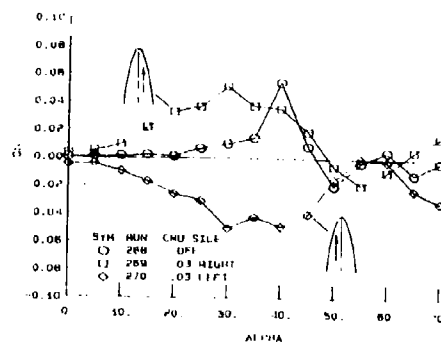
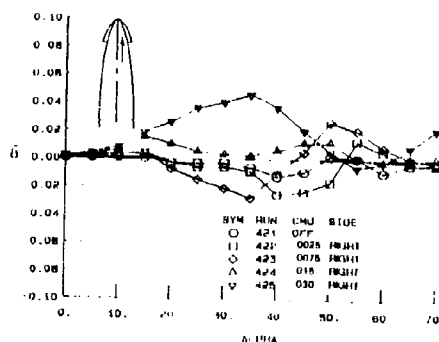
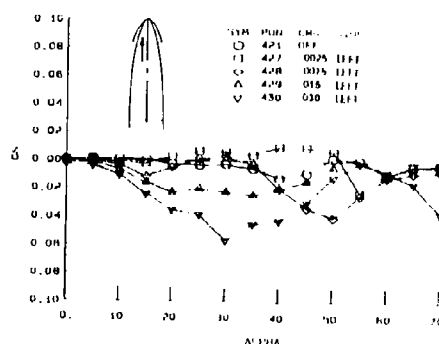
a. $x/d = 0.5$ b. $x/d = 1.0$

Fig. 25 - Yawing moment coefficient for configuration with clean forebody, blowing forward at $\phi = 135^\circ$, left or right, at different longitudinal locations.



a. Blowing right



b. Blowing left

Fig. 26 - Yawing moment coefficient for configuration with symmetric strakes, $\phi = 105^\circ$, $h_{ST} = 1.0d$, $h_{ST} = 0.05d$, and blowing forward at $\phi = 135^\circ$, $x/d = 1.0$.

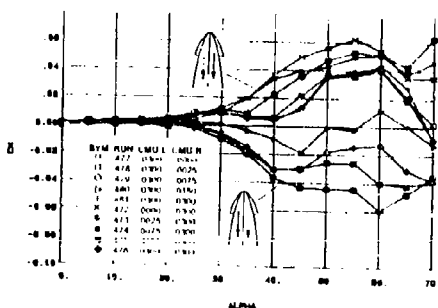


Fig. 27 - Yawing moment coefficient for configuration with symmetric forebody strakes, $\phi = 105^\circ$, $h_{ST} = 1.0d$, $h_{ST} = 0.05d$, and blowing simultaneously left and right.

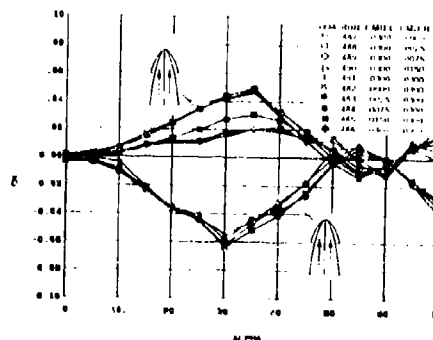


Fig. 28 - Yawing moment coefficient for configuration with symmetric forebody strakes, $\phi = 105^\circ$, $h_{ST} = 1.0d$, $h_{ST} = 0.05d$. Blowing simultaneously forward at $\phi = 135^\circ$, $x/d = 1.0$, left and right.

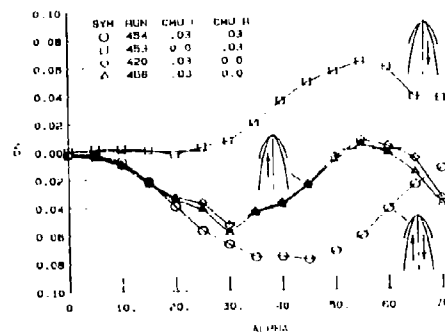
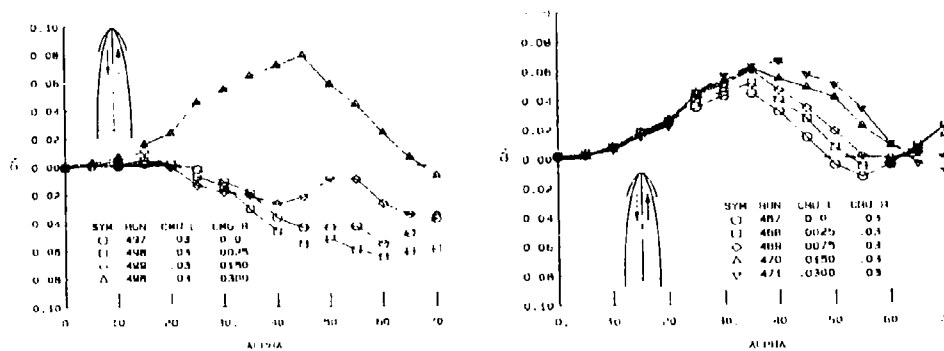


Fig. 29 - Yawing moment coefficient for configuration with symmetric forebody strakes, $\phi = 105^\circ$, $l_{S1} = 1.0d$, $h_{S1} = 0.05d$. Blowing forward left, $\phi = 135^\circ$, $x/d = 1.0$. Blowing aft right, $\phi = 135^\circ$, $x/d = 0.5$.



a. Blowing left ($C_{\mu} = 0.03$), blowing right variable

b. Blowing right ($C_{\mu} = 0.03$), blowing left variable

Fig. 30 - Yawing moment coefficient for configuration with symmetric strakes, $\phi = 105^\circ$, $l_{S1} = 1.0d$, $h_{S1} = 0.05d$. Blowing aft left, $\phi = 135^\circ$, $x/d = 0.5$. Blowing forward right, $\phi = 135^\circ$, $x/d = 1.0$.

CONTROL OF VORTEX AERODYNAMICS AT HIGH ANGLES OF ATTACK

by

Prof. L. Roberts

Department of Aeronautics and Astronautics
Stanford University
Stanford, CA 94305
United States

and

Dr. N.J. Wood

School of Mechanical Engineering
University of Bath
Bath, Avon BA2 7AY
United Kingdom

Summary

The concept of tangential leading edge blowing has been investigated as a means of controlling the vortical flow over delta wings at high angles of attack. At pre-stall angles of attack, tangential leading edge blowing exerts rapid control of the vortical flow and can control or impose asymmetries with either leading edge influence uncoupled from the other. At post-stall angles of attack, the response of the vortical flow to transient blowing is slower due to the presence of vortex burst. However, a burst vortex may be unburst by tangential leading edge blowing and significant rolling moments produced at conditions where conventional controls are ineffective. At these very high angles of attack, the left and right side vortical flows appear to be strongly coupled.

List of Symbols

A_j slot exit area
 b local semi-span
 c wing chord
 C_{μ} wing rolling moment coefficient
 C_{μ} wing normal force coefficient
 C_{μ} blowing momentum coefficient
 μ = jet momentum/($\rho_j S_j$)
 q free stream dynamic pressure
 S wing reference area
 x, y cartesian coordinates
 V_j jet velocity
 V_∞ free stream speed
 α angle of attack
 ρ free stream density
 Δp difference between internal plenum pressure and free stream static

Subscripts

L left side blowing only
R right side blowing only
T total wing blowing = L + R

Introduction

Increasing demands for greater manoeuvrability in combat aircraft at high angle of attack have stimulated new approaches to the control of aerodynamic flows with emphasis on the control of vortex flows over delta wings. At high angles of attack the flow over a delta wing is dominated by leading edge vortex shedding and subsequent breakdown. This may occur in an asymmetric and sometimes random way leading to a loss of aircraft stability and control. Restoration of an orderly and controlled vortex flowfield on the suction surface of the wing is considered to be the key to extending combat aircraft manoeuvrability to the very high angle of attack regime. To obtain maximum benefit from such a device the modified vortical flow should be controlled such that prolonged post-stall manoeuvres may be performed rather than simple transient excursions to high angle of attack.

Under normal conditions the flow over the lee-side of a delta wing is dominated by a pair of strong stable and well organised vortices formed by the vortex sheet shed from the leading edge[1]. As the angle of attack approaches the stall a vortex burst moves toward the apex of the wing from the trailing edge. At stall the burst reaches the apex and the normal force coefficient begins to decrease. Further increases in the angle of attack result in a complete breakdown of the organised flowfield and vortex shedding. These flow instabilities produce large oscillations in the forces on the wing and render any conventional moving surface controls ineffective.

There are at present a number of concepts being evaluated to provide control at high angles of attack. Thrust vectoring[2] and close coupled canards[3] are examples of devices under investigation to provide the control moments to maintain trim[4]. The proximity of the line of action of these devices to the centre of gravity would suggest that they are of little or no contribution to roll or yaw control. Concepts to control a burst vortex are rather more limited and recently modified strakes and fences have received attention.

There have been several attempts to control the vortical flow over a delta wing by blowing[5][6]. These schemes have, in general, relied upon an inertial, inviscid interaction with the vortical flow. Re-energisation of the vortex core has been shown to be capable of controlling vortex burst but the momentum required and the need to know the vortex location results in an inefficient solution. Spanwise blowing from the leading edge of a delta wing has also been investigated experimentally[7] and computationally[8][9]. Augmentation of the vortex strength was obtained pre-stall but the vortex burst was enhanced and the net lift closely matched the jet momentum resulting in no net augmentation.

Tangential leading edge blowing has as its basis the concept of vortex equilibrium on the lee-side of a delta wing. That is, the position and strength of the vortex core and its feeding sheet are maintained in a force-free condition. This observation forms the basis for several computational methods for vortex flows[10][11]. If the leading edge is rounded then the position of the leading edge separation provides an additional degree of freedom for the flowfield. Therefore for every position of the leading edge separation there exists a unique vortex strength and location. Normally the angle of attack would be the only variable to affect this equilibrium condition. However, if a thin tangential jet is injected into the crossflow boundary layer near the leading edge, figure 1, then the jet momentum will provide additional control of the boundary layer separation and hence the vortex. Thus the strength of the wall jet controls the equilibrium condition of the vortex. This is the concept of Tangential Leading Edge Blowing.

It is important to recognise that a key to the effectiveness of the jet blowing is the Coanda effect[12] by which the jet remains attached to the leading edge. The presence of a highly curved convex surface stimulates strong attachment and significantly enhances the mixing rate of the wall jet. Thus there is a very efficient transfer of momentum from the jet to the crossflow boundary layer. This viscous interaction takes place within the dimension of the boundary layer and results in delayed separation and consequently to large changes in the inviscid vortical flow and is therefore efficient. There have been several previous uses of boundary layer control and without exception it is those with the highest surface curvature which prove most effective. Examples of efficient boundary layer control are Circulation Control[13], Upper Surface Blowing for Powered Lift[14] and Wind Tunnel Boundary Layer Control[15].

Considering that a major problem of high angle of attack operation is one of control, the objectives of the present research were to investigate both the dynamic response of the flow to unsteady control input and the steady state control effectiveness over a wide range of angle of attack. This paper will report the results of two experiments. The first, a full-span wing on which the roll control effectiveness of tangential leading edge blowing was investigated at angles of attack up to 55° , steady state[16]. The second, a semi-span wing which was used to measure the unsteady response of the vortical flow to transient tangential leading edge blowing[17].

Experiment

Full-span Wind Tunnel Model

A sting mounted, full span delta wing has been tested in the 0.6m low speed wind tunnel at Stanford University. The wing was of constant thickness, approximately 6% at the root chord, and has a 60° leading edge sweep angle, figure 2. Two, separate internal plena were used to isolate the blowing supply for each of the leading edges. Leading edge slots extended over the majority of the leading edge and the slot width varied linearly from 0.1mm at the apex to 0.5mm at the wing tip. Since this model was to be operated only at steady state conditions, each plenum was supplied by an independent air source with manual pressure regulation monitored by separate pressure transducers. A typical wind tunnel free stream speed of 20m/s was used throughout the experiment giving a Reynolds number based on the root chord of 400,000.

The model was mounted on a sting which in turn was supported by two tubes which spanned the tunnel. These tubes were fixed to side windows such that rotation of the windows controlled the angle of attack. Angles of attack up to 55° were allowable before the support structure contacted the tunnel floor. The centre of rotation was the centroid of the wing so that any asymmetric blockage effects were minimised. The model support shaft could be rotated, through a worm gear system, from outside the test section to provide roll angles of up to 30° .

A single row of pressure tappings was included on the upper surface of the wing at the 35% chord location. The tappings extended 78% of the local semi-span on either side of the plane of symmetry and the surface pressure was monitored by a standard Scanivalve pressure measurement system. In addition the model was mounted on a simple 3-component strain gauge balance giving normal force, pitching and rolling moment. Care was taken with the alignment of the air inlet hoses so as to minimise the effects of induced loads due to pressurisation.

Semi-span Wind Tunnel Model

A semi-span delta wing model, figure 3, was also tested in the Stanford University 0.6m low speed wind tunnel. The wing was of constant thickness (approximately 6% at the root chord) and had a 50° leading edge sweep angle. The leading edge slot extended over the majority of the leading edge and the slot gap varied linearly from 0.1mm at the apex to 0.5mm at the tip.

The model could be configured for either steady or unsteady surface pressure measurement. Two rows of surface pressure instrumentation were included at the 32.5% and 54.5% root chord locations. For steady pressure measurement, a total of 27 and 24 tappings respectively were included, with the most outboard locations being at 7% and 84% of the semi-span. The model was floor mounted on a turntable which permitted angle of attack variation up to 50°. The experiments were performed at speeds of 20-30 m/s which gave Reynolds numbers of the order of 6.8×10^5 based on the root chord.

Transient blowing was provided by a simple pneumatic system. Based on previous experiments, a servo controlled, brushless D.C. motor was used to drive a rotating, variable area ratio valve assembly. A step input, differenced against a shaft angle potentiometer, provided the error signal which controlled the motion of the valve rotor. The damping and gain of the control system were adjusted to minimise the rise time and overshoot of the internal pressure signal. A system resulted which provided a typical plenum pressure rise time of 5ms with little or no overshoot.

Derivation of Results

The internal pressure of each plenum was used to estimate the blowing momentum assuming that the slot area was known and that the flow was incompressible.

$$C_\mu = 2 \frac{A_j}{S} \left(\frac{V_j}{V_\infty} \right)^2$$

where

$$V_j^2 = 2 \frac{\Delta p}{\rho}$$

The sting balance was calibrated wind-off and an on-line data acquisition system sampled the output signals and automatically derived the forces and moments. Any residual cross-coupling was accounted for in the balance calibration matrix.

No corrections for tunnel blockage have been applied. At the extreme angles of attack under investigation, the solid blockage could approach 1/4 of the wind tunnel cross sectional area. Obviously, this precludes the use of the results in absolute terms and also places the data outside the normal bounds of the approximate correction methods available. However, it is suggested that the magnitude of the effects of tangential leading edge blowing are representative. Note that all experiments were performed at fixed incidence and as such, the blockage effect would only impact the initial conditions. The stall angle in particular should be regarded as approximate but sufficiently accurate to delineate between the pre- and post-stall regimes. The ability to unburst a vortex and to reattach the flow over the entire delta wing for angles of attack up to 55° is thought to be of sufficient interest as to neglect concerns regarding tunnel boundary effects.

Results and Discussion

Results from the full-span experiment[16] will be used to illustrate the overall effects of tangential leading edge blowing. As previously reported[18] it is convenient to review the data in two separate regimes, pre-stall and post-stall, where the division relates to the absence or presence of burst vortical flow at the point of observation on the wing upper surface. Figure 4 shows spanwise pressure distributions for the full-span wing at 30° angle of attack with and without leading edge blowing. In the unblown case, the symmetry of the flow is apparent and the usual vortex induced suction peak indicates the presence of stable, strong vortical flow over the upper surface. For the blown cases, where both leading edges are blown with approximately equal momentum, the influence of the vortex is gradually reduced as is the extent of the separated flow. In the limit, the flow is fully reattached over the upper surface of the wing and the vortex influence is zero. Previous reports[18][19] have documented this effect where increasing leading edge blowing reduces the strength of the vortices and relocates them slightly inboard. The concept of an effective angle of attack of the vortical flow which is independent of the wing angle of attack has been proposed[17]. The effect of the blowing being to reduce the effective angle of attack of the vortices until, as the flow reattaches, it becomes zero. Notice that as the vortex influence reduces, the overall normal force stays relatively constant. This results from an additional normal force contribution due to the jet attachment around the leading edge[19]. Unfortunately there was insufficient volume to install pressure tappings on the leading edge of the full-span wing and the effect is not visible on the pressure distributions.

Thus, in the pre-stall regime the primary influence of blowing is to modify the spanwise pressure distribution but with little change of normal force.

Figure 5 shows the contrasting results for the post-stall condition. For this unblown case, there is no apparent vortex influence on the upper surface of the wing. However, as blowing is applied simultaneously to both leading edges, the vortical flow is gradually re-established. This illustrates the ability of tangential leading edge blowing to unburst a vortex. Increasing blowing removes the vortex burst point towards the trailing edge of the wing giving an increase in the vortex influence at any location on the upper surface. This effect correlates well with the effective angle of attack hypothesis previously mentioned. In the absence of blowing, rearward movement of the burst would usually be associated with a reduction in wing angle of attack. Here the effect is achieved at fixed angle of attack, with blowing.

For this post-stall case, recreating the vortical flow over the wing upper surface also increases the overall normal force. It has also been shown [19] that, once a maximum local vortex influence condition occurs, further increases in blowing momentum cause the vortex influence to decrease as for the pre-stall regime. This may be thought of as a continuing reduction of the effective angle of attack with increasing blowing.

The Production or Control of Rolling Moment

Since symmetric blowing is clearly able to control the vortical flow over a wide range of angles of attack, it is now of interest to examine the production of rolling moment by asymmetric blowing. For the same pre- and post-stall conditions, figures 6 and 7 show spanwise pressure distributions for asymmetric blowing. Consider first the pre-stall case, figure 6. At these conditions, blowing on the left leading edge modifies the left side vortex with little impact on the right side flow. As the blowing is increased, the vortex influence reduces and in the limit, the condition of fully reattached flow on the wing upper surface is achieved. It might be expected that a left wing down moment (negative) is produced, however this is contrary to the moment measured by the balance. Reference [19] showed that for pre-stall angles of attack, there were two contributions to rolling moment; one from the vortex and one from the leading edge suction induced by the wall jet attachment. It must be assumed that the contribution to roll from the leading edge suction is greater than that due to the reduced vortex influence. To what extent the net result of this balance is geometry dependent is not known but should be an area for further investigation. The slight increase in the vortex suction peak for very weak blowing momentum is not without significance. For this angle of attack the vortex burst is probably just aft of this chordwise measurement station. Consequently, the slight aft movement of the vortex burst caused by this weak blowing allows the vortex to initially strengthen and increase the local suction peak and to act as if the flow were conical thereafter.

The primary observation from figure 6 is that blowing asymmetrically at pre-stall angles of attack is an uncoupled phenomenon. Blowing on the left side does not significantly affect the right side flow and vice versa.

Consider now, figure 7 which shows the pressure distribution response to asymmetric blowing for a post-stall, 50° angle of attack. The form of the data is consistent with figure 3 in that the blowing is applied to the left leading edge only. Notice though that for all but the highest blowing momentum shown, the effects are concentrated on the right side of the wing. Also notice that instead of reducing the vortex influence on the right side it is actually enhanced. The distribution varies from one which is flat, showing no vortex influence, to one where a stable, organized vortical flow is present. Obviously, a number of effects of tangential leading edge blowing are present.

First, tangential leading edge blowing clearly is capable of unbursting a burst vortical flow as evidenced by the increasing vortex influence. Second, the left and right vortical flows are very strongly coupled. Blowing on the left leading edge appears to unburst the right side vortex, and for sufficient blowing, the left side vortex.

For this post-stall case, it is somewhat easier to correlate the pressure distribution with the balance measured rolling moment. The rolling moment that can be approximated from the pressure distribution agrees well with that measured on the balance. Reference [18] showed that for the post-stall case where a vortex has been unburst there is no additional leading edge suction effect until after the burst point has passed aft of the measurement location. This implies that the limited amount of pressure information has captured the majority of the pressure modifications which induce moments.

A significant result of this experiment is the recognition that the vortical flow at post-stall conditions is cross-coupled. The extent to which this is true for actual vehicle configurations with a fuselage present remains to be determined.

Further evidence of the vortical flow coupling at post-stall angles of attack is given in reference [17]. From spanwise pressure distributions (figures 13 and 14 of that reference), it was observed that, for the post-stall case, simultaneous blowing produces far greater modification of the flow than the individual asymmetric blowing cases combined. In contrast, for the pre-stall case, the effects of symmetric blowing could be predicted as the sum of the asymmetric results.

Figures 8 and 9 summarize the production of rolling moment by asymmetric leading edge blowing as functions of both angle of attack and blowing momentum. The control moment reversal that was evident from figures 6 and 7 is clarified and is bounded by the stall angle of the wing. It is therefore expected to be dependent upon the uncoupled/coupled nature of the flow in the two angle of attack regimes, pre- and post-stall. It is clear that tangential leading edge blowing has the potential to produce rolling moments which far exceed those produced by conventional moving surface devices. The data used for comparison [20] was acquired from a wind tunnel model similar to a YF-16. It is most important that the reason for the coupling of the post-stall response be understood so that this concept may be put to best use.

Figure 9 shows the symmetry of the rolling moment production for both left and right leading edge blowing. The slight variation in the blowing momentum at breakpoints, left and right, is probably due to a slight difference in the actual slot area. Since the actual slot dimension was rather small, the slot gap could only be estimated to $\pm 10\%$. This level of accuracy is unfortunately maintained in the values for blowing momentum coefficient. Even with this level of accuracy, the symmetry of the moment production is quite good. The ability to produce rolling moments of either sign suggests not only that roll control could be maintained over a broad range of angles of attack but also that asymmetric flows due to yaw or roll could be corrected and stabilised.

The Time Scales of Vortex Control

Having observed that tangential leading edge blowing is capable of producing or controlling rolling moment to very high angles of attack, it is of interest to investigate the speed at which the flow responds to control inputs. In this instance, the time for vortex reorganisation, in terms of the convective scale of the vehicle, following a rapid change in the blowing momentum is important. The semi-span wind tunnel model previously described has been used to derive these time scales [21]. By varying the angle of attack and the amplitude of the blowing momentum change for constant transient time, it is possible to determine time lags associated with vortex modification. These again will be examined in the two regimes, pre- and post-stall.

First, it is necessary to define some datum response against which the actual response can be compared. This datum is referred to as the "quasi-steady-state response". Reference [21] contains a full explanation of this derivation. In summary, the steady state pressure distributions, figure 10, may be used to identify steady state pressure coefficients at a fixed wing coordinate as a function of blowing momentum, figure 11. The transient internal pressure signals may then be transformed to transient blowing momentums from which an instantaneous surface pressure response may be interpreted. This technique produces an ideal surface pressure variation which assumes instantaneous response and can be compared to the actual response to identify unsteady aerodynamic effects.

Two primary regimes, pre- and post-stall, have been identified and it is of interest to investigate the vortex response in those regimes. It should be noted that a third possibility exists and that is at high wing angle of attack but with sufficient initial blowing momentum to unburst the vortex. This produces a pre-stall flow-field at post-stall wing angle of attack. Therefore three cases will be examined:

- pre-stall wing angle of attack, pre-stall vortex (unburst)
- post-stall wing angle of attack, post-stall vortex (burst)
- post-stall wing angle of attack, pre-stall vortex (unburst)

Figures 12, 13 and 14 show the results obtained from the semi-span model for these three cases. In each figure, both a positive and a negative change in blowing momentum is illustrated. In all cases the transition time of the internal pressure was maintained at 5mS but the amplitude was modified to maximise the change in the pressure coefficient. The quasi-steady response for each case is shown and the time lags due to unsteady effects may be determined. For all cases the convective time based on the root chord and the free stream speed was 14mS. Only a fraction of the actual data points are shown for clarity.

Examination of this data shows that there are two distinct time scales associated with vortex control by tangential leading edge blowing. A short time lag of less than 1 convective time appears to correlate with the pre-stall vortex condition regardless of the wing angle of attack. For that condition, the vertical flow may be considered almost conical and therefore would not exhibit any longitudinal dependency. Consequently the flow re-organisation is dominated by vortex equilibrium in the cross-flow plane and is a function of the semi-span and the cross-flow velocity. For slender wings at angle of attack this would produce a typical time scale much less than the convective time based on the root chord and the free stream speed and this would tend to correlate with previous observations. It is important to note that aerodynamic phenomena such as low speed wing rock (which is associated with vortex asymmetry rather than vortex burst [22]) tend to have periods of order 20 - 30 convective times [23][26][25]. These results would suggest that tangential leading edge blowing is capable of damping out periodic oscillations very quickly. This observation is also supported by previous work [26].

The second time scale is associated with the post-stall regime where a vortex burst is present. Under these conditions, the longitudinal motion of the vortex burst point has a significant impact upon the local surface pressure and introduces a longitudinal time scale. Consequently, the observation that for post-stall conditions the induced time lag is of the order of 5 convective times is not surprising. It is likely that this longer time scale is associated with longitudinal dimensions and velocities and the convective speed of the vortex burst. This may also explain the tendency for the response to exhibit larger magnitude pressure oscillations post-stall rather than pre-stall. Reference [27] also indicates the presence of two discrete time scales of similar order derived from experiments on oscillating delta wings at high angles of attack.

A number of uncertainties remain regarding tangential leading edge blowing.

- 1) It is difficult to accurately extrapolate the blowing requirements from model to full scale application. The model slot gap is limited by manufacturing constraints to a value which, relative to the span, may be an order of magnitude larger than necessary for full scale. Efficient boundary layer control has been achieved with a slot gap to boundary layer thickness ratio approaching 0.01 [15].

2) The Reynolds number at model scale is quite low, however its effects would be limited to the secondary flow and to the location of the jet slot. The jet slot is generally located just ahead of the cross flow separation for efficient operation. If the jet slot is located at the leading edge the result should be independent of Reynolds number.

3) The minimum radius for the leading edge compatible with vortex control is unknown and may be an area of compromise between cruise conditions and the requirement for agility.

Conclusions

The concept of tangential leading edge blowing has been applied to full-span and semi-span wind tunnel models. Results indicate that the concept is capable of controlling the vortical flow over the wing to very high angles of attack. Not only can burst vortices be unburst but asymmetric flows can be induced or controlled. Substantial rolling moments may be produced at conditions where existing control systems cease to be effective.

The effects of asymmetric leading edge blowing have been shown to be uncoupled at pre-stall angles of attack such that the overall forces and moments for asymmetric blowing can be obtained by superposition of asymmetric cases. The time lags associated with vortex flow control at pre-stall conditions are short, less than one convective time.

For post-stall conditions, the response of the vortical flowfield is strongly coupled for asymmetric blowing. The coupling produces a roll moment reversal which may be removed by the presence of a fuselage. The time lags associated with vortex flow control, post-stall are longer, of the order of 5 convective times. This may still be short enough for control of wing rock or divergence at low speed and high angle of attack.

Acknowledgement

This work was supported at Stanford University under AFOSR Grant #49620-86-10-0020-BR.

References

1. Kuchemann, D.
"The Aerodynamic Design of Aircraft"
Pergamon Press, 1978.
2. Aviation Week and Space Technology, May 29, 1989, pp 44-47.
3. Aviation Week and Space Technology, Oct 31, 1988 pp 36-38
4. Ashley, H. and Clarke, L.
"On the Feasibility of Low Speed Fighter Manoeuvres Involving Extreme Angles of Attack"
Stanford University Report SUDAAR 563, July 1987.
5. Shi, Z., Wu, J.M. and Vakil, A.D.
"An Investigation of Leading Edge Vortices on Delta Wings with Jet Blowing"
AIAA paper 87-0330, Jan 1987.
6. Visser, K.D., Iwanski, K.P., Nelson, R.C. and Ng, T.T.
"Control of Leading Edge Vortex Breakdown by Blowing"
AIAA paper 88-0504, Jan 1988.
7. Trebbie, W.J.G.
"Exploratory Investigation of the Effects of Blowing from the Leading Edge of a Delta Wing"
ARC R&M 3518, April 1966.
8. Tavelle, D.A.
"The Lift of Sharp Leading Edged Delta Wings with Blowing"
Stanford University Report JIAA TR-88, Dec 1985.
9. Yeh, D.T., Tavelle, D.A., Roberts, L. and Fujii, K.
"Navier-Stokes Computation of the Flow Field over Delta Wings with Spanwise Leading Edge Blowing"
AIAA paper 88-2558, 1988.
10. Brown, G.E. and Michael, W.H.
"On Slender Delta Wings with Leading Edge Separation"
Journal of the Aerospace Sciences, Vol 21, pp 134-135, 1956.
11. Smith, J.H.B.
"A Theory of the Separated Flow from the Leading Edge of a Slender Wing"
ARC R&M 3116, 1959.

12. Schlichting, H.
"Boundary Layer Theory"
McGraw Hill Book Co, 7th Edition, pp 750-752.
13. Wood, N.J. and Nielsen, J.N.
"Circulation Control Airfoils as Applied to Rotary-Wing Aircraft"
Journal of Aircraft, Vol 23, No 12, Dec 1986.
14. Englar, R.J.
"Further Development of Pneumatic Thrust-Deflecting Powered-Lift Systems"
Journal of Aircraft, Vol 25 No 4 pp 324-333 April 1988.
15. Wood, N.J., Ward, S. and Roberts, L.
"Wind Tunnel Wall Boundary Layer Control by Coanda Wall Jets"
AIAA paper 89-0149, Jan 1989.
16. Wood, N.J., Roberts, L. and Celik, Z.
"The Control of Asymmetric Flows over Delta Wings at High Angles of Attack"
AIAA paper 89-3347, Aug 1989.
17. Wood, N.J. and Roberts, L.
"The Control of Delta Wing Aerodynamics at High Angles of Attack"
Paper presented at 'Prediction and Exploitation of Separated Flows', Royal Aero. Society, April 1989.
18. Wood, N.J. and Roberts, L.
"Control of Vortical Lift on Delta Wings by Tangential Leading Edge Blowing"
Journal of Aircraft, Vol 25 No 3 pp 236-243, March 1988.
19. Wood, N.J., Roberts, L. and Lee, K.T.
"The Control of Vortical Flow on a Delta Wing at High Angles of Attack"
AIAA paper 87-2278, Aug 1987.
20. Ward, D.T. and Stout, L.J.
"Use of Differential Leading Edge Flaps for Lateral Control at High Angle of Attack"
AIAA paper 86-0168, Jan 1986.
21. Lee, K.T.
"Dynamic Control of Delta Wing Flows by Tangential Leading Edge Blowing"
PhD Thesis, Stanford University, 1989.
22. Ericsson, L.E.
"The Fluid Mechanics of Slender Wing Rock"
Journal of Aircraft, Vol 21 No 3 pp 322-328, May 1984.
23. Levin, D. and Katz, J.
"Dynamic Load Measurement with Delta Wings Undergoing Self-Induced Roll Oscillations"
Journal of Aircraft, Vol 21 No 1 pp 30-36, Jan 1984.
24. Jean Ross, A. and Nguyen, L.T.
"Some Observations Regarding Wing Rock Oscillations at High Angles of Attack"
AIAA paper 88-4371, Aug 1988.
25. Jun, Y.W. and Nelson, R.C.
"Leading Edge Vortex Dynamics on a Delta Wing Undergoing a Wing Rock Motion"
AIAA paper 87-0332, Jan 1987.
26. Mittelman, Z.
"Prediction of Unsteady Aerodynamics and Control of Delta Wings with Tangential Leading Edge Blowing"
PhD Thesis, Stanford University 1989.
27. Reynolds, G. and Abtahi, A.A.
"Instabilities in Leading Edge Vortex Development"
AIAA paper 87-2474, Aug 1987.

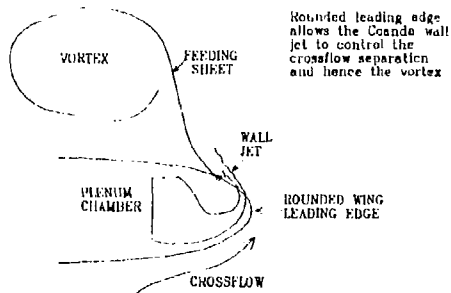


Figure 1: The Concept of Tangential Leading Edge Blowing.

Leading Edge Sweep 60 degs
Max Thickness 15.6 mm
Wing Span 200 mm
Wing Chord 250 mm

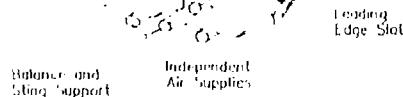


Figure 2: Full Span Wind Tunnel Model.

Leading Edge Sweep 55 degs
Max Thickness 18.75 mm
Wing Semi-span 187.5 mm
Wing Chord 300 mm

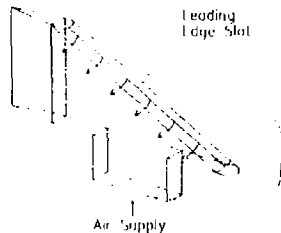


Figure 3: Semi-span Wind Tunnel Model.

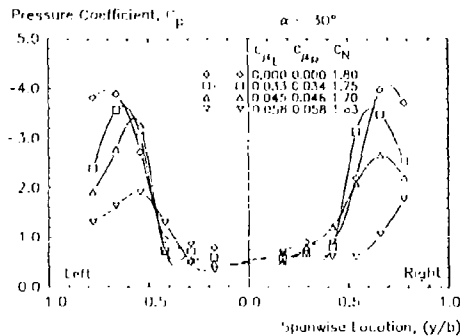


Figure 4: Pressure Distributions for Pre-stall Conditions with Symmetric Blowing.

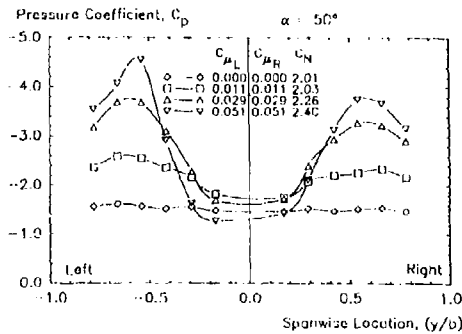


Figure 5: Pressure Distributions for Post-stall Conditions with Symmetric Blowing.

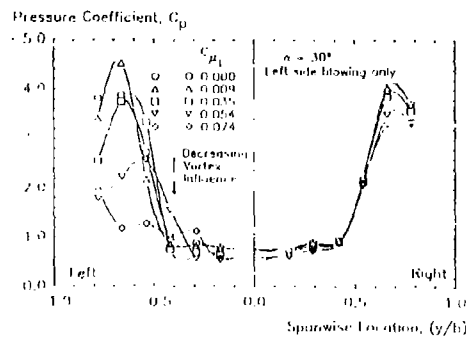


Figure 6: Pressure Distributions for Pre-stall Conditions with Asymmetric Blowing.

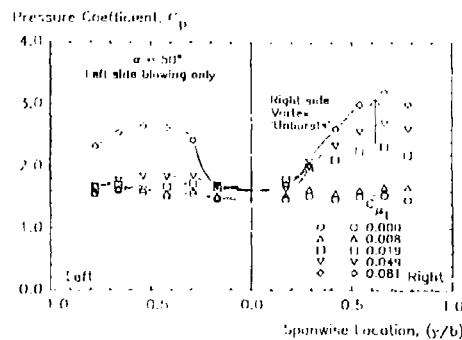


Figure 7: Pressure Distributions for Post-stall Conditions with Asymmetric Blowing.

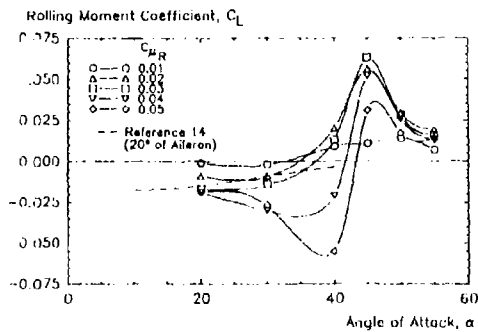


Figure 8: Rolling Moment Generated with Constant Asymmetric Blowing.

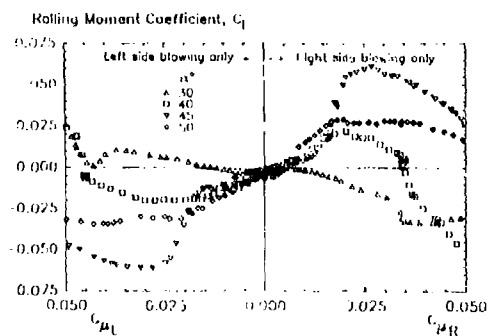


Figure 9: Rolling Moment Generated at Constant Angle of Attack.

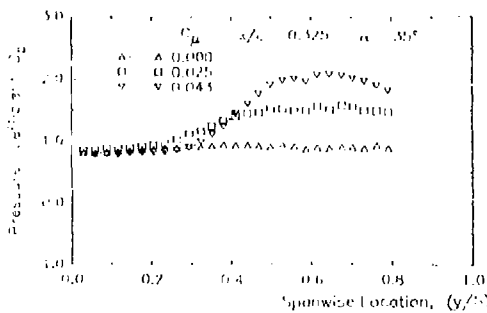


Figure 10: Pressure Distributions for the Semi-span Model, Post-stall.

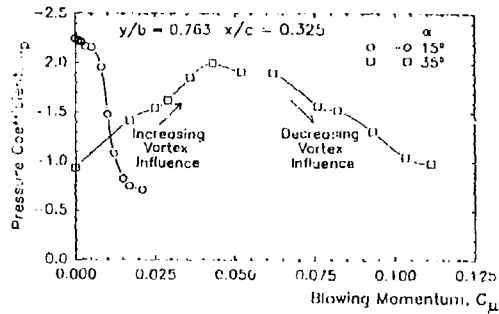


Figure 11: Characteristic Surface Pressure Response at a Fixed Location.

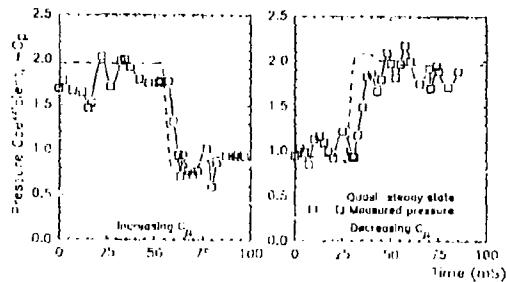


Figure 12: Unsteady Surface Pressure Response at Pre-stall Angle of Attack.

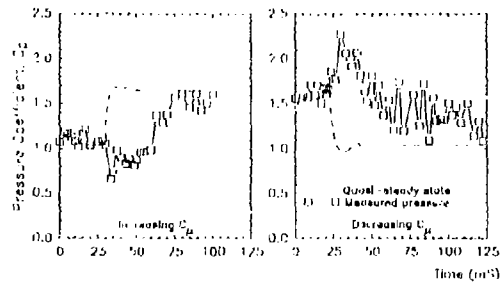


Figure 13: Unsteady Surface Pressure Response at Post-stall Angle of Attack.

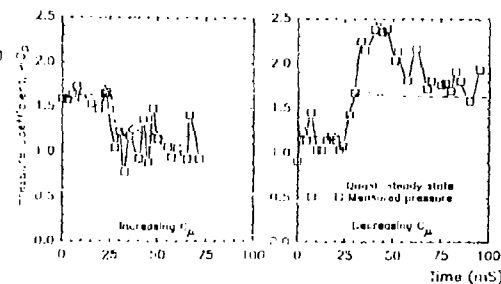


Figure 14: Unsteady Surface Pressure Response at Post-stall Angle of Attack with Pre-stall Initial Conditions.

A LOOK AT TOMORROW TODAY

Dr Lawrence A. Welch
 AF Wright Research and Development Center
 WRDC/PIHT, Wright-Patterson AFB OH 45433-6553
 USA

ABSTRACT

A broad overview of the X-29 forward swept wing technology demonstrator traces its development and test path during the past five years. Brief descriptions of the aircraft and its flight control system provide insight for evaluating this unique vehicle. Results are presented in several key technical areas and some general comparisons are made with current front-line fighters. The baseline flight control system provided a starting point for safe concept evaluation and envelope expansion for the aircraft. Subsequent up-dates resulted in performance levels favorably comparable to current fighter aircraft. Plans are cited for expanding the X-29's capabilities into the high angle-of-attack regime of flight. Aircraft and flight control system modifications are described which will permit the X-29 to fully exploit its technologies.

INTRODUCTION

Agility, maneuverability, integration-key words used to describe the successful development of the X-29 forward swept wing technology demonstrator.

The X-29 integrates several different technologies into one airframe as depicted in Figure 1. The aerodynamically tailored composite wing covers cause the forward swept wing to twist as it deflects, eliminating divergence. The thin supercritical airfoil, coupled with the discrete variable camber produced by the double-hinged full span flap, provides optimum wing performance at all flight conditions. The aircraft inherits its thirty-five percent static instability from the close-coupled, variable incidence canard. Without it the wing-body combination is near-neutrally stable. The canard, which has an area about twenty percent of the wing area, produces lift and its downwash delays flow separation at the wing root. The three-surface pitch control--the canard, flap, and strake flap-- is used by the digital fly-by-wire flight control system to control an otherwise unflyable unstable vehicle. The success of the X-29 really rests with the integration of these technologies into a single synergistic configuration.

Two X-29 aircraft were designed and built. The first entered flight testing in December 1984 and concluded in December 1988, completing 242 flights and over 200 flight hours. The primary objective of Ship 1 testing was to validate, evaluate and quantify the benefits of the technologies on board, both individually and synergistically.

The first two years of Ship 1 testing were primarily dedicated to altitude and Mach number in envelope expansion. Performance testing followed the envelope expansion and was completed in December 1987. Finally, Ship 1 testing provided evaluations of handling qualities, military utility and agility metrics below 20 degrees angle-of-attack (AOA). This paper presents data and results of Ship 1 testing in the areas of performance and handling qualities.

Ship 2 began flying in May 1989. It has been modified to allow high AOA testing. Its spin chute will allow the pilot to regain control in the event of a stall and spin. New instrumentation will help with this task. The flight control system software has been significantly modified to permit extension of flight in the longitudinal plane to a maximum trimmable AOA projected to be 70 degrees. To date, the aircraft has achieved 20 degrees while maneuvering in all axes during functional check flights. Following the upcoming envelope expansion, the aircraft will demonstrate the military utility and agility of a forward swept wing vehicle trimmed at 40 degrees angle-of-attack.

AIRCRAFT DESCRIPTION

The two X-29s were designed and built by the Grumman Aerospace Corporation, Bethpage, New York. They are essentially identical. To reduce overall program costs, the Air Force supplied several major components of the aircraft to Grumman. These included the F-5A forebody and nosegear; F-16 main gear, actuators, airframe-mounted accessory drive and emergency power unit; F-18 F404 engine; SR-71 BDP5301 flight control computers, and F-14 accelerometers and rate gyros. Use of these time-proven components also increased the reliability of the flight vehicle.

The X-29 flight control system (FCS) is a triplex digital fly-by-wire system with triplex analog back-up. Its schematic is shown in Figure 2. The fail-op/fail-safe system used MIL-F-8785C and MIL-F-9490D specifications as design guides. Flying quality design goals were Level 1 for the primary digital mode and Level II for the analog back-up mode.

The FCS contains both digital and analog modes. Normal aircraft operation is accomplished through the normal digital (ND) mode with its associated functional options such as automatic camber control (ACC), manual camber control (MCC), speed stability, precision approach control (PAC) and direct electrical link (DEL). ND also contains options in its gain tables for power approach (PA), up-and-away (UA), and degraded operation.

The normal digital mode has a pitch rate control law with gravity vector compensation, driving a discrete ACC system. This mode is gain-scheduled as a function of Mach number and altitude and incorporates a sophisticated redundancy management system allowing fail-op/fail-safe flight. MCC is a pilot-selected, fixed flap, flap, ND. The PAC function is a pilot-selected auto throttle system. The DEL function is a ground contact control law set. It is active when any landing gear

weight-on-wheel relay is open. This function fades out the longitudinal forward loop integrator, allowing direct pilot control of the canards during taxi, take-off, or landing roll-out.

Gain tables for degraded operation are activated by a failure of the Attitude Heading Reference System or any two of the three angle-of-attack sensors. This function cannot be pilot selected, nor can it be exited in flight. Degraded normal digital operation is the last option available during sensor failures prior to automatic down-moding to analog reversion.

The analog reversion (AR) mode is the back-up flight control system, designed to bring the aircraft safely back to base. The AR mode provides a highly reliable, dissimilar control mode to protect against generic digital control failures. It incorporates UA and PA functions similar to those of the ND mode. It contains no longitudinal trim capability or pitch loop gain compensation with dynamic pressure while the aircraft is on the ground. In all other aspects, it performs like the ND control system.

The initial X-29 Ship 1 flying was limited to 0.60 Mach number and 30,000 ft pressure altitude. As the flight envelope was expanded, the FCS evolved. Several gain and redundancy management modifications were made as a result of flight test data. The PAC and MCC modes were added to enhance the research capability of the aircraft. Addition of the Remote Augmented Vehicle (RAV) system, developed by NASA, provided the capability to pulse individual control surfaces so as to extract their effectiveness. As Ship 1 entered the military utility and agility phase of its flight test program additional changes were made. In order to enhance agility and improve handling qualities, control stick hysteresis was improved by reducing its longitudinal throw by about fifty percent. A further modification to the gains for both longitudinal and lateral axes was made to remove the earlier sluggishness in both pitch and roll response of the aircraft.

Late in 1987, Ship 2 was removed from storage and modifications begun for a high AOA program. A spin chute system was added to the aircraft to assist in recovery of the aircraft from an inadvertent departure. The system was designed for pyrotechnic deployment and mechanical jettison. A pyrotechnic emergency jettison is also available.

Cockpit instrumentation was changed to accentuate the importance of the angle-of-attack and yaw indicators. They are now large six inch meters centered on the console. Spin Chute system status lights and test switches were added as well as instructional lights to assist the pilot in applying spin-recovery control inputs.

The Ship 2 flight control laws have been modified to permit all-axis maneuvering to 40 degrees angle-of-attack, and pitch-only maneuvering to as high as 70 degrees AOA. Below 10 degrees, the control laws are identical to those last flown on Ship 1 in December 1988. Between 10 and 20 degrees, the high AOA modifications are faded in until above 20 degrees they are fully functional.

An angle-of-attack feedback loop has been added to complement speed stability. The longitudinal integrator has been removed above 40 degrees AOA. Three-break-point lateral-directional gain tables have been constructed to optimize maneuvering performance. The lateral integrator is removed above 10 degrees AOA. Logic has been added for spin prevention and recovery. Numerous other lesser changes have been incorporated into the high AOA control laws.

FLIGHT TEST RESULTS

Wing Performance

The interactive effects of the close-coupled wing and canard and the characteristics of the advanced thin supercritical airfoil were assessed through analysis of pressure measurements on these surfaces. Rows of pressure orifices are located on the left hand canard and wing at stations compatible with earlier wind tunnel model locations. Because of the flexible nature of the X-29, interpretation of the pressure data required knowledge of the local geometric angle-of-incidence of the wing section at each of the chords along which pressure data were taken.

A Flight Deflection Measurement System (FDMS) was installed on the right side of the aircraft. It consists of twelve infrared light-emitting diode targets, a target driver, two receivers, and a control unit which interfaces with the aircraft telemetry system. The purpose of the FDMS is to provide the deflection (twist) data needed for determining the true geometric angle-of-incidence.

Plots of selected pressure data are shown in Figures 3 and 4 for two values of lift coefficient. Data from each row of orifices along the five wing chord locations are compared to predictions which are based on wind tunnel results. Also shown is a set of data for about quarter span on the canard. The pressure data from the upper surface of the canard clearly shows the strong suction effect associated with a lifting surface in clear air. Likewise, the two inboard rows of wing pressure taps show the influence of the downwash from the canard. Although a row of wing pressure taps is located just inboard of the canard tip location, the canard flowfield propagates toward the fuselage as it encounters the forward swept leading edge of the wing. Thus, canard influence is confined to the two inboard rows of wing pressure data. Comparison of the pressure data with wind tunnel predictions shows relatively good agreement. It is apparent that a stronger shock wave exists in the flight data than in wind tunnel data.

Figure 5 shows predicted versus measured shock location at transonic conditions and at an intermediate value of lift coefficient. The agreement with wind tunnel predictions is excellent. The effect of the high trailing edge sweep of the wing has resulted in a more oblique (and weakened) shock wave, contributing lower wave drag than a similar aft swept wing. The thin supercritical airfoil has allowed the shock to move aft, producing a larger lift-producing region.

Aircraft Performance

The lift and drag characteristics of the X-29 were determined by performing push-over, pull-up (POPU) and wind-up turn (WUT) maneuvers at constant power settings. POPU maneuvers were used to obtain data for load factors under 2g's and the WUT maneuvers for 2g's and above. Data was obtained for angles-of-attack up to 20 degrees and for symmetric load factors up to 6.4 g's as corrected to 15,000 pounds gross aircraft weight. Both the automatic camber control (ACC) and manual camber control (MCC) options of the normal digital mode of the flight control system were investigated.

Drag polars were acquired for 0.4 to 1.3 Mach Numbers. The polars were compared to wind tunnel predictions which also used the ACC control surface schedules. In general, subsonic and transonic flight test results showed lower drag coefficients than predicted. Supersonically the test data either matched predictions closely or showed higher drag coefficients. The highest lift coefficient reached was 1.61 at 0.4 Mach number. This was a result of the conservative angle-of-attack and load factor limitations imposed on the aircraft, not from lack of engine thrust or control power.

Shown in Figure 6 is the comparison between a wind-tunnel-predicted drag polar and the actual flight-derived polar at 0.9 Mach and 30,000 feet pressure altitude. The wind tunnel data clearly over-predicted drag. Note the break in the curve which corresponds to an angle-of-attack of about seven degrees. It happened that the scheduled canard position reversed direction and the flaperon position schedule reached a limit simultaneously. This would suggest that at angles-of-attack below seven degrees, the ACC schedule was not correctly optimized for lift and drag.

The manual camber control (MCC) mode of the flight control system was also utilized during performance testing. The MCC uses fixed flaperon settings to achieve discrete values of wing camber. Figure 7 shows schematically how the ACC scheduling is derived from MCC results. Wind-tunnel-derived drag polars are plotted for specific flaperon settings. The dashed line, faired tangentially across the polars, then defines an optimum variable camber polar. The appropriate flaperon positions are then scheduled with angle-of-attack to achieve this polar (Reference 1).

Figure 8 shows both MCC and ACC data at 0.90 Mach number and 30,000 feet. As is evident, the ACC scheduling did an excellent job of optimizing the discrete camber polars.

The final aircraft performance data to be discussed here is directed toward answering the question: "Has the X-29 truly demonstrated technologies which are applicable to future high performance fighters?" If these technologies have been proven to provide tangible benefits in a fighter-class arena, then the answer is yes. Figures 9 through 12 provide performance comparisons between the X-29 and a current high performance fighter. An attempt has been made to normalize the data or optimize either aircraft. It is simply an aircraft-to-aircraft snapshot.

The induced drag polars presented in Figures 9-11 show a consistent trend. The polar shape of the X-29 has been greatly improved. Although the X-29 was specifically optimized for a 0.95 lift coefficient at 0.9 Mach number and 30,000 feet, the improvement exists through its entire performance map.

The X-29 maneuver design point chosen for the comparisons of lift to total drag and to induced drag only in Figure 12 obviously favors the X-29. But the point is quite representative of a nonmaneuvering condition of the "existing" aircraft. The X-29 data was acquired during automatic camber control operation. Using the ACC schedule should result in the optimum drag polar achievable. It might appear surprising, then, that Figure 12 shows a substantial decrement in maximum lift-to-drag ratio for the X-29. This is explicable by recalling that the X-29 was put together from many pieces and parts. This resulted in a rather large profile drag for the aircraft. However, at 0.95 lift coefficient, 0.9 Mach number and 30,000 feet altitude, the X-29 excels in spite of its high profile drag. In the fighter-class arena, performance of the X-29 is impressive.

Handling Qualities

Continuing the theme of the previous section, fighter-class performance testing must include handling qualities as a set of measurements. The original design goal for the X-29 control laws was to have this highly unstable aircraft exhibit Level 1 handling qualities. For about the first three and one half years of flying (186 flights), the X-29 exhibited level 11 handling qualities. These less-than-desirable ratings were a result of several programmatic decisions to trade design iterations and system performance for safety margin and cost/schedule savings. On early flights the control stick harmony was judged poor for a fighter aircraft, but adequate for a technology demonstrator. The flight control system values in pitch and roll were purposely reduced to achieve added margin of safety while validating the wing structure. Again, the resulting performance was acceptable for a demonstrator but did not represent current fighter capabilities.

The original control stick had a 10 inch travel in pitch and a 3.2 inch travel laterally. This uncomfortable situation made lateral tracking difficult during high g maneuvers and created slow pitch response. A hardware and software change was made after flight 186 which cut the pitch throw on the stick in half while maintaining the same force gradient. The pitch neutral point was also moved forward about one inch.

Following flight 213 another flight control system change was made. Pitch and roll gains were increased to permit better dynamic performance from the aircraft. However, the flight g limit of 6.4 has not been lifted since no structural proof test has ever been conducted (thereby limiting flight to 80 per cent design limit load). The results of these gain changes were a 41 per cent improvement in available maximum pitch acceleration and a 40 per cent increase in the maximum roll rate to 220 degrees per second. Figures 13 and 14 show the results over the 0.4 to 0.9 Mach number range. Note that no supersonic gain changes were made (Reference 2).

The handling quality pilot evaluation tasks are depicted in Figure 15. These tasks were performed only in the normal digital, ACC flight control system mode with the up-and-away gain set. They were flown within a flight envelope of 10,000 to 25,000 feet pressure altitude and 200 to 450 knots corrected air speed, to a maximum 0.9 Mach number. In all cases, the chase aircraft began either specified or random maneuvers and the X-29 pilot reacted to them.

The Cooper-Harper ratings for these tasks are presented in Figure 16. The height of the bars indicates the range of ratings received for each task. The horizontal lines show the average ratings for all of the pilots performing the task prior to flight 187. The ellipses show the average for data from flights 187 through 213, and the stars show the results for the final software flown in the military utility and agility flights after flight 213. The data shows an overall improvement in handling qualities from Level II to Level I.

The finger tip formation task was flown by virtually all of the pilots who flew the X-29 prior to flight 187, a total of thirteen. All pilots felt that the stick harmony between the longitudinal and lateral axes was poor. This resulted in an apparent sluggishness in pitch and an overcontrol tendency in roll/lateral direction. In general, they rated the task as medium-to-high workload. Following the control stick modification, four pilots repeated the task and three new pilots flew it for the first time. Comments referred now to good stick harmony, but perhaps too much sensitivity (gain) in roll. Cooper-Harper ratings for this task improved from Level II to Level I. The final 29 flights of Ship 1 had the increased pitch and roll response gains in the flight control system. Cooper-Harper ratings and pilot comments remained about the same. Roll response was better, although still too sensitive at elevated load factor.

The close trail formation task was performed by eleven pilots using the original control stick configuration. Again, the stick harmony was found to be a little annoying. One pilot noted that "as roll rates go up, the pilot starts chopping thru bank angle inputs to watch lead." Under elevated g maneuvering, another pilot commented that he could not fly the slot position with the X-29. Several of the pilots found a small overcontrol tendency in pitch. The Cooper-Harper ratings reflected borderline Level I handling qualities. The control stick modification was made and two pilots repeated the task. One other pilot flew it for the first time. All agreed no overcontrol tendency existed and aggressive pitch inputs could now be made. Good solid Level I ratings were given. Following the pitch/roll response flight control modifications, four pilots reflew the task. Ratings didn't appreciably change. Several comments indicated that roll sensitivity at elevated g could be decreased.

Two separate versions of the simulated terrain-following task were performed. All flights performed with the original control stick configuration used a smooth push-over/pull-up maneuver for this task. Ten pilots participated and all had problems with the task. Many suffered small pilot-induced oscillations in pitch. "Two to three high frequency overshoots in pitch" was the most-used expression. It was generally a high workload task because of the aircraft response lagging longitudinal stick inputs. A solid Level II rating was assigned to this task. The same task was repeated by three of the pilots (and two new ones) following the stick modification. The overshoots still occurred but the pilots were now able to anticipate and recover more quickly. Ratings improved, but were still Level II. The biggest improvement occurred as a result of the pitch and roll gain changes. At the same time, the task was refined to employ step inputs instead of smooth ones. Indeed, the task change was significant. The veteran X-29 pilots found little difference between the two, while the three new pilots found the step input task easier to perform. All pilots rated the step version of the simulated terrain following task Level I. The POPB maneuver was also rated Level I by the veterans, but Level II by the new pilots.

The final task being reported here is the air-to-air tracking task. As with the finger tip formation task, all of the early pilots flew the air-to-air tracking. Three different set-ups were used: first, 4g target; 90 degree heading crossing angle, 4g target; and 180 degree heading crossing angle, 4g target. Cooper-Harper ratings appeared independent of target set-up, although with so many variables it was difficult to interpret the results. Figure 16 shows that the average scores ranked as Level II handling qualities. The lack of control stick harmony did not seem to strongly influence the pilot comments. Once the stick harmony was improved, three X-29 veterans and two new pilots flew the task. All three veterans found gross acquisition acceptable and fine tracking excellent. The two guest pilots rated the task as Level II. Following the pitch and roll response improvements to the flight control system, the same three veteran X-29 pilots reflew the task and found more improvement. "Good control harmony." "Nice roll response." "Pitch fine tracking was excellent." "Fine tracks as well as my aircraft I have flown!" And finally, from a guest pilot, "Fine tracks as good as (current fighters)."

HIGH ANGLE-OF-ATTACK TESTING

The X-29 configuration is novel in that it was designed from inception by Grumman to fly to high angles-of-attack. This design requirement, in concert with high levels of longitudinal instability at low angles-of-attack and subsonic speeds, defined the need for horizontal foreplane strakes at the rear of the aircraft. These strakes move the center of pressure of the aircraft behind the center of gravity at very large angles-of-attack, thereby ensuring a nose-down pitching moment to eliminate the possibility of a hung stall condition. Wind tunnel tests of the X-29 have demonstrated its ability to trim at angle-of-attack through 70 degrees. In addition, lateral control is available to 90 degrees AOA. With this combination of low AOA instability and longitudinal and lateral control power to very high AOA, the X-29 is a uniquely useful vehicle for investigating the application of high AOA maneuverability in future tactical aircraft.

The X-29 Ship 2 high angle-of-attack flight test program has progressed through its five functional test flights (this past June) and into the envelope expansion phase. About fifty flights will completely open the envelope to the flight operating limits on the aircraft. Once the performance envelope is cleared, about twenty flights will explore the military utility and agility capabilities of the X-29. We should complete this work by October, 1990 and report on the results soon thereafter.

CONCLUDING REMARKS

In summary, X-29 Ship 1 testing has clearly demonstrated the viability of flying a highly unstable forward swept wing aircraft using a three surface digital flight control system. The aeroelastically tailored thin, composite, supercritical wing performed flawlessly, allowing the aircraft to achieve or exceed its transonic performance goals. Ship 1 testing produced the following partial list of accomplishments:

- o Performance
 - o Defined drag polars over the X-29 flight envelope
 - o Proved significant drag reduction with automatic versus manual camber control
 - o Proved superior induced drag coefficient over front-line fighter
 - o Exceeded design predictions
- o Loads Expansion
 - o Expanded envelope symmetrically and asymmetrically to obtain envelope for military utility flights
- o Military Utility
 - o Demonstrated Level 1 flying qualities in operations-oriented tasks
 - o Investigated fighter agility metrics and flight test techniques

The X-29 Ship 2 high AOA testing currently underway will revisit these areas above 20 degrees angle-of-attack.

REFERENCES

1. Moore, R., and Frel, D., "X-29 Forward Swept Wing Aerodynamic Overview," AIAA Paper 83-1834, July 1984.
2. Hoover, Al, Major, USAF, "Agility Flight Testing, A Progress Report," 32nd Annual Symposium of the Society of Engineering Test Pilots, September 1988.

HIGH STATIC
INSTABILITYDIGITAL
FLY BY WIREFORWARD
SWEEP WINGAEROELASTICALLY TAILORING
COMPOSITE WINGTHIN
SUPERCRITICAL
AIRFOILFULL AUTHORITY
CLUST COUPLED CANARDSDISCRETE VARIABLE
CAMBERTHIN SURFACE
PITCH CONTROL

FIGURE 1. X-29 ADVANCED TECHNOLOGIES

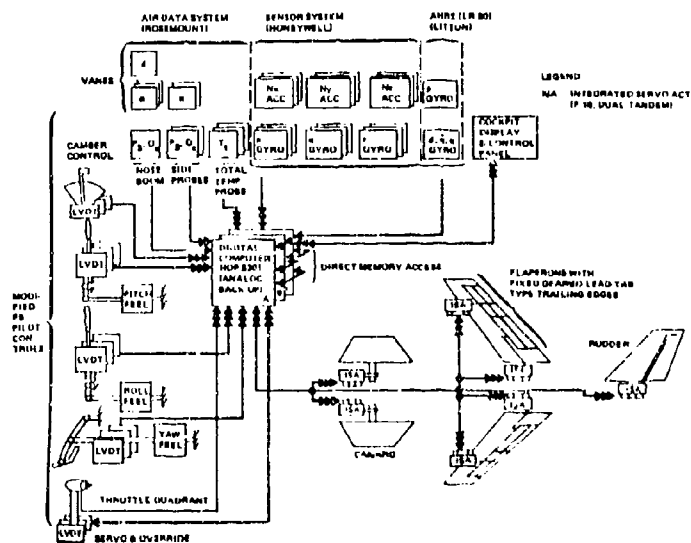


FIGURE 2. X-29 DIGITAL CONTROL SYSTEM ARCHITECTURE

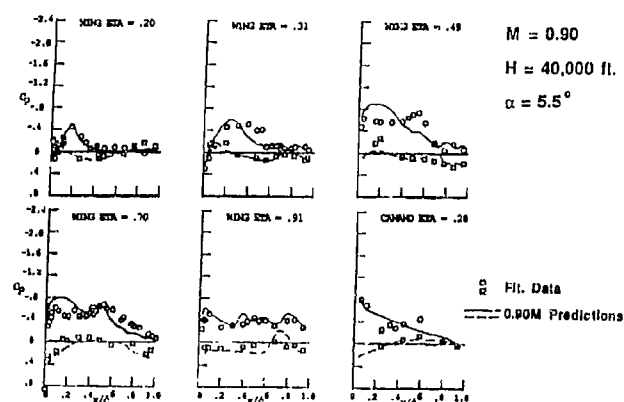


FIGURE 3. X-29 AERO-PERFORMANCE
 PRESSURE DISTRIBUTIONS - $C_L = 0.45$

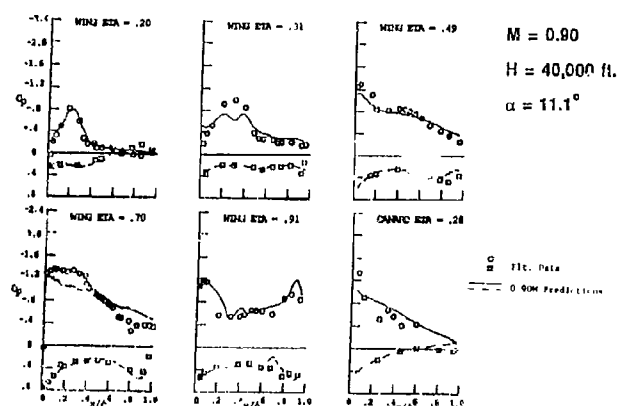


FIGURE 4. X-29 AERO-PERFORMANCE
 PRESSURE DISTRIBUTION - $C_L = 1.10$

$M = 0.90$, $H = 40,000 \text{ ft.}$, $\alpha = 5.5^\circ$

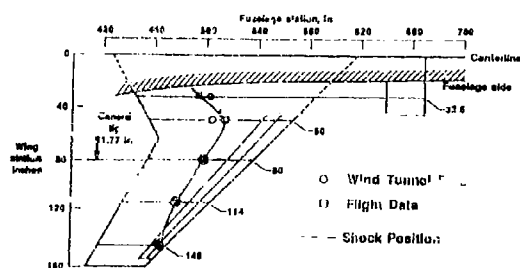


FIGURE 5. X-29 AERO-PERFORMANCE
 SHOCK LOCATION

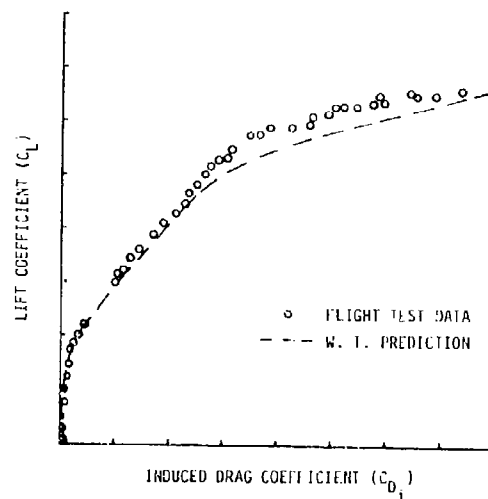


FIGURE 6. X-29 DRAG POLAR
PREDICTED VS. FLIGHT RESULTS

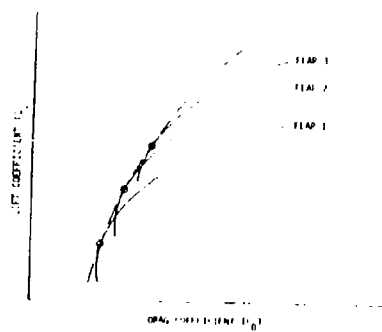


FIGURE 7. X-29 ALL SCHEDULE DERIVATION

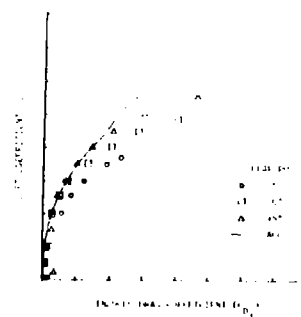


FIGURE 8. OPTIMIZED X-29 DRAG POLAR
FLIGHT RESULTS

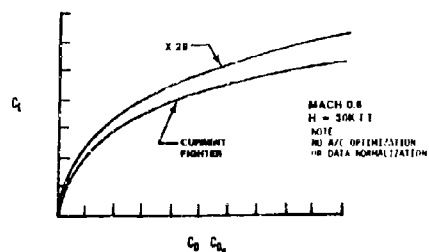


FIGURE 9. INDUCED DRAG POLARS - 0.6 M FLIGHT RESULTS

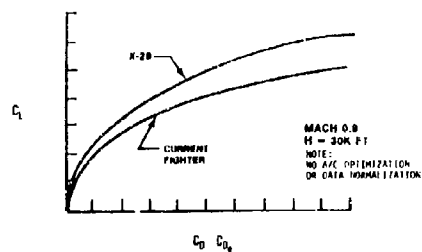


FIGURE 10. INDUCED DRAG POLARS - 0.9 M FLIGHT RESULTS

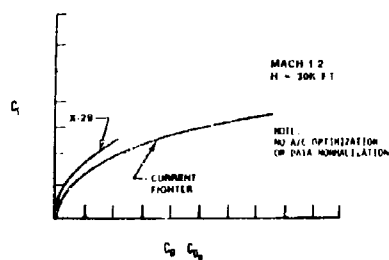


FIGURE 11. INDUCED DRAG POLARS - 1.2 M FLIGHT RESULTS

L/D INCREMENT X-29/CURRENT FIGHTER

	At $C_L = 0.95^*$		At $(L/D)_{max}$
	INDUCED DRAG	TOTAL DRAG	
MACH 0.6	-25%	-40%	13%
MACH 0.9	-30%	-55%	18%
MACH 1.2			9%

* X-29 MANEUVER DESIGN C_L FIGURE 12. LIFT/DRAG RATIO COMPARISONS
FLIGHT RESULTS

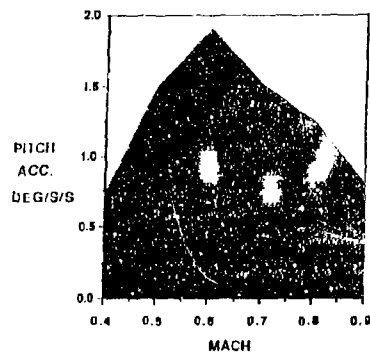


FIGURE 13. PITCH ACCELERATION - FLIGHT RESULTS

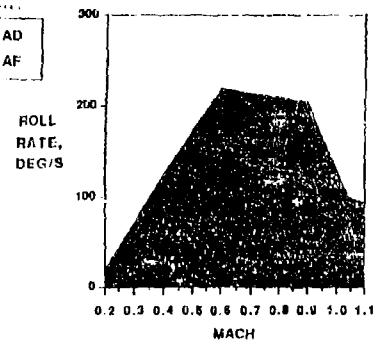


FIGURE 14. ROLL RATE - FLIGHT RESULTS

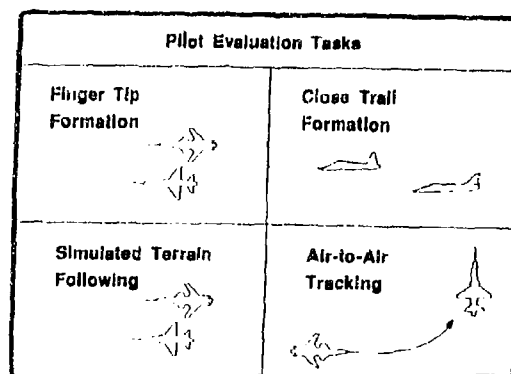


FIGURE 15. HANDLING QUALITY TASKS

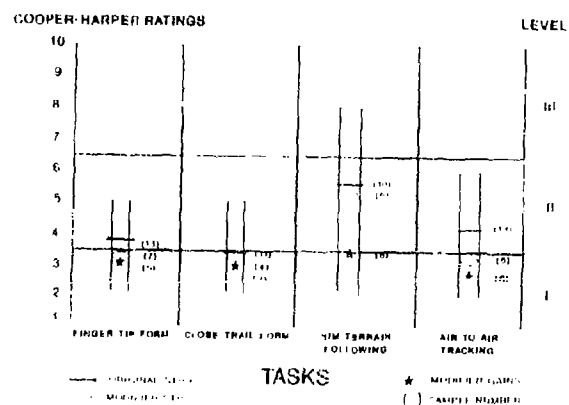


FIGURE 16. HANDLING QUALITY EVALUATIONS

UNSTEADY AERODYNAMICS OF CONTROLS

by

G.J. Hancock
Queen Mary College
University of London

and

D.G. Mabey
Royal Aerospace Establishment
Clapham, Bedford, MK41 6AE
United Kingdom

SUMMARY

The paper is divided into three parts.

The physics of quasi-steady aerodynamics are discussed. The concept of an aerodynamic rise time is defined, which indicates how quickly steady states are realized. Long rise times occur at low transonic speeds, but short rise times occur at high transonic speeds.

Predictions of control surface characteristics compare poorly with experimental results. Experimental errors are possibly due to small gaps and wind tunnel wall interference while in the theoretical methods boundary layer approximations may be suspect.

The interface of unsteady aerodynamics with control system design and validation is described. It is pointed out that the unsteady aerodynamic input is limited to approximate and tailored forms of linearized aerodynamics. It is not clear how more accurate, non-linear transonic aerodynamics can be incorporated in control design procedures.

INTRODUCTION

The topic of control surface characteristics in both steady and unsteady conditions is an extremely wide one with an extensive literature and folk lore. It is therefore necessary to be selective here, concentrating on some current problem areas, biased toward the interests of the authors, and suggesting future directions of research.

Three areas will be discussed:

- (i) physics of quasi-steady aerodynamics,
- (ii) comparison of prediction with experiment,
- (iii) interface of unsteady aerodynamics with control system design and validation.

Only attached flows are considered in this paper because of limitations of time and space.

Unsteady separated flows deserve another presentation which the authors are prepared to give on another occasion.

This presentation builds upon the contributions of both authors to the AGARD Special Course in 1983 on Aerodynamic Characteristics of Controls^(1,2) but includes some contemporary developments.

II PHYSICS OF QUASI-STEADY AERODYNAMICS

II.1 INTRODUCTION

First it is useful to clarify what is conventionally understood by unsteady aerodynamics. Unsteady aerodynamics are associated with two types of unsteady motion:

- (i) when a body, either a component such as a wing or a complete aircraft, is in unsteady motion, for example structural vibrations of a wing, or an aircraft in a transient manoeuvre;
- (ii) when a body is in steady motion but unsteady separations lead to buffeting.

The much higher frequency unsteadiness associated with acoustic noise or turbulence is not usually considered part of unsteady aerodynamics apart from their influence on the low frequency boundary layer and wake development.

The definition of steady and unsteady motion needs care in interpretation. The aerodynamics associated with an aircraft in a steady pull-out manoeuvre at a constant velocity in a still atmosphere are steady relative to axes fixed in the aircraft but unsteady relative to axes fixed in space, see Fig.1. It must be remembered that the basic equations of aerodynamics, the Navier-Stokes equations, are formulated in terms of inertial axes fixed in space and that there is always an axis transformation involved in using any other axis system. Essentially an unsteady motion arises when the mathematical formulation of that motion cannot be resolved into time independent equations and boundary conditions. The distinction between steady and unsteady motions are not always clear cut, especially when viscous effects are included.

Qualitative descriptions of unsteady aerodynamics are normally given in terms of

- (i) impulsive motions, following a rapid change in wing, or control displacement, usually a step displacement,
- (ii) oscillatory motions when a wing, or control surface, is oscillating in simple harmonic motion.

A reference unit of aerodynamic time t is the time taken for the relative air stream (U m/s) to travel the distance of one mean chord length (\bar{c} m), so

$$t = \bar{c}/U \quad \text{seconds} \quad (1)$$

With typical numbers at a low Mach number,

$$c = 3 \text{ m}, \quad M_\infty = 0.3, \quad U = 100 \text{ m/s, then } t = 30 \text{ ms.} \quad (2)$$

For low aspect ratio wings, $AR \sim 1$, the span ($2s$) should be used instead of \bar{c} in equation (1).

Unsteady motions and their aerodynamic responses are expressed in terms of non-dimensional time \bar{t} , where

$$\bar{t} = t/\bar{t}_0 \quad (3)$$

A ramp change in control surface angle $\gamma(t)$ at a rate of $200^\circ/\text{s}$ is

$$\gamma(t) = 200^\circ t = 6^\circ \bar{t}, \quad (4)$$

so with the above numbers in equation (2) the control rotates at the rate of 6° in the time the free stream air travels one mean chord.

For an oscillatory input

$$\gamma(t) = \gamma_0 \sin \omega t = \gamma_0 \sin(\omega \bar{c}/U)t = \gamma_0 \sin \nu \bar{t} \quad (5)$$

where

$$\nu = \text{frequency parameter} = \omega \bar{c}/U = 2\pi \bar{t}/\text{period.} \quad (6)$$

A frequency parameter of 1.0, with the numbers of equation (2), gives

$$\nu = 1.0, \quad \text{frequency} = 5.3 \text{ Hz.} \quad (7)$$

An alternative measure of non-dimensional frequency is the reduced frequency $k (= \nu/2)$.

A question of relevance at this Conference is

'what are the values of ramp rates and frequency parameters when unsteady aerodynamic effects need to be taken into account?'

or alternatively

'below what values of ramp rates and frequency parameters can unsteady aerodynamic effects be neglected and quasi-steady assumed?'

An attempt is made in the first part of this lecture to answer these questions, and to clarify such phrases as 'fast acting controls' which may be fast in real time as far as an actuator is concerned but which could be slow in terms of aerodynamic time.

11.2 STEP RESPONSE AT LOW MACH NUMBERS

Consider first a symmetric two dimensional aerofoil with a trailing edge control surface in a low Mach number stream, (see Fig.2). Suppose at time t equal to zero the control surface is suddenly displaced through an angle γ . Such a sudden displacement is not physically possible, nevertheless it is a most useful concept; mathematically it is a fundamental concept.

The sequence of aerodynamic developments which follow as time \bar{t} increases are sketched in Fig.2.

- (i) for very small time \bar{t} a starting vortex builds up just beyond the trailing edge;
- (ii) at \bar{t} about 0.25 the starting vortex leaves the trailing edge and convects downstream with the free stream velocity U ;
- (iii) vorticity is continuously shed from the trailing edge and is convected downstream with the free stream velocity U , forming a vortex sheet connecting the starting vortex to the trailing edge;
- (iv) a time-varying circulation around the aerofoil, $\Gamma(\bar{t})$, is generated which tends to a steady state value $\Gamma_\infty (= \Gamma(\infty))$ as \bar{t} tends to infinity.

The problem is to determine the time varying circulation $\Gamma(\bar{t})$, and hence the time varying forces on the aerofoil and control surface.

Using standard vortex lattice theory $\Gamma(\bar{t})$ can be estimated approximately by concentrating the total circulation $\Gamma(\bar{t})$ into a line vortex located on the quarter chord line (i.e. $c/4$ aft of the aerofoil leading edge) and the satisfying the boundary condition on the three quarter line (i.e. $3c/4$ aft of the aerofoil leading edge). At small time $\bar{t} \sim 0.25$, assuming that the starting vortex is located about $c/4$ aft of the trailing edge, and remembering that the total circulation around aerofoil and wake remains zero, by reference to Fig.3(i) both aerofoil circulation and starting vortex contribute equally to the downwash on the $3c/4$ line. In the final steady state at large time, $\bar{t} \rightarrow \infty$, only the aerofoil circulation $\Gamma(\infty)$ affects the flow about the aerofoil. Since, for a step input, the downwash conditions remain constant independent of time, it follows from Fig.3 that

$$\Gamma(\bar{t} \sim 0.25) \sim \Gamma(\infty)/2. \quad (8)$$

Thus the initial lift at small time, $\bar{t} \sim 0.25$, increases rapidly to half the final steady state lift.

At large time, when \bar{t} is of the order of 50, since most of the shed vorticity is concentrated within a length of $0.0c$ behind the starting vortex, the centre of the shed vorticity will be a distance approximately $(U\bar{t} - 3c)$ aft of the trailing edge, bearing in mind that the starting vortex itself contains half the total shed vorticity. Thus by reference to Figs. 3,4 the downwash condition on the $3c/4$ line is

$$\frac{\Gamma(\bar{t})}{2\pi c/4} + \frac{\Gamma(\bar{t})}{2\pi(U\bar{t} - 3c)} = \text{downwash.} \quad (9)$$

which leads, for large \bar{t} , to the asymptotic behaviour

$$\Gamma(\bar{t}) \rightarrow \Gamma(\infty)(1 - 1/2\bar{t}). \quad (10)$$

A simple formula which satisfies both equations (8, 10) is

$$\Gamma(\bar{t}) = \Gamma(\infty)(1 - 1/2(\bar{t}+1)) \quad (11)$$

so

$$\Gamma(\bar{t})/\Gamma(\infty) = \begin{cases} 0.90 & \text{when } \bar{t} = 4, \\ 0.95 & \text{when } \bar{t} = 9, \\ 0.99 & \text{when } \bar{t} = 49. \end{cases}$$

An aerodynamic rise time is defined in this paper as the time to reach 99% of the final steady state value. So the rise time for the two dimensional control surface deflection is about 50 \bar{t} (i.e. 1.5 s at $M_\infty = 0.3$).

As shown in Fig. 4, because of the downwash induced at the aerofoil by the wake vorticity the resultant force vector is inclined aft giving a drag component. This drag component manifests itself as a lag in the build-up of the leading edge pressures, i.e. in the leading edge suction force.

The above approximate approach can be extended to finite wings using shed horse shoe vortices in the wake. A simple analysis gives the build up of circulation as

$$\Gamma(\bar{t}) = \Gamma(\infty) \left(1 - \frac{AR}{1.5\bar{t}^2 + 3AR} \right). \quad (12)$$

The numbers 1.5 and 3 in equation (12) depend on aspect ratio but not significantly.

For a finite aspect ratio wing the lift builds up as (l/\bar{t}^2) , much more rapidly than for the two dimensional case, which builds up as (l/\bar{t}) .

According to equation (12) the rise time for a wing of aspect ratio 3 is about 4 \bar{t} (~ 0.12 s) ten times faster than for the two dimensional aerofoil of 50 \bar{t} (~ 1.5 s). Dynamic effects at low Mach number are much less pronounced on wings of finite aspect ratio than on two dimensional aerofoils. These trends are shown in Fig. 5.

Two basic flow features contribute to the lag effect at low Mach numbers:

- (i) the formation and convection of wake vorticity;
- (ii) the (almost) instantaneous induction of downwash at the aerofoil by the complete wake vorticity at each instant of time as implied by equation (9); when $M_\infty \ll 1$ the speed of propagation of information by sound waves is substantially higher than the free stream velocity, so the transfer of information is (almost) instantaneous.

II.3 STEP RESPONSE OF A BOUNDARY LAYER

The previous section has been concerned essentially with inviscid response characteristics acknowledging that local viscous effects are responsible for the trailing edge separation. It is of some interest to assess the step response characteristics of boundary layers.

In incompressible flow when an infinite plate, initially at rest in a viscous fluid, is suddenly moved parallel to itself with a constant velocity U , a boundary layer diffuses outwards normal from the plate surface, forming the so called Stokes layer⁽³⁾, as shown in Fig. 6.

The basic equation of motion is

$$\frac{\partial u}{\partial t} = \nu' \frac{\partial^2 u}{\partial y^2}, \quad (13)$$

where ν' is the kinematic viscosity; with boundary conditions

$$u(y, 0) = 0, \quad t > 0; \quad u(y, t) = U, \quad y > 0; \quad u \rightarrow 0 \text{ as } y \rightarrow \infty \text{ for } t > 0.$$

The solution of equation (13) is

$$\frac{u(y, t)}{U} = \left(1 - \frac{2}{\sqrt{\pi}} \int_0^{y/2\sqrt{\nu' t}} e^{-\tau^2} d\tau \right). \quad (14)$$

The time taken for a boundary layer thickness δ to develop is

$$\frac{\delta}{2\sqrt{\nu' t}} \sim 1.82; \quad t \sim \frac{\delta^2}{13\nu'}. \quad (15)$$

The value 1.82 comes from Table 1 of the standard error function in equation (14), taking $u(t)$ equal to 0.99.

Consider an aerofoil of chord c , initially stationary in stationary air, which is then moved forward suddenly with constant velocity U . If δ_s is the steady boundary layer thickness at the trailing edge after a long time, the time for the boundary layer to build up to δ_s is, from equation (15),

$$t \sim \frac{\delta_s^2}{13\nu'} \sim \frac{\delta_s}{c} \frac{U\delta_s}{13\nu'} \hat{t} \quad (16)$$

where \hat{t} ($=c/U$) is the same unit of aerodynamic time as that used earlier.

With a turbulent boundary layer an eddy viscosity representation for ν' can be taken; for example the Cochet-Smith formula (4) is

$$\nu'_{\text{turbulent}} \sim \frac{U\delta^*}{60} \sim \frac{U\delta}{500} \quad (17)$$

Furthermore the ratio δ_s/c would be expected to be of the order

$$\delta_s/c \sim 0.02 \quad (18)$$

Hence from equations (16,17,18) the rise time for a boundary layer is of the order of

$$t \sim 1.0 \hat{t} \quad (19)$$

which is significantly smaller than the inviscid response times shown in Fig. 5, even for the wing of aspect ratio 3. It would be expected that this boundary layer rise time would be independent of aspect ratio.

On the basis of these response times the separation delay in a typical dynamic stall is due primarily to the lag in the build up of the leading edge pressures in the outer inviscid flow; the viscous boundary layer behaves in a quasi-steady manner, unsteady effects in the boundary layer itself would be small.

II.4 RAMP INPUTS OF TRAILING EDGE CONTROL SURFACES

Next consider a ramp input of a trailing edge control surface over a finite time T ($=\hat{T}$) where

$$\eta(\epsilon) = \begin{cases} 0 & \epsilon < 0 \\ \eta_s(\epsilon/T) & 0 \leq \epsilon \leq T \\ \eta_s & \epsilon > T \end{cases} \quad (20)$$

The lift build up for two ramp rise times $\hat{T} = 4.0, 20.0$ for a trailing edge control surface on a two dimensional aerofoil at $M_\infty = 1$, are shown in Fig. 7; there is a noticeable lag even for the longer ramp rise time of $\hat{T} = 20.0$.

A quasi steady aerodynamic response is one which follows closely the input. In general a quasi steady aerodynamic response occurs when the ramp rise time \hat{T} is greater than the aerodynamic rise time, as defined earlier. Hence, for $M_\infty = 0.3$,

$$\begin{aligned} \hat{T} &> 50 \quad (T > 1.5 \text{ s}) \text{ for two dimensional aerofoil,} \\ \hat{T} &> 4 \quad (T > 0.12 \text{ s}) \text{ for AR = 3 wing.} \end{aligned} \quad (21)$$

are indicative of quasi-steady aerodynamic responses. At the end of the ramp rise time i.e. when $\hat{t} = \hat{T}$, the lift response should be within 97% of the final steady state value.

With an actuator rate of $200^\circ/\text{s}$ a control displacement of 35° takes about 0.16 s, which would be quasi steady for the wing of aspect ratio 3, but not for the two dimensional aerofoil.

II.5 STEP RESPONSE AT SUBCRITICAL SPEEDS

Now consider the sudden displacement of a trailing edge control surface at a higher free stream Mach number but where the flow remains shock free. The basic flow mechanisms are still the same as those described at low Mach numbers, namely the formation and convection of a starting vortex and subsequent wake vorticity, and its convection downstream with the free stream velocity. The important difference is that now there is an additional lag due to the finite time of upstream propagation of information from the developing wake to the aerofoil. The forward propagation speed is the speed of sound minus the free stream velocity, as shown in Fig. 8.

For a two dimensional aerofoil the induced downwash at the aerofoil at time t is the accumulated effect of two dimensional acoustic waves which arise during the time interval $0 \rightarrow t'$ where t' is evaluated from the condition that when the starting vortex is distance Ut' downstream of the aerofoil trailing edge, sound waves from that location reach the trailing edge at time t , hence

$$t = t' + \frac{Ut'}{a_\infty(1-M_\infty)} \quad \text{or} \quad t' = \frac{t}{1-M_\infty} \quad (22)$$

So in equation (11) \hat{t} can be replaced by $(\hat{t}/M_\infty)^{-1}$.

On this argument the aerodynamic rise time increases as a factor of $(1-M_\infty)^{-1}$. Calculations for two dimensional aerofoils follow this trend as shown in Fig. 9.

The actual mechanism is somewhat more complicated than that outlined above in the sense that the magnitude of the downwash at the aerofoil at time t depended only on the position of the starting vortex when it was a distance Ut' aft of the trailing edge. Firstly the strength of the waves reaching the aerofoil decrease as Mach number increases. Secondly two dimensional acoustic waves have 'tails' so all of the acoustic waves generated in the wake during the whole time interval $0 \rightarrow t'$ contribute to the downwash at time t .

It should be noted that the time lag for information to pass from the trailing edge to the leading edge becomes significant as M_∞ increases; for example, at $M_\infty = 0.8$ this time lag is $5\hat{t}$.

Although the non-dimensional aerodynamic rise time increases by $(1-M_\infty)^{-1}$, the unit of aerodynamic time \hat{t} ($=c/U$) also decreases, so the increases of the aerodynamic rise time in real time is not so pronounced. For example, quasi-steady aerodynamics can be assumed for two dimensional aerofoils for ramp rise times greater than

$$\begin{aligned} 50\hat{t} \quad (1.5 \text{ s}) & \text{ at } M_\infty = 0.3 \\ 175\hat{t} \quad (2.0 \text{ s}) & \text{ at } M_\infty = 0.8. \end{aligned}$$

The variation of the time lag for a finite wing of aspect ratio about 3.0 with increase in free stream Mach number M_∞ is not so clear. Since, at low Mach numbers it is the spanwise flow which dominates, it might be expected that the aerodynamic rise time of about $4\hat{t}$ will be little affected by increase in M_∞ at subsonic speeds. The forward speed of propagation of information from the trailing edge to the leading edge, which is of the order of $5\hat{t}$ at $M_\infty = 0.8$ may increase the aerodynamic rise time slightly.

11.6 COMPARISON OF STEP RESPONSES AT SUBSONIC AND SUPERSONIC SPEEDS

Before considering step responses at transonic speeds it is useful to consider the step responses in subsonic and supersonic flows about M_∞ equal to 1.0 in the absence of shocks, i.e. assuming linearized theory.

By reference to Fig.10 when the flow is subsonic, with $M_\infty < 1.0$, information is propagated upstream. Only when all of the information from the deflected control surface and the fully developed wake reaches the whole of the aerofoil will steady conditions be attained.

However when M_∞ is supersonic the situation is totally different. Now the lag effect is due to the downstream propagation of information from the leading edge of the control surface to its trailing edge. Steady flow will be attained when the aft part of the sound waves from the control surface leading edge reach the trailing edge, only the development of the flow over the control surface is relevant, there is no wake effect. At $M_\infty = 1.1$ the aerodynamic rise time is of the order of $(\text{control chord}/0.1 \text{ } M_\infty)$, which is about $3.6\hat{t}$ for a 30% control, a relatively short aerodynamic rise time. This supersonic aerodynamic rise time will be independent of aspect ratio.

Apparently there is a major change in aerodynamic rise times from the extremely long when M_∞ is slightly less than 1.0 to the extremely short when M_∞ is slightly greater than 1.0.

The reduction of the effect of the wake from subsonic to supersonic conditions is a continuous process with increase in Mach number on the argument that in the subsonic case as waves propagate slowly upstream the strengths of the waves diminish with time of propagation, hence the strengths of the waves reaching the aerofoil from the wake will tend to zero as $M_\infty \rightarrow 1.0$.

The reasons for these large variations in aerodynamic rise times are not altogether understood. As described next these differences are amplified by non linear effects in real transonic flows when shock waves appear.

11.7 STEP RESPONSE AT TRANSONIC SPEEDS

Above the subcritical speed at subsonic speeds embedded supersonic regions appear, mostly terminated by shock waves. A tentative explanation for the step response under these conditions is given below.

When a shock wave system stands in front of the leading edge in the initial steady state, as shown in Fig.11, the sudden deployment of a trailing edge control surface will generate complex systems of waves. Expansion waves from the upper surface of the control will move forward rapidly in the subsonic region aft of the upper surface shock, reducing the strength of this shock and moving it backwards (the aft motion reduces its strength). Other expansion waves travel up and over the supersonic region to affect conditions on the same line and then into the supersonic region itself. Opposite effects occur on the lower surface.

This initial package of waves will be followed by waves from the starting vortex. The low pressure region in the vortex core will generate more expansion waves over the aerofoil upper surface while the separating flow from the trailing edge will generate more compression waves over the aerofoil lower surface. This combination of expansion waves and compression waves is the mechanism for increasing the circulation around the aerofoil.

It is suggested that the combination of waves at small time will induce a large aft motion of the upper surface shock and a large forward motion of the lower surface shock. As the starting vortex leaves the trailing edge region and convects downstream the upper surface shock moves slowly forward to its final steady state position, and the lower surface shock similarly moves aft.

Because of the barrier of the embedded supersonic region to the upstream propagation of information, the aerodynamic rise times, relative to linearized aerodynamic rise times, are significantly increased, by a factor of 2, as shown in the next section on oscillatory motions.

At higher transonic Mach numbers, $M_\infty \approx 0.9$, when the initial steady state shocks are located close to the trailing edge, as shown in Fig. 12, the step response is similar to that shown in Fig.10 with a supersonic free stream.

Calculations from contemporary computational aerodynamic codes for step responses at transonic speeds are not readily available because of numerical difficulties. Edwards¹⁰ reports some calculations of impulsive pitch responses but there are doubts on the rise times deduced from these results. However useful estimates of aerodynamic rise times can be obtained from oscillatory responses as described in the next section.

11.8 OSCILLATORY MOTIONS

The aerodynamic characteristics of oscillatory motions complement the aerodynamic characteristics of step responses in developing overall understanding of unsteady aerodynamics.

Consider a trailing edge control oscillating with amplitude η_0 and frequency ω rad/s, so

$$\eta(t) = \eta_0 \sin(\omega t), \quad (23)$$

Vorticity is continuously shed from the trailing edge and convected downstream with the free stream velocity, forming a semi-infinite wake, as shown in Fig. 13. When $M_\infty \ll 1.0$ the circulation around an element of wake, distance z aft of the trailing edge, Fig. 13, is proportional to $(\partial \Gamma / \partial t)$ when it was generated at the trailing edge at the earlier time $t - (z/U)$.

The time varying circulation $\Gamma(t)$ about the aerofoil/wing is expressed in the form

$$\Gamma(t) = \tilde{\Gamma}_R \sin(\omega t) + \tilde{\Gamma}_I \cos(\omega t), \quad (24)$$

where $\tilde{\Gamma}_R$ is the amplitude of the in-phase component and $\tilde{\Gamma}_I$ is the amplitude of the out-of-phase component. A negative value of $\tilde{\Gamma}_I$ implies a phase lag whereas a positive value of $\tilde{\Gamma}_I$ implies a phase advance.

The force and moment coefficients can be expressed in the same form as equation (24).

If the time of (period/4) is comparable to the aerodynamic rise time of the step response as defined earlier then the oscillatory response can be treated as quasi-steady, where $\tilde{\Gamma}_R$ is within 97% of the steady state value and $\tilde{\Gamma}_I$ is negligibly small. On the basis of the aerodynamic rise times derived earlier quasi-steady oscillatory conditions occur at low Mach numbers as follows:

$$\text{for } AR = \infty \quad \text{when } (2\pi/\omega/4) > 50$$

$$\text{i.e. when } \nu = \text{frequency parameter} = \omega c/U \\ < 0.03 \text{ (i.e. } 0.03 \text{ Hz),} \quad (25)$$

$$\text{for } AR = 3 \quad \text{when } \nu < 0.4 \text{ (i.e. } 2.0 \text{ Hz),} \quad (26)$$

Similar arguments can be applied to the boundary layers. According to Section 11.3 the aerodynamic rise time for a boundary layer is about 1.0. Hence attached boundary layers in oscillatory motions remain quasi-steady for $\nu < 1.5$, irrespective of aspect ratio. The range of $\nu > 2.0$ is outside the practical range of flutter.

Typical variations of $\tilde{C}_{LR}(\nu)$ and $\tilde{C}_{LI}(\nu)$ for an oscillating trailing edge control surface at low Mach numbers are shown in Fig. 14.

To estimate the aerodynamic rise time from Fig. 14, for the case $AR = \infty$, if the gradient of the $\tilde{C}_{LR}(\nu)$ curve at $\nu=0$ cuts the ν -axis at ν_0 , then

$$\tilde{C}_{LR}(\nu) \sim 0.9 \tilde{C}_{LR}(0) \quad \text{when} \quad \nu \sim 0.03 \nu_0 \quad (27)$$

In Fig. 14 ν_0 is about 1.0 so the limit for quasi-steady conditions is about 0.03, which agrees with equation (25), as it should since both are based on the 97% factor for defining quasi-steady aerodynamics.

The quasi-steady limit for the aspect ratio 3 case has to be deduced by a closer inspection of the detailed graph in Fig. 14, but it is seen that the extent of quasi-steady aerodynamics covers a wider range of values of frequency parameter.

In Fig. 14 the out-of-phase component $\tilde{C}_{LI}(\nu)$ for the two dimensional aerofoil is negative at small values of ν (i.e. a phase lag) but becomes positive at larger values of ν (i.e. a phase advance). This behaviour can be tentatively explained in terms of the wake vorticity, as shown in Fig. 15. As the control surface is becoming positive through zero, inducing an upward lift force, the corresponding shed vorticity is anti-clockwise in the near wake and clockwise in the medium wake. The near wake induces a downwash at the aerofoil, creating a download on the aerofoil, hence a lag effect, while the medium wake induces the opposite effects. The extent of the near wake will be long at low frequencies, dominating the induced flow field, but the near wake becomes shorter as frequency increases and then the effects of the medium wake take over. These effects are substantially modified in the case of the wing of aspect ratio 3 because of the dominating role of the trailing vorticity.

Typical variations of $\tilde{C}_{LR}(\nu)$ for an oscillating control surface at subsonic speeds on the basis of linearized theory are shown in Fig. 16. For the case of infinite aspect ratio the value of ν_0 at $M_\infty=0.8$ is about 0.25 of the value of ν_0 at $M_\infty=0$, implying an increase in the aerodynamic rise time of a factor of 4, which agrees with Fig. 9.

For the finite wing of aspect ratio 3 there is a much smaller increase in the aerodynamic rise time between $M_\infty = 0.0$ and $M_\infty = 0.8$, of the order of 1.5 (this number cannot be seen from the graph in Fig. 16, it has been obtained from detailed calculations).

At highsubsonic speeds when there are embedded supersonic regions terminated by shock waves the flows are non-linear with a variety of types of oscillatory flow which depend on Mach number, frequency parameter, amplitude of oscillation and mean incidence.

A classic set of experiments were reported by Tijdeman⁽⁸⁾. A NACA 64006 aerofoil with a 25% trailing edge control surface was set at zero incidence and the control surface oscillated at 1° amplitude. Three types of flow were observed, and are sketched in Fig.17.

(i) Type A $M_{\infty} = 0.875$, $\gamma = 0.936$

At the highest Mach number the shock motion is virtually simple harmonic but with a phase relative to the control surface motion. There is also a phase difference between the shock motion and its strength; the maximum strength, which depends on the free velocity ahead of the shock wave relative to the shock motion, is not encountered at the most aft shock location but slightly later as the shock moves forward.

(ii) Type B $M_{\infty} = 0.854$, $\gamma = 0.716$

With a slightly reduced Mach number the shock motion is similar to that of Type A except that the shock disappears during part of the aft motion of each cycle.

(iii) Type C $M_{\infty} = 0.822$, $\gamma = 0.992$

At the lowest tested Mach number the embedded supersonic region disappears each cycle; a shock wave appears aft and then as it moves forward its strength decreases and eventually propagates forward of the aerofoil leading edge as a weak, free shock.

Calculations for two dimensional aerofoil at supercritical conditions are shown in Fig.18 for $M_{\infty} = 0.90$ (ref.6). Compared to linear conditions the aerodynamic rise time is approximately doubled to the order of 350°. Similar calculations for finite wings do not appear to be available in the open literature.

II.9 COMMENTS

In two dimensions with increasing Mach number at subsonic speeds aerodynamic rise times become extremely large, especially when there are embedded supersonic regions. The aerodynamic rise time decreases dramatically with further increase in Mach number at the higher transonic speeds. The reasons for this abrupt change is obscure, at least to the authors.

Neither is the effect of aspect ratio clear. Results from existing three dimensional transonic codes would provide further insight but such data do not appear to be available in the open literature, although it would be expected that industrial firms would have made such calculations.

It is well known that time accurate numerical codes experience convergence difficulties at low frequencies.⁽⁹⁾ It is not known whether these convergence difficulties are related to the long aerodynamic rise times discussed above.

III COMPARISON OF PREDICTION WITH EXPERIMENT

III.1 LOW MACH NUMBERS

The range of prediction methods at low Mach numbers, for both steady and unsteady flows, compares

inviscid linear theory
inviscid conformal mapping
inviscid surface singularity methods
inviscid/inviscid coupling, using the boundary layer lag entrainment method
direct coupling for attached flows
inverse coupling for weak separated flows
Navier Stokes

It is part of the folk-lore of aerodynamics that in attached flow at low Mach numbers and at high Reynolds number, inviscid linear theory gives reasonable estimates for C_L and C_M because thickness and boundary layer effects tend to cancel.

For conventional two dimensional aerofoils steady inviscid surface singularity/inviscid coupling methods give good estimates of pressure distributions, see Fig.19⁽¹⁰⁾ and even for C_L and C_M .⁽¹¹⁾ However, when these same prediction methods are applied to two dimensional aerofoils with moving control surfaces predicted values do not compare at all well with experimental results.⁽¹²⁾ A typical comparison is shown in Table 1.

	linearized theory	panel method	panel method + boundary layer	experiment
C_L	0.242	0.275	0.254	0.174
C_M	0.044	-0.050	0.046	-0.074
C_H	0.0025	0.0020	0.0012	0.0015

TABLE 1

There is a considerable difference between predicted and experimental values of C_L , of the order of 50%. The prediction of the centre of pressure is reasonable. The prediction of the hinge moment coefficient C_H is within 20%. Note that whereas, for C_L , as already mentioned, thickness and boundary layer effects tend to cancel, as far as C_H is concerned the effects of thickness and boundary layer are additive.

It has been pointed out that it is inadvisable to compare overall forces and moments because of wind tunnel interference uncertainties.

More recent comparisons from ONLRA for oscillatory motions ⁽¹³⁾ are shown in Fig. 20; the section is supercritical and rear loaded, with a 25% trailing edge control surface. The predicted values of $\{C_L\}$, based on the inviscid/viscid coupling method, which are now less than the linearized predictions in contrast to the results presented in Table I, are of the order of 35% greater than experiment. For the hinge moment coefficient the effects of thickness and boundary layer are dramatic, at low frequencies the inviscid/viscid coupling method predicts values about 35% less than the experimental values although at higher frequencies predictions agree well with experiment; the phase angle is poorly predicted. Although not shown here, in these experiments there were large non-linearities due to the mean angle of the control surface.

For finite wings there were many experiments in the 1950's to measure hinge moment characteristics, ⁽⁷⁾ comparisons were made with the approximate forms of linearized theory available at that time. Experiments were carried out in the 1970's on finite wings at low Mach numbers; comparisons were made with predictions from linear and inviscid panel methods. A typical result from refs. (14,15) is shown in Fig. 21 for a swept wing with a full span oscillating control surface. In Fig. 21 the experimental data lie between the predictions of inviscid thin and thick wing theories, which is at variance with the two dimensional results in Fig. 20.

III. TRANSONIC SPEEDS

Prediction methods for transonic speeds are listed

Inviscid

- linear theory
- steady transonic small perturbation (TSP), non conservative and conservative
- low frequency TSP, LTRAN2
- all frequency TSP, XTRAN, NLR, Watson.
- steady full potential, non-conservative and conservative
- two potential, approximate and exact
- Luber

methods of solution: finite difference, finite element, integral equation.

Inviscid/viscid coupling

- potential codes + boundary layer lag entrainment method, including higher order terms
- pressure gradient effects, wake curvature
- direct method for attached flows
- inverse method for weak separated flow.

Navier Stokes

For the two dimensional aerofoil, NACA 64006 section, and trailing edge control surface, 25% chord, 1° angular deflection, Homwak illustrates the main features for low frequency control surface oscillation, as shown in Fig. 22. (16)

The main points of interest from Fig. 22 are:

- (i) large corrections are introduced to account for wall interference especially around the front half of the aerofoil, it is important that such corrections are well founded, shocks are present about 60% chord.
- (ii) linear theory which does not include shocks appears to be in the right ball park over the aerofoil but not over the control surface.
- (iii) non-linear inviscid codes which include thickness (i.e. all transonic codes) give a high loading much in excess of the experimental loading, the shock is predicted too far aft.
- (iv) the inclusion of the boundary layer in any calculation method is essential.
- (v) the loading on the control surface appears to be reasonably well predicted by the inviscid/viscid coupling method.

More detailed comparisons for the same case are shown in Fig. 23, taken from ref. 6, the predictions are derived from the XTRAN code plus steady lag entrainment. At the lower value of μ thickness increases the loads, both in phase and out of phase, compared to linear theory, and then the effects of the boundary layer decrease the loads, however all estimates are significantly higher than the experimental values. It is not known whether the tunnel corrections outlined by Homwak, Fig. 22, have been included in Figs. 23. These results at the lower value of μ are not altogether consistent with Fig. 22 nor are they similar to the results at lower Mach numbers, as shown in Fig. 20. At the higher frequency parameter linear theory is closest to the experimental values but all predictions are now greater than experiment. Although not shown here the predictions for the hinge moment coefficients are more reasonable.

Turning to finite wings, in the 1970's considerable effort was devoted to the development of accurate linearized methods, incorporating the correct singular behaviour around all edges, including those around the control surface. ⁽¹⁷⁾ It is claimed ⁽¹⁸⁾ that the linearized methods give satisfactory results in shock free conditions, at higher frequencies, as shown in Fig. 24; the experiments were carried out at the NLR. It is not known how well linear theory predicts loadings at lower frequencies. However linearized theory does not appear in such a good light for out board control surfaces ⁽¹⁹⁾ as shown in Fig. 25, the experiments were carried out at the RPI, linear theory now seriously overestimates experiment. The frequencies in Fig. 25 are somewhat lower than in Fig. 24. And overall force coefficients are compared in Fig. 25 in contrast to the loading distributions in Fig. 24. The inconsistencies between Figs. 24, 25 are worrying.

There appears to be little information in the open literature on the application of the various transonic codes to predict control surface characteristics on finite wings, either steady or unsteady; again it would be expected that industrial firms would have made such calculations.

III.3 SOME COMMENTS ON PREDICTION/EXPERIMENTAL COMPARISONS

The prediction of control surface characteristics is, in general, not encouraging. The trends seem to be that predictions are somewhat better for finite wings than for two dimensional aerofoils and that prediction is better at higher frequencies than lower frequencies. The reasons for these trends are unclear.

Although the evidence is not presented here methods which give reasonable predictions for overall aerofoil motions, e.g. heave and pitch, give poorer estimates of control surface characteristics. So it would appear that the control surfaces themselves are introducing additional factors which need to be taken into account.

The inability to predict control surface characteristics has been a fact of life over the past 60 years. Design and operational information has been based on data sheets and similar compendia complemented by wind tunnel and flight testing. But in this present day the aeronautical fraternity ought to be able to do better. Some thoughts are presented for debate.

In appraising prediction versus experiment it should be borne in mind that both theory and experiment contain defects, which need to be clarified.

- (i) Control surface characteristics in tunnel tests and in full scale can be affected by small gaps between aerofoil, or wing, and the control surface leading edge. These gaps are of the order of 0.1% aerofoil chord, or less, and they are small compared to the boundary layer thicknesses on the upper and lower surfaces which pass over the gaps. Sometimes these gaps are sealed, perhaps completely, perhaps partially, leaving cavities.

Flows through unsealed gaps can have high velocities, the gap flow can laminarize, large pressure gradients exist across gap entrance and exit, and separation/reattachment bubbles can exist. Investigations into gap flows at Queen Mary College and Göttingen have been reported^(19,20); research is continuing at both establishments.

A related problem is that small production changes in geometry near the control surface leading edge can have a profound effect.

- (ii) Much of the data on overall loads comes from pressure measurements. There is a problem of accuracy when the number of pressure measurement stations is limited, which is always the case, especially in three dimensions.
- (iii) Tunnel interference needs to be borne in mind. The nature of wind tunnel interference is fundamentally different in steady and unsteady flows. In the steady case the size of the model in relation to the wind tunnel working section is the main parameter, although even here some care is needed, a 'two dimensional aerofoil' between parallel walls is only truly two dimensional in an infinitely long working section. Fox⁽²¹⁾ and Shao⁽²²⁾ have reported on this aspect.

In the unsteady case as already explained in Part II, unsteady flow effects are associated with the developing wake and the induced effects of that wake about the aerofoil/wing. But in a tunnel the wake proceeds downstream through a diffuser, slowing down the wake convection speed, and then around a corner, as shown in Fig. 26. Wake effects are considerably reduced by tunnel interference, especially in two dimensional at low frequencies. Such tunnel interference should be significantly less for finite wings. It is noted that in the 'Nora' series of tests, where a model was tested in different tunnels, differences in wind tunnel interference effects were small⁽²³⁾.

Usually oscillatory tests are carried out at range of discrete frequencies. An alternative approach in principle is to sweep continuously through a frequency range, however such an approach has not been altogether successful even at low Mach numbers when checks are absent. The reasons are obscure but it is thought that tunnel unsteadiness is a major factor.

- (iv) It has been commented on that boundary layers play a key role in control surface characteristics. On the theoretical side one wonders how far boundary layer approximations remain valid. Even with sealed gaps, velocities over the upper surface in the region of the control surface leading edge are high, accompanied by high accelerations and decelerations with extremely large curvatures. It would be of interest to check whether or not some of the higher order boundary layer methods improve predictions. If gap flows are present the large pressure gradients across the gap exit would certainly invalidate the boundary layer assumptions.

IV. ROLE OF UNSTEADY AERODYNAMICS IN CONTROL SYSTEM DESIGN

IV.1 INTRODUCTION

Aerorocketcraft is the name given to the interdisciplinary activity involving structural dynamics, aerodynamics (steady and unsteady), and control systems. All active control system applications involve aerorocketcraft whether for overall aircraft dynamics (e.g. relaxed stability, manoeuvre demand, handling qualities) or for those involving more specifically structural response (e.g. gust loads, ride quality, flutter suppression, manoeuvre load reduction).

There are two complementary aspects:

- (i) control system design;
- (ii) control system validation.

In control systems design the aim is to determine the optimum values of the gains, compensation factors, etc., in the control loops to meet design specifications. There is an hierarchy of levels of design specifications, which essentially utilise unsteady aerodynamics in different ways. Take for example the design of a flutter suppression system.

- (i) The specification may be to increase the flutter speed by a given amount. For a wing with given inertial, stiffness and actuator characteristics, the role of the unsteady aerodynamics would have parity with the structural dynamics.
- (ii) The specification may be more severe, namely to increase the flutter speed by a given amount of a given wing but accommodating the full range of weapons and stores to be carried by that wing. Such a system is known as a robust system. In this case the role of the unsteady aerodynamics is crucial, see refs. 25,26.
- (iii) A more direct approach is to design a self-adaptive system where an on-board system of sensors and computer estimates continuously the open loop characteristics throughout flight and computes and implements the optimum values for the closed loop performance. In this case, apart from full park estimates, unsteady aerodynamics are not really required.

In control system validation once the control system has been designed it has to be checked for safe operation through the entire flight envelope by extensive computational studies, incorporating the full range of aerodynamic codes, ground simulation, tunnel testing and flight testing.

In this section an attempt is made to explain how unsteady aerodynamics are used in control system design.

IV.2 SINGLE DEGREE OF FREEDOM SYSTEM IN STILL AIR

Before introducing any unsteady aerodynamics consider the single degree of freedom system of an aircraft with fixed control in pitch in still air, as shown in Fig.21. The equation of motion is

$$I \ddot{\theta} + D \dot{\theta} + K \theta = m g \alpha_0 \cos(\omega t) \quad (28)$$

where I = moment of inertia, D = structural damping, and K = stiffness, all assumed constant, and the input has a prescribed variation with time.

Equation (28) can be solved for $\theta(t)$:

(i) in the time plane,

(ii) via the frequency plane by solving for the Fourier Transform

$$\tilde{\theta}(\omega) = \int_{-\infty}^{+\infty} e^{-i\omega t} \theta(t) dt, \quad (29)$$

and then inverting back to the time plane by the inverse Fourier Transform

$$\theta(t) = \frac{1}{2\pi} \int_{-\infty}^{+\infty} e^{i\omega t} \tilde{\theta}(\omega) d\omega, \quad (30)$$

(iii) via the s plane by solving for the generalized Laplace Transform

$$\tilde{\theta}(s) = \int_{-\infty}^{+\infty} e^{-st} \theta(t) dt, \quad s = \alpha + i\omega, \quad (31)$$

and then inverting back to the time plane.

It is important to appreciate that whereas the time plane and frequency plane methods can be applied analytically or numerically, the s plane method is essentially analytic only. The reason is that in the s plane method, in equation (31), $\tilde{\theta}(s)$ can only be defined for $\text{Re}(s) < 0$, but for all practical damped motion, $\tilde{\theta}(s)$ is needed when $\text{Re}(s) > 0$. This difficulty is overcome mathematically by the concept of analytic continuation where analytic expressions which are valid for $\text{Re}(s) < 0$ are carried over to the region where $\text{Re}(s) > 0$. This approach is an extremely powerful tool which underpins control system design.

The other point to note is that the frequency and s plane methods are limited to linear differential equations, i.e. linear systems, only.

IV.3 SINGLE DEGREE OF FREEDOM SYSTEM IN MOVING AIR

Now consider the response of the single degree of freedom, shown in Fig.21, in a relative air stream of velocity U at Mach number M_∞ . The equation of motion is now

$$I \ddot{\theta} + D \dot{\theta} + K \theta = \frac{1}{2} \rho U^2 c^2 C_M(M_\infty, \alpha_m, \bar{c}) \theta(t) = m g \alpha_0 \cos(\omega t) \quad (32)$$

where $C_M(M_\infty, \alpha_m, \bar{c})$ denotes the time varying moment coefficient about the axis of pitch when the aircraft pitch motion $\theta(t)$ is about a mean incidence of α_m .

Codes for transient non-linear unsteady aerodynamics determine $C_M(M_\infty, \alpha_m, \bar{c})$ directly in a stepwise manner, i.e. C_M is calculated sequentially at time t_k , t_{k+1} , t_{k+2} , etc. Here it is straightforward to couple such aerodynamic codes with the structural dynamic terms and then equation (32) can be solved for $\theta(t)$ for a given input, directly in the time plane. The system is unstable if $\theta(t)$ tends to infinity with time, the system is marginally stable if $\theta(t)$ enters a limit cycle oscillation. In general such response calculations are part of the validation exercise, not part of the design procedures.

However unsteady linearized aerodynamics are substantially different because of the manner in which the topic has evolved over the past years. In general codes for linearized unsteady aerodynamics are limited to estimates

of oscillatory derivatives only, steady and quasi-steady derivatives are special cases as the frequency tends to zero. In the present example, if $\Theta(t)$ is simple harmonic, i.e.

$$\Theta(\bar{t}) = \Theta_0 \sin \omega \bar{t}, \quad (32)$$

the linearized aerodynamic moment coefficient has the form $C_M(M_\infty, \alpha_m, \bar{t} | \Theta(\bar{t})) = \tilde{C}_M(M_\infty, \nu) \Theta_0 \sin \nu \bar{t}$, (34) where the oscillatory derivative \tilde{C}_M , which is independent of α_m , has in-phase and out-of phase components $\tilde{C}_{MR}(M_\infty, \nu)$ and $\tilde{C}_{MI}(M_\infty, \nu)$, and ν is the non-dimensional frequency parameter. Codes give numerical estimates of $\tilde{C}_M(M_\infty, \nu)$ at discrete values of M_∞ and ν , usually for $\nu < 2$, the practical range for flutter investigations. Most codes become inaccurate for $\nu > 3.0$.

To solve equation (32) via the frequency plane, because the Fourier integral covers all frequencies from zero to infinity it is necessary to interpolate $\tilde{C}_M(M_\infty, \nu)$ from $\nu = 2.0$ to ∞ . The asymptotic limit at $\nu = \infty$ is known, it is given by piston theory; however the behaviour of $\tilde{C}_{MR}(M_\infty, \nu)$ from $\nu = 2 \rightarrow \infty$ is far from monotonic. Fortunately the asymptotic behaviour of $\tilde{C}_{MI}(M_\infty, \nu)$ is much more reasonable. Since the frequency plane method uses either $\tilde{C}_{HR}(M_\infty, \nu)$ or $\tilde{C}_{HI}(M_\infty, \nu)$, not both of them, $\tilde{C}_{MI}(M_\infty, \nu)$ is used in practice (see ref. 27).

To solve equation (32) in the time plane, formally on the basis of linear aerodynamics, the aerodynamic moment is given by the convolution integral

$$C_M(M_\infty, \alpha_m, \bar{t} | \Theta(\bar{t})) = \int_0^{\bar{t}} C_{MS}(M_\infty, \bar{t} - \bar{\tau}) \Theta(\bar{\tau}) d\bar{\tau}, \quad (35)$$

where $C_{MS}(M_\infty, \bar{t})$ is the moment coefficient of the impulsive response following a unit impulse input at time $\bar{t} = 0$; the impulse response is the differential of the step response described in section II. But $C_{MS}(M_\infty, \bar{t})$ is not usually known directly, it has to be calculated from the known values of the oscillatory derivatives, via the Fourier transform.

$$C_{MS}(M_\infty, \bar{t}) = \int_{-\infty}^{\infty} \tilde{C}_M(M_\infty, \nu) e^{-i\nu \bar{t}} d\nu. \quad (36)$$

Once $C_{MS}(M_\infty, \bar{t})$ is known numerically, with $C_M(M_\infty, \alpha_m, \bar{t} | \Theta(\bar{t}))$ given by equation (35), the response $\Theta(\bar{t})$ in equation (32) can be computed relatively easily.

But control system design is carried primarily in the s plane. Since the s plane formulation is linear, linear aerodynamics have to be used. On the basis of linearized aerodynamics the Laplace transform of the equation of motion, equation (32), is

$$(\bar{I}s^2 + Ds + K - \frac{1}{2}\rho U^2 c^2 \bar{C}_M(M_\infty, s)) \bar{\Theta}(s) = \overline{\text{input}}(s), \quad (37)$$

where the aerodynamic transfer function $\bar{C}_M(M_\infty, s)$ is given by

$$\bar{C}_M(M_\infty, s) = \int_0^{\infty} C_{MS}(M_\infty, \bar{t}) e^{-s\bar{t}} d\bar{t}. \quad (38)$$

Note that formally, from equation (38), $\bar{C}_M(M_\infty, s)$ only exists for $\text{Re}(s) > 0$.

Stability of the single degree of freedom system is ensured if, from equation (37),

$$\text{Re}(s_i) < 0$$

where $s_i, i = 1, \dots, n$ are the roots of

$$\bar{I}s^2 + Ds + K - \frac{1}{2}\rho U^2 c^2 \bar{C}_M(M_\infty, s) = 0. \quad (39)$$

The aim is to obtain an analytic expression which approximates $\bar{C}_M(M_\infty, s)$, which is valid for $\text{Re}(s) > 0$, and then to apply that analytic expression to solve equation (39) in the region $\text{Re}(s) < 0$.

The form of the aerodynamic transfer function can be deduced from Part II of this paper. For a two dimensional aerofoil an approximation for the step response is given by equation (II), namely

$$C_{MH}(M_\infty, \bar{t}) \sim \left[1 - \frac{1}{2\{(1-M_\infty)\bar{t}+1\}} \right], \quad (40)$$

the sign \sim denotes 'proportional to'. Now $C_{MS}(M_\infty, \bar{t})$ is the differential of $C_{MH}(M_\infty, \bar{t})$ so

$$C_{MS}(M_\infty, \bar{t}) \sim (1-M_\infty)\bar{t} + 1)^{-2} \quad (41)$$

Thus from equation (38) the aerodynamic transfer function is

$$\begin{aligned} \bar{C}_M(M_\infty, s) &\sim \int_0^{\infty} \frac{e^{-s\bar{t}} d\bar{t}}{((1-M_\infty)\bar{t}+1)^2} = \left\{ 1 - \frac{s}{1-M_\infty} \int_{s/(1-M_\infty)}^{\infty} \frac{e^{-\lambda}}{\lambda} d\lambda \right\} \\ &\sim 1 + \left(\frac{s}{1-M_\infty} \right) \ln \left(\frac{s}{1-M_\infty} \right) \quad \text{for small } s \\ &\sim \left(\frac{s}{1-M_\infty} \right)^2 \quad \text{for large } s \end{aligned} \quad (42)$$

Research has been aimed at formulating interpolation functions between these asymptotic limits e.g. ref. 28.

Once an analytic expression has been assumed for $\bar{C}_H(M_\infty, s)$, which is consistent with equation (42), it is necessary to investigate the system stability by solving equation (39). The first question to arise is 'how many roots (s_k) does equation (39) possess?'. The answer is 2, the same number as the number of roots in still air Q.Q. The values of these two roots can be tracked numerically by gradually increasing the speed U , a fairly intensive numerical exercise which is not altogether compatible with control system design methods. So further approximations to the aerodynamic transfer function are usually introduced.

The simplest approximation is to assume quasi-steady aerodynamics, where $\bar{C}_H(M_\infty, s)$ is replaced by

$$\bar{C}_H(M_\infty, s) = \bar{C}_H(M_\infty, 0) + \bar{s} \frac{\partial \bar{C}_H(M_\infty, \bar{s})}{\partial \bar{s}} \Big|_{\bar{s}=0} \quad (43)$$

The procedure to find the roots is then trivial but inaccurate if the roots are not located within the region $|\bar{s}|$ less than (non-dimensional aerodynamic rise time) $^{-1}$.

The most common approximation uses rational functions in the s plane. Essentially the impulse response is approximated by a combination of exponential decay functions. For example, if the step response response to a unit change in θ is approximated by the single exponential decay function

$$C_H(\bar{t}) \sim (1 - e^{-p\bar{t}}/2), \quad (44)$$

where the value of the constant p is determined from a best fit, then

$$C_H(\bar{t}) \sim p e^{-p\bar{t}}, \quad \bar{C}_H(s) \sim p/(s+p). \quad (45)$$

The stability equation (39) then becomes

$$I s^2 + D s + K - \frac{1}{2} \rho U^2 c^2 (\text{const}) \frac{p}{s+p} = 0. \quad (46)$$

It is seen that the order of equation (46) has been increased from a quadratic to a cubic. There are now three roots, so one root must be spurious with no physical meaning. Increasing the number of exponential terms in equation (44) to improve the accuracy of the impulsive response will also increase the number of spurious roots. These spurious roots can be a nuisance in a control design exercise.

An alternative approach recently investigated by Vepa⁽²⁹⁾ approximates the aerodynamic transfer function by

$$\bar{C}_H(M_\infty, s) = \int_0^\infty C_H(\bar{t}) e^{-s\bar{t}} d\bar{t} = \int_0^\infty \left(\sum_{n=0}^N a_n e^{-n\bar{t}} \right) e^{-s\bar{t}} d\bar{t} = \sum_{n=0}^N a_n \frac{1}{s+n}. \quad (47)$$

The coefficients a_n can be determined directly from the oscillatory derivatives $\bar{C}_H(M_\infty, \nu)$. The roots are then determined from

$$I s^2 + D s + K - \frac{1}{2} \rho U^2 c^2 \left(\sum_{n=0}^N a_n \frac{1}{s+n} \right) = 0. \quad (48)$$

This form of equation (48) is typical of a time delay differential equation which has been applied in other control system contexts. The advantage of this approach is that it does not introduce any spurious roots.

If now there is feedback through a trailing edge control surface, the closed loop equations

$$I \ddot{\theta} + D \dot{\theta} + K \theta - \frac{1}{2} \rho U^2 c^2 \bar{C}_H(M_\infty, \alpha_m, \eta_m, \bar{t} | \theta(\bar{t})) = \text{input}(\bar{t})$$

where, in general, assuming no actuator lag $\eta(\bar{t}) = A \theta(\bar{t}) + B \dot{\theta}(\bar{t}) + C \int_0^{\bar{t}} \theta(\bar{t}) d\bar{t}$. (49)

The aim of control system design is to determine values of A, B and C to best meet the specifications. All of the above discussion on aerodynamic transfer functions can be carried over to this closed loop problem.

This part of the paper shows that control system design is heavily dominated by linear synthesis methods which imply linear aerodynamics. But the linear aerodynamics themselves have to be further approximated and tailored in analytic forms which are consistent with control system strategies. This is an area of active research.

But it is known that linearized aerodynamics do not apply at transonic speeds. So there are two main questions.

- (i) How does control system design methodology cope with non-linear transonic unsteady aerodynamics? Modern aeroplanes are currently flying with sophisticated control systems. Do we deduce that satisfactory systems have been developed without the need to know about non-linear aerodynamics?
- (ii) Looking to the future, is there a need for closer dialogue between control designers and aerodynamicists to seek appropriate formulations of realistic aerodynamics in control design strategies?

V CONCLUSIONS

- (i) The aerodynamic rise time to attain steady state conditions has been shown to increase significantly at transonic speeds but then to drop abruptly as the Mach number approaches 1. The reasons why are unclear.
- (ii) Current techniques to predict steady and unsteady aerodynamics, which give reasonable estimates for overall aerofair/wing motions, give poorer estimates for control surface characteristics. At least one set of reliable experimental data exists for unsteady control surfaces⁽³⁰⁾ so perhaps effort in the near future should be focussed on estimation procedures. A coordinated effort, possibly sponsored by AGARD, could clarify the current state-of-the-art, identify problem areas, and propose future directions of research.
- (iii) The contribution of unsteady aerodynamics to control system design is limited to approximate forms of linearized aerodynamics. To use more accurate non-linear aerodynamics poses considerable difficulties. On the other hand accurate aerodynamics may not be required with modern control system techniques.

A closer dialogue between aerodynamicists, steady and unsteady, with control system designers, could be highly beneficial, mainly to aid mutual understanding but also to clarify the future role, and direction of research, of unsteady aerodynamics.

Perhaps an AGARDograph, where contributions from a number of experts, moulded into a unified text, might be one way of proceeding.

REFERENCES

1. G.J.Hancock Dynamic effects of controls. Special Course On Aerodynamics of Controls. AGARD Report No. 711, 1983.
2. D.G.Mabey Experimental methods to determine control effectiveness in wind tunnels. Special Course On Aerodynamics of Controls. AGARD Report No. 711 1983.
3. D. Telionis Review of unsteady boundary layers. Special Course on Unsteady Aerodynamics AGARD Report No. 675, 1980.
4. T.Cebeci Analysis of turbulent boundary layers. Academic Press 1974.
5. A.M.O Smith Some notes on sound waves. Special Course on Unsteady Aerodynamics AGARD Report No. 679, 1980.
6. G.J.Hancock Computational unsteady aerodynamics for lifting surfaces. AGARD Lecture Series: Unsteady Aerodynamics 1988-07.
7. AGARD Manual of Aeroelasticity 1961.
8. H.Tijdeman Investigations of the transonic flow around oscillating aerofoils. NLR TR 77090 U 1978.
9. W.J.McCroskey Status and prospects of computational fluid dynamics for unsteady viscous flows. P.Kutler AGARD CP 374, 1985.
10. J.O.Bridgeman An aerofoil with control surface in incompressible viscous flow Aero. Jour. December 1977.
11. B.C.Basu Comparisons of separated flow airfoil analysis Jour. Aircraft March, 1985.
12. I.D.Bascorich Measurements of two dimensional derivatives on a wing-aileron tab system with a 1541 section aerofoil. Part 1 Direct aileron derivatives. A.R.C. R&M 2934 1952.
13. K.C.Wright Effects instantanées d'une gouverne en encoulement bidimensionnel subsonique et transonique AGARD CP 252 1979.
14. A.Desopper Pressure measurements on a harmonically oscillating swept wing with two control surfaces in incompressible flow. R.Grenon J.Steels DLR-FB 70-47 1970.
15. H.Förschlag Non-linear unsteady potential calculations for three dimensional oscillating wings. H.Triebstein J.Wagener AIAA Jour. 16.
16. W.Geissler Some remarks on boundary layer effects on unsteady loads AGARD CP 296 1981.
17. R.Houwink On the pressure loading functions for oscillating wings with control surfaces. Proc. AIAA/ASME 8th Structures, Structural Dynamics & Materials Conference March 1967.
18. B.Laschka Unsteady aerodynamics; fundamentals and applications. AGARD CP 386 1985.
19. C.Michael On the effects of gaps on control surface characteristics AGARD CP 262 1979.
20. G.J.Hancock Some remarks on the unsteady airloads on oscillating control surfaces in subsonic flow AGARD CP 296 1981.
21. H.Försching The effect of finite test section length on wall interference in two dimensional ventilated wind tunnels AGARD CP 174 (1975).
22. J.W. Sluif Wind tunnel interference on unsteady two dimensional aerofoil motions in low speed flows. Aero. Jour. March 1988.
23. W.J. Piers European wind tunnels : unsteady pressures on an oscillating model (Nora experiments) AGARD Report R673 1979.
24. C.W.Chung R.Destuynder K.Kienappel R.Roos Effects of unsteadiness on the measurement of oscillatory pressures on a wind tunnel model with discrete and sweep excitation. R.A.E. Tech.Memo.Aero.2016 1984.
25. D.G.Mabey Flutter suppression using active controls based on the concept of aerodynamic energy. NASA TN D 6199 1971.
26. E.Nissim The aeroelastic loop and its robust control, to be published.
27. R.Vepa Aerodynamic modelling for studies of aircraft dynamics. RAE TR 810116 1981.
28. D.L.Woodcock General equations of motion for an elastic wing and method of solution. AIAA Journal August 1984.
29. V.Stark Practical techniques for modelling aeroelasticity systems for active controls - Eurocon Forum on Aeroelasticity and Structural Dynamics Aachen 1989.
30. N.C. Lumbourne Compendium of unsteady aerodynamic measurements. AGARD Report 702 1982.

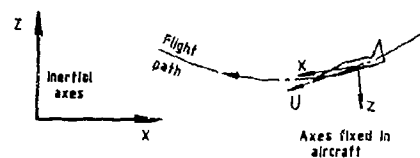


Fig.1 Axes systems

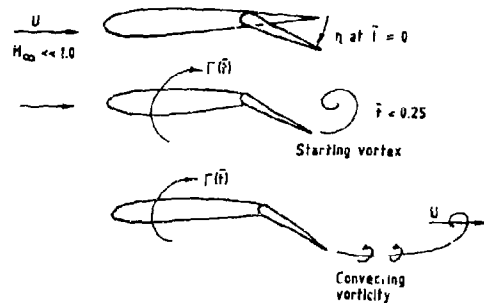


Fig.2 Aerodynamic flows following step input of control

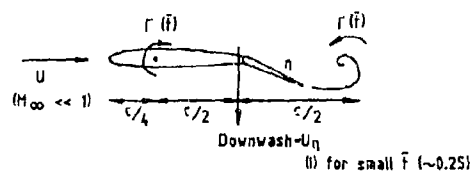
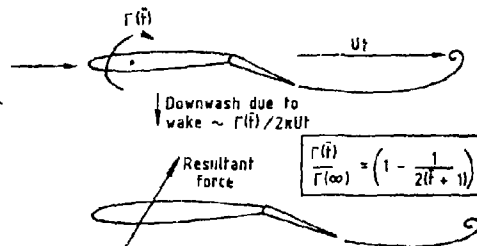
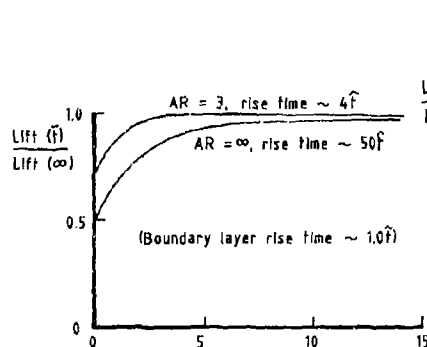
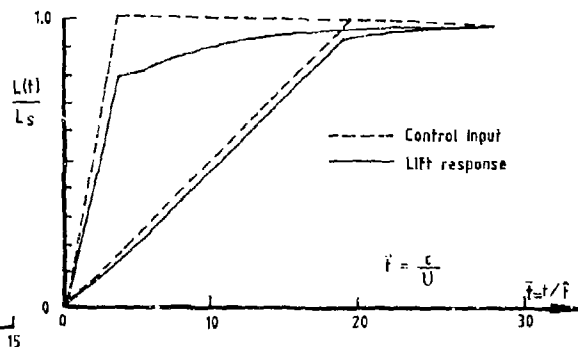
Fig.3 Consideration of $\Gamma(\bar{t})$ at small timeFig.4 Consideration of $\Gamma(\bar{t})$ at large timeFig.5 Build up of lift following step change in control ($M_\infty = 1.0$)

Fig.7 Lift response for ramp changes in trailing edge control

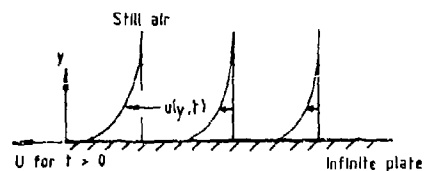


Fig.6 Impulsive boundary layer development

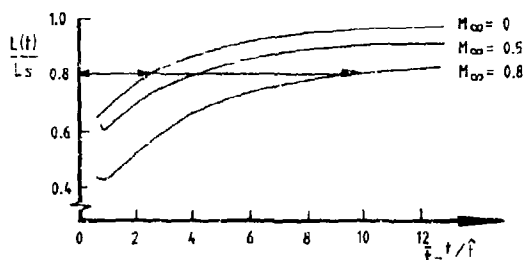


Fig.9 Effect of free stream Mach No. on transient lift

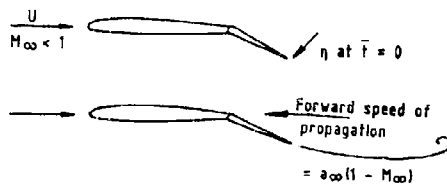


Fig. 8 Effect of compressibility

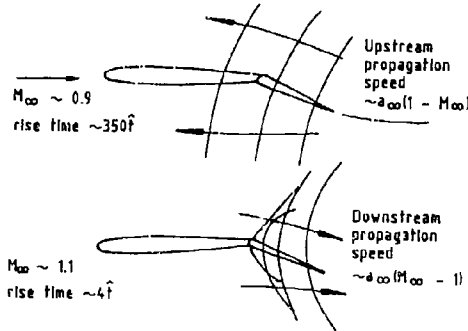
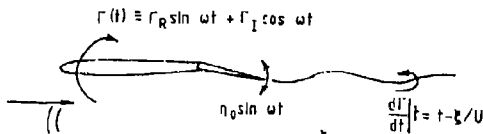
Fig. 10 Wave patterns about $M_\infty \sim 1.0$ 

Fig. 13 Aerodynamics of oscillating control

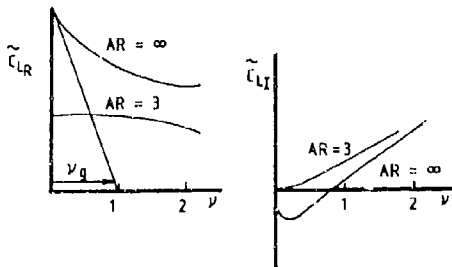
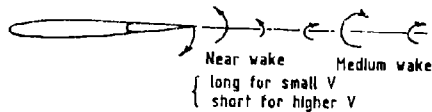
Fig. 14 Oscillatory control derivatives for $M_\infty \ll 1.0$ (Ref. 7)

Fig. 15 Oscillating wake

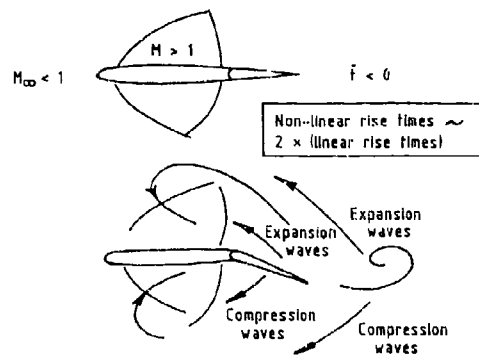


Fig. 11 Tentative wave patterns at transonic speeds

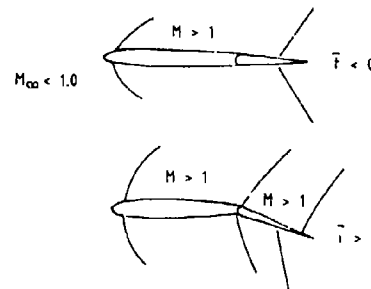


Fig. 12 Conditions at high subsonic speeds

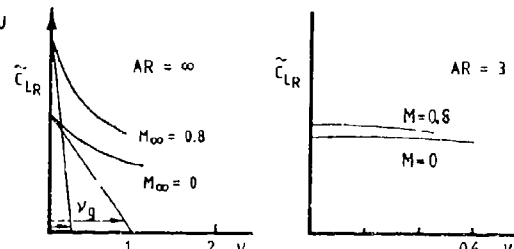


Fig. 16 Linearised oscillatory derivatives at subsonic speeds

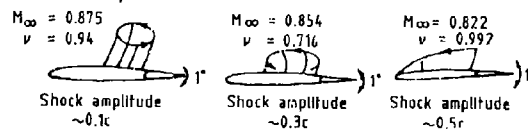


Fig. 17 Oscillatory shock movement (Ref. 8)

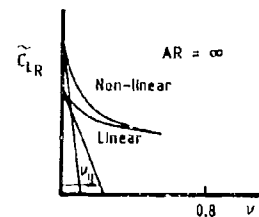


Fig. 18 Comparison of linear and non-linear derivatives

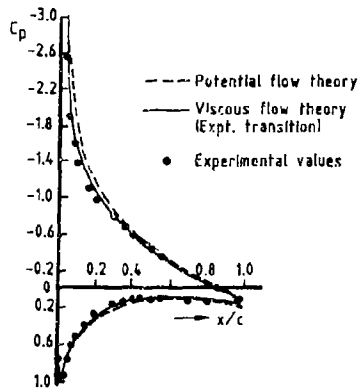


Fig. 19 Pressure distribution RAE 101, $t/c = 0.01$, $\alpha = 8.18^\circ$, (Ref. 9)

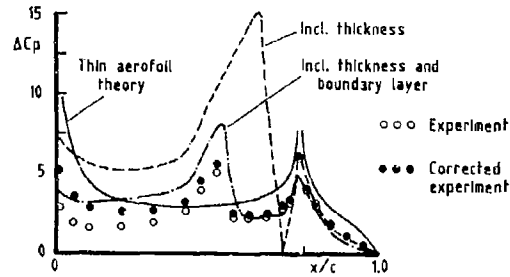


Fig. 22 Effect of thickness and boundary layer on the steady and quasi-steady pressure distribution in transonic flow (Ref. 15)

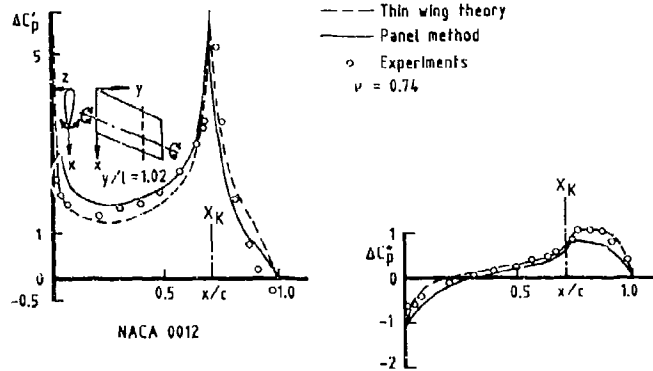


Fig. 21 Finite wing with control (Refs. 13, 14)

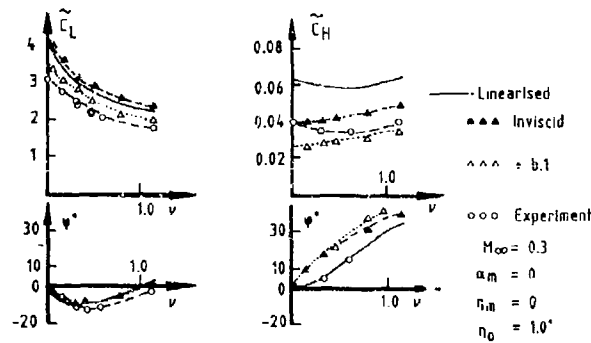


Fig. 20 Comparison of prediction and experiment at low Mach number (Ref. 12)

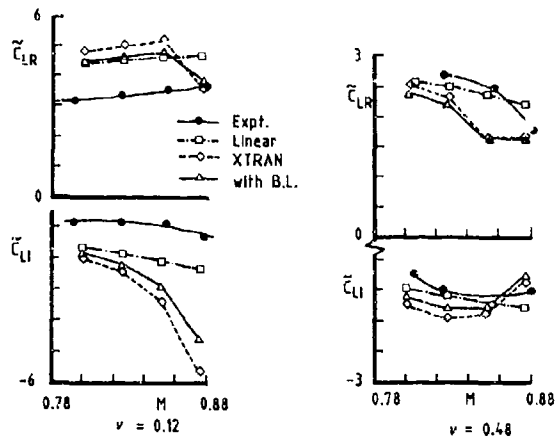


Fig 23 Aerofoil with control at high subsonic speed (Ref.6)

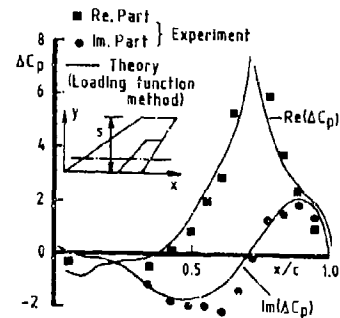


Fig.24 Comparison theory - experiment for a swept wing with oscillating flap in compressible flow (Ref.17)

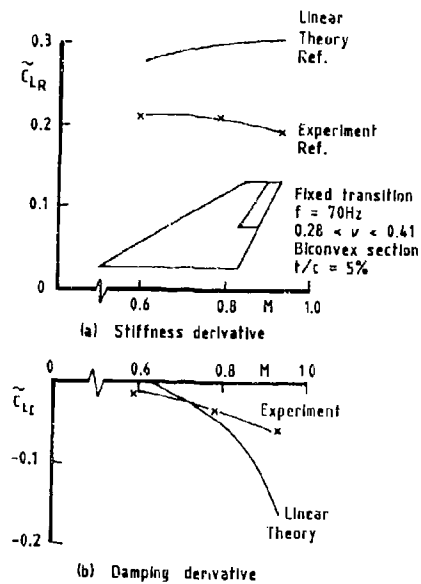


Fig.25 Lift due to oscillating flap v Mach number (Ref.2)

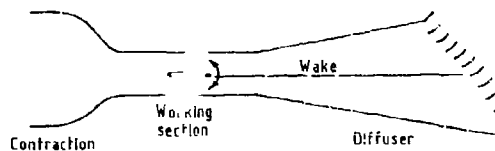


Fig 26 Tunnel interference

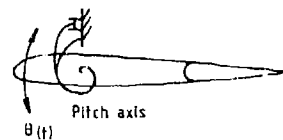


Fig.27 Single degree of freedom model

THE STEADY AND TIME-DEPENDENT AERODYNAMIC CHARACTERISTICS OF A COMBAT AIRCRAFT WITH
A DELTA OR SWEEP CANARD

by

D. G. Mabey
B. L. Welsh
C. R. Pyne

Aerodynamics Department
Procurement Executive, Ministry of Defence
Royal Aerospace Establishment
Bedford, MK41 6AE
UK

SUMMARY

The steady and time-dependent aerodynamic characteristics for a low speed half model of a typical combat aircraft configuration fitted with a 65° delta canard are compared with those for the same model fitted with a 44.3° swept canard. The tests were made in the RAE 13ft x 9ft Wind Tunnel on a large model of the RAE High Incidence Research Model (HIRM 1), modified to represent the Experimental Aircraft (EAP) configuration.

For the same planform area, the delta canard gives higher lift and comparable pitching moments for trimming. For canard and wing buffeting the differences are small. The pressures induced on the wing by oscillation of either the delta or the swept canard are very small and comparable.

Overall, these low speed measurements suggest that delta canards might have advantages over swept canards for future combat aircraft.

LIST OF SYMBOLS

C_{BC}	static bending moment coefficient (Eq.(1))
C_L, C_D, C_m	lift, drag and pitching moment coefficients
C_N	normal force coefficient
c	local chord
\bar{c}	aerodynamic mean chord of gross wing (868 mm)
C_p	pressure coefficient
f	frequency (Hz)
k_1	upwash factor due to wing and body (Eq.(3))
$\sqrt{n\delta(n)}$	buffet excitation parameter (Eq.(2))
m	generalised mass
\bar{p}	total broad band rms pressure fluctuations on wings
$q = \frac{1}{2}\rho U^2$	free stream kinetic pressure
S	gross wing area (1.031m ²)
S_w	exposed wing area (0.78m ²)
S_c	exposed canard area (0.092m ²)
s_c	exposed canard semi-span
s_w	wing semi-span from centre line
x	streamwise co-ordinate
y	spanwise coordinate
\ddot{z}	rms tip acceleration in mode
U	free stream velocity
α	wing and fuselage incidence

α_c	canard effective incidence (Eq.(3))
ζ	total damping fraction critical (Eq.(2))
$n = y/s_w$	semi-span ratio for wing pressure plotting section
η_c	canard setting
λ	function of η_c (Eq.(4))
ρ	free-stream density

1. INTRODUCTION

A detailed study of the steady and time-dependent aerodynamic characteristics at low speeds on advanced combat aircraft configurations fitted with canards is being made with a large half model of the RAE High Incidence Research Model (HIRM 1) in the RAE 13ft x 9ft Tunnel. For the unmodified model with an undrooped leading edge, reports have been issued giving a description of the complex interaction between the canard and wing flows¹ and of the wing pressures induced by the oscillation of the canard².

The model was then modified to represent the Experimental Aircraft Project (EAP) configuration with an undrooped leading edge. The modified model successfully reproduced the known general steady aerodynamic characteristics and also gave useful information about the time-dependent characteristics³. Hence it was decided to exploit this modified model to address other important questions.

This Paper assesses the possible advantages of replacing the EAP canard, (with a swept planform) by a canard with a highly swept delta planform (Fig 1). The advantages of the present swept planform include a compact design and the fact that the short root chord allows relatively small gaps at the fuselage when the control is deflected. A delta planform would be less compact and because of its longer chord, and the fuselage curvature, would have larger gaps when the control is deflected. However, a delta planform should give appreciably lower wave drag at supersonic speeds, due to the effects of increased sweep and possibly due to an improved area distribution.

Despite this important advantage, hitherto delta planforms have not been considered seriously because of fears that control power might become inadequate at high angles of incidence, or that vortex bursting might increase the wing buffeting. The present tests suggest that these fears are unfounded: control power is increased with the delta canard without any adverse effects on the wing buffeting. Hence delta canards should be included in future design studies of advanced combat aircraft.

A preliminary study of the buffeting due to canard, fuselage and wing separations has already been reported⁵, and includes measurements with both the swept and delta canards.

2. EXPERIMENTAL DETAILS

Complete descriptions of the model are included in Refs 1 and 3 and are summarized here. The model is mounted on the half model balance in the floor of the RAE 13ft x 9ft Wind Tunnel so that overall steady forces can be measured. Steady and time-dependent pressures are measured on both upper and lower surfaces at three spanwise sections on the wing (Fig 1) using the RAE PRESTO system⁶. The wing motion in the first bending mode at $f = 22$ Hz is measured by an accelerometer near to the tip (at $n = 0.8$).

2.1 Canards

Fig 2 shows the swept canard (described in Ref 3). Fig 3 shows the 65° delta canard, which is a flat plate of constant thickness with a chamfered leading-edge and which closely resembles the wing of Ref 4. Both canards are of similar construction and have a pair of glass fibre skins which are stiffened internally with polyurethane foam. The canard loads are diffused from this relatively weak structure into a steel root block, which has a strain gauge bridge configured to measure the bending buffeting response in the usual way⁷. The first bending frequency of the swept and delta canards were 58 Hz and 134 Hz respectively.

2.2 Analysis of measurements

For the delta canard the canard-root bending moment coefficient is given by

$$C_{Be} = \frac{\text{canard bending moment}}{q S_c (0.53 s_c)} \quad (1)$$

where S_c = exposed canard area (0.092 m²),

and s_c = exposed canard semi-span (0.293 m).

The factor 0.33 is introduced into the denominator of Eq.(1) to make the measured bending moment equivalent to a lift coefficient, C_{Lc} , for a lift force acting at the centre of area of the triangular planform.

As a safety precaution and as a measurement of the buffeting of the flexible wing, the wing accelerometer reading was recorded also for every data point, using a spectrum analyser (Brüel and Kjær Type 2120). For PRESTO the measurement time of 34 s gave about 750 cycles of buffeting at the wing first-bending frequency (22 Hz), so that accurate measurements of damping were possible from the signals recorded by the PRESTO system.

Buffeting response is measured as output from the strain-gauge bridge in volts. For the wing the buffet excitation parameter in any mode is given by the relation^{8,9}

$$\sqrt{n\delta(n)} = \frac{2}{\sqrt{\pi}} \frac{m\ddot{z}}{qS_w} \zeta^{\frac{1}{2}}, \quad (2)$$

where m = generalised mass in mode with respect to motion at tip,

\ddot{z} = rms tip acceleration in mode,

q = kinetic pressure,

S_w = exposed reference area,

ζ = total damping - as a ratio of critical damping.

Before the tests the generalised mass for the wing bending mode was measured. The wing-tip acceleration applicable to the first-bending mode was deduced from the accelerometer reading at $n = 0.8$ according to the relation

$$(\text{acceleration at } n = 1) = 1.56 (\text{acceleration at } n = 0.8) .$$

Damping coefficients were extracted from the spectra of the signals, using the half-power method. Knowing the generalised mass, the tip acceleration and the total damping the buffet excitation parameter could be calculated according to Eq.(2) for the wing.

Unfortunately Eq.(2) could not be applied for the delta canard because it proved impossible to obtain accurate values of the generalised mass for the bending mode at 134 Hz. [An attempt was made to measure the generalised mass in the usual way by adding small masses to the tip of the canard and noting the change in frequency. However, due to the high level of structural damping, and the corresponding flatness of the spectral peaks, these small changes in frequency could not be measured accurately.] Hence the canard root strain signals (in mV at 134 Hz measured by the spectrum analyser) were compared with previous buffeting measurements on an isolated 65° delta wing with a similar geometry" (cf Fig 10b).

2.3 Test conditions

A roughness band 3 mm wide of 0.36mm diameter ballotini was applied to fix transition at 3 mm from the leading-edge of both the wing and the canard. Most measurements were made at a speed of 60 m/s, giving a Reynolds number $R = 3.7 \times 10^6$ based on the wing aerodynamic mean chord, \bar{c} . Some additional measurements were made at reduced speeds of 40 and 20 m/s. Unless otherwise stated, all the measurements presented are at 60 m/s.

No corrections were made for tunnel interference. In this closed working section, corrections would be large for such a large half model, particularly at angles of incidence from 15-30° when the wing flow is well separated. The uncorrected steady lift coefficient will have large errors (up to 9.1 in C_L) following flow separation. This is shown by the comparisons of uncorrected and corrected lift curves (Ref 10, Fig 26) for a combat aircraft half model of almost the same semi-span ($s_w = 1350$ mm compared to $s_w = 1300$ mm) and planform (compare Fig 8 of Ref 10 with Fig 1) also tested in the RAE 13ft x 9ft Wind Tunnel. However wall corrections are unlikely to affect the character of the interactions between the canard and wing flows, which is the main objective of these tests.

The static forces and moments measured by the balance and the steady and fluctuating pressure and model motion measurements using the PRESTO system were restricted generally to $\alpha = 0^\circ, 5^\circ, 10^\circ, 12^\circ$ (buffet onset), $15^\circ, 20^\circ, 25^\circ$ and 30° . The tests of the delta canard were made in March 1987: the main series of tests on the swept canard were made in June 1986 and are reported fully in Ref 3.

3. RESULTS

The static force and buffeting measurements of the present tests conform to the general character of those found in previous experiments^{1,3}. Hence it is convenient first to consider briefly the overall static forces and moments (section 3.1), the wing and canard buffeting (section 3.2) and the canard/wing flow interactions in terms of the

canard effective incidence (section 3.3). The local steady pressures and buffet excitation on the wing are considered in detail (section 3.4) and wing pressures induced by canard oscillation are discussed briefly (section 3.5).

During these tests small surface minitufts gave a general indication of the development of the viscous flow on the wing (Ref 3, Appendix A). These minituft observations are carefully related with the steady and fluctuating pressures on the wing and the wing buffeting. It is helpful to recall the main conclusions from the tests with the swept canard. The strake vortex inhibits the growth of bubble separations, increases lift and reduces buffeting (Fig 4). The further effect of a swept canard (for positive canard effective incidence) enhances the favourable effect of the strake vortex. This beneficial effect of the canard is small compared to the large favourable effect of the strake. The minituft photographs on the wing are virtually the same with the swept and delta canards and hence are not reproduced here. Nevertheless they are the first indication that both canards have roughly comparable effects on the wing flow.

3.1 Overall static forces and moments

Fig 5 shows that the effect of both the canards on the overall lift is much the same. For the delta canard (Fig 5a) the lift increases steadily with incidence so that at $\alpha = 25^\circ$, the lift coefficient of $C_L = 1.58$ is developed for both $\alpha_c = -5^\circ$ and -10° . The measurements for the swept canard (Fig 5b) are comparable but generally a little lower at the higher angles of incidence, eg at $\alpha = 25^\circ$, $C_L = 1.55$ for $\alpha_c = -10^\circ$. We shall see later (section 3.3) that for $\alpha_c = -41^\circ$ even at $\alpha = 25^\circ$ the effective incidence is still negative for both canards so that the interference effect on the wing is adverse, yet small according to Ref 3. Fig 5 shows that for $\alpha_c = -41^\circ$ the lift curves for both delta and swept canards are virtually identical and below the 'canard off' value (equivalent to $\alpha_c = 0^\circ$ according to Refs 1 and 3) included in Fig 5b.

Fig 6 shows the different effects of each canard on the pitching moments. The incremental pitching moments generated by the delta canard (Fig 6a) are appreciably higher than those due to the swept canard (Fig 6b) presumably because the centre of lift is further forward of the moment centre. For a C_L of 1.3, the change in pitching moment between $\alpha_c = -5^\circ$ and -10° is about 100% higher for the delta canard but only about 20% higher between $\alpha_c = -5^\circ$ and -41° . No comparative measurements were made in the tests of Ref 3 for the swept canard at $\alpha_c = -25^\circ$ and $R = 3.7 \times 10^6$. However some measurements were made for $\alpha_c = -25^\circ$ at reduced speed ($U = 20$ m/s, $R = 1.2 \times 10^6$) and these are included in Fig 6b to provide a rough comparison to the delta canard. The increment in pitching moment between $\alpha_c = -5^\circ$ and -25° would then be about 40% higher for the delta canard compared to the swept canard.

Fig 6 suggests that if the area of the delta canard had been reduced by about 15% it would still have given improved control power compared to the swept canard over most of the range of the control. Alternatively, the delta canard could have been displaced downstream, to give the same control power as the swept canard.

It is interesting to note that the delta canard maintains its effectiveness ($dC_m/d\alpha_c$) for $\alpha_c = -41^\circ$ in the range from $0 < C_L < 1$ (Fig 6a). In contrast the swept canard for $\alpha_c = -41^\circ$ apparently starts to lose effectiveness near $C_L = 1$. This curious anomaly in the tests of Ref 3 is genuine and occurs at both $U = 60$ and 40 m/s. It has not yet been explained and would be worthy of further investigation on a specific project.

Fig 7 illustrates the effect on the canards on the overall drag. For a given canard setting the trimmed C_D values are a little lower with the delta canard than with the swept canard (Fig 7a), as are the corresponding lift/drag ratios (L/D) when expressed as a function of trimmed C_L (Fig 7b). The reduction in L/D with the delta canard is small despite the unrealistic base drag, particularly for $C_L < 1$. If the flat plate section of the delta canard (Fig 3) had been replaced by a thin airfoil section, its large base area (and base drag) would have been eliminated giving a somewhat higher L/D . This might have been much the same or possibly even a little higher than for the swept canard.

3.2 Wing and canard buffeting

3.2.1 Wing buffeting

Fig 8 shows that the addition of either canard for both $\alpha_c = -10^\circ$ and -41° only makes relatively small changes to the wing buffeting. Fig 8a shows the excitation parameter in the first bending mode plotted against α . For $\alpha_c = -10^\circ$ the canard effective incidence (defined later) is always positive, so that the interference on the wing is favourable. The wing buffeting is much the same for both canards and a little lower than for the wing alone. In contrast for $\alpha_c = -41^\circ$ the canard effective incidence is generally negative and the interference on the wing is unfavourable. The wing buffeting is much the same for both canards and generally somewhat higher than for the wing alone. For the delta canard at $\alpha_c = -41^\circ$ the measurements were extended down to $\alpha = 5^\circ$, although this represents an unrealistic condition. Such a high negative canard setting should never be combined with such a low incidence because high negative canard settings would be utilized only for recovery at high angles of incidence. Here the buffet excitation from the separated flow on the lower surface of the canard strongly excites the wing, when the wing flow is itself attached. [This wing motion causes a feedback process which increases the canard buffeting, as discussed in Fig 10b. No comparable measurements were made for the swept canard at $\alpha_c = -41^\circ$, but a comparable increase in wing response would

be expected.] Fig 8b shows the wing buffeting measurements plotted against the overall lift coefficient. The effects of the canards on the overall lift (an increase for $\alpha_c = -10^\circ$ and a decrease for $\alpha_c = -41^\circ$) make the effect of the canard on the wing buffeting more noticeable.

3.2.2 Canard static bending moments and buffeting

For the delta canard, static bending moment coefficients, C_{mq} , and buffeting signals were measured with $\alpha_c = -5^\circ, -10^\circ, -25^\circ$ and -41° , generally over the incidence range from $\alpha = 5^\circ$ to 30° . Fig 9a shows that for all canard settings C_{mq} increases steadily with α , apart from two exceptions. For $\alpha_c = -5^\circ$ there is a sudden discontinuity in the bending moment coefficient at $\alpha = 25^\circ$. For $\alpha_c = -41^\circ$ the canard appears stalled at $\alpha = 5^\circ$. [This is an unrealistic condition according to section 3.2.1 above.]

Fig 9b shows the corresponding canard buffeting signals at 144 Hz. The fluctuating signal in mV is plotted rather than the buffet excitation parameter because of the uncertainty about the generalised mass in this mode, as discussed in section 3.2. The main feature of these measurements is that for $\alpha_c = -41^\circ$, with the canard stalled at $\alpha = 5^\circ$, the buffeting signal is remarkably high (205 mV). Thereafter the buffeting decreases as α increases, reaching a minimum at 20° before increasing again. For $\alpha_c = -5^\circ$ the buffeting reaches a maximum at $\alpha = 25^\circ$, at the discontinuity in the static bending moment coefficient. For $\alpha_c = -10^\circ$ and -25° the canard buffeting is generally somewhat smaller than for $\alpha_c = -5^\circ$.

Following previous practice with diverse canard/wing configurations^{1,10,12,14}, the canard static bending moment coefficient, C_{mq} , and the buffeting signals may be expressed as unique functions of canard effective incidence, α_{eq} .

For the symmetric swept canard in the tests of Ref 4

$$\alpha_{eq} = (1 + k_1) \alpha + \alpha_c \quad (3)$$

where k_1 = upwash factor due to the wing and the fuselage.

In Eq.(3) k_1 is a function of α_c .

It was hoped that Eq.(3) would also apply for the delta canard, but this hope was not realised, probably because of more complex interactions between the canard and wing flows combined with the effects of the leading-edge chamfer and the base flow at the trailing edge (due to the constant thickness). The relationship observed was of the form

$$\alpha_{eq} = (1 + k_1) \alpha + \alpha_c + \lambda \quad (4)$$

where k_1 and λ are functions of α_c . The values of k_1 are identical with or close to the values found in Ref 4 for the swept canard. This is reasonable because according to the theory (Ref 1, Appendix C) the upwash due to the wing should be nearly the same for the delta and swept canards. Large values of λ (given a tentative explanation elsewhere) are required to ensure that for small effective angles of incidence,

$$C_{mq} = K \alpha_{eq} \quad (5)$$

A relationship of this type appears desirable because, despite the asymmetry caused by the leading-edge chamfer on the lower surface of the isolated 65° delta of Ref 4, the angle of incidence for zero normal force was very small. Using Eqs. (4) and (5) the measurements for the delta canard can now be presented as a function of α_{eq} (Fig 10).

For the static bending moment coefficient, Fig 10a shows a unique relationship between C_{mq} and α_{eq} for $\alpha_c = -10^\circ, -25^\circ$ and -41° , over the wide range of canard effective incidence from $-10^\circ < \alpha_{eq} < 40^\circ$. This relationship is in good agreement with the normal force coefficient, C_N , measured on the isolated 65° delta wing of Ref 4 over the incidence range from $0 < \alpha < 25^\circ$. However, for $\alpha_c > 25^\circ$, the present measurements are a little lower than the wing C_N measurements from $24^\circ < \alpha < 28^\circ$. The static bending moment coefficients for $\alpha_c = -5^\circ$ differ appreciably from those for $\alpha_c = -10^\circ$. This is an anomalous result because for the buffeting signals, Fig 10b, shows that the measurements for $\alpha_c = -5^\circ$ and -10° are consistent. There is a rapid rise above about $\alpha_c = 20^\circ$, which is the same in character as that observed on the isolated wing at vortex breakdown². In order to relate the present measurements of mV to the measurements of $\alpha_{eq}(n)$ for the isolated delta of Ref 4 it is reasonable to equate the present measurements at $\alpha_c = -41^\circ$ with the measurements on the isolated delta wing at $\alpha = 24^\circ$. [This has the advantage of making the 'plateau' level of the isolated delta wing the same as that for $\alpha_c = -5^\circ$ and -10° .] Hence a signal of 20 mV on the left hand axis corresponds approximately to moderate buffeting on the right hand axis or

$$20 \text{ mV} = 10^3 \alpha_{eq}(n) = 1.5 \quad (6)$$

According to eq.(6) the maximum level of the buffet excitation parameter, at $\alpha_c = 36^\circ$, is about $10^3/\eta_0(n) = 4.5$. (The measurements on the isolated delta were terminated at $\alpha = 28^\circ$, $10^3/\eta_0(n) = 2.0$).

For $\alpha_c = -25^\circ$, where $\alpha_c > 5^\circ$, the character of the measurements is comparable with those for $\alpha_c = -10^\circ$ and -15° , with a rapid rise above about $\alpha_c = 20^\circ$. However the buffeting levels for $\alpha_c < 15^\circ$ are appreciably higher than the plateau level. Here separated flow on the wing excites light canard buffeting.

For $\alpha_c = -41^\circ$ the character of the measurements is completely different. There is a very high level $10^3/\eta_0(n) = 16$ at $\alpha = -28^\circ$ (where the canard is 'stalled'), a minimum, $10^3/\eta_0(n) = 0.75$ or light buffeting about $\alpha_c = -9^\circ$ and then a steady increase to $\alpha_c = 5^\circ$. This unusual characteristic is discussed elsewhere.

3.3 Interaction between the canard and wing flows in the (α, α_c) domain

Using Eq.4, α_c may be evaluated as a function of α for each of the four canard settings. Hence contour plots of constant α_c can be prepared in the (α, α_c) domain. From Ref 4 six contours of constant α_c relevant to the buffeting of an isolated delta may be identified.

$$\alpha_c = +4^\circ$$

The contours defining buffet onset due to the formation of a small vortex close to the leading edge on upper and lower surfaces.

$$\alpha_c = +21.5^\circ$$

The contours for light buffeting, due to the vortex burst moving just upstream of the trailing edge.

$$\alpha_c = +25^\circ$$

The contours for moderate buffeting, due to the vortex burst moving further upstream of the trailing edge.

These six contours are included in Fig 11a. In the absence of interference from the wing, Fig 11a would be sufficient to define the canard buffeting. However interference does occur under certain conditions and the experimental results indicate that the situation is more complex (Fig 11b).

The good correlation of canard buffeting measurements for $\alpha_c = -5^\circ$ and -10° (Fig 10b) suggests that for these settings there is no strong interference of the wing on the canard buffeting despite the vortex breakdown on the upper surface of the canard interacting with the wing separations. For $\alpha_c = -25^\circ$ the canard buffeting differs somewhat from that for an isolated 65° delta. Fig 10b shows that the level of buffeting for $\alpha_c < \alpha_c < 15^\circ$, ie without a burst vortex, is appreciably higher than the plateau level for an isolated delta. Hence for this setting the canard receives additional excitation from the separated flow on the wing over a region indicated roughly in the (α, α_c) domain by the cross hatching (Fig 11b). The measurements for $\alpha_c = -41^\circ$ differ from those on an isolated delta because of the strong interaction between the canard and wing flows already noted in both Figs 10b and 9b. These and the stages 1 and 2 are discussed elsewhere.

In the tests of Ref 4 there were some anomalies in buffeting measurements on the swept canard when tested in conjunction with the EAP type wing. Hence it is not possible to make a direct comparison between the buffeting on the delta and swept canards.

Fig 12 shows the contours of wing buffeting (for onset, light, moderate and heavy buffeting) in the (α, α_c) domain for both the delta and swept canards. The canard off measurements from Ref 3 are represented along the line $\alpha_c = 0^\circ$ in the usual way^{1,3}. For positive canard effective incidence the favourable effect of the delta canard is indicated by the increasing distance between the contours (Fig 12a). It is important to notice that vortex breakdown on the upper surface of the delta canard ($\alpha_c = +21.5^\circ$) leaves the wing buffeting unaltered. In complete contrast vortex breakdown on the lower surface of the delta canard (for large negative values of α_c combined with low α) creates wing buffeting with attached flow. This is shown clearly by the sudden change of the wing buffet onset contour along the line $\alpha_c = -21.5^\circ$ at low angles of incidence. This is an interesting but unrealistic condition.

Fig 12b shows the corresponding buffeting contours for the wing tested with the swept canard. Here the canard off measurements were slightly different and have to be represented according to Eq.(3), rather than Eq.(4) as appropriate to the delta canard. With respect to buffet onset and light buffeting, comparison of Fig 12a&b shows that the contours for buffet onset and light buffeting on the wing are nearly the same with the swept and delta canards. However, for the moderate buffeting contour there are some differences. The swept canard is inferior to the delta canard for a realistic setting - say about $\alpha = 20^\circ$, $\alpha_c = -20^\circ$ but superior to the delta canard for an unrealistic setting of about $\alpha = 17^\circ$, $\alpha_c = 41^\circ$. The intermediate buffeting contour,

$10^3/\sqrt{Re(n)} = 2.6$, encloses a somewhat larger area for the swept canard than for the delta canard. The heavy buffeting contour is poorly defined for both swept and delta canards, but encloses a somewhat smaller area for the swept canard than for the delta canard.

These differences in wing buffeting are comparatively small, consistent with the small differences in the steady and random pressure fluctuations on the wing, which are now discussed.

3.4 Steady pressures and buffet excitation on the wing

The general development of the wing flow with the delta canard shown by the mini-tufts resembles closely that with the swept canard. Consistent with this the steady and random pressure distributions on the wing are virtually identical for both canards. This is illustrated by a direct comparison of the pressure distributions for $\alpha_c = -10^\circ$ and -41° over the incidence range when canard/wing interference is important, i.e. $15^\circ < \alpha < 30^\circ$.

For $\alpha_c = -10^\circ$, Figs 13, 14 and 15 show the steady and random pressure distributions at $\alpha = 15^\circ$, 20° and 30° respectively. There are no significant changes in character, although there are differences between the steady pressures (typically 0.2 in C_p) and also between the random pressures (sometimes as much as 0.05 in p/q). An indication of the favourable interference between the wing and canard flows is provided by the overall lift coefficients, which are shown for both canards and also with the canard off.

Figs 16, 17 and 18 show the corresponding pressure distributions for $\alpha_c = -41^\circ$. For this canard setting the interference on the wing is large and unfavourable for $\alpha = 15^\circ$ and 20° and small and favourable for $\alpha = 30^\circ$ (indicated by the C_l values) as discussed fully in Ref 3. Thus there is a radical change in interference between $\alpha_c = -10^\circ$ and $\alpha_c = -41^\circ$. Despite this change in the type of interference on the wing, there is again no change in character in the type of the wing pressure distributions with the two canards.

3.5 Pressures induced on the wing by canard oscillation

An important question about canard/wing interaction is the magnitude of the forces induced on the wing by the dynamic movement of the canard, particularly when the canard is operated in an active control mode over a range of frequencies. There are two specific questions:

- (1) Can dynamic movement of the canard (about a constant mean setting) alter the mean flow on the canard and hence alter the mean flow on the wing?
- (2) Can dynamic movement of the canard induce significant dynamic pressures on the wing, possibly reducing the pitching moment generated by the canard itself?

Both questions are being answered by tests for several different configurations of the large half model of the HIRM 1. With respect to the first question, a change in mean flow has not been observed for any configuration so far tested. This is an important negative conclusion because for conditions where the canard/wing interaction is large a variation in mean flow due to canard dynamic movement could have serious consequences.

With respect to the second question, Fig 19 gives an overview of the present position. When the standard HIRM 1 canard oscillates close to the basic HIRM 1 wing with an uncambered leading edge (Fig 19a) the dynamic pressures induced on the wing are small and the net dynamic pitching moment generated by the canard is reduced by a maximum of about 10% (Ref 2, Fig 16). [The dynamic lift and pitching moment induced on the wing are estimated approximately by integrating the local pressures on the upper and lower surfaces as described on the Appendix of Ref 2.] When the delta canard (Fig 19b) or the swept canard (Fig 19c) oscillate well upstream of the modified wing (present comparative tests) the local induced pressures on the wing are one order of magnitude smaller than for the basic HIRM 1 wing². Hence here the dynamic pitching moments induced on the wing must be very small - perhaps about 1% of those generated by the canard. Although the local pressures induced on the modified wing are very small (at least with a canard amplitude of only 1°), they have a good coherence with the canard motion for attached flow on the wing. This implies a high degree of causality on the wing. [See discussion of Figs 4 and 5, Ref 14.]

For completeness it may be added that when the standard HIRM 1 canard oscillates close to the HIRM 1 wing with a highly cambered leading edge (Fig 19d and unpublished tests made in December 1987) the dynamic pressures induced on the wing are two orders of magnitude smaller than with the uncambered leading edge², so that there is no reduction in dynamic pitching moment. Presumably this change is caused by the displacement of the wing leading edge relative to vorticity shed from the canard.

5. CONCLUSIONS

This Paper suggests six main conclusions with respect to the comparison of a delta canard and a swept canard used in conjunction with an EAP type wing. In spite of the unrealistic drag of the delta canard we may conclude from the experiments:

- (1) The delta canard has the same general effect on the wing flow as the swept canard, for the same canard area.

- (2) The delta canard provides comparable control power to that of the swept canard over a wide range of incidence.
- (3) For positive canard effective incidence and hence favourable interference, the delta canard provides a higher overall lift at a given incidence
- (4) For realistic conditions with positive values of canard effective incidence, vortex breakdown occurs on the upper surface of the canard at about $\alpha_c > 21.5^\circ$, leaving the wing buffeting unaltered.
- (5) For unrealistic conditions with negative values of canard effective incidence, vortex breakdown occurs on the lower surface of the canard at about $\alpha_c < -21.5^\circ$. Here the burst canard vortex excites significant wing buffeting even when the wing flow is attached.
- (6) Oscillation of either the swept or the delta canard (representing ACT application) does not alter the mean flow on the wing or induce significant dynamic pitching moments on the wing.

REFERENCES

1. D.G. Mabey, B.L. Welsh and C.R. Pyne: "Interaction between the canard and wing flows on a model of a typical combat aircraft". 1987 RAE Technical Report 87019
2. B.L. Welsh and C.R. Pyne: "Wing pressures induced by the oscillation of a canard on the High Incidence Research Model (HIRM 1)". 1986 RAE Technical Report 86039
3. D.G. Mabey, B.L. Welsh and C.R. Pyne: "Interaction between the canard and wing flows on a model typical of the EAP configuration". 1987 RAE Technical Report 87062
4. D.G. Mabey and G.F. Butler: "Measurements of buffeting on two 65° delta wings of different materials". 1977 Paper 6, AGARD CP 226
5. D.G. Mabey, B.L. Welsh and C.R. Pyne: "Fin buffeting at high angles of incidence on combat aircraft configurations". 1987 RAE Technical Report 87051
6. B.L. Welsh and D.M. McOwat: "PRESTO - a system for the measurement and analysis of time-dependent signals". 1979 RAE Technical Report 79135
7. D.G. Mabey: "Some aspects of aircraft dynamic loads due to flow separation". 1987 RAE Technical Memorandum Aero 2110, AGARD R750
8. J.G. Jones: "A survey of the dynamic analysis of buffeting and related phenomena". 1972 RAE Technical Report 72197
9. D.G. Mabey and B.E. Cripps: "Some measurements of buffeting as a flutter model of a typical strike aircraft". 1982 Paper 13 AGARD CP 339
10. P.R. Achill and R.F.A. Keating: "Calculation of tunnel wall interference from wall-pressure measurements". 1985 RAE Technical Report 85086
11. D.G. Mabey and B.L. Welsh: "Canard and wing buffeting on a model of an advanced fighter aircraft". 1985 RAE Technical Memorandum Aero 2035
12. D.G. Mabey and B.L. Welsh: "Wing and canard buffeting on a flutter model of the EAP aircraft". 1986 RAE Technical Report 86009
13. D.G. Mabey and B.L. Welsh: "Further measurements of wing and canard buffeting on a flutter model of the EAP aircraft and some flight comparisons". 1987 RAE Technical Report 87017
14. D.G. Mabey and B.L. Welsh: "The measurement of oscillatory pressures with discrete and sweep excitation". 1987 J. Fluids and Structures, Vol 1, No.1, pp 95-105

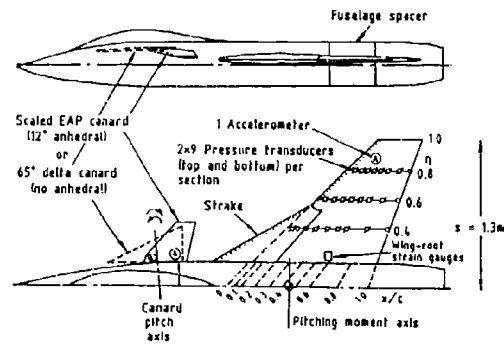


Fig.1 Details of model

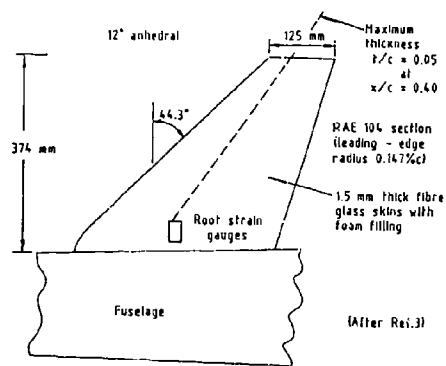
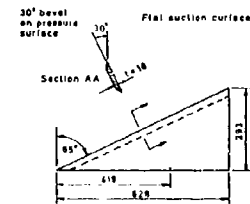


Fig.2 Details of swept canard



Dimensions in mm

Fig.3 Details of 65° delta canard

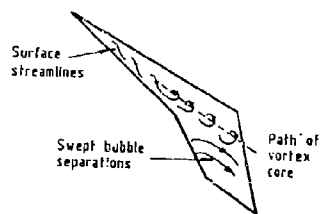


Fig.4 Effect of stroke vortex on wing flow

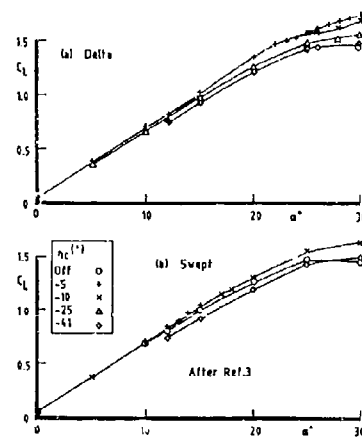


Fig.5 Effect of canards on lift

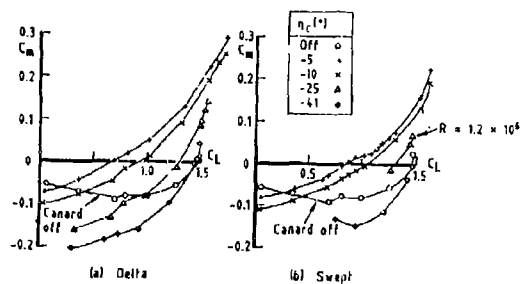


Fig. 6 Effect of canards on control power

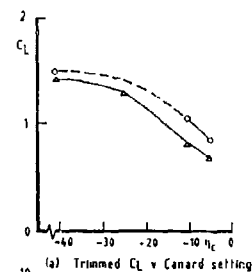
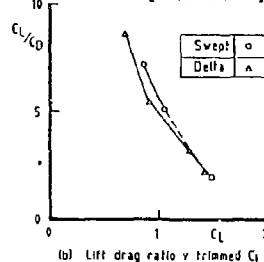
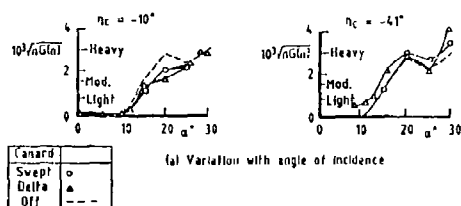
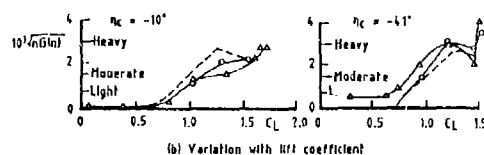
(a) Trimmed C_L v Canard setting

Fig. 7 Effect of canards on drag

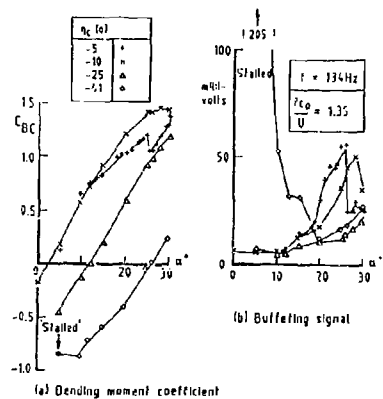


(a) Variation with angle of incidence



(b) Variation with lift coefficient

Fig. 8 Buffet excitation parameter in wing first bending mode for both canards.



(a) Bending moment coefficient

(b) Buffeting signal

Fig. 9 Delta canard bending moment coefficient and buffeting signal v incidence

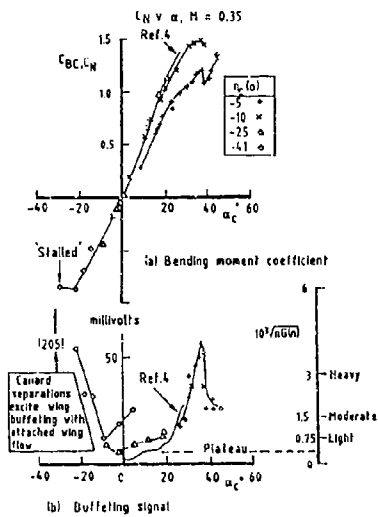


Fig. 10 Delta canard - bending moment coefficient and buffeting signal v canard effective incidence

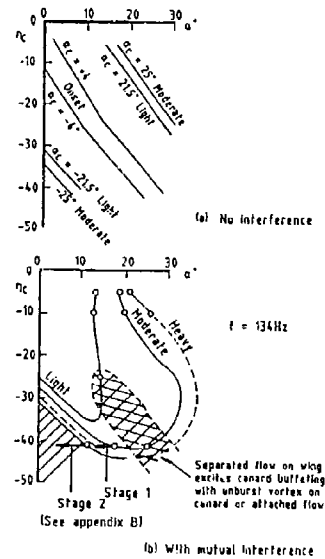


Fig. 11 Delta canard buffeting contours in first bending mode in (α, η_c) domain

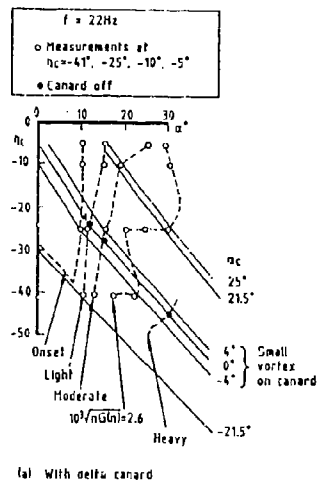


Fig. 12 (a) Wing buffeting in first bending mode in (α, η_c) domain

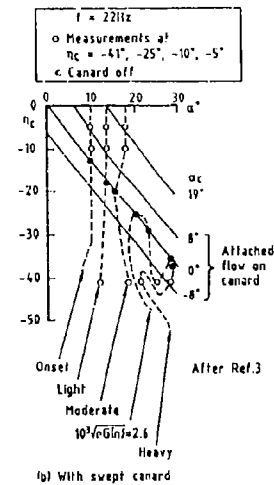


Fig. 12 (b) Wing buffeting in first bending mode in (α, η_c) domain

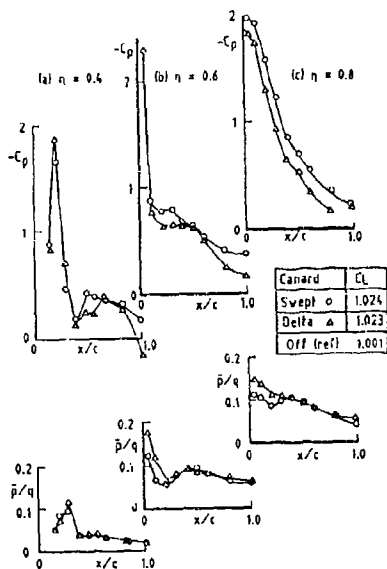


Fig.13 Effect of different canards on wing steady and random pressure distributions, $\eta_c = -10^\circ$, $\alpha = 15^\circ$

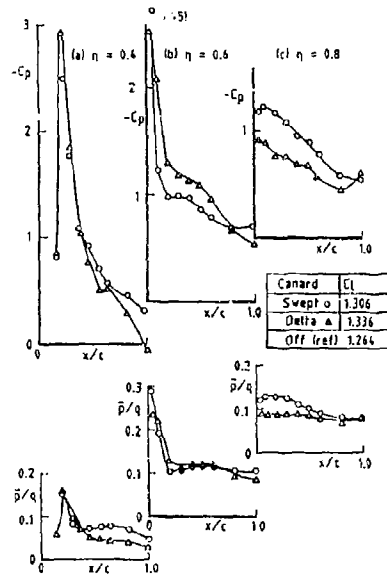


Fig.14 Effect of different canards on wing steady and random pressure distributions, $\eta_c = -10^\circ$, $\alpha = 20^\circ$

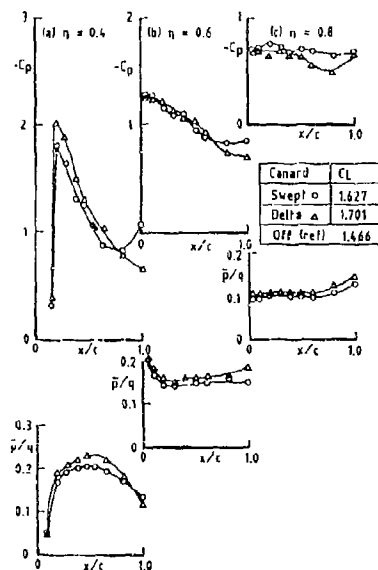


Fig.15 Effect of different canards on wing steady and random pressure distributions, $\eta_c = -10^\circ$, $\alpha = 30^\circ$

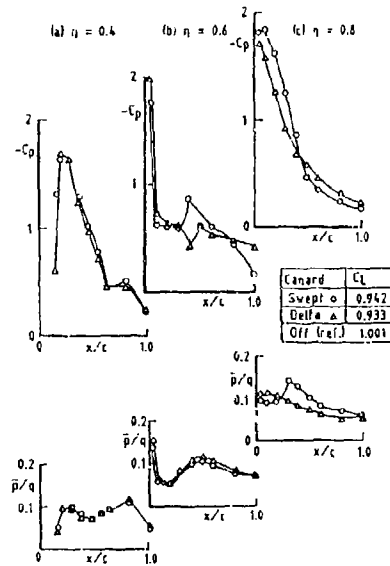


Fig.16 Effect of different canards on wing steady and random pressure distributions, $\eta_c = -41^\circ$, $\alpha = 15^\circ$

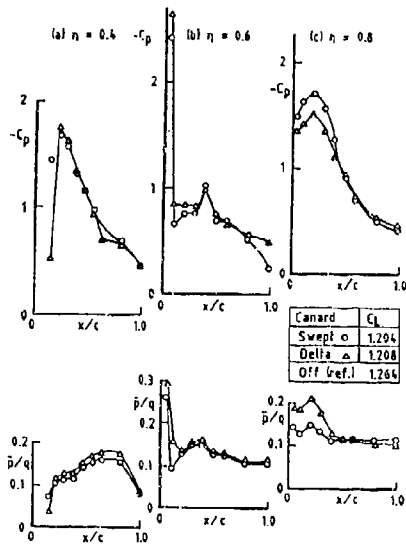


Fig.17 Effect of different canards on wing steady and random pressure distributions, $\eta_c = -41^\circ$, $\alpha = 20^\circ$

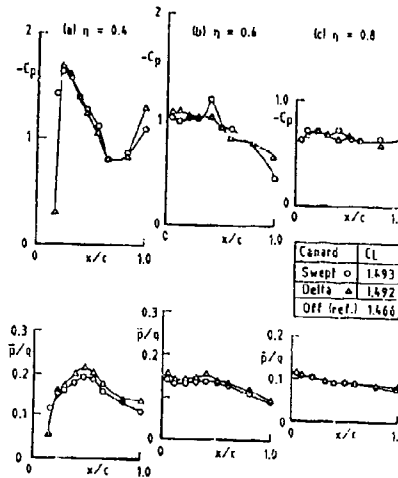


Fig.18 Effect of different canards on wing steady and random pressure distributions, $\eta_c = -41^\circ$, $\alpha = 30^\circ$

Configuration	(Date of test)	Induced effects
(a) HIRM 1 - Uncambered wing	(October 1985 Ref. 2)	Small $0^\circ \leq \alpha \leq 12^\circ$ None $\alpha \geq 12^\circ$
(b) EAL type wing - Delta canard	(March 1987)	Very small $0^\circ \leq \alpha \leq 10^\circ$ None $\alpha \geq 12^\circ$
(c) EAP type wing - Swept canard	(June 1986)	Very small $0^\circ \leq \alpha \leq 10^\circ$ None $\alpha \geq 12^\circ$
(d) HIRM 1 - Highly cambered wing	(December 1987)	None $0^\circ \leq \alpha \leq 30^\circ$

Fig.19 Overview of wing pressures induced by oscillation of canard

THE EFFECT OF RAPID SPOILER DEPLOYMENT ON THE TRANSIENT FORCES ON AN AEROFOIL

by

P.W. Bearman, J.M.R. Graham and P. Kalkanis

Department of Aeronautics, Imperial College, London, SW7 2BY

Summary

The Discrete Vortex Method (DVM) is used to simulate the two-dimensional separated flow generated by a spoiler over the upper surface of an aerofoil. Cases of fixed and moving spoilers are presented and particular attention is paid to the phenomenon of short duration adverse lift which can be induced by rapid spoiler deployment. Forces and pressure distributions on the aerofoil and spoiler are calculated and compared, where possible, with experimental results. The model that has been developed predicts the delay times to maximum adverse lift at very high spoiler deployment rates, as well as allowing the forces on the aerofoil and the spoiler to be computed separately. Numerical results are in good agreement with experiment.

1. Introduction

Spoilers for aeronautical applications are conventionally sited on the rear half of the upper surface of the wing of an aircraft, and when deployed have the long term effect of increasing drag and decreasing lift, thus controlling symmetric and asymmetric lift. Spoilers have become widely used to provide roll control on high manoeuvrability combat aircraft because of the reduced efficiency of conventional ailerons at high speeds. For obvious reasons they tend to become ineffective at high angles of attack when the wing section is fully stalled (WENTZ et al (1)). They also suffer from increasing time lag between operation and response the further forward they are sited on the aerofoil. There is now interest in the question of how far spoilers can be used as fast aerodynamic devices in active control technology (ACT) applications to improve the efficiency and cost effectiveness of military and civil aircraft. In order to use spoilers for rapid manoeuvre control or gust alleviation high rates of deployment ($\sim 400^\circ/\text{sec}$) are required. At such high rates of deployment, spoiler effects are aerodynamically unsteady. It has been observed (e.g. MABEY et al (2), CONSIGNY et al (3)) that in these cases a period of adverse lift increase is induced before the intended reduction in lift occurs. The cause of the adverse lift is the formation of a very strong vortex behind the spoiler which induces a large suction on the rear upper surface of the aerofoil. Eventually the vortex is convected away by the stream leaving a fluctuating region of reduced total pressure behind the spoiler and a reduction in overall circulation. This is rather similar to the vortex build up and shedding which occurs during dynamic stall of a rapidly pitching aerofoil. For slow rates of spoiler deployment the height reached by the spoiler tip above the aerofoil at the end of the vortex build up phase is much less and as a result the vortex and the vortex induced lift are both very weak. In this case adverse lift is not observed.

The adverse lift generated by spoiler deployment is induced by the formation and shedding of a strong coherent vortex along the span of the spoiler. This phenomenon is strongly two-dimensional and a two-dimensional calculation method which models the vortex sheet evolution can therefore be expected to give useful predictions for the initial phase of the flow. The discrete vortex method which has been used here is inviscid and incompressible but relatively inexpensive to compute and because of its Lagrangian basis gives a much better delineation of the structure of a rolled up vortex sheet at high Reynolds numbers than finite difference or element methods. The restriction to incompressible flow is not considered to be serious for the present purposes since adverse spoiler lift occurs over a range of Mach numbers and the qualitative development of the phenomenon is the same. However, inviscid vortex methods tend to become less accurate over long times as diffusion processes become more significant. The flow also becomes increasingly three dimensional with time.

Although spoilers have been used extensively over the years, there has been little theoretical information available on their performance characteristics, particularly transient behaviour. The mean flow about spoilers has been modelled by the wake source method, first applied to the problem by PARKINSON and JANDA (4). A later improved version of the method has been published recently (PARKINSON and YEHUNG (5)). In the wake source method the base pressure coefficient is an empirical input. In an attempt to remove this, TOU and HANCOCK (6) and (7) developed a different method based on a vortex sheet representation of the wake. The surface of the aerofoil and spoiler were modelled with panel elements of piecewise continuous vorticity. The separating thin shear layers from the spoiler tip and the trailing edge were modelled similarly using elements of constant vorticity. However, the length of the separated vortex sheets and the strength of the two point vortices used to "close" the wake were empirical inputs.

In the present work the discrete vortex method (using direct interaction between moving point vortices) has been used to represent the separated flow. The flow, which is assumed to be two dimensional, separates at the spoiler tip and the trailing edge of the aerofoil. The vorticity field is represented by concentrated vortex lines appearing as points in the cross sectional plane. Circulation is conserved on these vortices as they move with the fluid particles in the flow. The velocity field is calculated at the locations of each vortex as a sum of attached potential flow about the body and a velocity field calculated by the Biot-Savart law due to all the vortices in the flow. The computation of this interactive component at each time step is proportional to the square of the number of vortices in the flow and hence increases rapidly with time. Using a multi-stage analytical transformation a Joukowski aerofoil plus spoiler was transformed to a circle in which an image system for vortices was used. Vortex positions and velocities were calculated in the circle plane and, when needed, were transformed back to the aerofoil plane. An analytical transformation was used in preference to a numerical one, such as for example one based on Schwartz-Christoffel theory, because of its faster speed of computation. Since the study was concerned with investigating the general development and effect of the spoiler vortex, the restriction to a Joukowski aerofoil was not considered to be important. However, the transformation did have a disadvantage in that the spoiler could not be continuously modelled down to the fully closed position because of the implied curvature of the spoiler resulting from the transformation. At deployment angles below about 10° degrees the spoiler became increasingly distorted.

2. Computational Method

The following sequence of transformations (PARKINSON (8)) was used to map the field outside the Joukowski aerofoil (z_1 -plane) fitted with an upper-surface spoiler of arbitrary size, deployment angle and chordwise position, into the field outside the unit circle (z_7 -plane):

$$z_1 = z_7 - \eta e + \eta^2 / (z_7 - \eta e) \quad 1(a)$$

$$z_3 = \exp \{ i(\pi/2 - \delta) \} (\exp(-i\phi) z_2 - R) + C \quad 1(b)$$

$$z_4 = -i \ln \{ (z_3 - C) / (z_3 + C) \} \quad 1(c)$$

$$z_4 = -i\alpha/\pi \ln\{z_5 + \alpha/\kappa\pi\} + i\beta/\pi \ln\{z_5 + \beta/\kappa\pi\} + \beta \quad 1(d)$$

$$z_5 = \varepsilon + i\rho(z_6 - 1)/(z_6 + 1) \quad 1(e)$$

$$z_7 = \exp(i\alpha_0)z_6 \quad 1(f)$$

where

$$\kappa = \frac{1}{\pi} \exp\{\pi\gamma/(\alpha - \beta)\} \alpha^{a/(\alpha - \beta)} (-\beta)^{-b/(\alpha - \beta)} \quad 1(g)$$

The constant 'e' defines the aerofoil thickness. For the 11% thick aerofoil used here $e=0.09237$. The other constants are defined in fig. 1, which shows the sequence of boundaries generated. It is important to note that all equations 1(a) to 1(f) can be inverted simply except for 1(d). Thus, whereas z_1 can be found directly from any value z_7 in the circle plane, the reverse is not possible without time consuming iteration for each point. A direct non-numerical transformation from the circle plane in which the computation is performed to the physical plane greatly reduces the computing time for the discrete vortex method and this was a major reason for choosing such a transformation. In the present study a spoiler of length 10% of the aerofoil chord was used and tests were made with the spoiler sited at different locations on the upper surface of the aerofoil. It should be noted that the total transformation does not tend to the identity transformation for very large z_1 and z_7 but to

$$z_1 = A z_7 \quad (2)$$

where A is a constant. This implies a rotation and a magnification of the free stream between the two planes which can be calculated by an expansion of equation 1(a) to 1(f) for large z_1 . The correctness of the transformation method was checked for the case of a spoiler normal to the surface of a symmetric Joukowski aerofoil. Attached flow results for the pressure distribution were compared with results for the same Joukowski aerofoil with normal spoiler given by PARKINSON and JANDALI(4).

In the case of a moving spoiler the normal velocity at the surface of the spoiler, using an axis system fixed in the aerofoil, is non-zero. This was modelled using a distribution of sources and sinks on the spoiler. The source/sink distribution was defined for convenience in the straight-line plane (z_5 -plane), and was represented on the part of the real axis BD corresponding to the spoiler by piecewise constant surface panels. In cases where the spoiler was moving its position and hence the transformation were recalculated at each time step.

The flow field is modelled in the present study by a combination of an irrotational stream and a distribution of vortices representing the separated vortex sheets being shed into the flow. The aerofoil/spoiler combination was transformed into a circle. It was assumed that the flow separation occurred only at the two sharp edges located at the spoiler tip and the aerofoil trailing edge. Therefore, in the circle plane vortices were released from the transformed positions of the spoiler tip and the trailing edge on the circle. The complex potential in the transformed plane may be written as:

$$w(\zeta) = V_\infty \left(\zeta e^{i\alpha} + R^2 e^{i\alpha}/\zeta \right) + i \sum_{j=1}^N \frac{\Gamma_j}{2\pi} \ln \left\{ \frac{(\zeta - \zeta_j)}{(\zeta - R^2/\zeta_j)} \right\} + \frac{i\Gamma_b}{2\pi} \ln(\zeta) \quad (\zeta \equiv z_7) \quad (3)$$

The first term on the R.H.S. of eq. (3) represents the potential flow past the circle, the second term the vortices in the flow field and the third term bound circulation. The last term is the circulation which the aerofoil has, prior to the spoiler being raised (i.e. the initial condition ($t=0$) for the attached flow over the aerofoil prior to spoiler deployment). The velocity field is given by:

$$dW(\zeta)/d\zeta = u - iv \quad (4)$$

This equation is employed to calculate the induced velocity at a vortex position due to the free stream and all the vortices in the flow field. In the case of the moving spoiler eq. (3) includes a source density (m) contribution

$$w_1(\zeta) = w(\zeta) + \int_B^D \frac{m(s)}{2\pi} \ln(z_5 - s) ds \quad (5)$$

When a spoiler is deployed rapidly the flow forms a strong tightly rolled up vortex behind the spoiler and a weaker vortex sheet, not necessarily rolled up, is shed downstream from the trailing edge due to the changing aerofoil circulation. These vortex sheets, represented by an array of discrete vortices, were required to be shed from the spoiler tip and the trailing edge so that the condition of zero pressure jump across each sheet was satisfied. This condition implies that shed point vortices are convected with the local velocity of the fluid at their respective positions and that for sharp edges a Kutta-Joukowski condition applies. This condition can be applied with no ambiguity for point vortices if, as here, the edges are cusped. However, the strength of each vortex adjacent to an edge in the process of being formed and shed during the current time step is not fixed by the above conditions, since a finite strength vortex can only be placed in the flow at the non-zero distance from the edge. In order to avoid the need for an arbitrary distance parameter such as has been employed in some simulations, the segment of each vortex sheet adjacent to the edge was modelled by a point vortex of strength Γ_j growing from the start of each time step. Its strength and position at the end of the step were obtained by integration of the equations for the Kutta condition and a condition of zero net force on the vortex modelled as a concentrated core and a sheet (cut).

This procedure provides a rational method of shedding point vortices first used by BROWN and MICHAEL (9) for steady slender body flow, and by ROTT (10) for unsteady flow. It has been shown by GRAHAM (11) that this model also implies a similarity solution for the starting flow behind any aerofoil or other body over which a circulatory flow suddenly develops. For cusped edges and impulsively started flow where there is no preexisting flow off the edge in question the solution of the Brown and Michael equations for the initial growth and motion of the shed vortex is:

$$\Gamma_j \left(\frac{2V_0}{5} \right)^{1/2} \frac{\pi V_1}{\kappa} \Delta t^{3/2} \quad 6(a)$$

$$z_{1j} = z_{ic} + \frac{2}{3} V_0 \frac{\Lambda t}{\kappa} \quad 6(b)$$

where V_0 and V_1 are the asymmetric and symmetric parts of the velocity at the edge Z_0 and Δt is the time step. In this case the vortex moves initially along a line perpendicular to the bisector through the edge.

In the present investigation the starting condition for the development of the separated flow was normally an attached flowfield over the aerofoil at a specified incidence with appropriate circulation for the aerofoil with the spoiler fully retracted. In the case of a non-moving spoiler the starting condition corresponds to the sudden appearance of the spoiler fully deployed into the preestablished airstream at $t=0$. It is not equivalent to the infinite limit of increasing rate of spoiler deployment since the latter would also have an infinitely strong disturbance flowfield associated with the spoiler motion. This case will be referred to as the fixed spoiler. In the case of a spoiler deployed at a finite rate the spoiler moves continuously from a specified starting angle to its final position. This will be referred to as the moving spoiler.

Due to the nature of the velocity field generated by a point vortex, large velocities are induced when vortices come close together or near the surface of the aerofoil and spoiler. A number of different techniques have been devised over the years in an attempt to eliminate the instabilities inherent (MOORE (12)) in a vortex sheet of zero thickness and its representation by discrete points. The main technique applied in the present study was the use of a cut-off radius to limit the magnitude of the vortex induced velocities (CHORIN (13)). This is effectively a smoothing device for the velocity field. Here, vortices with a core size of $a/c=0.007$ (c =chord of aerofoil) were found to be sufficient.

A non-dimensional time step of $\Delta t = U_\infty \Delta t / c = 0.005$ was chosen as a compromise between accuracy and computational efficiency. For the moving spoiler tests a smaller time step was used, especially for the initial opening stage, which depended on the angular velocity of the spoiler.

The force Z_f induced on the body by the free stream and the vortices was calculated using the momentum theorem derived from Blasius' equation:

$$Z_f = -i\rho \frac{d}{dt} \sum_{j=1}^N I_j \left(\zeta_j - R^2 / \zeta_j^* \right) \quad (7)$$

The lift and drag force components along the y-axis and x-axis respectively are equal to the imaginary and real part of eq.7.

Forces on the aerofoil and spoiler were also obtained by surface pressure integration, using Bernoulli's unsteady equation for pressure. The unsteady term $(\partial\Phi/\partial t)_s$ was calculated by time differencing and integrating the surface velocity around the circle in the transformed plane.

3. Results

3.1 Fixed spoiler results

Figure 2 shows the development of the separated flow behind the fixed spoiler deployed at 90° at the 70% chord position. The aerofoil is at 12° incidence to the free stream. A strong vortex develops behind the spoiler growing in size until it starts to interact with the trailing edge. At that moment, the relatively weak vortex sheet shed from the trailing edge strengthens and starts to roll up due to the anticlockwise flow generated by the spoiler vortex. Subsequently, this trailing edge vortex starts to spread into the formation region of the spoiler vortex eventually disrupting the sheet from the spoiler tip, which feeds it. This in turn causes the spoiler vortex to be shed, after which the cycle repeats itself. The development of the spoiler vortex leads to a large suction pressure over the rear upper surface of the aerofoil which lies beneath it. The development of the pressure distribution over the aerofoil surface calculated from the unsteady Bernoulli equation is shown in figure 3.a. The spoiler angle and spoiler position determine the strength and duration of the suction pressure generated. The higher the spoiler angle and the further forward the spoiler on the aerofoil surface, the larger and longer duration generally is the suction pressure generated. The pressure distribution over the spoiler shown in figure 3.b is near stagnation at the upstream side of the root of the spoiler and then decreases and becomes negative near the spoiler tip. The back surface of the spoiler is characterised by suction of nearly constant strength, at any given time. As the flow develops further, the suction at the back of the spoiler drops, and this is associated with the rearward convection past the aerofoil trailing edge of the positive vortex cluster shed by the spoiler.

Figure 4 shows a long term averaged pressure distribution compared with experimental mean pressure measurements on a similar thickness aerofoil (PARKINSON and YEUNG (5)). The resulting lift force time history corresponding to the fixed case, is shown in figure 5.a and compared with experimental and theoretical (wake source model) long term mean results in figure 5.b. The 'adverse' positive lift phase due to the formation of the spoiler vortex is clearly visible in each case of the vortex computation. The lift starts to collapse at the time when the spoiler vortex starts to interact strongly with the trailing edge. For this reason the further forward the spoiler is located the longer the adverse phase. After the vortex is shed the lift oscillates as it decreases towards an asymptotically lower value. Figure 6 shows the variation of the long term mean lift with incidence compared with results from TOU and HANCOCK (6).

An advantage of the numerical method developed here is that unlike experimental methods (where overall forces on the aerofoil and spoiler have been obtained by integrating pressures measured on the surface of the aerofoil only), forces may be easily obtained separately on the aerofoil and on the spoiler. The spoiler normally carries negative lift force depending on the spoiler angle or the aerofoil incidence, decreasing in magnitude as the flow develops. Therefore in experiments, forces are overestimated if measured during the initial stages of the impulsive flow and the spoiler contribution is not included.

3.2. Moving spoiler results

When the spoiler is deployed at a finite rate starting at a small angle $\delta \rightarrow 0$ the inflow into the opening space behind the spoiler is initially very large leading to some difficulty in establishing a stable position for the initial vortex. This type of opening flow has been analysed by CHENG and EDWARDS (14). An exact comparison between this work and the spoiler flow described in the present paper was not possible because of the curvature of the spoiler imposed by the transformation. Very fast spoiler deployment rates have been investigated in the present study. The time T_0 between start and finish of deployment ranged between 0, the fixed case, and $U=T_0/c = 4.0$. A constant angular velocity was assumed. These rates correspond to the order of $500^\circ/\text{sec}$. and higher for full scale aircraft at high subsonic speeds.

Figure 7.a shows the initial flow development behind the spoiler as it moves continuously from 30° to 90° . A long term flow development is shown in Figure 7.b for the case when the spoiler has been deployed from 10° to 30° over a time in which the aerofoil travels two chord lengths. The phases of the flow development in both cases are very similar to the fixed spoiler case. Figure 8

shows the lift coefficient time history compared with measured results from KALLIGAS (15). The trends of the two time histories are similar but the starting conditions and hence the lift levels are different. Kaligas' experiment had a starting condition of a slightly raised spoiler with a pre-established separated flow which could not be reproduced conveniently in the numerical model. However, the incremental increase in C_L from the start of the calculation to maximum adverse lift ($\Delta C_{L,a}$) predicted by the numerical method is in good agreement with that predicted experimentally i.e. $\Delta C_{L,a} \approx 0.26$ and 0.25 respectively. Also it should be noted that the experimental lift (KALLIGAS (15)) was measured on the aerofoil only and not on the spoiler. However, integration of the computed pressure distribution over the spoiler and aerofoil separately showed that the spoiler only contributed on average a small lift coefficient (~ -0.025) after the initial period of motion. During the initial period when the spoiler is at low angles moving upwards rapidly there is a large suction force between the spoiler and the aerofoil. The latter therefore experiences a large upward force counterbalanced by a similar downward force on the spoiler.

Figure 9 shows a typical time history of lift for a rapid 40° spoiler deployment, for $U_\infty/c = 0.19$

Two delay times are significant:
 t_a : time to maximum adverse lift and
 t_o : time to onset of lift change.

For the deployment rates studied, the delay before the onset of adverse lift is very short, while maximum adverse lift is reached in the early stages of the spoiler motion (in agreement with experimental observations by MABEY et al (2)). Final lift levels are only reached long after the spoiler has come to rest. Fast but finite rates of spoiler deployment are often found to be associated with some apparent delay before the onset of adverse lift (point B in figure 9). This indicates that the separation immediately behind the spoiler may not develop into a concentrated vortex until higher spoiler deflections are reached (MABEY et al (2)). Also, it was found that the time to reach the peak of adverse lift increases for higher deployment rates due to the greater effective distance the vortex has to travel to reach the trailing edge. This was also found to be the case by KALLIGAS (15). The onset times and times to maximum adverse lift are plotted against non-dimensional time deployment in figure 10 and compared with measured data from KALLIGAS (15). The measured and predicted times are in good agreement.

4. DISCUSSION

The main feature of flow induced by rapid spoiler deployment is the formation of a strong vortex behind the spoiler. This vortex grows rapidly causing a region of suction on the rear upper surface of the aerofoil. This adverse lift continues to grow until the shear layer feeding the vortex starts to interact with the trailing edge. At this point fairly strong opposite signed vorticity is induced from the trailing edge and is convected round into the spoiler tip region interfacing with the main shedding sheet. The spoiler vortex then stops growing and starts to convect downstream causing the lift to drop. The flow pattern then repeats with the development of another but more diffuse vortex behind the spoiler causing another smaller rise in the lift and so on. The lift

continues to fluctuate with some periodicity evident but reduced amplitude. The asymptotic mean level reached is lower than the starting value which is the primary desired effect of the spoiler. The degree of adverse lift attained depends on fast rates of spoiler deployment, so that the spoiler has generated a significantly strong vortex before strong interaction with the trailing edge begins. For a spoiler at 70% chord this interaction starts at a non-dimensional time of order

$$U_\infty t/c \approx 0.6$$

and spoiler opening rates which are comparable with this will generate adverse lift. For spoilers sited further forward the time is proportionally longer, for example: $U_\infty t/c \approx 1.0$ at 50% chord, and the adverse lift effect is greater.

This raises the interesting possibility of using upper surface spoilers situated forward on the aerofoil to generate short bursts of controlled positive lift, particularly when the wing is close to the stall.

Even at slow rates of deployment some initial vortex shedding will pass relatively slowly across the aerofoil surface when the spoiler is located far forward. This may explain the observed slow aerodynamic response of spoilers located on the forward part of a wing.

5. Conclusions

- (1) Separated time dependent flow over an aerofoil with a spoiler has been simulated by a numerical Discrete Vortex Method. Cases of sudden spoiler appearance (fixed spoiler) and fast but finite deployment rates have been studied.
- (2) The results clearly show the adverse lift phase associated with the development of a strong vortex behind the spoiler.
- (3) Reasonable agreement is obtained where comparison is possible with experiment, both for the initial flow and the long time average flow.

6. REFERENCES

1. Wentz, W.H. Jr., Ostowari, C. and Seetharam, H.C. "Effect of design variables on spoiler control effectiveness, hinge moments and wake turbulence" AIAA paper 81-0072 (1981).
2. Mabey, D.G., Welsh, B.L., Stott, G. and Cripps, B.E. "The dynamic characteristics of rapidly moving spoilers at subsonic and transonic speeds" RAE Tech Rept. 82010 (1982).
3. Consigny, H., Gravelle, A. and Molinaro, R. "Aerodynamic characteristics of a two-dimensional moving spoiler in subsonic and transonic speeds", J. Aircraft 21, p. 687 (1984).
4. Parkinson, G.V. and Jandali, T. "A wake source model for bluff body potential flow", J. Fluid Mech. Vol. 40, pt. 3, p. 377 (1970).
5. Parkinson, G.V. and Yeung, W. "A wake-source model for aerofoil with separated flow" J. Fluid Mech. 179, p. 41 (1987).
6. Tou, H.B. and Hancock, G.J. "Supplement to an inviscid model prediction of steady two-dimensional aerofoil-spoiler characteristics at low speeds. Queen Mary College Rept. EP-1056 (1983).
7. Tou, H.B. and Hancock, G.J. "An inviscid model for the low speed flow past an aerofoil-spoiler flap configuration. Queen Mary College Rept. EP-1067 (1985).
8. Parkinson, G.V. Private Communication (1986).
9. Brown, C.E. and Michael, W.H. "On slender delta wings with leading edge separation". NACA Tech Note 3430 (1955).
10. Rott, N. "Diffraction of a weak shock with vortex generation" J. Fluid Mech. 1, p. 111 (1956).
11. Graham, J.M.R. "Vortex shedding from sharp edges" Imperial College Aero Dept Rept 77-05 (1970).
12. Moore, D.W. "A numerical study of the roll-up of a finite vortex sheet". J. Fluid Mech. 63, p. 225 (1974).
13. Chorin, A.J. "Numerical study of slightly viscous flow" J. Fluid Mech. Vol. 57, pp. 785 (1973).
14. Edwards, R.H. and Cheng, H.K. "The separation vortex in the Weiss-Fogh circulation-generation mechanisms" J. Fluid

- Mech 120, p.463 (1982).
 15. Kalligas, K. "A comparative assessment of different types of rapidly moving spoilers at low airspeeds" Bristol Univ. Aero Dept Rpt on MOD Agreement AT/2034/068 (1986)

7. ACKNOWLEDGEMENTS

This work has been carried out with the support of the Procurement Executive, Ministry of Defence. We are very grateful to J.H.B. Smith and D.G. Mabey who monitored and advised on the project.

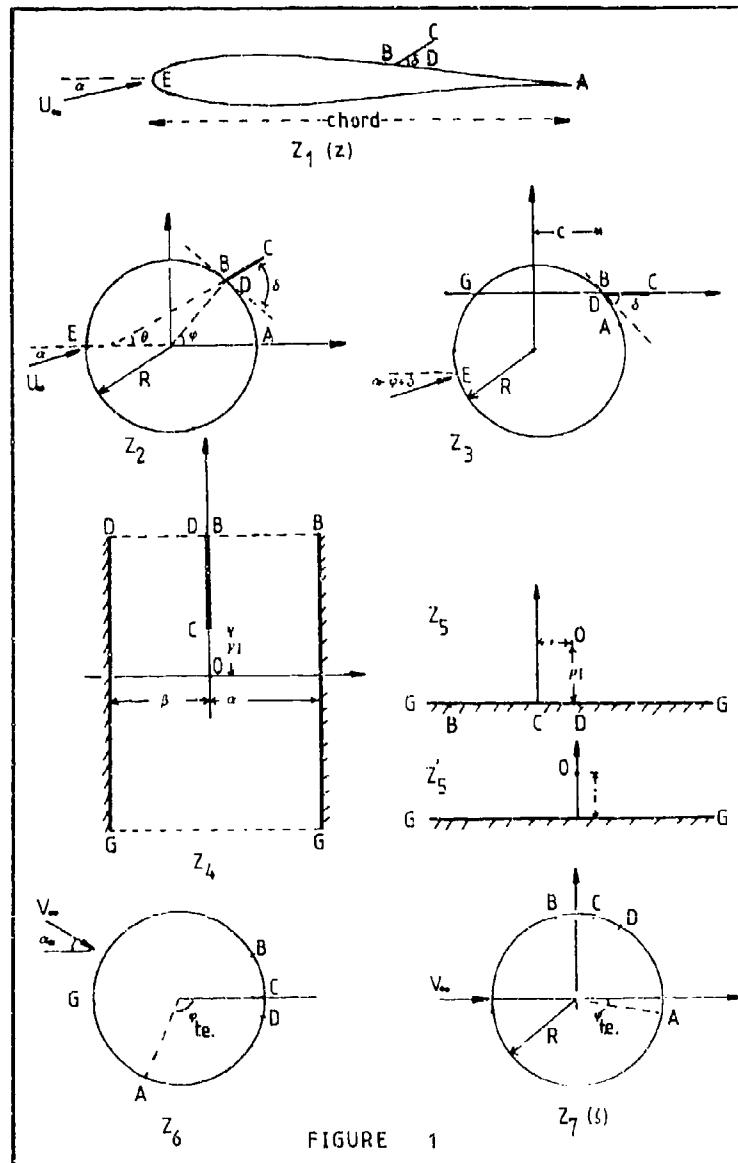


FIGURE 1

Transformation planes

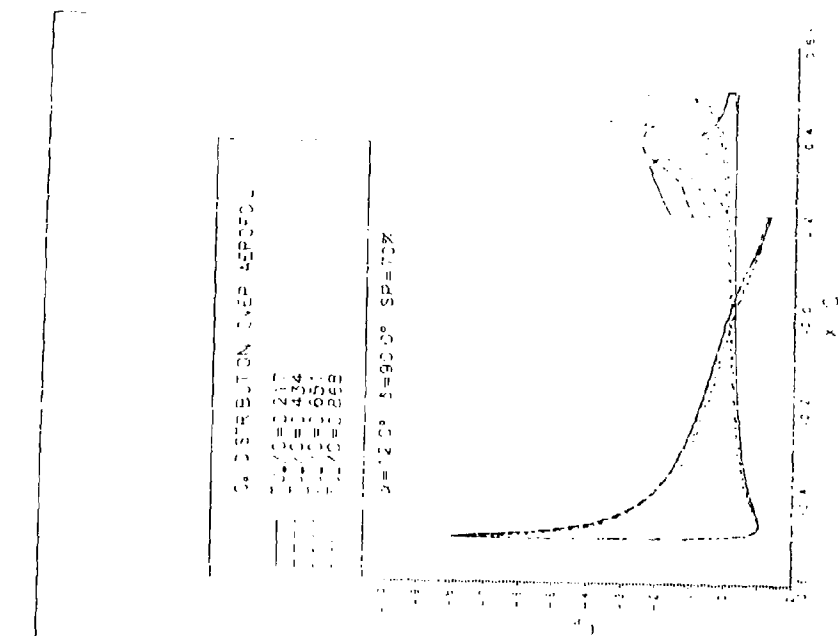


Figure 3.3. Inward-pointing arrows on the left.

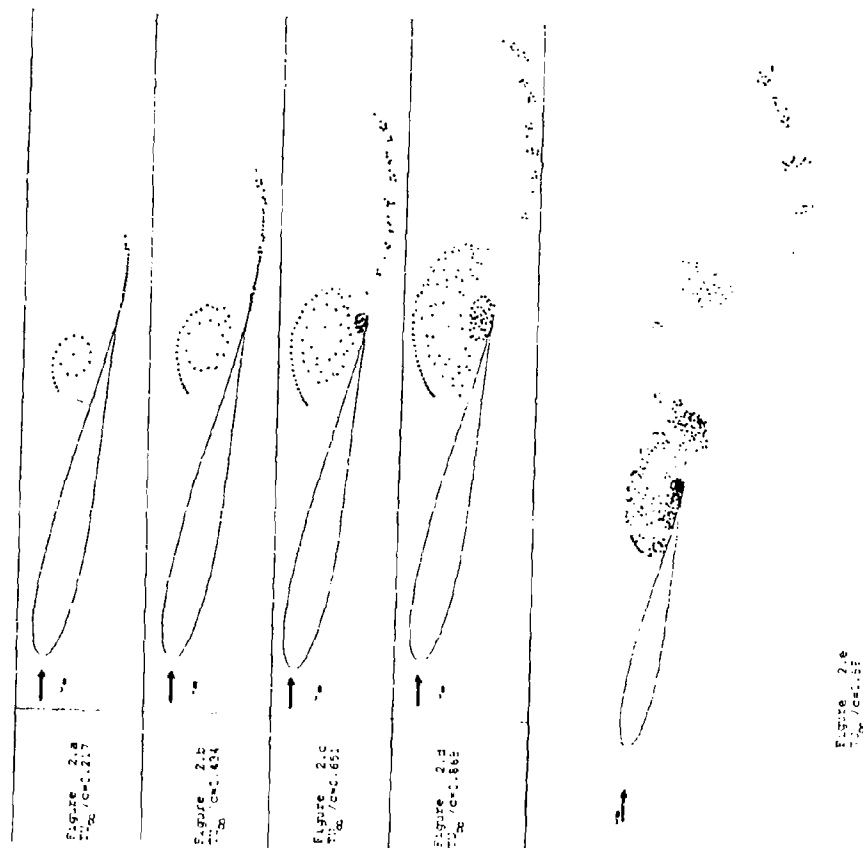


Figure 2. $\gamma = 12^\circ$, $\delta = 90^\circ$.
Fixed spider at T6 chord.

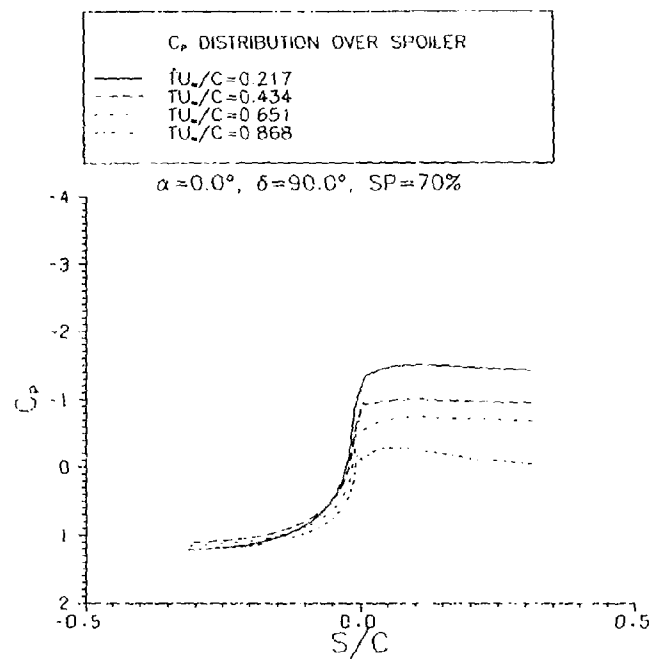


Figure 3 (b) Instantaneous pressure on spoiler.

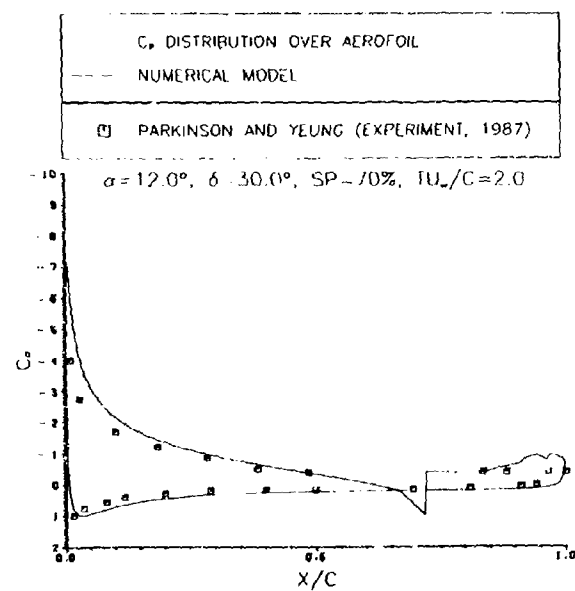


Figure 4 Mean pressure on aerofoil

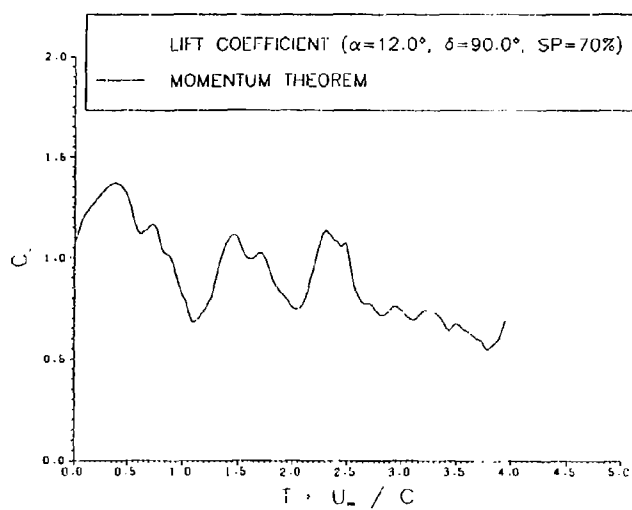


Figure 5a

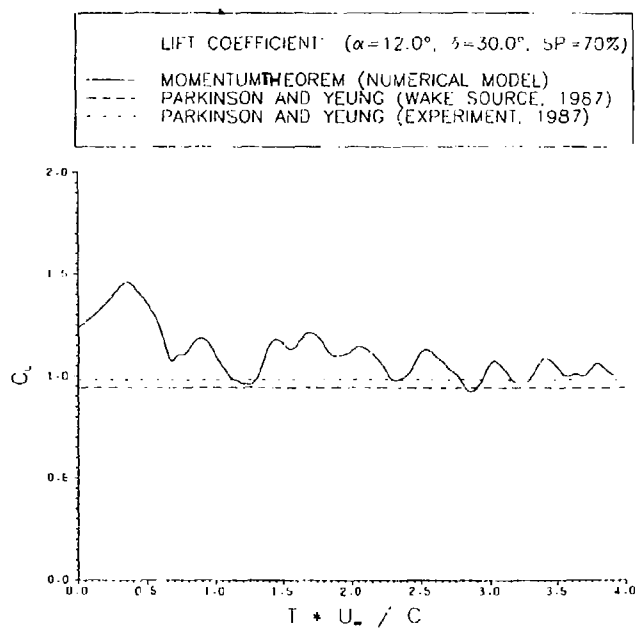


Figure 5b Lift coefficient time histories.

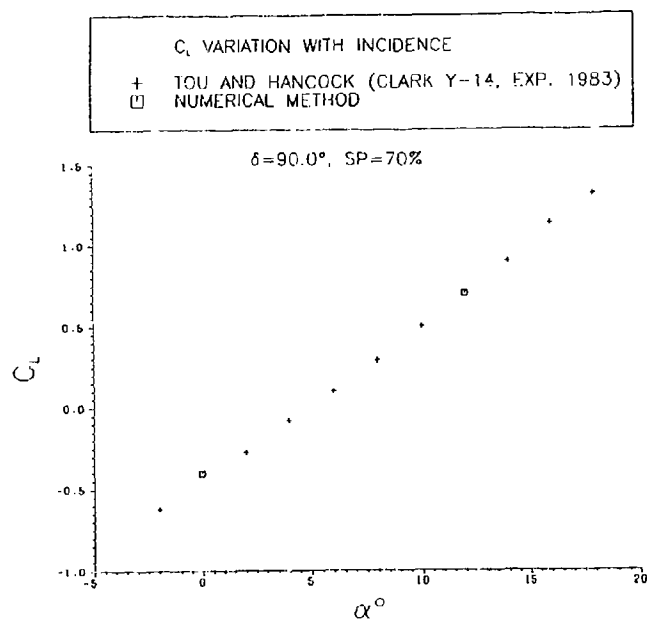
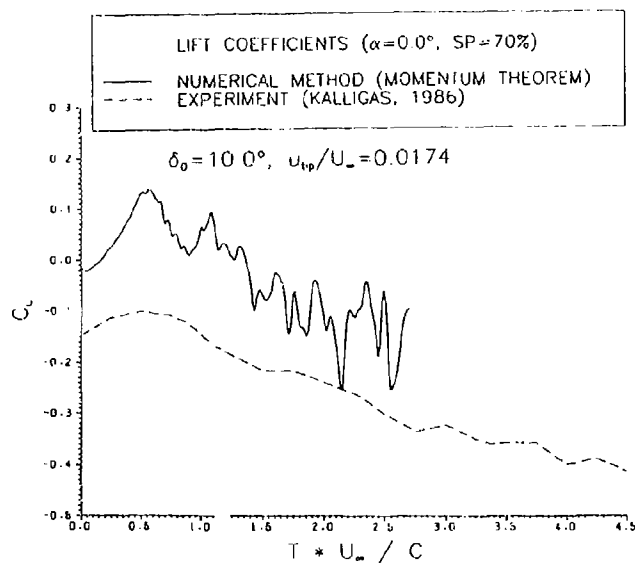
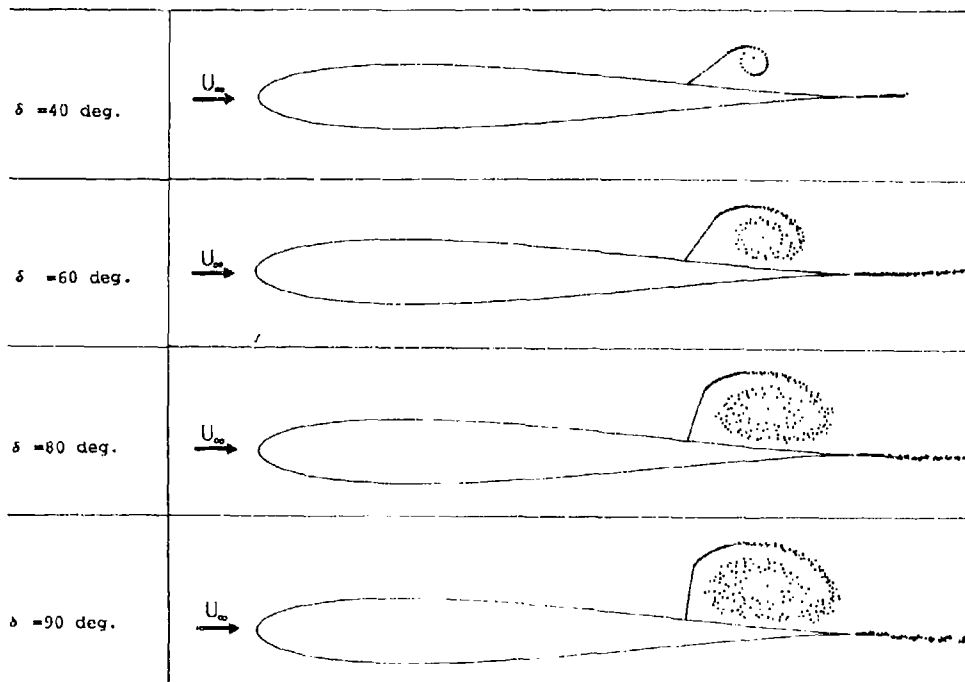
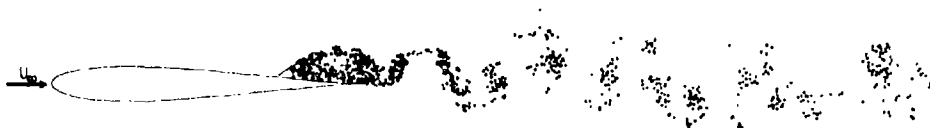
Figure 6 Lift coefficient versus incidence Fixed 90° spoiler at 70% chord.

Figure 8 Lift time history moving spoiler

Figure 7a Moving spoiler $30^\circ \rightarrow 90^\circ$ $U_\infty / c = 2.0$ Figure 7(b) 30° Spoiler long term flow

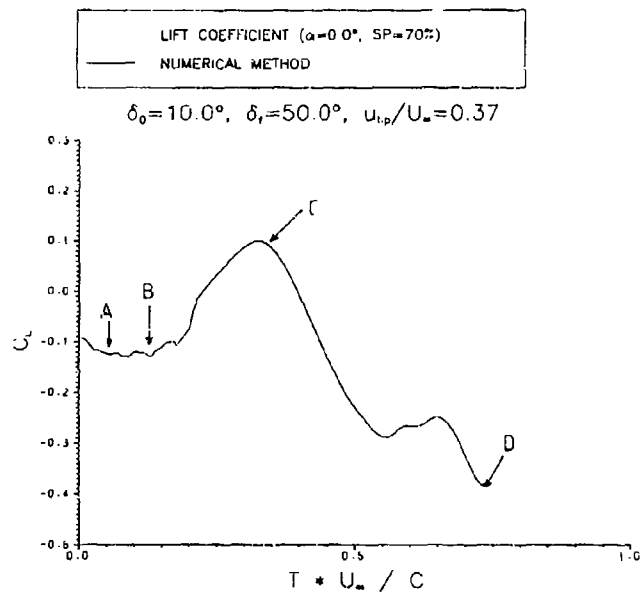


Figure 9 Lift coefficient delay times

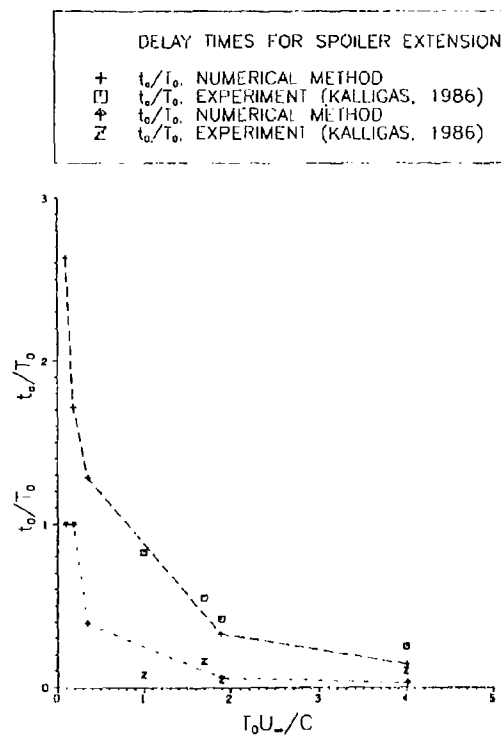


Figure 10 Delay times for spoiler extension

**"Inflight Thrust Vectoring" a Further Degree of Freedom
in the Aerodynamic/Flightmechanical Design
of Modern Fighter Aircraft**

P. Mangold
G. Wedekind
Dornier Luftfahrt GmbH
Postfach 1303
7990 Friedrichshafen
Federal Republic of Germany

1. ABSTRACT/SUMMARY

Within this paper two different aspects of Inflight Thrust Vectoring are discussed: In the first, more general part a rational for the future use of thrust deflection including reverser modes will be given by highlighting the overall possibilities and the potential of thrust vector devices within the aerodynamic/flightmechanical design of modern fighters. In the second part the most interesting results from 3 low speed wind tunnel test periods will be presented showing beneficial and detrimental effects of in flight thrust reverse on aerodynamic stability and control characteristics.

• **Flightmechanical Possibilities of Thrust Vectoring**

From the very beginning all the design phases of "New Generation" fighter aircraft are dominated by the attempt to find an optimum balanced concept within the frame of maximum performance, defined mass figures and limited costs. Especially the field of performance encompasses aspects on at least three planes, which are defined by the headlines "Mission, Point and Manoeuvre Performance". Requirements derived from these different items are often rather contradicting. So a pure optimization for maximum point performance (i.e. sustained and instantaneous turn rates) which requires maximum lift or minimum drag respectively may not be advantageous for a desired superior agility, because the preloaded aerodynamic controls do not leave enough power to initiate and stop manoeuvres in a way which lead to sufficient handling qualities. Furthermore, the general trend to enlarge the combat flight envelope towards higher angles of attack and lower dynamic pressures leads very quickly to the absolute limits of pure aerodynamic control devices. Hence these flight regimes cannot be exploited operationally unless additional control power is provided by thrust. The paper illustrates how these highly demanding design goals can be achieved by either an optimum blending between aerodynamic and thrust vector devices or even by a partial replacement of aerodynamic controls. It is shown in detail how thrust vectoring/thrust reverse can be used to enhance high angle of attack recovery, to ensure high angle of attack manoeuvres, to introduce a powerful device for acceleration and deceleration and how to optimize the approach and landing phase by additional control power especially usable for a shortened ground run.

• **Windtunnel Test Results of Inflight Thrust Reverse**

During a close cooperation between Dornier and Northrop from 1978 to 1986 a new generation fighter concept (N/D-102) equipped with PITCH THRUST VECTOR/THRUST REVERSE devices has been designed in some detail. Several low speed wind tunnel test phases have been carried out in order to study the problem areas and in order to optimize a reverser configuration which is feasible for inflight operation as well as for operation during approach and ground run after landing. The analyses of the inflight test results, which are discussed in this second part of the paper, have shown that the geometry of the reversed upper jets has to be optimized together with the vertical tail rudder concept. Especially the control efficiency at small rudder deflections may be reduced drastically during reverser operation which can lead to problematic nonlinear characteristics in some areas of the flight envelope. Furthermore some detrimental effects have been observed in sideslip test runs where rudder effectiveness vanishes rapidly versus sideslip and may even be reversed depending on the relative position of vertical tail and reversed jet.

A feasible optimum configuration could be identified if a combination of outboard cant of the upper jets is used together with a single vertical tail/rudder group. The effects of thrust reversers in ground effect are mainly dependent on the geometry of the lower jets. The most interesting results in this field and design rules derived from the tests are presented within the second paper submitted by the authors.

2. INTRODUCTION

During recent years the exploitation of thrust vectoring and thrust reverse for modern fighter aircraft has obtained growing importance. The availability of sufficient control power at low dynamic pressure and/or high angles of attack is forming the centre of flightmechanical design work. Thrust as a supplement or substitute for aerodynamic control devices offers attractive alternatives because it is able to provide effective angular accelerations even in unfavourable aerodynamic areas of the envisaged flight envelopes.

The first part of this paper will therefore discuss in detail the advantages and perspectives of a modern fighter equipped with Pitch Thrust Vectoring/Thrust Reverse (PTV/TR) devices as far as the flightmechanical and performance aspects are concerned. The second part will illustrate some problem areas within the optimization process of an inflight thrust reverser in windtunnel. Especially the geometry of the upper jets in combination with the vertical tail arrangement is a matter of concern and needs a careful optimization in order to minimize interferences on the basic stability and control characteristics.

3. FLIGHTMECHANICAL POSSIBILITIES OF THRUST VECTOR DEVICES

3.1 Design Requirements and Design Philosophies

During the recent past extreme requirements formulated by the customers have put growing pressure upon industry to improve the overall performance of the "New Generation" Fighter aircraft. From the very beginning all the design phases are therefore dominated by the objective to find optimum balanced concepts within the frame of maximum performance, fixed mass figures, limited costs and minimum risk. Especially the subject "Performance" is difficult to handle, because already the pure definition has to cover aspects on many planes: in general, the idea of "Performance" encompasses at least three different items:

- Mission Performance
- Point Performance
- Manoeuvre Performance.

The major points of interest hidden behind these head lines may be summarized in a table of "Modern Fighter Design Requirements" as listed below:

- Balanced sub- and supersonic point performance on a high level (i.e. sustained and instantaneous turn rates; specific excess power)
- High angle of attack manoeuvre capabilities
- Agility down to low dynamic pressure
- Superior handling and ride qualities within the entire operational envelope
- Unconventional manoeuvre modes (fuselage aiming; direct lift)
- Short take off and landing capabilities
- Small size and mass
- Stealth aspects.

The attempt to integrate the whole bunch of requirements into a single aircraft design leads to the conclusion that a great part of these nice features are rather contradicting and would lead to very different solutions. One possibility to reconcile some of the conflicting options is the use of automatic flight control systems: Aerodynamic Surface Scheduling and Active Controls will provide better point performances and may add some degrees of freedom by offering the possibility of unconventional manoeuvre modes. A further step towards optimized performance and/or smaller aircraft size can be done by the introduction of unstable basic longitudinal characteristics. This leads on one hand to a reasonable increase in maximum lift and a reduction in trimmed drag. But on the other hand some control potential at high angles of attack has to be sacrificed because of the preload on the aerodynamic surfaces. From the flightmechanical point of view a minimum pitch down capability has to be guaranteed at higher angles of attack (near maximum lift and beyond) in order to insure safe recovery and, if required, agility in this region. So the pitch down recovery margins shown in Fig. 1 have to cover in principal three different items:

- Control power for safe stabilization and good handling
- Control power for symmetrical pitch manoeuvring
- Pitch down potential for cancellation of pitch up acceleration due to roll manoeuvres (dumb-bell effect).

For the first two parts a minimum value of -0.3 rad/s^2 pitch acceleration should be sufficient whereas the inertial coupling term is directly connected with the required agility (i.e. roll performance) by:

$$\dot{\theta}_{1C} = \frac{1}{2} P_{\text{req}}^2 \cdot \sin 2\alpha.$$

So, if for example at 25° angle of attack and 200 KEAS a $65^\circ/\text{s}$ roll rate is required, an overall pitch down acceleration of $\dot{\theta} \leq -0.8 \text{ rad/s}^2$ has to be provided.

This lead to the conclusion that only horizontal tail concepts (aft tail or canard) are feasible in combination with a consequently unstable design in pitch. Unstable tailless configurations with pure aerocontrols are not able to produce the required pitch down at higher angles of attack. The desired instability level together with pitch-up tendencies and fading flap effectiveness reduce the available pitch recovery potential. So, for flightmechanical reasons such a concept seems to be "Not Acceptable" for a modern fighter design.

3.2 Replacement of an Aerodynamic by a Thrust Vector Tail

An enticing perspective of tailless configurations however is the possibility to reduce zero lift drag and to increase the freedom for a proper shape and arrangement of wing and fuselage. Pitch Thrust Vectoring as an internal substitute for an external aerodynamic horizontal tail brings back the opportunity to reconsider aerodynamically tailless aircraft as a proper solution in modern fighter design. As shown on the right hand side of Fig. 1 the pitch vector nozzle will provide control power in excess of the required margins. Especially at high angles of attack and/or low dynamic pressure, where the aerodynamic control power uses to fade, the thrust vector nozzle will be able to

produce high angular accelerations in both directions pitch-down and pitch-up. As a matter of fact the control potential will then be a function of thrust setting, but in the critical flight conditions where aerodynamic control power is low the thrust setting is normally on a high level anyway. This means that aerodynamic and thrust vector devices may be considered as highly supplementary to each other. A proper blending of the dynamic-pressure-dependent and thrust-setting-dependent control accelerations will then lead to real balanced concepts where most of the aspects of performance discussed above, may be integrated.

3.3 Special Features of a Pitch Thrust Vector/Thrust Reverse Design

From 1980 to 1986 the N/D-102 (Fig. 2) design has been developed by Northrop and Dornier to meet the objectives of next generation fighters. The most significant features which characterize this configuration may be summarized as follows:

- Non-afterburning, low-by-pass-ratio turbojet engines capable of high thrust persistence and of efficient supersonic cruise.
- Low aspect ratio supersonic trapezoidal wing with leading/trailing edge control surfaces optimized by a properly sized wing strake for minimum pitch-up and high trimmed max. lift at a chosen basic instability of SM = -8 %.
- Single vertical tail.
- Deletion of horizontal tail in conjunction with addition of pitch thrust vectoring (reduction of drag, radar signature).
- Two-dimensional convergent-divergent nozzle with pitch thrust vectoring and inflight thrust reverse (no aerodynamic speed brakes).

The two-dimensional exhaust nozzle, illustrated in Fig. 3, was designed to provide ± 30 degrees thrust vectoring in pitch and in addition the simultaneous function "thrust reverse". Both these nozzle functions as well as the thrust level have been integrated into the basic flight control system. So it was possible to give enhanced control effectiveness by blending thrust control with the normal aerodynamic control devices. In detail the nozzle divergent flaps act differential for the variation of the exit area and collectively for the vectoring mode with the provision that both functions can be performed simultaneously. For thrust reversing the convergent flaps, used to control the throat area, are equipped with additional motion, which allows to open the reverser ports while continuously controlling the total throat area.

The summary in Fig. 4 gives a general view about benefits, penalties and indifferent aspects of a tailless configuration equipped with thrust vector devices in comparison with a conventional aero-tailed design: High deceleration potential inflight, short ground roll, less zero-lift drag, high pitch control power during approach and high agility at low dynamic pressure outline the benefits which are more than a pure substitute for a horizontal tail. Penalties may be figured out by looking at the necessary development risk and cost of the nozzles, by the heat load on the vertical tail during thrust reverse and by the interferences which may alter the aerodynamic characteristics during the TR mode inflight and close to ground. The question of weight may be assumed to be of no significance because the saving on one hand (aero-tail/airbrake) is almost compensated by the increase of a 2D-PTV/TR nozzle.

• Inflight Deceleration Capability

Fig. 5 illustrates the superior inflight deceleration capability of a fighter equipped with thrust reverse devices in a straight level flight for a typical air defense combat altitude of 20000 ft. Once the reverser ports have opened the aerodynamic drag of the configuration plus inlet drag plus the reversed trim thrust act into the desired direction and may be used for effective longitudinal speed control within the limits of pilot's acceptance. If desired the effect can even be increased by setting the thrust to a higher level. When shutting the TR ports at the end of the braking manoeuvres the full acceleration potential will be available almost at once. For comparison Fig. 6 shows the deceleration capability of a fighter equipped with a conventional 1.5 square-metres airbrake deployable up to about 60 degrees. Assuming a realistic actuator, less than 0.5 g's are available to decelerate the aircraft at constant thrust setting at high subsonic mach numbers. The same manoeuvre with thrust reverser will almost double the longitudinal deceleration potential.

• Deceleration Capability after Touch-Down

The most important aspect of landing performance is the required ground roll after touch-down. Fig. 7 compares the optimized ground roll distances for three fighters using different deceleration devices on a dry runway. The longest ground roll is obtained by the "wheel-brake"-method including lift dump and anti-skid (friction coefficient = 0.7). A drag chute will shorten the required distance by about 10 % whereas the thrust reverser is able to save more than 45 % of the original ground roll. On a wet and slippery runway the advantage of thrust reversing is even more pronounced. For clarification Fig. 8 illustrates the principles of conventional high performance landings by showing the deceleration n_x [g's] versus time: After touch-down and an additional time of 1 sec for pitch-down and pilot's reaction, full wheel brake including lift dump is applied

giving an almost constant deceleration until the final stop of the aircraft. The relatively large idle thrust lowers the efficiency of the wheel brake by a remarkable amount, as shown in the upper sketch of Fig. 8. In lower diagram of the figure the effect of a 7 m^2 drag chute is added. It gets evident that a substantial increase in deceleration may only be expected during the first few seconds of ground roll where dynamic pressure is relatively high. - A possible automatic procedure for use of thrust reversers during a high performance approach, landing and ground roll is presented in Fig. 9: Approach and touch-down is performed with a thrust setting of 70 % max. thrust in partial reverse. After derotation full wheel braking, lift dump and full thrust reverse at constant power setting is applied until the permissible reingestion limit is reached ($q_1/q_{\infty} = 70$). Engine spool down to idle and afterwards partial reverse with continuous closing of the reverser ports will be scheduled to keep the dynamic pressure ratio q_1/q_{∞} below the reingestion limit until the stop of the aircraft is reached within 210 m from 115 kts touch-down speed.

A further advantage of the relatively high power setting with partial reverse during approach is the immediate availability of accelerating thrust if an unexpected go-around is required.

• Drag Characteristics

As already mentioned in chapter 3.2 some reduction in zero lift drag may be expected by replacement of the aerodynamic horizontal tail. Fig. 10 gives some indications for the possible drag improvement versus mach number: Changing the N/D 102 configuration from an aft tail towards a thrust tail (i.e. tailless) concept will save about 10 to 30 drag counts depending on mach number. The achievable improvement is of course dependent on the configuration itself and may vary with the overall design requirements. Of greater importance however, are the "Off-design"-induced drag characteristics which determine the losses in point performance if variations in centre of gravity have to be taken into account or if the desired design instability has to be reduced because of problems with the real flight control system. Fig. 11 shows the principal variation of induced drag (at constant lift coefficient and mach number) versus the basic stability margin. It can be shown that a pure tailless configuration is rather sensitive to deviations from the original design instability whereas an aft tail concept will exhibit smoother characteristics because of its powerful trim device. A considerable part of this favourable behaviour may be recovered by a thrust tail if the pitch thrust vectoring is used for trim in off-design conditions. So the losses concerning induced drag will not be too severe (see shaded area in Fig. 11) and be comparable to that of a canard configuration under the same circumstances.

• Pitch Control Power

Essential corner stones of a proper flightmechanical design are usually set by the available pitch control power within the several flight conditions. Especially the terminal flight phases (as i.e. Approach) or the low dynamic pressure areas require particular attention of the design engineers. Fig. 12 shows a comparison of the pitch acceleration capabilities between a conventional aft tail configuration and a tailless aircraft equipped with PTV. Excluding the potential of the trailing edge flaps, the aft tail configuration is able to produce about $\pm 1 \text{ rad/s}^2$ starting from a trimmed condition. The PTV fighter using the approach procedure of Fig. 9, will produce about 66 % more pitch control power which in emergency (aborted approach plus go around) condition can be increased to more than $\theta > 3 \text{ rad/s}^2$ by setting full power and closing the reverser ports.

If agility at high angles of attack is required the pitch-down acceleration capability is of major importance. Fig. 13 shows in detail that pitch thrust vectoring is a powerful mean to generate the angular accelerations which are necessary to install superior characteristics during manoeuvres near or even beyond stall at low dynamic pressure. Up to medium subsonic mach numbers the vector nozzles will be superior to any aerodynamic tail and therefore be capable to provide the necessary flightmechanical control potential even in aerodynamically critical areas.

• Unconventional Manoeuvre Modes

Fuselage Aiming represents one of the characteristics which usually are a matter to be looked at if performance improvements for future fighter aircraft are discussed. It is well-known that an aft tail concept can cover a relatively large range of trimmed pitch attitudes versus mach number if the configuration is trimmed with flaps up or flaps down as shown on the left-hand side of Fig. 14. A technical limit is usually set by the permissible load on the horizontal tail at increasing dynamic pressure. The diagram on the right hand side of the same figure presents the potential of a tailless aircraft equipped with PTV. Because of the slightly larger lever arm of the trim device it may be assumed that the usable fuselage aiming corridor is somewhat larger. So even for unconventional manoeuvre modes the thrust vector device will be at least a full and complete substitute for an aerodynamic horizontal tail.

4. WINDTUNNEL TEST RESULTS OF INFLIGHT THRUST REVERSE

Three test periods in low speed wind tunnels have been run during Dornier/Northrop co-operation in order to find feasible thrust reverser arrangements for the N/D-102 configuration, which should use these devices for efficient inflight deceleration, enhanced pitch manoeuvre and for high performance approach and landing. The photos in Fig. 15 are meant to give some insight into the overall arrangement of the windtunnel model and into the test techniques applied during the optimization work. Pressurized air has been used to feed the four reverser ports by independent tubes from the back in order to generate the required dynamic pressure of the jets. The whole reverser device has been kept separate from the windtunnel model so that the pure aerodynamic interferences could be evaluated with the forces and moments measured by the internal balance. Fig. 16 shows the principles of the upper and lower jet arrangement and the definition of the cant and reverser angles varied within the several windtunnel campaigns. A matter of discussion in advance of the tests are the relevant dynamic pressure ratios q_1/q_∞ which will occur during real operation. Fig. 17 gives an impression of the applicable relations "Average Dynamic Pressure in Thrust Reverser Exit" q_1 to "Free Stream Dynamic Pressure" q_∞ . A deceleration manoeuvre inflight will certainly be performed with q_1/q_∞ -ratios of less than 30. During ground roll however the ratio may become pretty large and the practical limit has to be set by the reingestion limit minus a considerable safety margin.

4.1 Objectives and Test Matrix

The optimization goals which have been considered within the windtunnel tests, were mainly defined by flightmechanical requirements. The main attention has been drawn upon the attempt to find a reverser solution which provided sufficient efficiency together with minimum aerodynamic interferences with respect to stability and control. It soon became evident that for inflight thrust reverse the geometry of the upper jets together with the position and arrangement of the vertical tail/rudder group are of major importance. The lower jets are a matter of concern in ground effect which will be discussed in detail in paper 19. Fig. 18 shows the matrix with the main parameters which have been varied within the several tests. Single and twin vertical tails in three different longitudinal positions relative to the reverser jets in combination with four jet cant angles have been investigated in order to find a well-balanced solution. As indicated in the table no overall satisfactory solution was found with the twin vertical tails. So the optimization process described in the following sections will be shown for the single vertical configuration only.

4.2 Identification of Problem Areas

The first test period was mainly devoted to identify the problem areas of the baseline configuration equipped with a single vertical tail/rudder in the forward position "F" and thrust reversers with 0° cant angle of the upper and lower jets. This reversed jet arrangement was originally chosen because the design effort for the reverser ports should be as simple as possible. Fig. 19 shows the longitudinal coefficients "lift" and "pitching moment" versus angle of attack for zero controls and a high lift flap setting at different q_1/q_∞ -ratios. In principle the data show no problematic changes in the overall characteristics besides the fact that for the high q_1/q_∞ the flap effectiveness is increased by a considerable amount. As the change in lift is not very pronounced the increase in pitch control power points towards an aft shift of the pressure point of the flap. A more suspicious change may be found in the lateral/directional coefficients at 10° of sideslip presented in Fig. 20. Especially directional stability is almost doubled at lower angles of attack and high reverser pressure ratios. At higher angles of attack (where the thrust reversers are not likely to be used operationally) the effect is almost reversed, although the deficiencies in $C_{Y\beta}$ might be compensated by a better lateral stability $C_{L\beta}$. The most problematic feature of this baseline thrust reverser configuration is pointed out in Fig. 21: The sideslip runs with variations of q_1/q_∞ show that rudder efficiency is heavily influenced in a negative sense. A total breakdown of effectiveness may be observed for small rudder deflections. In addition for large rudder inputs the yaw control power fades rapidly versus sideslip angle. Furthermore Fig. 22 shows a remarkable induced pitch-down effect once the rudder is deflected for directional control.

The overall characteristics exhibited above are of course totally unacceptable for a proper flightmechanical and control law design and alternative solutions with less severe interferences have to be found.

4.3 Influence of Vertical Tail Position

A first possibility to alter the detrimental interferences of thrust reverse on rudder efficiency was investigated by changing the relative position of vertical tail and reverser jets and retaining the zero cant angle. Fig. 23 shows the effect of a moving aft of the single vertical tail into position "A" (definition see Fig. 18): The smooth stable directional characteristics versus sideslip with efficient rudder power for $q_1/q_\infty = 0$ are deteriorated dramatically if the reverser jets are active. Large unstable ranges of $C_{Y\beta}$ versus β combined with a control reversal at small sideslip angles and a breakdown of rudder power at larger β 's indicate that this solution will not be acceptable in any case.

All other tests done with straight forward blowing upper jets ($\nu = 0^\circ$) in combination with the single vertical tail showed the same principle deficiencies. Slightly better results have been obtained with a twin vertical tail configuration. But non-steady directional data versus sideslip and again a β -dependent rudder power have proved to look for better solutions.

4.4 Influence of Reverser Cant Angle

The results discussed in the earlier sections have shown that nonlinearities of rudder power versus rudder deflection and directional stability versus sideslip is a major point of concern together with operation of an inflight thrust reverse device. The close proximity of the straight forward reversed jets and vertical tail/rudder seems to generate severe interferences which cannot be tolerated. The attempt to minimize interferences by changing the cant angle of the reversed thrust is presented in Fig. 24. The first diagram ($\nu = 0^\circ$) shows once more the original problems of the baseline (section 4.2) with the control power breakdown dependent on q_1/q_∞ and rudder deflection itself. An inboard cant of the jets ($\nu = -10^\circ$) towards the vertical tail doesn't solve the issue as illustrated in the right-hand diagram of the figure. Better results may be obtained by an outboard cant. An almost total separation of jet and vertical tail/rudder aerodynamics seems to be reached at 40° outboard cant. The diagram on bottom of Fig. 24 shows an essentially linear rudder power versus rudder deflection for all relevant q_1/q_∞ -ratios.

Outboard cant together with a twin vertical tail configuration however will again lead to problems with yaw control power at small rudder deflections.

4.5 Characteristics of an Optimized Configuration

The discussions above have shown that a considerable amount of reverser outboard cant may solve or minimize the interference problems between upper jet and rudder efficiency. Another problematic feature, which has been addressed before are the directional data versus sideslip. The yawing moments versus β test results of Fig. 25 show that the negative interferences obtained with the original baseline ($\nu = 0^\circ$) could almost been removed by the 40° cant of the upper jets. For all sideslip angles and all q_1/q_∞ -ratios rudder power proves to be linear and efficient. A small degradation in directional stability itself versus q_1/q_∞ has to be considered according to the presented results. But as the smoothness of the yawing coefficients is maintained, the control system to be installed will cope with this phenomenon. The lefthand graph of Fig. 26 shows the corresponding rolling moment coefficients versus sideslip. Again no suspicious interferences appear if the reverser is operative and/or the rudder is deflected. The same applies to the pitching moment coefficient on the right side of Fig. 26. If compared with the negative interferences of Fig. 21 and 22 it can be pointed out that nearly all the negative effects of inflight thrust reverse have disappeared if the tested single vertical tail/rudder configuration is equipped with upper reverser jets which are canted outboard by a considerable amount. However, it should be mentioned that such a solution may be likely to introduce some new problems as for example a higher sophisticated nozzle design and more severe safety requirements due to the large yawing moments in case of failure of one reverser port. On the other hand some additional flightmechanical advantage could be drawn out of canted upper and lower reverser jets if the yaw potential in asymmetric operation is used for enhanced directional control power.

5. CONCLUSIONS

The illustrations of section 3 of this paper have shown that the demanding design goals of "New Generation" fighter aircraft can be achieved more easily and with greater degrees of freedom by integration of thrust vector/thrust reverse devices. The flight-mechanical exploitation of these devices inflight and during ground roll provide an excellent supplement for the aerodynamic control surfaces and may even be used as a substitute for aerodynamic surfaces like horizontal tails or airbrakes.

The details of design with respect to stability and control has to be dominated by the attempt to find a proper arrangement for the geometry of the reverser jets which give minimum interferences and satisfactory efficiency of the thrust control simultaneously.

It has been shown in section 4 that for inflight thrust reverse the geometry of the upper jets in combination with the vertical tail/rudder group are of major importance. Matters of concern within the optimization processes in windtunnel may be found in the characteristics of directional stability and rudder efficiency versus sideslip with thrust reversers in operation. Straight forward blowing upper jets ($\nu = 0^\circ$) and inboard cant will not lead to real satisfactory solutions for single and twin vertical tail configurations. A feasible (optimum) configuration could be identified if a combination of outboard cant of upper jets is used together with a single vertical tail. The amount of cant angle and the relative position of vertical tail reverser ports will be a matter of detailed optimization in windtunnel and may heavily depend on the individual configuration.

Problems and optimization procedures for thrust reversers in ground effect will be discussed in paper 19, prepared by the same authors.

References

- Lorincz, D. Effect of Inflight Thrust Reverser Deployment on Tactical Aircraft
 Chiarelli, C. Stability and Control
 Hunt, B. 17th Joint Propulsion Conference, Colorado Springs
 AIAA-81-1446
- Miller, E. Nozzle Design and Integration in an Advanced Supersonic Fighter
 Protopapas, J. AIAA-paper-79-1813
- Bergmann, P. Thrust Vectoring Applied to Aircraft Having High Wing Loading
 AIAA-paper-79-1812
- Petit, J.E. Performance Characteristics of a Wedge Nozzle Installed on a F-18
 Capone, F.J. Propulsion Wind Tunnel Model
 AIAA-paper-79-1164
- Capone, F.J. The Nonaxisymmetric Nozzle - It is for Real
 AIAA-paper-79-1810
- Capone, F.J. Performance Characteristics of Nonaxisymmetric Nozzles Installed
 Growadia, N.S. on the F-18 Airplane
 Wooten, W.H. AIAA-paper-79-0101

Nomenclature:

α	[°]	angle of attack	} <u>see Fig. 16</u>
β	[°]	angle of sideslip	
ν	[°]	cant angle of reversed jet	
χ	[°]	longitudinal inclination of reversed jet	
ζ	[°]	rudder deflection	
\bar{c}	[m]	mean aerodynamic chord	
C_D	[-]	drag coefficient	
C_{D0}	[-]	zero lift drag	
C_l	[-]	rolling moment coefficient	
C_L	[-]	lift coefficient	
C_m	[-]	pitching moment coefficient	
C_n	[-]	yawing moment coefficient	
$C_{n\beta}$	[rad ⁻¹]	directional stability	
i_y	[m]	radius of inertia in pitch	
m	[kg]	aircraft mass	
Ma	[-]	mach number	
n_L	[g's]	load factor	
n_x	[g's]	longitudinal acceleration	
q_j	[N/m ²]	dynamic pressure within reversed jet	
q_∞	[N/m ²]	dynamic pressure (free stream)	
$\dot{\theta}$	[rad/s ²]	pitch acceleration	

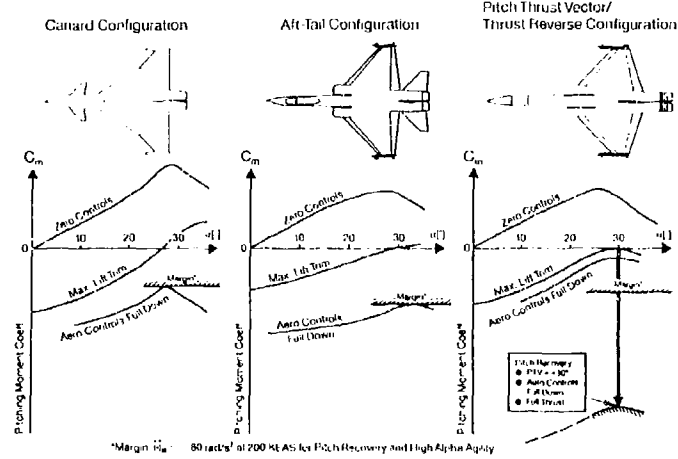
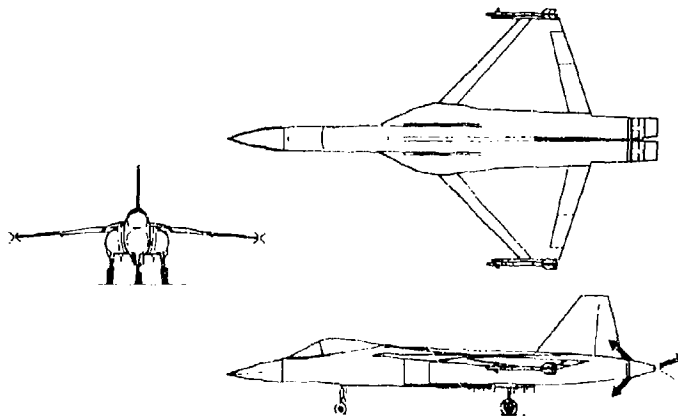
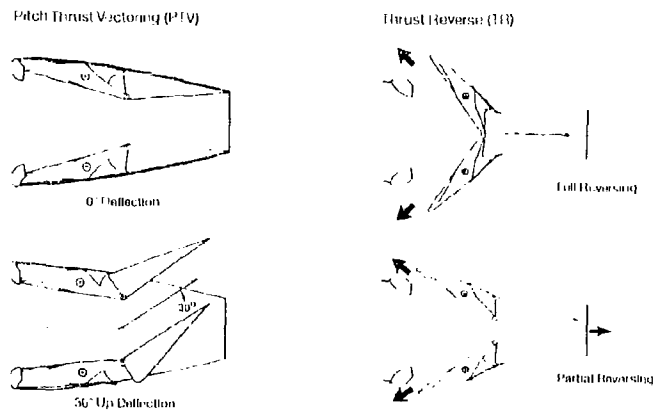
Fig. 1**Rationale for Necessity of a Horizontal Tail****Fig. 2****Example for a Modern Fighter with Thrust Reverse and Pitch Thrust Vector Devices****Fig. 3****Principles of Thrust Vector/Thrust Reverse Devices**

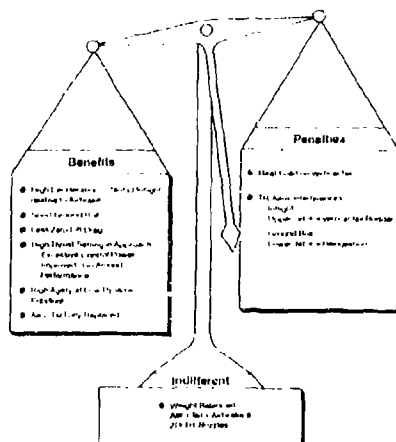
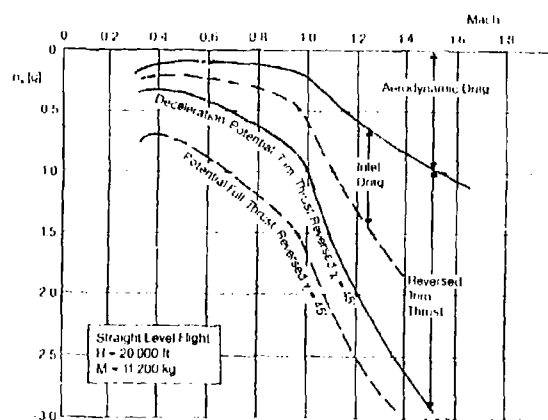
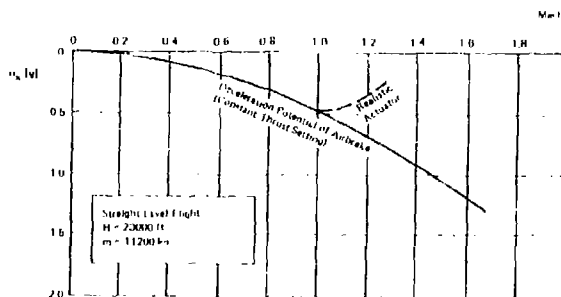
Fig. 4 Special Features of a Pitch Thrust Vector/Thrust Reverse Design**Fig. 5** Longitudinal Deceleration Capability with Thrust Reverse Devices**Fig. 6** Typical Longitudinal Deceleration Capability with Airbrakes
($S = 1.5 \text{ m}^2$; $\gamma = 60^\circ$)

Fig. 7 Optimized Ground Roll Distances During High Performance Landings (Mass = 10000 kg; Dry Runway; 115 kts Approach Speed)

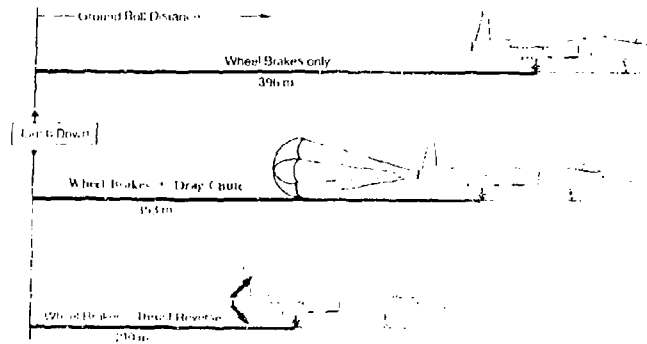


Fig. 8 Principles of Conventional High Performance Landings (Drag of Aircraft Neglected)

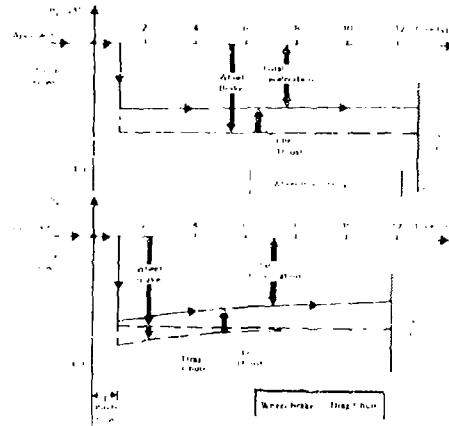


Fig. 9 Possible Automatic Procedure for Use of Thrust Reversers During a High Performance Short Landing

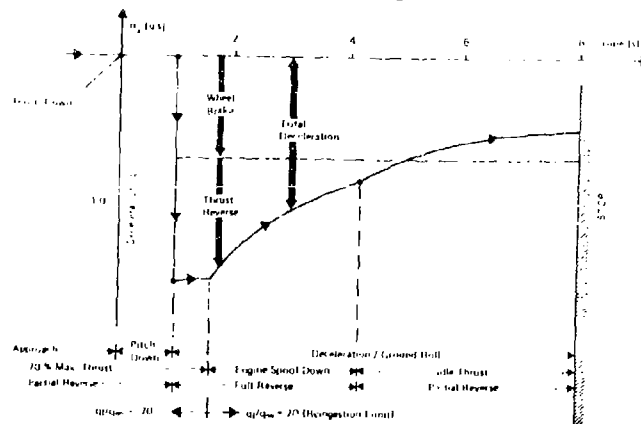


Fig. 10

Effect of Replacement of "Aero-Tail" by a "Thrust-Tail" on Zero Lift Drag

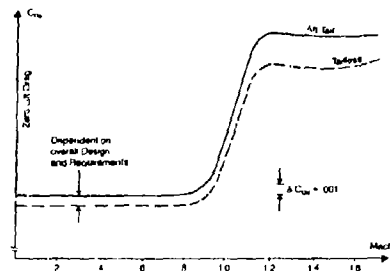


Fig. 11

"Off Design" - Drag Characteristics

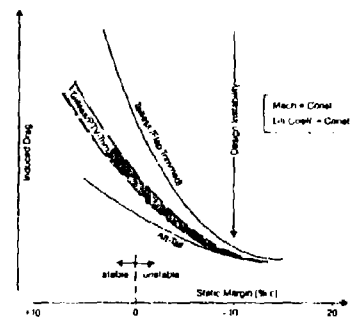


Fig. 12

Typical Pitch Control Power During Approach
(Approach Speed 115 kts)

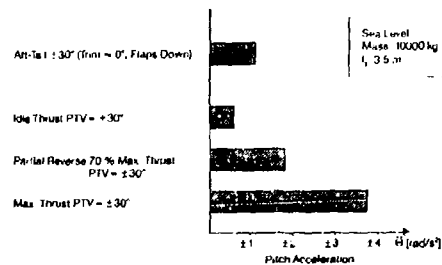


Fig. 13

Typical Pitch Down Capabilities near Maximum Lift
(Altitude: 20000 ft; Mass: 11000 kg; Radius of Inertia: 9.5 m; 20 AGA)

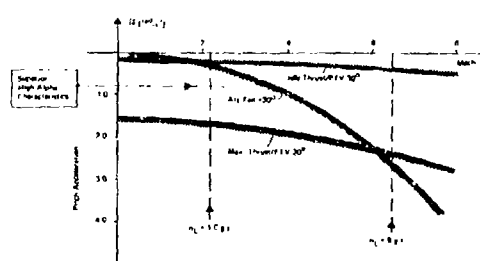


Fig. 14 Comparison of Fuselage Aiming Corridor "Aft Tail" Versus "Pitch Thrust Vectoring"

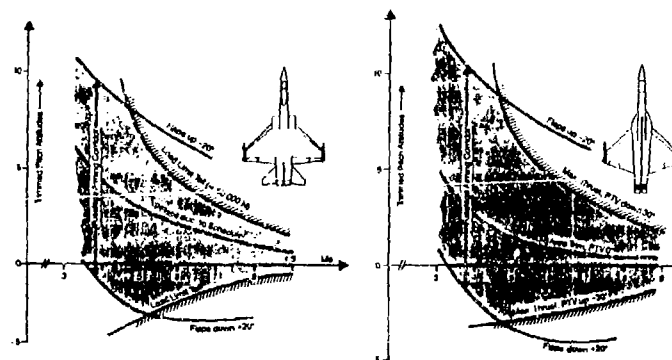


Fig. 15 Overall Arrangement of the Tested Model in Windtunnel

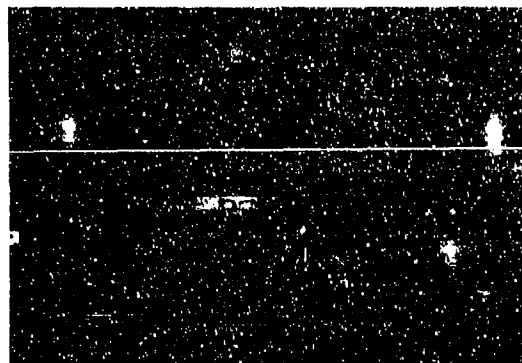
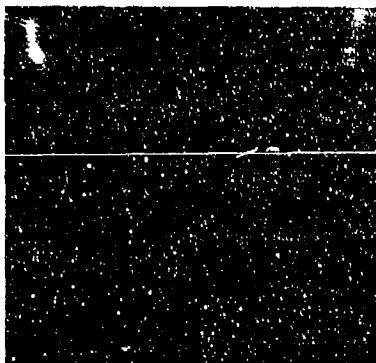
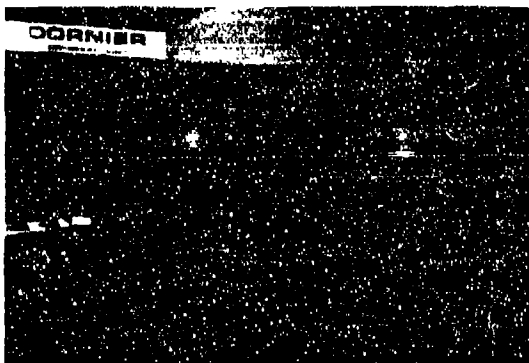
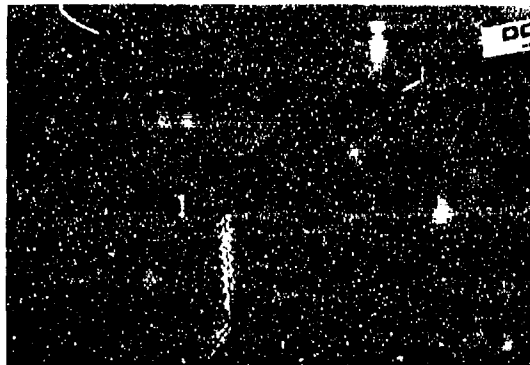
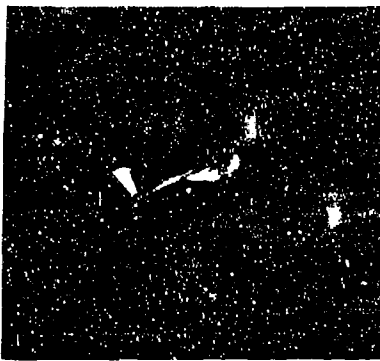


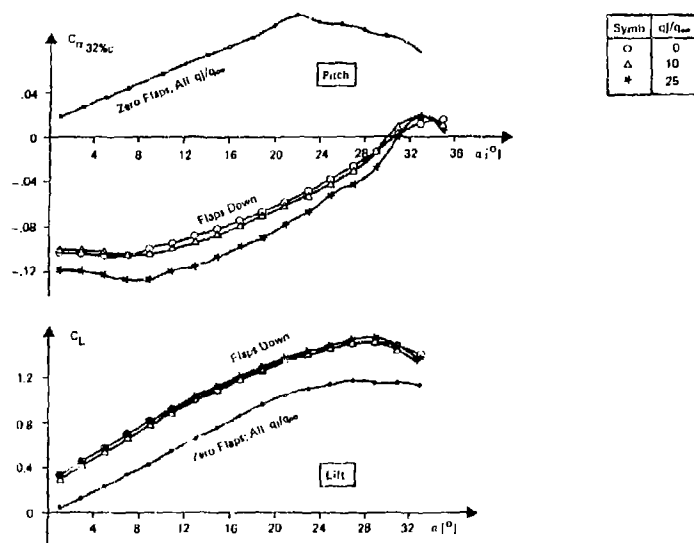
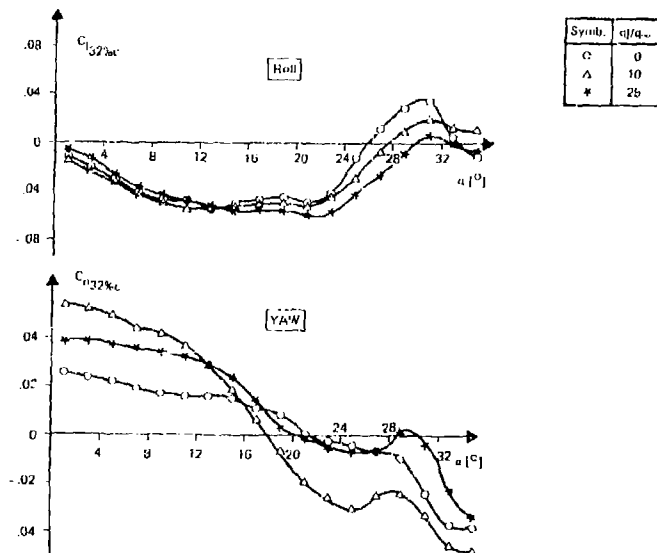
Fig. 19**Longitudinal Characteristics during Inflight Thrust Reverse**(Single Vertical Tail, Position F; Flaps down; $\nu = 0^\circ$; $\beta = 0^\circ$)**Fig. 20****Lateral/Directional Characteristics during Inflight Thrust Reverse**(Cant Angle: 0° ; Single Vertical, Position: F; Flaps down; 10° Sideslip)

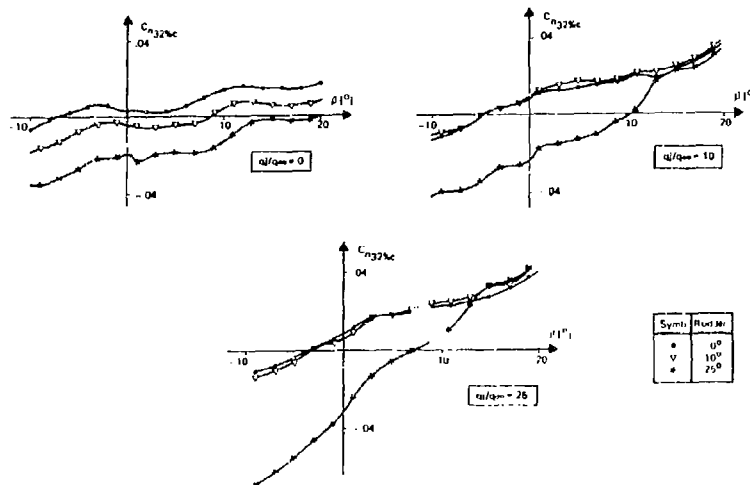
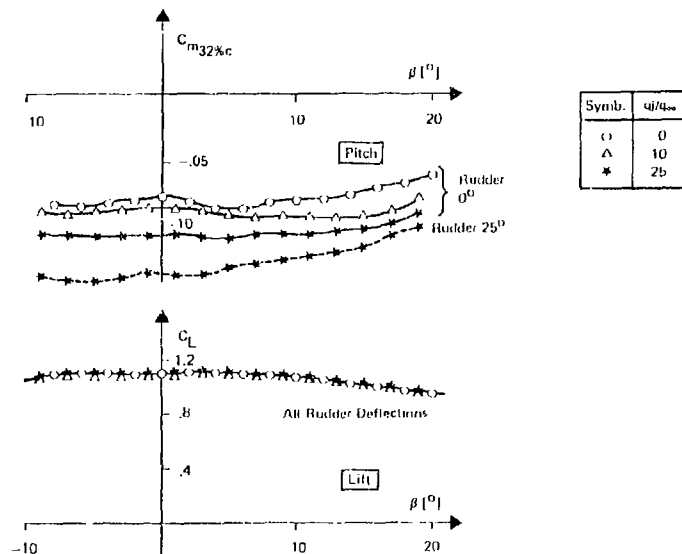
Fig. 21**Yawing Moment Characteristics and Rudder Effectiveness versus Sideslip/Inflight Thrust Reverse**(Single Vertical Tail, Position F; Cant Angle $\nu = 0^\circ$; $\alpha = 15^\circ$)**Fig. 22****Longitudinal Characteristics versus Sideslip**(Single Vertical Tail, Position F; Cant Angle $\nu = 0^\circ$; Flaps Down; $\alpha = 15^\circ$)

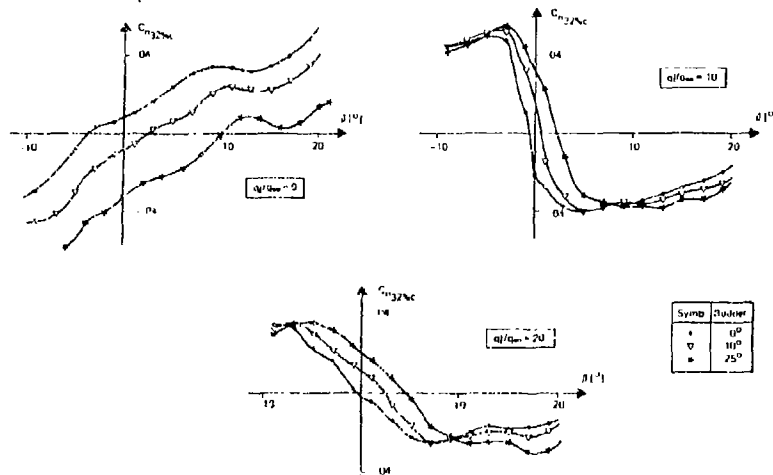
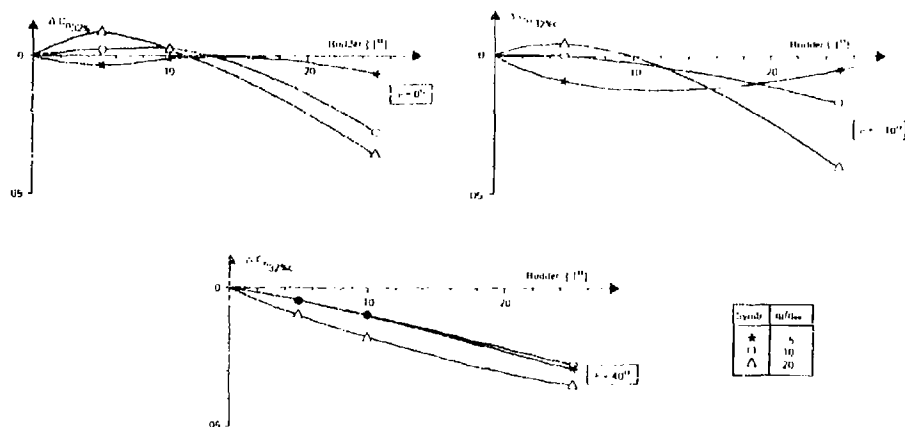
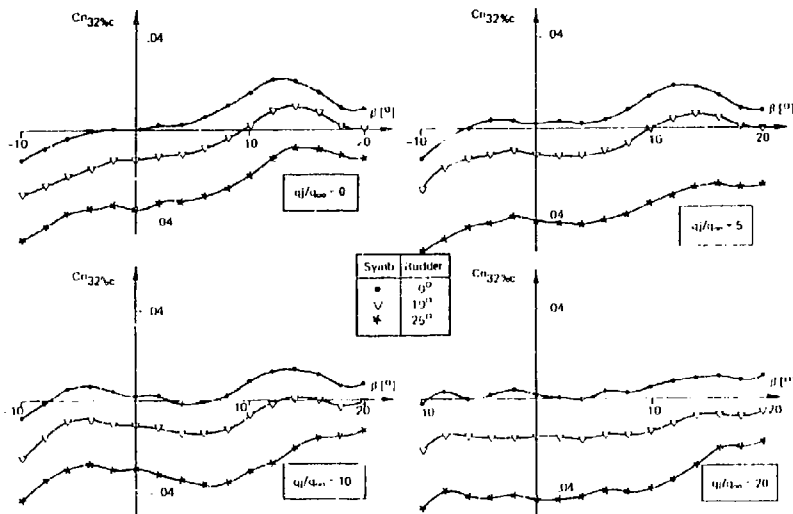
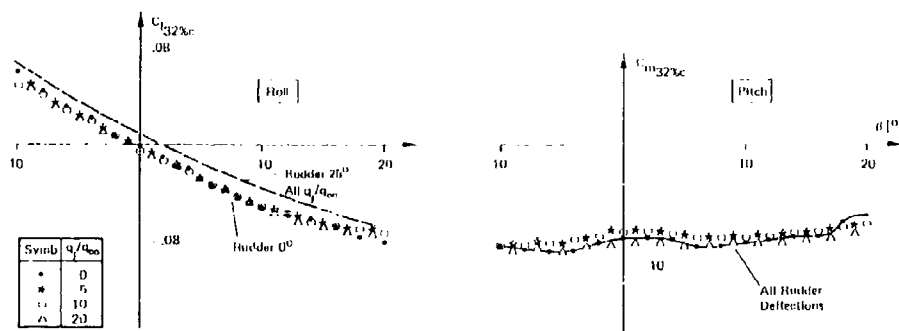
Fig. 23**Yawing Moment Characteristics and Rudder Effectiveness versus Sideslip**(Single Vertical Tail, Position A; Cant Angle $\nu = 0^\circ$; $\alpha = 15^\circ$)**Fig. 24****Optimization of Thrust Reverse Cant Angle ν with Respect to Rudder Effectiveness Inflight**(Single Vertical Tail, Position F; Flaps Down; $\alpha = 15^\circ$; $\beta = 0^\circ$)

Fig. 25**Yawing Moment Characteristics and Rudder Effectiveness of optimized Thrust Reverser**(Single Vertical Tail, Position F; $\alpha = 15^\circ$; Flaps Down; $\nu = 40^\circ$)**Fig. 26****Rolling and Pitching Moment Characteristics of Optimized Thrust Reverser**(Single Vertical Tail, Position F; $\alpha = 15^\circ$; Flaps Down; $\nu = 40^\circ$)

Aerodynamic Interferences of In-Flight Thrust Reversers in Ground Effect

G. Wedekind
P. Mangold
Dornier GmbH
Postfach 1420
7990 Friedrichshafen
Federal Republic of Germany

Abstract:

Overall design studies for future fighter aircraft have shown that it may be desirable or even necessary to install an in-flight thrust reversing mode during approach and landing in order to fulfil the growing requirements for optimum mission, manoeuvre, and point performance. With this device an additional optimization task is introduced into the aerodynamic design process, because adverse aerodynamic interference effects have to be avoided. - The problems related to approach and landing may roughly be divided into two main subjects:

- Reingestion of the hot exhaust gases into the inlet of the engines has to be retarded. The possibility to use the thrust reversers down to very low speeds on the runway during landing phases increases the potential to exploit this device for short landing capabilities.
- Detrimental aerodynamic interferences in terms of abrupt changes of the aerodynamic forces and moments are not tolerable, because the controllability of the aircraft has to be guaranteed within the whole approach and landing phase. The most critical situation has been found to occur shortly before touch-down when the lower jets hit the ground.

In a close cooperation between Dornier and Northrop a design study for a twin engine fighter equipped with an in-flight thrust-reverser (N/D-102) has been performed. During this period several low speed wind tunnel tests phases were run in order to study the principal effects of such a device. In this paper a summary of the test results including force measurements and flow visualisation are presented and some design rules for a reverser system are derived.

The conclusions to be drawn from these tests indicate that it is possible to separate the effects of the upper and lower jets:

- The upper jets can cause problems related to fin and rudder efficiency with operative thrust reversers. The effects near ground do not differ remarkably from those experienced in pure inflight situations. The test results obtained in this field will be discussed within paper 17.
- The lower jets - as can be presumed - may generate several problems in ground effect shortly before touch down with respect to reingestion and adverse aerodynamic interferences.

To illustrate a possible optimization procedure the most interesting results of two test periods are presented and discussed. During the first one "non-canted" lower jets were tested, because it had been assumed that such a jet configuration may cause less problems in a failure case (yawing moment during engine failure). Soon force measurements and flow visualisation made evident however that non-canted jets may not be feasible for reversers used during approach and landing. In ground effect a fountain is formed below the aircraft, the forward and side position of which is a tight function of jet pressure ratio (and hence air speed), bank angle, and side-slip of the aircraft itself. Especially the second parameter tends to cause extreme changes in lateral stability C_{δ} due to strong interference between fountain and wing. Force tests confirmed this effect.

During ground-roll the forward position of the fountain increases when speed of the aircraft is decreased. For the special fighter configuration tested, reingestion of the hot exhaust gases would have been occurred already at touch-down, and so the thrust reverser had to be cut off already prior to this point.

Therefore a second wind tunnel period has been performed where a variety of canted lower jets were tested. It will be shown that in-flight thrust reverse devices are applicable throughout the total approach and landing phases if a careful optimization with respect to cant angle is performed: The detrimental fountain can be avoided which then permits the reverser to be used down to relatively low (taxi) speeds. As a further consequence the adverse aerodynamic interference vanish leaving the stability and control characteristics close to the basic ones with reverser off.

So it can be concluded that the full potential of thrust reverse may also be exploited for flight mechanical optimization of final approach, landing, and for effective shortening of ground roll.

1. Introduction

In the preceding presentation (Paper 17) general aspects and highlights of an in-flight thrust reverser (TR) device have been demonstrated. Characteristic interference effects between upper TR-jets and vertical fin with rudder have been highlighted including the possibility to influence them in a positive manner at one type of aircraft configuration. This configuration has been developed from 1980 to 1986 by Northrop and Dornier, and has been described in the presentation mentioned above. The jet-fin interferences are a point of concern over the whole flight regime when thrust reverser mode is used.

At landing, in the approach, touch-down, and ground roll phases further problems arise from the lower TR-jets which interfere with the ground. In this condition mainly two aspects of concern exist, as illustrated in Fig. 1

- Aerodynamic interferences before touch-down

In free flight the lower jets are bent aft, away from the aircraft and especially from the wing. So no specific interference problems are to be expected as proved by the results of paper 17. At touch-down however the situation is totally changed, because the geometry of the reversed lower jets is heavily affected by the ground. Below some distance of the aircraft above ground they are turned forward and the flowfield of the wing is strongly influenced by these jets. This mechanism may cause abrupt changes in aerodynamic forces and moments on the aircraft and provoke serious and dangerous situations.

- Reingestion in ground roll

The more classical problem of reingestion is caused by the lower jets too. If reingestion occurs too early (that means at a too low q/q_{∞} -ratio) a thrust reverser is almost useless for deceleration after touch-down. The aim is to retard this event as far as possible.

In this presentation the interference effects near ground are described and a way is highlighted how to influence them positively for this special type of configuration.

Aerodynamic Interference in Ground Effect

Two windtunnel test phases were performed in order to study and optimize the interference effects of reversed jets close to ground. Phase I was run in the low-speed tunnel of DFVLR at Göttingen with simple uncanted jets ($\nu_{TR} = 0^\circ$) and a reverser angle of $\kappa_{TR} = 45^\circ$. For definition of these angles see Fig. 6. During the second phase (Phase II) in the Dornier low speed tunnel the lower jets were canted outboard by an angle of $\nu_{TR} = 30^\circ$.

In order to get a rough but more or less complete impression of the situation the tests were restricted to three attitudes of the aircraft:

- Approach near ground:

The flaps were deflected fully down (minus a certain reserve for roll control) and the aircraft was inclined to the angle-of-attack at landing of $\alpha = 15^\circ$.

The same attitude was tested with a bank angle ϕ of 10° , because it can be expected that a bank angle may have similar effects like a sideslip angle.

- Ground roll:

Tests were performed at $\alpha = 0^\circ$ with the correct distance between fuselage and ground representing the height of the landing gear.

Similar to the free flight tests only the aerodynamic interference forces on the model have been measured, excluding the jet forces themselves. The q -ratio q/q_{∞} has been varied from 25 to 75.

2.1 Phase I: Uncanted lower Reverser Jets

As mentioned above the tests started with the most simple TR configuration. That means that all thrust reverser jets were not canted.

2.1.1 Approach shortly before Touch Down

It soon became evident that this simple version would cause serious problems near ground which prohibits its use on a real aircraft.

- Aerodynamic forces and moments

The force measurements in approach demonstrated that a lot of adverse effects occurred. They are summarized in Fig. 2

Almost all the essential derivatives as rolling, yawing, pitching moment, and lift are strongly affected by the reversed jets. These values are plotted as function of sideslip angle β for a typical reverser setting in approach ($q/q_{\infty} = 27$), using as parameter the distance H of the lower TR nozzles above ground, reduced by wing span b .

The plots indicate that below $H/b=0.2$ (That means for the real aircraft that the bottom of the aftbody is about 2 meters above ground) the interferences increase rapidly and cause dramatic changes on those derivatives:

- Rolling moment is extremely stabilized in a small β range around $\beta = 0^\circ$. This overstabilization would be as critical as a strong destabilization, because a flight control system cannot cope with such an abrupt effect.
- The yawing moment is destabilized.
- The aircraft tends to pitch up due to a strong nose-up moment being in the amount of that generated by a full trailing-edge flap deflection.
- Lift decreases drastically.

These four adverse effects - especially their abrupt build-up and simultaneous occurrence - are unacceptable. Hence this simple TR configuration cannot be used in approach.

• Phenomenological Explanation

The reason for these adverse interferences can be understood by flow visualisation in ground roll as illustrated in Fig. 3 (The photos were of minor quality in this first test phase. Therefore a sketch derived from them is presented). On the left-hand side of the figure the footprint caused by reversing the jets with a q-ratio of $q/q_\infty = 50$ at zero sideslip (shaded region) is shown. As the jets blow directly against free-stream, a central fountain is formed below the cockpit. The sideward position of this fountain is strongly varied with sideslip (right side of the figure). This behaviour implies that in approach, where a q-ratio smaller than 50 can be expected, the fountain hits the aircraft more aft (see Fig. 4) which will then cause the stabilization in roll and the nose-up pitching moment. The reason for the loss in lift may be found in a suction below the wing which has its origin in the concave curvature of the jet surface.

2.1.2 Ground Roll

As indicated by Fig. 3 the central fountain which contains the hot exhaust gases of the engines is positioned considerably in front of the inlets already at a q-ratio of 50. Therefore the reverser thrust has to be cut back presumably to a q-ratio of about 25 in order to avoid reingestion. Comparing this value with typical dynamic pressure ratios needed for thrust reverse (see fig. 17 of presentation 17) it is evident that such a simple reverser configuration is almost useless not only in approach, but for deceleration after touch-down too.

2.1.3 Possible Improvements

As already implied by figure 3 the sideward position of the fountain is very sensitive to changes in crosswind. Hence a cant of the lower thrust reverser jets might be a promising measure to improve the situation. The footprint with canted lower jets should look like that sketched in Fig. 5. Several positive effects can be expected (Fig. 6):

- The central fountain will be deleted and replaced by two fountains in a sideward position which will not interfere with the inlets up to a relatively high q-ratio. Therefore the problem due to reingestion will be solved or at least retarded.
- By distributing the fountains to both sides, the problem related to the rolling moments may be relaxed because of the better symmetry of the flow.
- If the fountain is removed from fuselage and wing the large nose-up pitching moment will be likely to disappear.

Canting the lower jets outboard has of course some disadvantages too:

- The thrust reverser becomes heavier and its design will be more complicated due to vanes or similar devices which have to be installed.
- In case of single engine failure the reverser of the operating engine has to be closed immediately because of strong yawing moments induced. These certainly cannot be controlled by rudder, at least at low speed.

But in principle these disadvantages should not be too serious, and such a reverser seems to be feasible.

2.2 Phase II: Canted lower Reverser Jets

The minimum cant angle which will be sufficient to get rid of the aerodynamic problems cannot be evaluated without detailed optimization. From the design point of view this angle should be as small as possible. As a first step it has been decided to perform additional tests in a second wind tunnel campaign with a cant angle of $\alpha_{jet} = 30^\circ$. The modified model has been tested in the Dornier low speed wind tunnel, and flow visualisation was considerably improved. The results showed that the interference problems could already be solved by this first step variation.

2.2.1 Approach

- Aerodynamic forces and moments (Fig. 7)

In the most critical condition near ground ($H/b = .12$) no overstabilization in rolling moment has been measured, and the yawing moment is slightly stabilized by the reverser. Tests with bank angle showed that only a very slight destabilization in rolling moment was caused by banking. This is regarded to be uncritical. Furthermore the loss in lift and the nose-up pitching moment which occurred with non-canted jets was removed.

- Phenomenology

The expected aerodynamic effects discussed above proved to be correct. Fig. 8 shows a photo of the footprint at a $q/q_0 = .75$ and a sketch of the flow. This footprint was tested at ground roll, where the distance between model and ground plate was defined by the height of the landing gear. After the test the model has been removed. Its plan view is drawn on the ground plate to mark the exact position of the aircraft relative to the footprint.

Two definite regions can be distinguished by tracing the streamlines on the plate:

- a region dominated by free stream
- and another one which is dominated by the reverser jets.

The small region below the strakes in the plane of symmetry is not typical. Here the boundary-layer of the free stream is forced to separate by the reverser jets. In a real landing condition the aircraft itself moves relative to the ground and not the windtunnel airflow as in the case of the tests. Therefore this layer does not develop and hence cannot separate.

When following the streamlines on the floor a separation line can be detected on both sides. These lines imply that canted jets form no fountains but two side vortices. The central fountain does not develop and is replaced by a stagnation line being situated more aft than the fountain in the case of non-canted jets. Fig. 9 shows the geometry of the flow for the same q/q_0 but at a sideslip angle of $\beta = 10^\circ$. The footprint remains quite symmetrical even at sideslip which implies that it is relative insensitive to changes. This effect in combination with the others seems to be the reason for the good aerodynamic behaviour.

2.2.2 Ground Roll

In order to represent a whole ground roll, a set of pictures is composed in Fig. 10 with varying q/q_0 . The footprint and the flow on the side of the aircraft is illustrated. Comparing the pictures one can trace the development of the jet flow with increasing q -ratio - or decreasing dynamic pressure respectively. Up to a q -ratio of 75 which was the maximum value tested no reingestion occurred.

2.3 Jet Effect on Aircraft

In Fig. 11 the flow on bottom of the aircraft for $q/q_0 = 50$ is shown in more detail. On the central fuselage a small fountain of limited size can be detected, a zone which is dominated by the jets.

But when tracing the streamlines beginning at the sidewall of the inlets it is evident that the front limit of this zone is positioned somewhere on the aft part of the boxes which represent the inlets. The wing is already outside of this zone. No indication for reingestion can be detected on the fuselage at this q -ratio.

3. Conclusions

The in-flight thrust reverser tests performed at the N/D-102 configuration demonstrate that with respect to the lower thrust reverser jets several principal items have to be regarded for such a type of aircraft:

- In-flight no special problems have been detected.
- In approach aerodynamic interference effects can cause serious problems with non-canted lower jets. Hence they have to be canted outboard to a certain amount which still is a matter of detailed optimization. The cant angle tested $\alpha_{1/2} = 30^\circ$ indicates however that adverse interference effects can be avoided with such a reverser configuration.
- Reingestion problems can be resolved with canted lower jets too.

Further optimization tests have not been performed with this configuration. Therefore it is not definite that this cant angle is optimum. Nevertheless the tests demonstrate that an in-flight pitch thrust vectoring/thrust reversing device is feasible - at least on such type of configuration having a relatively small wing in a high position, a single vertical tail, and no aft-tail, and that it will provide an impressive increase in agility and performance to the aircraft.

5

References

- [1] Lorincz, D.
Chiarelli, C.
Hunt, B. Effect of In-flight Thrust
Reverser Deployment on
Tactical Aircraft Stability
and Control
17th Joint Propulsion Conference,
Colorado Springs
AIAA-paper-81-1446
- [2] Miller, E.
Protopapas, J. Nozzle Design and Integration
In an Advanced Supersonic Fighter
AIAA-paper-79-1813
- [3] Bergman, P. Thrust Vectoring Applied to
Aircraft having High Wing Loading
AIAA-paper-78-1812
- [4] Pettit, J. E.
Capone, F. J. Performance Characteristics of a
Wedge Nozzle Installed on a F-18
Propulsion Wind Tunnel Model
AIAA-paper-79-1164
- [5] Capone, F. J. The Nonaxisymmetric nozzle -
It Is for Real
AIAA-paper-79-1810
- [6] Capone, F. J.
Gowadia, N. S.
Wooten, W. H. Performance Characteristics of
Nonaxisymmetric Nozzles Installed
on the F-18 Aircraft
AIAA-paper-79-0101
- [7] Glezer, A.
Hughes, R. V.
Hunt, B. L. Thrust Reverser Effects on
Fighter Aircraft Aerodynamics

J. Aircraft Vol. 22, No. 6
(June 1985)

6.

Variables

b	wing span
C_l	lift coefficient
C	rolling moment coefficient
C_m	pitching moment coefficient
C_n	yawing moment coefficient
H	height of aft-body above ground
q_j	dynamic pressure of jet
q_∞	dynamic pressure of ambient flow
α	angle-of-attack
β	sideslip angle
κ_{10}	reverser angle of jet
ν_{10}	cant angle of jet
ϕ	bank angle of aircraft

Fig. 1 **Geometry of TR-Jets from Free Flight to Landing**



Fig. 2 **Aerodynamic Effects of Non-Canted Lower TR-Jets in Ground Effect**

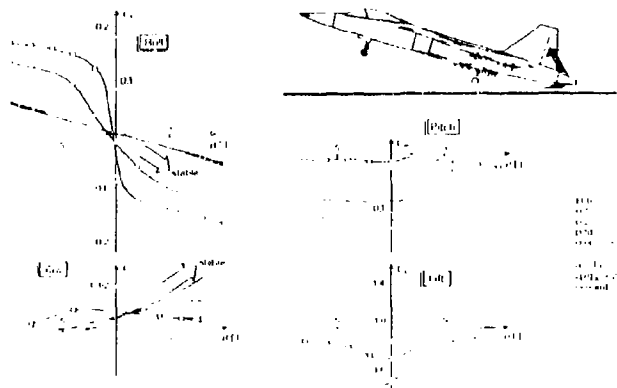


Fig. 3 **Footprint and Fountain with Non-Canted Jets at $q/q_{70} = 50$ (after Flow Visualisations)**

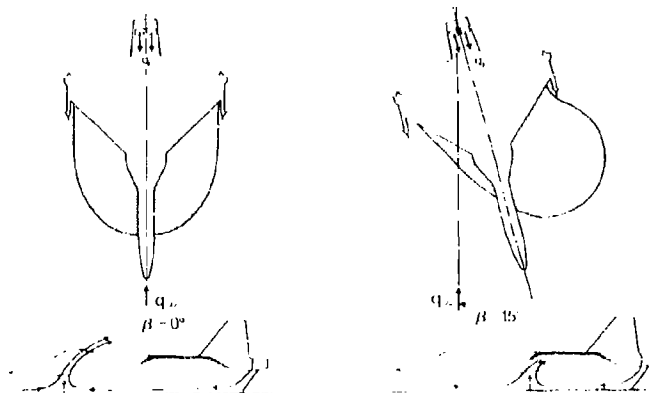


Fig 4 **Aerodynamic Effects of Non-Canted TR-Jets in Ground Effect**

Flow configurations causes:

- strong nose-up pitching moment due to fountain
 - loss of lift due to suction at lower wing surface
 - overstabilization in rolling derivative C_{δ}
 - destabilization in yawing derivative C_{δ}
 - reingestion already at touch-down speed
- Due to these adverse effects non-canted lower TR-jets are not tolerable

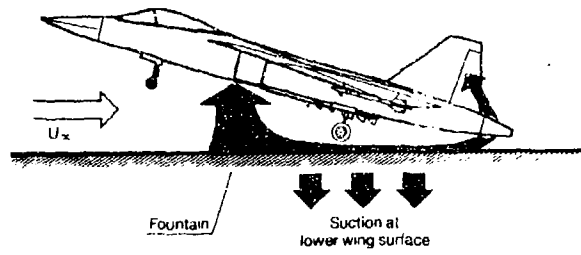


Fig 5 **Footprint with Canted Jets**

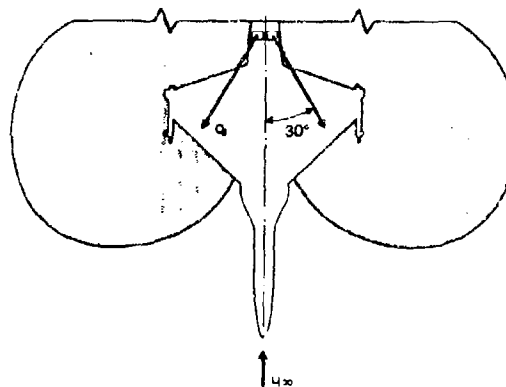


Fig 6 **Improvement due to Outboard Cant of Lower TR-Jets**

Advantage of cant:

Central fountain is reduced in strength or even avoided. Consequence:

- improved aerodynamic interference at touch-down
- retarded recirculation

Disadvantage of cant:

- TR-system more complicated
- some weight increase to be expected
- immediate closing of TR at engine failure required due to strong yawing moments

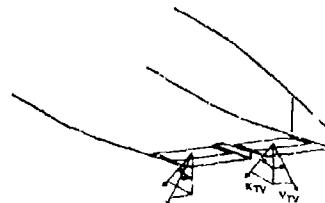


Fig. 7 **Aerodynamic Effects of Canted Lower TR-Jets ($V_{TR} = 30^\circ$) in Ground Effect**

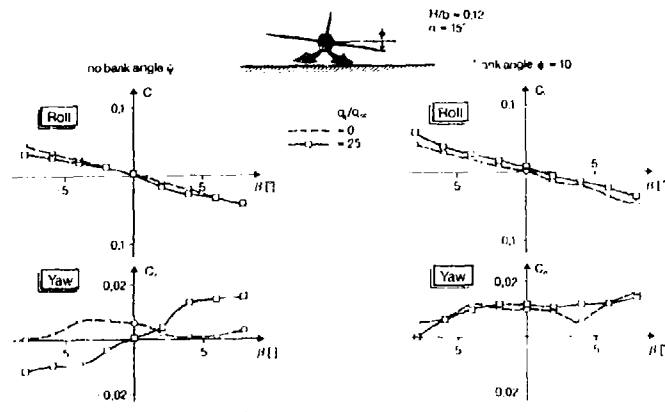


Fig. 8 **Effect of Canting**

- Central fountain reduced
- Replaced by two lateral vortices outside of wing span

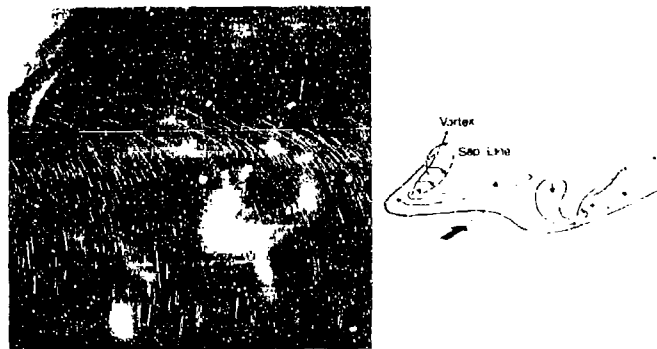


Fig. 9 **Footprint at $q/q_\infty = 75$, $\beta = 17^\circ$**

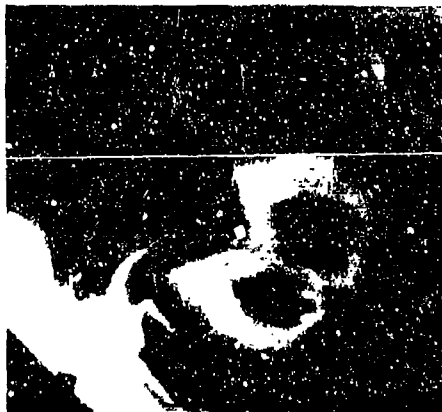


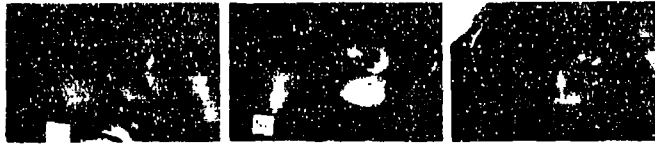
Fig. 10 **Reingestion in Ground Roll**

- Reingestion does not yet occur at $q/q_\infty = 75$

$q/q_\infty = 25$

$q/q_\infty = 50$

$q/q_\infty = 75$



Footprint



Side View

Fig. 11 **Aircraft from below ($q/q_\infty = 50$)**



Fig. 12 **In-Flight TR in Ground Effect**

Conclusions:

- Uncanted lower TR-jets give unacceptable aerodynamic interference related to
 - aerodynamic forces and moments shortly before touch-down
 - reingestion
- A cant cures the adverse aerodynamic effects of uncanted TR-jets

ETUDE DE L'EFFET DE SOL AU CEAT EXPLOITATION DES RESULTATS

par

Georges Vidal
Ingénieur d'Essais
TUNNEL AÉRO-HYDRODYNAMIQUE
CEAT -- (Toulouse)
23 Avenue Hemi Gullaumet
31056 Toulouse, Cedex
France

et

Jacques Deschamps
Ingénieur d'Etudes Aérodynamiques
MYSTERE FALCON ENGINEERING DIVISION
AMD-BA MERIGNAC

RESUME

Depuis 1979, le Tunnel Aéro-Hydrodynamique du CEAT est équipé d'une plate-forme entièrement carénée, propulsée par un moteur linéaire permettant d'atteindre la vitesse de 40 m/s.

Ce moyen d'essai est surtout utilisé en aérodynamique pour les études du comportement des avions en présence du sol.

L'objet de ce document est de présenter tout d'abord les moyens d'essai, puis de décrire les montages utilisés pour l'étude de l'effet de sol, et enfin de montrer quelques résultats de mesure.

Pour le constructeur d'avions, il est en effet essentiel de connaître l'influence de la proximité du sol sur les coefficients aérodynamiques longitudinaux et transversaux.

A titre d'exemple nous donnons quelques résultats d'essais effectués sur une maquette de l'avion d'affaire Falcon 900 au 1/10.

Les résultats montrent que l'effet de sol augmente le coefficient de portance et le moment longitudinal piqueur pour des incidences usuelles d'utilisation.

De même la traînée diminue et la finesse augmente quand l'aile s'approche du sol.

Au contraire le C_z et l'incidence de décrochage diminuent dans l'effet de sol.

Le calcul numérique de répartition de pression effectué sur ordinateur par la méthode des singularités, montre que sur un profil de voilure, l'effet de sol augmente la pression à l'intrados et la dépression dans la partie avant de l'extrados, le résultat global étant une augmentation de portance.

Ces résultats théoriques sont cohérents avec les essais effectués au Tunnel Aéro-Hydrodynamique.

ABSTRACT

Since 1979, the Aero-Hydrodynamic Tunnel of CEAT Toulouse is equipped with a faired platform powered by an electrical linear induction motor enabling a maximum speed of 40 m/s.

This method is chiefly used in aerodynamic tests to analyse the aircraft behaviour in ground effect.

The purpose of this document is to show the equipment and facilities used for the ground effect tests, and to provide a few measurement data.

For aircraft manufacturers it is essential to know the effects of ground proximity on the aerodynamics of the wing.

The ground effect has been studied on a Falcon 900 model (scale 1/10) at the A.H.T. of Toulouse.

Results show that ground effect increases the lift coefficient and the pitching moment (nose down) for usual angle-of-attack.

In the same way the drag decreases and the lift-to-drag ratio increases as the wing approaches the ground.

On the contrary, stall C_l and stall angle-of-attack decrease in the ground effect.

Numerical computation of pressure distribution by a panel method shows that on a wing profile the ground effect increases the pressure on the lower surface and decreases the pressure on the forward part of the upper surface.

The overall result of ground effect is an increase in the normal force.

These computation results are in good agreement with the test results obtained at the Aero-Hydrodynamic Tunnel.

NOTATION ---

C_p	Pressure coefficient $(p_l - p_{\infty})/q$
p_l	Local static pressure
p_{∞}	Static pressure in free stream
q	Dynamic pressure $1/2 \rho V^2$
V_S	Stall speed in flight
V_S'	Stall speed in ground effect
C_L	Lift coefficient
C_D	Drag coefficient
C_M	Pitching moment coefficient
α	Angle-of-attack
δ_m	Elevator
V_C	C.A.S. Calibrated Air Speed
V_I	Critical engine failure speed
T/P	Thrust/Weight ratio
Finesse Lift/Drag ratio $f = C_z/C_x$	
Z	Height of wheel/ground
H	Proximity ratio Z/b
b	Semi span

NOTATION

K_p	Coefficient de pression $(p_l - p_\infty)/q$
p_l	Pression statique locale
p_∞	Pression statique infini amont
q	Pression dynamique $1/2 \rho V^2$
V_S	Vitesse de décrochage vol
V_S'	Vitesse de décrochage dans l'effet de sol
C_Z	Coefficient de portance
C_X	Coefficient de traînée
C_M	Coefficient de moment de tangage
α	Incidence
δ_m	Gouverne de profondeur
V_C	Vitesse conventionnelle
V_l	Vitesse de panne au décollage
π/p	Rapport poussée/poids
Finesse	$f = C_Z/C_X$
Z	Hauteur roue/sol
H	Rapport Z/b
b	Demi envergure de l'aile

A - ETUDE DE L'EFFET DE SOL AU CEAT

1 - PREMIERS MOYENS UTILISES AU CEAT POUR L'ETUDE DE L'EFFET DE SOL

Les premiers essais d'effet de sol au tunnel aéro-hydrodynamique datent de 1974. Auparavant, deux souffleries du CEAT avaient permis l'étude de l'influence du sol sur des aéronefs, au moyen d'un plancher réglable en hauteur. Il s'agit des souffleries S 4 et S 5, où se sont déroulées les campagnes suivantes :

Soufflerie S 4

Date	Avion
06.61	Caravelle
10.64	MS 760
08.72	Falcon 10
08.74	Falcon 50 Mystère 20
07.76	Falcon 50

Soufflerie S 5

Date	Avion
05.54	Mystère IV A Breguet 940
08.54	SS 212 C 160 Motorisé
1968 1970	Mirage G 01
1968 1970	TSS (Concorde)
03.70	Falcon
05.74	Jaguar

On voit bien qu'à partir de 1976, les essais d'effet de sol ont été interrompus dans ces souffleries pour être transférés au Tunnel qui déjà à l'époque, semble être considéré comme le site le mieux adapté pour ce type d'essai, et ce, malgré l'utilisation d'une plate-forme mue par un réacteur ATAR 8 (induisant d'importantes perturbations aérodynamiques).

2 - LE TUNNEL AERO-HYDRODYNAMIQUE (TAH)

2.1 - Description (planche 1)

Le tunnel a été construit entre 1947 et 1952, et était destiné à l'étude de carènes d'hydravions.

C'est un tube horizontal en béton précontraint d'une longueur de 1200 mètres, au fond duquel est situé un bassin de 5,60 m de large par 3 m de profondeur.

La veine d'air pratiquement semi-circulaire ($S = 25 \text{ m}^2$) est formée à ses deux extrémités pour assurer l'immobilité de l'écoulement.

L'ensemble est recouvert d'un remblai de terre permettant une régulation naturelle de la température.

De part et d'autre du bassin ont été disposés des rails sur toute sa longueur (écartement 6 m). Ils ont la particularité d'épouser la courbure terrestre de façon à maintenir les maquettes à hauteur constante par rapport au plan d'eau.

2.2 - Intérêt des mesures d'effet de sol au TAH

Le fait que la maquette se déplace dans la veine d'air immobile est le principal avantage du tunnel par rapport aux autres souffleries. L'essai est beaucoup plus représentatif puisque c'est bien l'avion qui se déplace en réalité, et d'autre part, qu'il n'y a pas d'apparition de couche limite parasite près de la surface de l'eau, ce qui n'est pas le cas sur les planchers simulant le sol en soufflerie.

Enfin, le taux de turbulence relevé dans le tunnel lors de tirs à 40 m/s est inférieur à celui des souffleries en général.

Il faut noter que le plan d'eau est indéformable et les turbulences induites par le mouvement du chariot négligeables lorsque la maquette est située suffisamment en amont de la plate-forme d'essai (3 m minimum).

3 - LA PLATE-FORME A MOTEUR LINEAIRE (PML)

3.1 - Description -- performances (planche 2)

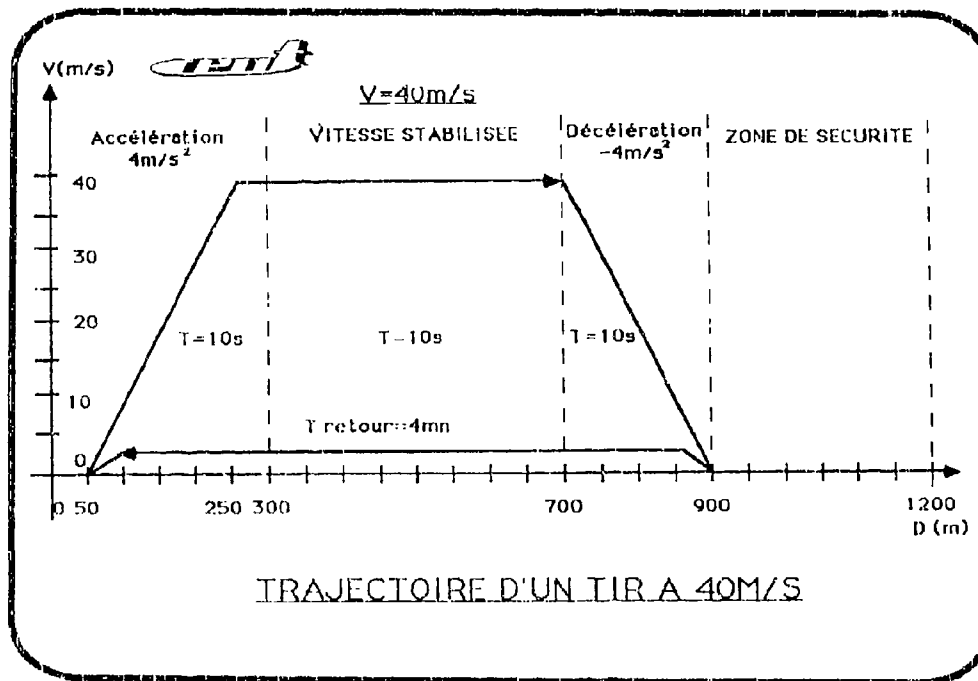
La plate-forme actuelle qui permet de déplacer la maquette à grande vitesse a été mise en service au tunnel en 1979 pour remplacer l'ancienne plate-forme à réacteur, difficile à piloter et trop bruyante.

Sa propulsion est assurée par un moteur triphasé asynchrone à induction linéaire dont l'inducteur en forme de U est fixé sur la structure du fuseau droit de la plate-forme.

Les montages d'essais viennent se fixer sur la poutre avant et sur une palette alvéolaire située au centre de la plate-forme. Pour les essais aérodynamiques, la plate-forme est équipée de carénages et de planchers canalisant mieux l'écoulement.

La plate-forme d'une masse à vide de 12,5 tonnes atteint la vitesse de 40 m/s au bout de 200 mètres (poussée du moteur ; 6000 daN).

La séquence du tir est la suivante :



3.2 - Historique "effet de sol"

Ancienne plate-forme à réacteur

Date	Avion
04.74	Mirage 2000
02.75	Mirage G 01
03.76	Mirage G 01
03.77	Mirage 2000
09.77	Mystère 50 Mirage 2000

Plate-forme à moteur linéaire

Date	Avion
12.82	A.C.T.
04.83	Falcon 900
03.84	Falcon 10
04.84	Falcon 20 F F.C.F.
12.85	Rafale A
04.86	
02.88	Rafale A

4 - MONTAGE "EFFET DE SOL"

4.1 - Montage en potence (planche 3)

C'est le premier montage réalisé au tunnel et fixé au départ sur l'ancienne plate-forme. Il permet de positionner la maquette 3 mètres en amont du bord d'attaque de la P.M.L. Un mât vertical reprend celle-ci (masse maxi : 100 kg) par l'extrados.

Une glissière verticale de course 700 mm permet de régler la hauteur de la maquette, son débattement en incidence étant assuré par un vérin hydraulique.

4.2 - Montage en dard (planche 4)

Ce montage a été réalisé en 1984 et validé juste avant le passage du "Rafale A" en 1985.

La maquette est montée en amont de la P.M.L. à l'extrémité d'un dard venant en prolongement du montage principal. Ce montage permet d'étudier l'effet de sol (à $V = 40$ m/s) sur des maquettes de moyennes dimensions (masse maxi : 100 kg). Le montage est constitué par un mât de 4,5 m de long placé en amont de la plate-forme d'essai. Son déplacement suivant un arc de cercle permet un débattement en incidence de 22° pendant les 10 secondes que dure le palier de vitesse. L'ensemble est monté sur un support à glissière verticale de course 1 520 mm, la hauteur maximale atteinte étant suffisante pour placer la maquette en position "hors effet de sol" et permettre le recouplement avec les essais réalisés en soufflerie.

Le montage d'origine a été modifié de façon à isoler le dard des accélérations parasites de la PML suivant l'axe Y (dus au déport du moteur linéaire). L'ensemble repose sur la poutre avant de la PML par l'intermédiaire d'un bloc qui autorise un pivotement en lacet et un déplacement suivant l'axe Y. Ces déplacements sont limités par un système amortisseur réglé lors de la mise en service de ce découpleur.

A l'arrière, le montage est en appui sur une plaque à billes par l'intermédiaire d'un étrier support de façon à verrouiller l'ensemble en tangage tout en laissant libres les déplacements suivant l'axe Y.

4.3 - Comparaison

	Potence	Dard	Observations
Position maquette/ bord d'attaque	3 m	4,2m	Pratiquement pas de perturbations avec le montage dard (d'après étude écoulement amont PML).
Débattement incidence (°)	22°	22°	Essais seulement effectués à dérapage fixe (0°, 5°, 10°, 20°)
Course glissière verticale (mm)	700	1520	Course du montage en dard suffisante pour toutes les hauteurs (pas de variation de niveau d'eau)
Poids maximum maquette (kg)	100	100	Un autre montage sous PML existe pour les grosses maquettes, mais problèmes de corrections importants. Pas besoin de correction de paroi ou de blocage avec les deux montages présentés dans le document.

5 - MESURES

5.1 - Types de mesures

Les mesures suivantes sont effectuées à chaque essai :

- Les 6 efforts aérodynamiques X, Y, Z, L, M, N.
- L'incidence maquette.
- Les accélérations longitudinales et transversales, γ_x et γ_y .
- Les pressions dynamiques mesurées par deux pitots permettant de déterminer la pression dynamique au niveau de la maquette (cf paragraphe 6.1).
- La vitesse du chariot.

5.2 - Chaîne de mesures actuelle (planche 5)

L'acquisition des mesures est effectuée par une chaîne de télémesure numérique, en modulation par impulsions codées (MIC ou PCM) dont le fonctionnement schématisé est le suivant :

Sur la plate-forme les signaux issus des différents capteurs sont conditionnés filtrés à 2 Hz, puis envoyés sur un multiplexeur codeur à format fixe qui élabore un message numérique série composé des valeurs codées sur 12 bits (32 voies maxi, cadence maxi : 1,3 kHz).

Le message série ainsi formé est alors transmis par un émetteur VHF, une antenne et un câble rayonnant vers la station sol. Dans la salle de mesure, un récepteur restitue le message numérique PCM qui est, dans tous les cas, sauvegardé sur bande magnétique.

Les mesures sont par ailleurs stockées sur une unité de disque (sous forme numérique) et restituées sous forme analogique pour visualisation en temps réel sur enregistreur graphique (validation partielle du tir).

Un premier traitement local permet de moyenner les fichiers mesures avant transmission vers le centre de calcul du CEAT.

5.3 - Premiers éléments d'exploitation

Les courbes classiques $C_Z = f(\alpha)$; $C_Z = f(C_X)$; $C_Z = f(C_m)$ sont systématiquement fournies au client.

Pour des configurations de dérapage, de gauchissement et de drapeau les courbes ($\gamma = 1$) ; $C_{Y1} = f(\alpha)$; $C_{I1} = f(\alpha)$ sont également fournies. Toutefois ces coefficients n'ont pas été étudiés pour les essais d'avions civils.

Toutes ces courbes sont accompagnées de leurs listings de résultats comportant les conditions d'essais et des précisions sur les calculs. Les groupages sont fournis ensuite à la demande du client.

6 - ESSAIS D'EFFET DE SOL

6.1 - Campagne préliminaire (planche 6)

Une campagne d'identification de la veine (sans maquette) a été effectuée pour chaque montage.

La pression dynamique de la maquette (Q_{maq}) est fournie par quatre pitots disposés au niveau de la maquette.

Un pitot supplémentaire fournit la pression dynamique de référence ($Q_{réf}$).

L'identification consiste d'abord à déterminer le coefficient de veine $R_v = \frac{Q_{max}}{Q_{ref}}$ en fonction de la hauteur maquette (planche 7).

La deuxième partie de la campagne permet de déterminer l'ascendance $\Delta\alpha$ de l'écoulement au niveau de la maquette en fonction de la hauteur de celle-ci (planche 7).

6.2 - Description des essais

Les campagnes débutent toujours par des essais de recouplement à hauteur supposée infinie pour valider le montage et les mesures.

Chaque tir comporte une prise de zéros maquette à incidence nulle, puis une polaire de gravité, plate-forme arrêtée, identique à la polaire de l'essai, enfin la polaire proprement dite à vitesse stabilisée.

B - EXPLOITATION DES RESULTATS

Effet de sol FALCON 900

Nous présentons ici une étude de l'effet de sol effectuée sur une maquette de l'avion d'affaire FALCON 900 au 1/10 au bassin hydrodynamique du CEAT de Toulouse.

La maquette est fixée sur un chariot qui se déplace à $V = 40$ m/s. Au cours des essais l'incidence avion varie de -2° à 20° . A chaque essai on fait varier l'altitude de l'avion, c'est-à-dire la hauteur de la roue du train principal par rapport au plan d'eau, de $Z/b = 1,578$ à $0,031$ (b demi envergure de l'aile).

Nous avons étudié les configurations de décollage et d'atterrissage. Plusieurs braquages de la gouverne de profondeur δ_m ont été réalisés dans le but d'obtenir les courbes équilibrées.

Description de l'avion

Le Falcon 900 est un avion d'affaire tri-moteurs à aile basse dont la hauteur de l'aile par rapport au sol au roulage est de $Z = 1,100$ m à l'emplanture et de $1,300$ m à l'extrémité. L'envergure de l'aile est de $19,300$ m et la longueur fuselage de $19,700$ m. L'allongement est $\lambda = 7,66$. La flèche au bord d'attaque interne est $\varphi = 35^\circ$ et $\varphi = 27^\circ$ dans la partie externe.

Les vues de profil et de face sont représentées sur la planche 3.

Etude des résultats

L'examen des résultats bruts permet de faire les remarques suivantes :

Quand l'avion se rapproche de sol,

- les $C_z = f(\alpha)$ se déplacent vers la gauche
- le C_z de décrochage diminue (planche 9)
- le moment longitudinal piqueur augmente (planche 10)

Les essais effectués à différents braquages de la gouverne de profondeur permettent de calculer les courbes équilibrées suivantes :

$$- C_z = f(\alpha) \quad \delta_m = f(C_z) \quad \text{Finesse} = f(C_z) \quad \text{Polaire} = f(C_z)$$

Considérons les C_z équilibrés :

A l'équilibre et suivant la configuration la perte de C_z max est de l'ordre de 12 à 14 % ; la diminution de l'incidence de décrochage étant de 5 à 6°. Au C_z d'utilisation correspondant à 1,2 VS ou 1,3 VS l'effet de sol déplace vers la gauche les incidences de - 2 à - 2,5° ; soit pour une incidence donnée une augmentation de C_z de l'ordre de 20 points (planche 11).

Dans l'effet de sol la vitesse décrochage augmente jusqu'à :

$$VS'/VS = \sqrt{CZ/CZ'} \text{ soit environ 8 \% .}$$

Gouverne δ_m d'équilibre

Dans la configuration décollage à 1,2 VS on voit que l'effet de sol conduit à une position de gouverne plus à cabrer d'environ $\delta_m = - 6^\circ$ pour équilibrer l'avion, ceci étant dû au moment piqueur qui apparaît au voisinage du sol (planche 12).

Finesse

La finesse augmente considérablement dans l'effet de sol, à 1,2 VS au décollage on note un gain de l'ordre de 75 %. A titre d'exemple ceci correspond à une augmentation de pente stabilisée de 3° pour un $M/P = 0,2$ (planche 13).

Trainée

Diminution importante de l'ordre de 45 % de la trainée à 1,2 VS dans la configuration décollage (planche 14).

On voit donc l'importance de l'effet de sol sur la modification de certains coefficients aérodynamiques qui caractérisent la stabilité longitudinale statique et les performances. Il est donc impératif d'appliquer ces variations aux bases de données qui servent à modéliser l'avion dans les codes de calcul de performance et de simulation de vol.

A titre d'exemple un calcul de performance au décollage effectué au poids maxi avec coupure d'un moteur à $V_L = 115 \text{ Kt}$ montre que l'effet de sol fait gagner 2 secondes sur le passage des 35 Ft, soit un gain de distance d'environ 130 mètres.

Simulateur de vol

On a effectué une simulation de décollage avec et sans effet de sol à partir de VR en supposant que le pilote affiche la même loi d'assiette dans les deux cas. On voit que l'effet de sol conduit à une loi de pilotage assez différente (planche 15). Les évolutions de Z et VC en fonction du temps figurent sur la planche 16.

Evolution des profils de KP dans l'effet de sol

Il est intéressant de connaître l'évolution des coefficients de pression autour d'un profil voilure dans l'effet de sol. Nous n'avons pas fait de mesure directe au bassin hydrodynamique de Toulouse, par contre nous avons effectué un calcul d'aérodynamique théorique par la méthode des singularités sur l'avion complet en présence de la piste (planche 17). Le calcul a été effectué pour une incidence de 10 degrés hors effet de sol et avec effet de sol.

Le calcul donne la répartition de pression sur l'avion complet et sur la piste, ce qui permet donc de connaître l'évolution des KP dans n'importe quel profil voilure ou empennage. Dans le profil voilure figurant sur la planche 18, on voit que l'effet de sol augmente la surpression sur tout l'intrados, et la dépression dans la partie avant du profil. On a la même chose sur l'empennage horizontal.

Ce calcul montre bien l'augmentation de portance à incidence donnée dans l'effet de sol et l'existence d'un moment piqueur dû au bras de levier de l'empennage horizontal. La diminution de trainée est due à l'augmentation de la succion de bord d'attaque.

Il est intéressant de connaître la contribution de chaque élément de l'avion dans les gains de C_z et de moment longitudinal :

Fuselage	: Delta C_z = 30 %	Delta C_m = - 17 %
Voilure	: " 45 %	" - 19 %
Empennage	: " 24 %	" + 134 %
Mâts	: " 1 %	" + 2 %
Total	: Delta C_z = 0.172	Delta C_m = - 0.08

Ces résultats de calculs théoriques sont tout à fait cohérents avec les résultats des essais effectués au bassin hydrodynamique du CEAT.

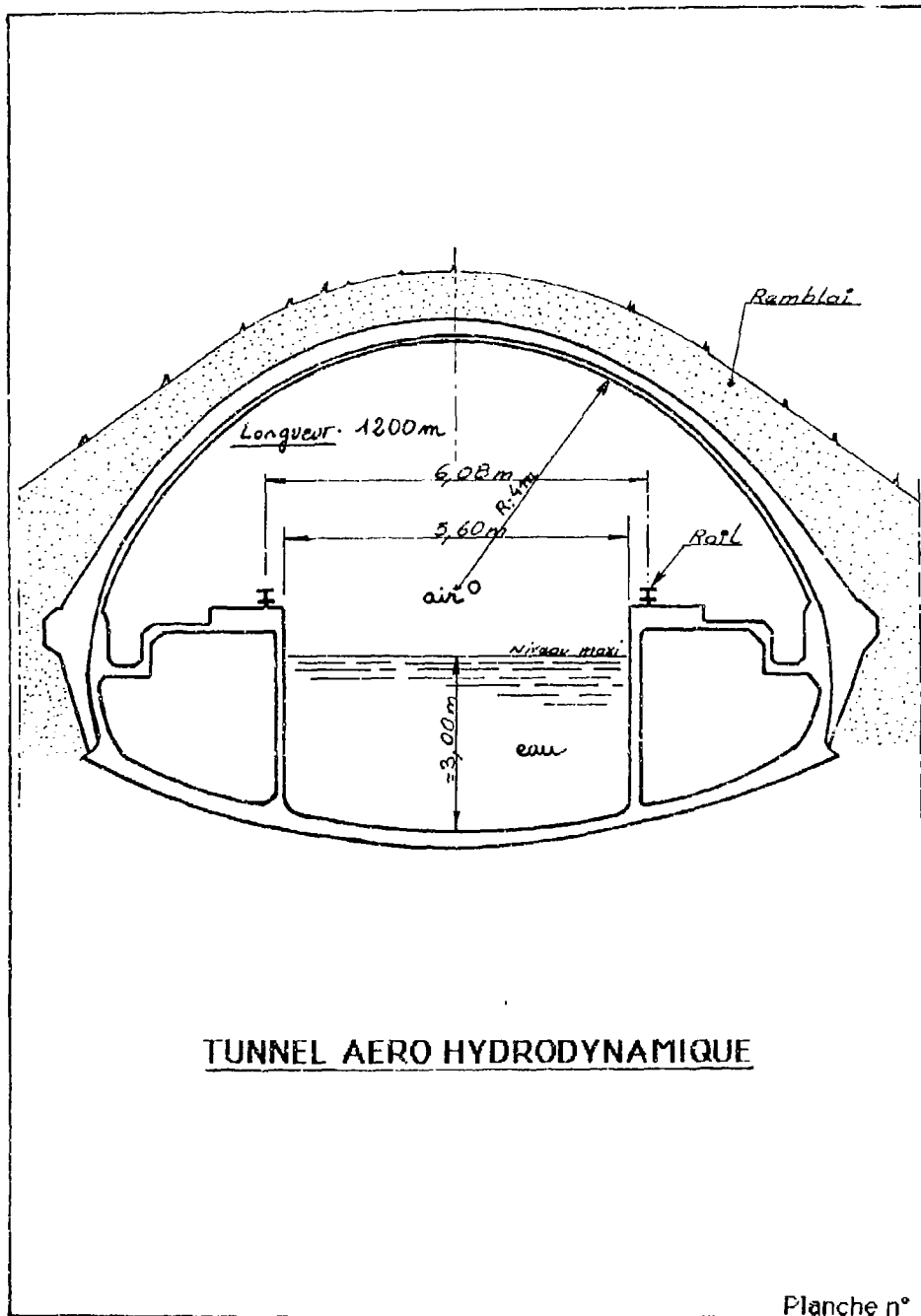
On peut expliquer l'effet de sol en disant que lorsque l'aile se rapproche du sol, la réduction du débit entre l'aile et la piste conduit à une augmentation de pression à l'intrados et à un recul du point d'arrêt ce qui entraîne un accroissement de la circulation autour du profil se traduisant également par une augmentation de la dépression à l'extrados.

Sur la planche 19 on a visualisé la répartition de pression sur l'ensemble de l'avion et sur la piste pour $\alpha = 10^\circ$ et $Z = 0$. On remarque l'étendue de la plage de surpression qui s'étend en amont de la pointe avant du fuselage. On note également la trace des tourbillons marginaux d'extrémité voilure sur la piste.

Conclusion

L'étude de l'effet de sol a montré l'importance de la variation de certains coefficients aérodynamiques quand l'avion se rapproche du sol jusqu'à l'impact. Ces variations de paramètre modifient considérablement le comportement et les performances de l'avion au voisinage du sol.

Il est donc essentiel d'introduire les corrections nécessaires en fonction de l'incidence et de l'altitude avion dans les modèles mathématiques utilisés pour les codes de calcul et les simulateurs de vol, afin de se rapprocher au mieux des performances et qualités de vol au décollage et à l'atterrissage.



1- Fuseau droit caréné support du moteur	Longueur: 7,5m
2- Rails d'alimentation basse tension (380V)	Largeur : 6,5m
3- Induit moteur linéaire	Poids : 12,5t
4- Rails d'alimentation haute tension moteur (5kV)	Vitesse : 0/40m/s (40m/s pendant 10s)
5- Inducteur moteur linéaire	Poussée moteur: 60000N (accélération max: 4m/s ²)
6- Carénage avant	
7- Fuseau gauche caréné comportant les boîtes de mesure	

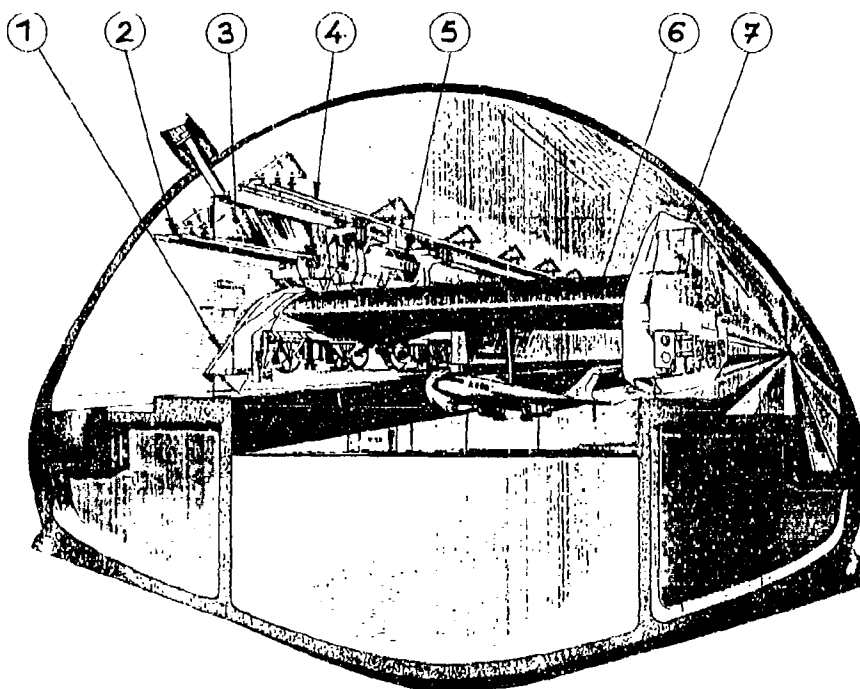
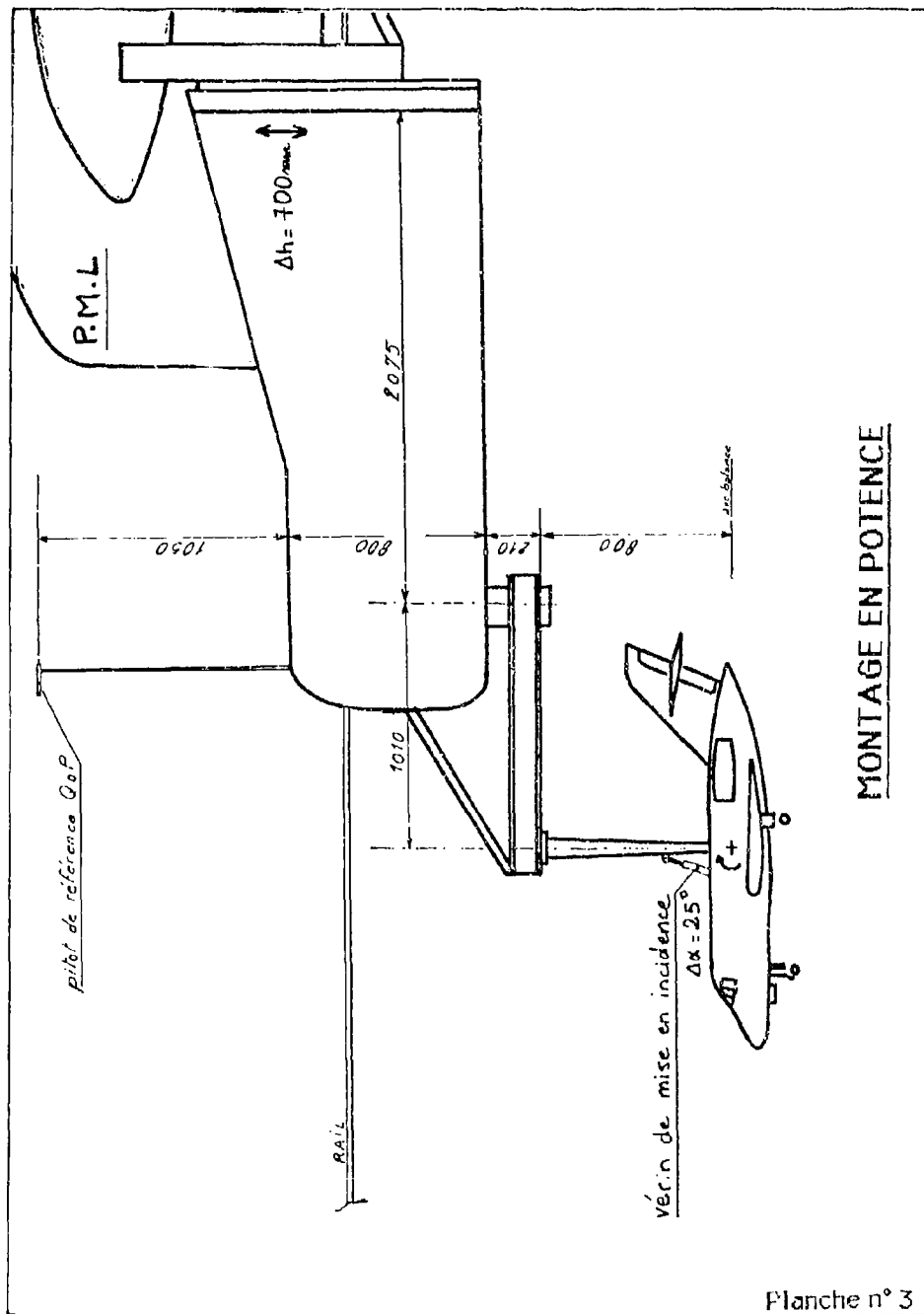
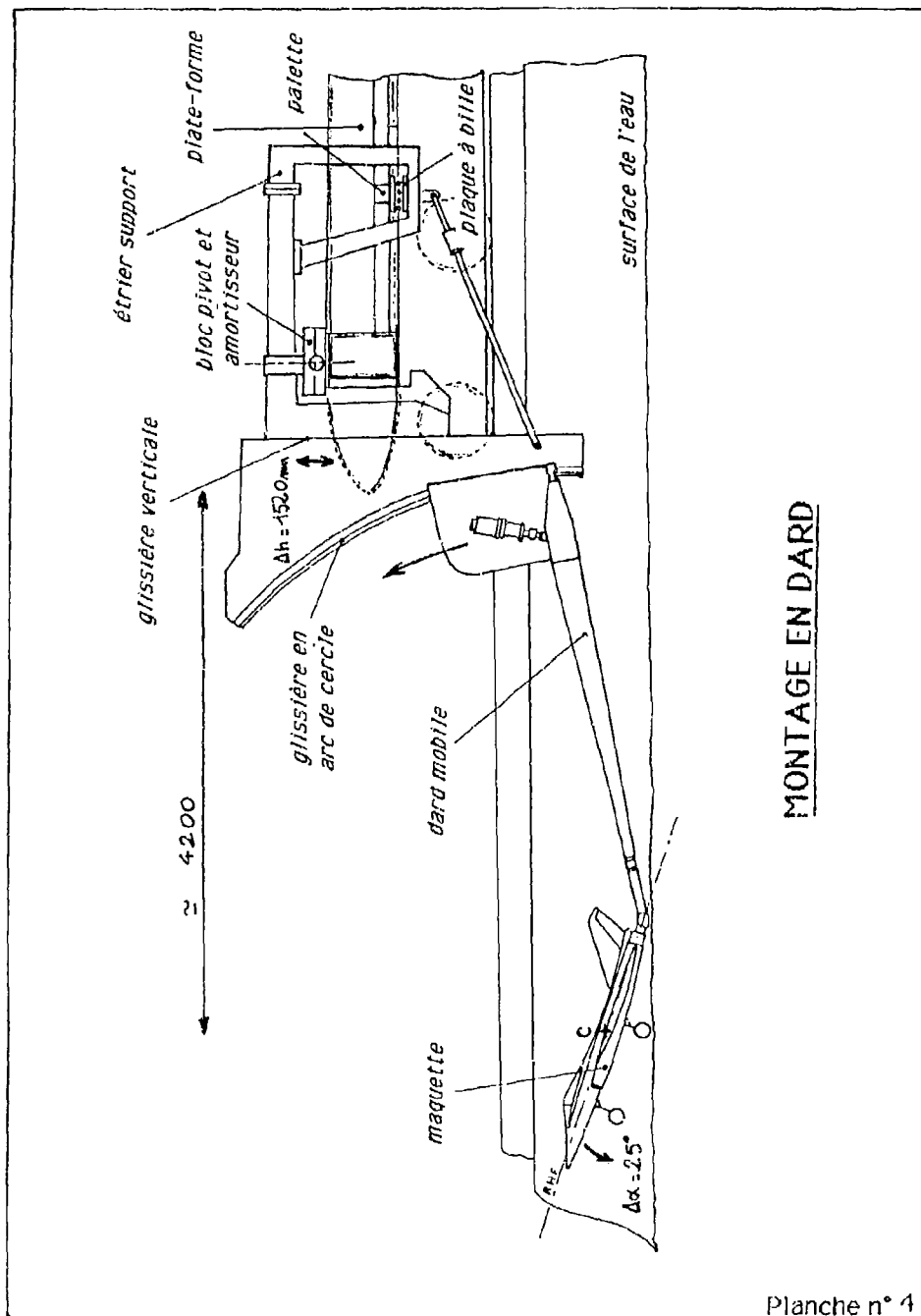
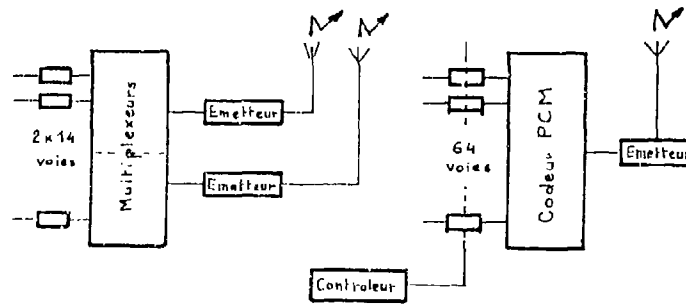


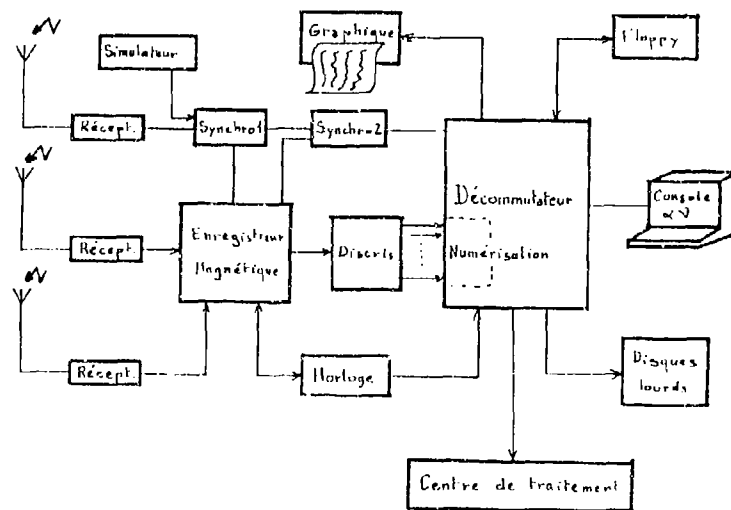
PLATE-FORME A MOTEUR LINEAIRE





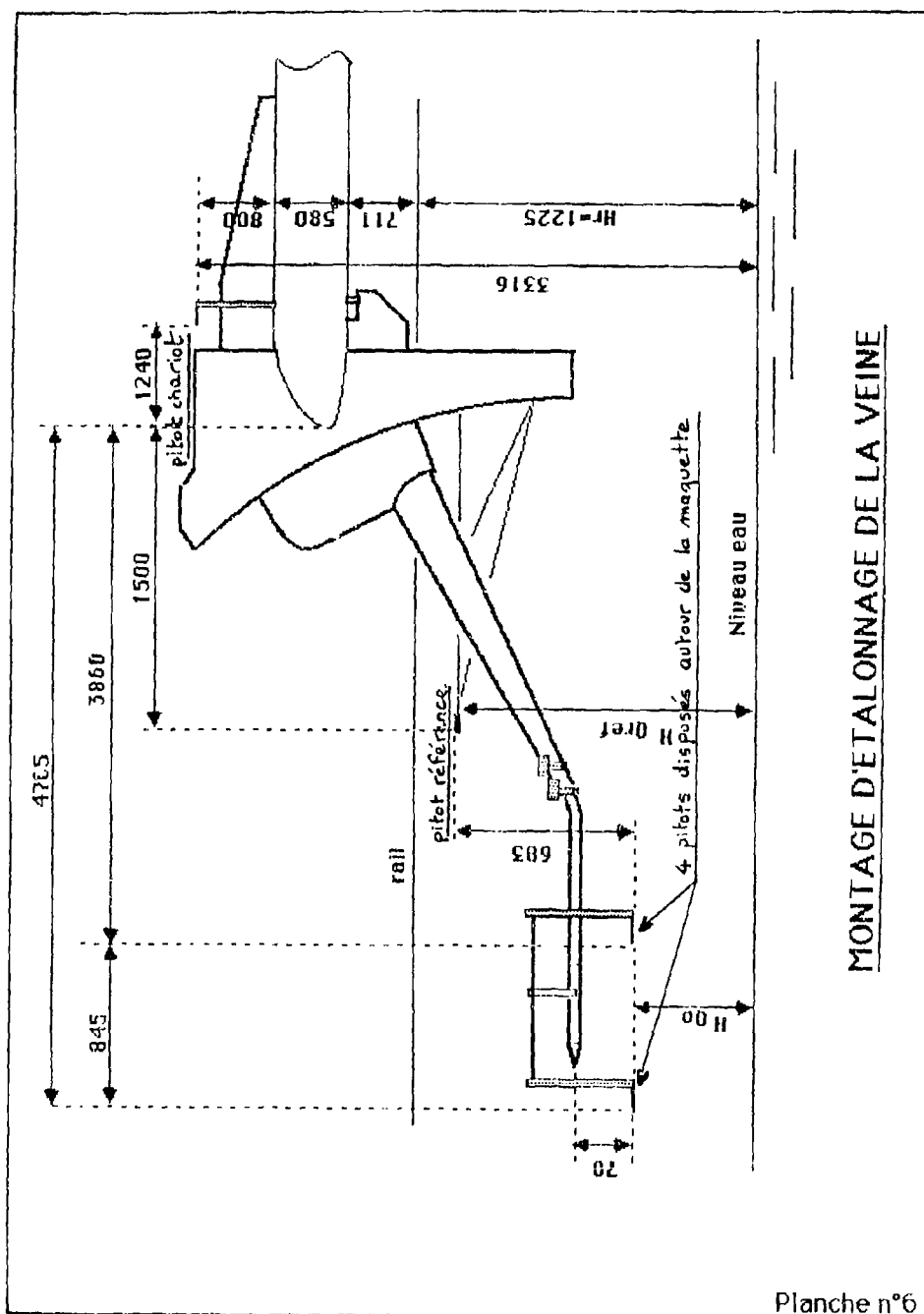


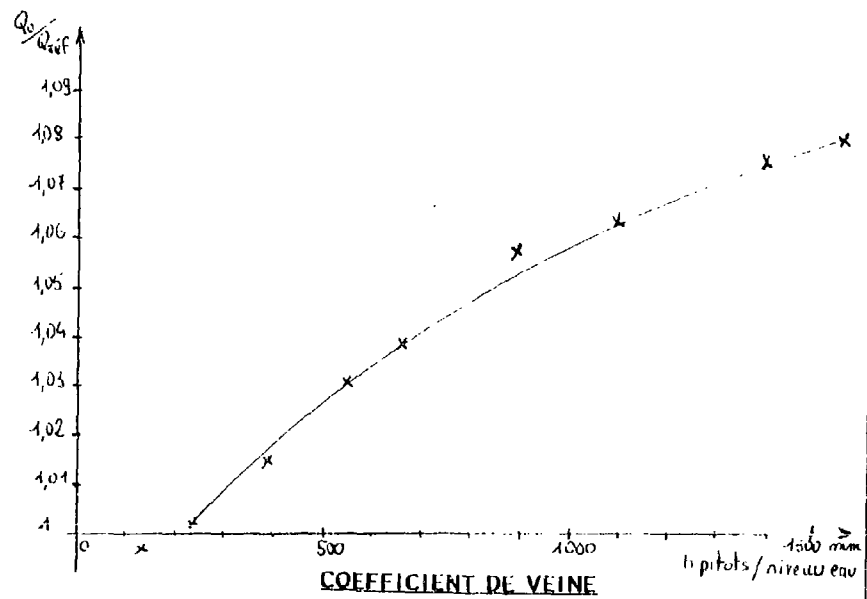
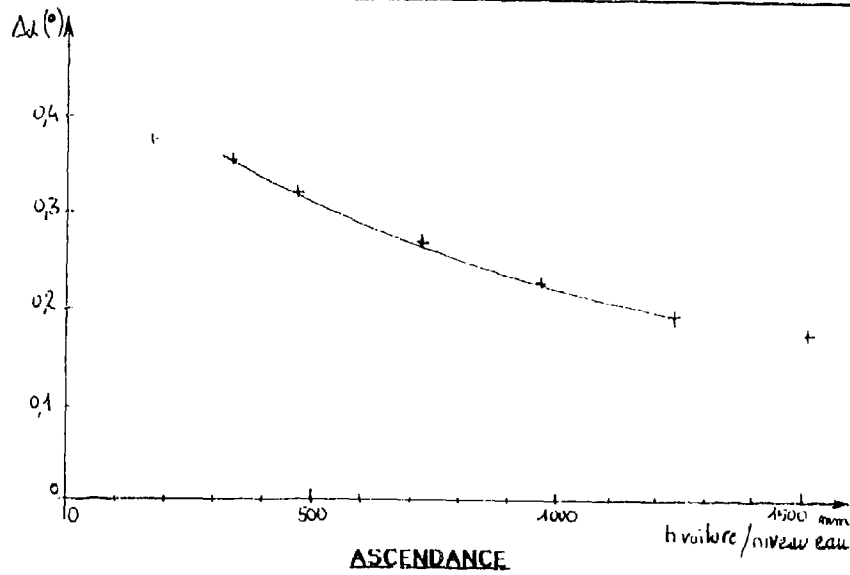
Sous ensemble Bord (P.M.L)



Sous ensemble Sol

CHAINE DE MESURES





CORRECTIONS APPLIQUEES

Planche n°7

FALCON 900

éch : 1/120

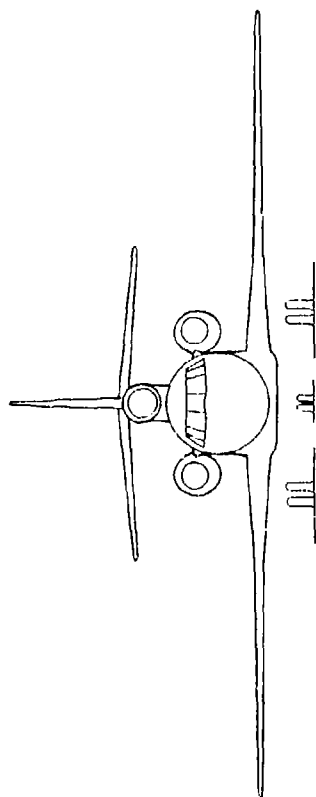
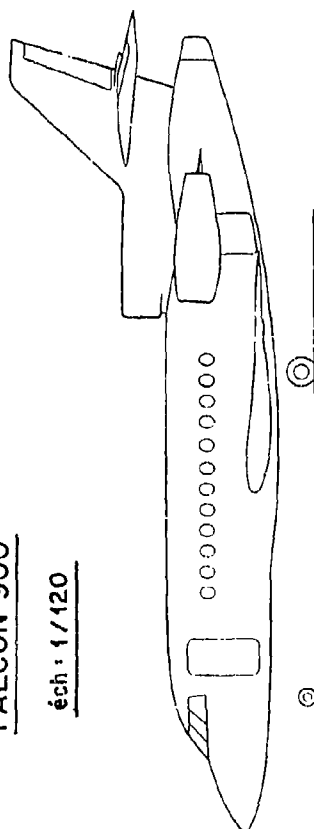
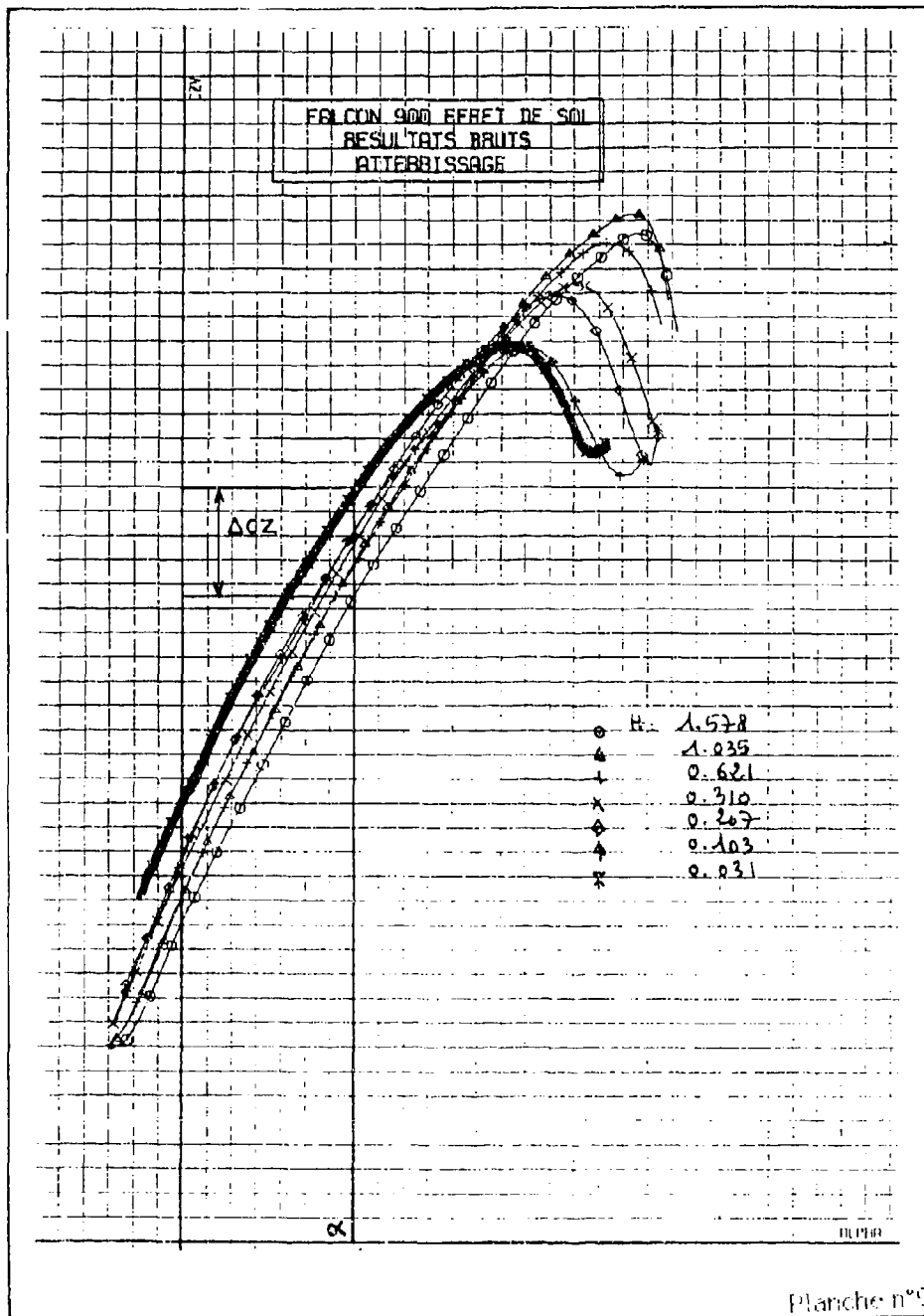
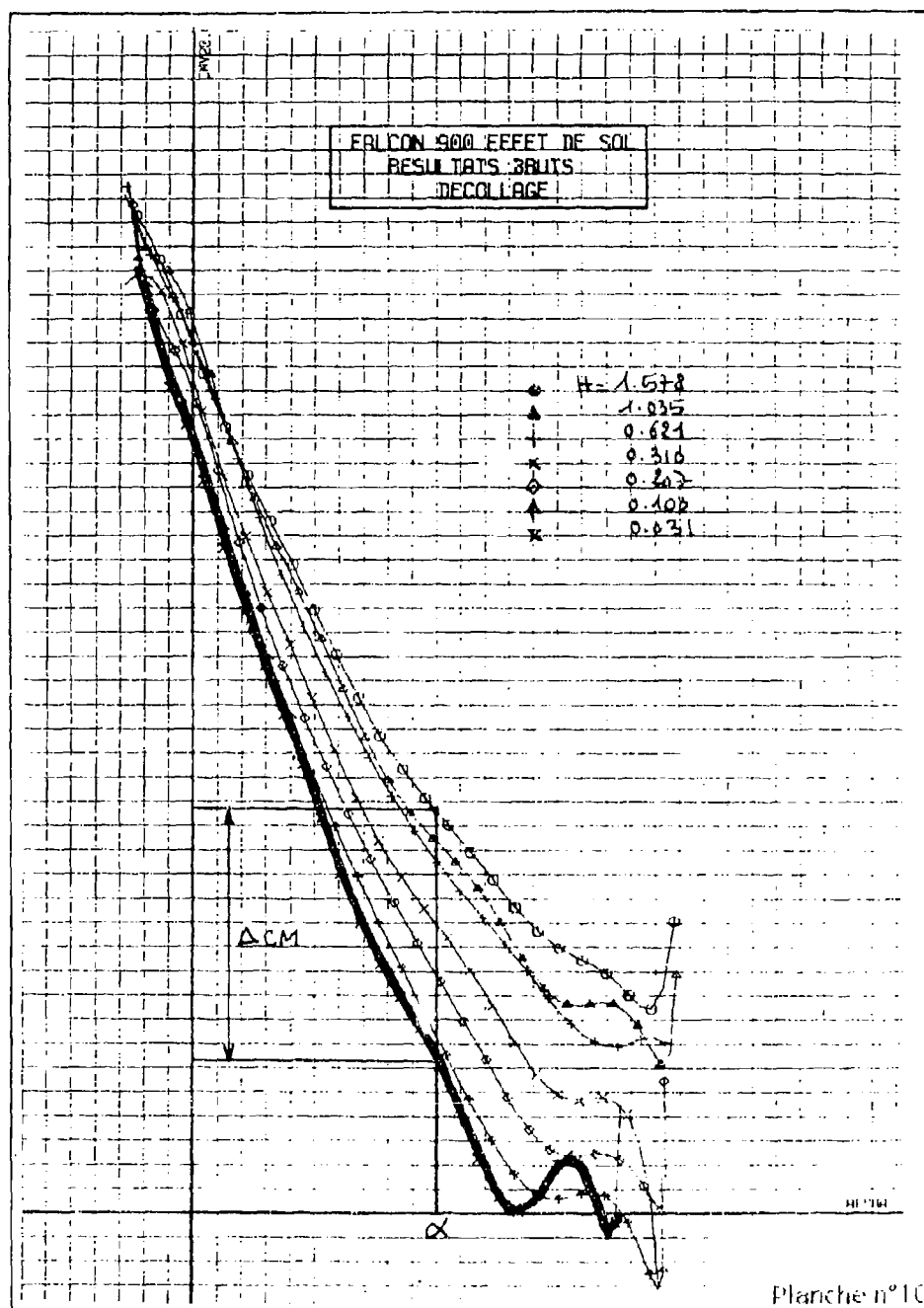
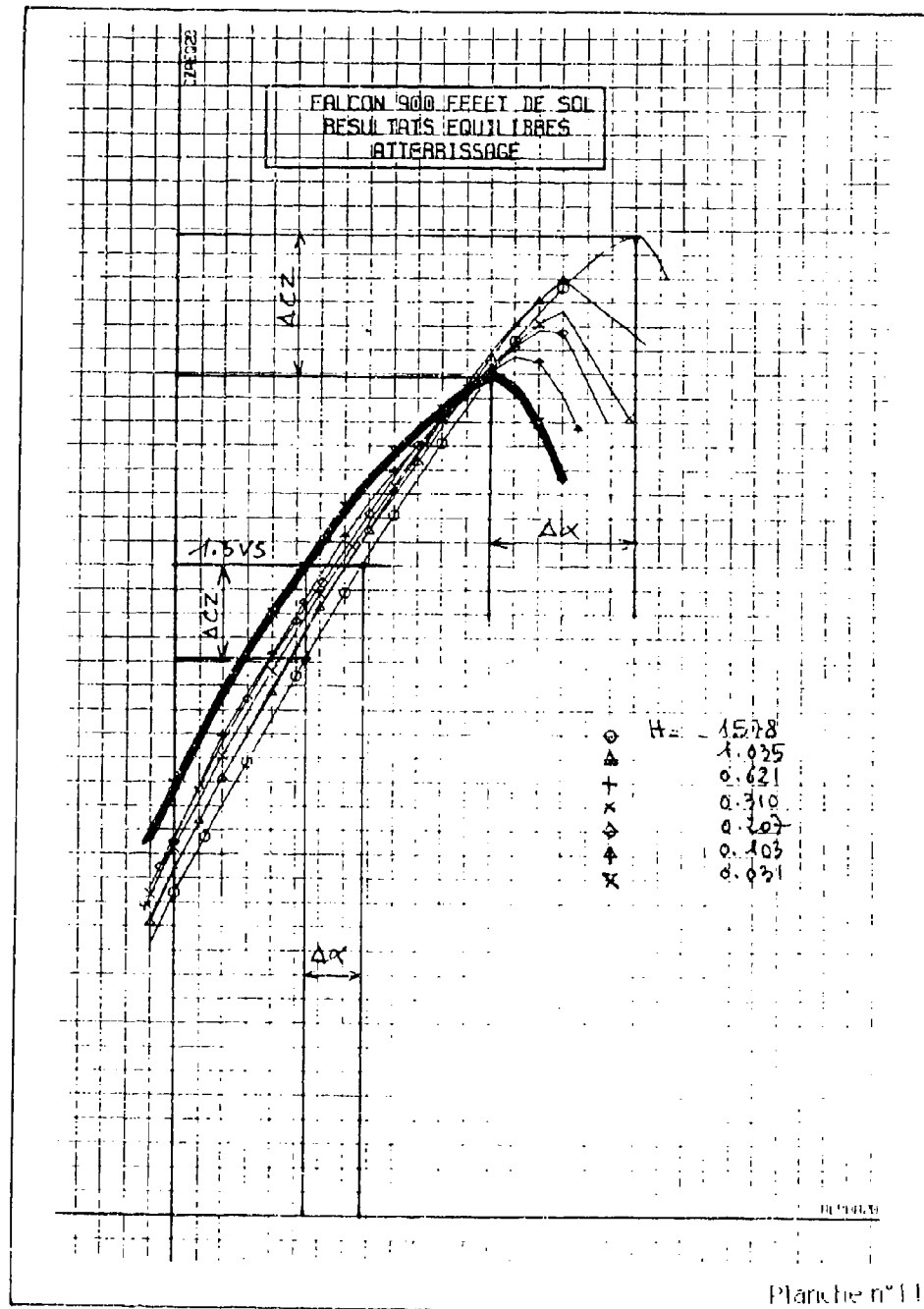
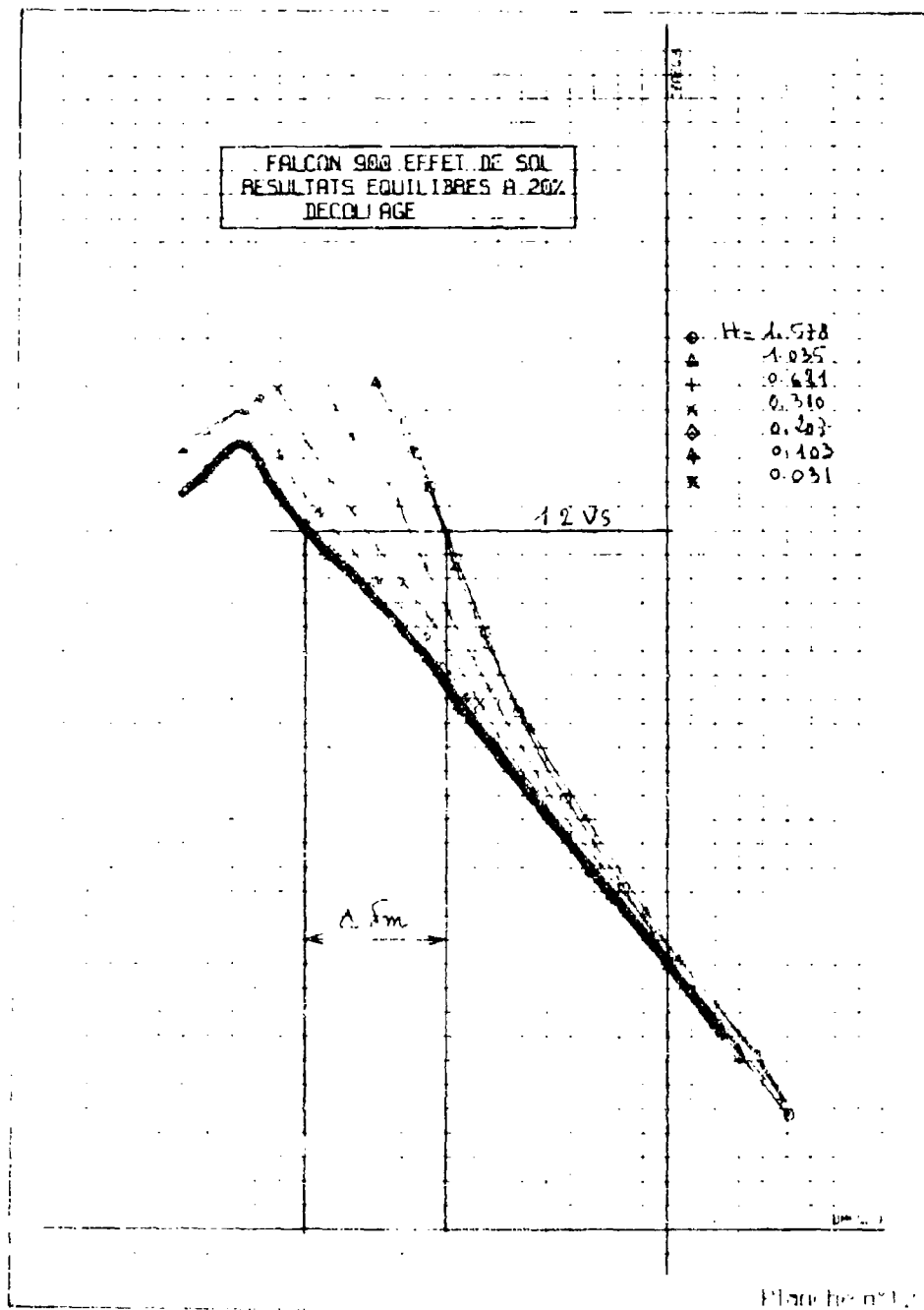


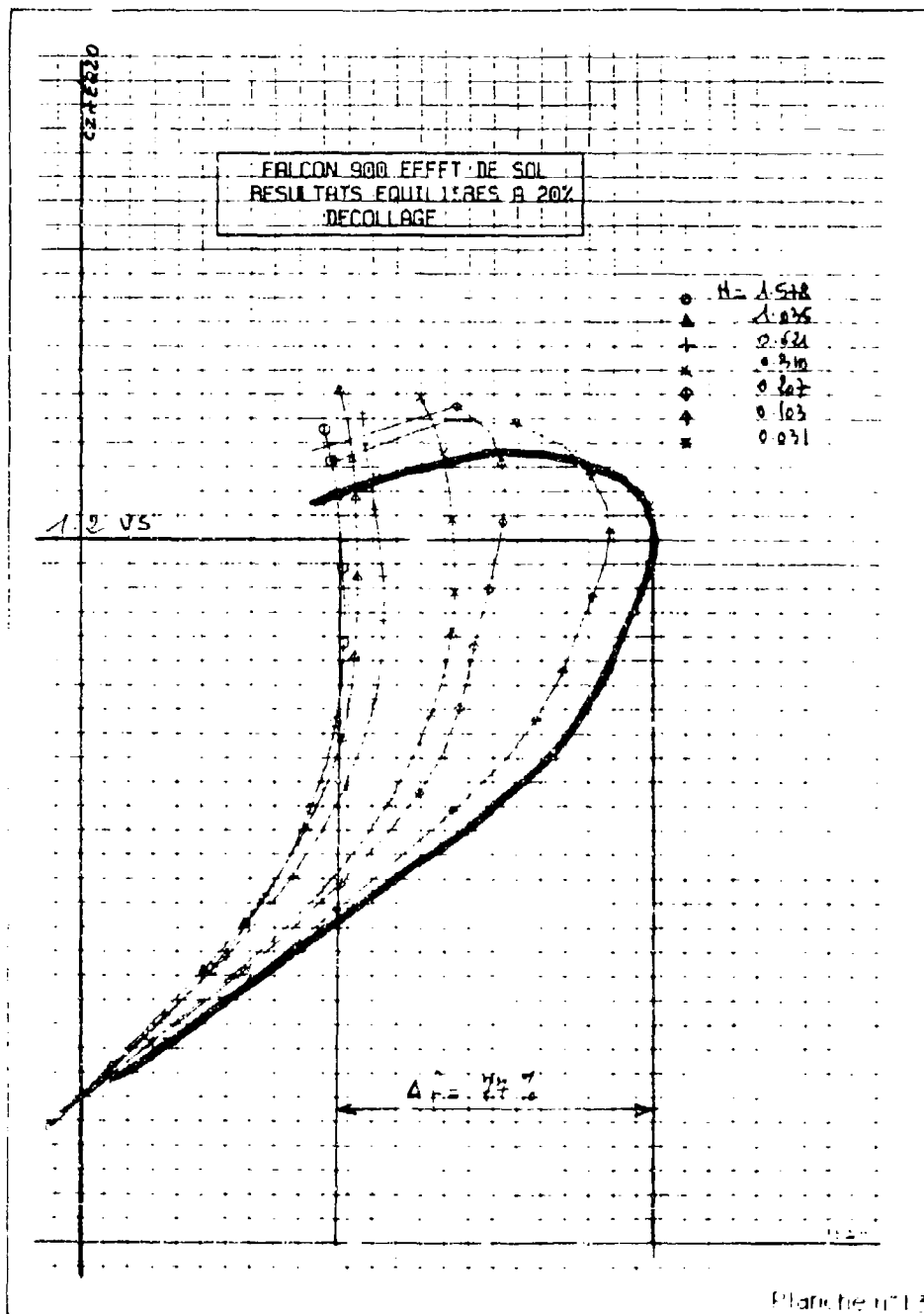
Planche n°3

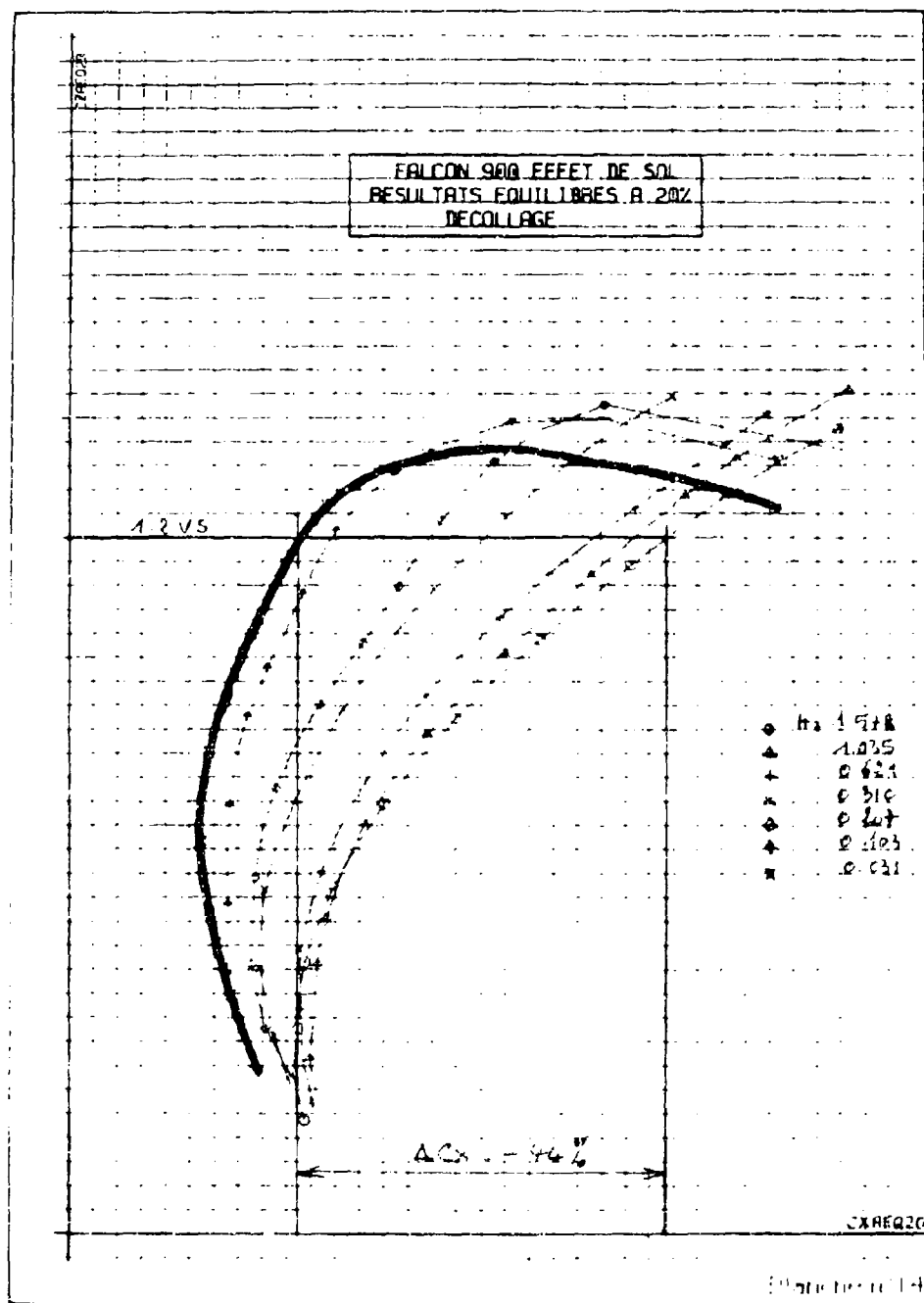












FALCON 900 EFFET DE SOL

DECOLLAGE

POIDS MAXI CENTRAGE=14% VR=126KT

- SANS EFFET DE SOL
 ■ AVEC EFFET DE SOL

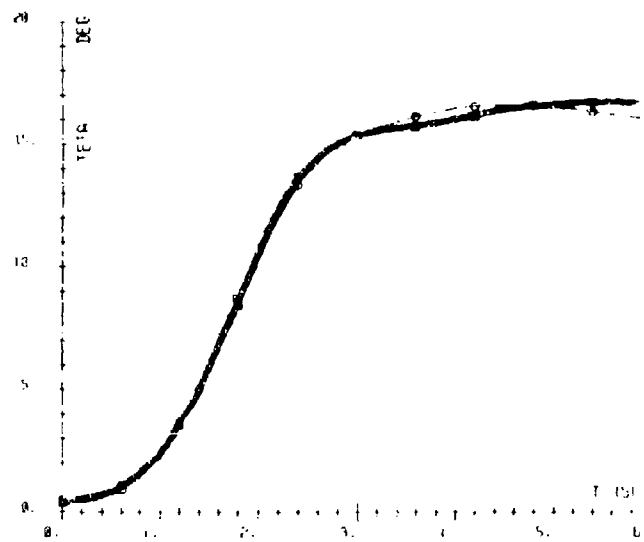
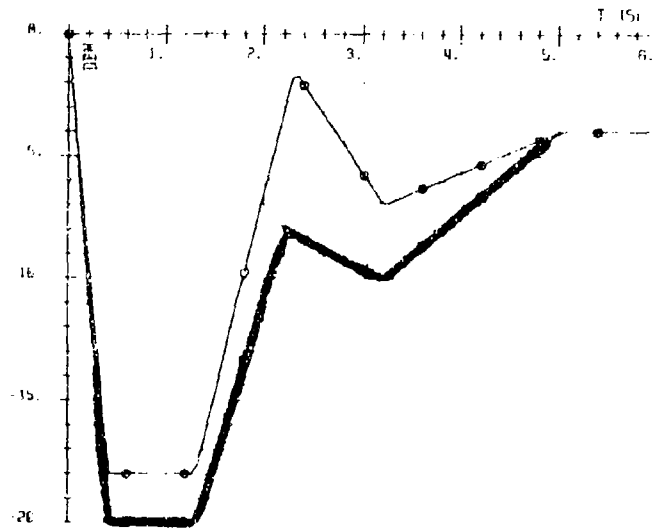


Planche n°15

FALCON 900 EFFET DE SOL

DECOLLAGE

POIDS MAXI CENTRAGE=14% VR=126KT

○ SANS EFFET DE SOL
 ■ AVEC EFFET DE SOL

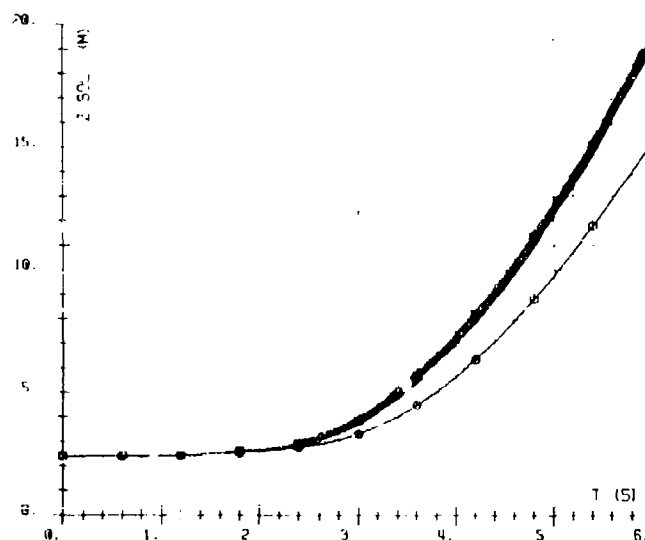
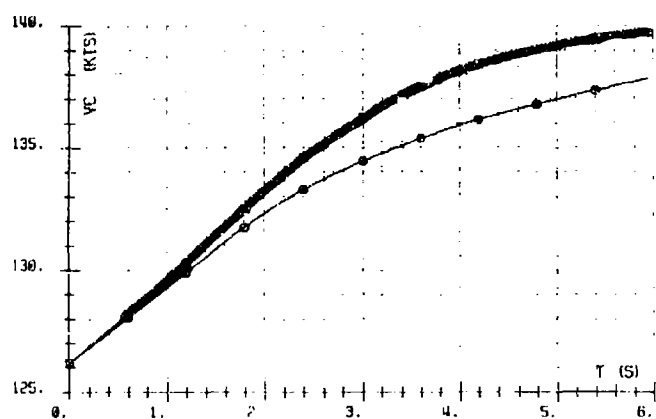
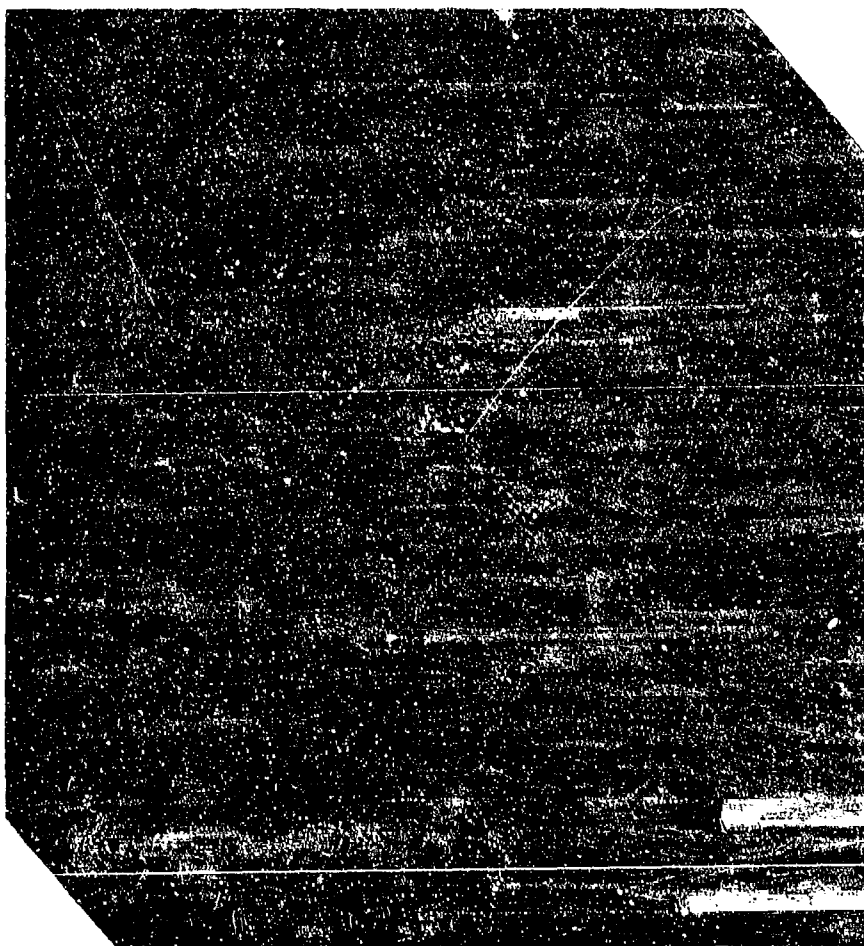


Planche n°16

FALCON 900 EFFET DE SOL

ATTERRISSAGE

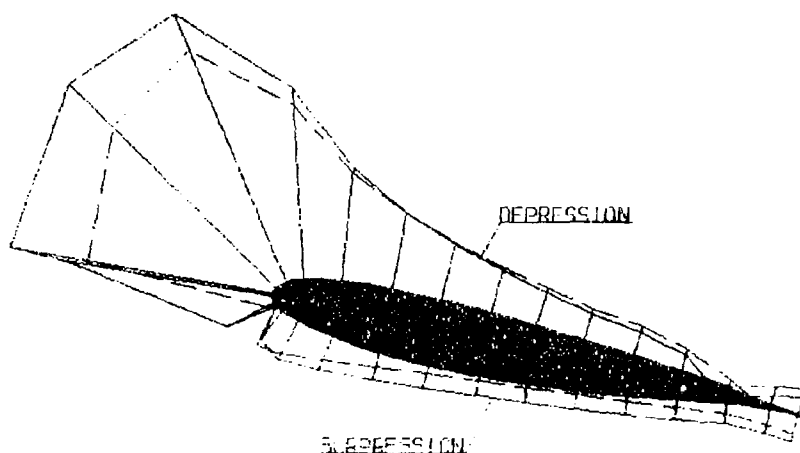
**CALCUL AERODYNAMIQUE THEORIQUE
METHODE DES SINGULARITES**



FALCON 900 EFFET DE SOL

PROFILS DE KP POUR $\alpha=100^\circ$

— Avec effet de sol
— Sans effet de sol



PISTE

Planche n°18

FALCON 900 EFFET DE SOL

ATTERRISSAGE

REPARTITION DE KP SUR L'AVION ET SUR LA PISTE

INCIDENCE 10 DG Z=0



DYNAMIC GROUND EFFECTS

by

John W. Paulson Jr., Guy T. Kemmerly and William P. Gilbert
 NASA Langley Research Center
 Mail Stop 286
 Hampton, VA 23665
 United States

SUMMARY

A research program is underway at the NASA Langley Research Center to study the effect of rate of descent on ground effects. A series of powered models have been tested in the Vortex Research Facility under conditions with rate of descent and in the 14- by 22-Foot Subsonic Tunnel under identical conditions but without rate of descent. These results indicate that rate of descent can have a significant impact on ground effects particularly if vectored or reversed thrust is used.

SYMBOLS

b	wing span, ft
C_L	lift coefficient, $l/q_\infty S$
$C_{L,\infty}$	lift coefficient out of ground effect
h	height above ground plane, ft
\dot{h}	time rate of change of height above ground plane, dh/dt , ft/sec
MAC	mean Aerodynamic Chord, ft
NPR	nozzle Pressure Ratio, P_t/P_∞
P_t	nozzle total pressure, psi
P_∞	freestream static pressure, psi
q_∞	freestream dynamic pressure, $1/2\rho V_\infty^2$
S	wing area, ft ²
V_∞	freestream velocity, ft/sec
$\Delta C_{L,\infty}$	$C_{L,\infty} - C_{L,\infty}$
α	angle of attack, deg
δ_a	aileron deflection, deg
δ_c	canard deflection, deg
δ_f	flap deflection, deg
δ_h	horizontal tail deflection, deg
δ_j	nozzle vector angle, deg
θ	pitch attitude, deg
γ	flight path nozzle, deg
ρ	density, slugs/ft ³

INTRODUCTION

Future fighter/attack aircraft will almost certainly use some form of thrust vectoring to achieve enhanced takeoff and landing performance. Additionally, reducing the ground roll after landing will require the use of reversed thrust. Studies have shown that, for thrust reversing to be most effective, the engines must be at a high power setting at touchdown so that reverse thrust may be applied immediately without waiting for engine spool-up. The configuration aerodynamics associated with the forward directed efflux of reversers will almost certainly be sensitive to ground effect. Accurate prediction of these effects is not always possible in wind tunnels, because the effects of power, floor boundary layer, and rate of descent may not be properly included.

Considerations of ground effects determined from wind tunnel tests and flight test (Reference 1) indicate that transient effects which occur in flight are not considered in typical wind tunnel ground effects testing. In particular, conventional wind tunnel ground-effects tests (that is, time-averaged tests of a stationary model at various ground heights) actually simulate an aircraft flying near the ground at a constant altitude rather than an aircraft descending through a given altitude, as

is the case in approach and landing. As shown in Figure 1, flight test results of an XB-70 in ground effect indicated less lift increase during approach than was predicted on the basis of wind tunnel testing. Dynamic testing of an XB-70 model (Reference 2) determined that ground-effect characteristics measured so as to include the effects of rate of descent match the flight test results much better than the conventional wind tunnel data, as can be seen in Figure 1. Other flight test results using a Concorde (Reference 3) showed that constant-altitude, low-level flight results agreed very well with the ground effects predicted by wind tunnel tests.

Another stimulus to do ground-effects testing with a moving model arose from a generic thrust reverser study, reported in Reference 4. During the study, the thrust-reverser flow field generated undesirable ground effects such as a severe lift loss and large rolling moments at ground heights above wheel touchdown. Questions arose as to whether the effects measured in these conventional static wind tunnel tests would be encountered during an actual approach. That is, would the flow field develop fully and interfere with the aircraft in the short time the aircraft was in ground effect, or would the aircraft fly through (or ahead of) the flow field and land before the ground could have a significant effect on the configuration's aerodynamic characteristics?

Figure 2 shows some of the differences between conventional static wind tunnel ground-effect testing and testing with a moving model. In the static technique, a model is set at a fixed height above the ground plane, the flow field develops to a steady-state condition, then the aerodynamic characteristics are measured. The moving model method measures the aerodynamic characteristics of the model with the flow field in a dynamic state similar to conditions encountered during an actual approach. On a normal approach without thrust reversers operating, the differences may have little effect on the measured aerodynamic characteristics, but the plumes created by forward blowing jets at low ground heights will react differently to the two test conditions. This can result in a substantial difference in measured aerodynamics between the two techniques. Not only are the plume dynamics different in the two methods of testing, but they also differ geometrically. If both methods are used to test a model at a given angle of attack, the moving model will be set at a lower angle of incidence to the ground board (reduced by the simulated glide path angle). This changes the impingement angle of the jet on the ground plane, resulting in distinctly different plumes.

As a result of concern over the information gathered in the above studies, and the known sensitivity of powered models to ground boundary-layer modeling, it appeared that conventional ground-effect testing techniques should be reevaluated. The main emphasis in the present study was to determine the effects of sink rate by comparing the results of current static testing methods with results from a dynamic procedure in which a model would be moved toward an inclined ground plane to simulate rate of descent. A second purpose of the study was to evaluate the need for using a moving-belt ground plane when testing models with thrust reversers in wind tunnels. Identical models and support systems were tested in both the NASA Langley 14- by 22-Foot Subsonic Tunnel and the NASA Langley Vortex Research Facility (VRF) to minimize any effects of using different hardware in the two tests. The 14- by 22-Foot Subsonic Tunnel was used for the static testing because it has both a boundary-layer removal system and a moving-belt ground plane. This paper presents the details of the dynamic testing technique and provides an assessment of the effects of both the moving-belt ground plane and the moving-model technique as they influence the development of aerodynamic ground effects.

Throughout this paper, the term "static" refers to results obtained in the 14- by 22-Foot Subsonic Tunnel with a stationary model; "dynamic" refers to results obtained in the VRF while the model was moving over the inclined portion of the ground board to simulate rate of descent; and "steady state" refers to the results obtained in the VRF while the model was moving at a fixed height over the level portion of the ground board.

MODEL DESCRIPTION

Three models were tested in this study: a generic flat wing planform and two complete configurations. The generic model was a 60° delta wing shown in figure 3. The other models were a 7-percent scale F-18 model and an 8-percent scale F-15 STOL and Maneuver Technology Demonstrator model (F-15 S/MTD) shown in figures 4 and 5.

The wing planform was made out of a 3/8-inch thick clear acrylic sheet and all edges were beveled sharp with a 7.5° half angle. The model was supported by a six-component strain-gauge balance mounted on the centerline of the model, forward of the trailing edge. Two non-metric axisymmetric jets were used to simulate reverse thrust and were mounted at the trailing edge to exhaust forward at a 45° angle. The nozzle exits were one inch below the trailing edge of the wing and were spaced 4 inches apart. Simple convergent nozzles were used and are detailed in figure 6.

The other two models were mounted on a six-component strain-gage balance inside the fuselage and were fitted with adjustable leading- and trailing-edge flaps and horizontal stabilizer. The F-15 S/MTD was also fitted with a movable canard. Reverse thrust simulation was supplied non-metrically using a thrust reverser simulator described in reference 4 and sketched in figure 7. The simulator provided for variability in both longitudinal reverser angle and splay angle (the angle that the jets are inclined spanwise).

These models were tested at several rates of descent, forward speeds, and thrust reverser settings. Dynamic ground effect tests were conducted on all three models in the VRF and the 60° delta wing and the F-18 were tested statically in the Langley 14- by 22-Foot Subsonic Tunnel. The same sting and air lines were used for both static and dynamic testing to minimize differences in the support interference effects between the two facilities. The F-15 S/MTD model was not tested in the 14- by 22-Foot Subsonic Tunnel. However, an F-15 model with the rotating vane thrust reverser has been tested in the 14- by 22-Foot Subsonic Tunnel (Reference 5) and other F-15 S/MTD models have been tested in various facilities. This static data base has been used in this paper as will be discussed in the following sections.

TEST FACILITIES AND PROCEDURES

The Vortex Research Facility (figure 8) at the Langley Research Center was modified for the present study by installing a 150-foot long ground plane assembly approximately in the center of the test section. The models were suspended on a variable-length strut extending from the bottom of the gasoline-engine powered cart. The strut supported the model, sting, and airline assembly as well as the instrumentation. It also provided a means for adjusting the minimum height over the level portion of the ground board. Angle of attack was changed by pitching the entire strut, sting, and model assembly at the point where the strut was attached to the cart. Velocity was controlled by a cruise-control system on the cart. High-pressure air bottles on the cart provided compressed air for the jets.

The ground board consisted of two parts: a ramp which was inclined upward 4° for a distance of 100 feet, followed by a horizontal section which extended for an additional 50 feet. As the model moved horizontally over the inclined portion, the height of the model above the ground board decreased, thereby simulating an approach along a glide slope of 4° . Rate of descent was dependent on the test velocity as given by the equation:

$$h = V_\infty \tan 4^\circ.$$

After moving across the ramp, the model passed over the horizontal section to simulate rollout or constant altitude flight (See figure 9).

In the VRF, 24 channels of data are transmitted from the cart through a modulated laser to a photo receptor and a mass storage unit. The channels are sampled at a rate of 111 samples per second for nearly 30 seconds. The data are then converted to engineering units using an HP-1000 A900 computer. For more information on the data acquisition in the VRF see Reference 6.

The static ground effects of the models were measured in the Langley 14- by 22-Foot Subsonic Tunnel, which has a suction ground boundary-layer removal system and a relatively large test section as illustrated in figure 10. The boundary-layer removal system is located at the beginning of the test section and is followed by a moving-belt ground plane used to minimize boundary-layer development in the test section. The models were supported from the aft bay of the test section and extended into the front bay over the moving-belt ground plane. Angle of attack was controlled by pitching the sting around the vertical strut and height was changed by driving the entire support system vertically. Angle of attack was measured by an accelerometer installed on the model, and height was computed from readings obtained by encoders on the support system. The data in the 14- by 22-Foot Tunnel is time averaged over a period of 4 seconds for each data point. The sample rate is 5 samples per second resulting in 20-sample averages.

SPECIAL CORRECTIONS

An inherent problem with moving-model testing is that model accelerations caused by cart and strut vibrations will contaminate the balance aerodynamic force data with inertial loads. These loads must be removed from the balance output to identify the aerodynamic data contained in the balance output. The strut and cart were therefore instrumented with several accelerometers to measure the vertical and lateral accelerations of the sting and the vertical, lateral, and longitudinal accelerations of the cart near the strut connection point.

As a first-order approximation of the inertial loads, the total mass of the model and all mounting hardware forward of the balance strain gauges was multiplied by the measured vertical acceleration of the sting. The resulting loads were then subtracted from the normal force outputs of the balance to obtain the aerodynamic normal force acting on the model. These corrections are discussed in detail in Reference 7.

RESULTS

The detailed discussion of the data obtained during this study are reported in references 7 through 12. To address all three configurations in this paper, highlights will be given for each configuration illustrating the characteristics defined during the testing. These characteristics were present to various degrees on all models depending on geometry, thrust conditions, angles of attack, and rates of descent.

Data for the 60° delta wing are presented in figures 11 and 12 and show the comparison between static data with and without the moving belt and the moving model dynamic data. The basic lift loss in the static data is to be expected as the reversed thrust plume envelopes the model as the ground plane is approached. The elimination of the ground boundary layer using the moving belt delays the onset of lift loss to a lower h/b , but does not fundamentally alter the characteristics of the data. However, the dynamic data indicates significant changes as the loss in lift does not occur until the model is over the horizontal portion of the ground board and steady state conditions are established.

Here, the model is, apparently, constantly moving away from the reversed thrust flow field and the plume does not envelope the model as long as rate of descent is present. As in the wind tunnel static conditions, the steady state condition gives time for the plume to begin to cover the model and cause the lift loss indicated.

The effect of increasing power is evident when the data of figures 11 and 12 are compared in that the ground effects begin to occur at a higher h/b at the higher power setting. This is reasonable in that when the power setting is increased, the exhaust flow should penetrate farther below and ahead of the model and begin to interact with the ground at a greater distance.

Results for the F-18 model are presented in figures 13 and 14. The basic characteristics in figure 13 are similar to the previous figures in that the differences between belt on and off static data are small and the differences between static and

dynamic data are larger. However, the effects in general are of less magnitude than those indicated in the 60° delta wing. This is also reasonably expected since the thrust reversers on the F-18 are located far aft on the model and relatively far away from the wing. The nozzles on the delta wing are located directly below the wing trailing edge and, thus, the exhaust flow should have a greater interaction with the wing than when the nozzles are located further aft of the wing.

The effect of power setting is evident again by comparing the data of figures 13 and 14. This time the high power setting is very high and actually much greater than would be expected during a reasonable aircraft operation. However, the point to be made is that this high power blows the exhaust plume so far ahead of the model that the interaction with the ground occurs at essentially the same h/b whether or not the data is static or dynamic.

The third model, the F-15 S/MTD is effectively a mid-point between the first two models in that the thrust reversers are not located as far aft on the fuselage as the F-18 nor are they directly below the wing trailing edge. The dynamic results from the VRF are compared with an estimate of the F-15 S/MTD characteristics, which were developed from static results, in figure 15. This static data set from Reference 12 is currently being used as the basis for F-15 S/MTD simulation and was developed from flight results from the F-15 and wind tunnel ground effects tests of several configurations of the S/MTD. The data set, completed before the dynamic results were available, was intended to represent the conditions that the F-15 S/MTD would encounter during final approach and landing. The purpose of this comparison is in no way intended to criticize the simulation data but to further point out the significant differences that may be present between static and dynamic ground effects, especially when vectored or reversed thrust is used.

The increase in lift as the ground is approached is present in both sets of data, but to much less extent in the dynamic results. The reduction in lift indicated in the static results at low heights is not present in the dynamic results. Differences in the level of lift vary, but do reach a very significant level of 0.3 to 0.4 in the extreme.

These data will be compared with flight data from the F-15 S/MTD program to determine the differences between static, dynamic and flight results. From this analysis the actual need for rate of descent modeling during ground effects testing in the wind tunnel will be determined.

PLANS

A program has been approved where new tunnel hardware will be designed and built to provide up to 15 ft/sec vertical rates and 60 deg/sec pitch rates for the 14- by 22-foot Subsonic Tunnel. This hardware will consist of a vertical post which will provide model support. It will be hydraulically powered and computer controlled to provide the required model motions. The vertical post assembly will be capable of yaw motion and the model cart will have provision for a moving belt ground plane. This testing hardware will allow complete ground effects modeling in that both elimination of the ground boundary layer and inclusion of rate of descent will be possible in the wind tunnel. In addition, a complete new data system will be included in this program to allow proper acquisition and reduction of transient data phenomena.

CONCLUDING REMARKS

A research program at the NASA Langley Research Center has demonstrated that rate of descent can be an important factor in determining accurate ground effects for aircraft during approach and landing. A series of models have been tested and the trends are consistent that significant differences can exist between ground effects obtained with and without rate of descent, especially if vectored or reversed thrust are present. In general, for the models tested, rate of descent tends to reduce the severity of any ground effect present. Finally, the effect of using the moving belt to eliminate the floor boundary layer in the wind tunnel, while significant, is much smaller than the effect of rate of descent.

A program is underway at LaRC to fabricate support system hardware and develop a data system to allow wind tunnel ground effects testing at rates of descent up to 15 ft/sec.

REFERENCES

1. Baker, P. A.; Schweikhard, W. G.; and Young, W. R.: *Flight Evaluation of Ground Effect on Several Low Aspect Ratio Airplanes*. NASA TN D 6053, 1970.
2. Chang, R. C.: *An Experimental Investigation of Dynamic Ground Effect*. Ph.D. Diss., Univ. of Kansas, 1985.
3. Pelagatti, C.; Pilon, J. C.; and Bardaud, J.: *Analyse Critique des Comparaisons des Resultats de Vol aux Previsions de Soufflerie Pour des Aéronefs de Transport Subsonic et Supersonic*. Facilities Correlation, AGARD CP 187, April 1976, pp. 23-1 23-24.
4. Joshi, P. B.; Widynski, T. C.; Chiarelli, C.; and Chapman, R. W.: *Generic Thrust Reverser Technology for Near Term Application. Volume 2. Testing, Method Application and Data Analysis*. AFWAL TR 83-3084 VOL. 2, U. S. Air Force, February 1985. (Available from DTIC as AD B094 293L.)
5. Banks, D. W., and Paulson, J. W., Jr.: *Aerodynamic Characteristics and Predicted Landing Performance of an F-15 Fighter with Two Thrust Reverser Configurations*. NASA TP 2466 (Confidential), April 1985.
6. Satran, D. R.; Neubart, D.; Holbrook, G. T.; and Greene, G. C.: *Vortex Research Facility Improvements and Preliminary Density Stratification Effects on Vortex Wakes*. AIAA 85-0050, January, 1985.
7. Kemmerly, G. T.; and Paulson, J. W., Jr.: *Investigation of a Moving Model Technique for Measuring Ground Effects*. NASA TM-4080, January, 1989.

8. Paulson, J. W., Jr.; and Kemmerly, G. T.: *An Assessment of Ground Effects Determined by Static and Dynamic Testing Techniques*. Ground Effects Workshop, NASA CP 10008, 1987.
9. Kemmerly, G. T.; Paulson, J. W., Jr.; and Compton, M.: *Exploratory Evaluation of a Moving Model Technique for Measurement of Dynamic Ground Effects*. AIAA-87-1924 San Diego, CA, June 29-July 2, 1987.
10. Kemmerly, G. T.; Paulson, J. W., Jr.; and Compton, M.: *Exploratory Evaluation of a Moving-Model Technique for Measurement of Dynamic Ground Effects*. AIAA Journal of Aircraft, Volume 25, No. 6, pp. 557-562, June 1988.
11. Humphreys, A. P.; Paulson, J. W., Jr.; and Kemmerly, G. T.: *Transient Aerodynamic Forces On a Fighter Model During Simulated Approach and Landing With Thrust Reversers*. AIAA/ASME/SAE/ASEE 24th Joint Propulsion Conference, July 11-13, 1988. AIAA-88-3222.
12. Kemmerly, G. T.: *A Comparison of the Ground Effects Measured With and Without Rate-of-Descent Modeling on the F-15 S/MTD Configuration*, AIAA-89-3280, August 18/1988.

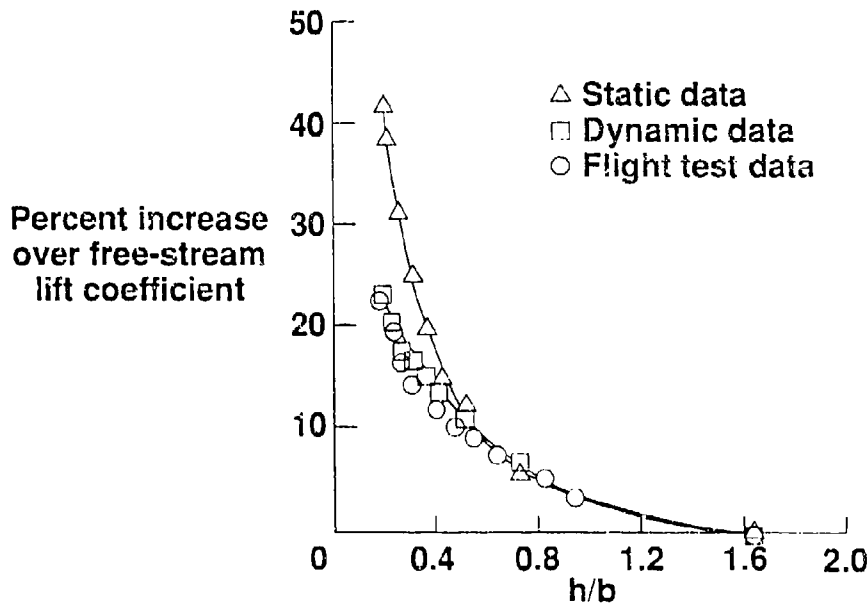


Figure 1. Comparison of static, dynamic and flight test data of an XR-70 at $\alpha = 9.3^\circ$

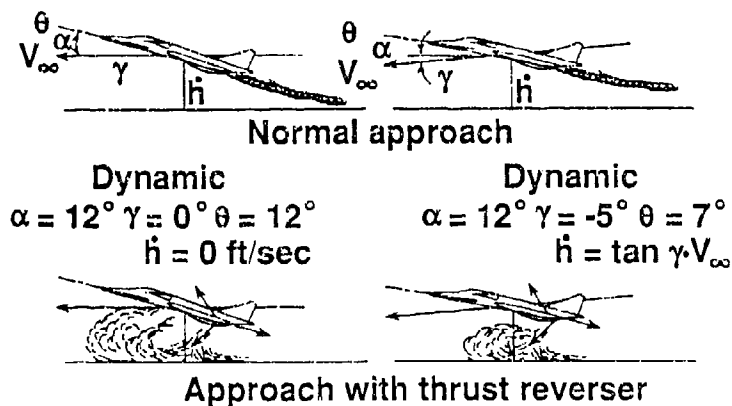


Figure 2. Schematic of dynamic and steady-state ground effects.

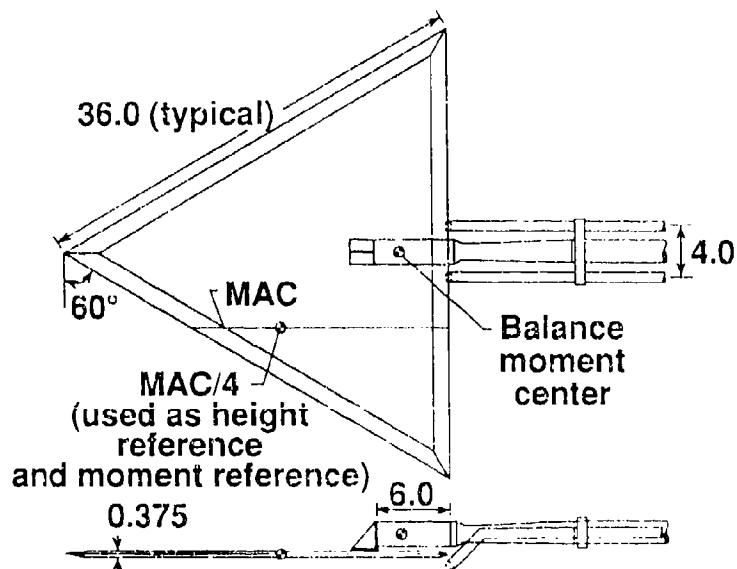


Figure 3. Sketch of the 60° delta wing mounted on the VRE strut. Dimensions in inches.

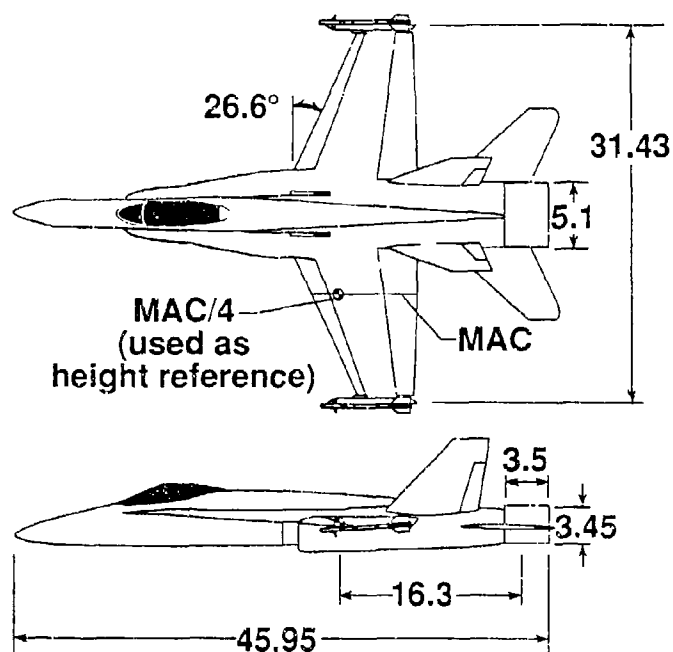


Figure 4. Sketch of the F-18 model tested. Dimensions in inches.

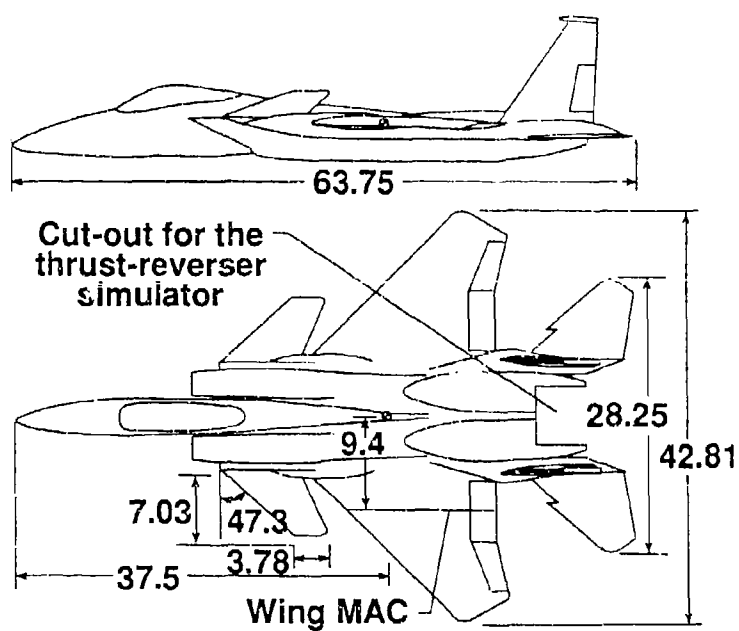


Figure 5. Sketch of the LF-15 S/MTD model tested. Dimensions in inches.

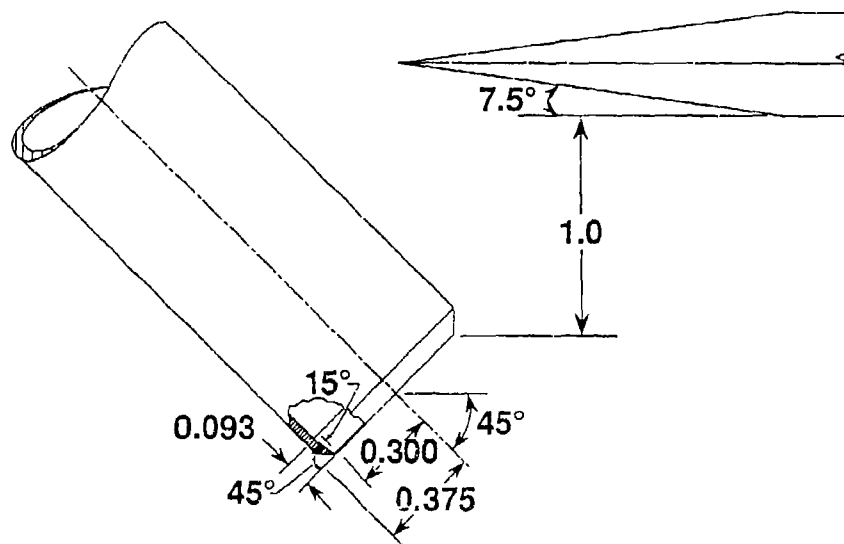


Figure 6. Cross section and relative position of the convergent nozzle used in the 60° delta wing test.

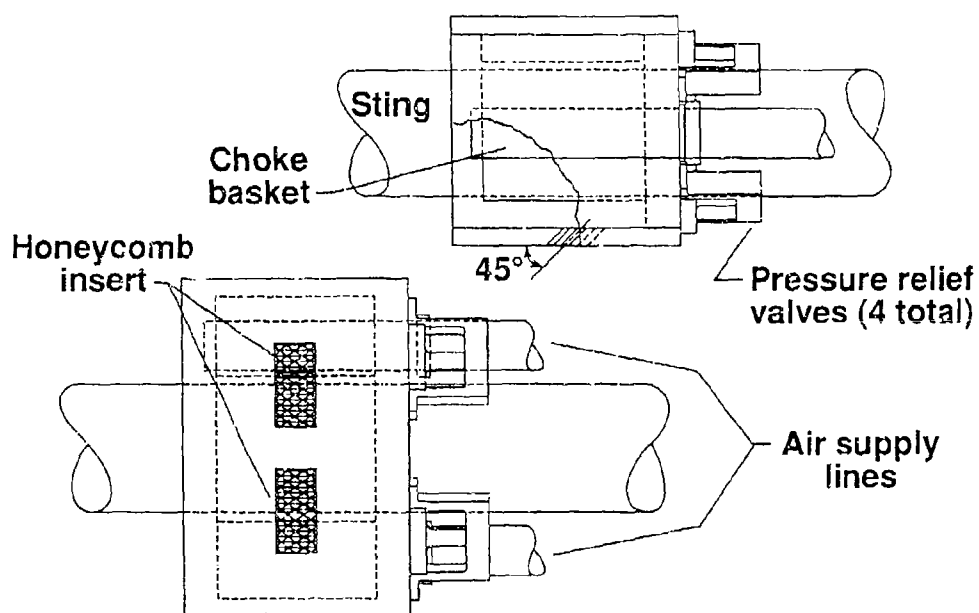


Figure 7. Sketch of the thrust reverser simulator used in the F-18 and F-15 S/MTD tests.

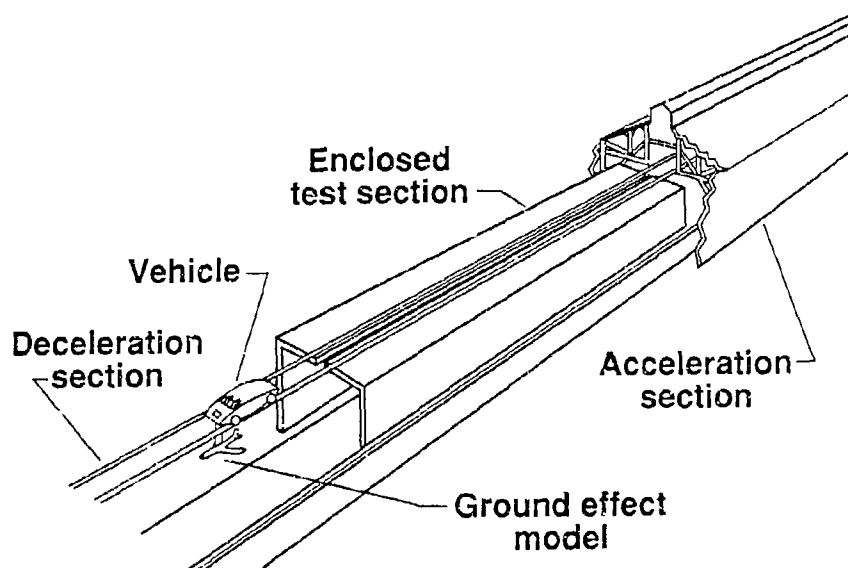


Figure 8. Schematic diagram of the Vortex Research Facility.

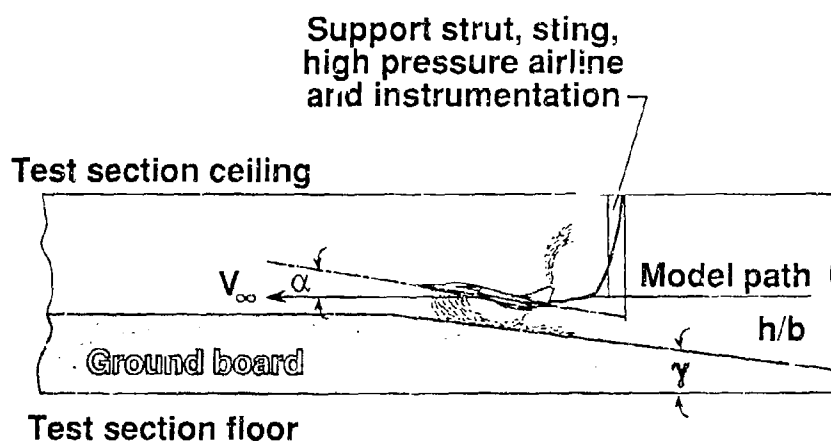


Figure 9. Experimental concept in the Vortex Research Facility.

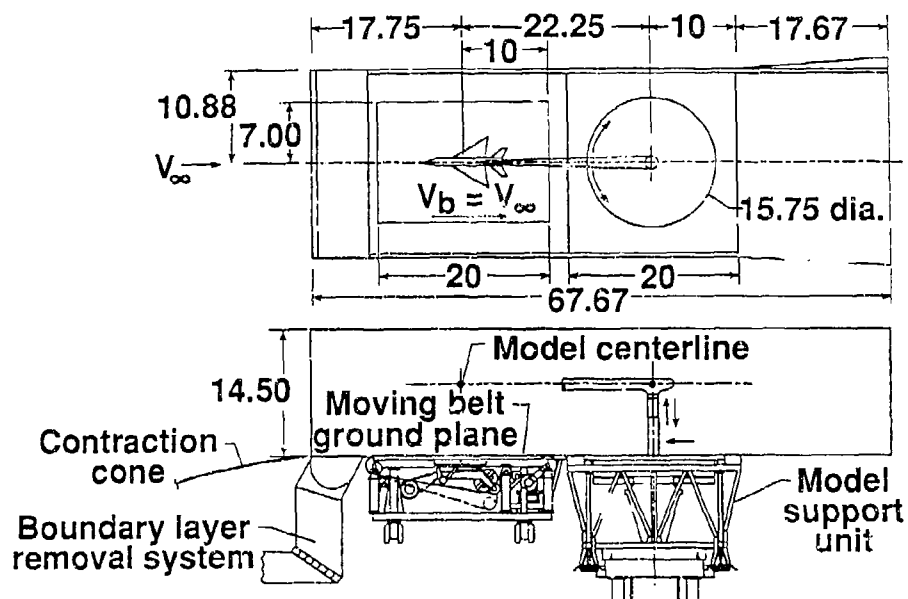


Figure 10. Sketch of the test section of the Langley 14- by 22-Foot Subsonic Tunnel. Dimensions are in feet.

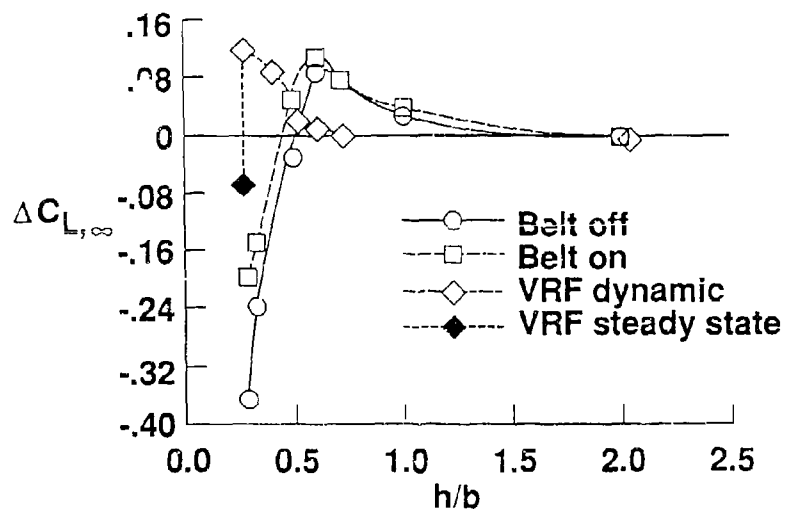


Figure 11. Effect of model height on the lift coefficient of the 60° delta wing at $\alpha = 10^\circ$ and $NPR = 1.6$.

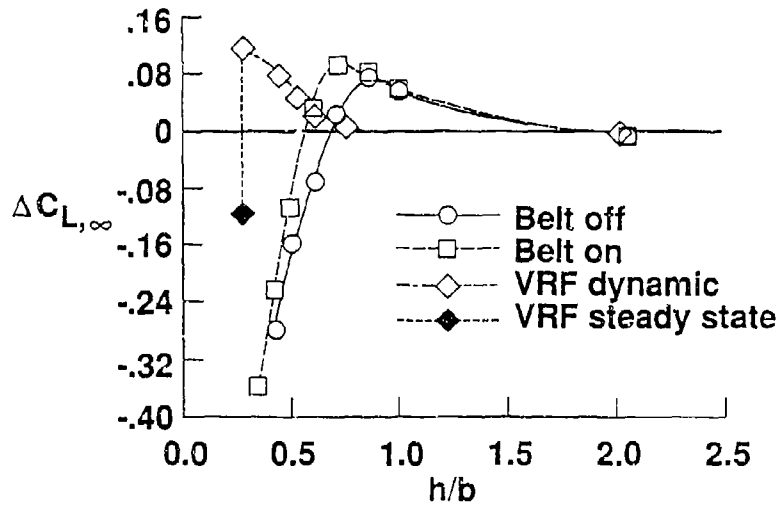


Figure 12. Effect of model height on the lift coefficient of the 60° delta wing at $\alpha = 10^\circ$ and $NPR = 2.0$.

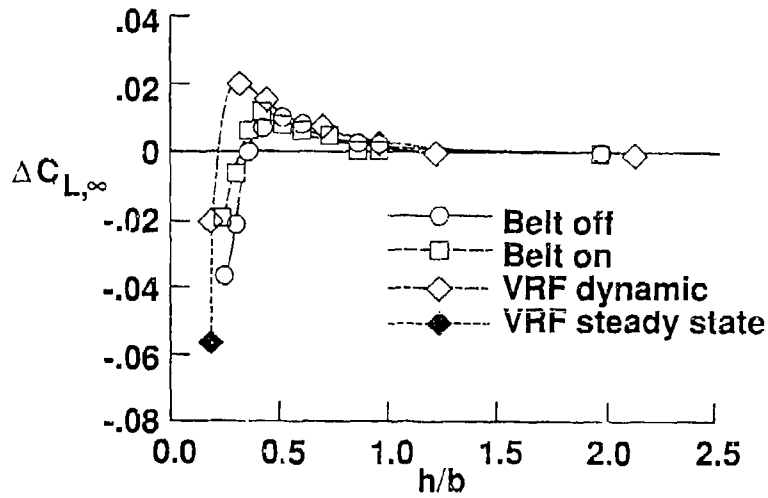


Figure 13. Effect of model height on the lift coefficient of the F-18 model at $\alpha = 8.4^\circ$ and $NPR = 1.5$. $\delta_j = 135^\circ$, $\delta_{f, \text{leading edge}} = 25^\circ$, $\delta_{f, \text{trailing edge}} = 20^\circ$, $\delta_h = -10^\circ$.

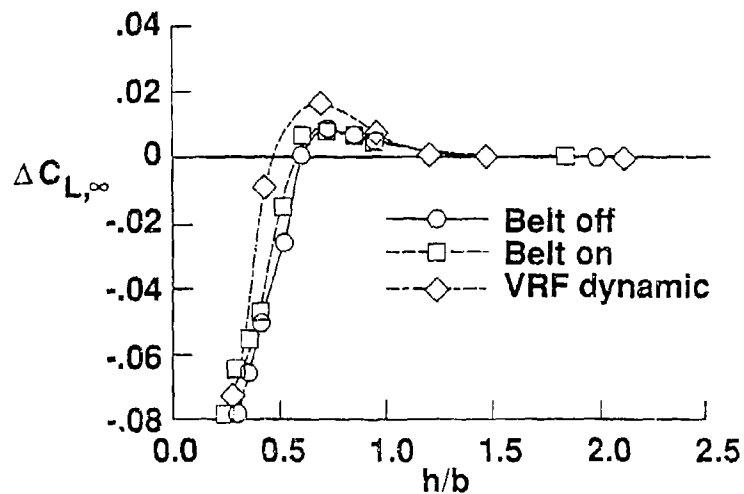


Figure 14. Effect of model height on the lift coefficient of an F-18 model at $\alpha = 8.4^\circ$ and $NPR = 2.5$. $\delta_j = 135^\circ$, $\delta_{f, \text{leading edge}} = 25^\circ$, $\delta_{f, \text{trailing edge}} = 20^\circ$, $\delta_h = -10^\circ$.

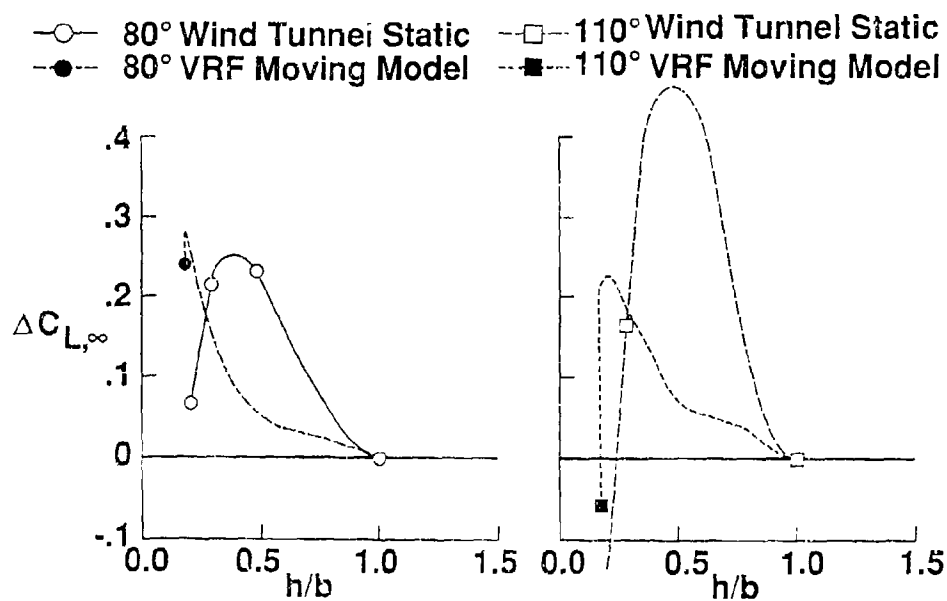


Figure 15. Comparison of static and dynamic ground effects on the lift coefficient of the F-15 S/MTD model. $\alpha = 12^\circ$, $\delta_f/\delta_n = 20^\circ/20^\circ$, $\delta_r = -13^\circ$, $\delta_h = 2^\circ$.

ETUDE DE L'EFFET DE SOL SUR MAQUETTE EN VOL*

par

J.L.Cocquerez, P.Coton and R.Verbrugge
IMFL - 5, boulevard Paul Painlevé, 59000 Lille
Tel. 20.49.69.00, Telefax 20.52.95.93, Telex 160010F
France

Résumé

L'Institut de Mécanique des Fluides de Lille (IMFL), établissement de l'ONERA (Office National d'Etudes et de Recherches Aéronautiques), développe depuis de nombreuses années des méthodes expérimentales originales fondées sur l'exploitation d'essais en vol de maquettes en laboratoire. Ces méthodes sont en particulier exploitées pour la caractérisation et la modélisation des qualités de vol des avions en milieu perturbé ou non. Elles ont été appliquées à l'étude de l'effet de sol en vue d'une meilleure maîtrise des phases terminales de l'approche et de l'atterrissage.

Les atouts de la technique expérimentale sont déterminants, en particulier pour ce type d'étude :

- Représentation directe du comportement de l'avion et des phénomènes aérodynamiques (représentation de l'effet de sol, absence de support, domaine incompressible, maîtrise de l'environnement, etc...)
- Précision élevée dans la connaissance des caractéristiques massique, inertielle et structurale des maquettes
- Accès aux caractéristiques du vol à partir d'informations redondantes permettant une restitution optimale des variables d'état et des coefficients aérodynamiques
- Utilisation directe des méthodes d'identification paramétrique
- Complémentarité de la technique vis-à-vis d'essais en tunnel et en soufflerie
- Mise en évidence d'effet de sol statique et dynamique

Dans ce document, nous développons les principaux aspects de la méthode mise en oeuvre et nous présentons quelques résultats expérimentaux sur l'effet de sol, notamment en dynamique. Les perspectives relatives à la modélisation du comportement longitudinal sont évoquées. Des développements ultérieurs sont suggérés concernant notamment l'appontage et l'atterrissage en présence de turbulence.

Summary

The Institute of Fluid Mechanics of Lille (IMFL), establishment of ONERA, has developed since many years specific experimental methods based on the exploitation of flying scaled models in laboratory. These methods are specially used to characterize and model the aircraft flight qualities in a disturbed or undisturbed environment. They have been applied to ground effect studies in order to get a better control on approach and landing phases.

The experimental technique and facilities are specially well adapted to this kind of study :

- Realistic representation of the aircraft behaviour and the involved aerodynamic phenomena (ground representation, no support interference, incompressible flow, well-known environment, etc...)
- High accuracy on weight, inertia and structural characteristics of the model
- Flight test data obtained through redundant measurements which allow an optimal restitution of the state variables and the dynamic coefficients
- Application of parameters identification techniques widely complementary with low speed wind tunnel and other moving model techniques
- Abilities to illustrate static and dynamic ground effect

This paper is particularly concerned with the experimental techniques. Some experimental results on ground effects, especially dynamic ones, are presented. The future developments of the mathematical modelling of the aircraft longitudinal behaviour are also mentioned. Some ideas are suggested concerning aircraft on carrier or landing with atmospheric disturbances.

* Etude financée par la Direction des Recherches, Etudes et Techniques (DRET)

I. INTRODUCTION

L'optimisation des procédures d'approche et d'atterrissage, et en particulier la précision de l'impact consécutif à la phase d'arrondi et au palier à vitesse décroissante, nécessite une reconnaissance des effets d'interaction aérodynamique entre l'avion et le sol.

Ces effets sont de deux types :

- L'effet de sol statique correspond à un vol en palier au voisinage d'un sol sans discontinuité (phase précédant l'impact ou phase de roulement au sol dans le cas du décollage). De nombreux moyens de caractérisation existent pour traiter cette phase.

- L'effet de sol dynamique est relatif à une vitesse verticale lors de la phase dite d'arrondi, à une vitesse de tangage, ainsi qu'à la proximité d'un sol discontinu (apportage). Peu de moyens sont actuellement disponibles pour prendre en compte ces phénomènes spécifiques ainsi que certaines caractéristiques liées à l'environnement telles que le vent latéral ou la turbulence.

Pour répondre à ces préoccupations, l'IMFL a récemment étendu l'usage d'une méthode expérimentale spécifique basée sur l'exploitation d'essais en vol de maquettes en laboratoire (planche 1). Celle-ci complète les méthodes classiques développées par ailleurs.

Les principaux avantages de cette méthode sont :

- la représentation directe des phénomènes caractéristiques,
- pas d'autre interaction que celle recherchée,
- un paramétrage des "entrées sensibilisantes",
- une possibilité de pilotage embarqué,
- une possibilité de simulation des phases complètes jusqu'à l'impact.

Ce document présente les moyens expérimentaux mis en oeuvre, fournit des illustrations de résultats statiques et dynamiques et propose quelques axes de développement ultérieurs, en matière de modélisation et vis-à-vis du domaine d'application de la méthode.

II. PRINCIPE ET METHODE EXPERIMENTALE - MOYENS MIS EN OEUVRE

2.1 - Principe de base - similitude

Les règles de similitude à adopter visent une représentation semblable des trajectoires et du mouvement de l'avion. Il s'agit d'une similitude cinématique.

Ainsi, dans l'inventaire des variables à prendre en compte pour ces essais en similitude sur maquettes volantes, il y a lieu de considérer les caractéristiques massique et inertielle du modèle. Les grandeurs primaires indépendantes en fonction desquelles peuvent être exprimées les variables du problème sont une longueur de référence (c), la masse volumique (ρ) et l'accélération de la pesanteur (g). Cette représentation conduit dans l'expression des grandeurs réduites caractéristiques à la conservation du nombre de Froude $F = V / (g \cdot c)^{1/2}$ entre maquette et avion (conservation du rapport des forces d'inertie aux forces de gravité).

Du point de vue de l'aérodynamique, cette similitude est restreinte car elle ne peut pas représenter simultanément l'identité des nombres de Reynolds ou de Mach. On notera cependant que le domaine de vol considéré, particulièrement pour la présente application, est subsonique incompressible. Le nombre de Reynolds, calculé sur la corde de référence (c), est voisin de $2,5 \cdot 10^6$. Ainsi, pour la maquette considérée présentée ci-après, l'identité des effets aérodynamiques est respectée.

2.2 - Maquette

La planche 2 présente une vue générale de la maquette utilisée pour ces travaux. Il s'agit d'une maquette d'avion d'armes à l'échelle 1/8,6. Sa longueur est 1,75 m, son envergure est 1,00 m et sa masse 21 kg.

Pour le calcul des vecteurs instantanés "accélération résultante" et "rotation" au centre de gravité l'équipement de la maquette comporte :

- trois accéléromètres "Q-Flex" verticaux disposés à l'avant, à l'arrière et au centre de gravité (CdG),
- un accéléromètre "Q-Flex" longitudinal au CdG,
- un gyromètre "SAGIM" en tangage,

Une sonde anémométrique Gruson au nez de la maquette mesure une pression cinétique locale et une pression différentielle pour le calcul de l'incidence.

Ces moyens de mesures dynamiques sont complétés par des systèmes opto-électroniques. Pour la trajectographie, le repère maquette est matérialisé par trois lampes de référence. Une photo-cellule provoque, par l'intermédiaire du codeur embarqué, l'initialisation de l'acquisition des données télémétrées et assure la datation du passage aux bases d'enregistrements optiques (synchronisation espace-temps).

2.3 - Moyens sol - Station d'essais

L'installation d'essais en vol est abritée dans un bâtiment de type Industriel occupant une surface au sol de 360 m². Sa longueur est 70 m et sa hauteur moyenne 10 m.

Tous les essais sont réalisés dans la configuration "vol plané".

La maquette est mise en vitesse au moyen d'une catapulte pneumatique, préalablement positionnée en pente et en hauteur (pente d'équilibre relative au vol plané de la maquette). L'énergie maximum libérable au largage est voisine de 20000 J. Sur la vue générale de l'installation, planche 3, on peut distinguer la zone de mise en vitesse sous la catapulte, la domaine d'évolution de la maquette où les trajectoires peuvent se développer sur des distances de 30 m, et le dispositif de récupération. La vitesse initiale est donnée par une barrière constituée d'un compteur et de deux faisceaux laser coupés par l'extrémité de la voile.

Dans le domaine d'évolution de la maquette, une soufflerie horizontale et une soufflerie verticale permettent de créer des sollicitations extérieures du type vent ou rafale latérale ou verticale.

La piste est représentée par un plancher, mis en place dans le domaine d'évolution de la maquette, sur tout ou partie de la longueur disponible, selon le type d'essai à réaliser. La pente de ce plancher est ajustable, sa largeur est de 2,50 m.

Le paramétrage de la hauteur initiale de largage de la maquette (H) par rapport au plancher est réalisé en modifiant la position de la catapulte.

Pour les essais en effet de sol permanent le plancher est prolongé en amont du point de largage de sorte que les effets aérodynamiques liés à l'effet de sol soient complètement établis aux conditions initiales du vol.

Le plancher, conçu en modules indépendants permet de solliciter dynamiquement la maquette par des discontinuités imposées telles que l'entrée en effet de sol et la sortie.

Ces dispositions peuvent représenter à la fois des conditions réalistes de vol du type appontage ainsi que des sollicitations correspondant à des entrées mathématiques qualifiées (crâneaux, échelons, etc...). Quelques exemples de configuration de sol sont représentés sur les planches 4 et 5.

Les informations nécessaires à la connaissance "au sol" de la trajectoire et de l'attitude de la maquette en vol sont obtenues sur quatre bases optiques implantées dans la zone d'évolution de la maquette (planche 6).

Chaque base est située dans un plan vertical, normal au plan de symétrie du vol, et comporte deux appareils photographiques à axes perpendiculaires. Les traces lumineuses des trois lampes de référence portées par la maquette ainsi qu'un référentiel local sont enregistrés. Les traces sont relevées en continu. Une batterie de flashes préprogrammée fournit sur chaque plaque photographique un instantané de la maquette en vol et active la photo-cellule portée par la maquette, générant ainsi une information de synchronisation espace-temps insérée dans le cycle de télémesure.

La géométrie de cet espace de vol est déterminée au moyen d'un système de mesures tridimensionnelles sans contact, utilisant deux théodolites reliés à un système d'acquisition et de calcul.

Les mesures effectuées dans la maquette durant le vol sont transmises au sol par émission HF en mode PCM et stockées sur des mémoires internes. Ce dispositif est bien adapté à la mesure de phénomènes rapidement variables. Les caractéristiques principales du codeur utilisé sont les suivantes :

- 30 entrées analogiques symétriques (-1 V à $+1\text{ V}$)
- fréquence de codage 150 Kbits/s (781 mesures par seconde et par voie - période d'échantillonnage : 1,28 ms)
- format de sortie : 30 mots de mesure et 2 mots de synchronisation de 12 bits chacun
- Insertion en mot 15 d'une voie numérique (tops)
- Insertion en mot 16 d'un compteur de cycles (datation avant émission)

La composition du cycle de télémesure est la suivante : deux mots de synchronisation, quatorze voies de mesures, deux mots numériques, quatorze voies de mesures. Cette composition permet de doubler la fréquence d'échantillonnage des 14 voies de mesure.

Un exemple de données brutes d'acquisition est présenté sur la planche 7, relatif aux accéléromètres longitudinal et vertical au CdG ainsi qu'au gyromètre de tangage. Le paramètre figurant en abscisse (T^*) est le temps réduit ou distance exprimée en nombre de cordes parcourues. La maquette, représentée à l'échelle sur la planche, est larguée hors effet de sol. Elle subit une première sollicitation brusque d'effet de sol avec une hauteur relative de 0,35 sur une longueur de deux cordes maquette, puis la hauteur relative augmente de 0,20 sur une longueur de 13 cordes. Ensuite la maquette n'est plus interconnectée par le plancher.

2.4 - Logiciels

On dispose donc, à partir des moyens mis en oeuvre, de trois sources d'information indépendantes (trajectographie sol, mesures dynamiques embarquées, anémoclinométrie) permettant une exploitation des redondances dans la procédure de traitement des essais en vol (restitution des variables d'état et des coefficients aérodynamiques globaux).

Trois programmes principaux sont mis en oeuvre (planche 8) :

- un programme de trajectographie traite les traces lumineuses des trois lampes de référence portées par la maquette, obtenues par dépouillement des enregistrements optiques. Pour chaque base on obtient les angles d'Euler (ψ , θ , ϕ), les coordonnées du centre de gravité (X , Y , Z), l'incidence (α), le dérapage (β) et la pente (γ).

- un programme traite les données accélérométriques et gyrométriques télémesurées pendant l'essai. Il opère sur les valeurs obtenues par différence entre le vol et les zéros pris sous rampe immédiatement avant la mise en vitesse de la maquette. Un premier ensemble de conditions initiales est déterminé soit par mesures directes (valeurs fournies par les capteurs de la maquette au début du vol), soit par des mesures faites au sol (angles, vitesse initiale, ...). A la cadence d'échantillonnage, toutes les 1,28 ms, les paramètres suivants sont calculés : X , Y , Z , ψ , θ , ϕ et leurs dérivées premières et secondes, V , α , β , γ .

- Un programme permet, à partir des mesures en vol d'une pression cinétique locale et d'une pression différentielle, le calcul de la vitesse et de l'incidence au nez de la maquette.

Les résultats obtenus à partir de ces trois sources d'informations indépendantes sont utilisés ensuite dans un test de validation des données et d'ajustement final des conditions initiales du vol. Les informations provenant de la trajectographie optique se permettent d'établir un recalage précis des données accélérométriques et gyrométriques intégrées, notamment en terme de conditions initiales. Les résultats du vol sont acquis lorsque, pour chaque paramètre, le recoupement s'établit à l'intérieur d'intervalle de précision définis sur les grandeurs géométriques.

Cette procédure permet de valider des vols en laboratoire sur des parcours de 35 m, avec une précision de 0,01 m sur les positions X, Y, Z et de 0,1 ° sur les angles ψ , θ , ϕ , α , β , γ . La qualité de l'information sur les accélérations et les vitesses angulaires et linéaires est donc particulièrement précieuse pour l'exploitation aérodynamique des vols.

III) ESSAIS REALISES

La procédure générale mise en oeuvre a consisté tout d'abord à caractériser la maquette en vol permanent non perturbé (vol de référence) et à solliciter le tangage hors effet de sol. Cette procédure permet la caractérisation aérodynamique de base de la maquette (C_x , C_z , C_m , δm). Sur la base des vols de référence, on établit ensuite un programme d'essais en effet de sol, associant des conditions initiales au largage variées (braquage des élévons, variation de l'incidence, du centrage ou de la vitesse initiale) et diverses configurations de plancher.

Les caractéristiques des vols réalisés représentent une configuration du type atterrissage :

- la vitesse est comprise entre 27,12 m/s et 31,84 m/s
- le domaine d'incidence couvert va de 2,61 ° à 20,29 °
- l'assiette longitudinale varie de 5,59 ° à 16,83 °
- le facteur de charge normal est compris entre 0,77 et 0,97

Les conditions initiales des vols ont été choisies pour sensibiliser différents paramètres entrant dans la formulation de l'effet de sol.

Les principales caractéristiques des vols réalisés sont les suivantes :

- des vols de référence, sans effet de sol
- des vols avec effet de sol "continu" (le plancher est installé sur toute la distance du vol y compris avant le largage).

Différentes hauteurs relatives du centre de gravité de la maquette par rapport au plancher ont été étudiées ($0,6 < H/c < 1,0$). Certains de ces vols peuvent être considérés comme effectués à la limite de l'effet de sol, d'autres se caractérisent par une hauteur relative (H/c) quasi constante ce qui permet des recoupements immédiats avec des résultats obtenus avec d'autres moyens d'essais. D'autres vols comportent une dynamique plus importante et un fort taux de chute, pouvant aller jusqu'à l'impact.

- des vols avec pénétration en effet de sol et sortie de l'effet de sol
- des vols avec pénétration en effet de sol, sollicitations "en créneau" sur des distances de deux et quatre cordes et sortie de l'effet de sol.

La planche 9 résume quelques caractéristiques d'un programme d'essais type. Des schémas illustrent différentes configurations du plancher.

IV) RESULTATS ET FORMULATION DE L'EFFET DE SOL

Les résultats obtenus lors d'essais en vol d'une maquette d'avion d'armes sont relatifs au vecteur d'état (positions, vitesses et accélérations linéaires et angulaires) et aux grandeurs aérodynamiques (coefficients globaux, incidence, pente et vitesse).

4.1 - Effet de sol statique et dynamique stationnaire

Pour un ensemble de vols avec effet de sol "continu", l'accroissement relatif du coefficient de portance globale est présenté sur la planche 10.

Le paramètre porté en abscisse est la hauteur du centre de gravité de la maquette par rapport au plancher, rapportée à la corde de la maquette.

La portance globale intègre les termes relatifs aux différents braquages des élévons ainsi que ceux liés à l'incidence ou à la vitesse de tangage. Elle traduit à la fois les effets de sol statiques et dynamiques liés à la vitesse verticale (V_z).

On relève une évolution très caractéristique du coefficient de portance (C_z). L'effet de sol se manifeste en deçà d'une hauteur relative voisine de 0,8 et croît de façon sensiblement hyperbolique jusqu'à la hauteur relative minimum correspondant à l'impact. Les variations relatives du coefficient de portance atteignent 40 % et peuvent se produire en un laps de temps de l'ordre d'une à deux secondes.

A partir de la base de données constituée des résultats des essais en vol de la maquette, l'IMFL a développé une formulation empirique de l'effet de sol pour tenter de restituer, à partir de cette hauteur relative d'apparition de l'effet de sol, l'évolution des coefficients aérodynamiques longitudinaux C_x , C_z , C_m . Cette formulation prend en compte la hauteur relative et la vitesse verticale réduite.

Chaque coefficient peut s'exprimer sous la forme suivante :

$$C_l (i = x, z, m) = C_{l0} + C_{l\alpha} \cdot \alpha$$

avec $C_{l0} = A + B / (H/c) + C / (H/c)^2$
 et $C_{l\alpha} = D + E / (H/c) + F / (H/c)^2 + G \cdot (V_z/V_{\infty}) / (H/c)$

Les constantes A, B, C, D, E, F, G sont identifiées par moindres carrés sur l'ensemble des vols.

Les résultats figurant sur la planche 11 présentent des comparaisons effectuées entre les coefficients mesurés en vol (x) et ceux obtenus avec la formule ci-dessus (0). L'ordonnée représente l'écart relatif de chaque coefficient par rapport à la valeur hors effet de sol. On peut constater que, pour des vols avec effet de sol "continu", la formulation est représentative.

4.2 - Effet de sol dynamique et stationnaire

Jusqu'à présent de nombreux auteurs ont montré l'importance des effets dynamiques liés notamment à la vitesse verticale. Bien que prise en compte dans la formulation présentée ci-dessus, celle-ci n'est pas appropriée à la description de phénomènes d'effet de sol comportant des effets transitoires importants. Ces conditions particulières sont rencontrées notamment lors de phases d'atterrissage ou de décollage d'avions embarqués. Elles sont reproduites dans les essais en vol de maquettes et constituent par ailleurs des sollicitations attractives du point de vue de la recherche de modèles généraux d'effet de sol (réponses indicielles).

Pour ces essais particuliers, les coefficients calculés (0) ne correspondent plus à ceux mesurés en vol (x). Les effets transitoires ne sont pas restitués comme le montrent les courbes présentées sur la planche 12. Dans cet exemple la maquette, représentée à l'échelle sur la planche, est larguée hors effet de sol. Elle subit une première sollicitation brusque d'entrée en effet de sol avec une hauteur relative de 0,35 sur une longueur de deux cordes maquette, puis la hauteur relative augmente de 0,20 sur une longueur de 13 cordes. Ensuite la maquette n'est plus interactionnée par le plancher.

On remarque que l'effet de sol n'est pas symétrique, que les effets liés à la pénétration en effet de sol sont très importants (gain et perte à l'origine) et que les réponses en portance et en moment de tangage sont relativement corrélées.

Pour mieux illustrer ces phénomènes spécifiques on présente sur la planche 13 les résultats comparés de phases transitoires de trois vols représentant le premier un atterrissage (-), le second une sollicitation d'effet de sol de type crêneau sur une longueur de deux cordes (0), le troisième une sollicitation d'effet de sol de type crêneau sur une longueur de quatre cordes (+).

On remarque, pour les coefficients de portance et de moment de tangage, que les pentes à l'origine semblent dépendre directement de la hauteur relative. On atteint 80 % des valeurs dynamiques stationnaires (+) après un parcours d'environ deux cordes.

L'intérêt de ces configurations de plancher, comportant une forte dynamique en effet de sol, est évident pour la détermination des temps de réponse et l'étude des effets transitoires.

4.3 - Concepts de modélisation

Sur la base des données généralement disponibles relatives à l'effet de sol stationnaire, les simulations réalisées en atterrissage ne sont pas confirmées par les essais en vol en ce qui concerne la précision de l'impact. Nous avons pour objectif de développer, à partir des données provenant d'essais en vol et en soufflerie de la maquette, une modélisation plus globale de l'effet de sol en vue d'optimiser les performances en configuration d'atterrissage et de décollage y compris dans la configuration d'avions embarqués. Cette modélisation sera développée sous une forme utilisable en mécanique du vol.

Les principales difficultés du problème sont relatives à :

- l'impact de l'architecture de l'avion sur son comportement en effet de sol,
- la non linéarité, l'asymétrie et la non stationnarité du phénomène,
- le choix de variables explicatives indépendantes, locales ou non.

Les outils à mettre en œuvre s'inspirent des développements déjà effectués dans des domaines similaires (vol à haute incidence ou en turbulence). Ils peuvent être de différents ordres :

- soit des tables et des fonctions de transfert, permettant de bien représenter mathématiquement les phénomènes mais ne pouvant pas a priori être extrapolables à un changement d'architecture de la maquette ou à l'ouverture du domaine de vol
- soit des fonctions indicielles, type Tobak et Schiff
- soit une modélisation par éléments, plus physique, permettant de prendre en compte l'architecture de la maquette et les aspects temporels du phénomène, notamment les effets de pénétration et de sortie.

V) CONCLUSION ET PERSPECTIVES

Ces travaux ont permis de confirmer les avantages de la technique d'essais en vol de maquettes en laboratoire employée à l'IMFL, en vue de la caractérisation statique et dynamique de l'effet de sol, et pour la validation de procédures simulées d'approche et d'atterrissage.

Les principaux enseignements dégagés concernent :

- la complémentarité de la technique expérimentale vis-à-vis d'autres moyens d'essais
- une bonne corrélation de l'effet de sol statique à l'égard d'autres sources de données
- la mise en évidence de l'importance des effets dynamiques liés notamment à la vitesse vorticale
- une première formulation de l'effet de sol dynamique stationnaire
- la caractérisation des effets dynamiques instantanés, répondant à des objectifs opérationnels relatifs à l'avion embarqué ainsi qu'à une possibilité de recherche et de validation d'un modèle mathématique global de l'effet de sol.

A l'avenir les travaux doivent être orientés en particulier vers une analyse plus approfondie des effets dynamiques, fondée sur une expérimentation diversifiée concourant à la mise au point d'un modèle de représentation performant. Cette approche nécessiterait l'emploi d'outils mathématiques tels que les tables et les fonctions de transfert, les fonctions indicielles et les modèles par éléments.

La méthode expérimentale sera par ailleurs exploitée pour la validation de performances ainsi que pour des études de sensibilité vis-à-vis d'erreurs du modèle d'effet de sol.

La possibilité de simuler des perturbations atmosphériques pourra être prise en considération ainsi que la représentation dans la maquette de la motorisation.

Références

- (1) Lee Pal-Hung, Lan C.E., Muirhead V.U. : Experimental investigation of dynamic ground effect. Journal of Aircraft, June 1989, vol 26, n° 6, p 497-498
- (2) Kemmerly G.T., Paulson J.W., Compton M. : Exploratory evaluation of moving-model technique for measurement of dynamic ground effects. Journal of Aircraft, June 1988, vol 25, n° 6, p 557-562
- (3) Plotkin A., Dobbela S.S. : Slender wing in ground effect. AIAA Journal, April 1988, vol 26, n° 4, p 493-494
- (4) Parks E.K., Wingrove R.C. : Flight test measurements of ground effect - STOL airplanes. Presented at the 8th annual symposium of the Society of Flight Test Engineers, Washington D.C., August 1977
- (5) Chang Ray Chung, Muirhead V.U. : Effect of sink rate on ground effect of low aspect ratio wings. Journal of Aircraft, March 1987, vol 24, n° 3, p 176-180
- (6) Er-EI J., Weihs D. : Ground effect on slender wings at moderate and high angles of attack. Journal of Aircraft, May 1986, vol 23, n° 5, p 357-358
- (7) Chen Yen-Sen, Schweikhard W.G. : Dynamic ground effects on a two dimensional flat plate. Journal of Aircraft, July 1985, vol 22, n° 7, p 638-640
- (8) Humbert Claude : Mesure de l'effet de sol dans le Tunnel Aérodynamique du Centre d'Essais Aéronautique de Toulouse, 20ème Colloque d'Aérodynamique Appliquée, Toulouse, Novembre 1983
- (9) Tobak M., Schlif L.B. : Aerodynamic mathematical modelling - basic concepts. Agard Lecture Series n° 114 on Dynamic Stability Parameters, paper n° 1, March 1981
- (10) Vaunois, Januel : Essais Aérodynamiques avec la Plate-forme à Moteur Linéaire du Centre d'Essais Aéronautique de Toulouse, 17ème Colloque d'Aérodynamique Appliquée, Grenoble, Novembre 1980
- (11) Parks E.K., Wingrove R.C. : Analysis of flight test measurements in ground effect. Presented at the 11th annual symposium of the Society of Flight Test Engineers, Atlanta, GA, August 1980
- (12) Berlin J.J., Smith M.L. : Aerodynamics for Engineers, Prentice-Hall, New Jersey, 1979
- (13) Lan C.E. : A quasi vortex lattice method in thin wing theory. Journal of Aircraft, Sept 1974, vol 11, n° 9, p 518-527
- (14) Glatzer L.B., Mahal A.S. : Ground effects in STOL operation. Journal of Aircraft, March 1972, vol 9, n° 3, p 236-242

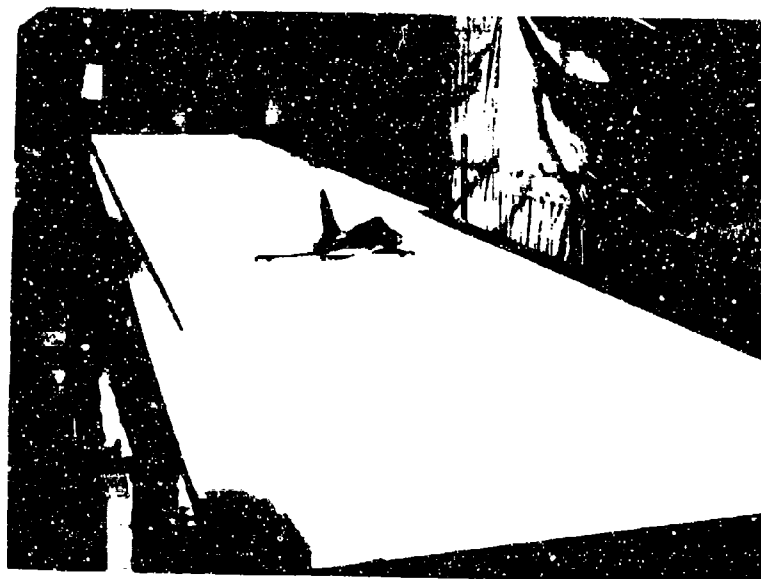


Planche 1 Etude de l'effet de sol sur maquettes en vol
Ground effect study on flying model



MAQUETTE en SIMILITUDE de FROUDE

FROUDE SCALED MODEL

REYNOLDS = 2.10^5

SPECIFICATIONS

ECHELLE	1 / 8.6	SCALE
MASSE	21 Kg	WEIGHT
LONGUEUR	1.75 M	LENGTH
ACCELEROMETRES	7	ACCELEROMETERS
GYROMETRES	2	GYROMETERS
V, α, β	1	V, α, β
FREQUENCE d'ACQUISITION	781Hz	RATE SAMPLING

Planche 2 Caractéristiques typiques d'une maquette
Typical model characteristics

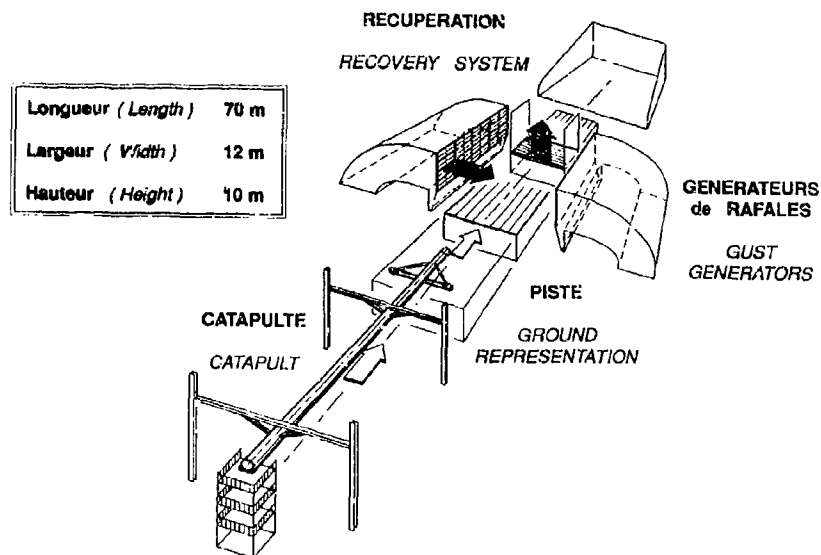


Planche 3 Vue générale du laboratoire d'essais en vol
General view of the flight test laboratory

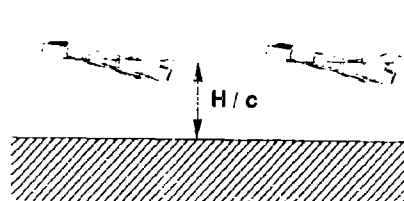
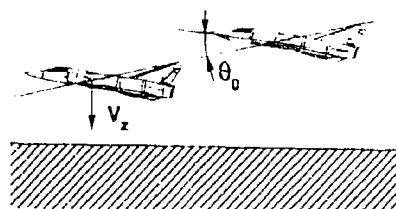


Planche 4 Effet de sol permanent
Steady state ground effect



Effet d'une vitesse verticale
Effect of sink rate

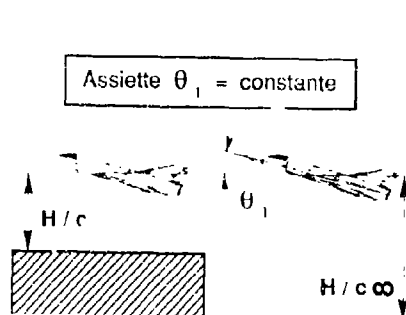
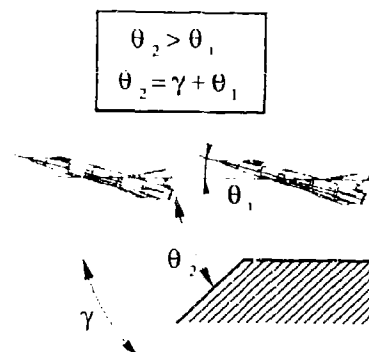


Planche 5 Simulation d'entrée ou de sortie
d'effet de sol
Ground effect steps simulation



Simulation d'un effet de variation d'assiette
Simulation of pitch angle variation effect

TRAJECTOGRAPHIE

- VITESSE INITIALE
- ANGLES d' EULER aux BASES
- POSITION du C.D.G.
- PENTE
- INCIDENCE, DERAPAGE

TRAJECTOGRAPHY SYSTEM

- INITIAL SPEED
- EULER ANGLES on BASES
- CG POSITIONS
- FLIGHT PATH ANGLE
- ANGLE of ATTACK, SIDESLIP

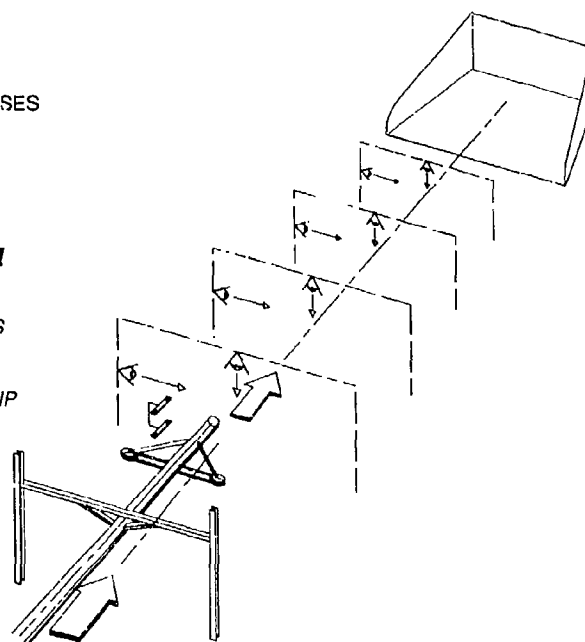


Planche 6 Moyens de mesure au sol
Ground based measurements

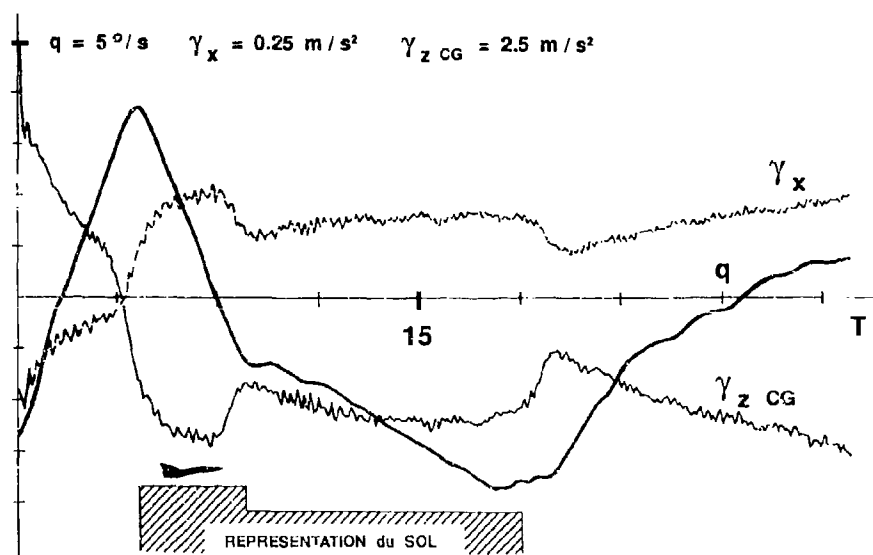


Planche 7 Données d'essais en vol
Flight test data

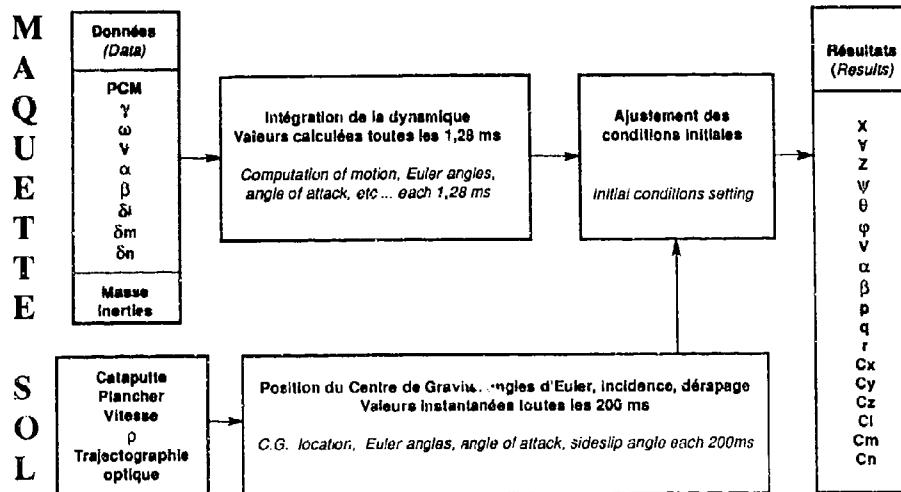


Planche 8 Diagramme schématique du traitement des données
 Schematic diagram of data processing

Configuration du plancher <i>Ground configuration</i>	Conditions initiales <i>Initial conditions</i>	Variation de hauteur <i>Height variation</i>	Variation de la vitesse de tangage <i>Pitch-rate variation</i>	Variation d'incidence <i>Angle of attack variation</i>
	H 0 / c	Δ H / c	Δ q (° / s)	Δ α (°)
_____	1	0.2	4	-1
_____	1	0.6	-2	-1
_____	0.6	Impact	-22	-1
_____	0.6	0.1	-10	4
┌ ┐	0.6	0.1	3	5
┌ ┐	0.4	0.1	9	3
┌ ┐	0.4	0.2	3	5
┌ ┐	0.4	0.3	2	6

Planche 9 Caractéristiques de vols "types"
 Typical flights characteristics

Planche 10 Ecart global en portance
dû à l'effet de sol
Total lift increment
due to ground effect

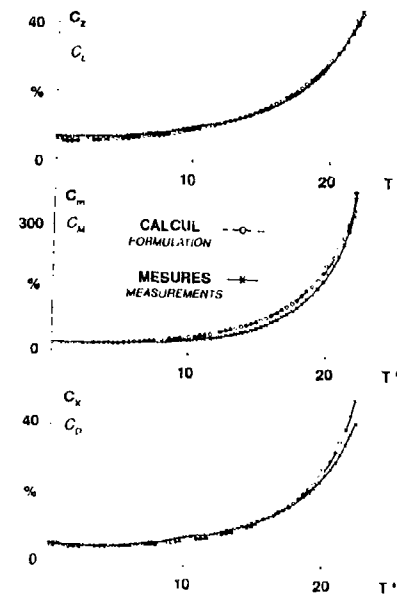
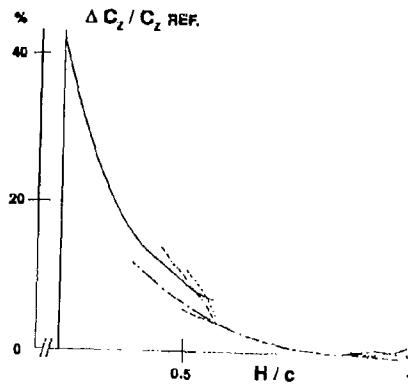


Planche 11 Effet de sol continu
Continuous ground effect

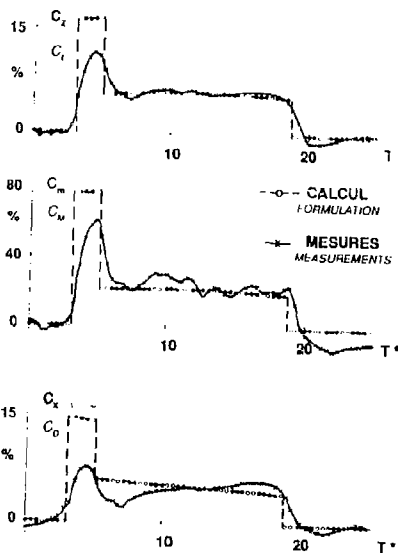


Planche 12 Effets instationnaires
Instationary effects

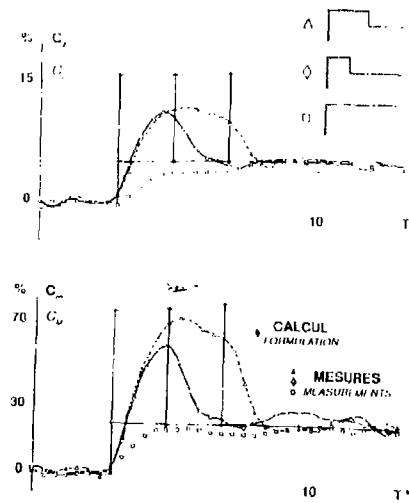


Planche 13 Effets instationnaires
Instationary effects

AN IN-FLIGHT INVESTIGATION OF GROUND EFFECT ON A FORWARD-SWEPT WING AIRPLANE

Robert E. Curry, Bryan J. Moulton, and John Kresse
NASA Ames Research Center
Dryden Flight Research Facility
P.O. Box 273
Edwards, California 93523-5000
U.S.A.

SUMMARY

A limited flight experiment was conducted to document the ground-effect characteristics of the X-29A research airplane. This vehicle has a unique aerodynamic planform which includes a forward-swept wing and close-coupled, variable incidence canard. The flight-test program obtained results for errors in the airdata measurement and for incremental normal force and pitching moment caused by ground effect. Correlations with wind-tunnel and computational analyses were made.

The results are discussed with respect to the dynamic nature of the flight measurements, similar data from other configurations, and pilot comments. The ground-effect results are necessary to obtain an accurate interpretation of the vehicle's landing characteristics. The flight data can also be used in the development of many modern aircraft systems such as autoland and piloted simulations.

NOMENCLATURE

AGL	above ground level
APAS	aerodynamic preliminary analysis system
b	span, ft
$C_{L_{\infty}}$	lift coefficient, out-of-ground-effect
$C_{N_{\infty}}$	normal force coefficient, out-of-ground-effect
h	height of airplane above minimum height, wheels on ground, ft
\dot{h}	vertical velocity, ft/sec
NASA	National Aeronautics and Space Administration
PANAIR	panel aerodynamics
q	pitch angular rate, deg/sec
α	angle of attack, deg
$\Delta C_{A_{GB}}$	axial force coefficient increment caused by ground effect
$\Delta C_{L_{GB}}$	lift coefficient increment caused by ground effect
$\Delta C_{m_{GB}}$	pitching moment coefficient increment caused by ground effect, reference center of gravity
$\Delta C_{N_{GB}}$	normal force coefficient increment caused by ground effect
$\Delta h_{p_{GB}}$	pressure altitude measurement error caused by ground effect, ft
δ_C	canard position, positive trailing-edge down, deg
δ_{STK}	longitudinal control stick position, positive aft, in.

1. INTRODUCTION

An understanding of ground effects is important for the development of many modern aircraft systems and for accurate interpretation of vehicle flying qualities. These data must include the ground effects on total vehicle forces and moments as well as perturbations of aerodynamic (angle-of-attack (α) and airspeed) sensors which may be used for control system feedback. Valid analytical models of these effects are required to support high fidelity simulators, used for flight-time equivalent pilot training. These models are also required in the development of advanced flight control systems such as autoland.

Ground effects for a variety of planform types such as aft-swept, delta, and low-aspect-ratio wings have been studied in the past (refs. 1-4). Recent studies (refs. 5-7) have indicated substantial variations between ground effects determined from steady-state conditions (constant height above ground) and dynamic conditions (such as landing approaches). Flight testing allows the determination of ground effects under dynamic conditions, which are typically not simulated in wind tunnels or computational analysis.

The X-29A forward-swept wing research airplane was developed and flight-tested to evaluate several concepts for application on future fighter aircraft. A general overview of the goals of the project can be found in references 8 and 9. As part of the flight-test program, a series of maneuvers was conducted to determine the ground effects related to this unique configuration. Flight data were obtained at angles of attack from 6.5 to 8.5° and indicated airspeeds from 145 to 160 kn.

Flight data were obtained from onboard sensors and a ground based optical tracking system during shallow approaches to the runway. The analysis included balancing the vehicle forces and moments and correcting for pilot inputs during the maneuvers. The data were correlated with a limited set of wind-tunnel data, obtained with a fixed ground board in a low-speed wind tunnel. In addition, two numerical techniques, aerodynamic preliminary analysis system (APAS) and panel aerodynamics (PANAIR), were also applied to the configuration in ground effect. The APAS code (ref. 10) uses a constant-pressure panel method with limited modelling capability. The PANAIR code (ref. 11) is a higher-order panel method which offers greater modelling capability but requires more computer resources and user effort.

This paper presents the flight data and compares the results with the wind-tunnel and theoretical predictions. In addition, the results are discussed with respect to the dynamic nature of the flight measurements, data from other configurations, and pilot comments regarding X-29A aircraft landing characteristics.

2. VEHICLE DESCRIPTION

The test vehicle is shown in figure 1. Table 1 gives a summary of the physical characteristics. A more complete description of the vehicle is given in reference 9. The most unusual external features include the forward-swept wing and close-coupled, variable incidence canard. The configuration has relaxed longitudinal static stability which requires the use of a highly augmented digital flight control system. The wing has a full-span trailing-edge flap. Pitch is controlled through a scheduled combination of the canard, wing trailing-edge flap, and the strake flap surfaces (fig. 1). In the "power approach" control system mode, the wing flap and gear are fixed in the down position and pitch control is achieved by the canard and strake flap surfaces. The airdata sensors used in this study were installed on a noseboom.

3. MEASUREMENTS

The principal onboard measurements in this study were inertial rates and accelerations, control surface positions, airdata, and fuel quantities. The data were encoded by a pulse code modulation system with 10-bit resolution and were telemetered to a ground station. The flight data were obtained at rates up to 200 samples/sec. Further details regarding the data acquisition system are found in reference 9.

A cine-theodolite (optical tracking) system was used to determine aircraft position with respect to a fixed ground reference system (ref. 12). Two calibrated motion picture cameras tracked the aircraft as it maneuvered close to the runway. The tracking provided elevation and azimuth values referenced to each

camera location. Triangulation of these measurements determined aircraft position. Sink rate, flightpath angle, and other pertinent parameters were derived from the position data. The accuracy of the measurements depended on the distance between the aircraft and the camera installations. Because of the small size of the X-29A aircraft and the shallow approaches used in this experiment, good optical data were available only for approximately the last 50 ft of descent. The optical data were obtained at a rate of 4 samples/sec.

4. FLIGHT MANEUVERS

All maneuvers were flown by the same general procedure, similar to that described in reference 13. While at a constant altitude in the landing pattern, the pilot selected the power approach configuration (wing flap and gear down) normally used for landing the airplane. After the airplane was aligned with the runway, the pilot established a shallow descent at a predetermined sink rate, and optical tracking began. During the descent the pilot minimized use of the control stick and throttle. As the airplane approached the runway and responded to ground effect, the pilot tried to maintain a constant indicated angle of attack using pitch stick inputs. On some maneuvers, the throttle was reduced in order to ensure touchdown. When the airplane leveled off or the main gear touched down, the optical tracking was terminated and the pilot conducted a "go around" maneuver. Ground-effect maneuvers were not attempted if surface winds exceeded 5 kn in any direction.

Figure 2 shows a time history of key parameters from a typical maneuver. In this example, the angle of attack, pitch rate, and canard position indicate an oscillation in the pitch axis during the first few seconds, probably caused by small flightpath adjustments or atmospheric turbulence (note the small amplitude of stick movement). As the airplane descends below 15 ft above ground level (AGL), it begins to flare, as the altitude and vertical speed data show. At the same time, the angle of attack generally decreases, indicating that additional lift is being generated because of ground effect. During the last 10 ft of vertical descent, stick commands diminish while the canard moves to a more positive (trailing-edge down) deflection. This movement is produced by the flight control system. The strake flap surface movement, not shown, is inversely proportional to the canard movement.

A total of 10 maneuvers were attempted over a series of four nonconsecutive test flights. Of these, four maneuvers were not analyzed because of gaps in the optical tracking data or excessive control inputs. For all maneuvers, the normal force coefficient ranged from 0.95 to 1.15 and angle of attack ranged from 6.5 to 8.5° prior to entering ground effect. Because of the limited flight time available for this study, a wider variety of flight conditions was not attempted, and the pilots had little opportunity to practice the technique.

For several reasons, the flight maneuver was a difficult task to perform with precision. In order to maintain quasi-steady flight conditions, the pilot had to monitor the angle-of-attack display inside the cockpit, while simultaneously verifying a safe approach to the runway. The maneuver relies on the increased lift caused by ground effect to help flare the airplane and provide an acceptable touchdown sink rate. The pilot does not experience this effective ground-effect cushion until the last few seconds of the descent.

As a safety precaution, on the first attempts the targeted descent rates prior to encountering ground effect were very shallow (approximately 100 ft/min). As confidence increased, the targeted descent rates were increased to 500 ft/min. In all maneuvers, the sink rate decreased substantially as the airplane descended below about 15 ft AGL ($h/b = 0.55$).

The pilots attempted to conduct the maneuvers near the midpoint of the runway in order to minimize distance from the tracking camera installations (fig. 3). Because of the shallow sink rates, it was difficult for the pilot to visually plan his descent to touchdown near the midpoint. On the last flight, ground radar tracking data, monitored in the control room, was successfully used to advise the pilot when to begin his descent. Figure 3 also shows the distance along the runway for the various maneuvers relative to the runway threshold.

5. FLIGHT DATA ANALYSIS

Data from the optical tracking system and aircraft telemetry stream were merged by linearly interpolating the telemetered data to fit the optical data sample times. The center of gravity, weight, and inertias were computed from the fuel quantity data. The acceleration and angular rate measurements were adjusted to the flight center of gravity. The noseboom static pressure and angle-of-attack vane measurements were adjusted for upwash and position error using corrections developed from "out-of-ground-effect" (altitudes above the point where ground effect influences aircraft behavior) flight calibrations. These calibrations were obtained from tower fly-by, radar tracking, and trajectory reconstruction techniques. The accuracy of the static pressure error calibration is approximately 20 ft (pressure altitude).

The effects of ground proximity on airdata measurements were determined by comparing the onboard aerodynamic sensor data (noseboom angle-of-attack vane and static pressure) to data from independent, nonaerodynamic, sources (optical tracking and inertial sensors). Pressure altitude above ground was determined by subtracting the current ground-level ambient pressure from the noseboom static pressure. The test site is at an altitude of approximately 2,300 ft above sea level. Altitude above ground was also determined from nonaerodynamic sensors by subtracting the runway altitude from the optically measured altitude. The runway was modeled as a sloped surface defined in three dimensional space. The optically measured altitude at touchdown on several runs showed the method to be accurate to within 1 ft. An angle-of-attack measurement which does not rely on aerodynamic sensors was made from a combination of the onboard pitch attitude data and the flightpath angle determined from optical tracking data.

The total vehicle normal force, axial force, and pitching moment were determined from the mass, inertias, and accelerations. These values include all aerodynamic forces (including ground effect) and thrust. The pitching moment was adjusted to the reference center of gravity. The contributions of out-of-ground-effect aerodynamics were estimated by the use of a nonlinear aerodynamic database developed from wind tunnel data. This database accounts for control surface positions, angle of attack, angle of sideslip, and pitch rates and has been extensively validated with flight-test results. The database estimates were subtracted from the flight measured forces and moments. The difference generally included a constant offset in the data at altitudes above ground effect. This offset was attributed to the effects of thrust or discrepancies in the database and was subtracted from the results. A nine-point moving average technique was used to fair the final data. This process eliminated extraneous variations in the data from sources such as gusts or inaccuracies in the nonlinear aerodynamic model. Figure 4 shows normal force coefficient data for a typical maneuver.

6. RESULTS AND DISCUSSION

6.1 Airdata Measurements

The difference between noseboom measured pressure altitude AGL and the optically measured altitude AGL represents the static pressure measurement error caused by ground effect (Δh_{pgs}). Results from two maneuvers (fig. 5), indicate an error of up to 7 ft at touchdown. This magnitude is consistent with results from other noseboom systems (ref. 14). The two maneuvers shown in figure 5 were conducted with constant throttle setting. Useful results were not obtained from the other four test maneuvers, which included variations in throttle setting. Changes in engine thrust level appear to produce static pressure measurement errors of sufficient magnitude to mask the errors caused by ground effect.

The comparison of angle-of-attack measurements from the aerodynamic sensor (noseboom vane) to those from nonaerodynamic sensors indicated no sensitivity to ground proximity. After this was determined, the angle-of-attack vane measurement was used in the analysis of the force and moment data.

6.2 Normal Force

Figure 6 shows the flight measured normal force increments from the six analyzed maneuvers. The data indicate that ground effect is negligible at altitudes above 15 ft AGL, or 0.55 h/b . The maximum

normal force increment (at touchdown) is about 17-percent greater than the out-of-ground-effect normal force coefficient. The consistency of the results from different maneuvers is excellent. Throttle adjustments were made during three of the maneuvers, but had no significant effect on the data.

The wind tunnel data shown in figure 6 were obtained at an angle of attack of 8° with control surface positions typical of the flight maneuvers (-5° -canard deflection, -12° -strake flap deflection).

The PANAIR program was used to determine the sensitivity of the panel method ground-effect predictions to modelling features for this configuration. In this limited PANAIR analysis, features such as the camber distribution and the orientation of wakes from the wing and canard were varied. The results indicated no strong sensitivities in the ground-effect increments; therefore, the remainder of the analysis was based on a simple flat plate model of the X-29A aircraft planform using the APAS code. As figure 6 shows, the APAS results, using a flat plate model, agree favorably with the wind tunnel data; however, both indicate larger ground effect than the flight data.

The wind tunnel and panel methods are based on a steady aerodynamic configuration at constant height above the ground. The lower normal force increments observed in flight could be the result of a lag in the aerodynamic flow field as the airplane approached the ground. Figure 7 shows the flight measured normal force increments as a function of the vertical velocity at $h = 9$ ft AGL. There is a slight indication that the normal force increments approach the steady-state data as the sink rate decreases. However, vertical velocity varied continuously during the flight maneuvers, and the data of figure 7 are based only on the instantaneous value of sink rate. It was not possible to obtain flight data at a constant sink rate throughout a flight maneuver for two reasons. First, the reduction in sink rate is at least partially a result of ground effect, and second, it is clearly necessary to have a low sink rate at touchdown.

Figure 8 shows the X-29A airplane ground-effect data compared with steady-state and dynamic wind tunnel data from other configurations, compiled in reference 5. The dynamic data for the XB-70 and F-104 airplanes were validated with flight-test measurements. Figure 8 shows that the differences caused by dynamic effects can be as significant as differences caused by planform variations. All configurations show a decrease in the ground effect caused by dynamics, although this decrease is minimal for the F-104 aircraft.

6.3 Pitching Moment and Axial Force

The flight and wind tunnel measurements of pitching moment increment caused by ground effect are shown in figure 9. It was found that even slight power adjustments during the flight maneuvers produced pitching moments which masked the ground-effect characteristics. Therefore, data from several maneuvers which included power adjustments could not be used. The flight data show variations at altitudes well above 30 ft AGL (out-of-ground-effect), presumably because of turbulence or other features which were not accounted for in the analysis. The magnitude of the ground-effect increments are small with respect to the total unrimmed pitching moments at these conditions, which may also account for some of the scatter in the flight data. The ground-effect increment at 9 ft AGL is about 0.01 nose down, equivalent to the pitching moment created by an angle-of-attack change of only 0.3° .

The flight and wind-tunnel data agree poorly. The discrepancies may be because of dynamic maneuver effects, as discussed in the normal force data, or the use of a static ground plane in the wind tunnel testing. The data are insufficient to explain the poor correlation of results. In figure 10, flight and wind-tunnel data at a height of 9 ft AGL are shown as a function of angle of attack.

Flight measurements of axial force increments caused by ground effect were inconclusive. The measurements were clearly sensitive to any variation in power setting and no reasonable trends could be developed from the data. Wind-tunnel measurements of axial force, also shown in figure 10, indicate that values at the flight-test conditions may be very small with respect to axial force of the total vehicle.

6.4 Pilot Comments Related to Landing

During early flight tests of the X-29A airplane, pilots commented that the airplane tends to float excessively if the landing flare is initiated too early, requiring the pilot to force the airplane down with forward stick inputs. As discussed in reference 15, this undesirable characteristic has been identified in other aircraft which, like the X-29A, incorporate pitch rate command, attitude hold flight control systems.

Data from the present analysis indicate moderate levels of lift and nosedown pitching moments caused by ground effect. It should be noted that the canard generates positive trim lift when used to balance nosedown ground-effect pitching moments. This is contrary to most configurations with aft-located longitudinal control surfaces. This additional trim lift may account for some of the float tendencies noted by the pilots.

7. CONCLUDING REMARKS

The flight-test program was successful in determining ground effects related to airdata measurements, normal force, and pitching moment of the X-29A airplane. The results were obtained from a minimal amount of total flight time (ten landing approaches). A longer flight program may have allowed a wider variation of flight conditions and would have allowed greater pilot proficiency in conducting the test maneuver.

The static pressure measurement error caused by ground effect was identified and is consistent with other aircraft which use noseboom systems. The angle-of-attack measurement was found to be insensitive to ground effect. The flight-measured normal forces in ground effect were up to 17-percent greater than the out-of-ground-effect values. The increases predicted by computational or wind-tunnel methods were substantially greater than those encountered in flight. This discrepancy has been demonstrated for other configurations and has been attributed to the dynamic nature of the flight maneuver. The difference between dynamic and steady-state ground-effect results can be of equal magnitude to differences related to configuration.

REFERENCES

1. Furlong, G. Chester, and Thomas V. Bollech, National Advisory Committee on Aeronautics, *Effect of Ground Interference on the Aerodynamic and Flow Characteristics of a 42 Degree Sweptback Wing at Reynolds Numbers up to 6.8×10^6* , 1955, Technical Report 1218.
2. Baker, P.A., W.G. Schweikhard, and W.R. Young, NASA, *Flight Evaluation of Ground Effect on Several Low-Aspect-Ratio Airplanes*, 1970, TN D-6053.
3. Rolls, L. Stewart, and David G. Koenig, NASA, *Flight-Measured Ground Effect on a Low-Aspect-Ratio Ogee Wing Including a Comparison With Wind-Tunnel Results*, 1966, TN D-3431.
4. Snyder, C. Thomas, Fred J. Drinkwater III, and A. David Jones, NASA, *A Piloted Simulator Investigation of Ground Effect on the Landing Maneuver of a Large, Tailless, Delta-Wing Airplane*, 1970, TN D-6046.
5. Chang, Ray Chung, and Vincent U. Muirhead, NASA, "Investigation of Dynamic Ground Effect," *Proc. NASA ARC Ground-Effects Workshop*, 1985, CP-2462.
6. Kemmerly, Guy T., and John W. Paulson, Jr., "Exploratory Evaluation of Moving-Model Technique for Measurement of Dynamic Ground Effects," *J. Aircraft*, vol. 25, no. 6, June 1988, pp. 557-562.
7. Lee, Fai-Hung, C. Edward Lan, and Vincent U. Muirhead, "Experimental Investigation of Dynamic Ground Effect," *J. Aircraft*, vol. 26, no. 6, June 1989, pp. 497-498.
8. Putnam, Terrill W., NASA, *X-29 Flight Research Program*, 1984, TM-86025.
9. Sefic, W., and C. Maxwell, NASA, *X-29A Technology Demonstrator Flight Test Program Overview*, 1986, TM-86809.

10. Bonner, E., W. Clever, and K. Dunn, NASA, *Aerodynamic Preliminary Analysis System II, Part I - Theory*, 1981, CR-165627.
11. Carmichael, R. L., and L.L. Erickson, AIAA, "PANAIR - A Higher Order Panel Method for Predicting Subsonic or Supersonic Linear Potential Flows About Arbitrary Configurations," June 1981, 81-1255.
12. Taylor, Albert E., U.S. Air Force Flight Test Center, "Evaluation of Take-off and Landing Facility," 1958, Tech. Memo. FTFF-TM-58-12.
13. Schweikhard, W.G., "A Method for In-Flight Measurement of Ground Effect on Fixed-Wing Aircraft," *J. Aircraft*, vol. 4, no. 2, Mar.-Apr. 1967, pp. 101-104.
14. Parks, Edwin K., NASA, *Flight-Test Measurement of Ground Effect for Powered-Lift STOL Airplanes*, 1977, TM-73256.
15. Gera, J., NASA, *Dynamics and Controls Flight Testing of the X-29A Airplane*, 1985, TM-86803.

Table 1. Physical characteristics of the X-29A aircraft.

Reference area, ft ²	185.0
Reference span, ft	27.2
Reference chord, ft	7.215
Aspect ratio	4.0
Quarter chord wing sweep angle, deg	-33.73
Reference center of gravity	Fuselage station 451
Empty weight, lb	13,948
Useful load, lb	3,882
Fuel load, lb	3,662
Gross weight, lb	17,830
Engine	GE-404-000
Sea-level static thrust, lb	16,012

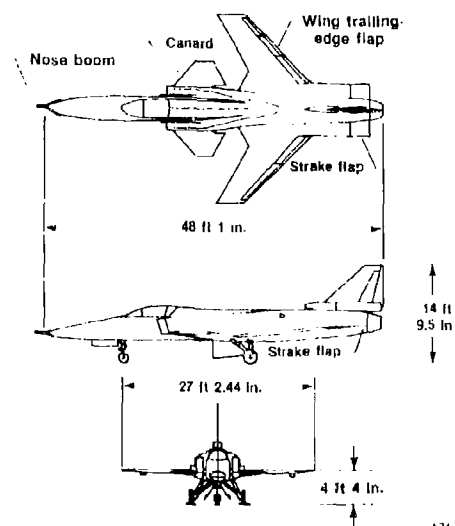


Figure 1. The X-29A airplane.

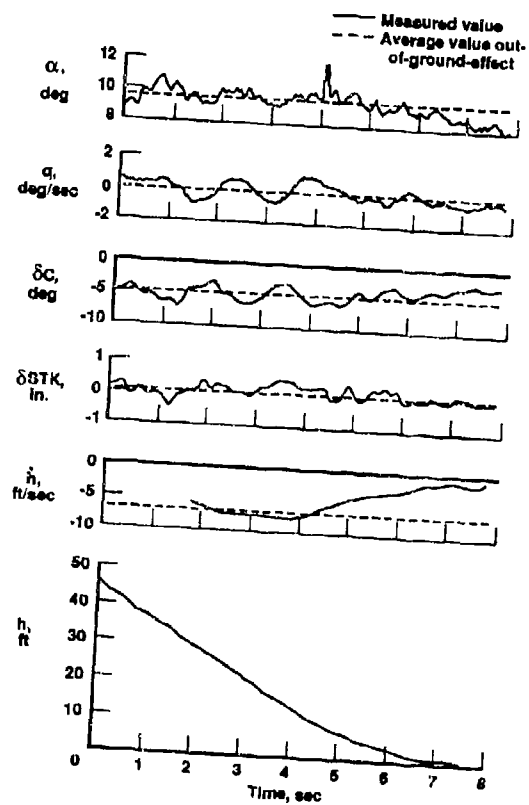


Figure 2. Time history of ground-effect flight-test maneuver.

0781

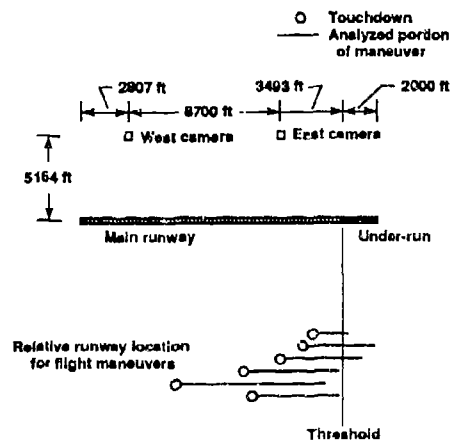


Figure 3. Runway and optical tracking system layout and relative location of ground-effect maneuvers.

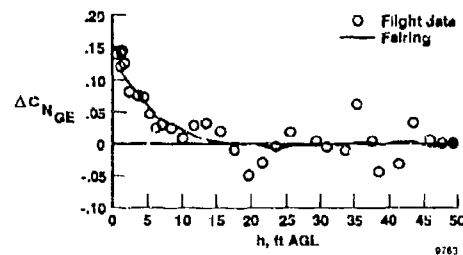


Figure 4. Flight data with fairing.

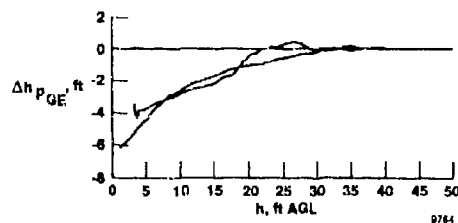


Figure 5. The $\Delta h_{p_{GE}}$ during two maneuvers.

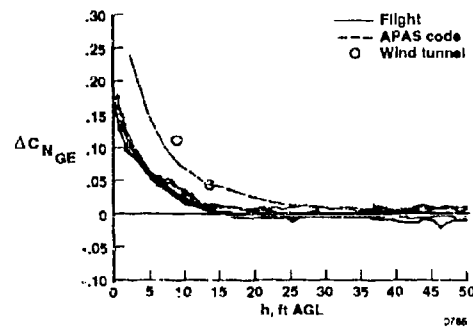


Figure 6. The $\Delta C_{N_{GE}}$ as a function of height AGL.

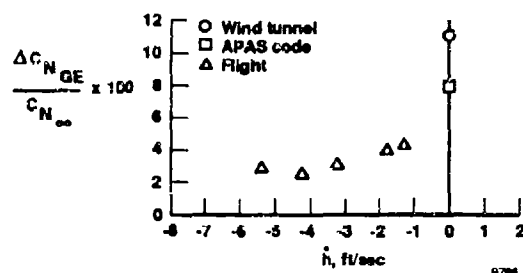


Figure 7. Percentage increase in normal force coefficient caused by ground effect as a function of instantaneous vertical velocity.

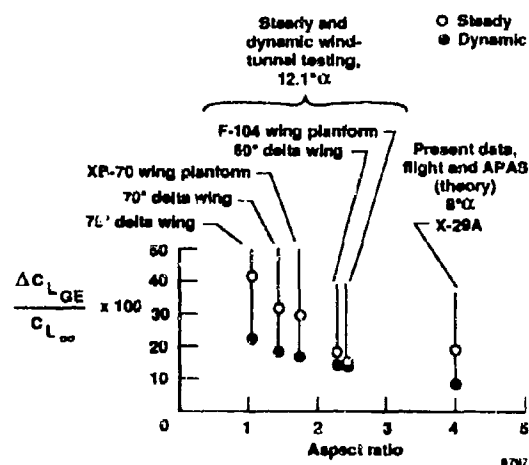


Figure 8. Percentage increase in lift coefficient caused by ground effect under dynamic and steady-state conditions for a variety of configurations. Data for delta wing, XB-70, and F-104 aircraft from reference 5.

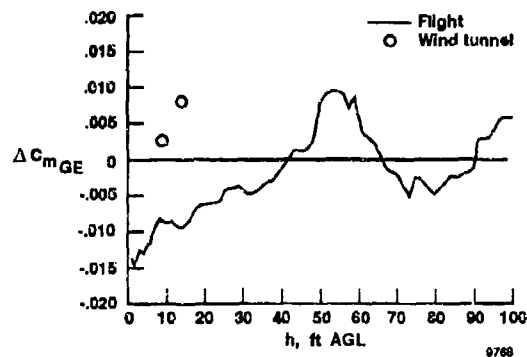


Figure 9. The $\Delta C_{m_{GE}}$ as a function of height AGL.

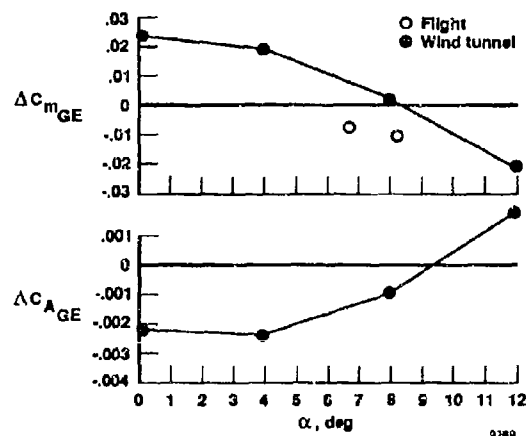


Figure 10. Variation in $\Delta C_{m_{GE}}$ and $\Delta C_{A_{GE}}$ as a function of angle of attack.

DETERMINATION DE L'EFFET DE SOL SUR LES CARACTERISTIQUES DE L'AVION A320

par

A. CONDOMINAS
Aérospatiale Toulouse
B.P. n° 3153, 31060 Toulouse Cedex 03, France

et

J.P. BECLE
ONERA
Centre d'Essais de Modane-Avrieux
B.P. n° 25, 73500 Modane, France

SUMMARY

ONERA and Aerospatiale have combined their means to solve the problems of the determination of ground effect in wind-tunnel : ground simulation, wall and support effects, aerodynamics conditions.

Tests have been carried out in SIMA wind-tunnel (ONERA, Modane center) on a large scale model of A320, with power simulation.

This paper presents :

- a description of the model and its installation in wind-tunnel ;
- the boundary layer processing for ground simulation ;
- the principle of support and wall corrections ;
- the comparison of the wind-tunnel tests results with flight tests results (anemometry, clinometry, deflexion on the tail, lift coefficient).

RESUME

L'ONERA et Aérospatiale ont joint leurs moyens pour résoudre au mieux les problèmes liés à la détermination des effets de sol en soufflerie : simulation au sol, effets des parois et des supports, conditions aérodynamiques.

L'effet de sol sur l'avion A320 a été établi à l'occasion des essais d'une maquette hyperventée à l'échelle 1/7,6, équipée de simulateurs de réacteurs. Cet essai a eu lieu durant l'hiver 1986-1987 dans la grande soufflerie SIMA du Centre de Modane-Avrieux de l'ONERA.

L'exposé présente :

- la description de la maquette et du montage d'essai ;
- le traitement de la couche limite du plancher pour la simulation du sol ;
- le principe des corrections de parois et de support ;
- la comparaison des résultats obtenus en soufflerie à ceux obtenus lors des essais en vol (anémométrie, clinométrie, déflexion moyenne au droit de l'empennage, coefficient de portance).

1 - INTRODUCTION

La détermination avant le premier vol de l'effet de sol auquel tout avion sera soumis est un des multiples objectifs d'un bureau d'études.

Les essais en soufflerie sur une maquette représentant au mieux l'avion réel ont toujours été l'instrument préféré de cette étude.

De Caravelle et de l'Airbus A300B jusqu'à l'A320 en passant par l'A310, bien des méthodes et des moyens d'essais ont évolué.

Si le principe de la simulation du sol par un plancher -quelquefois un plafond- est demeuré, le traitement de la couche limite est allé en s'améliorant ; les calculs de corrections de parois et de supports ont beaucoup progressé ; les maquettes ont crû en dimension et en finesse de représentation des détails. Et cette énumération n'est pas exhaustive.

L'avion A320 est le dernier des Airbus -mais certainement pas l'ultime- à avoir profité de cette expérience.

Nous allons exposer ce que furent les moyens d'essais développés par l'ONERA en ces circonstances, puis quels furent les résultats livrés par la soufflerie à l'Aérospatiale et comment ils se comparèrent à ce que donna le vol quelques mois plus tard.

2 - MAQUETTE

Les essais d'effet de sol ont été effectués sur une maquette de l'Aérospatiale, représentant à l'échelle 1/7,6 l'avion A320 (fig. 1). La similitude la plus parfaite possible avec l'avion réel, notamment dans les configurations de décollage et d'atterrissage a été nécessaire pour obtenir l'effet de sol, non seulement sur l'avion complet en terme de coefficients aérodynamiques, mais également sur l'instrumentation de l'avion (anémométrie et clinométrie), les efficacités de gouvernes ou la déflexion moyenne au droit de l'empennage ; ceci a conduit à une maquette des plus sophistiquée, tant du point de vue de la géométrie que de celui de l'équipement.

2.1 - Données géométriques - Configurations [fig. 2]

Conçue par l'Aérospatiale pour des essais d'effet de sol, mais également pour des essais d'inverseurs de poussée, la maquette est équipée de deux nacelles motorisées avec des simulateurs de 23 cm de diamètre (TPS, Turbo Powered Simulator). Ces nacelles représentent soit le moteur CFM56, soit le moteur IAE V2500, et ce, en jets directs ou inverses. Les résultats des inverseurs de poussée ont fait l'objet d'une publication particulière [1]. Les résultats présentés dans cette communication sont issus des essais de détermination systématique des effets de sol effectués avec simulation des moteurs CFM.

La voilure est équipée de toutes ses parties mobiles, dont le braquage est positionné à l'arrêt, à des valeurs prédéterminées. Les bords de bord d'attaque peuvent être braqués à 0,22 ou 40 degrés ; les volets de bord de fuite à 0, 20 ou 40 degrés ; les spoilers et aérofreins à 0 ou 50 degrés ; les ailerons à - 10, 0 ou 10 degrés.

Le train d'atterrissage de la maquette est escamotable ; dans la configuration "train sorti", il est positionné soit dans la configuration "amortisseurs enfoncés" dans le cas où l'avion est au sol, sans portance, soit dans la configuration "amortisseurs détendus", dans les phases d'approche et de décollage. L'écart de positionnement représente 0,43 m (56 mm à l'échelle de la maquette).

Le pointe arrière de l'appareil est composée de la dérive, avec gouverne de direction motorisée (+ 30 degrés), et de l'empennage horizontal, qui est démontable. La position angulaire de l'empennage est motorisée (+ 5 à - 15 degrés), ainsi que celle des deux gouvernes de profondeur gauche et droite (+ 15 à - 30 degrés).

L'envergure de la maquette est de 4,5 m ; le diamètre du fuselage est de 0,5 m pour une longueur de 5 m ; la masse de la maquette avec tous ses équipements est de 1 800 kg.

2.2 - Equipement - Mesures [fig. 3]

Les essais de la maquette de l'A320 ont comporté des mesures d'efforts aérodynamiques, de pression, de température, de débit, de positionnement de gouvernes, et de positionnement de la maquette (angles d'incidence et de dérapage, hauteur de la maquette par rapport au sol).

La mesure des efforts sur une maquette complète avec simulation des moteurs a nécessité la réalisation d'une balance dard à six composantes, avec traversée d'air comprimé (fig. 4). Cette balance monobloc est composée de deux tubes concentriques reliés par six lames dynamométriques. Le tube externe, pesé, reçoit le fourreau de la maquette sur deux portées situées à ses extrémités. Le tube interne, non pesé, supporte à l'amont le dispositif de découplage. Celui-ci est constitué de quatre soufflets, montés perpendiculairement à l'axe longitudinal de la balance entre les tubes fixe et pesé. La présence de ces soufflets engendre deux types de difficultés : ils présentent tout d'abord des rigidités en parallèle avec la partie sensible de la balance, qui peuvent agir sur les coefficients de sensibilité dynamométrique ; de plus des défauts résiduels dans la fabrication et le montage des découpleurs engendrent des efforts parasites lors de la mise sous pression des canalisations d'air comprimé. En conséquence l'étalonnage de la balance est effectué en présence du dispositif de découplage, avec et sans pression dans les

découpleurs. Pour la balance concernée, l'effort parasite sur la composante la plus sensible est au maximum de 0,4 % de la capacité nominale de la balance ; la variation de sensibilité avec la pression est négligeable. Il est tenu compte de ces corrections dans le calcul des résultats.

L'ensemble débitmétrique permettant la régulation et la mesure de débit d'air comprimé alimentant les nacelles est monté dans la pointe avant de la maquette. Il est fixé entre la partie pesée du dispositif de découplage à l'amont, et les canalisations traversant la voilure à l'aval. Cet ensemble est composé d'une vanne d'entrée, utilisée pour la mise sous pression de la balance, sans débit, de deux vannes de régulation permettant de régler indépendamment le débit sur chacune des nacelles, et de deux débitmètres à col sonique pour la mesure des débits ; ce dispositif a été étalonné avant les essais pour s'assurer du bon accord entre les différents moyens de mesure du débit au banc d'étalonnage des nacelles et en essais.

Toutes les vannes installées dans la maquette sont télécommandées depuis la salle de pilotage de la soufflerie.

La maquette est équipée de 600 prises de pression. Plus de 300 d'entre elles concernent seulement les nacelles ; elles sont réparties en prises de pression pariétale sur les entrées d'air et les mâts et en prises de pression interne dans les tuyaux primaire et secondaire du moteur ; ces dernières sont utilisées pour recalculer à partir des étalonnages le débit et la poussée des moteurs.

Quinze profils de la voilure et une corde de l'empennage sont équipés en prises de pression pariétale.

Des pressions statiques sont mesurées dans les deux zones du nez du fuselage où sont situées les prises anémométriques de l'avion (prises pilote, copilote et prise de secours).

Les incidences locales aux emplacements où se trouvent les girouettes d'incidence de l'avion sont mesurées par des sondes clinométriques à cinq trous, qui ont été étalonnées dans la soufflerie F2 de l'ONERA, au Centre du Fauga-Mauzac, dans des conditions de montage et de fixation analogues à celles sur la maquette.

L'assiette longitudinale de la maquette est fournie par des inclinomètres placés sur la pièce de fixation de la maquette sur la balance et étalonnés une fois en place. Le dérapage de la maquette, jusqu'à 180 degrés, obtenu par rotation du mât central, est calculé à partir des indications de ce mât et des déformations du support et de la maquette sous les charges qui leur sont appliquées.

L'altitude de la maquette est définie comme étant la hauteur du centre de gravité de l'avion par rapport au sol ; elle dépend donc de la position du mât support et de l'assiette de la maquette. La hauteur minimale admissible lors des essais en incidence est celle qui correspond aux roues à 1 cm du sol, à l'assiette maximum ; cette hauteur est de 0,473 m lors des essais avec le train d'atterrissage enfoncé, et de 0,53 m lors des essais avec les amortisseurs détendus. Pour les altitudes de la maquette inférieures à 1 m, les essais ont été menés en ajustant la position du mât à chaque position en incidence de manière à conserver la hauteur de la maquette constante. La précision de positionnement en hauteur est de l'ordre du millimètre.

Les répartitions de pression et les profils de vitesse sont relevés au plancher de la soufflerie simulant le sol.

L'ensemble de l'instrumentation a nécessité une centaine de voies de mesure, les températures et la plupart des mesures de pression étant pour leur part sous-commandées.

3 - MOYENS ET TECHNIQUES D'ESSAI

3.1 - Soufflerie - Montage

Les essais d'effet de sol ont été effectués dans la veine n° 2 de la soufflerie SIHA de l'ONERA, installée au centre de Modane-Avrieux.

La soufflerie SIHA est une soufflerie continue, atmosphérique, dont le domaine de vitesses s'étend depuis les très basses vitesses jusqu'à un nombre de Mach voisin de 1. Trois veines d'expérience interchangeables peuvent être utilisées. Ces veines ont une section circulaire de 8 m de diamètre et une longueur de 14 m.

La veine n° 2, utilisée pour les essais à basses vitesses, est équipée d'un dispositif de mécanique du vol (dénommé mât SILAT), à deux degrés de liberté : translation verticale et rotation.

Le sol est simulé par un plancher horizontal, situé à 1,985 m en-dessous de l'axe de la veine, dont la couche limite naturelle est soufflée par de l'air comprimé éjecté par une fente transversale. La mise au point de la simulation du sol a fait l'objet d'études particulières qui sont décrites au paragraphe 3.2.1.

Le montage de la maquette dans la veine est schématisé sur la figure 5. A l'extrémité supérieure du mât vertical est monté un dispositif de mise en incidence, autorisant des débattements angulaires de - 4 à + 15 degrés, et sur lequel vient se fixer la balance, supportant la maquette. L'étanchéité de la maquette dans la partie inférieure du fuselage, au niveau de la jonction avec le mât, est assurée par un tiroir coulissant lié à la maquette et dont la force d'appui sur le mât est mesurée par un dynamomètre.

L'air comprimé à haute pression nécessaire à l'entraînement des turbines provient d'un stockage d'air de 23 m³ à 270 bars alimenté en permanence par un compresseur débitant 2,7 kg/s. Cet air, filtré à 12 μ m et maintenu à température constante, transite à pression constante (45 bars) à l'intérieur du mât vertical, du dispositif de mise en incidence, de la balance et des découpleurs ; il est ensuite distribué à chacun des moteurs à l'aide du système débitmétrique embarqué ; le débit maximum pour les deux moteurs est de 5 kg/s.

3.2 - Technique des essais

La détermination de l'effet de sol sur une maquette en soufflerie a nécessité des études et expériences liées à la nature même du problème : la simulation du sol et le déplacement de la maquette dans la veine.

Le plancher de la soufflerie ne présente pas les mêmes caractéristiques que la piste d'un aéroport sur laquelle l'avion se pose du fait du développement, en soufflerie, de la couche limite. La simulation du sol consiste donc à s'affranchir de cette couche limite.

Il convient ensuite de ne pas attribuer à l'effet de sol d'éventuelles hétérogénéités de l'écoulement dans la veine d'essai. Ses caractéristiques en vitesse et direction doivent être parfaitement définies dans le volume balayé par la maquette.

Enfin, la présence du support et des parois de la veine engendrent des perturbations, différentes selon la position de la maquette, dont il faut tenir compte dans les résultats finaux.

3.2.1 - Simulation du sol

La simulation du sol est obtenue par soufflage de la couche limite qui se développe naturellement sur le plancher de la soufflerie. Le soufflage s'effectue par une fente de 6 m de long pour 1 mm de hauteur, située à 5,16 m du bord d'attaque du plancher, soit à deux cordes du centre de référence de la maquette situé à 25 % de la corde aérodynamique moyenne.

La simulation par soufflage a fait l'objet, dans un premier temps, d'études et d'expériences réalisées dans la soufflerie S10 du Centre d'Essais Aéronautiques de Toulouse.

L'adaptation au cas de la maquette de l'A320 a ensuite fait l'objet d'études théoriques en amont des essais et d'études expérimentales en soufflerie.

Des études théoriques ont été menées à partir d'un programme de calcul de couche limite soufflée, bidimensionnelle, en milieu incompressible, prenant en compte les effets de gradient de pression statique (veine d'essai et champ de la maquette). Le débit de soufflage a été ainsi optimisé de manière à obtenir, sur le plancher, une épaisseur de déplacement de la couche limite réduite, et sans variation notable au droit de la maquette, ainsi qu'un profil de vitesse dans la couche limite le plus acceptable possible, sans sous-vitesses ou survitesses trop importantes au plancher. Le débit optimum calculé était de 1,9 kg/s à un nombre de Mach de 0,2.

Les calculs ont également démontré que, sans soufflage de la couche limite, le gradient de pression positif dû au champ de la voilure provoquait un net épaissement de l'épaisseur de déplacement, mais sans provoquer cependant son décollement.

L'étude expérimentale a porté sur l'allure des lignes de courant au plancher de la soufflerie, devant simuler le sol d'un aéroport, sans couche limite, donc en fluide parfait.

Dans un premier temps, l'Aérospatiale a calculé les lignes de courant au plancher de la soufflerie en fluide parfait, pour deux incidences de la maquette ($\alpha = 0$ et $\alpha = 8$ degrés), à une altitude donnée ($H = 0,53$ m), (lignes "fluide parfait" dans les figures 6 et 7). Ces lignes sont celles que devraient suivre les filets fluides sans phénomène visqueux.

La Direction de l'Aérodynamique de l'ONERA a superposé à ce champ fourni en fluide parfait la couche limite de la soufflerie et a ainsi déterminé ce que devient la ligne de courant pariétale initiale en fluide parfait en présence de la couche limite (ligne "fluide visqueux"). Celle-ci, comme le montrent la figure 6 ou la photographie de la figure 7, est fortement déviée vers l'extérieur.

Une expérience a été menée en visualisant à l'aide de fils de laine la direction des lignes de courant au sol et en mesurant les profils de vitesse dans la couche limite à l'aide d'un peigne situé à 0,84 m en aval de la fente de soufflage. Le résultat est présenté sur la figure 6 pour une incidence de 8 degrés et un nombre de Mach de 0,20.

Sans soufflage de la couche limite, les fils de laine suivent assez bien la ligne de courant "fluide visqueux", excepté dans la zone à fort gradient transversal ; la couche limite associée présente un aspect classique, avec une épaisseur de l'ordre de 130 mm.

Un débit de soufflage moyen (1,6 kg/s) provoque un redressement des lignes de courant et les fils de laine se superposent bien avec la ligne de courant "fluide parfait" que ce soit en amont ou en aval de la voilure ; le niveau de survitesses observé dans la couche limite, dû au soufflage, est pratiquement nul.

Un débit de soufflage excessif (2,5 kg/s) redresse trop les lignes de courant au sol et provoque de grandes survitesses dans la couche limite à proximité du sol.

Les expériences réalisées, qui ne sont révélées être en bon accord avec les calculs théoriques préliminaires, ont conduit aux débits de soufflage de 1,75 kg/s à un nombre de Mach de 0,20 et de 2,2 kg/s pour un nombre de Mach de 0,25.

3.2.2 - Etalonnage de la veine

Les conditions génératrices de l'écoulement sont mesurées dans la chambre de tranquillisation de la soufflerie (24 m de diamètre). La pression statique de référence est mesurée par une sonde, dont les prises sont situées à 1 m en aval de l'entrée de veine. Un étalonnage de la veine a permis d'établir la relation liant cette pression statique à celle régnant au centre de réduction des efforts de la maquette.

L'étalonnage de la veine a été effectué avec une sonde, mesurant les répartitions longitudinales de pression statique sur une longueur de 6,6 m, et ce, à trois hauteurs au-dessus du plancher de la veine : 0,65 m, 1 m et 2,45 m. Les résultats ont démontré (fig. 8) une très bonne homogénéité de l'écoulement selon l'altitude. Au point de référence de la maquette, situé à 6,2 m de l'entrée de la veine, l'écart de nombre de Mach entre la prise de référence et la sonde de pression statique est constant quel que soit l'altitude ; le gradient de nombre de Mach est très faible (inférieur à 0,001/m) mais augmente cependant légèrement lorsque l'on se rapproche du sol. Le soufflage du plancher n'est perceptible qu'à l'altitude la plus basse et à un débit supérieur à 2 kg/s. Cet effet est cependant inférieur au demi-millième en nombre de Mach.

Le gradient de pression statique a engendré une correction de poussée d'Archimède, ne dépendant que de la hauteur de la maquette. Etant donné la grande dimension de la maquette, les prises de pression anémométrique ont été référencées à la pression statique régnant à leurs emplacements en l'absence de la maquette.

3.2.3 - Clinométrie de la veine

La détermination de l'ascendance du l'écoulement dans la veine d'essai ne peut se faire par la méthode classique du retournement de la maquette du fait de son mode de fixation par mât central.

L'ascendance de veine a été déterminée par sondage de l'écoulement, au droit du mât support, à l'aide de sondes clinométriques à cinq trous.

Un mât horizontal, équipé de dix sondes clinométriques espacées de 500 mm, est positionné à quatre altitudes dans la veine d'essai (0,5 m, 1 m, 2 m, 3 m) (fig. 9) ; les sondages sont effectués entre - 1,6 m et + 2,9 m en envergure.

Les résultats obtenus sont corrigés du défaut de sonde, déterminé par retournement de la sonde seule, et de l'effet de champ aérodynamique du mât support, calculé théoriquement, mais dont la valeur (0,06°) a été vérifiée expérimentalement par retournement du mât.

Les résultats obtenus selon l'envergure et l'altitude sont présentés figure 9 à un nombre de Mach de 0,25 ; les valeurs des ascendances de veine locales sont indépendantes du nombre de Mach. Pour l'exploitation des essais, une correction unique a été calculée par altitude, en faisant la moyenne des mesures locales dans la zone concernée par la maquette (+ 2,3 m). Cette valeur moyenne est de 0,09° à 0,5 m de hauteur, croît à 0,18° à 2 m de hauteur, et diminue à 0,12° à une altitude de 3 m.

Le soufflage du plancher n'a été perçu qu'à la hauteur minimum, mais avec une amplitude négligeable.

3.2.4 - Correction de support

L'influence du mât support central a été déterminée dans la soufflerie S4 du Centre d'Essais Aéronautiques de Toulouse (CEAT), sur une maquette à l'échelle 1/23, représentative d'un A320.

La maquette est reliée par un montage "3 mâts" à une balance qui mesure les efforts aérodynamiques ; le mannequin du mât ventral est approché du fuselage, sans contact avec celui-ci. Son influence est déduite, pour différentes configurations, incidences et altitudes, de la comparaison avec et sans mât. Trois sections de mât différentes ont été simulées.

Les résultats ont démontré que l'influence du mât sur les coefficients aérodynamiques longitudinaux est proportionnelle à la section du mât, mais est indépendante de l'incidence, de l'altitude et de la configuration d'hyper sustentation de la voilure.

Des corrections ont été apportées aux résultats [$\Delta C_Z = 0,03$; $\Delta C_M = 0,01$; $\Delta C_X = 0,001$] mais étant constantes, elles n'interviennent pas dans la détermination de l'effet de sol.

Il faut préciser également que les pressions anémométriques au nez de l'avion ont été corrigées d'un champ de pression du mât calculé théoriquement.

3.2.5 - Corrections des effets de parois

L'effet de sol est défini comme étant l'écart des caractéristiques aérodynamiques à iso incidence entre l'avion en atmosphère infinie et l'avion à proximité du sol.

Lors des essais en soufflerie, aucun de ces cas n'est parfaitement simulé à cause de la présence des parois de la veine ; les caractéristiques en milieu infini sont déduites des résultats obtenus avec la maquette centrée, corrigées de l'effet de toutes les parois (fig. 10A) ; à proximité du sol la maquette subit effectivement l'effet du sol, mais également l'influence des autres parois dont il faut tenir compte (fig. 10B). L'effet de sol est calculé à partir des résultats obtenus aux différentes altitudes, ainsi corrigés.

Les corrections de paroi sont calculées par une méthode analytique, décrite dans la référence [2] ; la veine circulaire de la soufflerie est remplacée par une veine rectangulaire équivalente, conservant le plancher, et respectant la section exacte de la veine.

Les faibles distances entre la maquette et les parois, et notamment en incidence entre le sol et l'empennage, ont nécessité une modélisation assez complexe de la maquette ; les singularités de volume des surfaces portantes (voilure et empennage) ont été réparties en envergure ; la portance de la maquette a été décrite par des nappes tourbillonnaires en séparant la portance de l'empennage de la portance de la voilure.

Les ordres de grandeur des corrections pour ramener les résultats en atmosphère infinie sont de 1 degré en incidence, 0,002 en nombre de Mach et 0,13 en moment de tangage ; les corrections de traînée sont très faibles.

4 - RÉSULTATS

4.1 - Généralités

Les moyens d'essais qui viennent d'être décrits ont été les instruments d'une longue expérimentation dont le premier objet était une étude d'inverseurs de poussée sur les moteurs de l'A320. Il est apparu intéressant d'en profiter pour développer une étude de l'effet de sol de cet avion.

L'effet de sol, c'est, chacun le sait, ce phénomène qui modifie les caractéristiques aérodynamiques d'un avion lorsque sa hauteur au-dessus du sol devient inférieure à environ une envergure (figure 11).

La portance et le moment de tangage cabreur propres à la voilure augmentent modérément, alors que sa traînée diminue. Au niveau de l'empennage horizontal, la déflexion chute et la portance de l'empennage augmente. Par conséquent, le pilote doit réduire l'incidence de l'avion et augmenter "à cabrer" le braquage de la gouverne de profondeur, pour maintenir la trajectoire.

Nous ne présenterons que des résultats obtenus en paliers, à pente constamment nulle. Cependant, nous montrons sur la figure n° 12, comment évoluent les paramètres d'un avion A320 lors d'un atterrissage. Il demeure, comme il est rappelé sur la figure n° 3, que la connaissance des effets de sol "en paliers", c'est-à-dire à pente nulle, est une étape nécessaire pour satisfaire les besoins de l'atterrissage automatique catégorie III et l'alimentation du simulateur de vol en données aérodynamiques.

4.2 - Expérimentation en soufflerie

La procédure d'essai a été présentée en détail dans la première partie de cet exposé. Il faut toutefois insister sur le fait que la vocation première de l'essai était une étude d'inverseurs de poussée. C'est ainsi que la motorisation des nacelles a imposé l'échelle de la maquette dont on aurait bien préféré qu'elle fût de dimensions plus réduites, eu égard à l'importance des effets de parois. Le montage sur un support ventral déjà existant n'était peut-être pas le mieux adapté à une étude d'effet de sol. Le régime des simulateurs de moteurs est représentatif des régimes correspondants en vol.

Les mesures ont été faites à des incidences comprises entre 0 et 12 degrés. Les hauteurs du centre de gravité de l'avion, à l'échelle 1/7,6, s'étagent entre 0,47 m et 2,7 m au maximum. Cette dernière ne représente que 60,5 % de l'envergure de l'avion. C'est dire toute l'importance du calcul des corrections de paroi pour accéder à la référence "milieu infini".

Les résultats sont mis sous une forme modélisée par le truchement de deux quantités. La première est la différence des valeurs que prend un paramètre entre le milieu infini et "avion, roues au sol" ; c'est une fonction de l'incidence. La deuxième est un facteur d'amortissement qui rend compte de l'effet d'altitude au-dessus de la piste. Cette formulation a pour mérite de rendre très simple le calcul d'un paramètre à une incidence et à une altitude données.

4.3 - Les mesures en vol

La figure n° 14 propose un résumé du programme d'essais en vol. Trois configurations ont été retenues, deux de décollage plus celle d'atterrissage. Pour chacune étaient prévus à peu près douze passages en palier, c'est-à-dire aux hauteurs au-dessus de la piste et deux incidences correspondant à 1,2 V_{s1} et V_{FE} (1,2 fois la vitesse de décrochage à $\alpha = 1$ et vitesse limite maximale avec volets sortis).

Sur la figure n° 15 sont schématisés les équipements permettant de définir les conditions de vol :

- un radioaltimètre détermine la hauteur de l'avion au-dessus de la piste ; la connaissance de cette hauteur associée par la loi de Laplace à la pression atmosphérique au sol donne accès à la pression statique de référence de l'avion ;
- les indications de trois prises de pression totale permettent de calculer le nombre de Mach ;
- la plateforme à inertie fournit l'assiette de l'avion, dans le cas qui nous intéresse, égale à l'incidence ;

- des prises de pression statique sont implantées sur la partie avant du fuselage. La correspondance entre les pressions mesurées et la pression statique de référence a été établie en milieu infini par la technique du cône remorqué. Un des buts de l'essai est d'étudier comment varie cette correspondance quand l'avion subit l'effet de sol ;
- des girouettes d'incidences sont, elles aussi, implantées sur la partie avant du fuselage. Des relations ont été établies entre ces incidences locales et l'incidence de l'avion en milieu infini. L'évolution de ces relations avec la proximité du sol est encore un des objets de l'essai.

Les figures qui suivent donnent une synthèse des procédures d'identification de l'effet de sol, en vol.

La figure n° 16 traite de l'anémométrie. Elle rappelle, en le précisant, tout ce que nous avons dit plus haut à propos de la détermination de l'altitude, des pressions statique et totale de référence, de l'incidence...

La figure n° 17 traite de la clinométrie. Elle constitue elle aussi un rappel de ce qui vient d'être exposé.

La figure n° 18 est consacrée à la détermination de l'effet de sol, en vol, sur la portance et le moment de tangage d'un avion non empenché et sur la déflexion moyenne au droit de l'empennage. La méthode est la suivante :

- avant tout calcul nous disposons de :

- . données aérodynamiques identifiées en vol, en milieu infini ;
- . données prévisionnelles relatives à l'effet de sol ; elles ont un caractère empirique ;
- . la situation de l'avion en vol, altitude, masse, vitesse, braquage des gouvernes de profondeur.

A ces trois groupes de données un programme de calcul fait correspondre une incidence, α_{SIMULE} et un calage de l'empennage, ih_{SIMULE} , nécessaires à l'équilibre. Ces deux valeurs diffèrent des incidence α et calage ih réels du cas de vol correspondant, dans la mesure où les données prévisionnelles d'effet de sol ne rendent pas exactement compte de la réalité.

Il faut donc les modifier en prenant :

$$\Delta C_{Zsol} = \Delta C_{Zsol} \text{ Données prévisionnelles} + \frac{dC_Z}{d\alpha} (\alpha_{SIMULE} - \alpha)$$

$$\Delta C_{m_{sol}} \quad \text{Inchangé (avion sans empennage)}$$

$$\Delta \epsilon_{sol} = \Delta \epsilon_{sol} \text{ Données prévisionnelles} + (ih_{SIMULE} - ih)$$

puis recommencer le calcul. L'itération converge rapidement.

REMARQUE : C'est en nous fondant sur des expériences antérieures et sur des comparaisons entre soufflerie que nous avons donné à $\Delta C_{m_{sol}}$ prévisionnel la valeur établie en soufflerie et l'avons maintenue pendant l'itération.

4.4 - Comparaison vol-soufflerie

Principe : la comparaison est faite aux altitudes et aux incidences des points de vol. Donc les valeurs comparées seront, pour le vol, celles directement mesurées et pour la soufflerie des valeurs élaborées à partir de la modélisation déjà mentionnée.

Résultats :

a) Anémométrie

Dans la plupart des cas examinés (figure n° 19), il apparaît que l'effet de sol sur les coefficients de pression K_p est plus faible en soufflerie qu'en vol. Mais, il faut observer qu'à un écart $\Delta K_p = 0,01$ correspond une variation de pression égale à 45 Pascals (0,0065 PSI) dans un cas de décollement à $M = 0,25$ et $Z = 0$. Il est aussi des cas où ΔK_p en vol ne semble pas tendre vers zéro quand l'altitude croît, ce qui peut être une erreur résiduelle associée à la précision de la mesure. Voyez aussi les figures n° 20, 21 et 22. Aujourd'hui, il semble que des méthodes de calcul théoriques assez fines ont été développées pour remettre en cause la nécessité de la mesure expérimentale.

b) Clinométrie

Les figures n° 23 et 24 montrent que la soufflerie sous-estime fortement l'effet de sol sur l'incidence locale au droit des girouettes. Pour autant que la sonde clinométrique soit correctement orientée, elle ne détecte qu'une incidence locale ponctuelle - à 18 mm de la peau du fuselage de la girouette, soit 136,8 mm à l'échelle avion-. La girouette montée sur l'avion indique une incidence locale prise en valeur moyenne sur une envergure de 76 mm. De plus, l'incidence à la sonde clinométrique est relevée dans une veine guidée de soufflerie ; or aucune variation ni de correction de paroi, ni d'ascendancy entre la voilure et l'emplacement de la sonde n'a été appliquée. Ici encore, et comme pour l'anémométrie, il semble bien que le calcul soit devenu plus simple et plus fiable que la mesure expérimentale.

c) Portance de l'avion sans empennage

Les figures n° 25 et 26 contiennent certainement les comparaisons les plus satisfaisantes de cet exposé. En effet, les plus fortes différences entre ΔC_Z du vol et de la soufflerie sont de l'ordre de 0,01 seulement.

d) Déflexion moyenne au droit de l'empennage

Les figures n° 27 et 28 montrent comment se comparent les effets de sol sur la déflexion. A un cas près (décollage à $\alpha = 6,5^\circ$ et $H = 39$ feet) les recouvrements sont excellents.

5 - CONCLUSIONS

L'ONERA et AEROSPATIALE ont mis en oeuvre un grand concours de moyens pour traiter expérimentalement, en soufflerie, le problème de l'effet de sol sur les caractéristiques aérodynamiques de l'avion A320.

Des essais en vol à très basse altitude au-dessus des pistes ont pu être exploités et comparés aux résultats issus de la soufflerie.

La comparaison vol-soufflerie a ainsi montré des recouvrements satisfaisants en portance et en déflexion moyenne au droit de l'empennage, malgré un montage et des dimensions de maquette qui ne sont pas sans prêter le flanc à la critique.

En anémométrie, les écarts observés sont de l'ordre de grandeur de la précision des capteurs de pression. Les écarts observés sur les résultats en clinométrie sont probablement dus à la différence des moyens de mesure et à un degré de correction des résultats soufflerie pas assez élaboré (ascendance locale, effets des parois et supports).

Sur ces deux points, les progrès obtenus dans les calculs théoriques permettront sans doute de s'attacher d'essais spécifiques.

REFERENCES BIBLIOGRAPHIQUES

- [1] C. CASTAN - Efficacité des Inverseurs - Colloque AAAF de POITIERS, France, le 28 octobre 1987
- [2] X. VAUCHERET - Progrès récents des calculs d'effets de parois en souffleries industrielles - La Recherche Aéronautique - N° 1988-3 (mai-juin 1988)

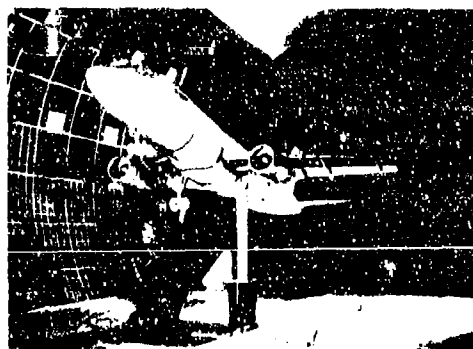
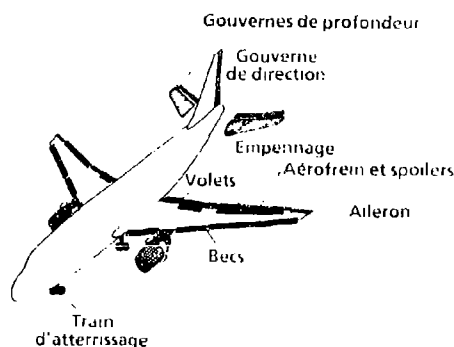


Fig. 1 - A320 à l'échelle 1/7,6 dans la soufflerie S1MA.



- Éléments mobiles par valeurs discrètes
- Éléments mobiles motorisés
- Nacelles motorisées par IPS
- Jets directs ou reverses
- Nacelles IAE (V 2500) ou CFM.

Fig. 2 - Configurations de la maquette.

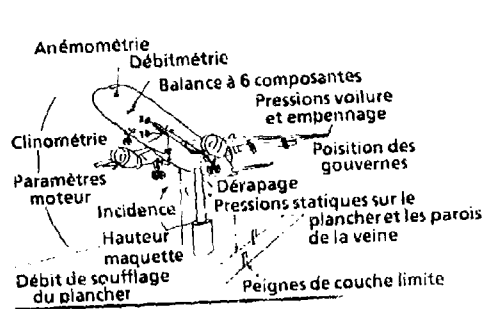


Fig. 3 - Equipement - Mesures.

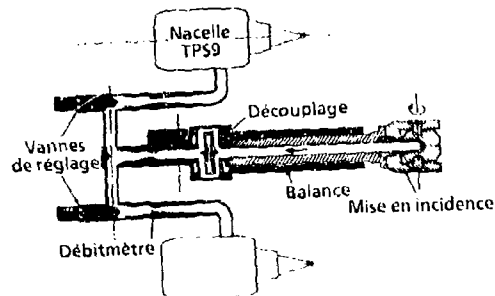


Fig. 4 - Balance - Découplage - Débitmètre.

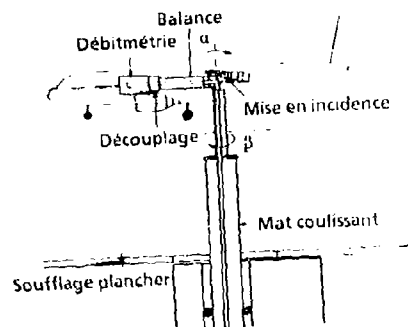


Fig. 5 - Montage de la maquette.

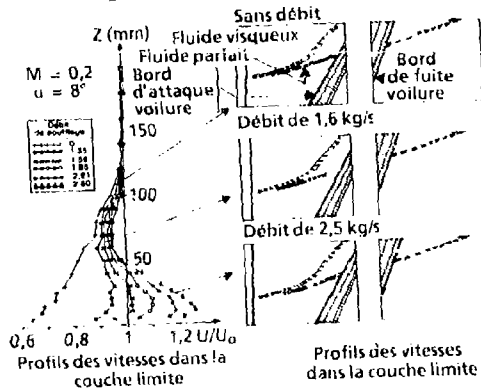


Fig. 6 - Simulation du sol.

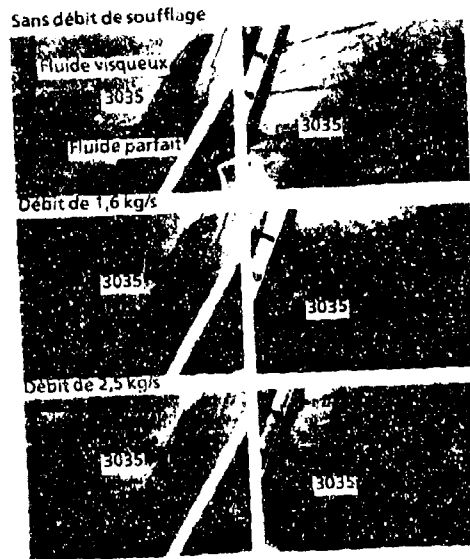


Fig. 7 - Visualisations des lignes de courant au plancher de la soufflerie.

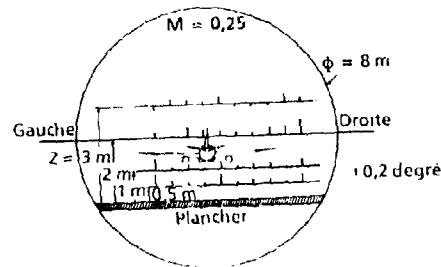


Fig. 8 - Etalonnage de la veine d'essai.

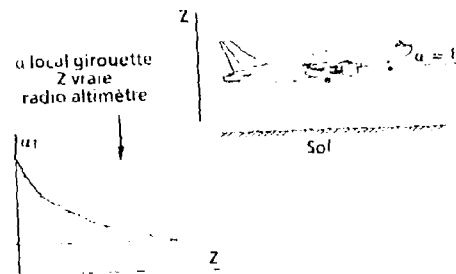


Fig. 9 - Sondage clinométrique de la veine d'essai.

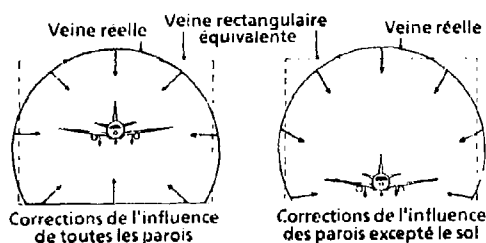


Fig. 10 - Corrections des effets des parois.

Modifications des caractéristiques aéronautiques	Conséquences essentielles
<ul style="list-style-type: none"> * Augmentation modérée de la portance et du moment cabreur de la voilure * Augmentation de la finesse * Diminution importante de la déflexion (CZ_h augmente) 	<ul style="list-style-type: none"> Réduction de u_{AC} et augmentation à cabrer du braquage de la profondeur

Effet de sol - paliers stabilisés

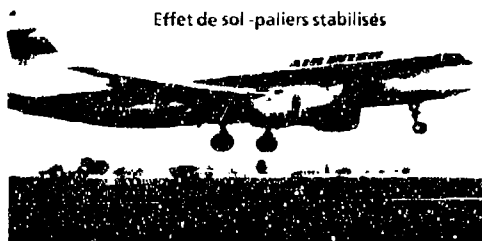


Fig. 11 - A 320 en présence du sol.

Centrale anémométrique ADC II et plate-forme à inertie IRS II

ADIRS

(f p)

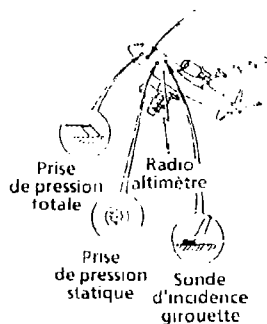


Fig. 12 - Evolution des paramètres avion lors d'un atterrissage.



Fig. 13 - Les besoins

Trains sortis	Configuration		Hauteur Z_1 (feet)	Vitesses stabilisées
	Becs	Volets		
18	10		~ 6 valeurs $10 \leq Z_1 \leq 130$	~ 1,2 V_{sig} et VFE
22	20			
27	35			

A 320 - Programme d'essais en vol en effet de sol

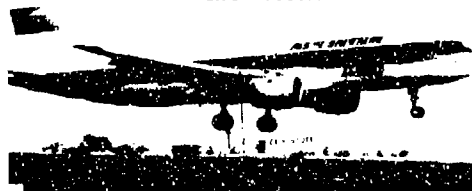


Fig. 14 - Programme d'essais en vol.

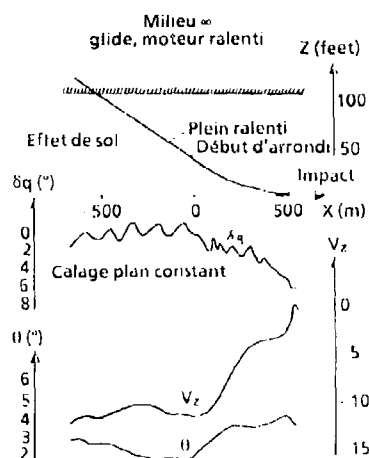


Fig. 15 - Mesure des conditions ambiantes et des repères avions.

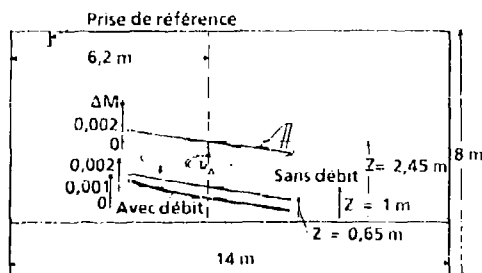


Fig. 16 - Détermination de l'effet de sol sur l'anémométrie - en vol

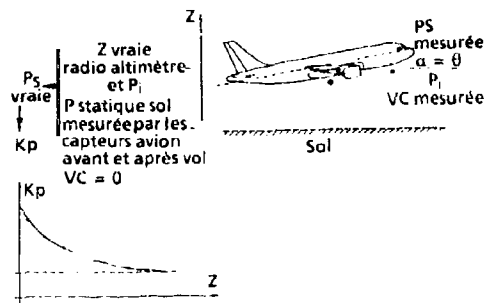


Fig. 17 - Détermination de l'effet de sol sur la cinométrie - en vol.

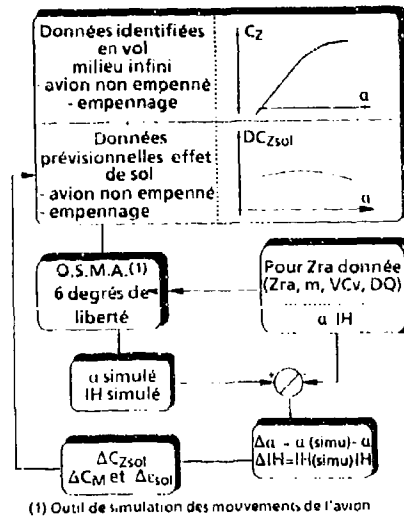


Fig. 18 - Méthode de la détermination de l'effet de sol sur les coefficients aérodynamiques - en vol

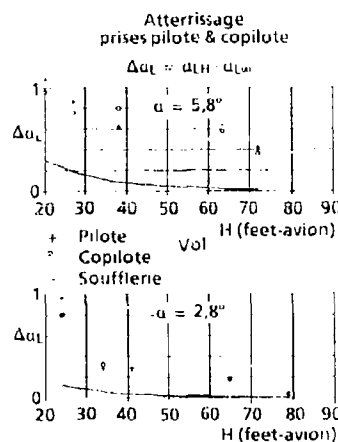


Fig. 19 - Comparaison des mesures en vol aux prévisions d'après soufflerie. Anémométrie : décollage.

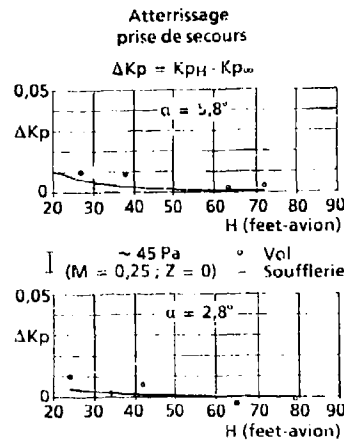


Fig. 20 - Comparaison des mesures en vol aux prévisions d'après soufflerie. Anémométrie : décollage.

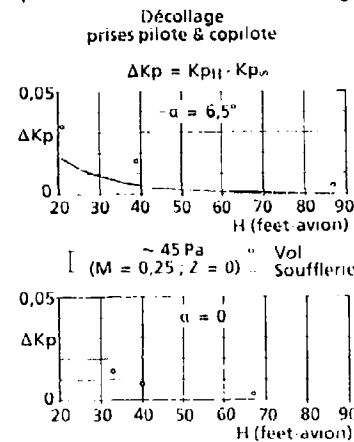


Fig. 21 - Comparaison des mesures en vol aux prévisions d'après soufflerie. Anémométrie : atterrissage.

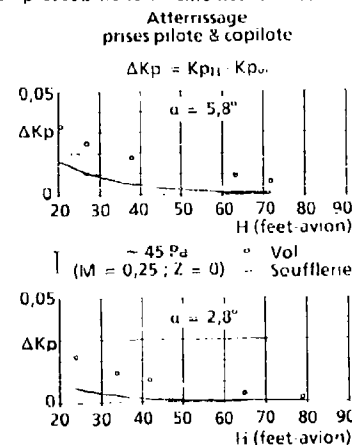


Fig. 22 - Comparaison des mesures en vol aux prévisions d'après soufflerie. Anémométrie : atterrissage.

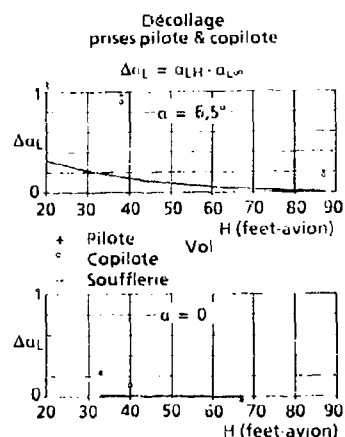


Fig. 23 - Comparaison des mesures en vol aux prévisions d'après soufflerie. Clinométrie : décollage.

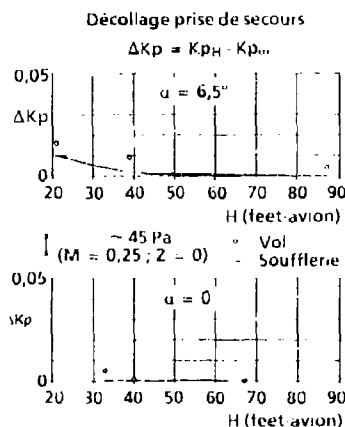


Fig. 24 - Comparaison des mesures en vol aux prévisions d'après soufflerie. Clinométrie : décollage.

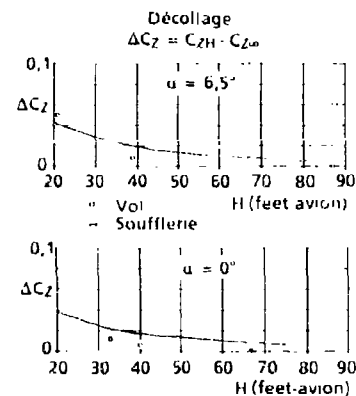


Fig. 25 - Comparaison des mesures en vol aux prévisions d'après soufflerie. Portance de l'avion sans empennage : décollage.

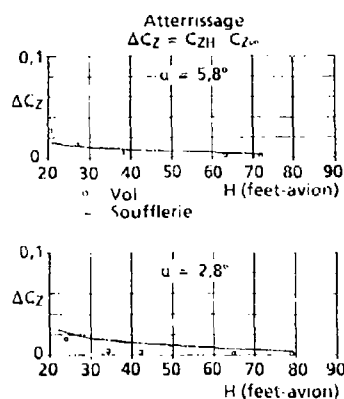


Fig. 26 - Comparaison des mesures en vol aux prévisions d'après soufflerie. Portance de l'avion sans empennage : atterrissage.

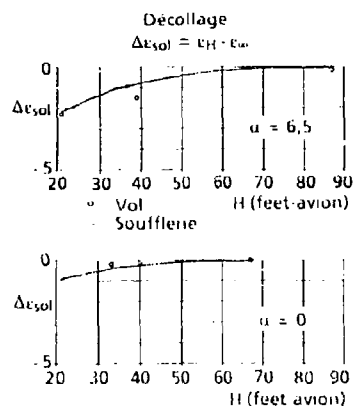


Fig. 27 - Comparaison des mesures en vol aux prévisions d'après soufflerie. Déflexion moyenne au droit de l'empennage : décollage.

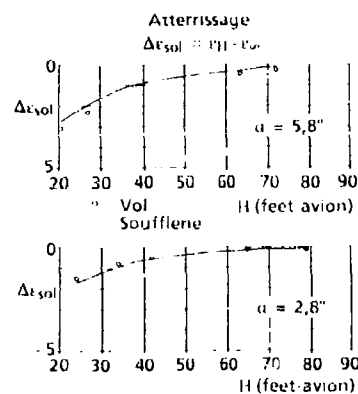


Fig. 28 - Comparaison des mesures en vol aux prévisions d'après soufflerie. Déflexion moyenne au droit de l'empennage : atterrissage.

ROUND TABLE DISCUSSION

Mr. D. Peckham (Chairman)

I would now like to re-introduce our Technical Evaluator, Dr. G. Keith Richey, who is Technical Director of the Wright Research and Development Center at Wright Patterson Air Force Base, Ohio in the USA. He was educated at the University of Michigan where he obtained his Ph.D. He has been with the US Air Force for 28 years, 26 years of this being associated with the Flight Dynamics Lab and 8 years of that time as Chief Scientist. For the last two years he has been the Technical Director of the Wright Research and Development Center. He is a past Panel member and was a member of the Fluid Dynamics Panel for 10 years from 1976 to 1986, and we are very pleased to see him back again as our Technical Evaluator.

Dr. K. Richey, USAF

Thank you Mr. Chairman. It is good to be back associated with AGARD and it is good to see that it is still in good hands. This was an excellent meeting with high quality presentations on a subject of keen interest to AGARD and to NATO. As you note from your program, the distribution of papers by country - if one counts paper Nr. 12 by Roberts and Wood as "half US and half UK" - is: US 8.5, UK 7.5, Germany 3, France 3, and Italy 1, for a total of 23. A good distribution, although wider participation by other AGARD member nations should be encouraged.

The aerodynamics of combat aircraft controls was covered in papers 1 through 17. I will not discuss them in order because you have all been very attentive. The papers and discussion made it clear that new requirements are emerging for combat aircraft for offensive and defensive manoeuvres. For example, automated missile avoidance could be considered for a defensive manoeuvre. The new requirements for the aircraft include high angles of attack and yaw, which I will refer to as alpha and beta, and a greatly expanded flight envelope, with high acceleration rates in all axes of flight, which is very important. A comment made from the audience after paper Nr. 4, that I think needs reinforcing, is that high alpha manoeuvres will be limited in their effectiveness if the aircraft cannot launch missiles at these conditions. This is an area that needs much more research.

Because of very high manoeuvring rates and accelerations, dynamic stability is much more important than ever before. So we need to fully understand the dynamics of controls including all the cross-coupling effects. In fact, the basic concept of stability derivatives may come into question in some very rapid non-linear manoeuvres. These trends dictate some new combat aircraft control requirements which were brought out in the meeting, particularly in papers 2 and 4. An expanded envelope of the aircraft will dictate an expanded controls envelope, requiring a search for favorable interference of control surfaces and wings in manoeuvres; rapid roll manoeuvres around the velocity vector will be used in order to rapidly change the plane of attack of the combat aircraft. It will become more important to account for aeroelastic effects in rapid manoeuvres at high dynamic pressure. It was pointed out that controls are now 10 to 15% of the empty weight, so there is already a need for light-weight controls.

A strong need, particularly at high angle of attack, is for flight-propulsion control integration, in fact multi-axis thrust-vectoring. The engine and the force it produces, in both direction and magnitude, is becoming a major control force and moment producer. Where aerodynamic forces are soft, particularly at short take-off or vertical landing conditions, then there is also a need for flight-propulsion control integration. During rapid manoeuvring, many of the aerodynamic control surfaces are undergoing time-dependent separation which can induce non-linearities in the aerodynamics of the aircraft and its control system. Again there is a need for dynamic control. It was pointed out that there was often times difficulty in obtaining both dynamic stability and favorable damping, while still maintaining a high level of agility. Active control of forebody, wing, and canard vortices seems to hold the key. Some authors proposed new dynamic stability criteria to improve on our old favorite CN_B -dynamic, but this will require a much more robust body of information on cross-coupling effects, requiring data on rotary balances and special forced oscillation balances such as those under development in Canada. Dr. Hanff of the NAE (Canada) showed you one example.

Another requirement for controls, going along with increased manoeuvrability/agility in the aircraft, is the strong requirement for nose down pitching moment control at high angle of attack. Nose-down pitch control is needed to arrest a nose-up manoeuvre, to quickly unload to reduced G's (to be able to accelerate), and to control pitch-due-to-rolling about the velocity vector at high angle of attack. It is impossible to keep the nose pointed precisely unless there is adequate nose-down pitch control. Most configurations have much more nose-up pitching moment capability than nose down authority.

Finally, a big driver in controls for agile aircraft is lateral-directional control at high angle of attack and high alpha rates. This was brought out by several authors. Providing the desired manoeuvres, i.e., to initiate the manoeuvres that we want and to stop the manoeuvres that we don't want, is often difficult because the tail, especially the vertical fin, has decreased effectiveness at high angle of attack; this situation may therefore require a strong propulsion-flight control coupling with multi-axis thrust vectoring. Lateral directional control at these extreme conditions will require innovative concepts, and several were discussed. One that wasn't discussed is a fin below the fuselage which could be deployed at high angle of attack to improve lateral-directional control. This is not a new idea.

How are we going to address all these problems of controls associated with very dynamic (unsteady) and extremely complex flow fields? There are some bright spots that we saw in this Conference. Our fundamental understanding of the phenomenon is improving. As shown, for example, by paper 14. Innovative approaches were shown by several authors, including deployable strakes on the forebody, tiperons and tip rudders, nose-blowing of air through ports or slots, and leading edge slot-blowing to control roll at high angles of attack. The static performance of these devices looks promising but we need more dynamic data, especially at higher Reynolds number to determine if these can actually be used as control devices. Just producing a force doesn't make a good control; the force has to have the right rate time response and must be able to be designed into an overall control system.

Another bright spot, as shown by the papers presented, is that dynamic stability test methods are improving. This is the subject of an AGARD FDP working group, which members of the audience should follow

its progress. It is noteworthy that hardly any computational or theoretical solutions of aerodynamic flows were presented at the meeting. One exception was in paper 16. I'll make the prediction, being bold, that we should be able to compute three-dimensional unsteady flows within 5 years. Using the large computers coming on, I think it is possible.

Another bright spot is that there are some major programs which are addressing the new requirements for control at high angle of attack and high alpha-beta rates. The F-15 STOL (short take off and landing)/Maneuver Technology Demonstrator program reviewed in paper 1 is a good example of propulsion-flight control coupling, although not currently evaluating the high angle of attack or high rate maneuvers. The two-dimensional nozzle being evaluated on the F-15 aircraft was first evaluated in research over 15 years ago by the Air Force and NASA. This shows the need to do research well before requirements are identified. On the STOL F-15, interactions between the canards and thrust vectoring, thrust reverse, etc produce non-linearities which can be verified through flight test. The F-15 is also a good test bed to verify thrust reverser effects on aerodynamics and controls as discussed in papers 17, 19 and 21, both up-and-away, and during landing. So we will be able to get some full-scale flight data on these effects.

The second major program that was reviewed was the NASA F-18 High Alpha Research Vehicle, or HARV. It is a good program to study high angle of attack with high rates of maneuverability, but in its present configuration is not evaluating propulsion-flight control coupling. This will come in a later phase. HARV will evaluate important aerodynamic parameters, both static and dynamic, to compare with windtunnel results and computational fluid dynamics calculations.

Another project, which was not reviewed at the meeting, is the US/German project on the X-31 experimental aircraft to evaluate high angle of attack maneuverability using thrust vectoring. This is a very important program because it combines the issue of high angle of attack at high rates of maneuverability with propulsion and control integration, not including thrust reversing, through a fairly simple implementation of thrust vectoring. These three projects, (F-15, F-18, X-31) will greatly increase our understanding of the aerodynamics of controls and propulsion integration for combat aircraft.

The second theme of this Conference was ground effects on combat aircraft. This is always important, but much more so when thrust vectoring and reverse is used on landing approach or for short take off. Landing and take-offs are always the most critical parts of flight. We are used to the thrust reverser being deployed after an airplane is at zero angle of attack on the runway, everything is settled down, and it is generally well understood. Combat aircraft will likely deploy their thrust reverser on approach, so the landing dynamics will have to include the effect of the thrust reverser.

Understanding complex ground effects, dynamic as well as static will be crucial to safe, routine operations of military and commercial aircraft that are attempting to operate under adverse conditions due to weather or under low speed conditions, such as a short take-off and landing or even vertical landing, where control surfaces are not very effective. Several interesting techniques for dynamic ground effects determination were shown particularly in papers 20 through 24. As stated earlier, the F-15 STOL and Maneuver Demonstrator represents a unique opportunity to better understand ground effects when thrust reverse and vectoring is used in landing approach.

In summary, the aerodynamics of combat aircraft controls and of ground effects was given a thorough treatment at this Conference. These are tough problems, but we are addressing them because we believe that stretching the combat maneuver envelope will enhance offensive and defensive combat capability. Will the Russians challenge us to an "agility duel"? Perhaps they have already at the 1989 Paris air show. By combining ideas and talents throughout NATO, by means of AGARD, we can collectively develop a superior technology base for combat aircraft of the future. This meeting is a step in the right direction. Let all AGARD participants bring forth their best ideas. Thank you.

Mr. D. Peckham

Thank you very much Dr. Richey for your stimulating remarks. Perhaps you would join us here as we now turn to the Round Table Discussion section. I would like to remind you that this session is being recorded and will appear in the proceedings of this Symposium. It is very important that everybody offering a comment or asking a question gives their name and affiliation. Otherwise there will be a gap in the proceedings. The floor is now open for questions or comments, either to the session chairmen or perhaps back to individual authors. I think I prefer to see discussion on the more general aspects as so ably outlined by Dr. Richey. Over to you, the audience.

Dr. W. Gildert, NASA Langley

I would like to amplify one of Dr. Richey's comments with regard to NASA's plans in the high angle attack technology program. We are committed to fly thrust vectoring and look at the integration of aerodynamic and propulsive controls. That will happen in the spring. We are moving into the area that he indicated is important, that of unsteady aerodynamic prediction. That is one of the major aspects of the program is to try to press for the improvement of the computational prediction methods for separated flows.

Dr. D. Woodward, RAE

I was very impressed and interested by the work that was being done on the deployment of thrust reversal on approach and therefore of the problem of the effects of thrust reversers in ground effect. What puzzles me a little is why, having all this background, that proposed vertical landing airplanes seem to be confined to a landing maneuver which involves coming to the hover out of ground effect and then landing vertically. I would have thought that a moving approach to a landing for a nominal vertical landing airplane would have solved a number of the problems, such as hot gas reinjection, etc. Has anybody got any comments to make on the way those two things might fit together?

Dr. K. Richey, USAF

I am familiar with the US/UK joint program on advanced short take-off/vertical landing technology. I think that your comment is valid. A "roll-on" vertical landing or a rolling short take-off, say with 30 to 50 feet per second forward velocity, can make a tremendous difference in ground effects, and in hot gas reinjection, so it is certainly worth considering.

Dr. G. Wedekind, Dornier

Concerning the argument that you can replace the short landing by vertical landing, I would say that the increase in weight due to devices you need for the vertical landing is so high that it will not pay off for fighter aircraft to carry this additional weight. I think that a better solution is to accept a short landing distance and spare a lot of weight in the aircraft.

Dr. K. Richey, USAF

Dr. Wedekind's comment is well taken, and except that if there was a requirement, he is quite right that there is an increment in weight and cost and complexity for the vertical landing, however some who have operated the Harrier aircraft, for example, the UK Royal Air Force and, the US Marine Corps, feel that the operational flexibility of being able to land and take off vertically is well worth some additional weight. With technology advancements, particularly in materials and high thrust-to-weight engines, the difference in weight to provide a vertical landing capability diminishes. I don't think that you would ever try to design an airplane that would take off vertically with fuel and payload to accomplish the mission; it would be far too heavy. But vertical landing, by itself, may not add too much weight for a combat aircraft that already has a large engine for combat maneuvering.

Mr. Dutcher, British Aerospace

I would like to reflect again on one of the comments that Dr. Richey made that full military utility of all these novel control schemes need to bear in mind the fact that weapons need to be fired, and also that we have radar scanners which need to slew across to keep the target in view and a number of avionic sensors. Indeed the cockpit arrangements need to be borne in mind, so that a pilot taking advantage of all the new aerodynamic capability that is foreseeable from the discussion in this Conference is actually able to operate his airplane in an operational sense. The point I am getting at is that we in the aerodynamic community, I think, have a responsibility to take along our colleagues in the weapon systems and avionics areas to make sure that they are aware of the potential capability that the aircraft is going to give them so that we don't end up with airplanes which are wonderful to fly for the pilot, but because of the low performance of the avionics system cannot actually perform their operational tasks effectively in the expanded envelope we have opened up.

Klaus Obel, IADG Germany

I would like to extend that. I think that it is not well understood where the operational value of the high angle of attack maneuvers in a conflict situation really are. I see the great value at the moment in the extent or in the improvement in terms of safety of the airplane, but not so much at the moment in the operational value. I think we need a lot of simulations where the entire weapon system is simulated including avionics, including weapons, including threat, including environment in terms of electronic disturbance so that we can really evaluate the aircraft as a weapon system for such capability. I think that there is a great need for it. Andy Skow touched that subject very briefly. We have done some research in our company in this respect, and we have I would think very questionable thoughts of the value.

R. Bradley, General Dynamics

Along the line that has just been mentioned, high alpha characteristics are extremely important, whether the post stall pointing has any operational value or not. One issue that was not raised at this Symposium that is very important is the ability to operate safely with asymmetric weapons loadings. Large asymmetries aggravate the high angle of attack characteristics, can cause departure, and can lead to great difficulties in recovery. From that standpoint these high alpha advances are extremely important.

Mr. B. Bufacchi, Aermacchi

Moving on from that in both the high and low alpha regimes, it seems that we place a strong emphasis on being able to harness the aerodynamics through control laws. Control laws seem fundamental to the aircraft. It is tempting to say that an aircraft is only as good as the control law design which went into it. Does the Panel agree with this assessment and do they think that this approach could pose any problems particularly in combat when you could only be left with the aerodynamics following control law failure?

Dr. K. Orlik-Ruckemann, NAE

I would like to highlight some cases of important dynamic effects, especially in connection with control considerations. One is that we have heard at this Symposium several concepts mentioned as to how to improve the combat aircraft's maneuverability through various control devices. We have heard about thrust vectoring, about moveable strakes and LEX's, about manipulation of leading-edge and forebody vortices, and about spoilers which could be very rapidly deployed.

The point that I would like to make is that all those methods have quite different applications and also different limitations. Therefore, not any single one of them, I think, will likely be sufficient. We must have a combination of these tools in our arsenal, and we should continue examining and investigating all those methods. It is not possible at the present time to say which one of them will be the winner, and most likely for different situations different methods will be required.

The second comment concerns Dr. Richey's remark about the changing role of stability derivatives. I could not agree more with Dr. Richey. It is quite clear and is further reinforced by the data we already have at NAE, that at high angles of attack, and especially if we combine high angles of attack with higher angular rates, moderate angles of side slip or larger amplitudes of motion, a situation will be reached where the whole stability and control domain will become very much non-linear and, therefore, no longer

describable by the relatively simple linear concept of stability derivatives. The effects will no longer be superimposable. You will have to devise completely non-linear methods both to represent the aerodynamics involved and to use the aerodynamic data for flight behavior prediction. This leads to my final comment which is that the magnitude and the importance of those effects on the final performance of the aircraft, I think, will be large enough to require that this kind of consideration be included at a much earlier phase in the aircraft design cycle than ever before. As you all know, in the past the design was practically frozen by the time somebody would come around and decide that one should check whether there are any dynamic problems that need fixing. Then, as an afterthought, some of the dynamic parameters would be determined and an analysis carried out. Usually, in the past, there were no problems so such an approach was justified. I think that in the future we have to include this kind of investigation at a much earlier stage because it will have much larger consequences.

Mr. T. Saunders, British Aerospace

I wonder if I could just combine the last two contributions there because I think there is quite an important conflict to be pointed out here. It is absolutely true that configurations that are being looked at are very non-linear and the dynamic effects of those non-linearities are significant. You can't represent them accurately by means of stability derivatives. We are already in the stage where we are producing large data bases of non-linear characteristics. Similarly, the FCS is important and is leading to an aircraft FCS pilot system of a very high order. Also, that means that you need powerful multi-variate optimization techniques to be able to design the FCS effectively. Those techniques are becoming available, but they are not becoming available in such a way that they can absorb also the degrees of non-linearity for very high orders that are being looked at and so there is a problem here. It is quite right that it is becoming increasingly ineffective to start off the design process with a simple linear model because it is just too far from what is eventually going to emerge. There is a need here for quite a major thrust in technology in developing multi-variate optimization techniques for the design of control systems which can deal with realistic aircraft descriptions.

Mr. D. Moorhouse, US Air Force

I would also go back to the comment on flight control system design. It used to be that aircraft were designed, optimized aerodynamically for performance, with the assumption that the flight control system designer can take care of things later. We currently measure aircraft agility in terms of deficiencies, and we compare deficiencies in capability. I think as I speak as a flight control system designer, the challenge to the aerodynamicist is to give me the control power to use, and then I can certainly design an aircraft that is controllable. We currently see aircraft that are incapable of rolling because the power to coordinate that roll from either pitch or yaw control just disappears. So as a flight control designer, the first step is for the aerodynamicist to provide me a control power to work with. I would also like to comment to Mr. Saunders that the nonlinearities that are a problem in multi-variable control are also the same problems as for the classical control system designers who all work with linear techniques as well.

Dr. G. Wedekind, Dornier

I, too, think that the design or the development of a new aircraft nowadays has to go the other way around. The flight control people should give the aerodynamicist the limits they can just tolerate. For example, when I install this or that instability or this or that non-linearity, I need from them the control power needed or the information that there is a limit where nothing can be handled any more. I think these are the first design rules we have to collect to be able to develop a new design. That is the situation today.

Dr. R. Bradley, General Dynamics

You have raised an interesting issue as to who should be first in the design process. Classically, aircraft design, as you well know, is a series of compromises, and all we have done here is add a few additional dimensions to the compromises involved. In that sense, demanding control power is not necessarily the answer because the solution will probably penalize your performance excessively. I have to agree that early testing in the dynamic sense is extremely important. I know in many cases, rather simple aircraft configuration features such as strake modifications may have very important performance results, but can lead to extreme dynamic problems in the damping modes. The point I'd like to make is that we just have a broader field of compromise that requires a lot earlier investigation of configurations from the dynamic sense.

Mr. D. Lovell, RAE

I would like to develop what has just been said. Drawing an analogy with flight control systems we need to think of graceful degradation of aerodynamic control systems. We have heard at this Conference of several novel aerodynamic systems. I think that we need to consider now graceful degradation of the aerodynamics, because if some of these devices go wrong we will have a much worse configuration to cope with than the basic shape. To put it operationally, we have to consider the envelope we wish to be able to fly in when our chosen aerodynamic configuration fails; thrust reversers that jam in flight, strakes on the nose which go out too far and stay there, a lot of potential problems I think.

Mr. D. Peckham

We have been talking largely about the control aspects, there are not many comments or questions on the ground effect side. Perhaps we can turn to that aspect at our meeting.

Mr. Mathieu, STPA

From the landing point of view and the ground effect point of view, do we have a sufficient prediction taking account of cross-winds for instance, which might make it possible for the pilot to anticipate this effect when the aircraft is going to land on the aircraft carrier?

Mr. J. Leynaert, ONERA

The test in ground effect can be done with yaw, but, concerning the unsteady effects, we have not studied this problem in the windtunnel of ONERA. That would be possible in the Institut de Mécanique des Fluides de Lille, because there we have the possibility of reproducing a side wind on the runway with a free flight model. This might be a partial possibility of solving your problem.

Mr. Verbrugge from this Institute might perhaps add something to this answer. I don't know whether he is here.

Dr. K. Richey, USAF

Most of the papers presented at this Conference indicated that it is very much an experimental situation. I think Mr. Mathieu's question is, "could ground effects be predicted or computed?". I think that this is a very difficult problem. Probably we will be dependent on test techniques for quite a while in that regard.

Mr. Mathieu, STPA

Yes, but let me add to this that if we didn't take account of the side wind effect from a longitudinal point of view would it be possible to anticipate on the piloting laws?

Mr. J. Leynaert, ONERA

I think that the last but one presentation indicated one tool, one possibility of obtaining indications in terms of piloting laws. I don't know to what extent they are accurate enough.

Mr. R. Bradley, General Dynamics

As far as piloting laws, in order to develop them you must be able to know the flow field. So we have a chicken and egg situation here as to which comes first.

Mr. D. Moorhouse, US Air Force

I was going to say the same thing. At the risk of being simplistic, on the STOL F-15, the ground effects became a control law design problem. The accuracy of the measurement was the only thing that drove the control law design and making them robust enough to where we removed the really severe effects so that what remained was controllable to the pilot.

Dr. D. Woodward, RAE

I was not aware before I came here of the large changes in ground effect that come from representing the vertical velocity towards the ground. This seems to have been well documented in Mr. Curry's paper - there were about 5 or 6 references which are much earlier than this Symposium. Is it now a firm conclusion that ground effect testing in a windtunnel at fixed height, the conventional ground effect testing, is of very little use? Do we need to do dynamic ground testing in windtunnels from now on to be of any use to the designer?

Dr. W. Gilbert, NASA Langley

I think that it is a function of configuration. One of the things that we found in our tests was that the impact of sink rate as I mentioned in my presentation is very much a function of the flow field that you are creating underneath the wing of the configuration. In the more conventional configurations, the dynamic effects are relatively modest as you come into ground effect with sink rate, but as you begin to introduce added flow fields or plumes the effect progressively grows. I think that it is safe to say that if you are going to talk about a vehicle that has deflected thrust in any significant amount where you are going to get interaction of the plume with the ground, yes, you probably need to model sink rate in your ground effects testing. For other configurations I guess I haven't seen enough test results to conclude that you would absolutely have to have sink rate effects, where you do not have very high lift or high deflection of the wake close to the ground. I guess the bottom line is if you are using deflected thrust, particularly if you are using reversers, you definitely want to model sink rate. In the more conventional cases, you can probably still get results that are useful without necessarily modelling sink rate.

Dr. K. Richey, USAF

I would agree with that assessment. If I recall from the data you were showing at the higher sink rates, without thrust vectoring there is not much difference. Is that right, Bill?

Dr. W. Gilbert, NASA Langley

One of the things that we are in the process of doing at Langley right now is that we are building a system to go in the 14 x 22 foot tunnel. This will allow us to very systematically run through sink rates, including flare and pitch rate. We want to do it in a systematic fashion where we look at a range of planforms with and without the effects of deflected thrust. That is something that will happen over the next several years. Right now we are not satisfied with the data base and the parameter variation that we have. For example, in the vortex facility we were not able to independently vary parameter because of the ground board system we use. When we varied our approach speed to the deflected plane, basically you varied your sink rate. You couldn't independently vary the test conditions that you wanted to look at.

I think in the next several years as we do some testing with a better apparatus we will get a lot better picture of what the guides ought to be in doing dynamic ground effects testing.

Dr. D. Woodward, RAE

Can I just come back for a moment then, because I think that is a very significant conclusion in relation to people who have to operate windtunnels. For some years we have dabbled with the idea that one of the important things that we ought to provide if we were going to take ground effect testing seriously was a moving ground plane. Now some of the data suggests that in fact the sink rate is vastly more important than the moving ground plane. If this were a general conclusion, this would indicate a fairly significant change in direction in the equipment being provided in windtunnels.

RTD-6

Dr. W. Gilbert, NASA Langley

I guess I would add a caution. The moving ground plane is still important when it comes to significant forward deflection of the thrust because of removal of the boundary layer. Even though in my presentation it shows being of less importance, it is still very important to remove the boundary layer.

Dr. D. Woodward, RAE

So you want both?

Dr. W. Gilbert, NASA Langley

Absolutely!

Mr. J. Leynaert, ONERA

I would like to add one remark. In the last presentation, you have seen that in the wind tunnel, we had a sort of mast so as to vary the altitude of the model. This system was defined to study the dynamic effects. It allows to apply a very sudden descent, for instance, so that you can measure also the dynamic effects. However, if you use a highly sensitive balance, the balance cannot withstand the inertial forces given by the model. Therefore, we should need a very light model or a stiffer balance. So there is a whole range of experimental problems that are very difficult to solve because the inertial forces are important, and it is very difficult to get rid of them with simple and accurate means. Apart from that the system has been defined so as to carry out the test precisely. It might very well be that one day we can solve the whole problem.

Mr. R. Curry, NASA Dryden

I would say that in the references that I did cite, there was some comment made that the distinction between dynamic and steady state ground effect is most pronounced for configurations which have a substantial amount of vortex lift. In both the more highly swept delta wing planforms and the X29 test in the landing configuration, we suspect there was a substantial level of vortex lift. I would agree with the other comments however, that the data base for side by side comparisons of dynamic and steady state data in control testing is very limited. I don't think that you can make a strong conclusion about this, but that is at least one proposed explanation for the varying sensitivity to dynamics in the ground effect testing.

Dr. K. Orlik-Ruckemann, NAE

I wonder whether I could go back to the control aspect? I have one or two additional points that I think should be mentioned. Someone mentioned the effect of asymmetric weapons distribution. This of course brings up the question of the importance of aerodynamic cross-coupling effects. This is something that I have been promoting for some time. One of the very good examples is in fact asymmetric weapon distribution. Once you have fired something on one side, you have an asymmetric configuration, which even at lower angles of attack will produce asymmetric aerodynamic effects. These have always been difficult to measure and more or less neglected, but some of the devices that we now have developed in Canada permit us to determine both static and dynamic cross-coupling effects, which should perhaps be kept in mind.

Another thing is the question which I think has somehow been slightly removed from being one of the urgent ones, but at one time we were all quite interested and excited by the prospects of being able to induce not only angular motions, but also translational motions to the aircraft. Somehow I haven't heard much about this in the last few years. I wonder if somebody could enlighten me whether this approach has become impractical and, if so, why? It seems that an independent possibility of controlling the aircraft in angular and translational degrees of freedom would go a long way towards, for instance, pointing the aircraft without changing the flight path. Finally, when I talked before about the importance of non-linear presentations, I should have included not only the need to consider the data in a non-linear fashion, which means that you no longer can superimpose them, but also the need to look at the various motions individually. One can no longer determine aerodynamic reactions to a certain motion and then superimpose them on reactions obtained for a different motion. One must examine the full complex motion and determine reactions to that. In an experimental environment, such as in a windtunnel, this is a relatively difficult problem. Nevertheless, the fact that it is difficult does not relieve us from the responsibility of having to deal with such a problem. Ultimately, however, this kind of study will probably have to be done more through flight testing or with free-flying models than in a windtunnel. There are exceptions, however, for instance at the Institut des Mécaniques de Lille there are possibilities of combining a coning motion with a superimposed oscillatory motion in pitch or yaw. We need more techniques which could produce arbitrary complex motions.

Mr. D. Peckham

Thank you for those comments Dr. Orlik-Ruckemann. In the middle you had a question about translational motions. I presume you mean the heave motion. Does anyone in the audience wish to comment on that?

Dr. R. Bradley, General Dynamics

As most of you know we have flown the AFTI program for a number of years now, which has produced a great deal of flight information on direct force control, direct translational motions, and so forth. These results have been published rather widely. You say you haven't heard much recently? Basically anything that goes on an aircraft has to earn its way in terms of payoff in use, and there are certainly some modes which have been shown to be useful for specific tasks. In many cases, however, those direct force modes do not really show great benefit in the field when evaluated by operational pilots, for example. Perhaps the reason you haven't heard much lately is that, although we have learned a great deal on different control modes, not too many of them were combined with such things as direct side force or nose pointing. There is quite a wealth of literature on this subject that is in the open and certainly can be researched.

Dr. K. Orlik-Rückemann, NAE

This is what I wanted to find out. I know about this work, but as I said, I didn't hear about any applications of these concepts, and you have answered that they are not too practical for various reasons. This means as far as I am concerned, that when we develop various experimental devices, we will probably de-emphasize to some degree the interest in constructing balances for translational oscillation in the vertical or lateral plane.

Dr. R. Bradley, General Dynamics

I might add that I didn't say they were not useful, I said they haven't earned their way on an operational aircraft yet. We have learned a great deal. We have learned a lot in the control law area and on how to use the more conventional control forces. Some of these are being integrated, incidentally, into the F-16 by the Air Force. However, the major direct force control modes have not yet earned their way on an aircraft.

Dr. W. Gilbert, NASA Langley

Dr. Orlik-Rückemann, the other reasons you may want to have those capabilities is to de-couple the classic forced oscillation measurements. Even though we not need the translational measurements for some of the applications that Dick Bradley talked about, many people still have interest in being able to break down the highly coupled derivatives that you get when you do the classic body axis forced oscillation dynamic testing, so I think that there is an interest from that standpoint.

Dr. K. Richey, USAF

I am generally familiar with the scope of the AGARD Working Group on Dynamic Balances. I think that we might look to them to solve these problems.

Dr. K. Orlik-Rückemann, NAE

Since I have been responsible for that particular Working Group, let me say that there is indeed a lot about mathematical modelling and the importance of various dynamic parameters in the Working Group report, which we hope will be available for distribution sometime next spring.

I would like to comment on Mr. Gilbert's comment. Indeed this is a very important consideration, and I fully agree that the translational oscillation experiments do produce an independent means of separating the so-called purely rotary effect from that due to translational acceleration effect which is usually called beta dot or alpha dot effect, depending on the degree of freedom. At high angles of attack it is very important, as shown by people at NASA Langley, to separate those two effects and put the proper derivatives at the proper places in the equations of motion. Thank you, Dr. Gilbert, for that remark.

Dr. K. Richey, USAF

I would like to go back to an earlier comment that was made about military utility of high rates of manoeuvrability and high angles of attack. Although I would tend to agree that the military utility of high angle of attack and high rates is yet to be fully explored, I think we have to explore the flight regime and then see what kind of combat tactics and military utility may result. You can't start with the assumption that it won't work. When you give pilots new degrees of freedom, they may figure out some very innovative ways to use that. We also need to keep in mind that when we are talking about those high rates and high angles of attack that we are not necessarily talking about low speed. We may be talking about transonic conditions, at least, and maybe even supersonic flight at high altitude. Let's not be drawn into the argument that it is only a low speed phenomenon.

Dr. W. Gilbert, NASA Langley

I would like to add an amplification of that. The other thing that we have noticed as you examine current aircraft, a lot of performance is lost long before maximum lift on current aircraft in terms of the ability to manoeuvre precisely both in pitch and laterally. A lot of the work that has gone on, not just the work that we have done, others have done in trying to find solutions to the separated flow problems will result in some rather impressive gains in manoeuvre capabilities prior to maximum lift and in the region of maximum lift. We have seen, for example, in comparisons with some current aircraft that you can expect with some fairly reasonable concepts to double roll performance, for example, in the region around maximum lift for current aircraft which is a region that, in air combat tactics today pilots fly in, how it is flying, and it doesn't involve going to the deep stall regime, it involves going into the regime approaching maximum lift where they fly frequently. So there are a lot of payoffs down to the edge of the sustained envelope and between there and maximum lift. I think that there is a lot to be gathered from it, and I agree with Dr. Richey's comment that explorations in this area will open some doors that we'll only understand the payoff as pilots begin to explore the tactics and work with the results.

Mr. Sjardij, Aeritalia

I have a question for Dr. Richey. Needless to say, I just followed closely the Symposium with the eyes of an unmanned systems engineer. Therefore, I ask him, "are there any future requirements in the field of unmanned aircraft systems" (as far as "agility" is concerned)?

Dr. Richey, USAF

My personal point of view is 'Yes'. I think that we are just beginning to understand the utility of unmanned vehicles. Several nations are exploring these types of vehicles for a wide variety of applications. I think that in the years ahead the controls community will have to pay a lot more attention to unmanned air vehicles because they will probably be able to operate certainly at higher g's and certainly more radical manoeuvres in some cases than manned aircraft. Also there may be a payoff for greatly reducing the control surface size to reduce signature. If the control surface is smaller, it will have to be more effective. I think that it is certainly fruitful to consider control characteristics of unmanned as well as manned aircraft.

Dr. J. Campbell, NASA Langley

Thus far, we have not discussed the crucial problem of extrapolating sub-scale wind-tunnel results to flight scales, which I will mention briefly. Scaling combat aircraft controls is very complicated because the control surfaces must function in separated flow fields that vary as the aircraft maneuvers. The airplane can have attached flow at cruise, mixtures of attached, separated, or vortical flows at moderate maneuvers, and fully separated flows at high alphas; these can be effected at high speeds by shock-induced separations, and vortex-shock interactions. As you see, this is a complex problem to scale with Reynolds number and Mach number.

Over the years, we have developed the capability of scaling attached 2-D boundary-layers from tunnel to flight for transport-type wings. Currently, there is no way to scale combat aircraft separated flows to flight, especially 3-D boundary layers and separations. When the fighter alpha increases, the boundary layer can become so strongly 3-D that it reaches a point where it goes out the span of wing without crossing the trailing edge. In addition, the boundary layer can separate at different locations such as at the wing leading-edges, at the leading-edge and trailing-edge flap hinge-lines, and around the forebody.

All of this may be affected by Reynolds number and compressibility, depending on the specific geometries involved, and represents a challenging technology area that requires more study. We are beginning to see some capabilities at Langley to help address this complicated problem. First, CFD codes are maturing that can calculate the full viscous, compressible flow around a complete airplane configuration; and second, the National Transonic Facility is unique in that it can obtain the effects of Reynolds number and Mach number to full-scale flow conditions. I believe that scaling of separated flows on combat aircraft is a major technology area to investigate.

Mr. Elsenaar, NLR

I wouldn't deny that scaling is a problem for these types of flow, but it might not be as bad as you point out here. Flows over bodies with sharp edges are Reynolds number independent, so from that point of view you do not have such a large problem. I agree we still have to find out for what conditions scalings laws are very important and for what conditions these scale effects can be neglected. I doubt if it is a severe problem for the whole area.

Dr. J. Campbell, NASA Langley

I will give one example. The Fairley Delta airplane had a 60° delta wing with a round leading-edge and was used in a tunnel-to-flight correlation which is the best that I have seen on leading-edge separation-induced vortex flows. In flight, the wing had attached flow on the inboard portion and a separated vortex flow about half way out at moderate angles of attack and at subsonic and transonic speeds. For the same alphas, the wind-tunnel would develop the leading-edge vortex all the way up the leading edge. The lower Reynolds number in the tunnel caused the flow to separate sooner from the round leading edge. That experiment, tunnel to flight, was very eloquent in pointing out the difference and it is very complicated. It is an issue.

Prof. A. Young, UK

We have heard a great deal this morning about the complexity of the problems that are being faced. Certainly the difficulties are immense. I wonder whether enough emphasis is being therefore put on fundamental well-organized programs of research. I was impressed in the particular session that I chaired by the well-devised coordinated programs described, admittedly on aspects of the problem which do not directly deal with dynamic effects in the way that we have been discussing this morning. However, it does seem to me that perhaps a little more thought should be given to what kind of fundamental programs of research should be developed in order to deal with the kind of problems that are arising. Complex as the problems are, we must not get so pessimistic that we will never be able to understand them at all. The more we can understand what is going on, the easier will the design problem be eventually.

Mr. D. Peckham

Thank you Professor Young. I think that we can allow one more question or comment.

D. R. Bradley, General Dynamics

Along the same lines as Alec mentioned here, I was surprised that no one had challenged Dr. Richey on his prediction, and I just would like to congratulate him on his forward-looking prediction that in five years we would be able to compute 3-dimensional unsteady flow fields. I hope you are right Keith.

Dr. K. Richey, USAF

Thank you Dr. Bradley. If we apply the necessary resources, we can do it.

Mr. D. Peckham

It is now time to bring this Symposium to a close. We on the Fluid Dynamics Panel hope that you have found it informative, stimulating and timely. My co-chairman, Jacky Leynaert, and I would like to thank all the speakers for their excellent presentations and for keeping to their allotted time and to you, the audience, for your active participation. Jacky Leynaert and I would also like to thank the members of the Program Committee for their efforts in putting the program together and for their chairmanship of the various sessions.

But the most hard working man this week has been our Technical Evaluator, Dr. Keith Richey. I invite you to join me in thanking him for his efforts. Turning to more general matters, I would like to express thanks on your behalf to the Spanish authorities for making our week so enjoyable, both at our technical meetings and the program for our wives and companions visiting Madrid and the cities nearby. In particular, I would like to record our thanks to General Michavila and General Battista for opening the meeting on Monday and the splendid reception on that evening. To Maria Cruse Gutierrez, the National Coordinator in Spain for all her work on arrangements and to our own Spanish Panel Members who have done so much to ensure that arrangements have run smoothly. Again, in particular, I would like to thank Mr. Simon for arranging the visit to CASA on Tuesday and the enjoyable lunch afterwards.

Now the smooth running of our meetings depends very much on our Panel Executive and we have a new executive, Dr. Winston Goodrich and his secretary Anne Marie Rivault who has been so busy in the lobby. It has been Winston's first meeting since he took over from Mike in July. Thank you Winston, well done on your first meeting.

These meetings would not be possible without our interpreters locked away in their booth at the back of the meeting room. I am sure they have had to cope with many problems during the week, and I would like to thank on your behalf Mrs. Main, Mrs. de Fushelle and Mr. de Liffiac for their interpretation efforts during the week. Also I would like to record your appreciation to Victoria Mascara who has operated the projection equipment for us during the week, and the staff of Niagara Travel Agency in the lobby who have looked after our hotel arrangements.

I would like to advertise our future program. Next year in the spring we have a meeting on Missile Aerodynamics in Germany. In the fall we have a meeting on Vortex Flow Aerodynamics in The Netherlands. For the Vortex Flow meeting, the copies of the "call for papers" are available outside in the entrance hall, and I hope that many of you will take copies and that many of you here will be able to attend our meetings next year. Finally, thank you all for coming to this meeting and have a safe journey home.

REPORT DOCUMENTATION PAGE			
1. Recipient's Reference	2. Originator's Reference AGARD-CP-465	3. Further Reference ISBN 92-835-0555-7	4. Security Classification of Document UNCLASSIFIED
5. Originator	Advisory Group for Aerospace Research and Development North Atlantic Treaty Organization 7 rue Ancelle, 92200 Neuilly sur Seine, France		
6. Title	AERODYNAMICS OF COMBAT AIRCRAFT CONTROLS AND OF GROUND EFFECTS		
7. Presented	and discussions held at the Symposium of the Fluid Dynamics Panel in Madrid, Spain, 2nd—5th October 1989.		
8. Author(s)/Editor(s)	Various		9. Date April 1990
10. Author's/Editor's Address	Various		11. Pages 352
12. Distribution Statement	This document is distributed in accordance with AGARD policies and regulations, which are outlined on the Outside Back Covers of all AGARD publications.		
13. Keywords/Descriptors	Fighter aircraft Control surfaces Aerodynamic characteristics/ Control equipment Design Ground effect		
14. Abstract	<p>The AGARD Fluid Dynamics Panel sponsored this Symposium to provide an updated review of the aerodynamic design of controls for combat aircraft. The scope included the aerodynamic design of controls for take-off and landing conditions, for manoeuvring at subsonic, transonic and supersonic speeds, for high angles of attack and yaw, and for departure prevention and post-stall manoeuvring. Also, part of the Symposium was concerned with novel control devices. Regarding ground effects, computational and experimental methods were reviewed, and included jet effects on flow-field forces and intake flows.</p> <p>In addition to the papers presented at the Symposium, the results of the one-hour Round Table Discussion recorded at the end of the Symposium are presented in this report. Here, basic insight and understanding of aerodynamic controls, provided by these papers and current research programmes, are reviewed and related to the design and effectiveness of controls for contemporary combat aircraft.</p>		

<p>AGARD Conference Proceedings No. 465 Advisory Group for Aerospace Research and Development, NATO AERODYNAMICS OF COMBAT AIRCRAFT CONTROLS AND OF GROUND EFFECTS Published April 1990 352 pages</p> <p>The AGARD Fluid Dynamics Panel sponsored this Symposium to provide an updated review of the aerodynamic design of controls for combat aircraft. The scope included the aerodynamic design of controls for take-off and landing conditions, for manoeuvring at subsonic, transonic and supersonic speeds, for high angles of attack and yaw, and for departure prevention and post-stall manoeuvring. Also, part of the Symposium was</p> <p>P.T.O.</p>	<p>AGARD-CP-465</p> <p>Fighter aircraft Control surfaces Aerodynamic characteristics Control equipment Design Ground effect</p>	<p>AGARD Conference Proceedings No. 465 Advisory Group for Aerospace Research and Development, NATO AERODYNAMICS OF COMBAT AIRCRAFT CONTROLS AND OF GROUND EFFECTS Published April 1990 352 pages</p> <p>The AGARD Fluid Dynamics Panel sponsored this Symposium to provide an updated review of the aerodynamic design of controls for combat aircraft. The scope included the aerodynamic design of controls for take-off and landing conditions, for manoeuvring at subsonic, transonic and supersonic speeds, for high angles of attack and yaw, and for departure prevention and post-stall manoeuvring. Also, part of the Symposium was</p> <p>P.T.O.</p>	<p>AGARD-CP-465</p> <p>Fighter aircraft Control surfaces Aerodynamic characteristics Control equipment Design Ground effect</p>
<p>AGARD Conference Proceedings No. 465 Advisory Group for Aerospace Research and Development, NATO AERODYNAMICS OF COMBAT AIRCRAFT CONTROLS AND OF GROUND EFFECTS Published April 1990 352 pages</p> <p>The AGARD Fluid Dynamics Panel sponsored this Symposium to provide an updated review of the aerodynamic design of controls for combat aircraft. The scope included the aerodynamic design of controls for take-off and landing conditions, for manoeuvring at subsonic, transonic and supersonic speeds, for high angles of attack and yaw, and for departure prevention and post-stall manoeuvring. Also, part of the Symposium was</p> <p>P.T.O.</p>	<p>AGARD-CP-465</p> <p>Fighter aircraft Control surfaces Aerodynamic characteristics Control equipment Design Ground effect</p>	<p>AGARD Conference Proceedings No. 465 Advisory Group for Aerospace Research and Development, NATO AERODYNAMICS OF COMBAT AIRCRAFT CONTROLS AND OF GROUND EFFECTS Published April 1990 352 pages</p> <p>The AGARD Fluid Dynamics Panel sponsored this Symposium to provide an updated review of the aerodynamic design of controls for combat aircraft. The scope included the aerodynamic design of controls for take-off and landing conditions, for manoeuvring at subsonic, transonic and supersonic speeds, for high angles of attack and yaw, and for departure prevention and post-stall manoeuvring. Also, part of the Symposium was</p> <p>P.T.O.</p>	<p>AGARD-CP-465</p> <p>Fighter aircraft Control surfaces Aerodynamic characteristics Control equipment Design Ground effect</p>

<p>concerned with novel control devices. Regarding ground effects, computational and experimental methods were reviewed, and included jet effects on flow-field forces and intake flows.</p> <p>In addition to the papers presented at the Symposium, the results of the one-hour Round Table Discussion recorded at the end of the Symposium are presented in this report. Here, basic insight and understanding of aerodynamic controls, provided by these papers and current research programmes, are reviewed and related to the design and effectiveness of controls for contemporary combat aircraft.</p> <p>ISBN 92-835-0555-7</p>	<p>concerned with novel control devices. Regarding ground effects, computational and experimental methods were reviewed, and included jet effects on flow-field forces and intake flows.</p> <p>In addition to the papers presented at the Symposium, the results of the one-hour Round Table Discussion recorded at the end of the Symposium are presented in this report. Here, basic insight and understanding of aerodynamic controls, provided by these papers and current research programmes, are reviewed and related to the design and effectiveness of controls for contemporary combat aircraft.</p> <p>ISBN 92-835-0555-7</p>
<p>concerned with novel control devices. Regarding ground effects, computational and experimental methods were reviewed and included jet effects on flow-field forces and intake flows.</p> <p>In addition to the papers presented at the Symposium, the results of the one-hour Round Table Discussion recorded at the end of the Symposium are presented in this report. Here, basic insight and understanding of aerodynamic controls, provided by these papers and current research programmes, are reviewed and related to the design and effectiveness of controls for contemporary combat aircraft.</p> <p>ISBN 92-835-0555-7</p>	<p>concerned with novel control devices. Regarding ground effects, computational and experimental methods were reviewed, and included jet effects on flow-field forces and intake flows.</p> <p>In addition to the papers presented at the Symposium, the results of the one-hour Round Table Discussion recorded at the end of the Symposium are presented in this report. Here, basic insight and understanding of aerodynamic controls, provided by these papers and current research programmes, are reviewed and related to the design and effectiveness of controls for contemporary combat aircraft.</p> <p>ISBN 92-835-0555-7</p>

Telephone (1)47.38.57.00 · Telex 610 176

DISTRIBUTION OF UNCLASSIFIED AGARD PUBLICATIONS

AGARD does NOT hold stocks of AGARD publications at the above address for general distribution. Initial distribution of AGARD publications is made in AGARD Member Nations through the following National Distribution Centres. Further copies are sometimes available from these Centres, but it may not be purchased in Microfilm or Photocopy form from the Sales Agencies listed below.

NATIONAL DISTRIBUTION CENTRES

BELEGUM

Coordonnateur AGRARD - VSI
Etat-Major de la Force Aérienne
Quartier Reine Elizabeth
Rue d'Ivère, 1140 Bruxelles

CANADA

Director Scientific Information Services
Dept of National Defence
Ottawa, Ontario K1A 0K2

D1-N°

National Aeronautics and
Space Administration

FILE A

Washington, D.C.
20546

**SPECIAL FOURTH CLASS MAIL
BOOK**

LUXEMBOURG

See Belgium

NETHERLANDS

Netherlands Delegation to AGARD
 National Aerospace Laboratory, NLR
 Kluyverweg 1
 3029 HS Delft

NORWAY

Norwegian Defence Research Establishment

Postage and Fees Paid
National Aeronautics and
Space Administration
NASA-451



tion to ACIARD
1995.

4:4-12

1. The above information is to be used for the purpose of the above-mentioned project only and is not to be used for any other purpose.

1121.

[illegible]

14-1

Revisi:lvik

67 Brown Street
Glasgow G2 8LX

MAY

Aeronautica Militare
Ufficio del Delegato Nazionale all'ACIARD
3 Piazzale Adenauer
00144 Roma EUR

UNITED STATES

National Aeronautics and Space Administration (NASA)
Langley Research Center
M/S 180
Hampton, Virginia 23665

THE UNITED STATES NATIONAL DISTRIBUTION CENTRE (NASA) DOES NOT HOLD STOCKS OF AGARD PUBLICATIONS, AND APPLICATIONS FOR COPIES SHOULD BE MADE DIRECT TO THE NATIONAL TECHNICAL INFORMATION SERVICE (NTIS) AT THE ADDRESS BELOW.

SALES AGENCIES

National Technical
Information Service (NTIS)
5285 Port Royal Road
Springfield
Virginia 22161, USA

ESA/Information Retrieval Service
European Space Agency
10, rue Maitre Nikis
75013 Paris, France

The British Library
Document Supply Centre
Boston Spa, Wetherby
West Yorkshire LS23 7BQ
England

Requests for microfiche or photocopies of AGARD documents should include the AGARD serial number, title, author or editor, and publication date. Requests to NTRS should include the NASA accession report number. Full bibliographical references and abstracts of AGARD publications are given in the following journals.

Scientific and Technical Aerospace Reports (STAR)
published by NASA Scientific and Technical
Information Branch
NASA Headquarters (NIT-40)
Washington D.C. 20546, USA

Government Reports Announcements (GIRA)
published by the National Technical
Information Service, Springfield
Virginia 22161, USA



Printed by Specialised Printing Services Limited
40 Chigwell Lane, Loughton, Essex IG10 3TZ

ISBN 92-835-0555-7